COMBINED THEORETICAL AND EXPERIMENTAL INVESTIGATIONS OF POROUS CRYSTALLINE MATERIALS

Daniel M. Dawson

A Thesis Submitted for the Degree of PhD
at the
University of St Andrews

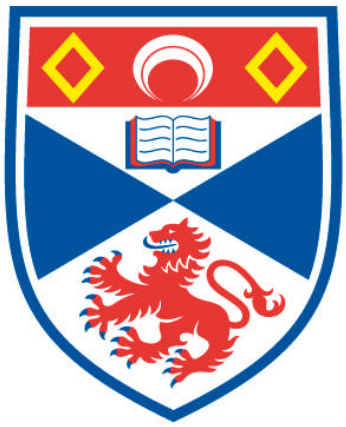

2014

Combined Theoretical and Experimental Investigations of Porous Crystalline Materials

Daniel McLean Dawson

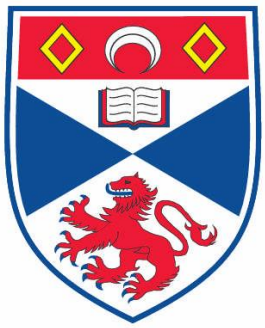

This thesis is submitted in partial fulfilment for
the degree of PhD at the University of St Andrews

January 2014

DECLARATION

I, Daniel McLean Dawson, hereby certify that this thesis, which is approximately 79,000 words in length, has been written by me, that it is the record of work carried out by me and that it has not been submitted in any previous application for a higher degree.

I was admitted as a research student in October 2009 and as a candidate for the degree of PhD in October 2010; the higher study for which this is a record was carried out in the University of St Andrews between 2009 and 2013.

Date Signature of candidate

I hereby certify that the candidate has fulfilled the conditions of the Resolution and Regulations appropriate for the degree of PhD in the University of St Andrews and that the candidate is qualified to submit this thesis in application for that degree.

Date Signature of supervisor

In submitting this thesis to the University of St Andrews I understand that I am giving permission for it to be made available for use in accordance with the regulations of the University Library for the time being in force, subject to any copyright vested in the work not being affected thereby. I also understand that the title and the abstract will be published, and that a copy of the work may be made and supplied to any bona fide library or research worker, that my thesis will be electronically accessible for personal or research use unless exempt by award of an embargo as requested below, and that the library has the right to migrate my thesis into new electronic forms as required to ensure continued access to the thesis. I have obtained any third-party copyright permissions that may be required in order to allow such access and migration, or have requested the appropriate embargo below.

The following is an agreed request by candidate and supervisor regarding the electronic publication of this thesis:

Access to printed copy and electronic publication of thesis through the University of St Andrews.

Date Signature of candidate

Signature of supervisor

ACKNOWLEDGEMENTS

I wish to thank my supervisor, Sharon Ashbrook, for her guidance in times of crisis and, on several occasions, for her guidance that would have allowed me to avoid said crises, had I listened to her the first time round. I would also like to thank Russell Morris, who has been an excellent source of advice, samples and encouragement to finish my thesis. I also wish to thank Iain Smellie for assisting me with all things organic, and introducing the disturbingly successful idea of the Dulux paint scale of MOF quality. Many other people have also helped this work by providing samples and experimental data – I will acknowledge their contributions more specifically in the relevant chapters.

It is traditional to thank the rest of one's group for keeping one sane during the writing-up process but, despite their best efforts, there was no saving me. Still, I would like to thank Team Solid-State NMR (featuring Team Isotopic Enrichment) for keeping me insane throughout the course of my PhD, especially during the writing-up. I would especially like to thank Valerie and Sharon, both of whom patiently proof-read the whole thesis.

Having been bribed with pizza, threatened with a cactus, and promised that it will make me a better person, I must also thank Charlotte, Rhiann and Naomi, whose combination of persistence, persuasion and stalking skills have amazed me on more than one occasion.

Honourable mention must also go to those project students who supplied cake at group meetings in the hope that it would improve their marks. If you are a project student, heed this advice: that tactic only works if you don't announce “I'm going home to bake cakes and play video games” at half past two the day before a group meeting. Of course, it could be argued that the world might be a better place if there were fewer students today and more cakes tomorrow.

And finally, I'd like to thank everyone else who has, over the past four years, if not actually made me stronger, at least not killed me.

To my friends and family, especially those no longer here.

ABSTRACT

This thesis combines solid-state nuclear magnetic resonance (NMR) spectroscopy, X-ray diffraction (XRD), chemical synthesis, isotopic enrichment and density-functional theory (DFT) calculations to provide insight into a number of microporous materials. The first class of materials studied is metal-organic frameworks (MOFs), where the presence of paramagnetic ions has a range of effects on the ^{13}C NMR spectra, depending on the nature of the ligand-metal interactions. For the Cu^{2+}-based MOFs, HKUST-1 and STAM-1, the assignment of the NMR spectra is non-intuitive, and unambiguous assignment requires specific ^{13}C labelling of the organic linker species. It is shown that ^{13}C NMR spectra of these two MOFs could act as a sensitive probe of the nature of "guest" molecules bound to the Cu^{2+}. The second class of materials is aluminophosphates (AlPOs). It is shown that, using a series of relatively simple linear relationships with the crystal structure, the NMR parameters calculated by DFT (with calculation times of several hours) can be predicted, often with experimentally-useful accuracy, in a matter of seconds using the DIStortion analysis COde (DISCO), which is introduced here. The ambient hydration of the AlPO, JDF-2, to AlPO-53(A) is shown to occur slowly, with incomplete hydration after ~3 months. The resulting AlPO-53(A) is disordered and some possible models for this disorder are investigated by DFT. The final class of materials is gallophosphates (GaPOs), particularly GaPO-34 and related materials. The two as-prepared forms of GaPO-34 are characterised by solid-state NMR, and their calcination investigated by TGA and *in-situ* powder XRD. An unusual dehydrofluorinated intermediate phase is isolated and characterised for the first time by solid-state NMR. The fully calcined material is shown to be stable under anhydrous conditions, but hydrates rapidly in air. The hydrated material is stable under ambient conditions, but collapses upon heating. Partial dehydration without collapse is achieved by gentle heating or room-temperature evacuation. The impurity phases, $GaPO_4$ berlinite and GaPO-X are investigated by solid-state NMR and, while the structure of GaPO-X remains unknown, much structural information is obtained.

PUBLICATIONS

Journal Articles

K. E. Johnston, J. M. Griffin, R. I. Walton, D. M. Dawson, P. Lightfoot and S. E. Ashbrook, *Phys. Chem. Chem. Phys*., **2011**, *13*, 7565.

A. L. Picone, S. J. Warrender, A. M. Z. Slawin, D. M. Dawson, S. E. Ashbrook, P. A. Wright, S. P. Thompson, L. Gaberova, P. L. Llewellyn, B. Moulin, A. Vimont, M. Daturi, M. B. Park, S. K. Sung, I.-S. Nam and S. B. Hong, *Micropor. Mesopor. Mater.*, **2011**, *146*, 36.

J. M. Griffin, L. Clark, V. R. Seymour, D. W. Aldous, D. M. Dawson, D. Iuga, R. E. Morris, and S. E. Ashbrook, *Chem. Sci.*, **2012**, *3*, 2293.

M. Amri, S. E. Ashbrook, D. M. Dawson, J. M. Griffin, R. I. Walton, and S. Wimperis, *J. Phys. Chem. C*, **2012**, *116*, 15048.

D. M. Dawson, L. E. Jamieson, M. I. H. Mohideen, A. C. McKinlay, I. A. Smellie, R. Cadou, N. S. Keddie, R. E. Morris and S. E. Ashbrook, *Phys. Chem. Chem. Phys.*, **2013**, *15*, 919.

S. E. Ashbrook and D. M. Dawson, *Acc. Chem. Res.*, **2013**, *46*, 1964.

S. Sneddon, C. J. Pickard, D. M. Dawson and S. E. Ashbrook, *Phys. Chem. Chem. Phys.*, **2014**, *16*, 2660.

S. E. Ashbrook, D. M. Dawson and V. R. Seymour, *Phys. Chem. Chem. Phys.*, **2014**, *16*, 8223.

A. C. McKinlay, P. K. Allan, C. L. Renouf, M. J. Duncan, S. J. Warrender, D. M. Dawson, S. E. Ashbrook, B. Gil, B. Marszalek, T. Düren, J. Williams, C. Charrier, D. Mercer, S. J. Teat and R. E. Morris, "Multirate delivery of multiple therapeutic agents from metal-organic frameworks", *in preparation*

Textbook Chapter

S. E. Ashbrook, D. M. Dawson and J. M. Griffin, "Solid-State Nuclear Magnetic Resonance Spectroscopy" in Local Structural Characterisation, ed. D. W. Bruce, D. O'Hare and R. I. Walton, Wiley, **2013**.

TABLE OF CONTENTS

THESIS OVERVIEW

With applications in almost all areas of modern life, functional microporous materials represent one of the most important recent developments in materials chemistry and much effort has gone into their synthesis, characterisation and development. Owing to the often very similar structures of these materials, their characterisation must involve several techniques, most often crystallographic diffraction and solid-state NMR spectroscopy. It is also increasingly common to support these experimental methods with theoretical approaches, which are often capable of providing valuable insight into structural features that may be overlooked by diffraction or ignored as "too challenging to assign in full" in NMR spectra.

This thesis is concerned with just a small number of the many chemically-distinct classes of microporous materials: metal-organic frameworks (MOFs), aluminophosphates (AlPOs) and gallophosphates (GaPOs). While compositionally different, the materials studied in this thesis all have the common property of microporosity. The presence of molecule-sized channels and pores within these materials suggests that their applications should involve manipulation of molecules – from storage and release of gas (*e.g.*, H_2, CO_2 and CH_4) or drug-type molecules (*e.g.*, NO, ibuprofen, metronidazole and caffeine) to changing molecules chemically (*e.g.*, by catalysis of a specific reaction) or magnetically (*e.g.*, altering their relaxation properties for magnetic resonance imaging (MRI) contrast enhancement). While it is tempting to dwell exclusively on the use of the free space within these materials, one must not neglect the portion of the material giving shape to these pores and channels, that is to say, the material itself. Depending on its composition, the material, may have uses as diverse as construction materials (as a consequence of negative thermal expansion), data storage (as a consequence of magnetic ordering of metal ions) and as a protecting group strategy in organic synthesis.

Given the impressive diversity of properties, applications and compositions available in just the three classes of materials mentioned above, it is unsurprising that the pace of analytical approaches for characterising these materials and understanding their behaviour is lagging somewhat behind the pace of synthesis of new materials. It is very common in the field of materials science to characterise a

material by crystallographic diffraction, and assume that this is "the" answer. However, most common diffraction techniques provide a long-range average structure, while many of the most important or unusual properties of microporous materials (catalysis, negative thermal expansion, *etc*.) involve local features (*e.g.*, interactions with dopant atoms) and dynamic processes (*i.e.*, motion on time and order scales to which diffraction is inherently insensitive). Solid-state nuclear magnetic resonance (NMR) spectroscopy should, in principle, be ideally suited to complement the data obtained by diffraction, providing information on any structural features occurring on the time and order scales to which diffraction is insensitive. While solid-state NMR has for decades been employed to characterise microporous materials, several challenges still remain in acquiring informative NMR spectra and relating them to the average diffraction-based structure of the material, and the true structure of the material. Some of these challenges are specific to a given material, for example, the NMR spectra of some MOFs containing paramagnetic metal ions are very challenging to acquire, at least with conventional NMR approaches, and guest molecules within the pores of certain AlPOs and GaPOs may be particularly mobile, affecting ^{27}Al and $^{69/71}$Ga NMR spectra significantly, but barely being observed by diffraction, whereas some of the challenges are more general to solid-state NMR. As an example, it is possible to have three chemically-identical carboxylic acid groups (as in benzene-1,3,5-tricarboxylic acid, or btc), yielding a single resonance in the solution-state NMR spectrum and yet, owing to crystal packing effects, yielding many distinct resonances in the solid-state. Work presented in this thesis aims to tackle a combination of material-specific and more general challenges in the field of solid-state NMR of microporous materials.

The first results chapter investigates the NMR spectra of paramagnetic MOFs. While NMR spectra of paramagnetic systems are typically challenging to acquire and assign, complete ^{13}C MAS NMR spectra for the two Cu^{2+}-based MOFs STAM-1 and HKUST-1 have been acquired and assigned in full. Part of the assignment relied on selectively ^{13}C-labelled linkers, and their syntheses are discussed. Based on the acquisition and assignment techniques developed, a number of medically-relevant multi-guest samples of HKUST-1 and STAM-1 are investigated, showing the sensitivity of solid-state NMR, even in the face of

paramagnetic samples and natural-abundance ^{13}C (1.1%). As a more challenging example of solid-state ^{13}C NMR spectra of paramagnetic MOFs, the CPO-27-M (M = Mg, Mn, Fe, Co, Ni, Zn) series has been studied, with spectra acquired but not assigned for all members of the series. A third series of MOFs, $Ln(btc)(dmu)_2$ (Ln = La or Nd, dmu = 1,3-dimethylurea) was also studied and, owing to the limited covalency of the lanthanide ions, the challenges faced in acquiring and assigning the NMR spectra were very different to the CPO-27-M series, demonstrating that the NMR spectra of paramagnetic materials are very sensitive to the chemical nature of the paramagnetic species, not just the number of unpaired electrons present.

The second results chapter deals with AlPOs. In order to aid the assignment of ^{17}O, ^{27}Al and ^{31}P NMR spectra of AlPOs, the relationships between the crystal structure and the NMR parameters of these nuclei are investigated. While some empirically-based relationships have been used in the literature to assign and interpret NMR spectra, the study here eliminates any errors of assumption of a correspondence between the (average) experimental crystallographic structure and the experimental NMR parameters by using density-functional theory (DFT) to calculate the NMR parameters for a series of exactly known (even if not physically realistic) structures. The DIStortion analysis COde (DISCO) has been developed to calculate various local structural distortion parameters and their relationships with the calculated NMR parameters were investigated. The version of DISCO included with this thesis is capable of predicting some NMR parameters, such as isotropic chemical shielding, with reasonable accuracy, while other parameters (particularly anisotropic shielding parameters) are still predicted too poorly to be of practical use. The chapter also explores the hydration of the AlPO, JDF-2, which converts to AlPO-53(A) by adsorption of water under ambient conditions. The local structure of AlPO-53(A) is then investigated using a combination of multinuclear solid-state NMR and DFT calculations to shed light on the presence of structural defects occurring upon hydration.

The final results chapter investigates the gallophosphate, GaPO-34. The structures of the as-prepared and calcined phases are studied by a combination of solid-state NMR and DFT calculations. A previously uncharacterised phase is also

observed as an intermediate between the as-prepared and calcined phases when the structure-directing agent used is 1-methylimidazolium fluoride. While no definite structure of this phase has yet been provided, many structural features are probed by solid-state NMR, and it is clear that the material exhibits a low-temperature dehydrofluorination prior to full calcination. The hydration of calcined GaPO-34 is also investigated, and it is shown that both calcined and hydrated materials are indefinitely stable, while heating the hydrated material appears to cause framework collapse. Various strategies to avoid this collapse are evaluated, and it would appear that vacuum treatment, rather than heating, can be used to regenerate the dried material without framework collapse. The synthesis of GaPO-34 is challenging, with two impurity phases commonly forming. The first, the dense phase, berlinite, is well known, while the second (here termed GaPO-X) appears to have a porous structure, and has not been fully characterised. The investigation of this material by multinuclear NMR experiments is carried out but, while many structural features can be identified, no overall structure has yet been determined.

INTRODUCTION TO MICROPOROUS MATERIALS

Microporous materials are one of the most important recent developments in materials chemistry. The presence of molecule-sized channels and pores within these materials immediately suggests their applications should involve manipulation of molecules – from simply storing and releasing "guest" molecules to changing molecules chemically (*e.g.*, by catalysis of a specific reaction) or magnetically (*e.g.*, altering their relaxation properties for magnetic resonance imaging (MRI) contrast enhancement). Furthermore, depending on the composition of the materials, they may have uses as diverse as construction materials, data storage, chemical sensing and as a protecting-group strategy in organic synthesis. With applications in practically all areas of modern life, it is little wonder that much effort has gone into the synthesis, characterisation and development of these materials.

The characterisation of microporous materials typically requires several techniques, of which crystallographic diffraction and solid-state nuclear magnetic resonance (NMR) spectroscopy are among the most common (but by no means the only). Solid-state NMR spectroscopy is ideally suited to the study of many microporous materials, as almost all elements have at least one NMR-active isotope, and microporous materials contain a large number of readily NMR-accessible (*i.e.*, suitable for routine study) nuclei, as summarised in Table 1.1. A combination of Bragg diffraction and solid-state NMR spectroscopy is particularly useful, owing to the fact that Bragg diffraction techniques yield the long-range "average" periodic structure, whereas solid-state NMR provides a very detailed, element-specific, picture of the local structure, symmetry and motion present, but at the cost of information on periodicity. A combination of these two complementary techniques can lead to a much deeper understanding of the structure of the material than either technique alone could provide. In support of these experimental methods, theoretical quantum chemical calculations are often capable of providing valuable insight into structural features that are difficult to interpret or understand by experiment alone. This thesis is concerned with the characterisation of some microporous materials by a combination of solid-state NMR spectroscopy, X-ray diffraction and theoretical calculations. These techniques are discussed in Chapters 2 and 3, while the present

Table 1.1. Summary of the nuclear magnetic properties – the spin quantum number, I, natural abundance, N, Larmor frequency (at 14.1 T), ν_0, relative receptivity, and (for I > 1/2) nuclear electric quadrupole moment, Q – of some nuclei commonly found in microporous materials.

Nucleus	I	N (%)	ν_0 at 14.1 T / MHz	Relative Receptivity[a]	Q / fm^2
^{1}H	1/2	99.99	600.13	1.00	
^{2}H	1	0.01	92.12	1.11×10^{-6}	0.268
^{13}C	1/2	1.07	150.90	1.70×10^{-4}	
^{14}N	1	99.64	43.37	1.00×10^{-3}	2.044
^{15}N	1/2	0.36	60.83	3.79×10^{-6}	
^{17}O	5/2	0.04	81.36	1.10×10^{-5}	–2.558
^{19}F	1/2	100.00	564.69	8.33×10^{-1}	
^{23}Na	3/2	100.00	158.75	9.26×10^{-2}	10.4
^{25}Mg	5/2	10.00	36.74	2.68×10^{-4}	19.94
^{27}Al	5/2	100.00	156.38	2.06×10^{-1}	14.66
^{29}Si	1/2	4.69	119.23	3.67×10^{-4}	
^{31}P	1/2	100.00	242.94	6.63×10^{-2}	
^{45}Sc	7/2	100.00	145.78	3.01×10^{-1}	–22.0
^{67}Zn	5/2	4.10	37.55	1.18×10^{-4}	15.0
^{69}Ga	3/2	60.11	144.04	4.16×10^{-2}	17.1
^{71}Ga	3/2	39.89	183.02	5.66×10^{-2}	10.7
^{87}Rb	3/2	27.83	196.37	4.88×10^{-2}	13.35

a. Receptivity is defined as $\gamma^3 N(I(I + 1))$, where γ is the gyromagnetic ratio of the nucleus. The relative receptivity is defined relative to ^{1}H.

chapter briefly introduces some of the main classes of microporous materials, and the terminology involved in describing their structures, properties and syntheses. More detailed descriptions of specific materials of interest are provided in later chapters.

Microporous materials are defined by the International Union of Pure and Applied Chemistry (IUPAC) as having pores of dimensions between 5 and 20 Å.[1] Non-porous materials have "pores" smaller than this and materials with larger pores

are classed as mesoporous (20 – 500 Å) or macroporous (> 500 Å). However, the recent increase in popularity of nanotechnology has led to a proliferation of the term "nanoporous". In the parlance of nanotechnology, anything having dimensions between 1 and 1000 nm may be regarded as "nano", and the term nanoporous covers materials ranging from the microporous to macroporous regimes. The term is, therefore, unhelpful, as it fails to describe the adsorption properties of a material (and also leads to the unusual situation where a pore may be "nano", while being too large to be "micro"). However, as the term "microporous" is often applied colloquially to materials that do not display microporosity (often being mesoporous instead), caution must also be exercised when interpreting this term, and no immediate conclusions must be made regarding the structure or behaviour of a material, based simply on how it is described. The remainder of this thesis uses the IUPAC terms as far as possible, but the reader is referred to primary literature for further details on the structures and properties of the materials discussed.

Microporous materials can be prepared with a vast range of chemical compositions, from entirely organic species (*e.g.*, van der Waals crystals[2]), *via* a mixture of organic and inorganic components (*e.g.*, metal-organic frameworks, or MOFs[3]) to wholly-inorganic materials (*e.g.*, zeolites[4]). Given this vast chemical diversity, it is impossible to provide even a brief overview of the whole field and, instead, this thesis will discuss only two such classes of microporous material; MOFs and inorganic phosphate zeotypes (*i.e.*, materials related to aluminosilicate zeolites). Even within these materials, there is a huge scope for chemical and/or structural variation, and it is these general features of the different classes of microporous materials that will be considered for the remainder of this chapter.

1.1 METAL-ORGANIC FRAMEWORKS

Metal-organic frameworks (MOFs) are composed of inorganic metal-based units connected by polytopic (*i.e.*, multiply connecting, as opposed to merely multidentate (*i.e.*, multiply binding)) organic "linkers". For example, the well-known chelating agent, ethylenediaminetetraacetic acid (EDTA), is hexadentate, but typically binds

six times to *the same cation*, whereas a polytopic ligand forms multiple bonds to *multiple cations*). The structural diversity of MOFs is vast, owing to the sheer number of combinations of possible linkers and metals, although the number of physically-possible structures is limited by the same underlying principles as all chemistry, *e.g.*, the overall charge of the material must be neutral and some electron configurations will favour certain coordination geometries of the metals. This means that the same framework may be formed with many different metals, as long as they are all capable of adopting the same coordination geometry. Some examples of such isomorphous frameworks are given in Table 1.2. The linker is typically a rigid (*i.e.*, based on benzene rings) polycarboxylate, as these species provide the least conformational flexibility, allowing a regular crystalline framework to form.[5] While this imposes some restrictions on the choice of linker species, many MOFs have been synthesised using linkers that do not obey this guideline.[6-10]

From Table 1.2, it can be seen that nomenclature in the field of MOFs is far from simple. The first issue is the name of the MOF itself, and there is no clear or unified consensus here. While the group of Yaghi *et al.* favour the nomenclature MOF-*n* for all MOFs, other research groups prefer to name their MOFs after the institution where they were discovered (*e.g.*, CPO = **C**oordination **P**olymer of **O**slo, MIL = **M**aterials **I**nstitute **L**avoisier and STAM = **St A**ndrews **M**OF), with the institution code generally suffixed by a number to distinguish between different materials (*e.g.*, CPO-27 and STAM-1). The case is further complicated by research groups working on the synthesis of other materials and who do not distinguish between different chemical compositions (*e.g.*, STA-13 (where STA = ST Andrews microporous material) is a MOF,[7] whereas STA-2 is an aluminophosphate zeotype[11]). It is, therefore, unsurprising that there can be confusion over the names of many of the more popular MOFs with, for example, CPO-27[12-14] also reported as MOF-74[5] and simply as M_2dhtp[15] (where dhtp = 2,4-dihydroxyterephthalate) in the literature. Throughout this thesis, a combination of all three styles of nomenclature will be used, depending on the nomenclature style adopted in the relevant literature. An area of greater (but by no means universal) agreement is the abbreviated names of the linker species. These are generally based on IUPAC nomenclature, *e.g.*, **b**enzene-1,4-**di**carboxylate is abbreviated to bdc and **b**enzene-1,3,5-**tri**carboxylate is

Table 1.2. Selected structurally-related MOFs known in the literature. The full names and chemical structures of linkers are provided in Appendix B. MOF names are discussed in the main text.

MOF	Linker(s)	Metal(s)	References
CPO-27	$dhtp^{4-}$	Mg^{2+}, Mn^{2+}, Fe^{2+}, Co^{2+}, Ni^{2+}, Zn^{2+}	5, 12-16
MIL-100	btc^{3-}	Sc^{3+}, V^{3+}, Cr^{3+}, Mn^{3+}, Fe^{3+}, Al^{3+}	17-22
MIL-53	bdc^{2-}, functionalised bdc^{2-}	Sc^{3+}, V^{3+}, Cr^{3+}, Fe^{3+}, Al^{3+}, Ga^{3+}, In^{3+}	23-30
MOF-5 and IRMOF-*n*	bdc^{2-}, bdc^{2-} analogues, functionalised bdc^{2-}	Zn^{2+}	31-33

abbreviated to btc. However, some abbreviations are based on the trivial name of the material, for example, 2,5-dioxobenzene-1,4-dicarboxylate is known as dhtp (from the neutral species, 2,5-**d**i**h**ydroxy **t**ere**p**hthalic acid, or 2,5-dihydroxy-benzene-1,4-dicarboxylic acid in IUPAC nomenclature). To add to the confusion, dhtp can also be referred to as dobc, emphasising the fact that the hydroxy groups have also been deprotonated – a fact that becomes important in cases such as CPO-26 (where only the acid groups of the linker are deprotonated) and CPO-27 (in which both the acid and hydroxy groups are deprotonated).[14] However, it is generally more convenient to define the abbreviation such that it represents the most deprotonated state of the linker likely to be encountered, and then indicate the protonation state by using the abbreviation itself as a surrogate chemical entity. Therefore, dhtp represents the tetraanion, $dhtp^{4-}$, H_2dhtp represents the dianion (note that the charge is rarely made explicit, unless required), and H_4dhtp represents the neutral species, as summarised in Appendix B for some common linkers.

MOFs are typically synthesised under hydro- or solvothermal conditions, in which the desired linker and metal salt are dissolved in the reaction solvent, either water (hydrothermal), or a polar organic species such as *N*,*N*-dimethylformamide (DMF) or methanol (solvothermal). For many MOFs, it is common to use a mixed

solvent system to obtain the optimum yield or quality of the MOF although, as Bauer *et al.*[34] demonstrated in a high-throughput study of the Fe^{3+}/aminoterephthalic acid system, the outcome of the reaction can be sensitive to factors such as scale and reaction temperature as well as the solvent used. The reaction mixture is then heated, typically under autogenous pressure in a sealed autoclave, with reaction temperatures and times varying for different MOFs, but typically on the order of 80 to 200 °C and 0.5 to 14 days. In recent years, more economic and "green" routes to the room-temperature synthesis of some MOFs, such as CPO-27[33] have been developed. Additionally, the reaction time may be drastically reduced (to under a minute) by the use of microwave irradiation of the reaction mixture, as demonstrated by Marquez *et al.*, who achieved reaction times of a few minutes for MIL-100,[35] and Ni and Masel, who achieved reaction times of 35 s for IRMOF-1, IRMOF-2 and IRMOF-3.[36]

The structures of MOFs can be considered as three-dimensional nets with the metal-based secondary building units (SBUs) at vertices of the net interconnected by the organic portion of the linker, as shown schematically in Figure 1.1(a). The nature of the SBU depends on the MOF, but can be mononuclear (*e.g.*, MOF-77[37]), binuclear (*e.g.*, HKUST-1[38]), trinuclear (*e.g.*, MIL-100[20]), tetranuclear (*e.g.*, MOF-5[31]) or may contain even larger clusters[39] or infinite chains[12] of metal ions. These example SBUs are shown in Figure 1.1(b). Despite the diversity of SBUs so far prepared, the range of linkers used in the most common MOFs is relatively small, as, depending on the nature of the SBU, one linker species may form several different types of framework. For example, bdc can connect MO_6 octahedra (MIL-53), M_3O trigonal clusters (MIL-101),[40] and Zn_4O tetrahedra (MOF-5). Trimesate (btc) is another commonly-used linker, which can connect mono-, bi- and trinuclear SBUs, in Zn-BTC,[41, 42] HKUST-1 and MIL-100, respectively. However, this is not to suggest that the choice of available linkers is limited, and many MOFs have used less conventional (*i.e.*, non-rigid[6, 7, 9] or non-carboxylate-based[7, 8, 10]) linkers and combinations of two or more linkers, as in the so-called "jungle gym" MOFs, which contain two-dimensional layers of bdc-connected di-zinc tetracarboxylate SBUs, with connections between the layers formed by the diamine, DABCO (1,4-diazabicyclo[2.2.2]octane).[43]

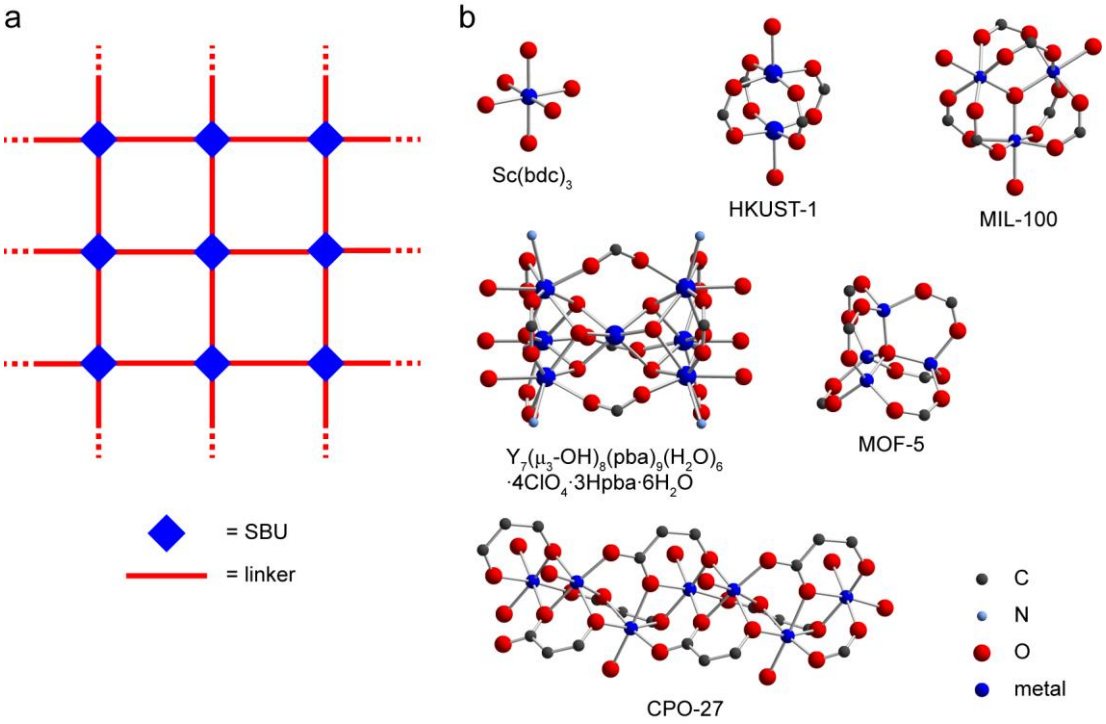

Figure 1.1. (a) Schematic representation of a MOF, composed of inorganic-based SBUs (blue) interconnected in an infinite network by organic-based linkers (red). (b) Examples of SBUs found in $Sc(bdc)_3$,[37] HKUST-1,[38] MIL-100,[20] MOF-5,[31] $[Y_7(\mu_3\text{-}OH)_8(pba)_9(H_2O)_6\cdot 4ClO_4\cdot 3Hpba\cdot 6H_2O]$ (pba = 4-pyridin-4-ylbenzoate)[39] and CPO-27.[12] In all cases, H atoms are omitted for clarity.

The highly modular nature of MOFs (*i.e.*, the SBUs and linkers can essentially be considered as separate entities) allows for the concept of isoreticularity, where isoreticular frameworks have a different chemical composition, but the same underlying connectivity as the parent framework. Isoreticularity has been demonstrated several times, most dramatically by the IRMOF-n (IRMOF = **i**so**r**eticular **MOF**) series, in which the tetranuclear Zn clusters of MOF-5 (or IRMOF-1) remain connected in the same cubic framework structure while the free volume of the MOF (*i.e.*, the size of the pores) can be varied from 7.8 Å (IRMOF-0, acetylene dicarboxylate linker) to 28.8 Å (IRMOF-16, terphenyldicarboxylate linker). This series demonstrates that, to a first approximation, providing two linkers possess the same geometry of coordinating functional groups, the same framework is likely to form with both (unless the pore volume exceeds that of the SBU and associated linkers, in which case it is possible that multiple, interpenetrating

frameworks will form instead[44]). As demonstrated by IRMOFs 1 to 7, isoreticularity also allows the same framework to be prepared with different pore chemistry, *e.g.*, using aromatic, aliphatic, basic (NH_2) or brominated linkers.[32] This ability to tune the reactivity of the MOF towards any adsorbed guest species, in a straightforward and predictable manner (in most cases), makes MOFs very appealing for many applications. The strategies for introducing additional chemical functionality depend largely on the chosen framework and the desired functionality. In some cases, the MOF can simply be synthesised using the modified linker but, as demonstrated by IRMOF-6, in order to modify the pores with a hydrophobic ethylene functionality, a sacrifice in free pore diameter (which dictates the maximum size of guest species admissible to the pores) of 3.7 Å must be made.[32] Therefore, it may sometimes be preferable to use a mixture of the modified and unmodified linker species.

In many cases, synthesising the MOF with the desired functionalised linker is not possible, either because the desired functional group reacts with another component of the reaction mixture – for example, reaction with the solvent[45] or coordinates to the SBU[43] – or because its steric bulk is such that formation of the framework is hindered. In such cases, post-synthetic modification of the framework may be possible, and this is generally achieved by installing a precursor functional group during the synthesis and then carrying out the required chemical transformation once the framework has been assembled.[46] At the most basic level, this can be as simple as removing one type of solvent molecule from the pores of the MOF and replacing it with another. Chui *et al*. provided the first demonstration of such modification by exchanging pyridine for H_2O within the pores of HKUST-1.[38] In recent years, more elaborate modifications have been demonstrated, including the immobilisation of NO as 4-methylaminopyridine-*N*-diazeniumdiolate in HKUST-1,[47] attachment of ferrocene to the pores of MOFs *via* amide linkages,[48] attaching catalytically-active vanadyl groups *via* catecholate tethers to the metal centres of MIL-101[49] and the growth of bimetallic metal nanoparticles within the pores of MOF-5 by chemical vapour deposition techniques.[50] In rare cases, it is also possible to functionalise the linker species *in situ*, which provides a further avenue to the preparation of new frameworks with interesting properties. For example, the *in-situ* methylation of btc in the synthesis of STAM-1[51] leads to a MOF that contains both

methyl-lined (hydrophobic) and water-lined (hydrophilic) pores, and which has interesting dual- and pressure-gated adsorption properties. Such behaviour may be of use in applications including the separation and purification of gases.

The above discussion gives the impression that the reactivity of the MOF arises predominantly from the linker and any reactive species introduced post synthesis. However, many of the most important MOFs contain solvent molecules such as H_2O, DMF or pyridine bound to the metal centre as part of the SBU. These small molecules can generally be removed by heating under vacuum to generate "coordinatively unsaturated" sites (CUSs) on the metal centre. These CUSs are generally highly reactive and will bind any suitable ligands (making anhydrous conditions essential for the handling of such evacuated or "activated" MOFs). The metal centres, therefore, represent an additional target for modification, as demonstrated above by the use of many different metal species for the preparation of the CPO-27 framework. When Mg^{2+} or Zn^{2+} is used, the MOF has favourable adsorption properties for CO_2,[52] the Mn^{2+} form is suitable for adsorbing fuel gases (*e.g.*, CH_4 and H_2),[15] the Fe^{2+} form has been shown to be catalytically active for the oxidation of phenols[16] and the Co^{2+} and Ni^{2+} forms have excellent NO adsorption behaviour[53] and have also recently been shown to have even more advanced medical applications. McKinlay *et al*. recently demonstrated the release of three antibacterial agents (metronidazole, NO and copper ions) from multiply-loaded HKUST-1 over a range of timescales from minutes to days; a function that is effective in combatting notoriously drug-resistant "biofilm" bacterial colonies.[54] The properties of the MOF may be tuned even more subtly by the use of multiple-metal SBUs, in which a combination of two (or, potentially, more) metals are involved. This approach could combine the favourable properties of the two metals in one MOF, and is currently an area of growing research interest. An example of this strategy is the synthesis of mixed-metal HKUST-1, which contains a mixture of Cu^{2+} and Zn^{2+} within the SBUs.[55]

Owing to their vast diversity of structures and resulting physical and chemical properties, MOFs find an equally wide range of applications (or potential applications), as mentioned in some of the examples discussed above. These

applications typically involve the selective adsorption of a guest species, with the selectivity owing to size, shape or chemical discrimination by the pores of the MOF. Once within the pores, the guest species may be stored or converted to a new species (*e.g.*, by catalysed reactions) and then released (either by diffusion, or in response to a stimulus). In recent years, these processes have found applications in most areas of modern life, including medicine (predominantly drug storage and controlled delivery),[53, 56] gas separation/purification and storage (particularly related to H_2, CH_4 and CO_2),[3, 57-60] catalysis (including stereo- and enantioselective reactions),[16, 61, 62] polymerisation[63] and as components within high-performance Li-ion fuel cells.[64]

For other applications, the physical or chemical properties of the MOFs themselves are of interest, rather than the processes of guest adsorption, storage, transformation and release. For example, HKUST-1 has been shown to have inherent antibiotic activity (owing to the slow degradation of the framework and release of Cu^{2+} ions over several days).[54] Several Fe-containing MOFs can be used as contrast agents in MRI owing to their inherent paramagnetism and low toxicity.[65] Many MOFs are magnetically active, making them potential candidate materials for applications such as data storage, sensing and imaging, although magnetic ordering in MOFs is typically confined to the low-temperature regime at present.[3, 66] Lanthanide-containing MOFs may exhibit luminescence, owing either to the inherent luminescence of many lanthanide ions, or to guest-induced luminescence,[67] giving such materials possible applications from optical imaging/sensing to communication technology. The extreme flexibility of many "breathing" MOFs[68] suggests that they may find applications in composite materials with unusual expansion properties, which may be of use in many technologies.

The use of solid-state NMR in the study of MOFs is typically limited to ^{1}H and ^{13}C (both spin I = 1/2), as these are the most readily-accessible NMR-active nuclei present. Solid-state ^{1}H NMR spectra are typically of relatively low resolution, but can still be of use in, *e.g.*, studying the hydration state of a MOF.[69, 70] Solid-state ^{13}C NMR spectra are generally of higher resolution and can provide information on the crystallographic symmetry of the MOF and, when the MOF contains carbon-based guests, on the presence of guests[50, 54] and guest dynamics.[71] ^{2}H (I = 1) NMR is

also possible, although the low natural abundance (0.01%) means that isotopic enrichment is typically required. The use of deuterated bdc in the synthesis of scandium terephthalate MOFs enabled a variable-temperature ^{2}H NMR study to monitor the flipping of the benzene rings in the framework.[37] In some MOFs, particularly those containing Al and Sc (and to some extent Mg, Zn and Ga), the metal centre is also NMR-accessible. The ^{27}Al (I = 5/2) NMR spectrum of MIL-53(Al) showed changes in the NMR parameters upon changes in the conformation and hydration state of the MOF,[70] and a series of ^{45}Sc (I = 7/2) NMR studies on scandium-based MOFs have shown that the ^{45}Sc NMR parameters are sensitive to the nature of the SBU present.[45] However, unlike ^{27}Al, the ^{45}Sc NMR parameters were relatively insensitive to conformational changes occurring within the MOFs, including MIL-53(Sc) (*i.e.*, changes analogous to those influencing the ^{27}Al NMR parameters in MIL-53(Al)). Ga has two NMR-active isotopes, ^{69}Ga (I = 3/2) and ^{71}Ga (I = 3/2), both with reasonably high natural abundance (60 and 40%, respectively) and moderate gyromagnetic ratios, making acquisition of solid-state Ga NMR spectra relatively easy, although the large nuclear quadrupole moments, particularly for ^{69}Ga, mean that the use of high field and high-resolution NMR techniques is essential to obtaining relevant structural information. To date there have been relatively few Ga NMR studies of MOFs, and these have been predominantly focused simply on confirming the number of distinct Ga species present.[72, 73] ^{25}Mg (I = 5/2) NMR is considerably more challenging, owing to its moderate nuclear quadrupole moment, low gyromagnetic ratio and moderate natural abundance (10%). ^{25}Mg NMR spectra have recently been used by Rangus *et al*. to characterise some novel MOFs,[74] and Xu *et al.* have probed dehydration-induced disorder in CPO-27-Mg using ^{25}Mg NMR.[75] ^{67}Zn (I = 5/2) NMR is also very challenging owing to low natural abundance (4%), low gyromagnetic ratio and moderate quadrupole moment. However, many of the zeolitic imidazolate framework (ZIF) class of MOFs[76] contain Zn^{2+} in relatively high-symmetry tetrahedral environments, allowing ^{67}Zn NMR spectra to be recorded on a reasonable timescale (predominantly at very high magnetic field strengths).[77] Other metal centres may also be NMR active, and can be studied by solid-state NMR, including ^{113}Cd (I = 1/2)[78] and ^{207}Pb (I = 1/2).[79-81] While ^{17}O (I = 5/2) at natural abundance (0.04%) is typically

a very unfavourable nucleus to study, He *et al.*[82] recently reported the synthesis of some ^{17}O-enriched MOFs, and showed that ^{17}O NMR can be used to distinguish between disordered hydroxide and oxo ligands in the MOF, UiO-66. Many MOFs are paramagnetic and, as discussed in Chapters 2 and 4, this complicates the acquisition and analysis of NMR spectra for these systems. However, ^{13}C NMR spectra of paramagnetic MOFs are, in some cases, more sensitive to the presence and behaviour of guest species, owing to the larger shift range resulting from interactions between ^{13}C and the unpaired electrons present.[64, 69, 83] Wu recently presented the natural-abundance ^{17}O NMR spectrum of HKUST-1, where the resonance for the Cu-bound oxygen species was observed at ~6000 ppm, although the work was more a proof of concept than an attempt to extract structural information.[84] In addition to studying the framework or guest species, the free volume of MOFs can be investigated by hyperpolarised ^{129}Xe (I = 1/2) NMR spectra, which allow information such as pore volume (number of Xe atoms per pore) and pore connectivity (the ease of diffusion of Xe between pores) to be determined.[85]

1.2 ZEOLITES AND ZEOTYPES

Naturally-occurring microporous aluminosilicate frameworks were first reported in 1756.[86] Zeolites (derived from the Greek *zeo* = boiling and *lith* = stone) were named after their ability to release the water stored within their pores upon heating. Since the early 20th century, a large number of synthetic zeolites have been prepared, either as analogues of natural zeolites, or as entirely new materials. The basic building units of zeolites are SiO_4 and AlO_4 tetrahedra, which can be arranged to give Si-O-Si and Si-O-Al linkages but, according to Lowenstein's rule, Al-O-Al linkages are unfavourable and do not form at low Al content.[87] These tetrahedra can combine to give SBUs, named according to the number and connectivity of the tetrahedra in the SBU, *e.g.*, the 6-6 SBU contains a ring of 6 TO_4 tetrahedra bonded to another 6-membered ring. Some examples of SBUs are shown in Figure 1.2(a). The SBUs can combine to give composite building units (CBUs), in the form of chains, rings and cages, as shown in Figure 1.2(b). (It should be noted that many authors do not make the somewhat arbitrary distinction between SBUs and CBUs, with the term SBU

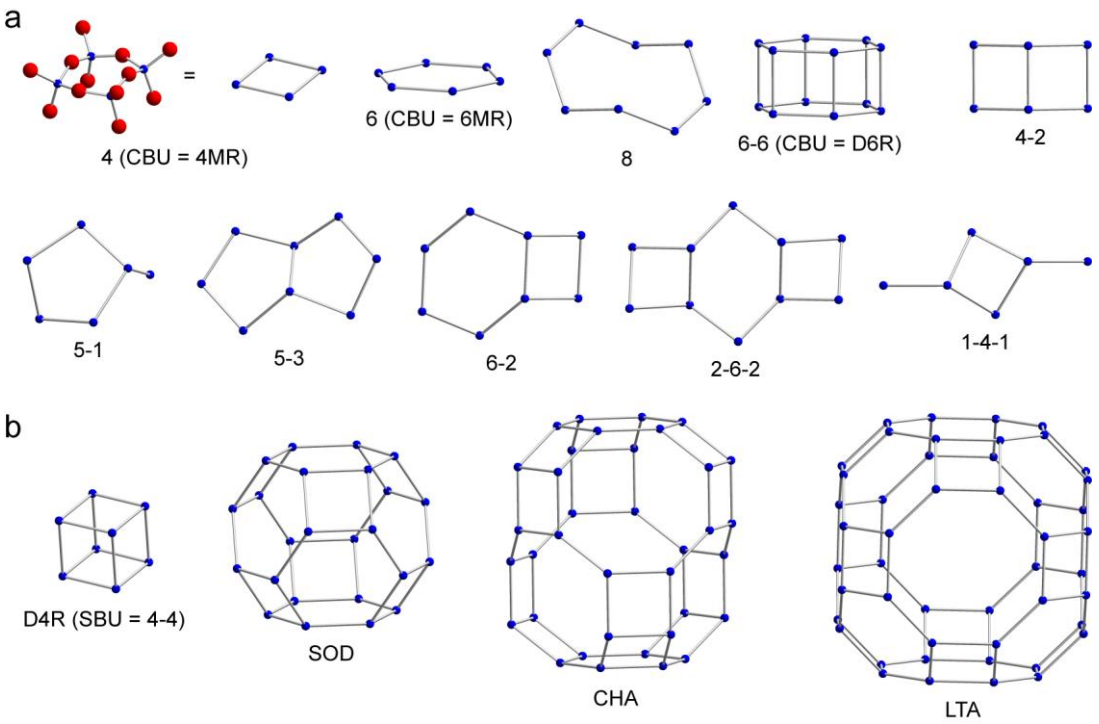

Figure 1.2. (a) The ten most common zeolite SBUs and (b) four example CBUs. The vertices represent Si or Al atoms (blue), with the bridging O atoms located along the edges of the SBU/CBU, as illustrated for the example of the 4 SBU in part (a), where the O atoms are shown in red. Where a structural motif can be considered as both a SBU and a CBU, the alternative nomenclature is given in parentheses.[88]

often being used for both.) CBUs are typically given a three-character code based on either the structure of the SBU (*e.g.*, a double six-membered ring (6-6 SBU) is known as a D6R when considered as a CBU) or the zeolite in which it was first observed (*e.g.*, the CHA cage was first observed in chabazite). The arrangement of the CBUs in the zeolite determines the overall pore structure and connectivity, and the suitability of the zeolite for different applications. The framework structure is classified by the International Zeolite Association (IZA) by a three-letter code, *e.g.*, CHA for **cha**bazite and LTA for **L**inde **T**ype **A** (zeolite A). There are currently 213 different framework types[88] but, typically, more are added every year.

The parent material for all zeolites is SiO_2, which contains exclusively Si^{4+} in the tetrahedral building blocks of the framework. Therefore, including Al^{3+} in an aluminosilicate framework introduces an overall negative charge, which is counter-

balanced by the presence of cations (typically of group 1 or 2 metals) within the pores of the framework, or Brønsted acid sites (H^+) on the framework. In addition to the inherent Brønsted acidity of aluminosilicates, Lewis acidity and/or redox behaviour may be introduced by the substitution of different elements into the tetrahedral framework sites. The reason that there is such interest in zeolites, and that they have so many applications, is that the pores and channels present are the same size scale as small molecules, while their shapes allow for the selective adsorption of molecules of specific shapes. This selective adsorption allows zeolites to act as "molecular sieves" and, in combination with the (electro)chemically-active sites present, allows them to act as very effective catalysts for a wide range of reactions.[4] For example, the zeolite, ZSM-5 (MFI topology), selectively catalyses *para* methylation of toluene, yielding exclusively *p*-xylene (1,4-dimethylbenzene), and none of the *m*- or *o*- isomers obtained in an alternative Friedel-Crafts approach.[89]

The synthesis of zeolites is typically hydrothermal, where the reagents are combined in an aqueous solution or gel, which is then heated until the product zeolite precipitates. The reagents required are sources of Si and Al and a cationic species, which can be either inorganic (*e.g.*, Na^+, Ca^{2+} or NH_4^+) or organic (*e.g.*, HNR_3^+ or R_4N^+). The choice of cation can influence the framework that forms, which has led to the name "template" for these species although, since the same "template" may lead to different zeolites under different conditions and the same zeolite may form from many different "templates", a more accurate term is generally structure-directing agent (SDA). An organic solvent (solvothermal route) or ionic liquid (ionothermal route) may also be used in the synthesis of zeolites. These approaches allow for the use of different Al- and Si-containing precursors, SDAs and reaction conditions and can lead to the synthesis of different framework types. The reaction times of all of these synthetic methods can be reduced drastically (from hours or days to minutes or seconds) by microwave irradiation (microwave-assisted synthesis), which is of interest owing to the time and energy savings involved. However, reaction methods must generally be modified to be suitable for microwave-assisted synthesis.

Solid-state NMR has been widely applied to zeolites, with the integrated intensities of the (typically well separated) ^{29}Si (I = 1/2) resonances corresponding to

$Si(OSi)_{4-n}(OAl)_n$ allowing the Si : Al ratio of the zeolite (an important parameter related to catalytic behaviour and thermal stability) to be determined, assuming Lowenstein's rule is applicable. In addition, the ^{29}Si chemical shift can be affected by the Si-O bond lengths and Si-O-T bond angles (T = Si or Al), with a variety of empirically-determined relationships between these parameters having been determined in the literature.[4, 90] These relationships will be discussed in further detail in Chapter 5. ^{27}Al (I = 5/2) is also a favourable nucleus to study by solid-state NMR, although the second-order quadrupolar broadening generally necessitates the use of high-resolution MQMAS experiments[91, 92] (see Chapter 3). As for ^{29}Si, there are various proposed relationships between the ^{27}Al NMR parameters (chemical shift and quadrupolar coupling) and the local structure (described by geometrical parameters, *e.g.*, bond angles and lengths) of zeolites.[90] While ^{17}O is not a favourable nucleus to study at natural abundance, isotopic enrichment of zeolites is relatively straightforward and involves either synthesising the zeolite in $H_2{}^{17}O$ (~€1000 per gram, 90% enriched), or heating the sample under an isotopically-enriched environment to allow exchange of O in the zeolite with $^{17}O_2$ gas (~£6600 per litre, 60% enriched). However, the large excess of ^{17}O required for these approaches means that ^{17}O enrichment is often prohibitively costly. Despite this, isotopic enrichment of ^{17}O has allowed some investigations into the ^{17}O NMR parameters of these materials. Both the chemical shift and quadrupolar coupling of ^{17}O are sensitive to the type of Si-O-T linkage formed and the Si-O-T bond angle, indicating that the nucleus can provide relevant structural information for zeolites.[93, 94]

^{1}H and ^{2}H NMR spectra are also commonly applied to zeolites, as ^{1}H can act as a sensitive probe of Brønsted acid sites, whereas variable-temperature ^{2}H NMR studies can provide valuable information on the motion of deuterated guest species within the pores of zeolites – a process fundamentally linked to the ability of the zeolite to absorb a particular species, or catalyse a specific reaction. It is also possible to study the SDA and guest species by ^{13}C and ^{15}N (I = 1/2) NMR spectra if the SDA is organic, and ^{23}Na (I = 3/2) NMR spectra if Na^+ is the SDA. Other NMR-active group 1 or 2 elements may also be present (Li^+, Rb^+, Sr^{2+}, Ca^{2+} and Mg^{2+}, *etc.*) and, like MOFs, the inner surface and pore connectivities can be investigated by the diffusion of hyperpolarised Xe.[85]

1.2.1 Aluminophosphates

The aluminophosphate analogues of zeolites (AlPOs) have generated intense interest since their relatively recent discovery in 1982.[95] Unlike zeolites, these AlPO "zeotypes" have an overall neutral framework (of formula $AlPO_4$), owing to the strict alternation of the AlO_4 and PO_4 tetrahedra from which AlPOs are constructed. It can be seen that SBUs containing 3- and 5-membered rings (*e.g.*, 5-1 and 5-3 in Figure 1.2) violate this alternation and are, therefore, not found in AlPOs. The conventional synthesis of AlPOs is similar to that of zeolites, with the P and Al sources mixed to form a gel, paste or solution in the desired solvent system (both hydrothermal and solvothermal syntheses are common) in the presence of the desired SDA and, if required, a mineraliser (commonly HF or tetraethyl orthosilicate (TEOS)). The reaction mixture is then heated at temperatures of up to ~230 °C with reaction times of up to ~7 days. However, in recent years, the popularity of the ionothermal synthesis route has increased, owing to the greater control over the water content of the reaction that this affords. Ionic liquids are typically salts of organic species such as alkylimidazoliums, which have a melting point close to room temperature, so that the salt is molten at the reaction temperatures common for the synthesis of AlPOs. Deep eutectic solvents (DESs) result when a mixture of two high-melting-point solids (*e.g.*, urea, m.p. = 134 °C and choline chloride, m.p. = 298-305 °C) has a greatly depressed melting point (*e.g.*, the mix of urea and choline chloride has a melting point of 12 °C), and can be used in an analogous manner to ionic liquids as solvents for the synthesis of zeolitic frameworks.[96] Ionic liquids and DESs offer safety benefits: as they have essentially no vapour pressure, the risk of explosion or fire during the synthesis is minimised. In addition, the solvent can act as the SDA, increasing the range of SDAs (and, hence, potential AlPO structures) possible.[97, 98] The SDA, which is typically a cationic nitrogen-based species, remains in the pores of the AlPO after synthesis and its positive charge is balanced by the presence of either F^- or OH^-, which bind to the Al to give five- or six-coordinate Al species in addition to the expected four-coordinate species. The structures of as-prepared AlPOs may also contain H_2O, depending on the synthetic route used. An example of these species is shown in Figure 1.3(a) for the CHA-type AlPO-34, prepared in the presence of morpholine and HF (AlPO-34[morpholinium fluoride]).[99] As Al, P and

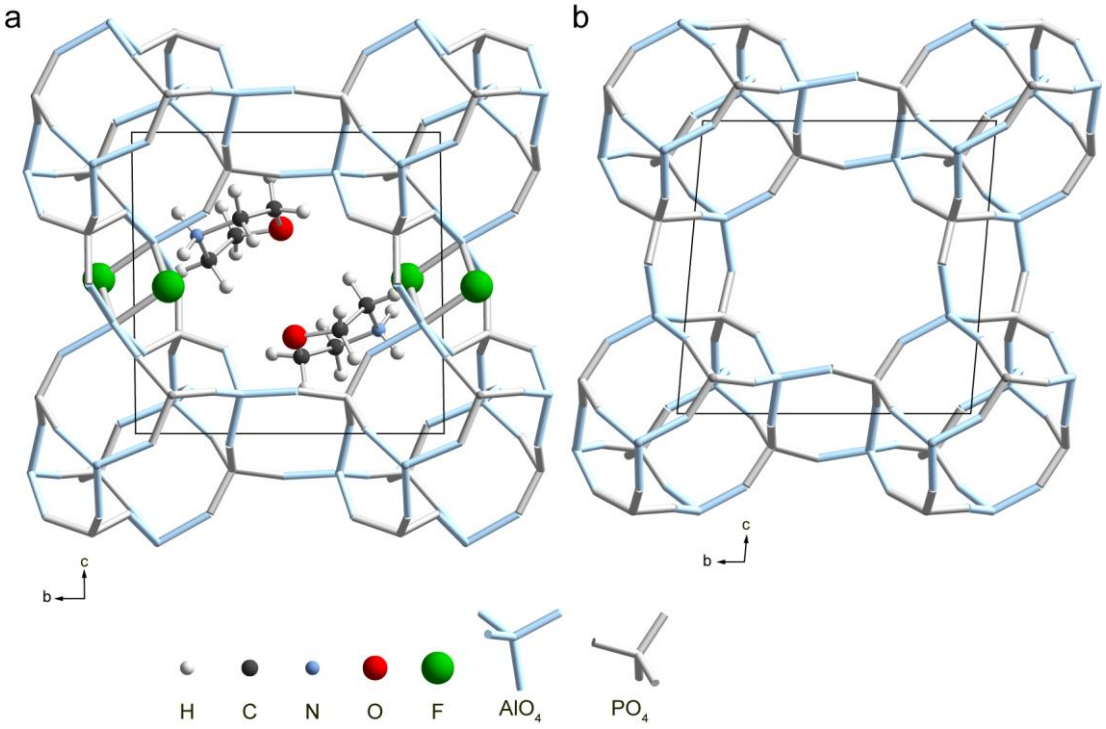

Figure 1.3. Structures of (a) the chabazite-type AlPO-34[morpholinium fluoride] and (b) calcined AlPO-34 ($AlPO_4$-CHA).

Si are in the same period of elements, AlPOs can form many structures isomorphous to aluminosilicates, and AlPO analogues of many important zeolites have been prepared.[88] However, AlPOs also have access to many structures not (yet) known for aluminosilicates – for example, AlPO-11 (AEL framework),[100] AlPO-14 (AFN framework),[101] and AlPO-41 (AFO framework)[102] do not have aluminosilicate analogues recorded in the IZA database.[88]

To complicate the issue of determining whether an AlPO is analogous to either an aluminosilicate or another AlPO, there are (as for MOFs) several different nomenclature schemes in existence. Initially, AlPOs were prepared with little knowledge of their structure and so they were named simply in order of their synthesis,[95] giving the nomenclature system AlPO-*n* (or, sometimes, $AlPO_4$-*n*). However, as for MOFs, many research groups prefer to name the material after the institution at which it was first prepared, *e.g.*, VPI-5 was prepared at the Virginia Polytechnic Institute[103] and JDF-2 was prepared as a collaboration between Jilin University and the Davy-Faraday Research Laboratory.[104] Some authors seek to

simplify the search for AlPO analogues of zeolites by including the IZA structure code in the name, *e.g.*, AlPO-CHA has the chabazite topology. Alternatively, some authors wish to highlight the synthetic procedure used, as in the SIZ-*n* series (SIZ = St Andrews Ionothermal Zeolite).[97, 98] In order to avoid confusion, this thesis uses the nomenclature of the primary literature relating to the AlPOs of interest. However, where possible, the IZA structure code[88] is also provided.

Unlike aluminosilicate zeolites, which possess inherent acidity, the AlPO framework has an overall neutral charge and the pores can be completely cleared of all extra-framework species by calcination. This process involves heating the AlPO until the organic material decomposes (normally between ~250 and 600 °C) to CO_2, H_2O and N_2 and the anionic species is lost as H_2O (for HO^-) or HF (for F^-), resulting in a stable microporous $AlPO_4$ framework. The calcined AlPO-34 framework is shown in Figure 1.3(b). Further heating to higher temperatures can cause additional transformations, as exemplified by the case of the AlPO-53 system (AEN framework type).[105, 106] The as-prepared AlPO-53(A) is dehydrated at low temperature, giving JDF-2[104] (which can also be prepared directly). Calcination to AlPO-53(B) occurs at 400 °C, the framework of which rearranges to give the non-porous AlPO-53(C) at 700 °C (AlPO-53(C) no longer has the AEN framework type). At temperatures above 700 °C the framework collapses to the fully dense phase, $AlPO_4$ tridymite (some tridymite was present in the sample heated to 700 °C, suggesting that the framework rearrangement may occur at lower temperatures than this), as shown in Scheme 1.1. Calcined AlPOs are usually stable to air and moisture, although they can be extremely hygroscopic, typically absorbing large quantities of water on the timescale of a few hours or days.[107, 108] This absorbed water can be removed by gentle heating (~110 °C) without damaging the framework.

In order to introduce chemical activity to an $AlPO_4$ framework several strategies are possible. The most common approach is to synthesise the material with substitution of either iso- or aliovalent cations for Al or P. The term generally used in the literature is either MeAPOs or MAPOs (where Me or M = "metal"), although MAPOs containing specific Me/M species are generally indicated by MgAPO (containing Mg^{2+}), FeAPO (containing $Fe^{2/3+}$), CoAPO (containing $Co^{2/3+}$), *etc*.,

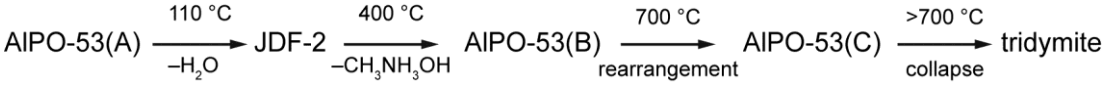

Scheme 1.1. Phase changes occurring on heating of AlPO-53 (AEN framework type, except for AlPO-53(C), which does not currently have an IZA structure code).

except for the case of Si-substituted AlPOs, which are called SAPOs,[109] and some authors rather confusingly use the term MAPO to refer specifically to MgAPOs. While MAPOs and SAPOs have yet to be used extensively in industry, they have been demonstrated to have activity and size and shape selectivity comparable to zeolites for industrially-relevant processes. For example, Lischke *et al*. demonstrated that a series of MAPOs and a SAPO with the AFI topology were capable of catalysing the conversion of methanol to dimethylether or light alkenes, with the products dependent on the metal (or Si) present in the framework.[110]

An alternative to including the active centre in the framework is to include active centres in the pores of the framework, as shown by Picone *et al*., who incorporated catalytically-active Cu^{2+} ions within SAPO STA-7,[111] and Mathiesen *et al*., who compared CuAPO-5 (AFI topology) and ZSM-5 containing Cu^{2+} within the pores.[112] In both cases, good activity was achieved for the selective reduction of NO – a toxic pollutant gas in the context of that work – and the "free" Cu^{2+} was observed to be significantly more active than the Cu^{2+} within the framework, particularly at lower temperatures. A third method for introducing active sites in AlPOs is to synthesise "interrupted" frameworks, in which the AlO_4 and PO_4 tetrahedra are not fully condensed and some "dangling" P-OH and Al-OH species remain. Examples of such materials include SIZ-1[97] and DNL-1 (DNL = Dalian National Laboratory).[113] The applications of such materials are relatively unexplored, but are likely to be similar to those of other zeolitic materials containing Brønsted acidic sites.

However, even without modification of their composition, AlPOs can display useful properties, notably, the phenomenon of negative thermal expansion (NTE), which occurs owing to rotation of the flexible Al-O-P linkages around the Al-P axis. This rotation becomes more pronounced at higher temperatures, reducing the Al-O-P angle and leading to a reduction in the Al-P distance. This atomic-level contraction

causes a (typically anisotropic) reduction in the unit cell dimensions and, consequently, a decrease in the volume of the bulk material. This effect, investigated by Amri and Walton for the CHA-type calcined AlPO-34 and the AEI-type calcined AlPO-18, can amount to a contraction of up to 0.02 Å in the Al-P distance over a temperature range of ~300 K.[114]

The frameworks of AlPOs are highly amenable to study by solid-state NMR, as both ^{27}Al and ^{31}P (I = 1/2) have 100% natural abundance and high sensitivity. As shown in Figure 1.4(a), the ^{27}Al isotropic chemical shifts are very different for four- five- and six-coordinate Al[90] and it is possible to obtain information about the nature of extra-framework anions from the ratio of Al(IV) to Al (V/VI) – where the Roman numerals denote the coordination number.[45] An example of this is shown in Figure 1.4(b) for AlPO-14 containing isopropylammonium hydroxide (AlPO-14-ipa). The crystal structure of AlPO-14-ipa contains two distinct Al(IV), one distinct Al(V) and one distinct Al(VI) species, which can be readily identified by their isotropic chemical shifts. Owing to the second-order quadrupolar broadening, which is evident in the spectrum shown in Figure 1.4(b), the ^{27}Al resonances for a given coordination number will overlap significantly in many cases and high-resolution experiments are required to resolve these resonances and determine the number of distinct Al species present. The ^{27}Al satellite transitions (see Section 2.3) are typically sensitive to motion on the microsecond timescale and variable-temperature ^{27}Al NMR spectra may be used to investigate the motion of any guest species within the framework.[115] ^{31}P NMR spectra can provide much valuable information on the structure of AlPOs, including the number and proportions of crystallographically-distinct P species present and, through empirically-derived relationships,[90, 116-118] information on the local structure (*e.g.*, the mean Al-O-P bond angle or P-O bond length – discussed further in Chapter 5). It is often very useful to carry out a heteronuclear correlation between ^{27}Al and ^{31}P in AlPOs. Depending on the design of the experiment, the spectrum can provide direct information on the through-bond or through-space relationships of the Al and P atoms in the framework. This allows the framework connectivity to be probed and can be invaluable in assisting the assignment of both the ^{27}Al and ^{31}P NMR spectra. While ^{17}O is less frequently studied, owing to the issues of sensitivity and cost discussed previously, recent experiments on the

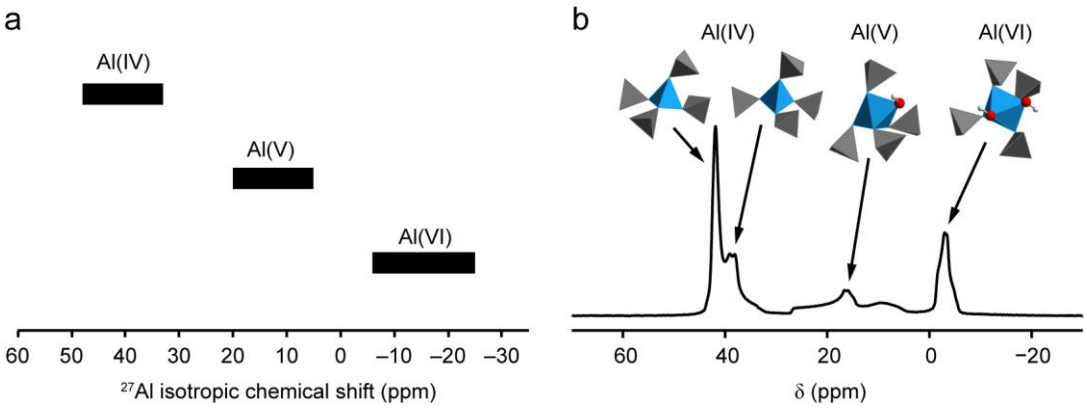

Figure 1.4. (a) Isotropic chemical shift ranges for ^{27}Al in AlPOs. (b) ^{27}Al (14.1 T, 20 kHz MAS) NMR spectrum of AlPO-14 containing isopropylammonium hydroxide as the SDA/anion pair.

isotopically-enriched (~4% abundance) CHA-type calcined SIZ-4 have indicated relationships between the ^{17}O NMR parameters and the local structure.[119] ^{17}O is of interest since the inner surfaces of AlPOs are lined with O atoms and, therefore, this nucleus should be one of the most sensitive probes of the chemistry occurring within AlPOs. However, the work of Griffin *et al.*[119] was more a proof of the isotopic enrichment process, which used an ionothermal synthesis to reduce the amount of expensive (~£500 / g, 35% enriched) $H_2{}^{17}O$ required for the level of enrichment achieved. Very recent work in the ^{17}O-enrichment of AlPOs, using 90%-enriched $H_2{}^{17}O$ has led to an even greater level of enrichment (~9%) in SIZ-4,[120] which paves the way for the use of more complicated and informative NMR experiments.

The extra-framework species found in AlPOs are also often amenable to study by solid-state NMR spectroscopy, particularly of ^{1}H, ^{13}C, ^{19}F and, to some extent, ^{2}H and ^{15}N. These nuclei can provide information on the crystallographic symmetry, guest species present (particularly useful when two "co-templates" are used to direct the structure of the material and it is unclear whether they are both incorporated), guest dynamics, and the hydration state of the material.

1.2.2 Gallophosphates

Like AlPOs, gallophosphates (GaPOs) are zeolite analogues although, owing to the differences in the chemistry of Ga and Al, and the different studies carried out into the syntheses of AlPOs and GaPOs, some zeotypic frameworks are known only for GaPOs. For example, the GaPO form of the large-pore zeolite, cloverite (CLO framework type) was synthesised hydrothermally with quinuclidine as the SDA in 1991,[121] whereas the AlPO analogue (DNL-1) was only reported in 2011 and was prepared ionothermally using 1-ethyl-3-methylimidazolium bromide and 1,6-diaminohexane as co-SDAs.[113] The synthesis of GaPOs has, to date, been mainly hydro- and solvothermal, with very few ionothermal syntheses reported. This is, in part, owing to the high solubility of Ga^{3+} in ionic liquids, meaning that crystallisation of the GaPO is not typically possible under the same conditions as used for the synthesis of AlPOs.[96] Another key difference between AlPOs and GaPOs is the greater prevalence of F^- as the extra-framework anion, as evidenced by the so-called "fluoride route", which gained prominence in the 1990s.[122] As such, there are currently many more known GaPOs containing F^- than HO^-.

While GaPOs are structurally similar to AlPOs, it is considerably harder to calcine GaPOs to leave a neutral microporous material. In a theoretical study, Girard *et al.*[123] proposed that this is a consequence of the inherent instability of many microporous $GaPO_4$ frameworks with respect to the dense phase $GaPO_4$ quartz. However, a study by Schott-Darie *et al.*,[124] subsequently confirmed by the work of Amri and Walton,[114] Amri *et al.*[125] and work reported in Chapter 6 of this thesis, has shown that the calcined chabazite-type framework of GaPO-34 is not inherently unstable. Like AlPOs, calcined GaPO frameworks hydrate rapidly in air.[125] However, as Amri *et al.* showed, unlike in the case of the AlPO form of the framework, heating of calcined, hydrated GaPO-34 does not remove H_2O. Instead, upon heating, the hydrated material collapsed to an amorphous state. While this sensitivity to moisture has so far restricted the applications of GaPOs, Richter *et al.* demonstrated that cloverite can be calcined and used (under anhydrous conditions) to catalyse the conversion of isobutene and methanol or ethanol to the fuel additives, methyl *tert*-butyl ether or ethyl *tert*-butyl ether, respectively.[126, 127] It should be noted, however, that Richter *et al.* were unclear whether the catalytically-active species was the

Brønsted-acidic P-OH and Ga-OH species of the interrupted framework, or residual HF that was not removed by calcination.[127] The frameworks of GaPOs, like AlPOs, also exhibit NTE. However, to emphasise again the "similar but very different" nature of AlPOs and GaPOs, Amri and Walton showed that the calcined CHA-type $AlPO_4$ and $GaPO_4$ frameworks both displayed NTE, but along different crystallographic axes, owing to the different behaviours of some of the Ga-O and Al-O bonds. [114]

As for AlPOs, solid-state NMR can provide much information about the local structure in GaPOs. Of the nuclei in the framework, ^{31}P is by far the most favourable nucleus to study, and provides much the same information as for AlPOs. ^{19}F NMR spectra are very useful in GaPOs, as the three common F-containing motifs; terminal, bridging and contained within a D4R unit, shown in Figure 1.5(a), have distinct chemical shift ranges, as shown in Figure 1.5(b). This information can be of use when attempting to determine the structure of a new material. As for AlPOs, ^{1}H, ^{2}H, ^{13}C and, in principle, ^{15}N can be used to provide information on the SDA or guest species, including the number of crystallographically-distinct species, the protonation state of the SDA and the presence of H_2O.[125] Ga has two NMR-active isotopes, ^{69}Ga (60.1% natural abundance) and ^{71}Ga (39.9% natural abundance), both of which are accessible to NMR experiments. However, both nuclei are quadrupolar (I = 3/2) and spectra are dominated by the second-order quadrupolar broadening. The nuclear quadrupole moment of ^{69}Ga is ~ 1.6 times greater than that of ^{71}Ga,[128] meaning that the resonances in ^{71}Ga NMR spectra are significantly narrower than those of ^{69}Ga. ^{71}Ga is, therefore, the isotope of choice for most Ga NMR experiments, although Amri *et al*. demonstrated that comparison between ^{69}Ga and ^{71}Ga NMR spectra could increase the confidence in the values determined for the chemical shift and quadrupolar parameters in the as-prepared forms of GaPO-34.[125] By analogy to ^{27}Al NMR for AlPOs, the shift ranges of $^{71/69}Ga$ in GaPOs are characteristic of Ga(IV), Ga(V) and Ga(VI).[129, 130] However, as the nuclear quadrupole moment of either isotope of Ga is greater than that of ^{27}Al, the overlap of the resonances is typically greater, and high-field, high-resolution ^{71}Ga NMR spectra are usually required to resolve distinct Ga species.

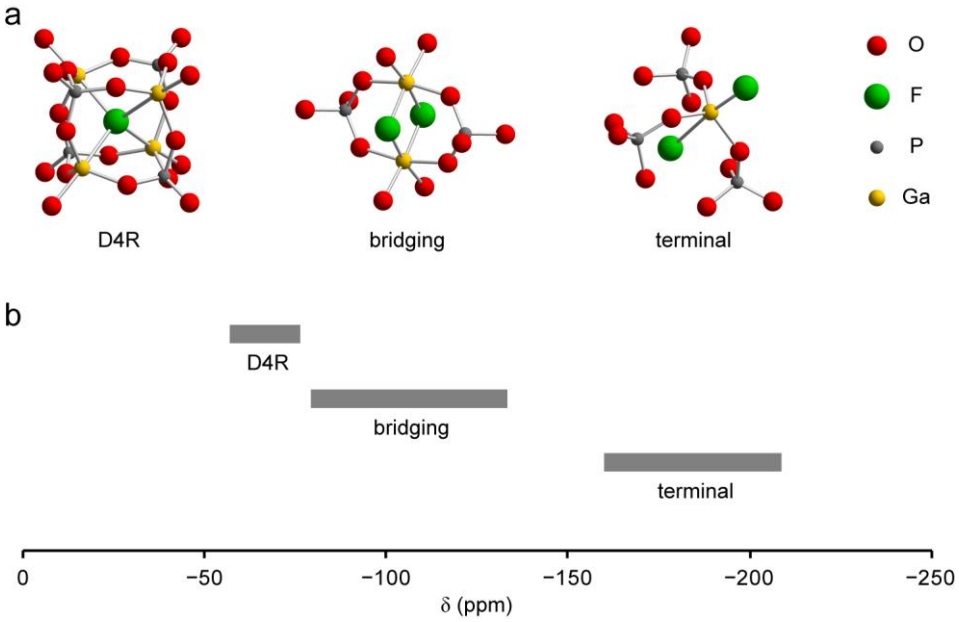

Figure 1.5. (a) F-containing structural motifs found in GaPOs; D4Rs, bridging, and terminal. (b) A plot of ^{19}F chemical shifts for F species assigned to the different structural motifs in the literature.[124, 131-148]

1.3 SUMMARY

It can be seen that the chemical and physical properties of microporous materials are as varied as their chemical compositions and longer-range framework structures. This great diversity of properties leads to a correspondingly large number of applications and potential applications of relevance to today's society. While the structures of the frameworks themselves are typically well-characterised by Bragg diffraction methods, the detailed picture of processes occurring during use of the framework materials are often poorly-understood at the local structural level. It has been shown that solid-state NMR experiments are capable of providing a great variety of element-specific information on the local structures present in microporous materials, making solid-state NMR spectroscopy an ideal investigative technique to assist in better understanding this important and fascinating class of materials.

1.4 REFERENCES

1. J. Rouquerol, D. Avnir, C. W. Fairbridge, D. H. Everett, J. H. Haynes, N. Pernicone, J. D. F. Ramsay, K. S. W. Sing and K. K. Unger, *Pure Appl. Chem.*, **1994**, *66*, 1739.

2. M. Mastalerz, *Chem. Eur. J.*, **2012**, *18*, 10082.

3. G. Férey, *Chem. Soc. Rev.*, **2008**, *37*, 191.

4. P. A. Wright, *Microporous Framework Solids*, 1st edn., The Royal Society of Chemistry, Cambridge, UK, 2008.

5. N. L. Rosi, J. Kim, M. Eddaoudi, B. L. Chen, M. O'Keeffe and O. M. Yaghi, *J. Am. Chem. Soc.*, **2005**, *127*, 1504.

6. A. D. Burrows, C. G. Frost, M. F. Mahon, P. R. Raithby, C. Richardson and A. J. Stevenson, *Chem. Commun.*, **2010**, *46*, 5064.

7. M. T. Wharmby, S. R. Miller, J. A. Groves, I. Margiolaki, S. E. Ashbrook and P. A. Wright, *Dalton Transact.*, **2010**, *39*, 6389.

8. P. K. Allan, B. Xiao, S. J. Teat, J. W. Knight and R. E. Morris, *J. Am. Chem. Soc.*, **2010**, *132*, 3605.

9. Y. S. Xue, Y. B. He, S. B. Ren, Y. F. Yue, L. Zhou, Y. Z. Li, H. B. Du, X. Z. You and B. L. Chen, *J. Mater. Chem.*, **2012**, *22*, 10195.

10. G. K. H. Shimizu, R. Vaidhyanathan and J. M. Taylor, *Chem. Soc. Rev.*, **2009**, *38*, 1430.

11. G. W. Noble, P. A. Wright and A. Kvick, *J. Chem. Soc. Dalton Transact.*, **1997**, 4485.

12. P. D. C. Dietzel, Y. Morita, R. Blom and H. Fjellvåg, *Angew. Chem. Int. Ed.*, **2005**, *44*, 6354.

13. P. D. C. Dietzel, R. E. Johnsen, R. Blom and H. Fjellvåg, *Chem. Eur. J.*, **2008**, *14*, 2389.

14. P. D. C. Dietzel, R. Blom and H. Fjellvåg, *Eur. J. Inorg. Chem.*, **2008**, 3624.

15. H. Wu, W. Zhou and T. Yildirim, *J. Am. Chem. Soc.*, **2009**, *131*, 4995.

16. S. Bhattacharjee, J.-S. Choi, S.-T. Yang, S. B. Choi, J. Kim and W.-S. Ahn, *J. Nanosci. Nanotechnol.*, **2010**, *10*, 135.

17. A. Lieb, H. Leclerc, T. Devic, C. Serre, I. Margiolaki, F. Mahjoubi, J. S. Lee, A. Vimont, M. Daturi and J. S. Chang, *Micropor. Mesopor. Mater.*, **2012**, *157*, 18.

18. H. Reinsch and N. Stock, *Cryst. Eng. Commun.*, **2013**, *15*, 544.

19. G. Férey, C. Mellot-Draznieks, C. Serre, F. Millange, J. Dutour, S. Surble and I. Margiolaki, *Science*, **2005**, *309*, 2040.

20. P. Horcajada, S. Surble, C. Serre, D.-Y. Hong, Y.-K. Seo, J.-S. Chang, J.-M. Greneche, I. Margiolaki and G. Férey, *Chem. Commun.*, **2007**, 2820.

21. C. Volkringer, D. Popov, T. Loiseau, G. Férey, M. Burghammer, C. Riekel, M. Haouas and F. Taulclle, *Chem. Mater.*, **2009**, *21*, 5695.

22. J. P. S. Mowat, S. R. Miller, A. M. Z. Slawin, V. R. Seymour, S. E. Ashbrook and P. A. Wright, *Micropor. Mesopor. Mater.*, **2011**, *142*, 322.

23. C. Serre, F. Millange, C. Thouvenot, M. Nogues, G. Marsolier, D. Louer and G. Férey, *J. Am. Chem. Soc.*, **2002**, *124*, 13519.

24. G. Férey, M. Latroche, C. Serre, F. Millange, T. Loiseau and A. Percheron-Guegan, *Chem. Commun.*, **2003**, 2976.

25. S. R. Miller, P. A. Wright, C. Serre, T. Loiseau, J. Marrot and G. Férey, *Chem. Commun.*, **2005**, 3850.

26. F. Millange, G. Férey, M. Morcrette, C. Serre, M. L. Doublet, J. M. Greneche and J. M. Tarascon, *Proceedings of the 15th International Zeolite Conference*, **2007**, 170.

27. E. V. Anokhina, M. Vougo-Zanda, X. Q. Wang and A. J. Jacobson, *J. Am. Chem. Soc.*, **2005**, *127*, 15000.

28. K. Barthelet, J. Marrot, D. Riou and G. Férey, *Angew. Chem. Int. Ed.*, **2001**, *41*, 281.

29. S. Couck, J. F. M. Denayer, G. V. Baron, T. Remy, J. Gascon and F. Kapteijn, *J. Am. Chem. Soc.*, **2009**, *131*, 6326.

30. T. Devic, P. Horcajada, C. Serre, F. Salles, G. Maurin, B. Moulin, D. Heurtaux, G. Clet, A. Vimont, J.-M. Greneche, B. Le Ouay, F. Moreau, E. Magnier, Y. Filinchuk, J. Marrot, J.-C. Lavalley, M. Daturi and G. Férey, *J. Am. Chem. Soc.*, **2010**, *132*, 1127.

31. H. Li, M. Eddaoudi, T. L. Groy and O. M. Yaghi, *J. Am. Chem. Soc.*, **1998**, *120*, 8571.

32. M. Eddaoudi, J. Kim, N. Rosi, D. Vodak, J. Wachter, M. O'Keeffe and O. M. Yaghi, *Science*, **2002**, *295*, 469.

33. D. J. Tranchemontagne, J. R. Hunt and O. M. Yaghi, *Tetrahedron*, **2008**, *64*, 8553.

34. S. Bauer, C. Serre, T. Devic, P. Horcajada, J. Marrot, G. Férey and N. Stock, *Inorg. Chem.*, **2008**, *47*, 7568.

35. A. G. Marquez, A. Demessence, A. E. Platero-Prats, D. Heurtaux, P. Horcajada, C. Serre, J.-S. Chang, G. Férey, V. Antonio de la Pena-O'Shea, C. Boissiere, D. Grosso and C. Sanchez, *Eur. J. Inorg. Chem.*, **2012**, 5165.

36. Z. Ni and R. I. Masel, *J. Am. Chem. Soc.*, **2006**, *128*, 12394.

37. P. S. Mowat, S. R. Miller, J. M. Griffin, V. R. Seymour, S. E. Ashbrook, S. P. Thompson, D. Fairen-Jimenez, A. M. Banu, T. Duren and P. A. Wright, *Inorg. Chem.*, **2011**, *50*, 10844.

38. S. S. Y. Chui, S. M. F. Lo, J. P. H. Charmant, A. G. Orpen and I. D. Williams, *Science*, **1999**, *283*, 1148.

39. W.-H. Fang, L. Cheng, L. Huang and G.-Y. Yang, *Inorg. Chem.*, **2013**, *52*, 6.

40. O. I. Lebedev, F. Millange, C. Serre, G. Van Tendeloo and G. Férey, *Chem. Mater.*, **2005**, *17*, 6525.

41. T. B. Čelič, M. Mazaj, N. Guillou, V. Kaučič and N. Logar, *3rd Croatian-Slovenan Symposium on Zeolites*, Zagreb, Croatia, 2010.

42. T. Cendak, T. B. Čelič, M. Rangus, N. Z. Logar, G. Mali and V. Kaučič, *7th Alpine Conference on Solid-State NMR*, Chamonix-Mont Blanc, France, 2011.

43. K. Uemura, F. Onishi, Y. Yamasaki and H. Kita, *J. Solid State Chem.*, **2009**, *182*, 2852.

44. T. M. Reineke, M. Eddaoudi, D. Moler, M. O'Keeffe and O. M. Yaghi, *J. Am. Chem. Soc.*, **2000**, *122*, 4843.

45. V. R. Seymour, *Ph.D. Thesis*, University of St Andrews, 2013.

46. K. K. Tanabe and S. M. Cohen, *Chem. Soc. Rev.*, **2011**, *40*, 498.

47. M. J. Ingleson, R. Heck, J. A. Gould and M. J. Rosseinsky, *Inorg. Chem.*, **2009**, *48*, 9986.

48. J. E. Halls, A. Hernan-Gomez, A. D. Burrows and F. Marken, *Dalton Transact.*, **2012**, *41*, 1475.

49. H. G. T. Nguyen, M. H. Weston, O. K. Farha, J. T. Hupp and S. T. Nguyen, *Cryst. Eng. Commun.*, **2012**, *14*, 4115.

50. F. Schröder, S. Henke, X. Zhang and R. A. Fischer, *Eur. J. Inorg. Chem.*, **2009**, 3131.

51. M. I. H. Mohideen, B. Xiao, P. S. Wheatley, A. C. McKinlay, Y. Li, A. M. Z. Slawin, D. W. Aldous, N. F. Cessford, T. Dueren, X. Zhao, R. Gill, K. M. Thomas, J. M. Griffin, S. E. Ashbrook and R. E. Morris, *Nature Chem.*, **2011**, *3*, 304.
52. P. D. C. Dietzel, V. Besikiotis and R. Blom, *J. Mater. Chem.*, **2009**, *19*, 7362.
53. A. C. McKinlay, B. Xiao, D. S. Wragg, P. S. Wheatley, I. L. Megson and R. E. Morris, *J. Am. Chem. Soc.*, **2008**, *130*, 10440.
54. A. C. McKinlay, P. K. Allan, C. L. Renouf, M. J. Duncan, S. J. Warrender, D. M. Dawson, S. E. Ashbrook, B. Gil, B. Marszalek, T. Düren, J. J. Williams, C. Charrier, D. Mercer, S. J. Teat and R. E. Morris, *in preparation*.
55. F. Gul-E-Noor, B. Jee, M. Mendt, D. Himsl, A. Pöppl, M. Hartmann, J. Haase, H. Krautscheid and M. Bertmer, *J. Phys. Chem. C*, **2012**, *116*, 20866.
56. P. Horcajada, R. Gref, T. Baati, P. K. Allan, G. Maurin, P. Couvreur, G. Férey, R. E. Morris and C. Serre, *Chem. Rev.*, **2012**, *112*, 1232.
57. A. U. Czaja, N. Trukhan and U. Mueller, *Chem. Soc. Rev.*, **2009**, *38*, 1284.
58. J.-R. Li, R. J. Kuppler and H.-C. Zhou, *Chem. Soc. Rev.*, **2009**, *38*, 1477.
59. S. S. Han, J. L. Mendoza-Cortes and W. A. Goddard III, *Chem. Soc. Rev.*, **2009**, *38*, 1460.
60. L. J. Murray, M. Dinca and J. R. Long, *Chem. Soc. Rev.*, **2009**, *38*, 1294.
61. J. Lee, O. K. Farha, J. Roberts, K. A. Scheidt, S. T. Nguyen and J. T. Hupp, *Chem. Soc. Rev.*, **2009**, *38*, 1450.
62. L. Ma, C. Abney and W. Lin, *Chem. Soc. Rev.*, **2009**, *38*, 1248.
63. T. Uemura, N. Yanai and S. Kitagawa, *Chem. Soc. Rev.*, **2009**, *38*, 1228.
64. G. de Combarieu, M. Morcrette, F. Millange, N. Guillou, J. Cabana, C. P. Grey, I. Margiolaki, G. Férey and J. M. Tarascon, *Chem. Mater.*, **2009**, *21*, 1602.
65. P. Horcajada, T. Chalati, C. Serre, B. Gillet, C. Sebrie, T. Baati, J. F. Eubank, D. Heurtaux, P. Clayette, C. Kreuz, J.-S. Chang, Y. K. Hwang, V. Marsaud, P.-N. Bories, L. Cynober, S. Gil, G. Férey, P. Couvreur and R. Gref, *Nature Mater.*, **2010**, *9*, 172.
66. M. Kurmoo, *Chem. Soc. Rev.*, **2009**, *38*, 1353.
67. M. D. Allendorf, C. A. Bauer, R. K. Bhakta and R. J. T. Houk, *Chem. Soc. Rev.*, **2009**, *38*, 1330.
68. G. Férey and C. Serre, *Chem. Soc. Rev.*, **2009**, *38*, 1380.

69. F. Gul-E-Noor, B. Jee, A. Pöppl, M. Hartmann, D. Himsl and M. Bertmer, *Phys. Chem. Chem. Phys.*, **2011**, *13*, 7783.

70. T. Loiseau, C. Serre, C. Huguenard, G. Fink, F. Taulelle, M. Henry, T. Bataille and G. Férey, *Chem. Eur. J.*, **2004**, *10*, 1373.

71. X. Kong, E. Scott, W. Ding, J. A. Mason, J. R. Long and J. A. Reimer, *J. Am. Chem. Soc.*, **2012**, *134*, 14341.

72. R. Hajjar, C. Volkringer, T. Loiseau, N. Guillou, J. Marrot, G. Férey, I. Margiolaki, G. Fink, C. Morais and F. Taulelle, *Chem. Mater.*, **2011**, *23*, 39.

73. C. Volkringer, T. Loiseau, G. Férey, C. M. Morais, F. Taulelle, V. Montouillout and D. Massiot, *Micropor. Mesopor. Mater.*, **2007**, *105*, 111.

74. M. Rangus, M. Mazaj, N. Z. Logar, G. Mali and V. Kaučič, *7th Alpine Conference on Solid-State NMR*, Chamonix-Mont Blanc, France, 2011.

75. J. Xu, V. V. Terskikh and Y. Huang, *J. Phys. Chem. Lett.*, **2013**, *4*, 7.

76. K. S. Park, Z. Ni, A. P. Cote, J. Y. Choi, R. D. Huang, F. J. Uribe-Romo, H. K. Chae, M. O'Keeffe and O. M. Yaghi, *Proc. Nat. Acad. Sci. USA*, **2006**, *103*, 10186.

77. A. Sutrisno, V. V. Terskikh, Q. Shi, Z. Song, J. Dong, S. Y. Ding, W. Wang, B. R. Provost, T. D. Daff, T. K. Woo and Y. Huang, *Chem. Eur. J.*, **2012**, *18*, 12251.

78. A. V. Kuttatheyil, J. Lincke, D. Lässig, M. Handke, H. Krautscheid, J. Haase and M. Bertmer, *54th Annual Rocky Mountain Conference on Analytical Chemistry*, Copper Mountain, CO, 2012.

79. B. J. Greer, V. K. Michaelis, M. J. Katz, D. B. Leznoff, G. Schreckenbach and S. Kroeker, *Chem. Eur. J.*, **2011**, *17*, 3609.

80. M. J. Katz, P. M. Aguiar, R. J. Batchelor, A. A. Bokov, Z. G. Ye, S. Kroeker and D. B. Leznoff, *J. Am. Chem. Soc.*, **2006**, *128*, 3669.

81. M. J. Katz, V. K. Michaelis, P. M. Aguiar, R. Yson, H. Lu, H. Kaluarachchi, R. J. Batchelor, G. Schreckenbach, S. Kroeker, H. H. Patterson and D. B. Leznoff, *Inorg. Chem.*, **2008**, *47*, 6353.

82. P. He, J. Xu, V. V. Terskikh, A. Sutrisno, H.-Y. Nie and Y. Huang, *J. Phys. Chem. C*, **2013**, *117*, 16953.

83. D. M. Dawson, L. E. Jamieson, M. I. H. Mohideen, A. C. McKinlay, I. A. Smellie, R. Cadou, N. S. Keddie, R. E. Morris and S. E. Ashbrook, *Phys. Chem. Chem. Phys.*, **2013**, *15*, 919.

84. G. Wu, 54th *Annual Rocky Mountain Conference on Analytical Chemistry*, Copper Mountain, CO, 2012.

85. M.-A. Springuel-Huet, A. Nossov, Z. Adem, F. Guenneau, C. Volkringer, T. Loiseau, G. Férey and A. Gedeon, *J. Am. Chem. Soc.*, **2010**, *132*, 11599.

86. A. F. Cronsted, *Akad. Handl.*, **1756**, *17*, 20.

87. W. Lowenstein, *Am. Miner.*, **1954**, *39*, 92.

88. C. Baerlocher and L. B. McCusker, *Database of Zeolite Structures*, http://www.iza-structure.org/databases, Accessed 20th Oct, 2013.

89. W. W. Kaeding, C. Chu, L. B. Young, B. Weinstein and S. A. Butter, *J. Catal.*, **1981**, *67*, 159.

90. K. J. D. MacKenzie and M. E. Smith, *Multinuclear Solid-State NMR of Inorganic Materials*, 1st edn., Elsevier Science Ltd, Oxford, UK, 2002.

91. L. Frydman and J. S. Harwood, *J. Am. Chem. Soc.*, **1995**, *117*, 5367.

92. A. Medek, J. S. Harwood and L. Frydman, *J. Am. Chem. Soc.*, **1995**, *117*, 12779.

93. H. K. C. Timken, G. L. Turner, J. P. Gilson, L. B. Welsh and E. Oldfield, *J. Am. Chem. Soc.*, **1986**, *108*, 7231.

94. H. K. C. Timken, N. Janes, G. L. Turner, S. L. Lambert, L. B. Welsh and E. Oldfield, *J. Am. Chem. Soc.*, **1986**, *108*, 7236.

95. S. T. Wilson, B. M. Lok, C. A. Messina, T. R. Cannan and E. M. Flanigen, *J. Am. Chem. Soc.*, **1982**, *104*, 1146.

96. E. R. Parnham, *Ph.D. Thesis*, University of St Andrews, 2006.

97. E. R. Cooper, C. D. Andrews, P. S. Wheatley, P. B. Webb, P. Wormald and R. E. Morris, *Nature*, **2004**, *430*, 1012.

98. E. R. Parnham and R. E. Morris, *Chem. Mater.*, **2006**, *18*, 4482.

99. M. M. Harding and B. M. Kariuki, *Acta Crystallogr.*, **1994**, *50*, 852.

100. J. M. Bennett, J. W. Richardson, J. J. Pluth and J. V. Smith, *Zeolites*, **1987**, *7*, 160.

101. R. W. Broach, S. T. Wilson and R. M. Kirchner, *Micropor. Mesopor. Mater.*, **2003**, *57*, 211.

102. R. M. Kirchner and J. M. Bennett, *Zeolites*, **1994**, *14*, 523.

103. M. E. Davis, C. Saldarriaga, C. Montes, J. Garces and C. Crowder, *Nature*, **1988**, *331*, 698.

104. P. L. Gai-Boyes, J. M. Thomas, P. A. Wright, R. H. Jones, S. Natarajan, J. S. Chen and R. R. Xu, *J. Phys. Chem.*, **1992**, *96*, 8206.

105. R. M. Kirchner, R. W. Grosse-Kunstleve, J. J. Pluth, S. T. Wilson, R. W. Broach and J. V. Smith, *Micropor. Mesopor. Mater.*, **2000**, *39*, 319.

106. S. E. Ashbrook, M. Cutajar, J. M. Griffin, Z. A. D. Lethbridge, R. I. Walton and S. Wimperis, *J. Phys. Chem. C*, **2009**, *113*, 10780.

107. S. Caldarelli, A. Meden and A. Tuel, *J. Phys. Chem. B*, **1999**, *103*, 5477.

108. M. Roux, C. Marichal, J. M. Le Meins, C. Baerlocher and J. M. Chezeau, *Micropor. Mesopor. Mater.*, **2003**, *63*, 162.

109. B. M. Lok, C. A. Messina, R. L. Patton, R. T. Gajek, T. R. Cannan and E. M. Flanigen, *J. Am. Chem. Soc.*, **1984**, *106*, 6092.

110. G. Lischke, B. Parlitz, U. Lohse, E. Schreier and R. Fricke, *Appl. Catal. A*, **1998**, *166*, 351.

111. A. L. Picone, S. J. Warrender, A. M. Z. Slawin, D. M. Dawson, S. E. Ashbrook, P. A. Wright, S. P. Thompson, L. Gaberova, P. L. Llewellyn, B. Moulin, A. Vimont, M. Daturi, M. B. Park, S. K. Sung, I.-S. Nam and S. B. Hong, *Micropor. Mesopor. Mater.*, **2011**, *146*, 36.

112. K. Mathisen, D. G. Nicholson, A. M. Beale, M. Sanchez-Sanchez, G. Sankar, W. Bras and S. Nikitenko, *J. Phys. Chem. C*, **2007**, *111*, 3130.

113. Y. Wei, Z. Tian, H. Gies, R. Xu, H. Ma, R. Pei, W. Zhang, Y. Xu, L. Wang, K. Li, B. Wang, G. Wen and L. Lin, *Angew. Chem. Int. Ed.*, **2010**, *49*, 5367.

114. M. Amri and R. I. Walton, *Chem. Mater.*, **2009**, *21*, 3380.

115. S. Antonijevic, S. E. Ashbrook, S. Biedasek, R. I. Walton, S. Wimperis and H. X. Yang, *J. Am. Chem. Soc.*, **2006**, *128*, 8054.

116. D. Müller, E. Jahn, G. Ladwig and U. Haubenreisser, *Chem. Phys. Lett.*, **1984**, *109*, 332.

117. K. Kanehashi, T. Nemoto and K. Saito, *J. Non-Cryst. Solids*, **2007**, *353*, 4227.

118. V. Campomar, *Ph.D. Thesis*, Université P. et M. Curie, 1990.

119. J. M. Griffin, L. Clark, V. R. Seymour, D. W. Aldous, D. M. Dawson, D. Iuga, R. E. Morris and S. E. Ashbrook, *Chem. Sci.*, **2012**, *3*, 2293.

120. O. Steward, *MChem Thesis*, University of St Andrews, 2012.

121. M. Estermann, L. B. McCusker, C. Baerlocher, A. Merrouche and H. Kessler, *Nature*, **1991**, *352*, 320.

122. G. Férey, *C. R. Acad. Sci. Ser. IIC*, **1998**, *1*, 1.

123. S. Girard, J. D. Gale, C. Mellot-Draznieks and G. Férey, *J. Am. Chem. Soc.*, **2002**, *124*, 1040.

124. C. Schott-Darie, H. Kessler, M. Soulard, V. Gramlich and E. Benazzi, *Stud. Surf. Sci. Catal.*, **1994**, *84*, 101.

125. M. Amri, S. E. Ashbrook, D. M. Dawson, J. M. Griffin, R. I. Walton and S. Wimperis, *J. Phys. Chem. C*, **2012**, *116*, 15048.

126. M. Richter, H. L. Zubowa, R. Eckelt and R. Fricke, *Micropor. Mater.*, **1996**, *7*, 119.

127. M. Richter, H. Fischer, M. Bartoszek, H. L. Zubowa and R. Fricke, *Micropor. Mater.*, **1997**, *8*, 69.

128. P. Pyykko, *Mol. Phys.*, **2008**, *106*, 1965.

129. S. M. Bradley, R. F. Howe and R. A. Kydd, *Magn. Reson. Chem.*, **1993**, *31*, 883.

130. D. Massiot, T. Vosegaard, N. Magneron, D. Trumeau, V. Montouillout, P. Berthet, T. Loiseau and B. Bujoli, *Solid State Nucl. Magn. Reson.*, **1999**, *15*, 159.

131. L. Lakiss, A. Simon-Masseron and J. Patarin, *Micropor. Mesopor. Mater.*, **2005**, *84*, 50.

132. L. Lakiss, A. Simon-Masseron, V. Gramlich, G. Chaplais and J. Patarin, *Micropor. Mesopor. Mater.*, **2008**, *114*, 82.

133. T. Loiseau, F. Taulelle and G. Férey, *Micropor. Mater.*, **1996**, *5*, 365.

134. T. Loiseau, F. Taulelle and G. Férey, *Micropor. Mater.*, **1997**, *9*, 83.

135. T. Loiseau, C. Paulet, N. Simon, V. Munch, F. Taulelle and G. Férey, *Chem. Mater.*, **2000**, *12*, 1393.

136. A. Matijasic, J. L. Paillaud and J. Patarin, *J. Mater. Chem.*, **2000**, *10*, 1345.

137. A. Matijasic, V. Gramlich and J. Patarin, *J. Mater. Chem.*, **2001**, *11*, 2253.

138. A. Matijasic, V. Gramlich and J. Patarin, *Solid State Sci.*, **2001**, *3*, 155.

139. A. Matijasic, B. Marler, J. C. M. Acevedo, L. Josien and J. Patarin, *Chem. Mater.*, **2003**, *15*, 2614.

140. A. Merrouche, J. Patarin, H. Kessler, M. Soulard, L. Delmotte, J. L. Guth and J. F. Joly, *Zeolites*, **1992**, *12*, 226.

141. V. Munch, F. Taulelle, T. Loiseau, G. Férey, A. K. Cheetham, S. Weigel and G. D. Stucky, *Magn. Reson. Chem.*, **1999**, *37*, s100.
142. P. Reinert, C. Schott-Darie and J. Patarin, *Micropor. Mater.*, **1997**, *9*, 107.
143. P. Reinert, J. Patarin, T. Loiseau, G. Férey and H. Kessler, *Micropor. Mesopor. Mater.*, **1998**, *22*, 43.
144. F. Taulelle, A. Samoson, T. Loiseau and G. Férey, *J. Phys. Chem. B*, **1998**, *102*, 8588.
145. D. S. Wragg, A. M. Z. Slawin and R. E. Morris, *J. Mater. Chem.*, **2001**, *11*, 1850.
146. T. Wessels, L. B. McCusker, C. Baerlocher, P. Reinert and J. Patarin, *Micropor. Mesopor. Mater.*, **1998**, *23*, 67.
147. Z. Yan, C. W. Kirby and Y. Huang, *J. Mater. Chem.*, **2010**, *20*, 10200.
148. B. Zibrowius, M. W. Anderson, W. Schmidt, F. F. Schuth, A. E. Aliev and K. D. M. Harris, *Zeolites*, **1993**, *13*, 607.

2 THEORETICAL BACKGROUND

2.1 ACKNOWLEDGEMENT

Dr Barbara Montanari (STFC), Professor Chris Pickard (UCL) and Dr Jonathan Yates (University of Oxford) are thanked for their kind and patient explanations of the principles of density functional theory, and for proof-reading Section 2.4.

2.2 CRYSTALLOGRAPHIC DIFFRACTION

2.2.1 The Unit Cell

A crystalline structure consists of a periodically repeating arrangement of atoms. The periodicity can be described by the crystallographic lattice; a three-dimensional array of equivalent points, related to each other by translations along the crystallographic vectors, **a**, **b** and **c** (where the bold typeface is used to denotes a vector). The lattice is described according to its type, which may be primitive (P), body-centred (I), face-centred (F) or side-centred (A, B or C), as shown in Figure 2.1. The lattice contains no chemical information and only shows the points in space that are equivalent by symmetry. The simplest repeating portion of the chemical structure is the asymmetric unit, which can be used to construct the unit cell by a series of symmetry operations (rotations, reflections, inversions and translations). The primitive unit cell is the smallest volume unit of the structure that can, through only translation along **a**, **b**, and **c**, generate the bulk structure of the material. It is also possible to define larger cells, which may enable more ready comparison between chemically-related structures with primitive unit cells of very different sizes. The symmetry operations define the crystal system of the lattice and, except for the triclinic crystal system, the lattice vectors are not totally independent. There are seven crystal systems, which define the relationships between the lattice vectors, as described by the unit cell dimensions, a, b and c, and angles α, β and γ, as given in Table 2.1 and shown in Figure 2.2. The combination of the crystal system and lattice type determines the Bravais lattice and, of the 28 possible combinations, there are 14 unique Bravais lattices.

The symmetry group of a crystal describes the symmetry operations required to reconstruct the entire crystal structure from the asymmetric unit. As much of the

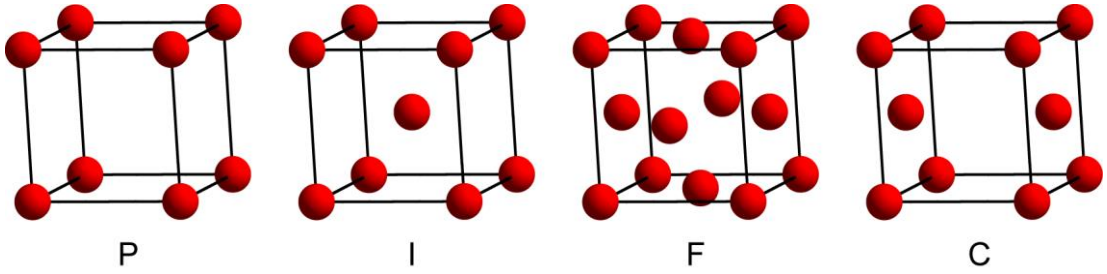

Figure 2.1. The four different lattice types are primitive (P), body-centred (I), face-centred (F) and side-centred (C-centred is shown). Lattice points are indicated in red.

Table 2.1. The seven crystal systems, minimum symmetry operations required for a unit cell to belong to these systems, and constraints imposed on the unit cell.[1]

Crystal System	Required Symmetry	Unit Cell Constraints
Triclinic	none	none
Monoclinic	one two-fold axis or symmetry plane	$a \neq b \neq c$ $\alpha = \gamma = 90°, \beta \neq 90°$
Orthorhombic	any combination of three mutually-perpendicular two-fold axes or symmetry planes	$a \neq b \neq c$ $\alpha = \beta = \gamma = 90°$
Trigonal	One three-fold axis	$a = b = c$ $\alpha = \beta = \gamma \neq 90°$
Tetragonal	One four-fold axis or four-fold improper axis	$a = b \neq c$ $\alpha = \beta = \gamma = 90°$
Hexagonal	One six-fold axis or six-fold improper axis	$a = b$ $\alpha = \beta = 90°, \gamma = 120°$
Cubic	Four three-fold axes in a tetrahedral arrangement	$a = b = c$ $\alpha = \beta = \gamma = 90°$

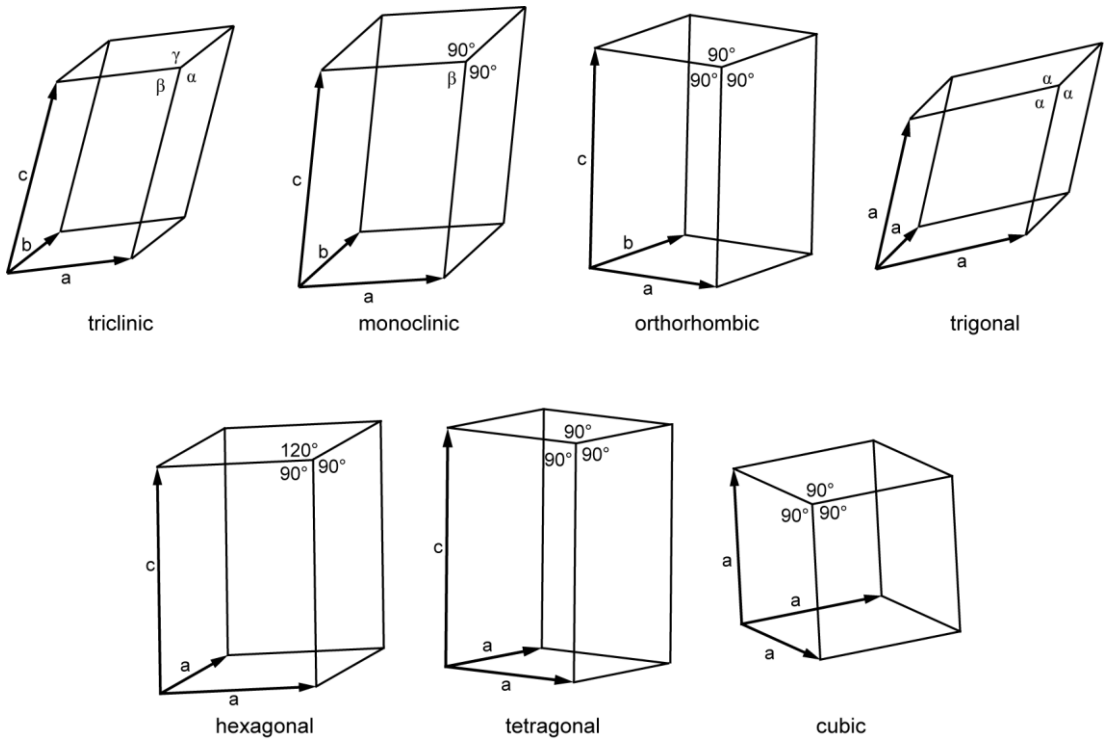

Figure 2.2. Unit cells for the seven crystal systems.

symmetry in crystals is at least partially translational in nature, crystal structures are described by space a space group, rather than the point groups (which just contain reflections, rotations and inversions) used for molecules. There are 230 unique space groups, characterised in the International Tables for Crystallography, Volume A.[2]

2.2.2 Miller Planes and Diffraction

A crystal can be considered as a series of equally-spaced planes (which need not contain any atoms), known as Miller planes and separated by the d-spacing, d_{hkl}. Each Miller plane is defined by the indices, h, k and l, which define how many of a given plane intersect the a, b and c axes of a single unit cell. If radiation of wave-length, λ, passes through an array of Miller planes, inclined at an angle, θ, to the incident radiation, some of the radiation will be reflected from the first plane, at an angle, 2θ, to the incident radiation. Some of the transmitted radiation will be reflected from the second plane at the same angle, and so on through the rest of the crystal. If the difference between the distance travelled by the radiation reflected from the different planes is an integer multiple, n, of λ, the radiation exiting the crystal at the angle of θ to the Miller planes will be in phase, resulting in constructive

interference, as shown in Figure 2.3. This is the basis of Bragg's Law,[3]

$$n\lambda = 2d_{hkl}\sin\theta \quad , \tag{2.1}$$

which can be seen to place strict constraints on the occurrence of constructive interference. An experiment in which 2θ is varied while the position of the crystal is held constant, therefore, provides very accurate values of d_{hkl} and, hence, a, b and c.

In order to satisfy Bragg's Law, it can be seen that λ must be on the order of d_{hkl}, which is typically on the Å scale. The X-ray region of the electromagnetic spectrum has wavelengths of ~1 Å and the electrons of atoms are capable of reflecting X-rays. As such, X-rays are commonly used in crystallographic diffraction techniques, but such experiments can suffer from a number of problems. The first of these is that X-rays are reflected by electrons and, as such, cannot distinguish between different species with the same (or very similar) electron density. The most pertinent example of this is the case of HO^- and F^-, mentioned briefly in the preceding chapter. These chemically different species are isoelectronic and, therefore, cannot be distinguished by X-ray diffraction (XRD). Furthermore, XRD lacks a good contrast range, so that if there are atoms that reflect X-rays very strongly (*i.e.*, atoms such as heavy metals, which have a high electron density), then these reflections will dominate those from any lighter atoms (*e.g.*, C, N and O). In almost all cases, there are elements substantially heavier than H present, so the locations of H atoms determined by XRD are very rarely reliable (and, indeed, are often added manually after determining the rest of the structure). This can be problematic for materials such as GaPOs, which contain relatively electron-rich Ga and P, less electron-rich C, N, O and F, and very electron-poor H. In addition, atoms with similar numbers of electrons will have similar scattering behaviour so that it can be difficult to distinguish between, *e.g.*, Al and P or C and N in the framework or SDA, respectively, of an AlPO. In order to improve the quality of XRD data, it is possible to use a more intense radiation source, such as a synchrotron rather than a laboratory source. This provides improved intensity of the observed reflections, allowing a higher-resolution structure to be obtained, but the experiment requires access to a national or international facility. Furthermore, the fundamental problems discussed above still remain, particularly in terms of locating light elements and H.

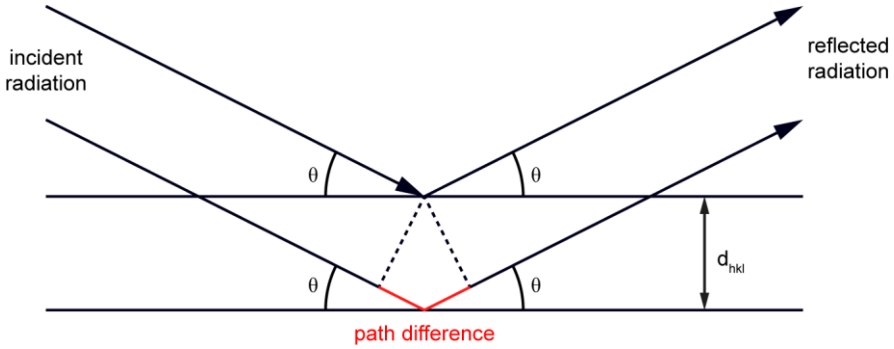

Figure 2.3. Schematic representation of radiation reflected by adjacent Miller planes.

Neutrons can be used as an alternative to X-rays for the incident radiation. Neutrons with λ similar to d_{hkl} can be generated, although the process requires a nuclear reactor, restricting the technique to a few national and international facilities. Nevertheless, neutron diffraction is still popular as it has several advantages over XRD. The most important of these is that neutrons interact with the nuclei rather than the electron clouds of atoms, meaning that the technique is both isotope-specific and much better equipped to locate lighter elements (although it is normally necessary to enrich with ^{2}H, as ^{1}H nuclei are still difficult to locate). Neutrons also possess a magnetic dipole moment, making them suitable probes for any magnetic ordering within the material. However, the much smaller scattering cross-section of an atomic nucleus compared to the electron cloud surrounding that nucleus makes neutron diffraction experiments very insensitive compared to XRD. Consequently, a very large sample mass (typically several grams of material) is required for neutron diffraction experiments, compared to a few dozen milligrams for XRD.

The main disadvantage of Bragg diffraction techniques (*i.e.*, experiments that determine the unit cell from Bragg's Law) is that these approaches require an ordered system with repeating Miller planes. This case is often true for simple materials but, for more interesting materials such as drug-loaded MOFs, there may be little or no long-range ordering (*e.g.*, of the guest species). Bragg diffraction techniques are, therefore, a poor choice for the characterisation of such systems, where the most important questions often relate to factors such as the location(s) and relative spatial distribution (*e.g.* "clustering" or "avoidance" behaviour) of the disordered species.

2.3 NUCLEAR MAGNETIC RESONANCE

As discussed above, while Bragg diffraction techniques provide a rapid and robust tool for the structural characterisation of ordered materials, their use is limited for disordered materials in which the overall periodicity is not changed (*e.g.*, in a SAPO, the framework remains the same in terms of connectivity, but the positions occupied by P in the parent framework are now occupied by either Si or P atoms, which appear as some "average" atom in any structure determined by Bragg diffraction). Nevertheless, local variations in periodicity (*e.g.*, Si clustering in SAPOs) may have a profound effect on the physical and chemical behaviour of the material and, therefore, a technique capable of investigating the local structure on an atomic level, rather than ordering on a bulk level, is required. As this section will discuss, solid-state NMR spectroscopy is a very sensitive probe to both structure and order on this level, and also to dynamic processes occurring on timescales covering more than ten orders of magnitude.

2.3.1 Fundamentals of NMR Spectroscopy

Key to NMR spectroscopy is the intrinsic quantum-mechanical property of spin angular momentum, described by a spin angular momentum vector, **I**, with corresponding spin quantum number, I. Both protons and neutrons have I = 1/2, meaning that, depending on the number of each, and their distribution in the atomic nucleus, atomic nuclei may also possess an overall spin. Nuclei with non-zero spin possess an overall nuclear spin angular momentum vector, **I**, which gives rise to a nuclear magnetic dipole moment, **μ**

$$\boldsymbol{\mu} = \gamma \mathbf{I} \ , \tag{2.2}$$

where the gyromagnetic ratio, γ, is the proportionality constant between **μ** and **I**. In the absence of an external magnetic field, **I** is quantised along an arbitrary z axis in units of $m_I\hbar$, such that

$$I_z = m_I\hbar \ , \tag{2.3}$$

where m_I is the magnetic quantum number, and may take values between +I and −I in integer steps, giving rise to 2I+1 degenerate spin states. It can be seen that **μ** must

also be quantised along the z axis, with

$$\mu_z = \gamma I_z \quad . \tag{2.4}$$

Nuclear magnetic moments interact with an external magnetic field (the Zeeman interaction), with the energy, E_0, of each spin state now dependent on its orientation with respect to the magnetic field vector, $\mathbf{B}_0$, which has magnitude B_0 and lies along the z axis by convention. E_0 depends only on the interactions of the z components of $\boldsymbol{\mu}$ and $\mathbf{B}_0$, such that

$$E_0 = -\mu_z B_0 \quad . \tag{2.5}$$

The energy difference between two spin states under the influence of an external magnetic field is, therefore

$$\Delta E = \Delta m_I \gamma \hbar B_0 \quad . \tag{2.6}$$

As the observation of transitions with $\Delta m_I \neq \pm 1$ is forbidden by the NMR selection rules (*i.e.*, only single-quantum transitions, in which the orientation of a single spin is changed, may be observed), all observable transitions in a system are degenerate with an energy difference of

$$|\Delta E| = \gamma \hbar B_0 \quad . \tag{2.7}$$

These transitions may be effected by electromagnetic radiation at the resonant frequency (termed the Larmor frequency), of

$$\omega_0 = -\gamma B_0 \quad , \tag{2.8}$$

in units of rad s^{-1}, or

$$\nu_0 = \frac{-\gamma B_0}{2\pi} \quad , \tag{2.9}$$

in units of Hz. In most NMR experiments, B_0 is between 4 and 24 T, and the Larmor frequency falls within the radiofrequency (rf) regime (~5-1000 MHz)

In a macroscopic ensemble of spins, the nuclear energy levels will be populated according to the Boltzmann distribution, with the equilibrium population

difference between adjacent energy levels given by

$$\frac{N_{m_I+1}}{N_{m_I}} = e^{\frac{-\gamma\hbar B_0}{k_B T}} \quad , \tag{2.10}$$

where N_{m_I} is the nuclear population of the m_I state, k_B is Boltzmann's constant and T is the absolute temperature. For spin I = 1/2 nuclei, the macroscopic magnetisation can be described in terms of a bulk magnetisation vector, **M**, which is composed of the sum of all the individual nuclear magnetic moments and whose magnitude, therefore, depends on the equilibrium population difference, ΔN_{eq},

$$\Delta N_{eq} = N_{m_I} - N_{m_I+1} \quad . \tag{2.11}$$

M can be considered as the measurable quantity for NMR experiments involving spin I = 1/2 nuclei, and it can be appreciated from Equation 2.10 that the number of spins contributing to **M** is very small, with some typical values given in Table 2.2. NMR is, consequently a very insensitive technique, requiring a large number of NMR-active nuclei to produce a small bulk magnetisation vector. For nuclei with spin I > 1/2, there are 2I + 1 possible orientations of the nuclear magnetic moments, and the concept of a bulk magnetisation vector is less applicable. However, some feel for the sensitivity of a NMR experiment involving a particular nucleus is given by the nuclear receptivity,

$$\text{receptivity} = \gamma^3 N\big(I(I+1)\big) \quad , \tag{2.12}$$

where N is the natural abundance of the nucleus of interest. It can be seen that the receptivity is greatest for nuclei with high γ, high N, and high spin, as shown in Figure 2.4 although, as discussed in later sections, the receptivity is not necessarily representative of the ease of conducting an experiment for a given nucleus.

2.3.2 Basic NMR Experiments

In a basic NMR experiment, the ensemble of nuclei (or "sample") is placed into a strong external magnetic field and allowed to achieve thermal equilibrium. The nuclear population is then disturbed from equilibrium by application of a short burst, or "pulse" of rf irradiation with frequency, ω_{rf}, at or near the Larmor frequency. While the pulse is applied in the static, or laboratory frame, it is convenient to

Table 2.2. Comparison of the nuclear population differences (expressed as nuclei per 10^6 contributing to **M**) resulting from the Zeeman interaction for some common nuclei with external magnetic fields of B_0 = 9.4, 14.1 and 20.0 T.

Nucleus	Population difference at B_0		
	9.4 T	14.1 T	20.0 T
^{1}H	32.0	48.0	68.1
^{13}C	8.1	12.1	17.1
^{15}N[a]	3.2	4.9	6.9
^{31}P	13.0	19.5	27.6

a. ^{15}N has a negative gyromagnetic ratio, and so the positive nuclear population difference is for the transition $m_I = +1/2 \rightarrow m_I = -1/2$ rather than $m_I = -1/2 \rightarrow m_I = +1/2$, as for the other nuclei, all of which have positive gyromagnetic ratios.

consider its effects on **M** in the "rotating frame"; a frame in which the z axis is coincident with the laboratory z axis (defined by $\mathbf{B}_0$) and the x and y axes rotate in the laboratory xy plane at $+\omega_{rf}$. In the laboratory frame, the pulse appears as two counter-rotating components with angular frequencies of $\pm\omega_{rf}$, whereas in the rotating frame, the component rotating at $+\omega_{rf}$ appears static while the component rotating at $-\omega_{rf}$ in the laboratory frame appears to rotate at $-2\omega_{rf}$ in the rotating frame and its effects can be ignored. The pulse, therefore, can be considered as a fixed magnetic field, $\mathbf{B}_1$, applied somewhere in the xy plane of the rotating frame. The orientation of the nuclear magnetic moments can then be altered by $\mathbf{B}_1$, with the result that **M** appears to nutate around the static $\mathbf{B}_1$ axis at a rate of

$$\omega_1 = -\gamma B_1 \quad , \tag{2.13}$$

where B_1 is the magnitude of $\mathbf{B}_1$ along the axis of application. Since the $\mathbf{B}_1$ axis may, in principle, have any orientation within the xy plane, it is necessary to define the phase, ϕ, of the pulse, which describes the relative orientations of $\mathbf{B}_1$ and the x and y axes. The extent of the nutation about the $\mathbf{B}_1$ axis, described by the "flip angle" of the pulse, β, is dependent on ω_1 and the duration of the pulse, τ_p

$$\beta = \tau_p \omega_1 \quad . \tag{2.14}$$

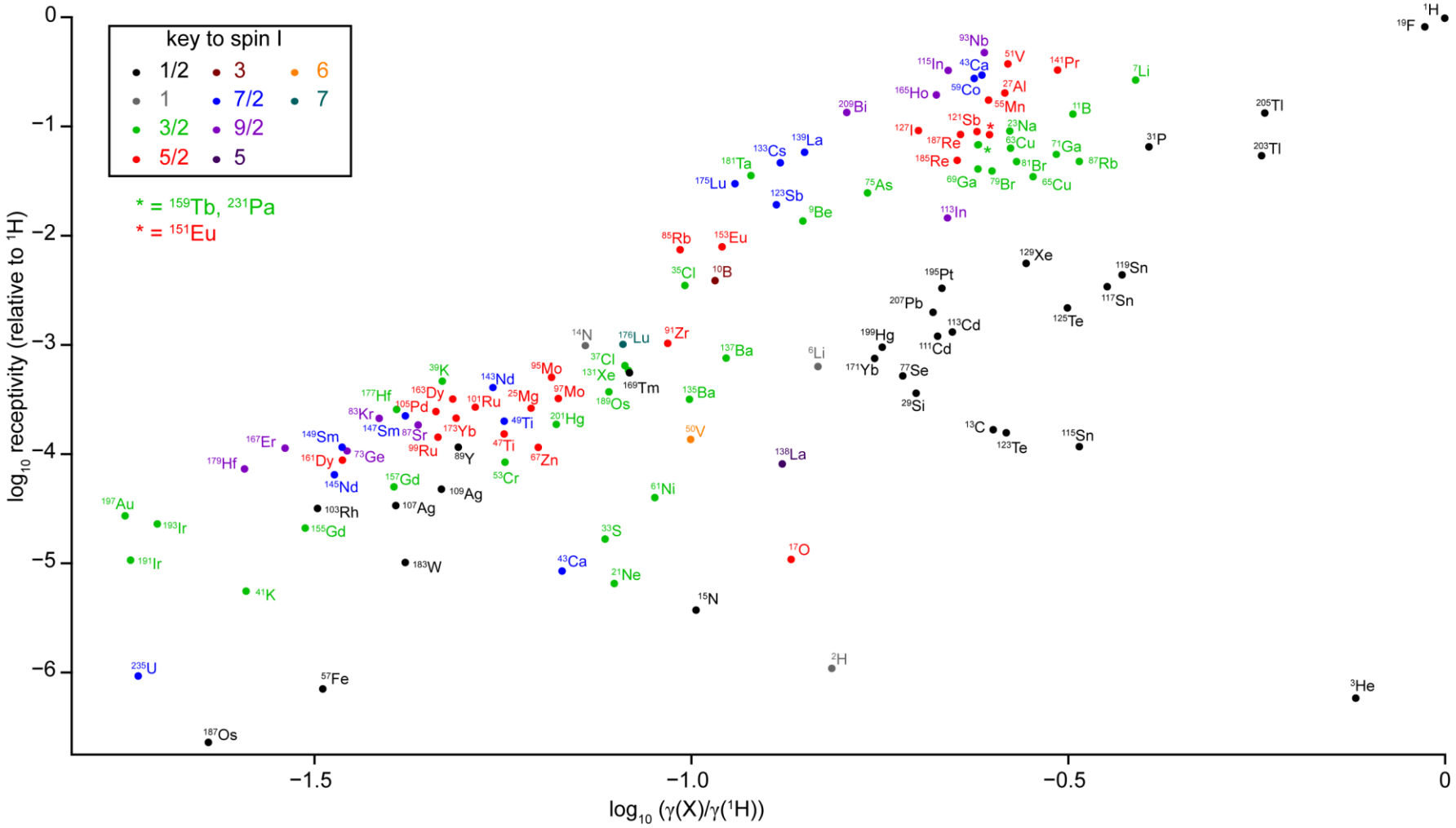

Figure 2.4. Plot of receptivity against ω_0 for some NMR-active nuclei. Both axes are logarithmic and values are plotted relative to ^{1}H.

It is common to describe pulses using the β_ϕ notation, where β may be given in degrees or radians, and ϕ may be given in degrees, radians, or in terms of the Cartesian axes, so that $\pi/2_{90}$, $\pi/2_{\pi/2}$, $\pi/2_y$, $90°_{90}$, $90°_{\pi/2}$ and $90°_y$ all describe the same pulse. Throughout this thesis, β will always be given in degrees and ϕ will be given either in degrees or in terms of Cartesian axes (when the phase coincides with one of these axes). Once the magnetic field supplied by the pulse is removed, the magnetic moments will continue their precession around the z axis at a frequency of ω_0, which, in the rotating frame, appears as precession in the xy plane at an offset with respect to ω_{rf} of

$$\Omega = \omega_0 - \omega_{rf} \quad . \tag{2.15}$$

If the pulse is "on resonance", *i.e.*, $\omega_{rf} = \omega_0$, then $\Omega = 0$ and **M** is static in the rotating frame.

Following a pulse, the system is in a non-equilibrium state and will return to equilibrium on a timescale described by the exponential longitudinal "spin-lattice" relaxation constant, T_1. There are many possible spin-lattice interactions, including motional processes and electronic and nuclear effects, giving a wide range of T_1 values in solids, on the order of ms to hours, depending on the nucleus and system of interest. In addition to spin-lattice relaxation, many spin-spin interactions contribute to transverse relaxation or "dephasing", described by the exponential time constant, T_2. Transverse relaxation is a loss of coherence in the xy plane, caused by different components of **M** precessing at frequencies between $\Omega + \Delta\Omega$ and $\Omega - \Delta\Omega$. After a time, t, the vector **M** will have a distribution of $2\Delta\Omega t$. Again, there are many possible internuclear and nucleus-electron interactions that can contribute to this relaxation, but it is generally observed that $T_1 \gg T_2$, with T_2 on the ms timescale for solids.

The precession of **M** in the xy plane is recorded as the complex time-dependent signal, S(t), which is often known as the free induction decay or FID. The acquisition use of a complex signal (or "quadrature detection") allows the sense of precession of **M** to be determined. By recording the precession with two different receiver phases, differing by 90°, the real and imaginary components of the FID are obtained. The part of the FID arising from precession has the form $e^{i\Omega t}$, which is

damped by the relaxation terms, e^{-t/T_1} and e^{-t/T_2}. However, by neglecting the e^{-t/T_1} term, which is typically ~1 when e^{-t/T_2} ~0 (assuming $T_1 \gg T_2$ for solids), the FID can be written as

$$S(t) = e^{i\Omega t}e^{-t/T_2} \quad . \tag{2.16}$$

An example FID is shown in Figure 2.5(a). Fourier transformation of S(t) yields the frequency-domain signal, S(ω), which contains a real "absorptive" component, A(Δω) and an imaginary "dispersive" component, D(Δω)

$$S(\omega) = A(\Delta\omega) - iD(\Delta\omega) \quad , \tag{2.17}$$

with

$$A(\Delta\omega) = \frac{1/T_2}{(1/T_2)^2+(\Delta\omega)^2} \quad , \tag{2.18}$$

and

$$D(\Delta\omega) = \frac{\Delta\omega}{(1/T_2)^2+(\Delta\omega)^2} \quad , \tag{2.19}$$

where $\Delta\omega = \omega - \Omega$. A(Δω) is an absorptive Lorentzian function centered on a frequency, Ω, with a full width at half height (FWHH) of $1/\pi T_2$, in Hz, as shown in Figure 2.5(b). D(Δω) is a dispersive Lorentzian function, as shown in Figure 2.5(c). By altering the phase of S(ω) so that the real component is purely absorptive (and the imaginary component is purely dispersive), it is possible to obtain spectra containing pure adsorption-mode lineshapes, as are generally reported. In almost all solids, there are multiple contributions to T_2; leading to a more Gaussian-like lineshape, with

$$A(\Delta\omega) = e^{\frac{-\Delta\omega^2}{2s^2}} \quad . \tag{2.20}$$

The FWHH given of a Gaussian function is $s\sqrt{2\ln 2}/2\pi$, where s is the second moment of the lineshape. It can be seen from Figure 2.5(d) that the Gaussian lineshape is significantly narrower at the base than the Lorentzian lineshape, whereas the Lorentzian lineshape is significantly sharper as $\Delta\omega \rightarrow 0$. Almost all experimental lineshapes (for solids) must, however, be described by a mixture of Lorentzian- and Gaussian-type behaviour.

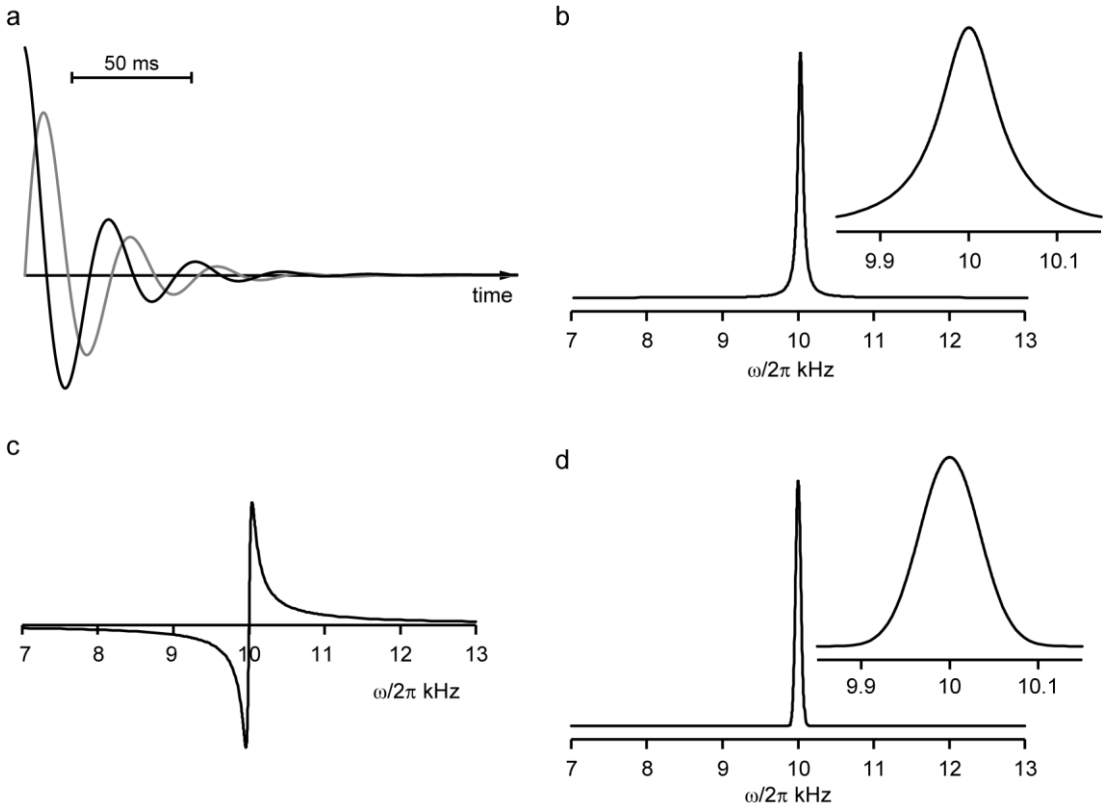

Figure 2.5. (a) A FID simulated according to Equation 2.16, with Ω = +10 kHz and T_2 = 25 ms. Real and imaginary components are shown in black and grey, respectively. Absorptive (b) and dispersive (c) Lorentzian functions simulated for T_2 = 25 ms (FWHH = 80 Hz). (d) Absorptive Gaussian function simulated with FWHH = 80 Hz (σ = 33.97 Hz).

In cases of very rapid transverse relaxation (*i.e.*, short T_2 leading to very broad lines), the FID intensity may decay to nearly zero by the time experimental data acquisition begins. This arises because a small amount of "dead" time must be included at the beginning of the experiment to avoid acquiring the distorted signal arising from the effects of the rf pulse on the probe hardware (often termed "ringing"). The dead time is typically ~10-100 μs, which can be a significant proportion of the FID for signals with very short T_2. In order to overcome this, a "spin echo" experiment may be used instead of the simple "one-pulse" or Bloch decay experiment outlined above. In simple terms, a spin-echo experiment consists of a $180°_x$ pulse applied at a time, τ, (often called the "echo duration") after the initial $90°_x$ pulse. The second pulse inverts the magnetic moments about the x axis

and, consequentially, after a second echo delay, τ, the dispersion of the magnetic moments is once again zero and the magnetisation has been "refocused". By setting τ to be greater than the dead time, one may record broad lines without distortion. The spin echo is also fundamental in many more advanced NMR experiments.

As NMR is an inherently insensitive technique, a single FID typically contains a very weak signal and a large amount of random "noise". Therefore, "signal averaging" is almost always carried out, in which the experiment is repeated N times and the resulting FIDs (or "transients") are coadded. Signal averaging improves the signal-to-noise ratio (SNR) of the resulting spectrum, as the true signal relating to the sample is the same in every FID and increases linearly with N. On the other hand, the noise is random and increases as $\sqrt{N}$, giving a $\sqrt{N}$-fold increase in the SNR. Signal averaging is extensively used in NMR, especially in cases where the signal per transient is low. In order for signal averaging to be successful, the population of spin states must be returned to thermal equilibrium prior to the start of each experiment. Once the magnetisation is in the xy plane, the time taken to return to equilibrium is determined by T_1, with the xy magnetisation at time, t, after the end of the pulse given by

$$M_{xy}(t) = M_0 e^{\frac{-t}{T_1}} , \tag{2.21}$$

and the z magnetisation given by

$$M_z(t) = M_0 \left(1 - e^{\frac{-t}{T_1}}\right) . \tag{2.22}$$

These functions are plotted in Figure 2.6, and it can be seen that the time taken to return to equilibrium is ~$5T_1$. This means that NMR spectra of nuclei with slow T_1 relaxation may require very long experimental times to achieve an acceptable SNR.

2.3.3 The Density Operator Formalism

While the vector model can describe experiments involving a single spin I = 1/2 nucleus, experiments involving more than one nucleus, or nuclei with higher spin quantum number, cannot be described by such a simplified approach. In principle, each spin system (*i.e.*, the nucleus and any other nearby nuclei or electrons) may be described completely by a wavefunction, $\Psi(t)$, which can be expanded in an

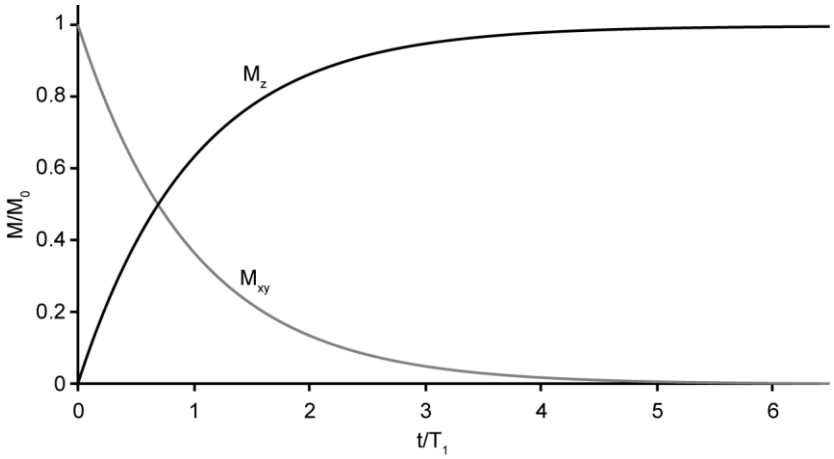

Figure 2.6. Plot of the magnetisation aligned with the $\mathbf{B}_0$ field (black) and remaining in the xy plane (grey) as a function of time, t/T_1, after the start of an experiment.

orthogonal basis set, $|i\rangle$

$$\Psi(t) = \sum_i c_i(t)\,|i\rangle\,, \tag{2.23}$$

where $c_i(t)$ are time-dependent coefficients. This approach to describing the system during an NMR experiment requires solving the Schrödinger equation for each component of the nuclear ensemble, which is unattractive for systems with more than a few atoms. The density operator, $\sigma(t)$, is a more compact representation of the ensemble spin density. In its matrix representation, $\sigma(t)$ has elements $\sigma_{i,j}(t)$

$$\sigma_{i,j}(t) = \langle i|\sigma(t)|j\rangle = \overline{c_i c_j^*}\,, \tag{2.24}$$

where the overbar denotes the ensemble average and the asterisk denotes the complex conjugate. From the density matrix, it is possible to determine the expectation value of any observable, O, from its appropriate operator, $\hat{O}$, as

$$\langle O\rangle = \mathrm{Tr}\{\sigma(t)\hat{O}\}\,, \tag{2.25}$$

where Tr{A} denotes the trace (*i.e.*, the average of the diagonal elements) of matrix A.[4] Of interest to NMR are the operators corresponding to the x, y and z components of the spin angular momentum (proportional to the magnetisation) in the rotating frame, I_x, I_y and I_z, respectively. Using these operators, S(t) may be expressed as

$$S(t) = \gamma \mathrm{Tr}\{\sigma(t)I_+\}\,, \tag{2.26}$$

where I_+ is defined as $I_x + iI_y$ (such that the x component of the magnetisation is real

signal and the y component is imaginary). The matrix representations of these operators are given in Appendix C.

Rather than expanding $\sigma(t)$ in the basis set, $|i\rangle$, it is often more convenient to use the eigenstates of the Zeeman Hamiltonian, $|m_l\rangle$, as the basis set, giving $\sigma(t)$ as a $(2I + 1) \times (2I + 1)$ square matrix. The diagonal elements, $\sigma_{ii}(t)$, represent the population of the corresponding Zeeman state, whereas off-diagonal elements represent coherent superpositions of eigenstates (*i.e.*, the population of the superposition is not averaged to zero over the ensemble), or "coherences". The elements, $\sigma_{i,i\pm1}(t)$, represent single-quantum coherences (with $\Delta m_l = \pm1$) with coherence order, p, of ±1 and, as mentioned above, are NMR observable. However, the use of quadrature detection means that only one of these coherences, by convention $p = -1$, is observed. Elements corresponding to higher coherence orders represent multiple-quantum coherences, which, while not directly observable, are important in many experiments, particularly for nuclei with $I > 1/2$.

2.3.4 The Product Operator Formalism

The matrix representation of the density operator quickly becomes unwieldy as the number of spin states of the system increases, and it is more convenient to express $\sigma(t)$ as a linear combination of the operators, I_x, I_y and I_z

$$\sigma(t) = a_x(t)I_x + a_y(t)I_y + a_z(t)I_z \quad , \tag{2.27}$$

where $a_x(t)$, $a_y(t)$ and $a_z(t)$ are time-dependent coefficients. The evolution of $\sigma(t)$ as a function of time is given by the Liouville-von Neumann equation

$$\frac{d\sigma(t)}{dt} = -i\left[\hat{H}(t),\sigma(t)\right] \quad , \tag{2.28}$$

where $\hat{H}(t)$, is the time-dependent Hamiltonian for the system. The solution to Equation 2.28 is

$$\sigma(t) = e^{-i\hat{H}t}\sigma(0)e^{i\hat{H}t} \quad , \tag{2.29}$$

where $\hat{H}(t)$ is given by

$$\hat{H}(t) = \Omega I_z \quad , \tag{2.30}$$

for periods of free precession and

$$\hat{H}(t) = \omega_1 I_x \ , \tag{2.31}$$

during pulses (assuming that the pulse is "hard", *i.e.*, $\omega_1 \gg \Omega$). Equation 2.29 can be rewritten in terms of the sine and cosine functions starting with $\sigma(0) = I_x$, I_y or I_z, as shown in Table 2.3,[5] where the angle, θ, is Ωt for free precession and $\omega_1 t$ for a pulse. The evolution of $\sigma(t)$ can be presented in the arrow notation:[5]

$$\sigma(0) \overset{\hat{H}t}{\rightarrow} \sigma(t) \ , \tag{2.32}$$

so that, for example, a conventional NMR experiment may be represented as:

$$I_z \overset{90°_y}{\longrightarrow} I_x \overset{\Omega t}{\rightarrow} \cos(\Omega t) I_x + \sin(\Omega t) I_y \ , \tag{2.33}$$

where the first arrow represents the pulse, and the second, free precession in the xy plane. The final operator is equivalent to S(t) in Equation 2.26.

The real power of the product operator approach, however, is in describing two coupled (or interacting) spins. For a single spin, three operators are required, I_x, I_y and I_z (plus the fourth identity operator, E, which is neglected as it never gives rise to observable magnetisation), whereas for two spins, 16 operators are required. These are all the possible products of an operator for the first spin, E_1, I_{1x}, I_{1y}, or I_{1z} and an operator for the second spin, E_2, I_{2x}, I_{2y}, I_{2z}. E can be neglected since, as for a single spin, it does not give rise to observable magnetisation. Terms involving one identity operator and one angular momentum operator (*e.g.*, I_{2x}) are single-quantum coherences, corresponding to coherent magnetisation on one of the spins. Operators in which both components describe x or y magnetisation (*e.g.*, $2I_{1x}I_{2x}$, where the factor of 2 is for normalisation purposes) represent double-quantum coherences, operators in which one of the components describes z magnetisation while the other describes x or y magnetisation (*e.g.*, $2I_{1x}I_{2z}$) are anti-phase (*i.e.*, only one of the pair of spins in the coherence is in the xy plane) and $2I_{1z}I_{2z}$ represents non-equilibrium population on both spins, aligned along the z-axis (*i.e.*, non-observable magnetisation). The use of such operators will be revisited in Chapter 3, for the interpretation of more advanced NMR experiments involving the transfer of magnetisation between two spins.

Table 2.3. Expressions for σ(t) following rotation of σ(0) around the, x, y or z axes by an angle, θ.[5]

σ(0)	rotation about	σ(t)
I_x	x	I_x
I_x	y	$\cos\theta\, I_x - \sin\theta\, I_z$
I_x	z	$\cos\theta\, I_x + \sin\theta\, I_y$
I_y	x	$\cos\theta\, I_y + \sin\theta\, I_z$
I_y	y	I_y
I_y	z	$\cos\theta\, I_y - \sin\theta\, I_x$
I_z	x	$\cos\theta\, I_z - \sin\theta\, I_y$
I_z	y	$\cos\theta\, I_z + \sin\theta\, I_x$
I_z	z	I_z

2.3.5 Phase Cycling

In general, a pulse will not only excite the desired coherence(s), but will result in a signal that contains a mixture of the desired coherence and several unwanted coherences. These unwanted coherences have the effect of distorting or cluttering the observed spectrum, and it is desirable to remove these wherever possible. By "phase cycling", *i.e.*, repeating the experiment several times with the relative phases of the pulses and receiver changed, and coadding the resulting FIDs, it is possible to select only the desired coherence and cancel out the unwanted coherences.[6]

2.3.6 Two-Dimensional NMR Experiments

Although a one-dimensional NMR experiment can often provide the desired information on a system, when probing the interaction between spins, it may be necessary to use a two-dimensional (2D) experiment. A 2D experiment typically comprises four basic blocks: preparation, evolution, mixing and detection. The preparation stage involves excitation of the first spin, *via* a pulse or series of pulses. During the evolution stage, the magnetisation evolves, either over time, or through a combination of time intervals and pulses. The duration of the evolution period is described by the variable, t_1. The mixing stage involves transfer of the magnetisation

between the two spins and, finally, the signal from the second spin is recorded during the detection stage. The detection period is characterised by the time variable, t_2. Evolution during t_1 is not recorded directly but, rather, the signal during t_2 is recorded with $t_1 = 0$, and then the experiment is repeated while t_1 is incremented. The intensity of the signal recorded during t_2 is, therefore, proportional to the intensity of the signal remaining after the t_1 evolution period. In this way, a 2D dataset, $S(t_1,t_2)$ is constructed from a series of one-dimensional FIDs. The fact that t_2 evolution is recorded directly, whereas the t_1 evolution is recorded indirectly leads to the two dimensions being known as the "direct" and "indirect" dimensions, respectively.

The 2D time-domain signal, $S(t_1,t_2)$ is converted to the frequency-domain signal, $S(\omega_1,\omega_2)$ by a 2D Fourier transform. As for a one-dimensional dataset, quadrature detection is an important part of 2D NMR experiments. Quadrature detection (for amplitude-modulated experiments, discussed in more detail in Chapter 3) during t_2 is achieved as described above. Two common methods exist for achieving quadrature detection in the indirect dimension, both involving manipulation of the phase of the t_1 signal. The method of States *et al.*,[7] involves acquisition of two data sets per t_1 increment, with the phase of the t_1 data incremented by 90°/p in the second dataset, where p is the coherence order present in the evolution period. Alternatively, for the time-proportional phase incrementation (TPPI) approach,[8] the t_1 increment is halved and the phase of the t_1 data incremented by 90°/p for each increment of t_1.

2.3.7 Interactions in NMR

From the above discussion, every element within a sample may be assumed to give rise to a resonance at its Larmor frequency, making NMR essentially an elaborate (and costly) means of elemental analysis. However, interactions between the nucleus and its surroundings (nuclei, filled electronic orbitals, unpaired electrons, and electric field gradients) alter the local magnetic field present at a specific nucleus, leading to a small but measurable difference in the observed resonance frequency. This fine structure in the NMR spectrum allows the technique to determine not simply *which* nuclei are present within a sample, but also *where* those nuclei are, with respect to their surroundings. As will be seen, this allows information on local geometry,

symmetry, chemical bonding, disorder and dynamics to be extracted from NMR spectra, making the technique a powerful probe of the local structures of materials.

2.3.7.1 The Chemical Shift

The Larmor frequency, ω_0, describes the resonant frequency of a free nucleus in a vacuum; an unlikely case in most materials. The electrons surrounding nuclei occupy either atomic or molecular orbitals, and their "motion" within these orbitals generates a small magnetic field, $\mathbf{B}'$, which, in a free atom, is opposed to $\mathbf{B}_0$, but may oppose or augment $\mathbf{B}_0$ when the electrons are located in molecular orbitals. The effective field at the nucleus, $\mathbf{B}_{\text{eff}}$, is

$$\mathbf{B}_{\text{eff}} = \mathbf{B}_0 - \mathbf{B}' = \mathbf{B}_0 (1 - \sigma) , \tag{2.34}$$

where σ is the dimensionless field-independent shielding constant. The resonant frequency of a nucleus subject to a chemical shielding interaction is, therefore

$$\omega_{\text{obs}} = \omega_0(1 - \sigma) . \tag{2.35}$$

As the absolute value of σ is hard to measure, it is common to report the ω_{obs} as a chemical shift, δ, relative to a known reference frequency, ω_{ref}

$$\delta = \frac{\omega_{\text{obs}} - \omega_{\text{ref}}}{\omega_{\text{ref}}} , \tag{2.36}$$

where normalisation by ω_{ref} ensures that δ is both dimensionless and field independent. The relationship between δ and σ is

$$\delta = \frac{\sigma - \sigma_{\text{ref}}}{1 - \sigma_{\text{ref}}} , \tag{2.37}$$

where σ_{ref} is the shielding constant giving rise to ω_{ref}. In most cases, $\sigma_{\text{ref}} \ll 1$, and Equation 2.37 can be simplified to

$$\delta = \sigma_{\text{ref}} - \sigma . \tag{2.38}$$

It can be seen that, whereas σ describes the shielding of the nucleus, δ describes the deshielding of the nucleus, as it is opposite in sign. Typically, $\delta \ll 1$ and is reported in parts per million (1 ppm = 10^{-6}). The chemical shift of the primary reference compound is set to zero, with various secondary reference compounds of known (but non-zero) chemical shifts used for different nuclei for reasons such as ease of

handling, toxicity, or ready availability. In some cases (*e.g.*, $^{14/15}$N), there exist multiple primary reference frequencies, and care must be taken in interpreting reported chemical shift values for these nuclei. A table of primary and secondary reference compounds used in this work is given in Appendix D. Except in cases of very high symmetry, the electron density around a nucleus cannot be described as spherical and the chemical shielding must be described by the anisotropic shielding tensor, $\boldsymbol{\sigma}$, rather than the isotropic scalar, σ. In the laboratory frame, $\boldsymbol{\sigma}$ is given by

$$\boldsymbol{\sigma}^{\text{lab}} = \begin{pmatrix} \sigma_{xx} & \sigma_{xy} & \sigma_{xz} \\ \sigma_{yx} & \sigma_{yy} & \sigma_{yz} \\ \sigma_{zx} & \sigma_{zy} & \sigma_{zz} \end{pmatrix}. \tag{2.39}$$

$\boldsymbol{\sigma}^{\text{lab}}$ may be defined with respect to a set of orthogonal axes – the Principal Axis System, or PAS, such that $\boldsymbol{\sigma}^{\text{PAS}}$ is diagonal

$$\boldsymbol{\sigma}^{\text{PAS}} = \begin{pmatrix} \sigma_{11} & 0 & 0 \\ 0 & \sigma_{22} & 0 \\ 0 & 0 & \sigma_{33} \end{pmatrix}. \tag{2.40}$$

The corresponding chemical shift tensor, $\boldsymbol{\delta}^{\text{PAS}}$, is given by

$$\boldsymbol{\delta}^{\text{PAS}} = \begin{pmatrix} \delta_{11} & 0 & 0 \\ 0 & \delta_{22} & 0 \\ 0 & 0 & \delta_{33} \end{pmatrix}, \tag{2.41}$$

where

$$\delta_{ii} = \sigma_{\text{ref}} - \sigma_{ii} \ , \tag{2.42}$$

and, by the IUPAC, or "standard" convention,[9] $\delta_{11} \geq \delta_{22} \geq \delta_{33}$. These three principal components may also be reported in the Haeberlen notation,[10] where they are known as δ_{xx}, δ_{yy} and δ_{zz}, and ordered so that $|\delta_{zz} - \delta_{iso}| \geq |\delta_{yy} - \delta_{iso}| \geq |\delta_{xx} - \delta_{iso}|$, where the isotropic chemical shift, δ_{iso}, is the trace of $\boldsymbol{\delta}^{\text{PAS}}$. The PAS is related to the laboratory frame by the three Euler angles, α (rotation around the PAS 11 axis), β (rotation around the new 22′ axis) and γ (rotation around the new 11″ axis), as shown in Figure 2.7(a). For every crystallite in the sample, $\boldsymbol{\delta}^{\text{PAS}}$ is the same, but α, β and γ are different. In the secular approximation, only the z component of the shielding tensor (in the laboratory frame) can interact with $\mathbf{B}_0$ (in the laboratory frame by definition). The chemical shift of a nucleus will depend not only on $\boldsymbol{\delta}^{\text{PAS}}$, but also the relative

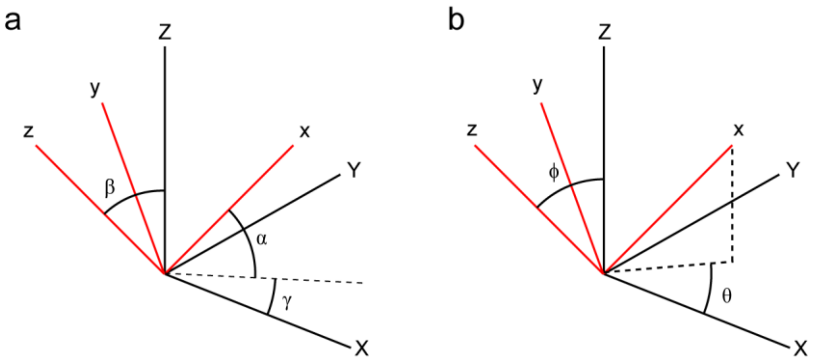

Figure 2.7. Rotation of a set of axes from one frame (red; x, y and z) to another (black; X, Y and Z) by (a) three successive rotations described by the Euler angles, α, β and γ, or (b) two successive rotations described by the polar angles, θ and ϕ. In part (a), the dotted line is normal to the zZ plane and in part (b) the dotted lines represent the XY and Z components of the x axis.

orientations of the internal and external magnetic fields. The orientation of **δ** with respect to $\mathbf{B}_0$ can also be described in terms of the polar angles, θ and ϕ, which represent a rotation about and a tilt away from the laboratory z axis, respectively, as shown in Figure 2.7(b). Using these angles, the observed chemical shift of a nucleus in a given crystallite is

$$\delta = \delta_{iso} + \frac{\Delta_{cs}}{2}\left[(3\cos^2\theta - 1) + \eta_{CS}\left(\sin^2\theta\cos 2\phi\right)\right] \quad . \qquad (2.43)$$

The chemical shift anisotropy (CSA), Δ_{cs}, and asymmetry, η_{cs}, are defined, using the Haeberlen convention, as

$$\Delta_{CS} = \delta_{zz} - \delta_{iso} \quad , \qquad (2.44)$$

and

$$\eta_{CS} = \frac{\delta_{yy} - \delta_{xx}}{\Delta_{cs}} \quad , \qquad (2.45)$$

It can be seen that, when $\Delta_{CS} \geq 0$, $\delta_{11} = \delta_{zz}$ and $\delta_{33} = \delta_{yy}$, whereas these two identities will be swapped when $\Delta_{CS} \leq 0$. For a single crystallite, the anisotropic part of $\boldsymbol{\delta}^{PAS}$ results in an orientation-dependent chemical shift whereas, for a powdered sample, in which a statistical distribution of all crystallite orientations is present, the result is a broadened resonance, with frequency extremes of δ_{11} and δ_{33} (or δ_{xx} and δ_{zz}), as

shown in Figure 2.8. As indicated above, several conventions exist for relating the spectral lineshapes to $\boldsymbol{\delta}^{PAS}$. The Haeberlen convention is popular as the parameters, δ_{iso}, Δ_{cs} and η_{cs}, describe how the lineshape will appear, as shown in Figure 2.9(a). The standard (but by no means the most common) notation simply lists the three principal components of $\boldsymbol{\delta}^{PAS}$, which define the tensor exactly, and provide the location of the three singularities in the spectrum, as shown in Figure 2.9(b). The Herzfeld-Berger,[11] or "Maryland",[12] convention uses the same ordering convention for δ_{ii} as the standard notation, but describes the lineshape in terms of its span, or "width", Ω_{cs}, and skew, or "shape", κ_{cs}, defined as

$$\Omega_{cs} = \delta_{11} - \delta_{33} \ , \tag{2.46}$$

and

$$\kappa_{cs} = \frac{3(\delta_{22} - \delta_{iso})}{\Omega_{cs}} \ . \tag{2.47}$$

These parameters also indicate the appearance of the lineshape, as shown in Figure 2.9(b). It is important to note that these conventions all describe the same tensor, $\boldsymbol{\delta}^{PAS}$, although, to cause confusion, δ_{ii} may be ordered in two different ways, and the δ_{11}, δ_{22} and δ_{33} labels are often used in place of δ_{xx}, δ_{yy} and δ_{zz} in the literature. The remainder of this thesis uses the standard notation.

2.3.7.2 The Dipolar Interaction

In addition to the chemical shift, the resonant frequency of a nucleus is often affected by interactions with other nuclei. The through-space internuclear dipolar coupling between two nuclear spins, I and S, has the interaction tensor, **D**, or $\mathbf{D}^{PAS}$ in the PAS. $\mathbf{D}^{PAS}$ is traceless and axially symmetric, meaning that there is no isotropic dipolar shift. However, there is an anisotropic component, ω_D

$$\omega_D = \omega_D^{PAS} \frac{1}{2}(3\cos^2\theta_{IS} - 1) \ , \tag{2.48}$$

where

$$\omega_D^{PAS} = -\frac{\mu_0}{4\pi}\frac{\gamma_I\gamma_S\hbar}{r_{IS}^2} \ . \tag{2.49}$$

As shown in Figure 2.10(a), the nuclei, I and S (with gyromagnetic ratios of γ_I and γ_S,

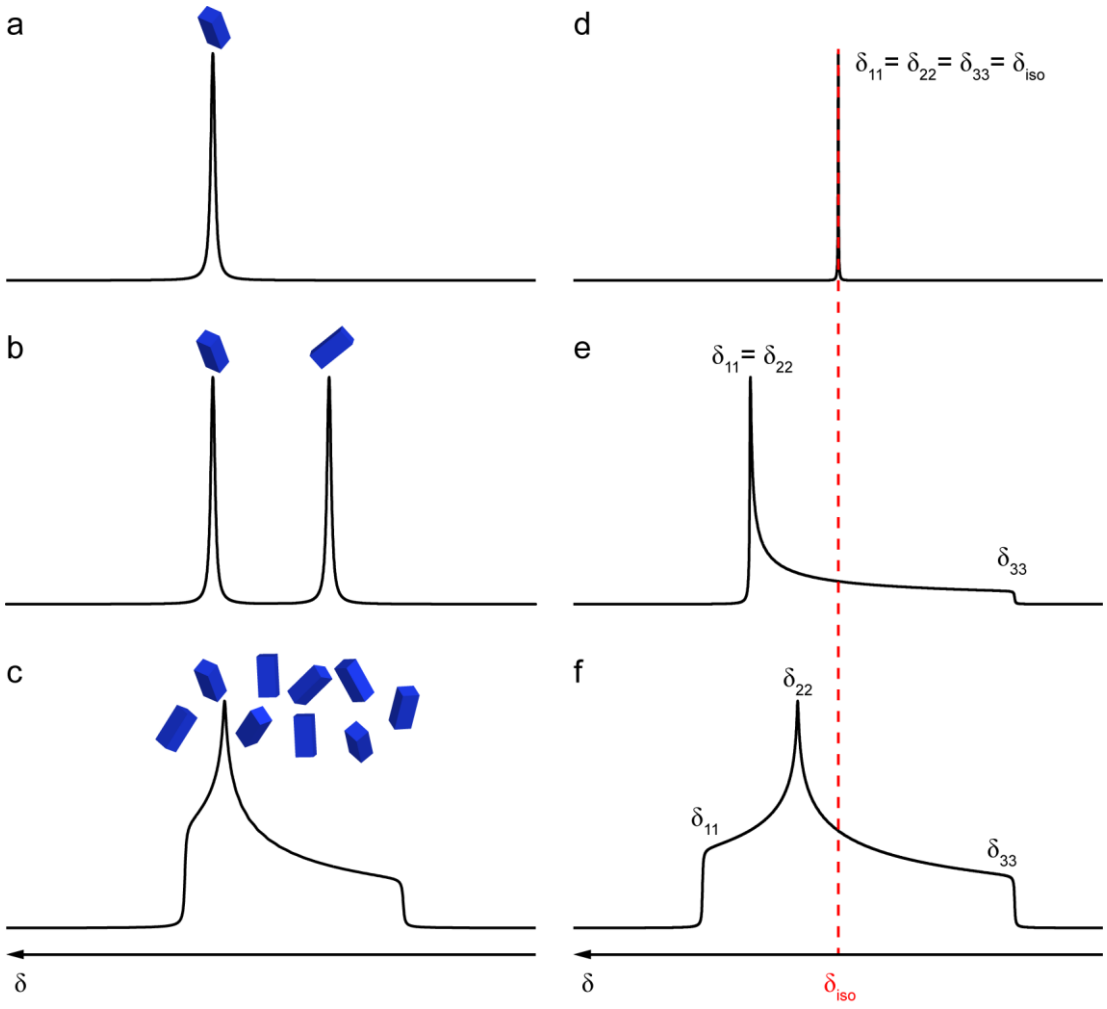

Figure 2.8. The anisotropic nature of the chemical shift tensor gives rise to (a) an orientation-dependent shift for a single-crystal sample, (b) distinct resonances for two identical crystallites with different orientations and (c) a broad "powder pattern" lineshape for a polycrystalline sample. The appearance of the lineshape depends on the symmetry of δ^{PAS}, described by Δ_{cs} and η_{cs}. Schematic spectra are shown for (d) spherically-symmetric ($\Delta_{cs} = 0$, $\eta_{cs} = 0$), (e) axially-symmetric ($\Delta_{cs} > 0$, $\eta_{cs} = 0$) and (f) axially-asymmetric ($\Delta_{cs} > 0$, $\eta_{cs} \neq 0$) shielding tensors. The positions of the principal components of δ are indicated using the standard notation.

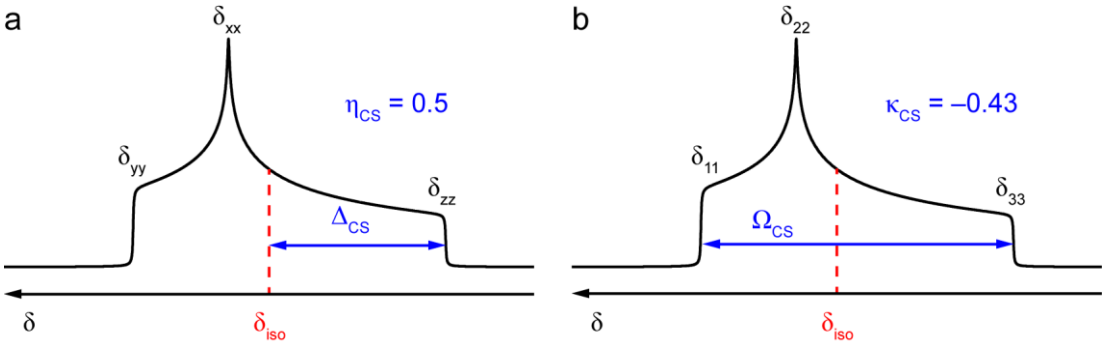

Figure 2.9. Schematic spectrum of a spin I = 1/2 nucleus, broadened by an anisotropic chemical shift interaction, with the parameters describing the CSA in terms of (a) the Haeberlen notation and (b) the standard and Herzfeld-Berger notations indicated.[9-11]

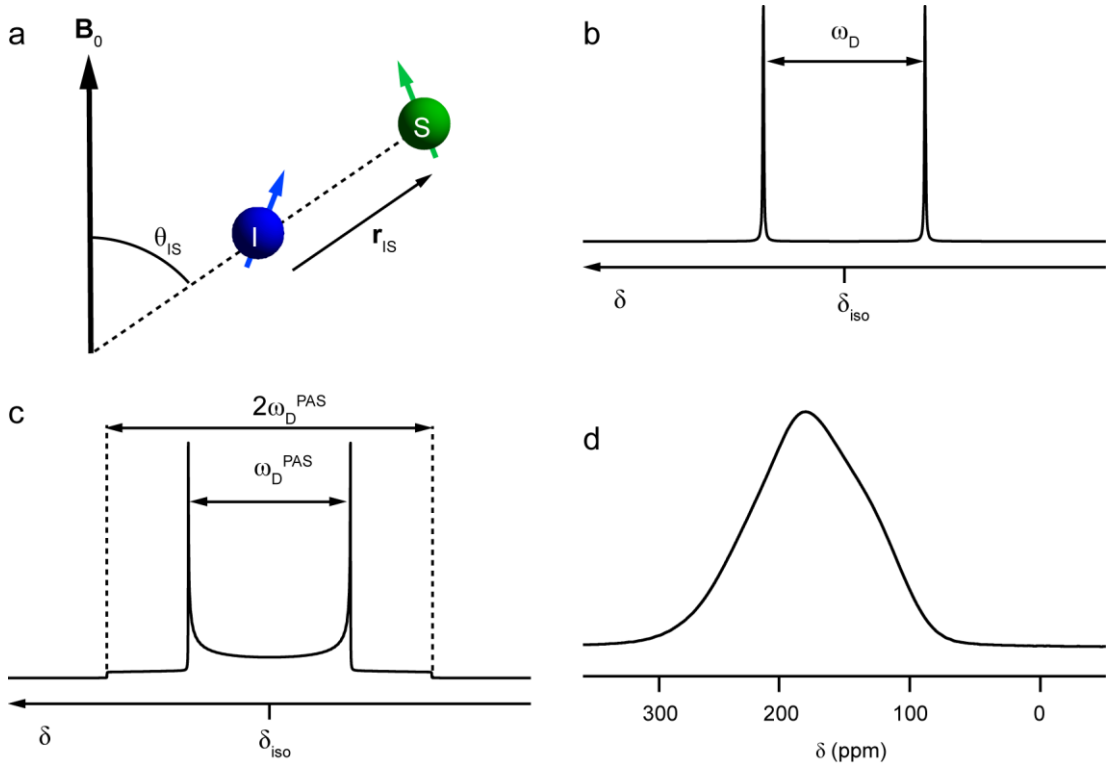

Figure 2.10. (a) Schematic representation of the dipolar interaction between two nuclei, I = 1/2 and S = 1/2. Schematic spectra for (b) a single crystallite and (c) a powdered sample of a material containing isolated heteronuclear I-S spin pairs, with I = 1/2, S = 1/2. (d) Experimental (9.4 T) ^{13}C NMR spectrum of 1[^{13}C]-glycine, showing the Gaussian-like broadening of the resonance.

respectively) are joined by the internuclear vector, $\mathbf{r}_{IS}$, of length r_{IS}, oriented at an angle θ_{IS} relative to $\mathbf{B}_0$. For a single-crystallite containing isolated spin pairs, this results in a doublet with an orientation-dependent splitting of ω_D, as shown in Figure 2.10(b). In a polycrystalline sample, this leads to a lineshape known as a Pake doublet,[13] which is composed of two powder-pattern lineshapes superimposed on one another with a peak separation of ω_D^{PAS} and an overall width of $2\,\omega_D^{PAS}$ for the heteronuclear dipolar interaction ($I \neq S$), as shown in Figure 2.10(c), or $3\omega_D^{PAS}$ for the homonuclear dipolar interaction ($I = S$). Isolated spin pairs are rare in practice, however, owing to the relatively long-range influence of the dipolar interaction, which means that each spin experiences many different dipolar interactions with different magnitudes and orientations. Consequently, the dipolar interaction is typically observed as a Gaussian broadening of the lineshape, as shown in Figure 2.10(d) for the ^{13}C NMR spectrum of 1[^{13}C]-glycine.

2.3.7.3 The Scalar Coupling

In addition to the direct through-space internuclear dipolar interaction, it is also possible for information on nearby nuclear spins to be transferred between nuclei *via* the through-bond (*i.e.*, electron-mediated) "scalar" (or J) coupling interaction. While strictly described by an anisotropic tensor, **J**, giving rise to both an isotropic splitting component (*i.e.*, the coupling constant, J) and an anisotropic broadening, these effects are typically on the order of a few tens or hundreds of Hz, meaning that this interaction is rarely observed in solids, as the other interactions influencing the spectral lineshapes are typically several orders of magnitude greater. However, the scalar coupling is still present in solids and, as discussed below, is used as the basis of some magnetisation transfer experiments.

2.3.7.4 Interactions with Unpaired Electrons

Electrons have spin $S = 1/2$, and can interact with atomic nuclei. In diamagnetic solids, the electrons are paired and only the indirect effects of electron-nuclear interactions (chemical shielding and scalar couplings) are observed. In paramagnetic materials, the unpaired electrons interact with their parent nucleus (*i.e.*, the nucleus of the atom formally bearing the half-filled orbital), any nearby bonded nuclei, and

other nuclei within a radius of up to ~100 Å from the parent nucleus. The magnitude and spatial extent of this interaction are generally very large as γ of an electron is ~660 times greater than that of ^{1}H. The interaction between a nucleus and an unpaired electron has four main contributions – a through-space dipolar interaction leading to an isotropic shift and anisotropic broadening of the nuclear resonance; a through-bond orbital polarisation leading to another isotropic shift; a bulk susceptibility leading to an additional anisotropic broadening; and a relaxation enhancement leading to very rapid nuclear T_1 and T_2 relaxation in most cases. Typically, the isotropic and anisotropic shift contributions are collectively called the "paramagnetic shift" and "paramagnetic shift anisotropy" (PSA), respectively.

In the most common case, the electronic T_1 and T_2 relaxation constants are several orders of magnitude faster than the nuclear relaxation, such that, on the NMR timescale, the nuclear magnetic moment, $\boldsymbol{\mu}_N$ interacts with the thermally-averaged electronic magnetic moment, $\bar{\boldsymbol{\mu}}_e$

$$\bar{\boldsymbol{\mu}}_e = \frac{\mu_B^2 S(S+1)}{3k_B T}\mathbf{g}\cdot\mathbf{g}\cdot\mathbf{B}_0 \ , \tag{2.50}$$

where S is the electronic spin, μ_B is the Bohr magneton and **g** is the electron g tensor. The interaction Hamiltonian is

$$\hat{H} = \bar{\boldsymbol{\mu}}_e\cdot\mathbf{D}_{eN}\cdot\boldsymbol{\mu}_N \ , \tag{2.51}$$

where the dipolar interaction tensor, $\mathbf{D}_{eN}$, has components

$$D_{ij} = \frac{1}{r^3}\left(\delta_{ij} - 3e_i e_j\right) \ , \tag{2.52}$$

where δ_{ij} is the Kronecker delta function ($\delta_{ij} = 1$ if $i = j$ and 0 if $i \neq j$), and e_i and e_j (i, j = x, y or z) indicate the x, y and z components of the vector between the electron and the nucleus. When **g** is isotropic, $\bar{\boldsymbol{\mu}}_e$ is aligned with $\mathbf{B}_0$ and $g\cdot g\cdot\mathbf{D}_{eN}$ will be traceless and axially symmetric. This may, at first sight, appear similar to the internuclear dipolar interaction tensor but, as the nucleus experiences a thermally-averaged electronic spin, the result of this interaction is a powder-pattern lineshape rather than a Pake doublet. In general, however, **g** is not isotropic and $\mathbf{g}\cdot\mathbf{g}\cdot\mathbf{D}_{eN}$ is not traceless. This results in a dipolar-induced isotropic shift, termed the pseudocontact

shift (typically of a few ppm) in addition to the anisotropic broadening.[14]

As well as interacting directly with the nucleus, the unpaired electron spin density may induce spin polarisation of the orbitals of the nucleus. This direct interaction is known by various names, including the contact, Fermi contact, hyperfine and transferred hyperfine interaction, and has the Hamiltonian

$$\hat{H} = \frac{\mu_0}{4\pi}\frac{8\pi}{3}\gamma_e\gamma_N \mathbf{I}\cdot\mathbf{S}\delta(r) \ , \tag{2.53}$$

where γ_N and γ_e are the gyromagnetic ratios of the nucleus and electron, respectively, I and S are their respective spins, and $\delta(r)$ is the Dirac delta function ($\delta(r) = 1$ if $r = 0$ and 0 everywhere else). As the s orbitals of the nucleus have finite value at $r = 0$, polarisation of these orbitals induces a contact shift of frequency

$$\nu_c = \frac{A\gamma B_0}{\hbar}\langle S_z\rangle \ , \tag{2.54}$$

where $A/\hbar$ is the hyperfine coupling constant in Hz and $\langle S_z\rangle$ is the expectation value of the z component of the electronic magnetic moment. As discussed above, this is thermally averaged by the rapid electronic relaxation, and has a value of

$$\langle S_z\rangle = \frac{\mu_B J(J+1) g_J\left(g_J - 1\right)B_0}{3k_B T} \ , \tag{2.55}$$

where the Landé g factor, g_J, is

$$g_J = \frac{3J(J+1) - L(L+1) + S(S+1)}{2J(J+1)} \ , \tag{2.56}$$

J is the total angular momentum quantum number for the electron state, L is the orbital angular momentum and S is the spin angular momentum.[15] The contact shift is very large (typically thousands of ppm) for the nucleus of the parent atom, and smaller contact shifts (thousands to tens of ppm) may be observed for the nuclei of nearby atoms that are bonded to the parent atom. The transfer of spin polarisation between atoms is mechanistically similar to the scalar coupling and the magnitude of ν_c rapidly decreases as the number of bonds increases between the nucleus in question and the unpaired electron. In addition to the shifts and anisotropic broadening arising from the contact and pseudocontact interactions, both of these

interactions can contribute to transverse and longitudinal relaxation, leading to typical values on the order of a few ms for T_1 and on the μs – ms timescale for T_2.[16]

In addition to the relatively local effects discussed above, the bulk magnetic susceptibility (BMS) may also be important.[17] In a region of uniform magnetisation, the demagnetising field, $\delta\mathbf{B}(r)$, exists

$$\delta\mathbf{B}(r) = -\boldsymbol{\nu}(r,s)\cdot\chi(s)\cdot\mathbf{B}_0 \ , \qquad (2.57)$$

where $\chi(s)$ is the volume susceptibility tensor for the volume enclosed within the surface, s, and $\boldsymbol{\nu}(r,s)$ is the demagnetisation tensor. The effect of this demagnetisation is an anisotropic shift dependent on the size and shape of the sample holder and the size and shape of the crystallites within the sample. In addition, a distribution of shifts is present, owing to different $\mathbf{B}_0$ fields at different locations within the sample holder, and it is difficult to predict the effects of the BMS shift on a spectrum.[16] Kubo *et al.* have attempted to determine the overall demagnetisation for a sample consisting of spherical crystals contained within a non-spherical holder.[17] However, given the complexity of calculating the BMS shift for a real sample, this term is often neglected in the analysis of the NMR spectra of paramagnetic nuclei.

Overall, the presence of paramagnetic species within a sample can give rise to large isotropic shifts, anisotropic broadening and very rapid relaxation, with all of these effects dependent on temperature. This makes solid-state NMR experiments on paramagnetic materials challenging but, as will be discussed in Chapter 4, by changing the experimental techniques used, it is still possible to acquire high-resolution NMR spectra of paramagnetic materials and obtain relevant information. The effects of paramagnetic species can be observed even for nominally-diamagnetic samples containing small amounts of paramagnetic impurities (*e.g.*, natural minerals containing $Fe^{2+/3+}$ ions[18]). In such cases, although the large shifts and anisotropies discussed above are present, the majority of the nuclei are not affected by these, but will typically have more rapid T_1 and T_2 relaxation (the latter sometimes leading to line broadening in the NMR spectrum). In such cases, unless specific experimental techniques are employed to allow the observation of the species close to the paramagnetic centres, these species will be "invisible" in the NMR spectrum.

2.3.7.5 The Quadrupolar Interaction

Quadrupolar nuclei (with $1 > 1/2$) are subject to the interactions affecting the nuclear dipole moment, described above. In addition, the interaction of the nuclear electric quadrupole moment, eQ, (arising from non-spherical nuclear charge distribution) with the electric field gradient (EFG) (arising from non-spherical symmetry of the surrounding structure) must be considered. The EFG is described by the tensor, **V**, which is traceless and is diagonalised in the PAS to give

$$\mathbf{V}^{\mathrm{PAS}} = \begin{pmatrix} V_{xx} & 0 & 0 \\ 0 & V_{yy} & 0 \\ 0 & 0 & V_{zz} \end{pmatrix}, \tag{2.58}$$

with $|V_{zz}| \geq |V_{yy}| \geq |V_{xx}|$. The magnitude of the quadrupolar coupling, C_Q, between the nuclear quadrupole moment, Q, and **V** is

$$C_Q = \frac{eQV_{zz}}{h}. \tag{2.59}$$

The asymmetry of **V** is described by the normalised asymmetry parameter, η_Q

$$\eta_Q = \frac{V_{xx} - V_{yy}}{V_{zz}}, \tag{2.60}$$

with $0 \leq \eta_Q \leq 1$. Is also useful to define the quadrupolar product, P_Q, as

$$P_Q = C_Q\left(1 + \frac{\eta_Q^2}{3}\right)^{1/2}. \tag{2.61}$$

It can be seen that $C_Q \leq P_Q \leq 1.155C_Q$ for corresponding values of $0 \leq \eta_Q \leq 1$.

When the electric field surrounding a quadrupolar nucleus is spherically symmetric, C_Q is zero and the nucleus behaves as a fictitious spin $I = 1/2$ nucleus, as all single-quantum transitions ($\Delta m_I = \pm 1$) occur with frequency ω_0. For small EFGs, the quadrupolar interaction may be treated as a first-order perturbation of the energy levels and, for larger EFGs, both first- and second-order perturbations must be considered. For exceptionally large EFGs, higher-order perturbation terms may also be required,[19] but are not relevant to this thesis. As the effects of these perturbations in the NMR spectra of integer-spin ($I = 1, 2, 3\ldots$) and half-integer-spin ($I = 3/2, 5/2, 7/2\ldots$) nuclei are quite different, these cases shall be considered separately.

2.3.7.5.1 Nuclei with Half-Integer Spin

For a quadrupolar nucleus with half-integer spin, the transitions between the Zeeman levels can be categorised as: the central transition (CT) ($m_I = +1/2 \leftrightarrow m_I = -1/2$); single-quantum satellite transitions (STs) ($m_I \leftrightarrow m_I \pm 1$), symmetric multiple-quantum (MQ) transitions ($m_I = +n/2 \leftrightarrow m_I = -n/2$ (n = 3, 5, 7…)), and non-symmetric MQ transitions ($m_I = n/2 \leftrightarrow m_I = n'/2$ (where n and n′ differ by at least 2)). The CT, STs and symmetric triple-quantum (3Q) transition are shown for a spin I = 3/2 nucleus in Figure 2.11(a). The perturbation of the Zeeman levels by the quadrupolar interaction lifts the degeneracy of the STs and CT, giving rise to 2I transitions, with frequencies,

$$\omega = \omega_0 + \omega_Q\left(m_I^2 - m_{I+1}^2\right) , \tag{2.62}$$

where the quadrupolar frequency, ω_Q, is

$$\omega_Q = \frac{\omega_Q^{PAS}}{2}\left(3\cos^2\beta - 1 + \eta_Q\sin^2\beta\cos 2\gamma\right) , \tag{2.63}$$

where

$$\omega_Q^{PAS} = \frac{3\pi C_Q}{2I(2I-1)} , \tag{2.64}$$

in rad s^{-1} and β and γ are two of the Euler angles relating the PAS of the EFG to the laboratory frame. The quadrupolar frequency may also be reported as ν_Q ($= \omega_Q/2\pi$) in Hz. For a single crystallite, lifting of the degeneracy of the transitions results in the splitting of the resonance into 2I resonances, separated by $2\nu_Q$, as shown in Figure 2.11(b), whereas for a powdered sample, the STs are broadened, while the CT remains sharp (Figure 2.11(c)). The symmetric MQ transitions are unaffected by the first-order perturbation, but cannot be observed directly by NMR spectroscopy.

For larger EFGs, a second-order perturbation must also be considered. The second-order perturbation of a single energy level, $E^2(m_I)$ is

$$E^2(m_I) = \frac{\left(\omega_Q^{PAS}\right)^2}{2\omega_0}\begin{pmatrix} A^0_{I,m_I}B^0(\eta_Q) + A^2_{I,m_I}B^2\left(\eta_Q, \alpha, \beta, \gamma\right) \\ + A^4_{I,m_I}B^4\left(\eta_Q, \alpha, \beta, \gamma\right) \end{pmatrix} , \tag{2.65}$$

where the coefficients, A^l_{I,m_I}, and functions, B^l, are given in Appendix E.[20] In the

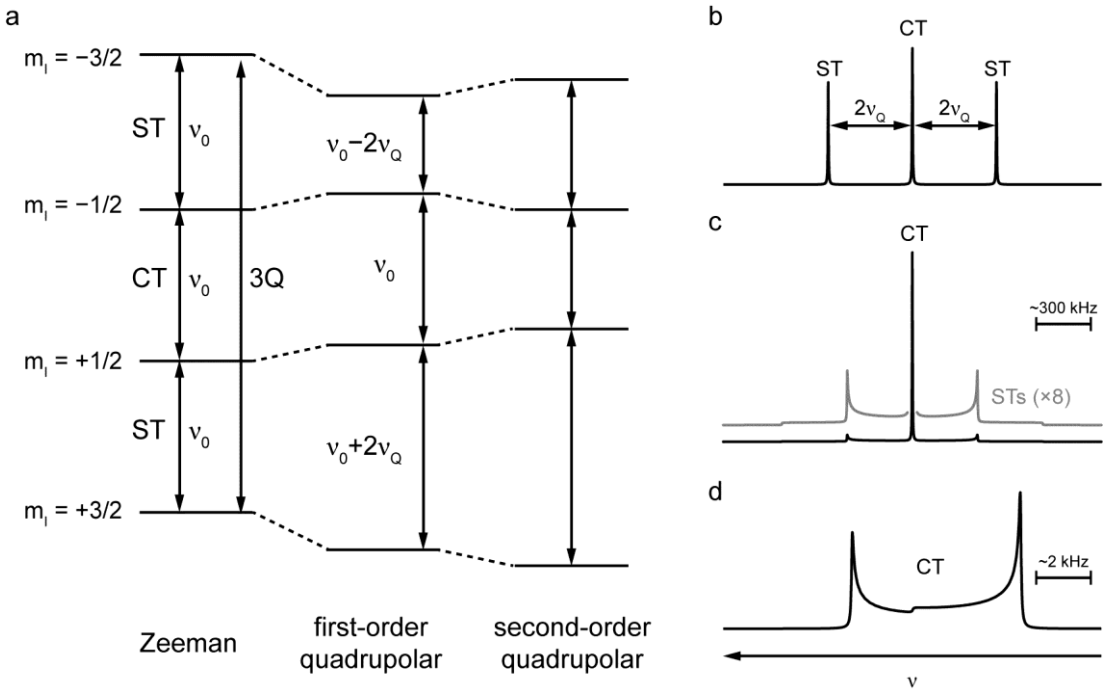

Figure 2.11. (a) Perturbation of the Zeeman energy levels of a spin I = 3/2 nucleus by the quadrupolar interaction. Schematic spectra showing the effect of the first-order quadrupolar interaction for (b) a single crystallite and (c) a powdered sample. (d) The anisotropic broadening of the CT by the second-order quadrupolar interaction (with $\eta_Q = 0$).

simplest case of axial symmetry ($\eta_Q = 0$), Equation 2.65 becomes

$$E^2(m_I) = \frac{\left(\omega_Q^{PAS}\right)^2}{2\omega_0}\left(A^0_{I,m_I} + A^2_{I,m_I}D^2_{0,0}(\alpha, \beta, \gamma) + A^4_{I,m_I}D^4_{0,0}(\alpha, \beta, \gamma)\right), \quad (2.66)$$

where the Wigner rotation matrix elements, $D^l_{m,m'}(\alpha, \beta, \gamma)$, are given in Appendix E. The second-order perturbation consists of an isotropic shift, δ_Q, given by the $A^0_{I,m_I}B^0(\eta_Q)$ term, and two terms corresponding to anisotropic broadening. The orientation dependence of this perturbation affects all transitions, including the CT, as shown in Figure 2.11(d). In cases where the second-order broadening of the CT is significant (more than a few kHz), the STs are typically broadened (with frequency dispersions reaching several MHz) such that their observation can be challenging. In such cases, it is normally only the relatively sharp CT that is observed.

2.3.7.5.2 Integer-Spin Nuclei

Integer-spin nuclei have no CT and all single-quantum transitions are anisotropically broadened in the presence of even a small EFG. However, as shown in Figure 2.12, symmetrical MQ transitions with $m_I = +n \leftrightarrow m_I = -n$ (n = 1, 2, 3…) are not affected by the first-order perturbation. As for half-integer-spin nuclei, the symmetrical MQ transitions become anisotropically broadened by the second-order perturbation. Direct observation of the spectra for integer-spin nuclei is typically limited to those with relatively narrow resonances (arising from small nuclear quadrupole moments, highly-symmetric environments, or high B_0 field strengths), owing to the difficulty of observing the resonances, which may have a frequency range of several MHz.

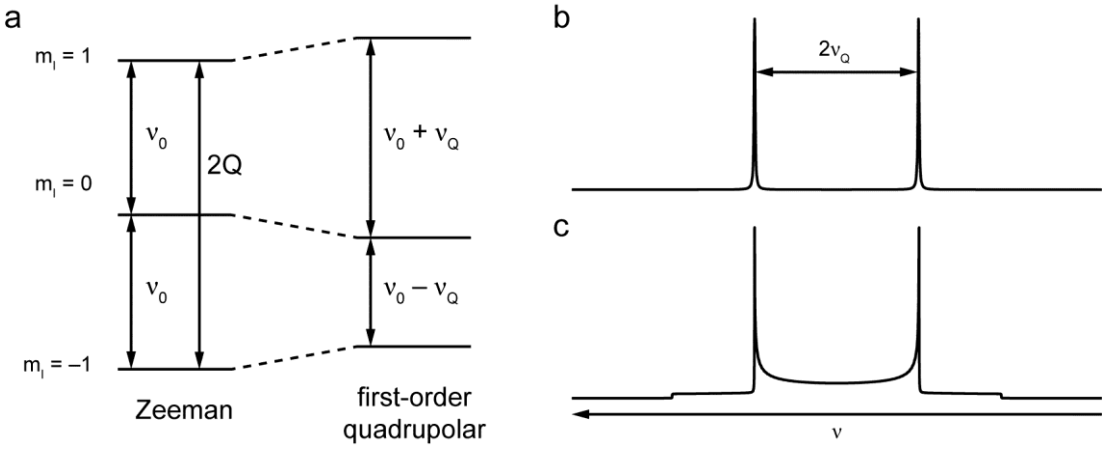

Figure 2.12. Perturbation of the Zeeman energy levels of a spin I = 1 nucleus by the quadrupolar interaction. Schematic spectra showing the effect of the first-order quadrupolar interaction for (b) a single crystallite and (c) a powdered sample (with $\eta_Q = 0$).

2.4 COMPUTATIONAL CHEMISTRY

2.4.1 Assigning an NMR Spectrum

As discussed above, the NMR spectra of solids can be considerably more complicated than for the solution state, owing to the presence of numerous anisotropic broadening effects not observed in solution. It seems somewhat unfair, therefore, that assigning NMR spectra can also be considerably more challenging for solids than molecules in solution. Assignment of solution-state NMR spectra is based on the principle that (except in cases of resonances split into multiplets by the J coupling) each chemically-different nucleus in the molecule will give rise to a single resonance in the spectrum, with a chemical shift that can be compared to extensive databases (at least for the most commonly-studied nuclei; ^{1}H, ^{13}C, ^{15}N, ^{19}F and ^{31}P) to give a rapid and confident assignment (in most cases). However, in solids, the number of possible arrangements of atoms (*i.e.*, chemically-distinct species possible), and the number of commonly-studied nuclei is considerably greater, and so few databases and "correlation" tables exist, with fewer still being comprehensive enough to be generally useful. Furthermore, depending on the packing (of molecules) and symmetry present within a crystal structure, chemically-identical species may not be related by symmetry, *i.e.*, their surroundings (and hence, magnetic environments) will be different, giving rise to multiple isotropic shifts for a single chemical species. An example of this is trimesic acid (H_3btc), which has three chemically-distinct C species within a molecule (Figure 2.13(a)), giving rise to three resonances in the solution-state ^{13}C NMR spectrum, shown in Figure 2.13 (b). However, in the solid, owing to the packing of the molecules, there are six distinct molecules of H_3btc within the unit cell, as shown in Figure 2.13(c), and the C_3 rotational symmetry of each molecule is no longer present, giving rise to 54 crystallographically-distinct carbon species (but still only three chemically- distinct carbon species).[21] As can been seen in Figure 2.13(d), the solid-state NMR spectrum is, therefore, significantly more complicated than the solution-state spectrum of the same material. In terms of assigning solid-state NMR spectra, it is insufficient, therefore, merely to improve the quality of databases of chemical shifts (and other NMR parameters) for solids, and an approach capable of considering crystallographic (*i.e.*, longer-range) as well as chemical (*i.e.*, local) structure is required. In recent years, such a role has

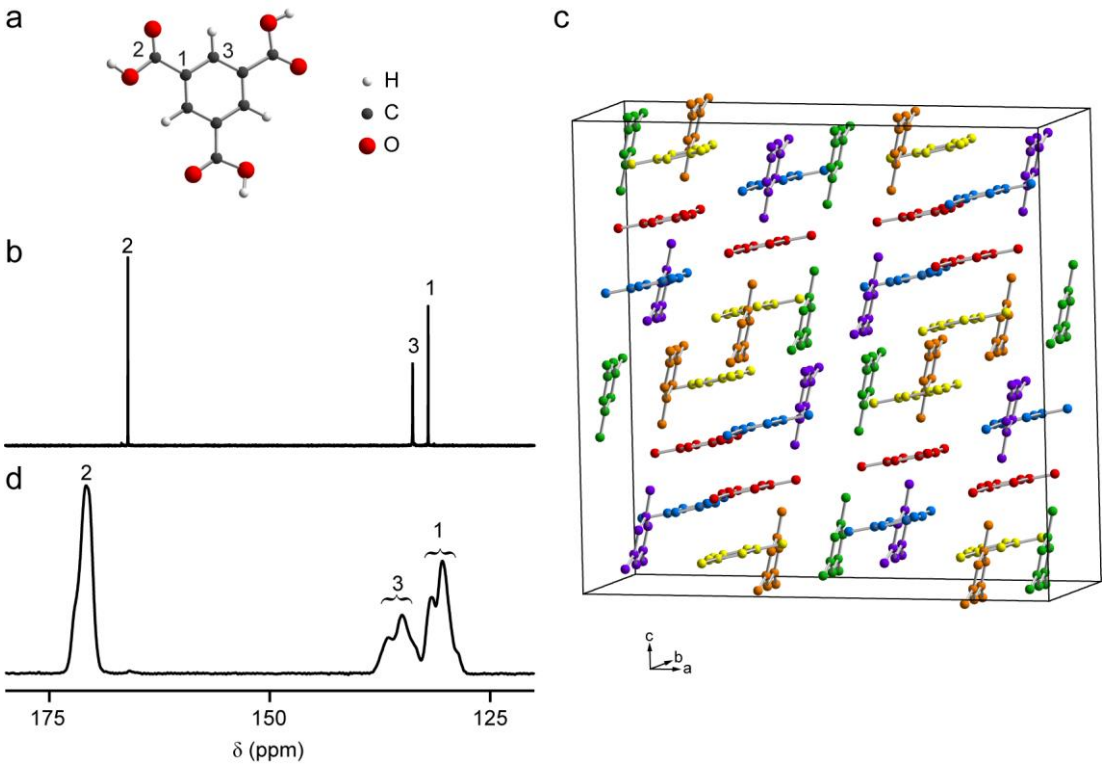

Figure 2.13. (a) The structure of benzene-1,3,5-tricarboxylic acid (H_3btc) as a single molecule in solution. (b) Solution-state ^{13}C NMR spectrum (7.05 T, $(CD_3)_2SO$) of H_3btc, assigned according to the numbering scheme in part (a). (c) The structure of solid H_3btc,[21] with the C atoms of the six crystallographically-distinct molecules highlighted in different colours for ease of interpretation and O and H atoms omitted for clarity. The unit cell is indicated by the black lines. (d) ^{13}C NMR spectrum (14.1 T) of solid H_3btc. Various techniques discussed in Chapter 3 (magic angle spinning, decoupling and cross polarisation from ^{1}H) have been used to maximise resolution and sensitivity.

increasingly been occupied by quantum-chemical calculations, which consider the electronic wavefunction of either a part or the whole of a given crystal structure, and are capable of determining the resulting NMR parameters, often with a high degree of accuracy. While a full understanding of the principles of these calculations is not required in order to use them as a method of assigning and interpreting NMR spectra, the following section provides a brief summary of the steps required to calculate the NMR parameters of a solid material, and highlights some of the recent developments and current limitations of the techniques described.

2.4.2 Fundamentals of Computational Chemistry and Density Functional Theory

The basic aim of computational chemistry is to find the ground state of a many-electron system, from which all observables for the system can be calculated through the appropriate operators. The most useful observable is the energy of the system, E, given by the Schrödinger equation

$$\hat{H}\Psi = E\Psi \ , \tag{2.67}$$

where $\hat{H}$ is the Hamiltonian operator and Ψ is the ground-state wavefunction. In a system composed of electrons and nuclei, there are several contributions to the Hamiltonian operator, corresponding to kinetic energy, T, of electrons (e) and nuclei (n), and electrostatic interactions, V, giving

$$E = -T_e - T_n - V_{ne} + V_{ee} + V_{nn} \ . \tag{2.68}$$

Interactions with a negative sign are stabilising and interactions with positive sign are destabilising. This expression may be simplified by employing the Born-Oppenheimer approximation, which regards nuclei as stationary on the timescale of electronic motion. T_n is, therefore, zero and electrostatic terms involving nuclei are constant for a given arrangement of atoms. Nuclei can then be treated as providing a constant background potential, V_{ext}, with which electrons interact. Of course, the electrons do not behave simply as classical point charges and point masses and, therefore, in addition to terms describing the classical kinetic energy of electrons and electron-electron repulsion, one must also consider two additional terms with a quantum-mechanical origin, the exchange, E_X, and correlation, E_C, interactions. Exchange modifies T_e to account for the fact that electrons may not occupy the same region of space, as this is forbidden by the Pauli Exclusion Principle. The V_{ee} term assumes the localisation of one electron at a time, with all other electrons providing a repulsive background "electron gas" potential. This oversimplification is corrected by the correlation term, which accounts for the fact that all electrons are partially localised simultaneously. The total energy is then given by

$$E = -T_e - V_e + E_X + E_C \ . \tag{2.69}$$

Exchange and correlation may be calculated separately or as a single term, E_{XC}, depending on the computational approach used.

Energy can be calculated either in terms of the wavefunction of a system (Hartree-Fock (HF) theory) or in terms of electron density of a system (density functional theory, DFT).[22] As HF calculations attempt to solve explicitly an equation with 4N variables for an N-electron system, (3 spatial and one spin variable per electron), their computational cost (in terms of processor power and time required) soon becomes prohibitive for larger systems. As such, the details of HF theory are not discussed further here, owing to the size of the systems of interest in this thesis. DFT takes as a variable the probability density, $\rho(r)$, of the sum of the individual electronic wavefunctions, $\psi_i(r)$, of an N-electron system according to the Kohn-Sham approach[23]

$$\rho(r) = \sum_{i=1}^{N} \psi_i^*(r)\psi_i(r) \quad . \tag{2.70}$$

While $\rho(r)$ is strictly the probability density of the wavefunction, it is generally referred to as the electron density, and this term shall be used throughout the remainder of this thesis. The Hohenberg-Kohn theorem,[24] demonstrates that $\rho(r)$ is a feasible variable to use, as each configuration of $\rho(r)$ can correspond only to exactly one value of V_{ext}. As such, $\rho(r)$ contains the same information about the system as the set of one-electron wavefunctions, $\{\psi_i(r)\}$, but in a much more manageable form, since all N electrons present in the system will contribute to a single $\rho(r)$. The original work by Hohenberg and Kohn proves that the energy of a system can be written in terms of the external (nuclear) potential, V_{ext}, and the universal Hohenberg-Kohn functional, $F_{HK}[\rho(r)]$

$$E[\rho] = \int \rho(r)V_{ext}dr + F_{HK}[\rho(r)] \quad , \tag{2.71}$$

where the square brackets denote a functional (*i.e.*, a function that takes another function as its argument). As the Hohenberg-Kohn theorem states that each unique configuration of atoms (*i.e.*, V_{ext}) gives rise to a unique $\rho(r)$, it is possible to iteratively alter the structure, calculate $\rho(r)$ and minimise $E[\rho]$ to determine the ground-state atomic positions and electron density of a system. The Hohenberg-Kohn functional, $F_{HK}[\rho(r)]$ describes exactly the inter-electron interactions and, if solved,

would provide the exact solution to the $\rho(r)$.[22, 24] However, while it is clear from the original work that such a functional *should* exist, its actual form remains unknown and, instead the inter-electron interactions must be expressed by the exactly-known Coulombic repulsion, and approximate exchange-correlation functionals.[22] Equation 2.69 can, therefore, be expressed a functional of $\rho(r)$[22, 23]

$$E = -T_S[\rho(r)] + V_{ext}[\rho(r)] + E_{XC}[\rho(r)] \ , \qquad (2.72)$$

where $T_S[\rho(r)]$ describes the kinetic energy of non-interacting electrons and $E_{XC}[\rho(r)]$ includes all electron-electron interactions . Early E_{XC} functionals used the local density approximation (LDA), or the closely-related local spin density (LSD) approximation,[22] which assumes that, over a sufficiently small unit of space, dr, $\rho(r)$ is constant. Despite its simplicity, this approximation works well in regions of space where the electron density changes little, but cannot provide an accurate description of the electronic structure near nuclei, where the potential well is very steep.[22] To account for this, the first derivative of electron density, $\nabla\rho(r)$, is also considered as a variable. Functionals that include the density gradient are known as gradient generalised approximation (GGA) functionals, and generally provide a much better approximate electronic wavefunctions. However, as with the LDA (or LSD) approaches, the description of the exchange interaction, $E_X[\rho(r)]$, is not exact for GGA functionals. Hybrid functionals, of which the most universally popular is the B3LYP functional,[25] attempt to correct for this difference by mixing the exact $E_X[\rho(r)]$ term from HF theory with the approximate correlation energy estimated from DFT (Becke's 3-parameter LDA functional,[26] B3, and the GGA functional of Lee, Yang and Parr,[27] LYP, in the B3LYP functional). The degree of contribution from the HF and DFT components of the calculation is parameterised to obtain the best possible results on a training set of small molecules. Even more recently, GGA and hybrid GGA functionals have been superseded by meta-GGA functionals, which provide small gains in accuracy, but are generally restricted to smaller systems owing to the more computationally-intensive calculations required.

Careful thought is required before choosing the correct functional for a given calculation, as these functionals are typically parameterised, either by fitting results to empirical parameters for a training set of molecules (*e.g.*, B3LYP) or by

consideration of theoretical boundary conditions (*e.g.*, PBE; the GGA functional of Perdew, Burke and Enrzerhof[28]). Calculations involving these functionals are commonly termed "first-principles". The choice of functional must be considered carefully, as functionals trained on sets of molecules similar to the system of interest are generally more likely to yield accurate results, but some functionals are considerably more robust than others.[22] In many cases in the literature, it is now known which functionals will perform well for which systems (*e.g.*, the PBE functional is generally suitable for strongly-correlated or periodic systems).

2.4.3 Basis Sets

While it is possible to calculate the electronic wavefunctions of a system numerically, this method becomes increasingly more cumbersome and computationally intensive as the number of electrons in the system increases. Instead, it is common to decompose the unknown wavefunction into a series of known mathematical "basis" functions, φ_i. Ideally, the basis functions would describe the atomic orbitals (AOs) of the electrons, $\psi_i(r)$, with the overall wavefunction of the system being composed of a linear combination of the AO wavefunctions. However, as the basis functions must be implemented in computer code, they are generally selected as much for computational efficiency (allowing the calculations to be extended to systems of relevant size) as for any physical relationship to $\psi_i(r)$. The choice of basis functions (the basis set) depends on the system under consideration, but basis sets can, in general, be classified as atom-centred or planewave.

2.4.3.1 Atom-Centred Basis Sets

The "ideal" atom-centred wavefunctions are Slater-type orbitals (STOs), of the form

$$\varphi_i^{STO} = Nr^{n-1}e^{-\zeta r}Y_{lm_l}(\Theta,\phi) \quad , \tag{2.73}$$

where N is a normalising factor (such that the one-electron orbital integrates to one electron), n is the principal quantum number, ζ is the effective nuclear charge and $Y_{lm_l}(\Theta,\phi)$ is an angular component, dependent on the orbital and angular momentum quantum numbers, l and m_l. It can be seen from Figure 2.14(a) that the radial part of φ_i^{STO} has the behaviour that one would expect, given the shape of the electronic

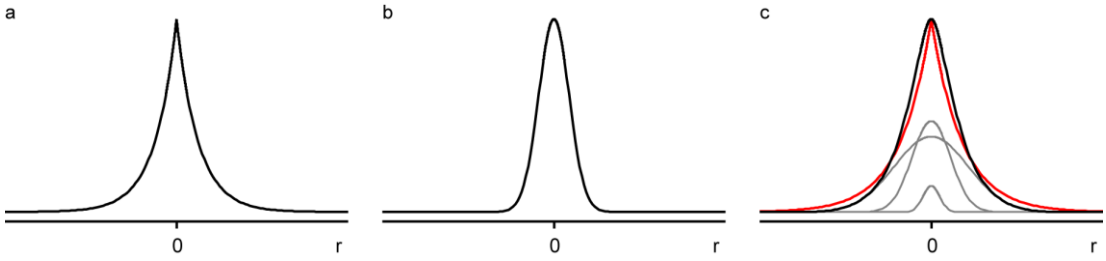

Figure 2.14. The radial components of (a) a Slater-type 1s orbital and (b) a Gaussian-type 1s orbital. Both orbitals are plotted to the same vertical and horizontal scale, and only their shapes should be compared. (c) Comparison of a single STO (red) and the sum (black) of the three GTOs shown (grey), demonstrating how an approximate STO can be constructed from GTOs (this example uses the STO-3G basis set for the 1s orbital of H with an effective nuclear charge, ζ, of 0.7[29]).

potential around a nucleus (located at r = 0): at the nucleus, there is a cusp in the function and as $r \rightarrow \infty$ the STO decays exponentially. The major problem with STOs is that calculation of inter-electron interactions requires calculation of the overlap of electronic wavefunctions, and there is no analytical way to determine the overlap of two STOs. Therefore, these must be calculated numerically, which rapidly becomes prohibitively costly as the number of orbital overlaps increases. Instead, it is possible to use Gaussian-type orbitals (GTOs), of the form

$$\varphi_i^{GTO} = Nr^L e^{-\alpha r^2} Y_{lm_l}(\Theta,\phi) \,, \tag{2.74}$$

where L is an integer (for a three-dimensional GTO there is a separate integer for each of the three Cartesian axes) and α is the orbital exponent.[22] At first sight, GTOs are not a sensible choice – it can be seen from Figure 2.14(b) that a GTO is a poor approximation of a STO (having a stationary point rather than a cusp at r = 0 and decaying too rapidly as $r \rightarrow \infty$). However, GTOs have the advantage that the overlap of two Gaussian functions is a third Gaussian function, meaning that orbital overlaps have an exact mathematical expression and can be calculated analytically rather than numerically, making the calculation far more efficient for larger systems. In addition, as shown in Figure 2.14(c), a STO can be approximated as the sum of multiple GTOs, known as a contracted Gaussian function (CGF). CGFs composed of more GTOs (larger basis sets) generally provide better approximations of their

corresponding STOs. As such, CGF basis sets are a popular choice in many DFT codes. The accuracy of a CGF basis set can be increased by the inclusion of "diffuse" functions, with small N and α, to describe the "tail" of the STO, which can be seen in Figure 2.14(c) to be poorly described by the sum of the three GTOs used.

The choice of basis set size is typically a trade-off between accuracy and computational cost. The "right" basis set is heavily dependent on the system in question as, like exchange-correlation functionals, basis sets are parameterised for different training sets of molecules and some basis sets are optimised for the calculation of specific parameters (*e.g.*, the pcS-n and pcJ-n sets have N and α selected to give optimum results in the calculation of shielding tensors and J-couplings, respectively[30]), whereas others, such as 6-311G[31, 32] are more general. Basis sets must always be "converged" to within the desired level of accuracy for the parameter of interest, such that increasing the number of basis functions does not significantly (to within the desired accuracy) affect the calculated result. However, the bewildering number of "families" of atom-centred basis sets means that it is often difficult to determine exactly which one is likely to be "best" and one must either conduct an extensive and time-consuming investigation to determine this prior to commencing the work of interest, or search the literature for a study in which similar properties were calculated for similar systems with a reasonable degree of accuracy.

2.4.3.2 Planewave Basis Sets

An alternative to atom-centred basis sets is to use planewaves of the form

$$\varphi(\mathbf{r}) = e^{i\mathbf{k}\mathbf{r}} \quad , \tag{2.75}$$

where k is the wavevector (related to the momentum of the planewave). Planewaves are an even larger deviation from the true physical form of the orbitals present than the GTOs discussed above. As such, a large number of planewaves is required in order to construct a reasonably accurate approximate wavefunction. The wavefunction is, then, a sum of the planewaves

$$\psi_{n,\mathbf{k}}(\mathbf{r}) = \sum_{\mathbf{G}} C_{n,\mathbf{k}}(\mathbf{G}) e^{i(\mathbf{G}+\mathbf{k})\mathbf{r}} \quad , \tag{2.76}$$

where $C_{n,k}(G)$ are the Fourier coefficients of the reciprocal lattice vectors, G. The

sum runs over all values of G up to the cut-off value, G_{max}, which is set by the kinetic energy cut-off, E_{cut}

$$E_{cut} = \frac{h^2}{2m}(G_{max} + k)^2 \quad . \tag{2.77}$$

By varying E_{cut}, the number of basis functions is varied. This is one of the key advantages of planewave basis sets over atom-centred basis sets, since the size of the basis set is controlled by a single parameter, which can be varied systematically. Increasing E_{cut} will make calculations more computationally expensive but more accurate, up to the limit of the theory, when the calculation is "converged". Above this limit, calculations will continue to become more costly, with little gain in accuracy. An example of this is shown in Figure 2.15(a) for the calculated total energy of SiO_2 coesite[33] as a function of E_{cut}. It can be seen that the energy of the system converges to a value of *ca.* –16789.3 eV at $E_{cut} \geq 50$ Ry (~680 eV). At higher cut-off energies, the computational cost, here measured as the computational time, continues to increase, but the total energy of the system is constant to within 38 meV.

In a solid in which the arrangement of atoms is periodic (*i.e.*, a crystalline material), the electronic potential energy is also periodic and satisfies Bloch's theorem.[36] Planewaves also satisfy the periodic conditions found in crystals, making them a natural choice of basis function for calculations involving crystalline solids (although it should be noted that it is possible, although computationally more challenging, to use atom-centred basis functions in such calculations as well[37, 38]). Planewave calculations are typically carried out in both real and reciprocal space, as some of the potential energy terms are more efficiently computed in real space, whereas it is more efficient to calculate kinetic and some potential energy terms in reciprocal space.[35] The accuracy of the planewave calculations, therefore, also depends on the level of sampling of the Brillouin zone (the reciprocal primitive unit cell), which is determined by the spacing of a grid of regularly-spaced "k-points" within this zone. It can be seen that, for the example of SiO_2 coesite shown in Figure 2.15(b), the total energy (calculated with $E_{cut} = 50$ Ry) converges when 5 or more k-points are used (k-point grid spacing ≤ 0.05 Å^{-1}).

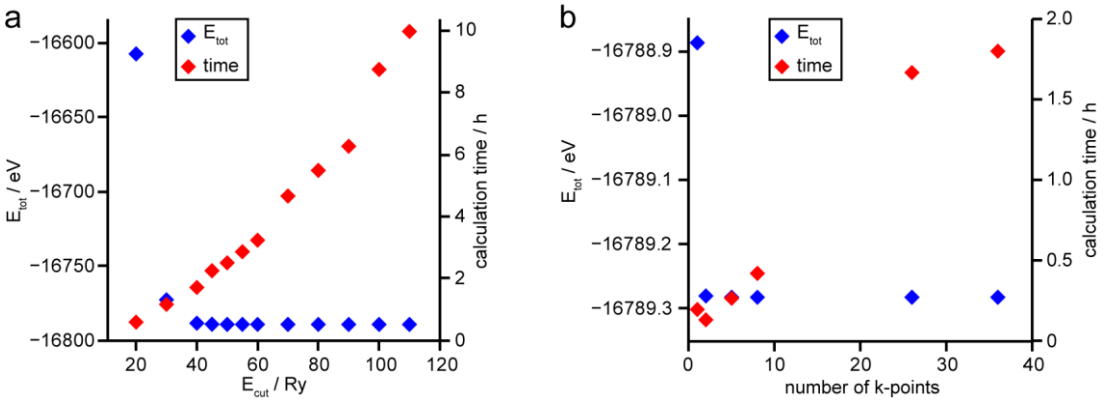

Figure 2.15. (a) The calculated total energy, E_{tot}, of SiO_2 coesite as a function of the planewave cut-off energy, E_{cut}. (b) The calculated total energy of SiO_2 coesite as a function of the number of k-points used for the calculation. On both plots, the time taken for each calculation is shown as a measure of the computational cost. Calculations were carried out with CASTEP 6[34, 35] using the PBE GGA functional.[28]

2.4.4 Reducing the Cost of Calculations

The explicit description of core electrons is computationally costly (especially for heavier atoms) and generally unnecessary, since it is typically the valence electrons that are responsible for most chemical phenomena. It is, therefore, sensible to employ a "frozen core" approximation, which treats electrons with energies below a "core" level as part of the background potential. The electrons with energies higher than this level are treated explicitly, but even their wavefunctions may be further simplified with little impact on the accuracy of the results. Since electronic wavefunctions must be mutually orthogonal, the explicit description of the core electrons forces the wavefunctions of the valence electrons to contain many nodes, which can only be approximated accurately with very large basis sets. By removing the explicit description of the core electrons in the frozen core approximation, it is possible to describe the valence electrons with a function that is nodeless within a core radius from the nucleus, r_{core}. This nodeless "pseudopotential" is computationally cheaper, as a smaller basis set may be used to provide a good degree of accuracy, as long as the valence electrons are still described adequately outside r_{core}.

The frozen core and pseudopotential approximations are very useful for reducing the cost of energy minimisations and other calculations depending only on

valence electrons. However, calculation of many properties (most pertinently the NMR parameters) requires a full description of the electrons close to the nucleus. The projector-augmented wavefunction (PAW) method[39] reconstructs the full wavefunction from a pseudised wavefunction by introducing the transformation operator, $\hat{T}$, such that

$$\psi_{\text{all electron}} = \hat{T}\psi_{\text{pseudised}} \ . \tag{2.78}$$

This allows calculation of expectation values (observables) related to the core electrons, but is still insufficient for calculation of NMR parameters, as the PAW method does not take into account the effects of a magnetic field.

2.4.5 Calculating NMR Parameters

An external magnetic field, B_0, induces a current, the effects of which can be calculated by several methods. For atom-centred orbitals, the most common methods are the Gauge-Including Atomic Orbitals (GIAO) and Continuum Set Gauge Transformation (CSGT). GIAO uses modified atomic orbitals, $\varphi_i(B)$,

$$\varphi_i(B) = e^{-\frac{1}{2c}(B \times B_i)r}\varphi_i \ , \tag{2.79}$$

where B and B_i are the external and induced fields, respectively, and φ_i is the field-independent orbital. The CSGT method, on the other hand, calculates the induced current density with the gauge origin at one location, then repeats calculations with the origin moved to different locations. The total effect of the magnetic field is then calculated by integrating over all gauge origins. The Single Gauge Origin (SGO) method is similar, but calculates the current density with only a single gauge origin, sacrificing accuracy for speed.

For pseudised wavefunctions, the Gauge-Including PAW (GIPAW) method is required.[40] GIPAW is an extension to the PAW method, analogous to the GIAO approach, with the wavefunctions of core electrons are reconstructed using an operator chosen to include translational invariance in the presence of a magnetic field. It should be noted that the GIPAW (and PAW) method only reconstructs the full wavefunction within r_{core} for pseudised electronic wavefunctions, and does not reconstruct the wavefunctions of electrons that have been omitted from explicit

description by the frozen core approximation. The importance of implementing the GIPAW algorithm in planewave pseudo-potential DFT codes (such as CASTEP[34, 35]) cannot be overestimated, as it has allowed the efficient and accurate calculation of NMR parameters for crystalline solids with large unit cells; enabling the direct comparison between the experimental and calculated NMR parameters for a given material. This approach solves the problem mentioned at the start of this section – that the assignment of solid-state NMR spectra cannot be made simply by reference to correlation tables, especially in the case of crystallographic (and hence magnetic) inequivalence of chemically-equivalent species. The GIPAW approach has been used extensively to interpret and assign a number of complicated NMR spectra of materials representing almost every class of crystalline compound currently of interest. This wide applicability of the approach is highlighted in recent reviews of the topic by, *e.g.*, Bonhomme *et al*.[41] and Charpentier.[42] The calculated NMR parameters can also be used to guide experiments, particularly those involving nuclei with unfavourable features such as low receptivity, large quadrupole moments and large shift ranges. For example, the ^{25}Mg (I = 5/2) NMR spectrum of clinoenstatite ($MgSiO_3$) contains a sharp resonance (C_Q = 3 MHz) that is readily observed, and a much broader resonance (C_Q = 14 MHz) that was only observed after DFT calculations suggested its presence.[43]

DFT calculations determine the absolute shielding tensor, $\boldsymbol{\sigma}$, giving calculated σ_{iso} and σ_{ii} that must be converted to δ_{iso} and δ_{ii} for comparison with experiment. This can be achieved either by calculating σ_{iso} for a reference compound of known structure and δ_{iso}, and calculating the reference shielding, σ_{ref}, as

$$\sigma_{ref} = \sigma_{iso}^{calc} + \delta_{iso}^{exp} \quad , \tag{2.80}$$

where "calc" and "exp" refer to the origin of the values in calculation or experiment, respectively. However, this method of calculating σ_{ref} from a single point is not advisable, as it does not take into account any errors associated with the calculation, structure, or experimental NMR spectrum. A better (but more laborious) approach is to calculate σ_{iso} for a number of compounds with known structure and plot these as a function of the experimental δ_{iso}. An example of this is shown in Figure 2.16, where the ^{29}Si σ_{iso} was calculated for 14 Si species in nine Si-containing materials (quartz,

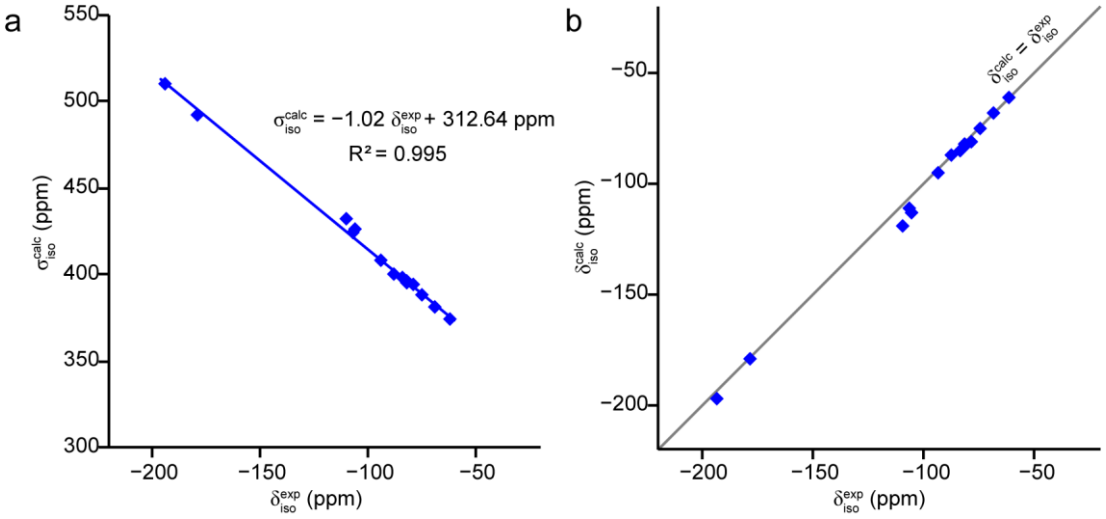

Figure 2.16. (a) Plot of calculated ^{29}Si σ_{iso} against experimental δ_{iso} for a range of solid silicates. The best fit line, determined by linear regression, is shown, and allows σ_{ref} and m to be determined, as described in the text. (b) Plot of calculated ^{29}Si δ_{iso} as a function of experimental δ_{iso}, with the ideal 1:1 relationship indicated. DFT calculations were carried out with CASTEP 6[34, 35] using the PBE GGA functional,[28] with E_{cut} = 50 Ry and a k-point spacing of 0.05 Å^{-1}.

coesite, clinoenstatite, protoenstatite, akimotoite, majorite, ringwoodite, wadsleyite and forsterite).[44] Plotting a line of best fit allows σ_{ref} to be determined (as the y intercept), the gradient of the straight line allows a scaling factor, m, to be determined, and the scatter of the data points from the straight line gives an indication of the associated error in σ_{iso}. The calculated chemical shift is then

$$\delta_{iso}^{calc} = \frac{\sigma_{ref} - \sigma_{iso}^{calc}}{-m}, \qquad (2.81)$$

where m is –1 if σ_{ref} is calculated from a single data point. In principle, m should be exactly –1 in all cases, but this is not always true and some notable examples where m deviates significantly from the ideal value are known in the literature. For example, Griffin *et al.* needed to use m = –0.68 to obtain reasonable calculated ^{19}F chemical shifts.[18] However, in cases where $-0.95 \leq m \leq -1.05$, it may be unclear whether a scaling factor is required, or whether the deviation from the ideal gradient arises from the inherent scatter of the data points. In the example in Figure 2.16, σ_{ref} is 312.64 ppm and m is –1.02 (*i.e.*, essentially –1.00). When the calculated and

experimental δ_{iso} are plotted against each other (with m = –1.00), as shown in Figure 2.16(b), the gradient is 1.02 and the mean absolute error (MAE) is 3.6 ppm, which is ~1.5% of the chemical shift range of ^{29}Si. The MAE can be decreased to 2.8 ppm by using m = 1.02 rather than 1.00 but, as discussed above, it is unclear whether this is simply over-fitting the relationship to better describe the experimental and computational errors present in the test dataset used. In a similar manner, σ_{ii} can be converted to the calculated δ_{ii} using the same value of σ_{ref}

$$\delta_{ii} = \sigma_{ref} - \sigma_{ii} \ . \tag{2.82}$$

The MAE in the calculated values of δ_{ii} is typically larger than for calculated δ_{iso}, although it should also be noted that the experimental error in determining δ_{ii} is typically greater than for δ_{iso}. For convenience, the calculated anisotropic values are typically reported either in standard or Herzfeld-Berger notation (see Section 2.3.7.1). The choice of the Herzfeld-Berger rather than Haeberlen notation is made by some authors,[45, 46] as a small error in σ_{22} can alter the sign and magnitude of Δ_{CS}, as well as affecting the value of η_{CS}. Such an error cannot affect Ω_{CS}, but may alter the sign and magnitude of κ_{CS}. It is, therefore, convenient to use the convention in which the value most prone to calculation errors corresponds to the value most difficult to determine experimentally. The "size" parameters of the anisotropy, Δ_{CS} or Ω_{CS}, are generally able to be more accurately measured from experiment than its "shape" parameters, η_{CS} or κ_{CS}, and the Herzfeld-Berger notation is, therefore, less likely to suffer from errors in the calculated σ_{22}, which will mainly be observed as an error in the sign of κ_{CS} (which may be hard to measure experimentally, anyway). However, errors in the calculated values of σ_{11} and σ_{33} will affect all anisotropy parameters.

2.4.6 Calculating the NMR Parameters of Solids

Whereas the above discussion has centred on how it is possible, mathematically, to calculate the NMR parameters of materials, the current discussion will focus on how these methods are implemented in practice. This thesis employs two DFT codes; GAUSSIAN,[47] which contains a large library of atom-centred basis sets, and CASTEP,[35] which uses a planewave basis set and pseudopotentials.

For small molecules, calculation of the NMR parameters may be carried out on a single molecule in the gas phase. This approach is achieved most efficiently using atom-centred basis sets, since the number of planewaves required to describe accurately a single atom is actually more than the number of planewaves required to describe an infinite array of atoms (the planewaves must interfere destructively at all locations but the atom, meaning that empty space is actually more computationally costly than an atom for planewave basis sets).

For crystalline systems, it is clear that calculation of the NMR parameters is best carried out using a planewave basis set and an effectively infinitely-repeating system. However, it is also possible to employ the "model cluster" approach, in which a small cluster of atoms is extracted from the infinite crystal structure, centred on the atom of interest. This cluster is then treated as a molecule, as described above, for the purposes of the calculation. The model cluster approach works relatively successfully for molecular solids, where no bonds must be broken in order to extract a sensible cluster (*i.e.*, the molecule of interest). However, for an inorganic solid, there will inevitably be some "dangling" bonds present on the surface of the cluster, and these are generally terminated with H. This cluster approach is useful for structures with exceedingly large unit cells, for which the calculation involving the full crystal structure is too computationally expensive to be feasible, and also in cases where the crystal structure is not known in detail, and various possibilities are to be investigated. As might be expected, the accuracy of this method is poor if the cluster is too small to provide a reasonable description of the infinite structure but, on the other hand, the costs of the calculation quickly become prohibitive as the number of coordination spheres included in the cluster is increased. An example of this is shown in Figure 2.17, in which the model cluster approach is used to calculate the ^{13}C isotropic shielding for diamond. It can be seen that the calculations are very inaccurate for the small clusters (essentially methane and neopentane) but become exponentially more expensive as the cluster size is increased, with no clear sign of convergence even when 4 coordination spheres (83 C atoms) are considered.

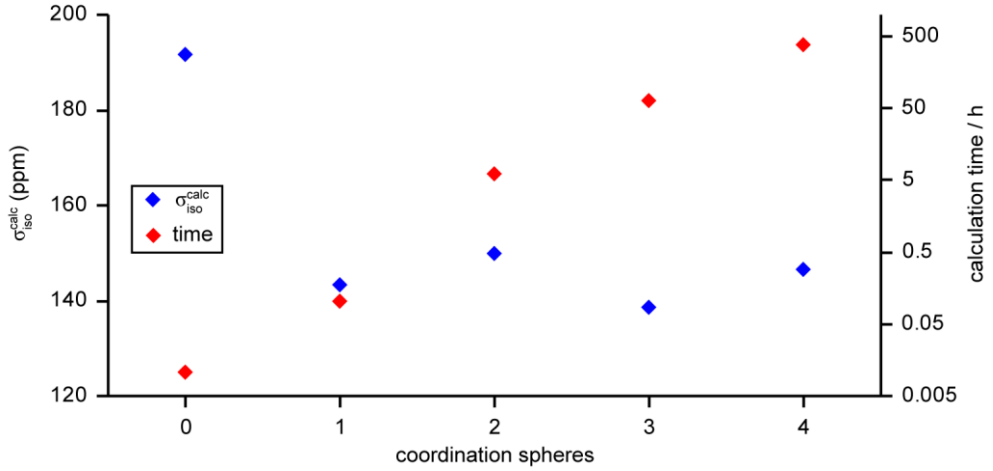

Figure 2.17. Plot of the calculated ^{13}C isotropic shielding for the central atom of a cluster of diamond containing the indicated number of coordination spheres. The computational cost (in terms of calculation time) is also shown – note the logarithmic scale used. Calculations were carried out using GAUSSIAN09[47] using the B3LYP GGA functional[25] and the 6-311+G(d,p) basis set.[31, 32]

2.4.7 The "Correct" Structure

While it is crucial to the understanding of an NMR spectrum that the NMR parameters calculated from a structure are as accurate as possible, it is of equal importance that the structure used as input for the calculations truly represents the sample used in the NMR experiments. The source of the structure (or structural model) must, therefore, be carefully considered prior to calculating its NMR parameters. It is well known that XRD is ill suited to, for example, locating H atoms, distinguishing between isoelectronic species, and determining the positions of light elements in the presence of heavier elements. In addition, incomplete diffraction data,[48] disorder, motional behaviour, an inherent inability to distinguish between different structural models (*e.g.*, those that differ only in terms of the positions of atoms that cannot be located accurately) or a desire to refine a structure in a higher-symmetry space group with a smaller unit cell than is strictly valid have led, in some cases, to structures that are unlikely for real chemical species. While single-crystal diffraction (either X-ray or neutron) and the use of high-resolution national facilities rather than local laboratory facilities may reduce many of these errors, and many such high-quality structures do yield NMR parameters in excellent agreement with experiments, the validity of a published crystal structure cannot simply be assumed.

Prior to calculating the NMR parameters for a material, it is, therefore, generally necessary to optimise its structure, to ensure that the structure for which the NMR parameters are calculated is an energy minimum for the material. Optimisation is achieved by calculating the forces exerted on individual atoms by the rest of the structure, and iteratively minimising these by changing the structure. The results of such a procedure are shown in Figure 2.18 for calcined AlPO-14. It can be seen that the ^{27}Al and ^{31}P NMR parameters calculated using the experimental (powder XRD[49]) structure yield simulated NMR spectra that are in very poor agreement with the experimental NMR spectra but, upon optimisation of the structure (using the TS semi-empirical dispersion correction scheme, discussed below), the spectra simulated from the calculated NMR parameters agree almost perfectly with the experimental spectra. In addition, the changes in calculated ^{31}P chemical shifts between the experimental and optimised structures alter the assignment of the ^{31}P NMR spectrum, highlighting the importance of using the correct initial structure for a calculation.

When optimising a structure with DFT, care must be taken to ensure that the structure reaches a reasonable energy minimum. The problem arises as many DFT functionals tend to underestimate long-range effects such as van der Waals' forces, π-π interactions and hydrogen bonding. For systems held together by strong, short-range interactions (*i.e.*, ionic or covalent bonds), the unit cell may expand by ~10% upon optimisation, but systems held together by weaker, longer-range interactions (*e.g.*, molecular crystals and some MOFs), may expand far more. Unlike the coordinates of the atoms, which are generally correct to within the experimental error of most diffraction techniques, such changes in the unit cell volume lead to significant disagreement with the experimental diffraction data. For many years, the options for correcting this problem were to accept that the optimised structure would give NMR parameters in better agreement with the experimental data despite disagreeing with the experimental diffraction structure, to constrain the unit cell to the experimental values during optimisation, or to re-scale the unit cell at the end of the optimisation to match diffraction data. None of these options is particularly satisfying, since the first contains an admission that the structure is only seen as "better" because it matches one experimental technique at the cost of agreement with another, and the latter two assume that the experimental diffraction-based unit cell is

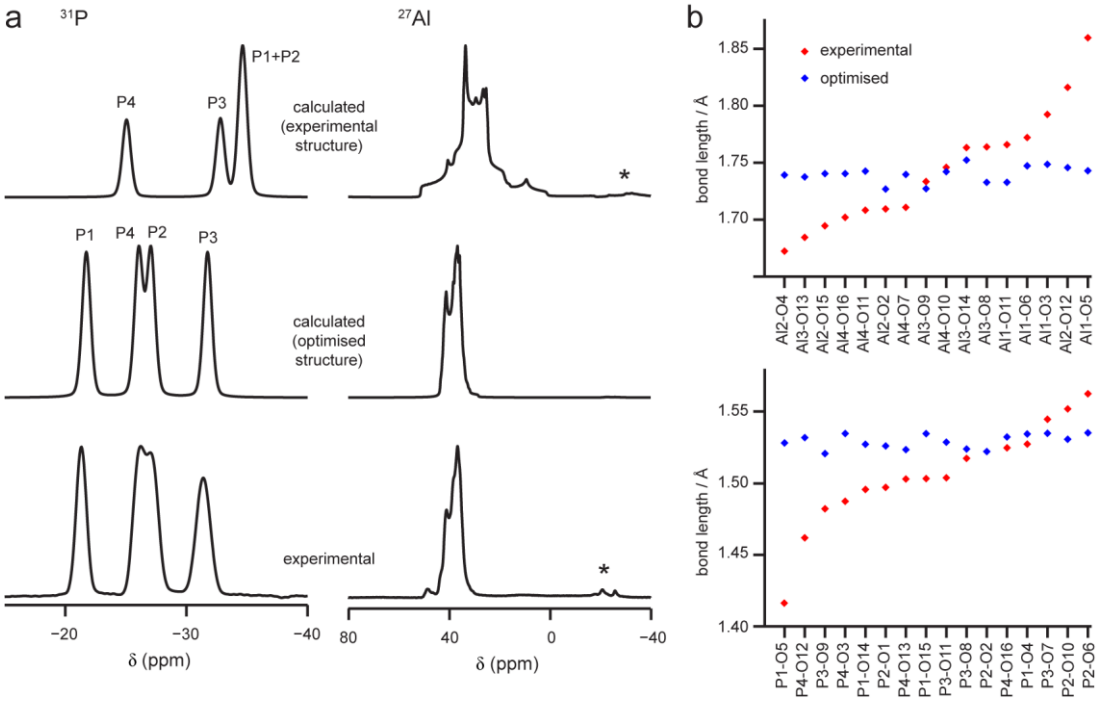

Figure 2.18. (a) Experimental (14.1 T, 14 kHz MAS) and simulated ^{31}P and ^{27}Al NMR spectra for calcined AlPO-14. Simulated spectra used NMR parameters calculated for the experimental[49] and optimised structures. (b) Plots of the changes in the local structure (Al-O and P-O bond lengths) of calcined AlPO-14 upon optimisation. DFT calculations were carried out with CASTEP6,[34, 35] using the PBE GGA functional,[28] with E_{cut} of 60 Ry and a k-point spacing of 0.04 Å^{-1}. For the geometry optimisation, all unit cell parameters and atomic coordinates were allowed to vary and long-range dispersion interactions were taken into account using the correction scheme of Tkatchenko and Scheffler.[50]

perfectly correct. In recent years, semi-empirical dispersion correction (SEDC) schemes[51] have been introduced as a fourth option to obtain structures that are in better agreement with both diffraction and NMR experimental data.

SEDC schemes modify the total energy of the system, adding the "missing" dispersion terms, E_{disp}, to the energy calculated in a normal DFT calculation, E_{DFT}

$$E_{tot} = E_{DFT} + E_{disp} \quad . \tag{2.83}$$

E_{disp} is calculated as the sum of the London potentials, $s_6 C_{6,ij} r_{ij}^{-6}$, between the i^{th} and j^{th} atoms, where s_6 is a scaling factor, $C_{6,ij}$ is the empirically-determined dispersion

coefficient between the i^{th} and j^{th} atoms, and depends on the nature of the two atoms. At shorter range, the London potential is modified by a damping function, $f(S_r r_{ij}^0, r_{ij})$, which reduces the dispersion correction to zero below a cut-off radius, r_{ij}^0, dependent on the van der Waals' radii of the i^{th} and j^{th} atoms. S_r is an empirical term introduced to match the damping function to the DFT potential. E_{disp} can, then, be expressed as

$$E_{disp} = s_6 \sum_{i=1}^{N} \sum_{j>i}^{N} f(S_r r_{ij}^0, r_{ij}) C_{6,ij} R_{ij}^{-6} \quad . \tag{2.84}$$

Three SEDC schemes have been introduced into CASTEP by McNellis *et al.*,[51] all of which use different parameterisation schemes for $s_6 C_{6,ij}$ and $S_r r_{ij}^0$. The first scheme, developed by Ortmann, Bechstedt and Schmidt (OBS)[52, 53] has only been parameterised for the GGA PW91 functional and is not, therefore, universally applicable. The second scheme, developed by Grimme in 2006 (G06)[54] is far more transferrable and, although introduced relatively recently, has gained popularity, with the original work cited ~3000 times to date. The most recent scheme, by Tkatchenko and Scheffler (TS)[50] is similar to G06. However, as seen in Table 2.4, when the three SEDC schemes were used to optimise the structures of NaCl[55] (ionic bonding), diamond[56] (covalent network) and metronidazole[57] (packed molecules), G06 achieves a very similar (or identical) result to experiment, whereas TS and OBS tend to lead to a contraction of the experimental unit cell. However, the small unit cell sizes considered here may overemphasise the differences between G06 and TS, and work on larger unit cells, such as those relevant to this thesis, does not show such a pronounced difference.[58-60] Application of a SEDC scheme generally results in either a reduction of, or no change to, the experimental unit cell, whereas the optimisations carried out with no SEDC scheme always expanded the experimental unit cell, especially in systems where dispersive interactions play a significant role in determining the overall structure (*e.g.*, metronidazole). SEDC schemes can be included in gas-phase calculations, but their impact is only really noticeable for intermolecular interactions, or intramolecular interactions for larger molecules.

Table 2.4. The unit cell volumes, in $Å^3$, obtained experimentally or calculated for a 2 × 2 × 2 supercell of NaCl, a 2 × 2 × 2 supercell of diamond and a single unit cell of metronidazole with CASTEP 6.[34, 35] Calculations were carried out for this work using the PBE[28] GGA functional (or the PW91 GGA functional for the OBS SEDC scheme) and the indicated SEDC scheme. In all calculations, E_{cut} was 60 Ry and the k-point spacing was 0.04 $Å^{-1}$.

	Unit cell volumes for		
SEDC scheme	NaCl[a]	diamond[b]	metronidazole[c]
experimental	1448.497	362.992	745.074
no SEDC scheme	1479.498	363.430	895.243
OBS[d]	1375.937	357.653	683.363
G06	1448.497[e]	360.861	728.403
TS	1247.876	357.335	763.875

a. Experimental data and starting structure from Ref. 55. (ICSD 165592).

b. Experimental data and starting structure from Ref. 56. (ICSD 28858).

c. Experimental data and starting structure from Ref. 57. (CSD MINIMET).

d. The GGA PW91 functional was used for calculations involving the OBS SEDC scheme, whereas all other calculations used the GGA PBE functional.

e. The experimental structure was not changed (*i.e.*, already represented an energy minimum at the given theory level).

As a final caveat, it must be remembered that DFT calculations are typically carried out with an effective temperature of 0 K, most modern diffraction experiments are carried out at temperatures below room temperature, and most NMR experiments are carried out at just above room temperature. As such, one should not be too surprised when the three techniques give slightly different structures, and perhaps a perfect match between the structures obtained by the three techniques should not (and cannot) be the ultimate goal of structural optimisation, as there will be real structural differences at different temperatures.[60] However, by careful optimisation of the structures of materials, it is possible to achieve a set of calculated parameters that agree well with both diffraction and NMR experiments, which can allow valuable insight into the structural origins of observed spectral features.

2.5 REFERENCES

1. M. T. Weller *Inorganic Materials Chemistry*, Oxford University Press, Oxford, UK, **1994**.

2. *International Tables for Crystallography*, 4th edn., **1995**.

3. W. L. Bragg, *Nature*, **1912**, ***90***, 410.

4. A. Abragam, *Principles of Nuclear Magnetism*, 6th edn., Oxford University Press, Oxford, UK, New York, **2002**.

5. J. Keeler, *Understanding NMR Spectroscopy*, John Wiley & Sons Ltd., Chichester, UK, Chippenham, UK, **2005**.

6. P. J. Hore, J. A. Jones and S. Wimperis, *NMR: The Toolkit*, 1st edn., Oxford University Press, New York, **2006**.

7. D. J. States, R. A. Haberkorn and D. J. Ruben, *J. Magn. Reson.*, **1982**, *48*, 286.

8. D. Marion and K. Wuthrich, *Biochem. Biophys. Res. Commun.*, **1983**, *113*, 967.

9. R. K. Harris, E. D. Becker, S. M. Cabral de Menezes, P. Granger, R. E. Hoffman and K. W. Zilm, *Pure Appl. Chem.*, **2008**, *80*, 59.

10. U. Haeberlen, *Advances in Magnetic Resonance*, Academic Press, New York, **1976**.

11. J. Herzfeld and A. E. Berger, *J. Chem. Phys.*, **1980**, *73*, 6021.

12. J. Mason, *Solid State Nucl. Magn. Reson.*, **1993**, *2*, 258.

13. G. E. Pake, *J. Chem. Phys.*, **1948**, *16*, 327.

14. A. Nayeem and J. P. Yesinowski, *J. Chem. Phys.*, **1988**, *89*, 4600.

15. K. J. D. MacKenzie and M. E. Smith, *Multinuclear Solid-State NMR of Inorganic Materials*, 1st edn., Elsevier Science Ltd, Oxford, UK, **2002**.

16. V. I. Bakhmutov, *Solid-State NMR in Materials Science*, 1st edn., CRC Press, Boca Raton, FL, Boca Raton, FL, **2012**.

17. A. Kubo, T. P. Spaniol and T. Terao, *J. Magn. Reson.*, **1998**, *133*, 330.

18. J. M. Griffin, J. R. Yates, A. J. Berry, S. Wimperis and S. E. Ashbrook, *J. Am. Chem. Soc.*, **2010**, *132*, 15651.

19. S. Cavadini, *Prog. Nucl. Magn. Reson. Spectrosc.*, **2010**, *56*, 46.

20. S. E. Ashbrook and S. Wimperis, in *NMR of Quadrupolar Nuclei in Solid Materials*, eds. R. E. Wasylishen, S. E. Ashbrook and S. Wimperis, John Wiley & Sons, Chichester, UK, 1st edn., **2012**.

21. D. J. Duchamp and R. E. Marsh, *Acta Crystallogr.*, **1969**, *B25*, 5.

22. W. Koch and M. C. Holthausen, *A Chemist's Guide to Density Functional Theory*, 2nd edn., Wiley VCH, Moerlenbach, Germany, **2007**.

23. W. Kohn and L. J. Sham, *Phys. Rev.*, **1965**, *140*, A1133.

24. P. Hohenberg and W. Kohn, *Phys. Rev.*, **1964**, *136*, B864.

25. P. J. Stephens, F. J. Devlin, C. F. Chabalowski and M. J. Frisch, *J. Phys. Chem.*, **1994**, *98*, 11623.

26. A. D. Becke, *J. Chem. Phys.*, **1993**, *98*, 5648.

27. C. T. Lee, W. T. Yang and R. G. Parr, *Phys. Rev. B*, **1988**, *37*, 785.

28. J. P. Perdew, K. Burke and M. Ernzerhof, *Phys. Rev. Lett.*, **1998**, *77*, 3865.

29. J. C. Slater, *Phys. Rev.*, **1930**, *36*, 57.

30. F. Jensen, *J. Chem. Theor. Comput.*, **2008**, *4*, 719.

31. P. C. Hariharan and J. A. Pople, *Theor. Chim. Acta*, **1973**, *28*, 213.

32. W. J. Hehre, R. Ditchfield and J. A. Pople, *J. Chem. Phys.*, **1972**, *56*, 2257.

33. K. L. Geisinger, M. A. Spackman and G. V. Gibbs, *J. Phys. Chem.*, **1987**, *91*, 3237.

34. S. J. Clark, M. D. Segall, C. J. Pickard, P. J. Hasnip, M. J. Probert, K. Refson and M. C. Payne, *Z. Kristallogr.*, **2005**, *220*, 567.

35. M. D. Segall, P. J. D. Lindan, M. J. Probert, C. J. Pickard, P. J. Hasnip, S. J. Clark and M. C. Payne, *J. Phys.: Condens. Matter*, **2002**, *14*, 2717.

36. N. W. Ashcroft and D. N. Mermin, *Solid State Physics*, Holt, Rinehart and Winston, New York, NY, **1976**.

37. R. Dovesi, R. Orlando, B. Civalleri, C. Roetti, V. R. Saunders and C. M. Zicovich-Wilson, *Z. Kristallogr.*, **2005**, *220*, 571.

38. R. Dovesi, V. R. Saunders, C. Roetti, R. Orlando, C. M. Zicovich-Wilson, F. Pascale, B. Civalleri, K. Doll, N. M. Harrison, I. J. Bush, P. D'Arco and M. Llunell, *CRYSTAL09 User's Manual*, University of Torino, Torino, Italy, **2009**.

39. P. E. Blöchl, *Phys. Rev. B*, **1994**, *50*, 17953.

40. C. J. Pickard and F. Mauri, *Phys. Rev. B*, 2001, **63**, 245101.

41. C. Bonhomme, C. Gervais, F. Babonneau, C. Coelho, F. Pourpoint, T. Azaïs, S. E. Ashbrook, J. M. Griffin, J. R. Yates, F. Mauri and C. J. Pickard, *Chem. Rev.*, **2012**, *112*, 5733.

42. T. Charpentier, *Solid State Nucl. Magn. Reson.*, **2011**, *40*, 1.

43. J. M. Griffin, A. J. Berry and S. E. Ashbrook, *Solid State Nucl. Magn. Reson.*, **2011**, *40*, 91.

44. S. E. Ashbrook and D. M. Dawson, *Acc. Chem. Res*, **2013**, *46*, 1964.

45. M. R. Mitchell, D. Carnevale, R. Orr, K. R. Whittle and S. E. Ashbrook, *J. Phys. Chem. C*, **2012**, *116*, 4273.

46. J. M. Griffin, F. R. Knight, G. Hua, J. S. Ferrara, S. W. L. Hogan, J. D. Woollins and S. E. Ashbrook, *J. Phys. Chem. C*, **2011**, *115*, 10859.

47. GAUSSIAN 09, Revision A.02, M. J. Frisch, *et al.*, Gaussian, Inc., Wallingford, CT, **2009**.

48. M. Estermann, L. B. McCusker, C. Baerlocher, A. Merrouche and H. Kessler, *Nature*, **1991**, *352*, 320.

49. R. W. Broach, S. T. Wilson and R. M. Kirchner, *Micropor. Mesopor. Mater.*, **2003**, *57*, 211.

50. A. Tkatchenko and M. Scheffler, *Phys. Rev. Lett.*, **2009**, *102*, 073005.

51. E. R. McNellis, J. Meyer and K. Reuter, *Phys. Rev. B*, **2009**, *80*, 205414.

52. F. Ortmann, W. G. Schmidt and F. Bechstedt, *Phys. Rev. Lett.*, **2005**, *95*, 186101.

53. F. Ortmann, F. Bechstedt and W. G. Schmidt, *Phys. Rev. B*, **2006**, *73*, 205101.

54. S. Grimme, *J. Comput. Chem.*, **2006**, *27*, 1789.

55. V. L. Cherginets, V. N. Baumer, S. S. Galkin, L. V. Glushkova, T. P. Rebrova and Z. V. Shtitelman, *Inorg. Chem.*, **2006**, *45*, 7367.

56. M. E. Straumanis and E. Z. Aka, *J. Am. Chem. Soc.*, 1951, **73**, 5643.

57. N. M. Blaton, O. M. Peeters and C. J. Deranter, *Acta Crystallogr.*, **1979**, *B35*, 2465.

58. O. Steward, *MChem Thesis*, University of St Andrews, **2012**.

59. V. R. Seymour, *PhD Thesis*, University of St Andrews, **2013**.

60. S. Sneddon, D. M. Dawson, C. J. Pickard and S. E. Ashbrook, Ph*ys. Chem. Chem. Phys.*, **2014**, *16*, 2660.

3 EXPERIMENTAL TECHNIQUES FOR SOLID-STATE NMR

3.1 HIGH-RESOLUTION SOLID-STATE NMR SPECTRA OF I = 1/2 NUCLEI

It can be seen from Section 2.3 that a solid-state NMR spectrum will contain information on the number of magnetically-distinct atoms, the chemical species present, the relative locations of the nuclei, the connectivity of the atoms and the local symmetry. The anisotropic (broadening) interactions are generally greater than the isotropic (separating) contributions, meaning that, in practice, solid-state NMR spectra typically consist of multiple, broad and overlapping lineshapes with contributions from many different interactions. As a result, limited information can be obtained without employing experimental techniques to simplify the spectrum (*e.g.*, by removing anisotropic broadening causing an overlap of resonances), whilst retaining some information (*e.g.*, isotropic positions of resonances). These techniques may involve a manipulation of the sample in physical space, manipulation of the spins in spin space, or a combination of the two.

3.1.1 Magic Angle Spinning

In solution, molecular tumbling (typically rapid on the NMR timescale) results in an averaging of all anisotropic interactions to their isotropic value. In solids, such motional averaging is generally absent, but can be mimicked using the technique of Magic Angle Spinning (MAS).[1, 2] For MAS, the sample is packed into a "rotor"; a cylindrical sample holder with "fins" at one end. The rotor is aligned along an axis inclined at an angle, θ_R, to $\mathbf{B}_0$ and rotated about this axis at a frequency, ν_R, of up to ~110 kHz, as shown in Figure 3.1. It is convenient to describe the orientation of a crystallite in the rotor frame, in which the z axis is aligned with the rotor axis and the xy plane is perpendicular to this. Under rotation of the sample, it can be seen that the angle between the crystallite and the z axis of the rotor frame, β', remains constant (but is different for each crystallite), whereas the orientation of the crystallite with respect to $\mathbf{B}_0$, θ, takes on all possible values. The orientation, θ, of a crystallite depends on β' and θ_R, such that the magnitude of any orientation-dependent interaction is dependent on both $d^2_{0,0}(\beta')$ and $d^2_{0,0}(\theta_R)$. In the limit of infinitely rapid

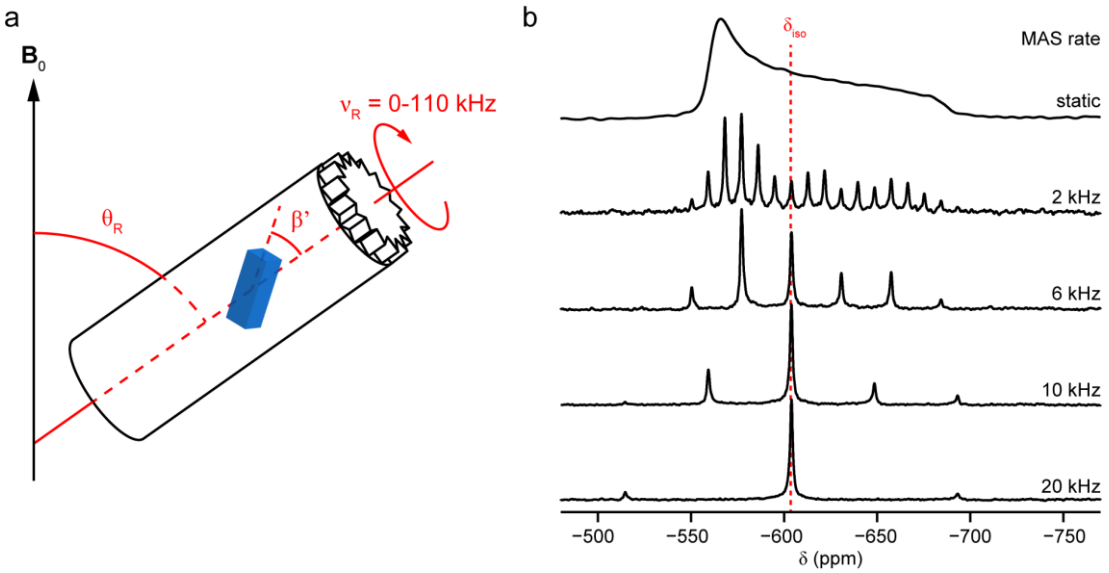

Figure 3.1. (a) Schematic representation of MAS, with a single crystallite shown in blue. (b) The effects of MAS at the indicated rate on the ^{119}Sn spectrum of SnO_2 (14.1 T). The single resonance is broadened by the CSA interaction, with δ_{iso} = –604 ppm, Ω = 124 ppm (27.8 kHz) and κ = 1.0 ($\delta_{11} = \delta_{22}$ = –563 ppm, δ_{33} = –687 ppm).

rotation, the average orientation, $\langle d^2_{0,0}(\theta)\rangle$, may be considered, where

$$\langle d^2_{0,0}(\theta)\rangle = \frac{1}{2} d^2_{0,0}(\theta_R) d^2_{0,0}(\beta') \ , \qquad (3.1)$$

which is zero when $\theta_R = \theta_m$, the so-called "magic" angle of 54.736°. In principle, MAS can, therefore, remove the chemical shift, dipolar, J and paramagnetic anisotropies, which are the main broadening interactions for spin I = 1/2 nuclei. However, the MAS rate must be "fast" relative to the anisotropic broadening, otherwise the lineshape is split into a series of spinning sidebands (SSBs), spaced at integer multiples of ν_R from the isotropic resonance, as shown in Figure 3.1(b). SSBs arise from incomplete averaging of the anisotropic interaction in question. At "slow" MAS rates, the envelope of the SSBs mimics the static lineshape, whereas, at intermediate MAS rates, the SSBs become less intense and the isotropic resonance begins to dominate the spectrum. Only in the fast MAS regime are the SSBs essentially negligible. The magnitude of the anisotropy that can be removed by MAS is limited by current MAS hardware, with commercial systems capable of achieving up to ~110 kHz MAS, meaning that chemical shift, heteronuclear dipolar and J

anisotropy can be removed, but large homonuclear dipolar and paramagnetic anisotropies may not be fully averaged to their isotropic value.

When carrying out fast MAS experiments, two important factors must be considered. The first is that the sample temperature will increase with increasing friction between the rotor and the drive and bearing gas flows required to achieve the MAS. This effect depends on the ratio of the MAS rate and the mass of the sample (*i.e.*, the rotor diameter), While this effect is not particularly significant (only a few °C) at MAS rates of ~10 kHz, it can contribute ~30 °C to the sample temperature at 60 kHz MAS. This has important implications for the temperature-dependent paramagnetic interactions, which require the fastest MAS for efficient averaging. Such heating may also change the rates of any dynamic processes present. The second practical consideration is the sensitivity of the experiment, which is proportional to the number of NMR-active nuclei within the rotor. In order to achieve more rapid MAS, rotors with smaller diameters (and, hence, sample volumes) are required. Table 3.1 summarises the sample volume and maximum MAS rates accessible by rotors of different diameter.

3.1.2 Decoupling

Despite the impressive resolution enhancements that may be achieved by MAS, the technique often cannot completely remove spin-spin interactions (*e.g.*, dipolar and isotropic J terms). These broadenings arise from interactions between two spins, I and S, where the resonant frequency of I depends on the state of S. By continuously irradiating S while acquiring the spectrum of I, the state of S is constantly changed and the I-S interaction averaged to zero. Such continuous wave (CW) decoupling is the simplest means of removing heteronuclear spin-spin interactions. More efficient composite-pulse decoupling schemes have been developed,[3] and the two-pulse phase modulation (TPPM) decoupling scheme[4] is used extensively in this thesis. TPPM involves a train of pulses of flip angle ~165° (typically optimised experimentally), with their phase alternating between ϕ and $-\phi$ applied to the S spins. The difference between ϕ and $-\phi$ is typically small, and ϕ is indicated by the notation TPPM-ϕ, in the name of the decoupling scheme. In this thesis, TPPM-15 was routinely used. The effects of decoupling can be seen in Figure 3.2 for the ^{13}C NMR spectrum of

Table 3.1. The sample volume and maximum MAS rates accessible by rotors of different outer diameters.

outer diameter / mm	approx. sample volume / μl	max. MAS rate / kHz
7	300-500	7
4	50-90	14
3.2	20-40	24
2.5	14	35
1.9	10	42
1.3	1.5	67
1	0.8	80
0.75	0.4	110

1[^{13}C]-glycine acquired with and without MAS. The static NMR spectrum (Figure 3.2(a)) shows a powder-pattern lineshape arising from the CSA interaction, with additional Gaussian-like broadening arising from heteronuclear dipolar interactions with ^{1}H. Decoupling removes the spin-spin contributions from the broadening,

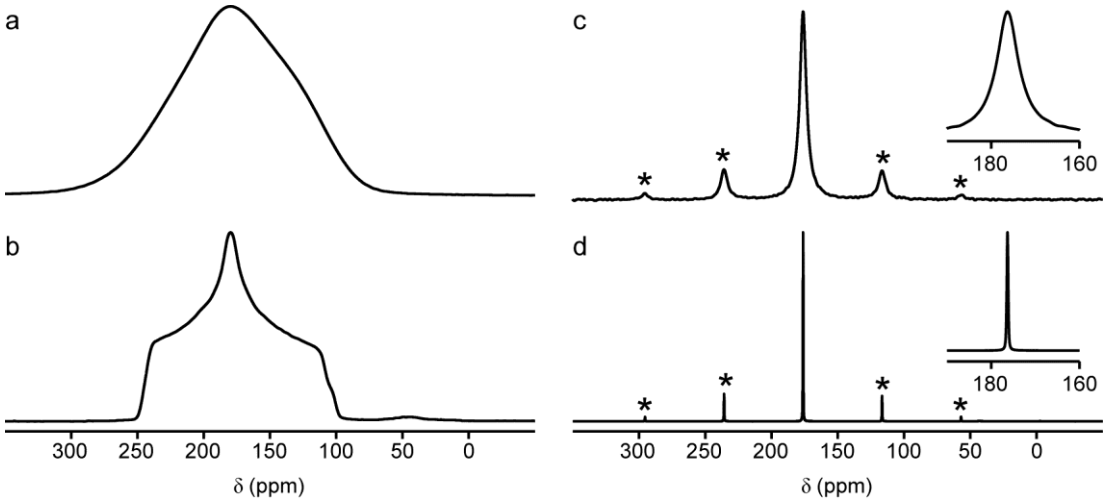

Figure 3.2. ^{13}C (9.4 T) NMR spectra of 1[^{13}C]-glycine with (a) no resolution enhancement, (b) TPPM-15 decoupling ($\nu_1 \approx 50$ kHz), (c) 6 kHz MAS, (d) 6 kHz MAS and TPPM-15 decoupling ($\nu_1 \approx 50$ kHz). Insets in parts (c) and (d) show the isotropic resonance and asterisks are denoted by spinning sidebands.

leaving a resonance broadened only by the CSA (Figure 3.2(b)). MAS (6 kHz) removes the CSA, but it can be seen that some broadening of the isotropic resonance remains (Figure 3.2(c)). The residual broadening arises from the coupling of ^{13}C to the essentially infinite spin network of ^{1}H, and can be removed by decoupling (Figure 3.2(d)). Therefore, it is common to combine MAS and decoupling, to achieve the most efficient enhancement of resolution. In the example shown here, the lineshape is narrowed by a factor of ~290 (from 10.9 kHz to 38 Hz) by combining MAS and decoupling.

3.2 HIGH-RESOLUTION NMR SPECTRA OF QUADRUPOLAR NUCLEI

Quadrupolar nuclei ($I > 1/2$) are subject to the same interactions with their local magnetic environment as spin $I = 1/2$ nuclei, but the interaction between the nuclear quadrupole moment and the EFG typically dominates the spectrum. Therefore, while the above techniques to remove the interactions affecting spin $I = 1/2$ nuclei may still be used, it is the removal of the first- and second-order quadrupolar interactions that provides the greatest resolution enhancement for NMR spectra of quadrupolar nuclei.

3.2.1 High-Field Techniques

As the second-order quadrupolar broadening is inversely dependent on ω_0, it should be possible to reduce this broadening simply by increasing the B_0 field strength used (although an infinite field would be required in order to achieve a truly isotropic spectrum). Technologically, however, this approach is challenging – as can be seen in Figure 3.3(a), while a B_0 field strength of 20.0 T does, indeed, lead to a narrowing of the ^{71}Ga resonance of $GaPO_4$ berlinite relative to that at $B_0 = 14.1$ T, the resonance is still 55 kHz wide at the higher field (*cf.* 80 kHz at 14.1 T). For fields significantly above 24 T – close to the current limit for superconducting magnets – it is necessary to use hybrid superconducting-resistive magnets, which tend to suffer from greater field instability and inhomogeneity. Therefore, although the ^{27}Al NMR spectrum of $Al_{18}B_4O_{33}$ shown in Figure 3.3(b) is essentially free of second-order quadrupolar broadening at 40.0 T, the resonances are broadened by B_0 field imperfections, which cannot be modelled mathematically (unlike the quadrupolar interaction, whose mathematical form is known).[5] In addition, the vast size and cost (both outlay and maintenance) of such magnets means that there are very few such facilities globally.

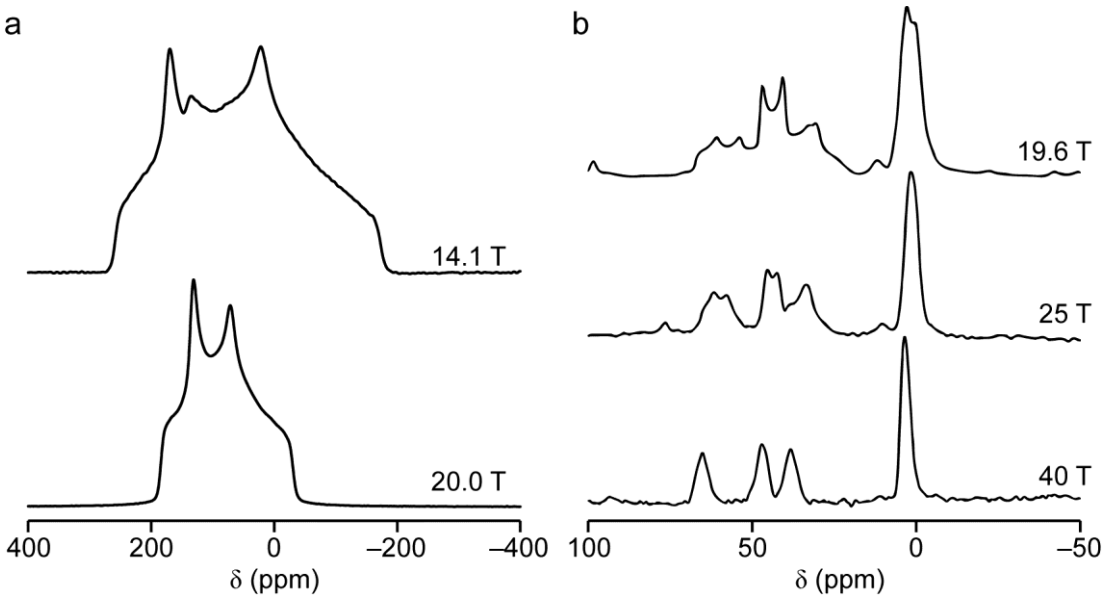

Figure 3.3. (a) ^{71}Ga NMR spectra of static $GaPO_4$ berlinite recorded at B_0 field strengths of 14.1 T and 20.0 T. (b) ^{27}Al MAS NMR spectra of $Al_{18}B_4O_{33}$, recorded at the indicated B_0 field strengths. Adapted with permission from Z. Gan *et al.*, *J. Am. Chem. Soc.*, **2002**, *124*, 5634.[5] Copyright 2002 American Chemical Society.

3.2.2 Physical Rotation of Samples

3.2.2.1 MAS

MAS can, in principle, remove the first-order quadrupolar broadening, which is proportional to $d^2_{0,0}(\beta')$. However, as the first-order broadening typically leads to resonances spanning several MHz (with the exception of the CT, which is unaffected by this broadening), spectra appear as a broad envelope of SSBs even at very rapid MAS rates, as demonstrated by the ^{27}Al MAS NMR spectrum of SIZ-4, shown in Figure 3.4(a). In order to consider the effects of MAS on the second-order broadening, it is necessary to consider the orientation of the EFG tensor in the laboratory frame during MAS. For a static sample, the PAS of the EFG tensor is related directly to the laboratory frame by the Euler angles, α, β and γ. However, when the sample is spinning, the PAS of the EFG is related to the rotor frame by the Euler angles, α', β' and γ'. The rotor frame is related to the laboratory frame by the two angles, θ_m and $-\omega_r t + \xi$, where ω_r is the MAS rate (in rad s^{-1}) and ξ is the initial phase of the crystallite relative to the rotor. The transformation from the PAS of the

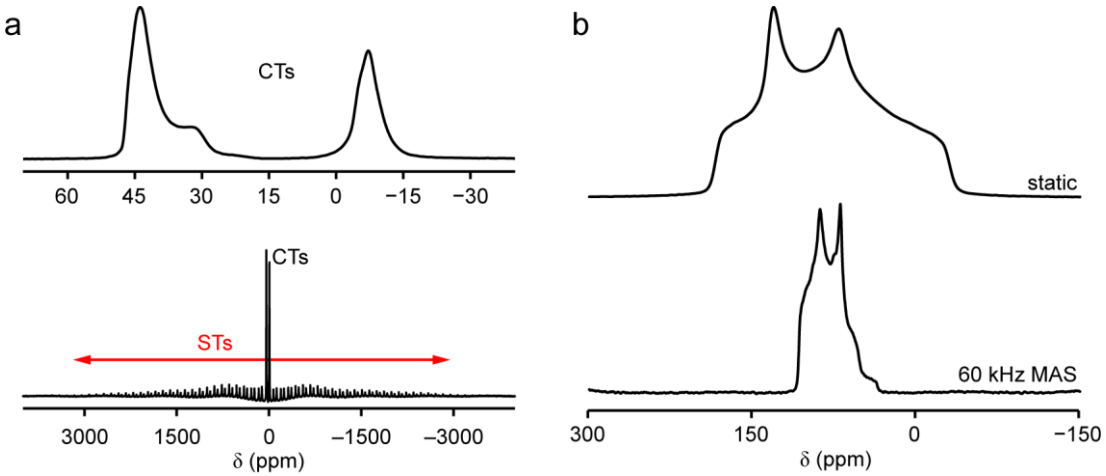

Figure 3.4. (a) ^{27}Al (9.4 T, 12.5 kHz MAS) NMR spectrum of SIZ-4. (b) ^{71}Ga (20.0 T) NMR spectra of $GaPO_4$ berlinite, acquired with and without MAS (60 kHz).

EFG to the laboratory frame is

$$D^{l}_{0,n}(\alpha, \beta, \gamma) = \sum_{m=-l}^{l} D^{l}_{0,m}(0, \theta_m, \omega_r t + \xi) D^{l}_{m,n}(\alpha', \beta', \gamma') \ . \qquad (3.2)$$

For a whole number of rotor periods, Equation 3.2 is non-zero only when m = 0, *i.e.*,

$$\begin{aligned} D^{l}_{0,n}(\alpha, \beta, \gamma) &= D^{l}_{0,0}(0, \theta_m, 0) D^{l}_{0,n}(0, \beta', \gamma') \\ &= d^{l}_{0,0}(\theta_m) D^{l}_{0,n}(0, \beta', \gamma') \ . \end{aligned} \qquad (3.3)$$

The perturbation of the m_I level, over a whole number of rotor periods, is then

$$E^{2}_{m_I} = \frac{\left(\omega_Q^{PAS}\right)^2}{2\omega_0} \begin{pmatrix} A^{0}_{I,m_I} b^{0}\left(\eta_Q\right) + A^{2}_{I,m_I} d^{2}_{0,0}(\theta_m) b^{2}\left(\eta_Q, \beta', \gamma'\right) \\ + A^{4}_{I,m_I} d^{4}_{0,0}(\theta_m) b^{4}\left(\eta_Q, \beta', \gamma'\right) \end{pmatrix} , \qquad (3.4)$$

where expressions for $b^0(\eta_Q)$, $b^2(\eta_Q, \beta', \gamma')$ and $b^4(\eta_Q, \beta', \gamma')$ are given in Appendix E. The second-order quadrupolar contribution to the frequency of the CT in a MAS experiment is, therefore,

$$E^{2}_{1/2} - E^{2}_{-1/2} = \frac{\left(\omega_Q^{PAS}\right)^2}{\omega_0} \begin{pmatrix} A^{0}_{I,1/2} b^{0}\left(\eta_Q\right) + A^{2}_{I,1/2} d^{2}_{0,0}(\theta_m) b^{2}\left(\eta_Q, \beta', \gamma'\right) \\ + A^{4}_{I,1/2} d^{4}_{0,0}(\theta_m) b^{4}\left(\eta_Q, \beta', \gamma'\right) \end{pmatrix} . \qquad (3.5)$$

It can be seen that Equation 3.5 still contains an isotropic shift and two anisotropic components. As the roots of $d^{4}_{0,0}(\theta)$ and $d^{2}_{0,0}(\theta)$ are not the same, the second-order broadening cannot be completely removed by MAS, or spinning at any other angle.

However, MAS does achieve a narrowing of the linewidth by a factor of ~3, (corresponding to averaging to zero the second-rank anisotropic broadening), as shown in Figure 3.4(b) for the ^{71}Ga resonance of $GaPO_4$ berlinite.

3.2.2.2 Double Rotation

Perhaps the most obvious way to remove the second-order anisotropic broadening is to extend the principles of MAS and solve $d^4_{0,0}(\theta)$, which is zero at an angle, ϕ_m, of 30.56 or 70.12°. Therefore, instead of rotating the sample at an angle of θ_m to $\mathbf{B}_0$, it can be rotated at the angle, ϕ_m, (typically 30.56° rather than 70.12°) around an axis inclined at an angle θ_m to $\mathbf{B}_0$. This process of DOuble Rotation (DOR)[6] averages the second-order quadrupolar broadening to zero, as well as removing all interactions that would be removed by MAS. However, DOR is practically limited by the fact that the sample must be held in a small rotor, placed within a bulky outer rotor, which typically achieves spinning rates < 2 kHz, while the inner rotor typically has a maximum spinning rate of ~10 kHz. Therefore, while the technique provides true isotropic peaks and very high-resolution spectra, they are cluttered by SSBs, making identification of isotropic resonances challenging, especially in complicated samples with multiple sites present in the same spectrum. Additionally, DOR is likely to remain a niche technique, owing to the requirement for a special rotor and probe.

3.2.2.3 Dynamic Angle Spinning

Dynamic Angle Spinning (DAS)[7] can be considered as a combination of MAS and DOR, in that the sample is spun in a single rotor, but the axis of rotation relative to $\mathbf{B}_0$ is changed during the experiment. Like DOR, DAS is likely to remain a niche technique owing to the requirement for a specialist probe and a sample with a suitably slow T_1 relaxation constant.

3.2.3 Spin-Manipulation Techniques

3.2.3.1 Multiple-Quantum MAS

The first high-resolution technique for quadrupolar nuclei that did not require the construction of a new magnet, probe or rotor was Multiple-Quantum (MQ) MAS.[8] The MQMAS experiment is a two-dimensional experiment, which correlates MQ evolution during t_1 with single-quantum evolution during t_2. Under MAS, the

frequency of a symmetric MQ transition is given by

$$E^2_{m_I} - E^2_{-m_I} = \frac{\left(\omega_Q^{PAS}\right)^2}{\omega_0}\left(A^0_{I,m_I} b^0\left(\eta_Q\right) + A^4_{I,m_I} d^4_{0,0}(\theta_m) b^4\left(\eta_Q, \beta', \gamma'\right)\right). \quad (3.6)$$

In a two-dimensional experiment, in which the magnetisation evolves as a MQ coherence in t_1 and as the CT in t_2, the time-domain signal will be

$$S\left(t_1,t_2\right) = e^{-i\omega_{(+m_I \leftrightarrow -m_I)}t_1} e^{-i\omega_{(+1/2 \leftrightarrow -1/2)}t_2} \quad . \quad (3.7)$$

As A^0_{I,m_I} and A^4_{I,m_I} are always different for the CT and any given symmetric MQ transition, the isotropic and fourth-rank terms will be refocused at different values of (t_1, t_2). Fourier transform of $S(t_1,t_2)$ leads to a spectrum containing "ridge" lineshapes that lie along a gradient, R, determined by the ratio of A^0_{I,m_I} and A^4_{I,m_I}. These gradients, or MQMAS ratios, are given in Appendix F. A projection of the spectrum perpendicular to this gradient yields a spectrum, in which the fourth-rank broadening has been refocused, the second-rank broadening has been averaged to zero (by MAS) and the isotropic information remains. In addition, the projection of the ridge parallel to δ_2 is still affected by the anisotropic broadening. However, crucially, as the lineshapes are separated in the isotropic dimension, a cross-section can be obtained for each individual lineshape, allowing information about C_Q and η_Q to be obtained. In practice, it is challenging to obtain the isotropic projection along an arbitrary gradient and it is more straightforward to shear the spectrum and obtain the isotropic spectrum as a sum projection perpendicular to δ_2. This also allows more ready extraction of the cross sections of the lineshapes, which lie parallel to δ_2.

The original pulse sequence for MQMAS involved the excitation of 3Q coherences by two pulses, separated by a short delay, τ_e.[8] A single pulse can then convert the 3Q coherences to the observable single-quantum magnetisation. MQ coherences can also be excited by a single high-power pulse and, when C_Q is significant (*i.e.*, when MQMAS is likely to be required), single-pulse excitation is more efficient than the two-pulse process.[9-11] However, in all cases, single-quantum coherences will be excited far more efficiently than the desired MQ coherence, and phase cycling must be used to remove these coherences from the signal.

Using a two-pulse MQMAS experiment (*i.e.*, with a single excitation pulse), a spectrum is obtained that contains "phase-twist" lineshapes. These lineshapes arise from a combination of absorptive and dispersive components in the real part of the signal as a consequence of modulation of the phase of $S(t_1)$ in the experiment. These lineshapes are undesirable, as they reduce the spectral resolution and can make it hard to obtain reliable information from the spectrum. The phase-twist lineshapes can be removed either by amplitude-modulation of $S(t_1)$, or the acquisition of a whole echo in t_2 of a phase-modulated experiment. An amplitude-modulated experiment selects two symmetrical coherence pathways (*e.g.*, $p = \pm 3$ for 3QMAS), and is usually combined with a "z filter",[12, 13] as shown in Figure 3.5(a). In a z-filtered experiment, the MQ coherence is converted to non-equilibrium magnetisation aligned along the z axis rather than directly to single-quantum transverse magnetisation. The magnetisation is stored along the z axis for the duration of the z filter (usually a few μs) to allow any unwanted coherences remaining in the transverse plane to dephase. Following this, the desired magnetisation is converted to single-quantum transverse magnetisation by application of another pulse, which is generally chosen to be of low power, such that the CT is excited efficiently whereas the STs are not (thereby preventing loss of population from the CT to the STs). A ^{87}Rb (I = 3/2) 3QMAS NMR spectrum of $RbNO_3$ acquired using the z-filtered amplitude-modulated experiment shown in Figure 3.5(a) is shown in Figure 3.5(b). The sheared spectrum and corresponding isotropic projection are shown in Figure 3.5(c).

Unlike an amplitude-modulated experiment, a phase-modulated experiment selects a single coherence pathway, and modulates the phase of $S(t_1)$.[14] The selected coherence pathway depends on the sign of the MQMAS ratio (given in Appendix F), which is positive for all MQ coherences except the highest-order coherence available for a given spin (*e.g.*, the 3QMAS ratio is negative for I = 3/2, but positive for I = 5/2, 7/2 or 9/2). When the ratio is negative, the $p = -n$ coherence in t_1 must be correlated with the $p = -1$ coherence in t_2 and, for a positive ratio, the $p = +n$ coherence is selected instead. Acquisition of the whole echo, as shown in the pulse sequence in Figure 3.6, allows a phase-pure lineshape to be obtained in both ω_1 and ω_2. However, as the whole echo must be acquired, the echo delay, τ, must be chosen

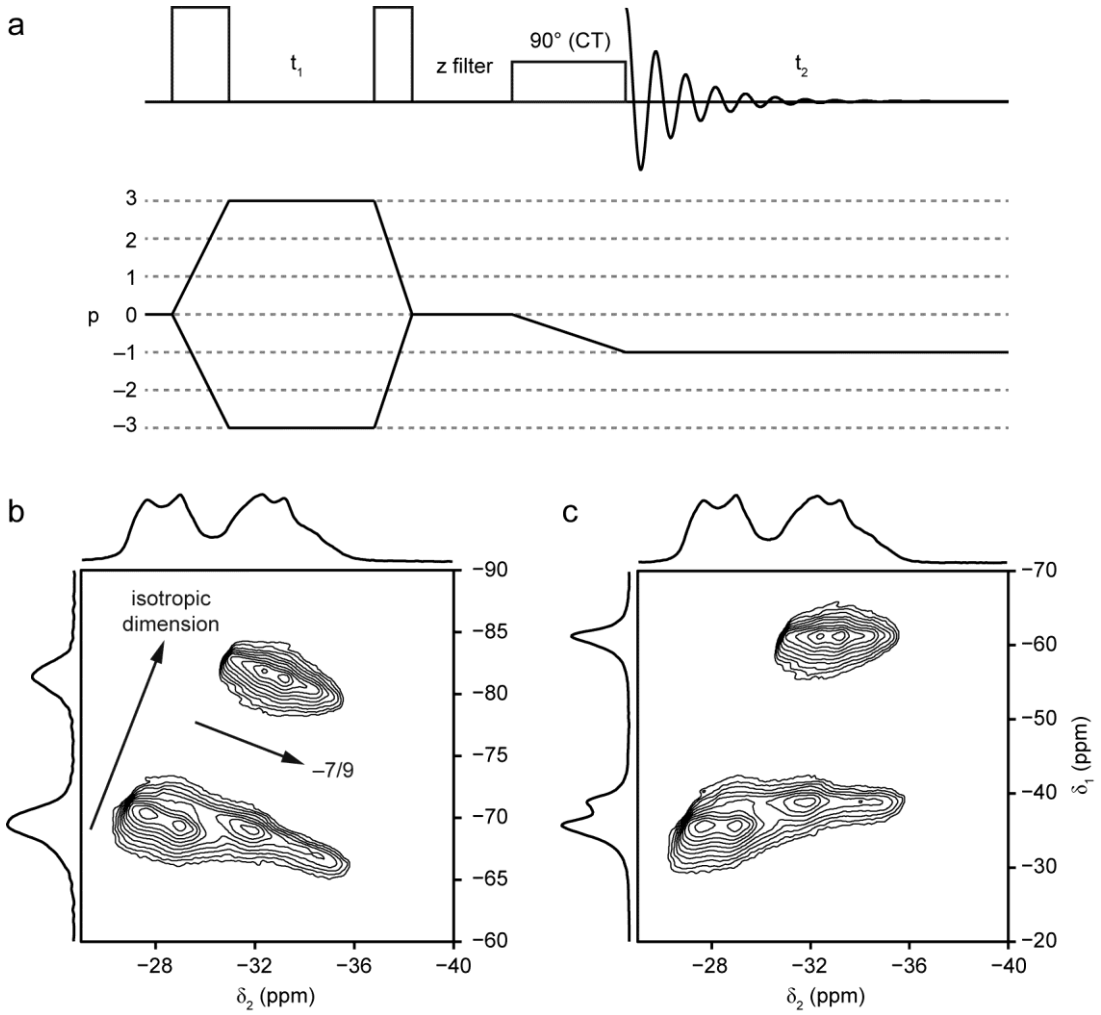

Figure 3.5. (a) The pulse sequence and coherence transfer pathway for a z-filtered amplitude-modulated MQMAS experiment, shown here for 3QMAS. (b) ^{87}Rb (14.1 T, 20 kHz 3QMAS) NMR spectrum of $RbNO_3$, acquired using the experiment from part (a). (c) The spectrum from part (b) after a shearing transformation has been applied. In parts (b) and (c) the sum projections perpendicular to δ_1 and δ_2 are shown.

to be at least the length of the FID, which can sometimes lead to a significant (and, in some cases, total) loss of signal, owing to transverse relaxation.

Both amplitude- and phase-modulated experiments can be modified by the "split-t_1" approach, in which the magnetisation evolves as the desired MQ coherence for a portion of t_1, kt_1, and as single-quantum magnetisation for the remainder of t_1, $k't_1$, where k and k′ are related to the MQMAS ratio.[15] The pulse sequence for a split-t_1 shifted echo MQMAS experiment is shown in Figure 3.7(a). The advantage of this

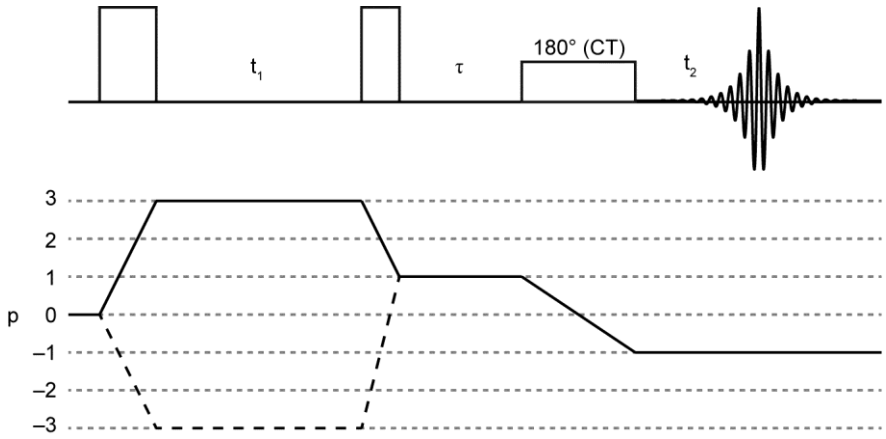

Figure 3.6. The pulse sequence and coherence transfer pathway for a shifted-echo phase-modulated MQMAS experiment, shown here for 3QMAS, with solid lines indicating the coherence transfer pathway for nuclei with I > 3/2, and the dashed line indicating the pathway for nuclei with I = 3/2.

approach is that the fourth-rank anisotropic term is refocused at the end of t_1 rather than at some point in t_2, and the resulting spectrum contains ridge lineshapes that are parallel to δ_2 without the need to apply a shearing transformation, as shown by the ^{87}Rb NMR spectrum of $RbNO_3$ in Figure 3.7(b). Lineshapes extracted from this spectrum for each Rb species, assigned according to Skibsted and Jakobsen,[16] are shown in Figure 3.7(c), and demonstrate the ability of the MQMAS experiment to separate the isotropic and anisotropic components of the quadrupolar interaction.

For a crystalline material with sharp, well-defined isotropic resonances, it is possible to obtain the NMR parameters (δ_{iso}, C_Q and η_Q) from the lineshape extracted parallel to δ_2 for each resonance. Such a lineshape is most easily extracted for sheared spectra (or those acquired using a split-t_1 experiment). However, where there exists – through disorder, *etc*. – a distribution of NMR parameters, the lineshape will be broadened along an additional gradient dependent on whether the distribution is of chemical shift or EFG parameters (or both). These gradients are given in Appendix F. When the resonances are broadened by distributions of both chemical shift and EFG parameters, it may be impossible to observe distinct resonances or determine readily the gradients along which broadening occurs. In such cases, the average P_Q, $\langle P_Q \rangle$, may still be approximated by the position of the centre of gravity, (δ_2, δ_1). The

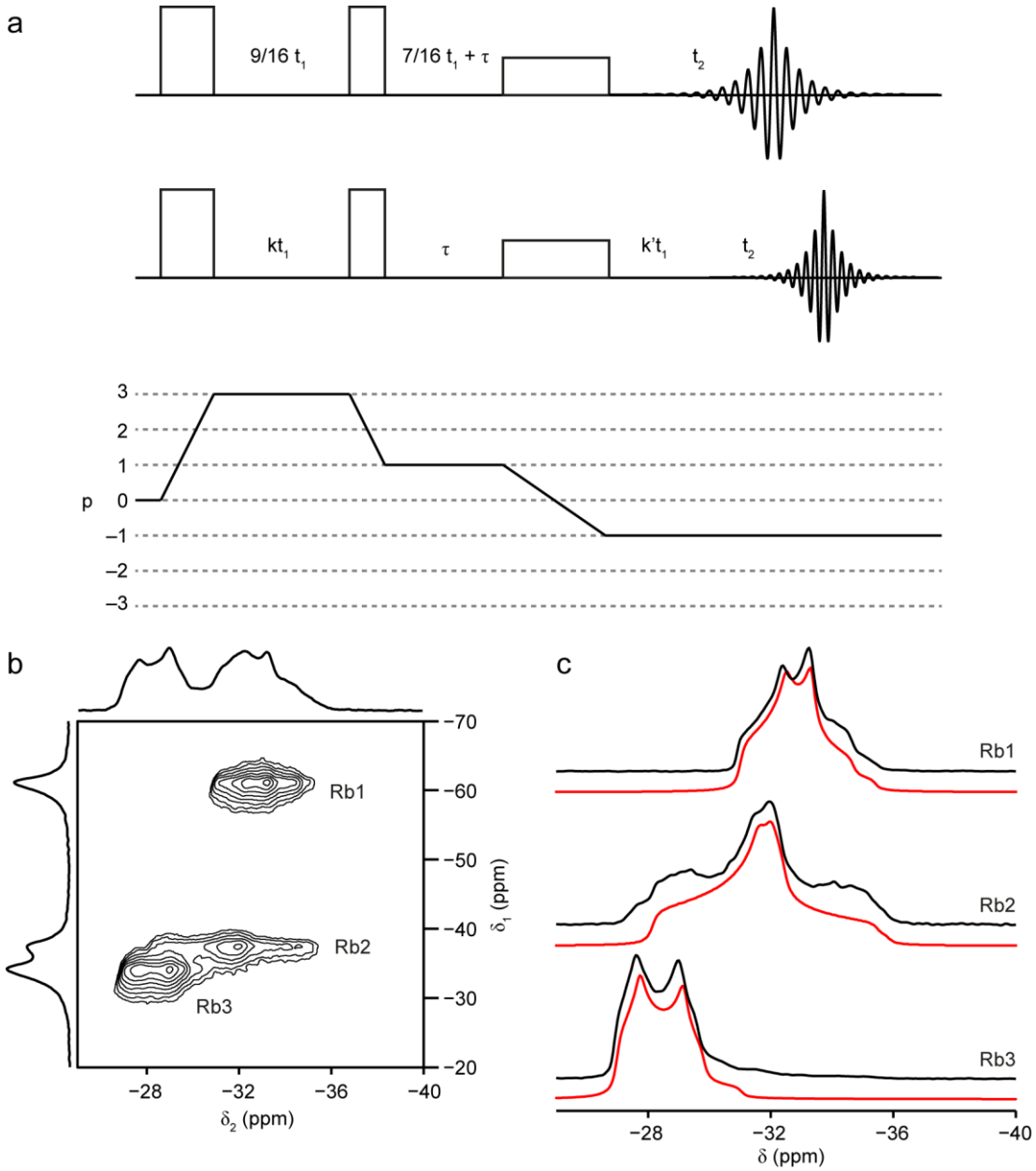

Figure 3.7. (a) The pulse sequence and coherence transfer pathway for a split-t_1 shifted-echo phase-modulated MQMAS experiment, shown here for 3QMAS for I = 3/2 (top) and I > 3/2 (below), where k and k′ depend on I. (b) ^{87}Rb (14.1 T, 20 kHz 3QMAS) NMR spectrum of $RbNO_3$, acquired using the experiment shown in (a). The projections perpendicular to δ_1 and δ_2 are shown. (c) Cross-sections parallel to δ_2, extracted from the spectrum in (b) Fits to the cross-sections are shown in red, with δ_{iso} = –30.9 ppm, C_Q = 1.62 MHz, η_Q = 0.6 for Rb1, δ_{iso} = –28.1 ppm, C_Q = 2.06 MHz, η_Q = 0.9 for Rb2, and δ_{iso} = –26.6 ppm, C_Q = 1.63 MHz, η_Q = 0.3 for Rb3.

δ_1 and δ_2 positions of the centre of gravity of a resonance depend on δ_{iso} and the isotropic quadrupolar shift, δ_Q, as given in Appendix G and it can be seen that both δ_{iso} and δ_Q can, therefore, be determined from the centre of gravity of the resonance. P_Q (in units of Hz) is then

$$P_Q = \frac{2I(2I-1)\omega_0\sqrt{\delta_Q}}{3\pi \times 10^3} \quad . \tag{3.8}$$

3.2.3.2 Satellite-Transition MAS

Satellite-Transition (ST) MAS can be used to overcome the inherently low sensitivity of MQMAS by avoiding the excitation of multiple-quantum transitions. Instead, the experiment correlates the STs with the CT. By careful setting of the θ_m (*i.e.*, 54.736° rather than 54.74°) and careful rotor synchronisation of pulses and delays, STMAS can typically provide ~4-8 times more sensitivity that the corresponding MQMAS experiment.[17] However, if there is motion present on the microsecond timescale, this can broaden the STs (which are of the order of the inverse of the correlation time, τ_c) while leaving the CT and MQ transitions unaffected. This leads to a significant loss of resolution in the STMAS spectrum compared to the MQMAS spectrum.[18] While this is undesirable when isotropic information is sought, the difference in resolution between STMAS and MQMAS spectra as a function of temperature can be a very useful probe of dynamic processes occurring within the sample. However, despite the vast improvement in sensitivity (and the correspondingly vast time saving) achieved by using STMAS rather than MQMAS, the requirement for high precision angle setting and rotor synchronisation has, so far, prevented the technique from gaining the same degree of universal popularity as MQMAS.

3.3 SENSITIVITY-ENHANCING EXPERIMENTS

The sensitivity of a NMR spectrum may be enhanced simply by a combination of MAS and decoupling, as all of the spectral intensity of a resonance is contained within a much narrower frequency range, resulting in an increased peak-height-to-noise ratio. (The peak-height-to-noise ratio is a measure of the maximum spectral intensity relative to the noise in a spectrum, and is distinct from the SNR, which measures the integrated intensity of the signal relative to the noise.) However, this

sensitivity enhancement is often insufficient to yield high-quality (*i.e.*, good SNR) NMR spectra on a reasonable timescale, and several techniques have been developed to provide further improvements in the sensitivity of NMR experiments.

3.3.1 Cross Polarisation

Cross polarisation (CP) was introduced by Hartmann and Hahn in 1962.[19] The technique involves creating transverse magnetisation for a nuclear spin, I and then, as shown in Figure 3.8(a), applying a "spin-lock" pulse simultaneously to the I spins, and spins of another type, S. During this pulse, the spins are "locked" in the rotating frame, and do not dephase. If the Hartmann-Hahn match condition

$$\omega_{1I} = \omega_{1S} \ , \tag{3.9}$$

(or, when combined with MAS at a rate of ω_R (in units of rad s^{-1}) the Hartmann-Hahn "spinning sideband" condition[20, 21]

$$\omega_{1I} = \omega_{1S} \pm n\omega_R \ , \tag{3.10}$$

where n is typically 1 or 2) is satisfied, then the S spins are then polarised by this "contact" with the locked I spins. The match conditions can be relaxed by using amplitude-modulated pulses to satisfy the match condition for more crystallites throughout the spin-locking period (a "ramped" pulse is applied to the I spins in Figure 3.8(a)).[22] The polarisation of the S spins leads to a signal, M_S^{CP}, whose intensity relative to the corresponding one-pulse experiment, M_S^{BD} is given by[23]

$$\frac{M_S^{CP}}{M_S^{BD}} = \frac{\gamma_I}{\gamma_S}\frac{1}{1+\varepsilon} \ , \tag{3.11}$$

where

$$\varepsilon = \frac{S(S+1)N_S}{I(I+1)N_I} , \tag{3.12}$$

where N_S and N_I are the number of S and I spins, respectively, that are present. In the case of $\varepsilon \ll 1$, and for I = S = 1/2, Equation 3.11 can be approximated as

$$\frac{M_S^{CP}}{M_S^{BD}} = \frac{\gamma_I}{\gamma_S}\left(1 - \frac{N_S}{N_I}\right) \ . \tag{3.13}$$

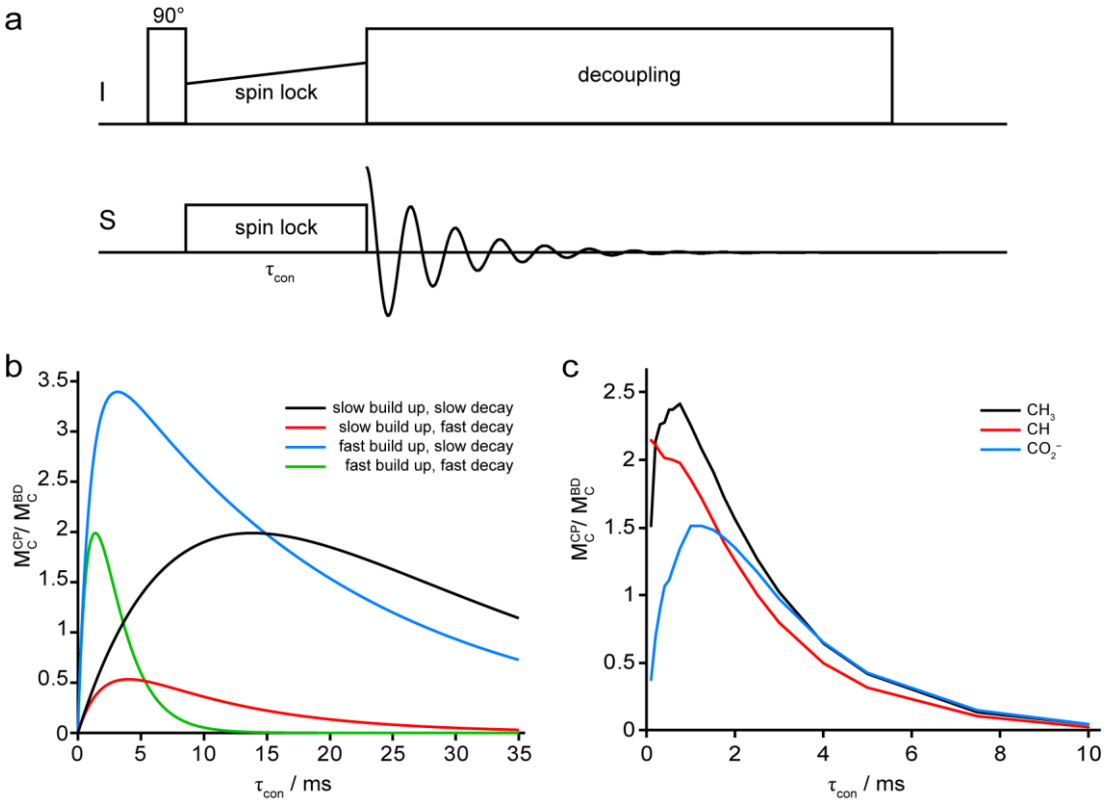

Figure 3.8. (a) The pulse sequence for CP, with a ramped pulse for I. Decoupling of I is normally applied during t_2. (b) Build up of CP magnetisation (given by Equation 3.14) in a ^{1}H-^{13}C CP experiment as a function of the contact time, τ_{con}, for various combinations of build up and decay rates. Slow build up is defined as T_{IS} = 10 ms, and fast build up is defined as T_{IS} = 1 ms. Slow decay is defined as $T_{1\rho}^{I}$ = 20 ms and fast decay is defined as $T_{1\rho}^{I}$ = 2 ms. A static ^{1}H-^{13}C spin pair is assumed, with no amplitude modulation of the spin-locking pulses. (c) Experimental CP build-up curves for L-alanine (9.4 T, 10 kHz MAS).

It can be seen that, when $\gamma_I > \gamma_S$ and $N_I > N_S$, CP leads to a signal enhancement, which is often significant. For example, CP is routinely used in ^{13}C NMR spectroscopy, where $N_S/N_I \approx 1/180$ and $\gamma_I/\gamma_S = 3.98$, giving a theoretical maximum signal enhancement of a factor of ~4. In addition, in the case when $T_{1I} < T_{1S}$, the experimental repeat rate can be increased, as the source of the S magnetisation in the CP experiment is the population of faster-relaxing I nuclei. In the case of CP between ^{1}H and ^{13}C, typical ^{1}H T_1 values are on the order of ~1-5 s, whereas for ^{13}C, T_1 is often on the order of minutes, and CP allows for an increase in repeat rate of ~1-2

orders of magnitude, in addition to decreasing the number of transients that must be coadded to achieve a reasonable SNR.

During the spin-locking period, or "contact time", τ_{con}, the rate of polarisation of S spins is dependent on the dipolar interactions linking the I and S spins, and the build up of S polarisation is described by the time constant, T_{IS}. Relaxation of the I and S spins in the rotating frame, described by the time constants, $T_{1\rho}^{I}$ and $T_{1\rho}^{S}$, will lead to an exponential decay of the polarisation. In the most common case of $\varepsilon \ll 1$ and $T_{IS} \ll T_{1\rho}^{I}$, the build-up of S magnetisation as a function of τ_{con} is given by[24]

$$M_S^{CP} = \frac{\gamma_I}{\gamma_S} M_S^{BD} \left(1 - \frac{T_{IS}}{T_{1\rho}^{I}}\right)^{-1} \left(e^{\frac{-\tau_{con}}{T_{1\rho}^{I}}} - e^{\frac{-\tau_{con}}{T_{IS}^{I}}}\right) . \qquad (3.14)$$

However, it should be noted that Equation 3.14 is an approximation and relies on the coupling of S spins to an infinite network of I spins. It can be appreciated that CP is not quantitative, as S spins that are closer in space to I spins will experience a more rapid build up of polarisation. Figure 3.8(b) shows the build up of ^{13}C magnetisation in a ^{1}H-^{13}C CP experiment in the case of slow build-up (large T_{IS}) and slow decay (large $T_{1\rho}^{I}$), slow build-up and fast decay (small $T_{1\rho}^{I}$), fast build-up (small T_{IS}) and slow decay, and fast build-up and fast decay. It can be seen that the theoretical maximum signal of 3.98 is only approached in the case of rapid build-up and slow decay of polarisation and, in the case of slow build-up and rapid decay of polarisation, the signal is actually *always* less intense when CP is used (with the parameters used for the simulation). While this does not allow CP to provide quantitative information, the spectral "editing" afforded by the technique can often be used to assist the assignment of resonances, as chemically different species are likely to have different CP dynamics. An example of this is shown in Figure 3.8(c) for the ^{1}H-^{13}C CP MAS NMR spectrum of L-alanine, where it can be seen that magnetisation builds up very rapidly for the CH and CH_3 resonances, owing to the close proximity of ^{1}H to these ^{13}C. However, magnetisation builds up more slowly for the CO_2^- resonance, as there are no protons in close spatial proximity (the molecule exists as a zwitterion in the solid form). The decay of the intensity of the CH_3 resonance is slower than that of the CH resonance, owing to the fact that the

CH_3 group can rotate rapidly around the C-C bond, effectively decoupling this moiety from the rest of the structure, whereas the CH group is held much more rigidly in space, leading to more rapid $T_{1\rho}$ relaxation.

3.3.2 Saturation Trains

When T_1 is slow (> ~120 s), the repeat interval of an NMR experiment (Figure 3.9(a)) can be prohibitively long, particularly if the SNR is low and extensive signal averaging is required. Using a repeat interval shorter than $5T_1$ is not advisable, as the equilibrium magnetisation recovered will be reduced after each subsequent experiment. This "saturation" is particularly problematic if the phase cycling scheme of the experiment requires signals with different phase to be coadded with equal amplitude.. In such cases, rather than wait ~$5T_1$ before acquiring each FID, it is possible to apply a saturation train – a series of pulses separated by a delay, τ_{sat}, at the start of the repeat interval, as shown in Figure 3.9(b). Following the saturation train (provided that the number of pulses in the train is sufficient), the nuclear magnetic moments are randomly oriented in the xy plane, and will gradually return to equilibrium. After the repeat interval (now significantly shorter than $5T_1$), a small proportion of the equilibrium magnetisation has been restored, and can be used to generate coherent xy magnetisation for the experiment. In this way, although the signal per FID is decreased, the overall experimental time can still be reduced significantly, particularly for two-dimensional spectra. In addition, as a constant signal is obtained for each FID, phase cycling is possible, allowing the quality of the recorded spectra to be improved.

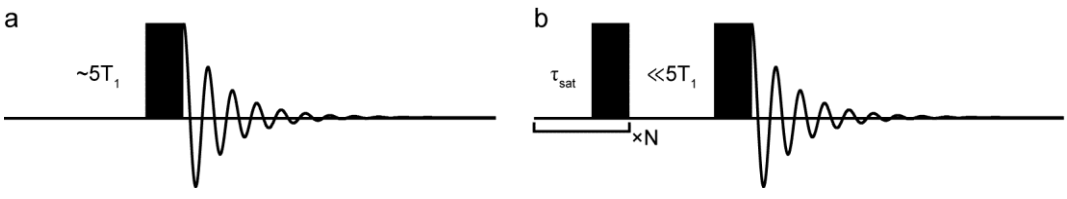

Figure 3.9. Pulse sequences for (a) a one-pulse experiment and (b) a one-pulse experiment preceded by a saturation train. 90° pulses are indicated by rectangles. Typically, N ≈ 20-100 and τ_{sat} ≈ 20-100 ms, depending on the system of interest.

3.4 RELAXATION MEASUREMENTS

3.4.1 Longitudinal Relaxation

The longitudinal relaxation constant, T_1, can be measured using either the inversion recovery experiment shown in Figure 3.10(a), or the saturation recovery experiment shown in Figure 3.10(b). Inversion recovery starts with the magnetisation, M_0, aligned along the z axis at thermal equilibrium. This magnetisation is then inverted by the first pulse, giving $-M_z$. During the "recovery delay", τ_{rec}, the magnetisation returns to equilibrium at a rate of $e^{-\tau/T_1}$, so that the magnetisation after τ_{rec} is

$$M(\tau_{rec}) = M_0(1 - 2e^{\frac{-\tau_{rec}}{T_1}}) \cdot \tag{3.15}$$

After τ_{rec}, transverse magnetisation is generated, with intensity proportional to $M(\tau_{rec})$. By increasing τ_{rec} from 0 to $>5T_1$, a plot of $M(\tau_{rec})$ against τ_{rec} (shown schematically in Figure 3.10(c)) can be constructed and, by iterative line fitting, T_1 can be obtained. Provided a sufficient number of measurements are made, and that the SNR is reasonable, inversion recovery can provide a very accurate measurement of T_1. However, the experiment is not practically suited to measuring very long T_1 relaxation constants, owing to the requirement for the magnetisation to be at thermal equilibrium at the start of each experiment. Because of this requirement, there must be a repeat interval equal to the largest τ_{rec} value (generally $> 5T_1$) for every experiment, regardless of the value of τ_{rec} actually used. Saturation recovery offers a faster alternative to inversion recovery, as the magnetisation is saturated prior to the recovery delay, meaning that the repeat interval of the experiment can essentially be zero for all values of τ_{rec}. The recovery of magnetisation as a function of τ in a saturation recovery experiment (shown schematically in Figure 3.10(d)) is

$$M(\tau_{rec}) = M_0(1 - e^{\frac{-\tau_{rec}}{T_1}}) \cdot \tag{3.16}$$

3.4.2 Transverse Relaxation

The FWHH of a Lorentzian resonance, Δ, is $1/\pi T_2$, and the transverse relaxation constant, T_2, can in principle be determined simply by measuring Δ (assuming $T_1 \gg T_2$). T_2 may also be measured using a series of spin echo experiments with different values of τ. The intensity of the magnetisation, $M(\tau)$, decays exponentially as a

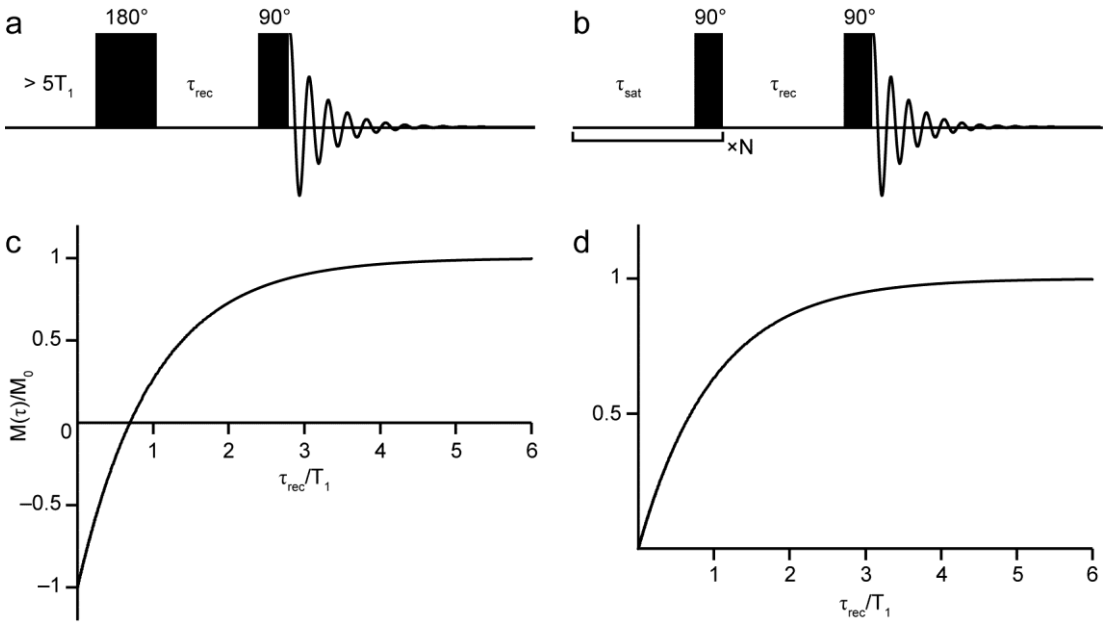

Figure 3.10. Pulse sequences for the (a) inversion recovery and (b) saturation recovery experiments. The magnetisation, $M(\tau_{rec})$ (normalised to M_0) as a function of τ_{rec} for (c) inversion recovery and (d) saturation recovery.

function of τ

$$M(\tau) = M_0 e^{\frac{-\tau}{T_2}} \quad . \tag{3.17}$$

A more efficient means of recording such a dataset is the CPMG experiment,[25, 26] in which a train of spin echoes repeatedly refocuses the magnetisation with many different values of τ in one acquisition period. The intensity of the echo maxima in the FID can be used to determine T_2. In solids, however, it is generally not possible to refocus the magnetisation completely at the end of each τ period (owing to non-refocusable interactions, *e.g.*, higher-order dipolar terms).[27] As a result, the transverse relaxation constant measured in a spin echo experiment, T_2' in the notation of Lesage *et al.*,[27] is typically smaller than the true T_2. The "non-refocusable" linewidth, Δ' can be defined as $1/\pi T_2'$. However, the experimentally-observed linewidth, Δ^*, is $1/\pi T_2^*$, where T_2^* is the apparent transverse relaxation time constant and can have additional contributions from B_0 and B_1 inhomogeneity. In solution, all three time constants are roughly equal but, typically, in solids, $T_2 \geq T_2' > T_2^*$. Therefore, in solids, the linewidth can often be a poor indicator of the true T_2.

3.5 TWO-DIMENSIONAL CORRELATION EXPERIMENTS

3.5.1 Homonuclear Correlations

There are many possible homonuclear correlation experiments that make use of the dipolar or J coupling interactions to transfer information between like spins. In this thesis, only the dipolar interaction was used in this way, using the homonuclear double-quantum correlation experiment shown in Figure 3.11(a). In this experiment, double-quantum coherences (DQCs) are generated by an excitation scheme, evolve with $p = \pm 2$ during t_1, are converted to zero-quantum populations by the conversion scheme (which is the same as the excitation scheme), and then converted to transverse single-quantum magnetisation by a final 90° pulse. The excitation and conversion schemes used here were the BAck to BAck (BABA) sequence,[28, 29] shown in Figure 3.11(b), and the POST-C7 sequence of Hohwy *et al.*,[30] shown in Figure 3.11(c). The BABA sequence involves four 90° pulses applied over the course of one rotor period, with the whole sequence repeated with (typically) N = 1-5. Using more blocks of BABA pulses excites DQCs between pairs of spins linked by weaker dipolar interactions (*i.e.*, spin pairs with a greater spatial separation). The POST-C7 sequence comprises a repeating series of pulses, typically applied for N = 7n rotor periods, where n is typically 3-8. While this achieves the same effect as BABA, a requirement of POST-C7 is that $\omega_{1I} = 7\omega_R$, which restricts the experiment to slower MAS rates. BABA is, therefore, more suitable for ^{1}H and ^{19}F, for which fast MAS is normally required in order to achieve good resolution, but POST-C7 can be used to recouple weaker dipolar interactions at slower MAS rates.

A schematic homonuclear double-quantum correlation experiment is shown in Figure 3.12. For every two spins, I_i and I_j, between which a DQC can be excited, there will be a pair of resonances at a position, (δ_2, δ_1), of $(\delta_i, \delta_i+\delta_j)$ and $(\delta_j, \delta_i+\delta_j)$. In the case of $I_i = I_j$, there will be a single resonance at $(\delta_i, 2\delta_i)$. The spectrum therefore contains a series of peaks symmetrically spaced from the $\delta_1 = 2\delta_2$ "diagonal" indicating close spatial proximities between pairs of different I spins, and on-diagonal resonances indicating close spatial proximities between pairs of like I spins. These features can be seen in the schematic spectrum of the A_2BC spin system shown in Figure 3.12. It is possible to excite DQCs between the two A spins (as they

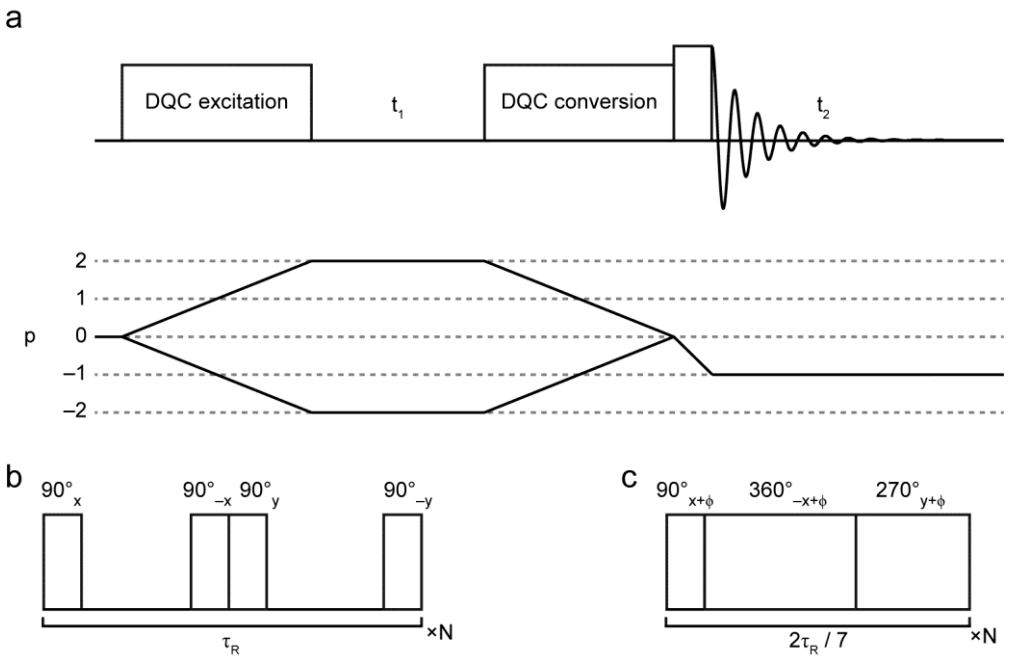

Figure 3.11. (a) The general pulse sequence and coherence transfer pathway for a homonuclear double-quantum correlation experiment. The (b) BABA and (c) POST-C7 schemes for exciting and converting DQCs. In part (c), $\phi = N/7$.

are either close in space, or connected *via* a short bonded pathway), giving rise to an on-diagonal resonance at (δ_A, $2\delta_A$). In addition, DQCs can be excited between A and C, and C and B, giving rise to pairs of resonances at (δ_A, $\delta_A + \delta_C$) and (δ_C, $\delta_A + \delta_C$) for the A-C DQC, and (δ_B, $\delta_B + \delta_C$) and (δ_C, $\delta_B + \delta_C$) for the B-C DQC. No A-B DQC is observed, and there are no on-diagonal resonances corresponding to B-B or C-C DQCs. It should be noted that spatially-isolated spins (*e.g.*, ^{1}H in HO^-) do not give rise to resonances in this experiment, as spins must have evolved as double-quantum coherences during t_1.

3.5.2 Heteronuclear Correlations

Like homonuclear correlation experiments, heteronuclear correlation (HETCOR) experiments transfer magnetisation between I and S spins (where I ≠ S) through bonds (*via* the J coupling) or through space (*via* the dipolar interaction). In this thesis, two heteronuclear correlation methods were used; CP-HETCOR, which uses spin-locking to transfer magnetisation *via* the dipolar interaction, and refocused Insensitive Nuclei Enhanced by Polarisation Transfer (INEPT),[31, 32] which uses a

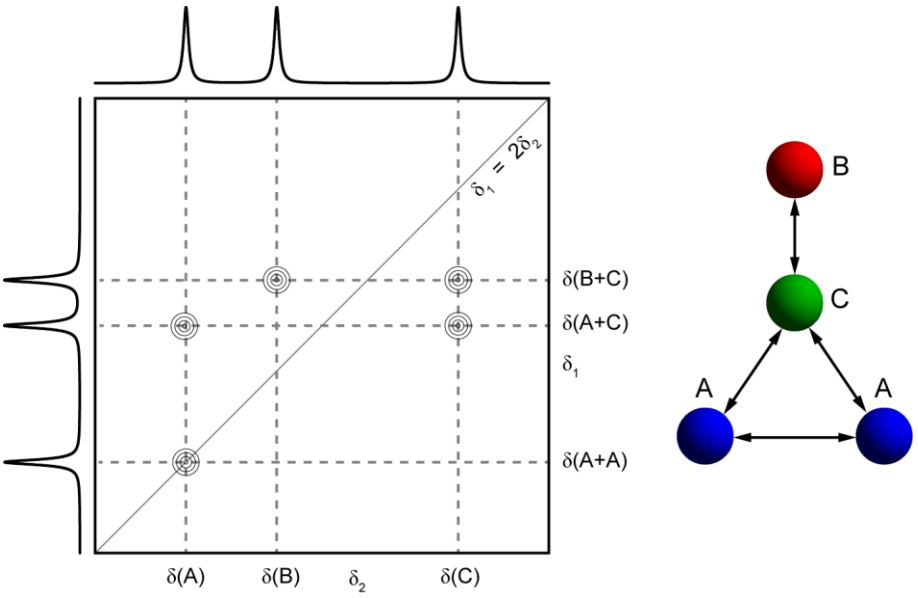

Figure 3.12. Schematic homonuclear double-quantum correlation spectrum for the A_2BC spin system shown.

series of pulses on the I and S spins to transfer the magnetisation *via* the J coupling. The pulse sequences for these experiments, as used here, are shown in Figure 3.13. The CP-HETCOR experiment works in a manner analogous to the CP experiment described above, but with the addition of a t_1 evolution period for the I spins before the spin-lock pulses are applied. Evolution of the I spins during t_1 modulates the polarisation available for transfer during the spin lock, allowing a 2D dataset to be constructed as described in Section 2.3.6. The refocused INEPT experiment can be understood using the product operator notation introduced in Section 2.3.4.[33] The experiment starts with the creation of transverse I magnetisation, $-I_y$, of intensity k_I

$$k_I I_z \xrightarrow{90°_x} -k_I I_y \quad , \tag{3.18}$$

which evolves, under a scalar coupling of magnitude J_{IS} (in Hz), over the period $2\tau_1$, with the spin echo used to refocus any evolution due to offsets (*e.g.*, chemical shifts) during this time. At the end of $2\tau_1$, the product operator description of the system is

$$k_I \sin(2\pi J_{IS}\tau_1) 2I_x S_z - k_I \cos(2\pi J_{IS}\tau_1) I_y \quad . \tag{3.19}$$

The Iy term can be neglected (as discussed below, τ_1 is normally $1/4J_{IS}$, so that I_y is zero), and only the anti-phase $2I_xS_z$ term is affected by the $90°_y$ pulse on I, or the $90°_x$ pulse on S. Although the pulses are applied simultaneously, their effects can be considered

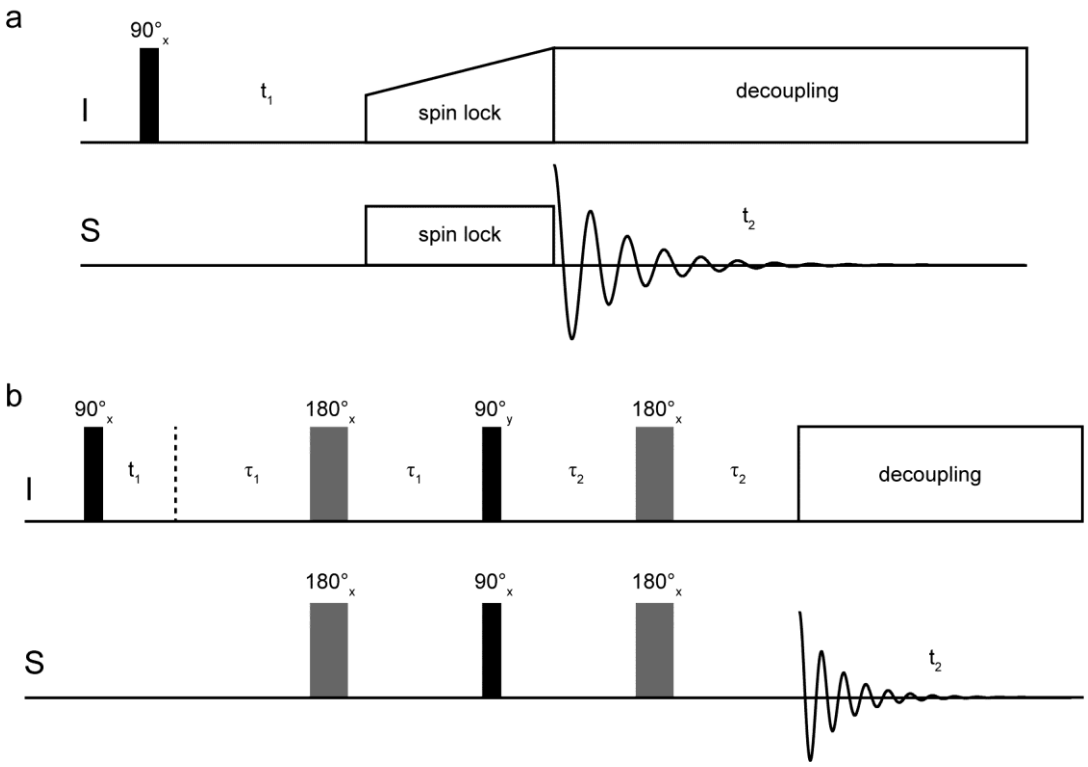

Figure 3.13. The pulse sequences for heteronuclear I = S = 1/2 (a) CP-HETCOR and (b) refocused INEPT correlation experiments.

sequentially, in either order. The description of the system becomes

$$k_I \sin(2\pi J_{IS}\tau_1) 2I_xS_z \xrightarrow{(\pi/2)I_y} -k_I \sin(2\pi J_{IS}\tau_1) 2I_zS_z \xrightarrow{(\pi/2)I_y} k_I \sin(2\pi J_{IS}\tau_1) 2I_zS_y \ . \quad (3.20)$$

The anti-phase $2I_zS_y$ coherence then evolves under the scalar coupling during the period $2\tau_2$, with any evolution during this time arising from offsets again refocused by the spin echo. At the end of the second period, the magnetisation is given by

$$k_I \cos(2\pi J_{IS}\tau_2) \sin(2\pi J_{IS}\tau_1) 2I_zS_y - k_I \sin(2\pi J_{IS}\tau_2) \sin(2\pi J_{IS}\tau_1) S_x \ . \quad (3.21)$$

It can be seen that when $\tau_1 = \tau_2 = 1/4J_{IS}$, the in-phase transverse S_x magnetisation is a maximum (k_I). As a one-pulse experiment would yield a signal $-k_SS_y$, the signal of the S spins has been enhanced by a factor of k_I/k_S by the experiment, although this theoretical enhancement is not always achieved. By including the t_1 evolution period prior to magnetisation transfer, the experiment becomes two dimensional, with any evolution due to offsets occurring during t_1 being retained at the end of the period, $t_1 + 2\tau_1$. The INEPT experiment, therefore, provides both sensitivity enhancement and information on the through-bond connectivity of chemical species.

In solids, the scalar coupling is typically orders of magnitude smaller than the heteronuclear dipolar interaction and transverse relaxation can lead to a significant loss of magnitude of the signal over the evolution and transfer periods, meaning that optimum signal transfer often occurs with τ_1 and $\tau_2 < 1/4J_{IS}$. Transverse relaxation and these non-optimal τ periods mean that the observed signal will be enhanced by less than the theoretical factor of k_I/k_S. Experimental optimisation is, therefore, essential to ensure the maximum signal intensity is observed. In addition, when the I spins experience significant homonuclear dipolar interactions (*e.g.*, when I is ^{1}H), homonuclear decoupling[34] is required in order to achieve high resolution in the spectrum of the I spins.

3.6 General Experimental Details

3.6.1 Solid-State NMR Spectroscopy

Solid-state NMR spectra were recorded using Bruker Avance III spectrometers equipped with wide-bore superconducting magnets with B_0 field strengths of 9.4, 14.1 or 20.0 T (respective ^{1}H Larmor frequencies of 400, 600 and 850 MHz). For spectra acquired at 9.4 T, samples were packed into zirconia MAS rotors with outer diameters of 4 or 7 mm and rotated at MAS rates of up to 14 kHz (4 mm rotors) or 7 kHz (7 mm rotors) using Bruker double-resonance (4 mm and 7 mm rotors) or quadruple-resonance (4 mm rotors) MAS probes. For spectra acquired at 14.1 T, samples were packed into standard zirconia MAS rotors with outer diameters of 4, 3.2, 2.5 or 1.3 mm and rotated at MAS rates of up to 14 kHz (4 mm rotors), 22 kHz (3.2 mm rotors), 12.5-35 kHz (2.5 mm rotors) or 40-62.5 kHz (1.3 mm rotors) using standard Bruker double-resonance MAS probes. Spectra acquired at 20.0 T were recorded at the UK 850 MHz solid-state NMR Facility, which was funded by EPSRC and BBSRC, as well as the University of Warwick including *via* part funding through Birmingham Science City Advanced Materials Projects 1 and 2 supported by Advantage West Midlands (AWM) and the European Regional Development Fund (ERDF). Dr Dinu Iuga is gratefully acknowledged for his patient assistance with the experiments carried out at the UK 850 MHz solid-state NMR Facility. Samples were packed into zirconia MAS rotors with outer diameters of 4, 2.5, 1.3 or 1.0 mm and

rotated at MAS rates of up to 14 kHz (4 mm rotors), 12.5-35 kHz (2.5 mm rotors), 40-62.5 kHz (1.3 mm rotors) or 77 kHz (1 mm rotors) using Bruker triple-resonance (4, 2.5 and 1.3 mm rotors) or Jeol double-resonance (1 mm rotors) MAS probes. Further details of specific experiments can be found in the text and figure captions, with full details of all NMR experiments given in Appendix A.

3.6.2 First-Principles Calculations

First-principles calculations were carried out using the codes, GAUSSIAN03 (revisions D.01[35] and E.01[36]), GAUSSIAN09 (revision A.02[37]), CASTEP 4.3, CASTEP 5, CASTEP 5.5.2, and CASTEP 6.[38, 39]

Calculations using GAUSSIAN03 (E.01), CASTEP4.3 and CASTEP5 were carried out using the former EaStCHEM Research Computing Facility, consisting of 148 AMD Opteron processing cores partly connected by Infinipath high-speed interconnects. Calculations using GAUSSIAN03 (D.01) and CASTEP 5.5.2 were carried out on a local cluster comprising four Intel Core i7-930 quad-core processors with 6 GB memory per core. Calculations using, GAUSSIAN09 (A.02) and CASTEP 6 were carried out using the current EaStCHEM Research Computing Facility, consisting of a 198-node (2376 core) Intel Westmere cluster with 2 GB memory per core and QDR Infiniband interconnects.

For calculations using GAUSSIAN, the B3LYP hybrid GGA functional was used, with the basis set dependent on the size of the system in question and the desired accuracy. GAUSSIAN calculates the EFG tensor in atomic units, which were converted to S. I. units by multiplying by 9.7177×10^{21} kg A^{-1} s^{-3}.

For CASTEP calculations, the PBE GGA functional was used with the core-valence interactions described by ultrasoft pseudopotentials. Where stated, geometry optimisations carried out with CASTEP 6 used the SEDC schemes of Grimme,[40] or Tkatchenko and Scheffler,[41] as implemented by McNellis *et al.*[42] Earlier versions of CASTEP did not include the SEDC module. In all series of calculations, the parameter of interest (typically the isotropic shielding of the relevant nucleus) was converged as far as practically possible with respect to the planewave cut-off energy, E_{cut}, and the *k*-point spacing. CASTEP generates the chemical shielding tensor,[43, 44]

which was referenced as described in the relevant chapters. CASTEP generates both the magnitude and sign of V_{ZZ}[45] and, consequently, where calculated values for C_Q are reported, sign information is included (unless otherwise stated), although only $|C_Q|$ is readily determined from the experiments used here. Further details of specific calculations can be found in the relevant chapters.

3.7 REFERENCES

1. E. R. Andrew, A. Bradbury and R. G. Eades, *Nature*, **1958**, *182*, 1659.

2. E. R. Andrew, A. Bradbury and R. G. Eades, *Nature*, **1959**, *183*, 1802.

3. A. K. Khitrin, B. M. Fung and G. McGeorge, "*Heteronuclear Decoupling in Solids*", in *Encyclopaedia of Magnetic Resonance*, John Wiley & Sons, Chichester, UK, **2007**.

4. A. E. Bennett, C. M. Rienstra, M. Auger, K. V. Lakshmi and R. G. Griffin, *J. Chem. Phys.*, **1995**, *103*, 6951.

5. Z. H. Gan, P. Gor'kov, T. A. Cross, A. Samoson and D. Massiot, *J. Am. Chem. Soc.*, **2002**, *124*, 5634.

6. R. Dupree, "*Double Rotation (DOR) NMR*", in *NMR of Quadrupolar Nuclei in Solid Materials*, eds. R. E. Wasylishen, S. E. Ashbrook and S. Wimperis, John Wiley & Sons, Ltd., Chichester, UK, 1st edn., **2012**.

7. P. J. Grandinetti, "*Dynamic Angle Spinning*", in *NMR of Quadrupolar Nuclei in Solid Materials*, eds. R. E. Wasylishen, S. E. Ashbrook and S. Wimperis, John Wiley & Sons, Ltd., Chichester, UK, 1st edn., **2012**.

8. L. Frydman and J. S. Harwood, *J. Am. Chem. Soc.*, **1995**, *117*, 5367.

9. A. Wokaun and R. R. Ernst, *J. Chem. Phys.*, **1977**, *67*, 1752.

10. S. Vega and Y. Naor, *J. Chem. Phys.*, **1981**, *75*, 75.

11. M. J. Duer and C. Stourton, *J. Magn. Reson.*, **1997**, *124*, 189.

12. O. W. Sorensen, M. Rance and R. R. Ernst, *J. Magn. Reson.*, **1984**, *56*, 527.

13. J. P. Amoureux, C. Fernandez and S. Steuernagel, *J. Magn. Reson. A*, **1996**, *123*, 116.

14. D. Massiot, B. Touzo, D. Trumeau, J. P. Coutures, J. Virlet, P. Florian and P. J. Grandinetti, *Solid State Nucl. Magn. Reson.*, **1996**, *6*, 73.

15. S. P. Brown and S. Wimperis, *J. Magn. Reson.*, **1997**, *124*, 279.

16. J. Skibsted and H. J. Jakobsen, *J. Phys. Chem. A*, **1999**, *103*, 7958.

17. S. E. Ashbrook and S. Wimperis,, "*Quadrupolar Coupling: An Introduction and Crystallographic Aspects*", in *NMR of Quadrupolar Nuclei in Solid Materials*, eds. R. W. Wasylishen, S. E. Ashbrook and S. Wimperis, John Wiley and Sons, Chichester, UK, 1st edn., **2012**.

18. S. Antonijevic, S. E. Ashbrook, S. Biedasek, R. I. Walton, S. Wimperis and H. X. Yang, *J. Am. Chem. Soc.*, **2006**, *128*, 8054.

19. S. R. Hartmann and E. L. Hahn, *Phys. Rev.*, **1962**, *128*, 2042.

20. E. O. Stejskal, J. Schaefer and J. S. Waugh, *J. Magn. Reson.*, **1977**, *28*, 105.

21. B. H. Meier, *Chem. Phys. Lett.*, **1992**, *188*, 201.

22. G. Metz, X. L. Wu and S. O. Smith, J. *Magn. Reson. A*, **1994**, *110*, 219.

23. A. Pines, M. G. Gibby and J. S. Waugh, *J. Chem. Phys.*, **1973**, *59*, 569.

24. M. Mehring, *Principles of High Resolution NMR in Solids*, Springer-Verlag, Berlin, **1983**.

25. H. Y. Carr and E. M. Purcell, *Phys. Rev.*, **1954**, *94*, 630.

26. S. Meiboom and D. Gill, *Rev. Sci. Instrum.*, **1958**, *29*, 688.

27. A. Lesage, M. Bardet and L. Emsley, *J. Am. Chem. Soc.*, **1999**, *121*, 10987.

28. W. Sommer, J. Gottwald, D. E. Demco and H. W. Spiess, *J. Magn. Reson. A*, **1995**, *113*, 131.

29. M. Feike, D. E. Demco, R. Graf, J. Gottwald, S. Hafner and H. W. Spiess, *J. Magn. Reson. A*, **1996**, *122*, 214.

30. M. Hohwy, H. J. Jakobsen, M. Eden, M. H. Levitt and N. C. Nielsen, *J. Chem. Phys.*, **1998**, *108*, 2686.

31. G. A. Morris and R. Freeman, *J. Am. Chem. Soc.*, **1979**, *101*, 760.

32. G. A. Morris, *J. Am. Chem. Soc.*, **1980**, *102*, 428.

33. J. Keeler, *Understanding NMR Spectroscopy*, John Wiley & Sons Ltd., Chichester, UK, Chippenham, UK, **2005**.

34. B. Elena, A. Lesage, S. Steuernagel, A. Bockmann and L. Emsley, *J. Am. Chem. Soc.*, **2005**, *127*, 17296.

35. GAUSSIAN03, revision D.01, M. J. Frisch *et al.*, Gaussian, Inc., Wallingford, CT, **2004**.

36. GAUSSIAN03, Revision E.01, M. J. Frisch *et al.*, Gaussian, Inc., Wallingford,

CT, **2004**.

37. GAUSSIAN09, revision A.01. M. J. Frisch *et al*., Gaussian, Inc., Wallingford, CT, **2009**.

38. S. J. Clark, M. D. Segall, C. J. Pickard, P. J. Hasnip, M. J. Probert, K. Refson and M. C. Payne, *Z. Kristallogr.*, **2005**, *220*, 567.

39. M. D. Segall, P. J. D. Lindan, M. J. Probert, C. J. Pickard, P. J. Hasnip, S. J. Clark and M. C. Payne, *J. Phys.: Condens. Matter*, **2002**, *14*, 2717.

40. S. Grimme, *J. Comput. Chem.*, **2006**, *27*, 1787.

41. A. Tkatchenko and M. Scheffler, *Phys. Rev. Lett.*, **2009**, *102*, 073005.

42. E. R. McNellis, J. Meyer and K. Reuter, *Phys. Rev. B*, **2009**, *80*, 205414.

43. J. R. Yates, C. J. Pickard and F. Mauri, *Phys. Rev. B*, **2007**, *76*, 024401.

44. C. J. Pickard and F. Mauri, *Phys. Rev. B*, **2001**, *63*, 245101.

45. M. Profeta, F. Mauri and C. J. Pickard, *J. Am. Chem. Soc.*, **2003**, *125*, 541.

4 SOLID-STATE NMR SPECTROSCOPIC STUDY OF PARAMAGNETIC METAL-ORGANIC FRAMEWORKS

4.1 CHAPTER OVERVIEW

Metal-organic frameworks (MOFs) display a wide and versatile range of chemistry, thanks to the "modular" nature of their structures. This structural and chemical versatility gives MOFs application in many important areas, *e.g.*, catalysis, drug storage and delivery, the "hydrogen economy" and carbon capture and storage. The first section of this chapter investigates the acquisition and assignment of the ^{1}H and ^{13}C MAS NMR spectra of the copper-based MOFs, HKUST-1 and STAM-1. Acquisition of complete spectra was achieved by a combination of rapid MAS, frequency-stepped experiments and use of a spin-echo. Assignment of the spectra is demonstrated to be challenging, but was achieved using a combination of NMR experiments and isotopic labelling (both ^{13}C and ^{2}H). The effects of B_0 field strength and temperature upon the spectra are investigated, and the ability of solid-state ^{13}C NMR spectra to provide useful information on a series of samples of HKUST-1 loaded with medically-relevant guest species is demonstrated. The second MOF system investigated in this chapter is CPO-27-M (M = Mg, Mn, Co, Ni, Zn). The acquisition of ^{13}C NMR spectra for all members of this series was considerably more challenging than for the Cu-based systems discussed in the first part of the chapter, owing to the different chemical and electronic structures of the MOFs. The challenges associated with recording the NMR spectra of these MOFs mean that spectral assignments remain incomplete. The final section of the chapter investigates Ln(btc)(dmu)$_2$ (Ln = Nd or La, dmu = 1,3-dimethylurea), for which the NMR spectra are dominated by the chemical shift interaction, with only small pseudocontact shifts arising from the presence of Nd^{3+}. Assignment of the ^{13}C CP MAS NMR spectrum of the diamagnetic La(btc)(dmu)$_2$ is supported by DFT calculations, but assignment for the paramagnetic Nd(btc)(dmu)$_2$ has not yet been achieved. This chapter demonstrates a range of possible effects that paramagnetic species may have on the NMR spectra of MOFs, and presents various strategies for acquiring and interpreting spectra despite these effects, and the information that may be available from such spectra.

4.2 ACKNOWLEDGEMENTS

Work reported here would have been impossible without the group of Professor Russell Morris (University of St Andrews), particularly Drs Infas Mohideen, Alistair McKinlay and Farida Aidoudi and Miss Siobhan Day, who provided many of the samples, and Dr Paul Wheatley, who assisted with guest loading of ^{2}H(3)-HKUST-1. Collaboration with Drs Iain Smellie, Neil Keddie and Romain Cadou was essential to the ^{13}C isotopic labelling work. Miss Lauren Jamieson and Miss Harriet Hopper carried out syntheses of isotopically-enriched MOFs and NMR experiments as part of their undergraduate research projects at the University of St Andrews. Miss Hanna Boström carried out syntheses and NMR experiments in her summer project at the University of St Andrews. Dr Dinu Iuga is thanked for his kind and patient assistance with work carried out at the UK 850 MHz solid-state NMR facility. Dr Marko Bertmer (University of Leipzig) is thanked for the spectrum shown in Figure 4.2(b).

4.3 EXPERIMENTAL DETAILS

4.3.1 Synthesis

4.3.1.1 Benzene-1[^{13}C],3,5-tricarboxylic acid

As previously reported,[1] a mixture of 3,5-dimethylbromobenzene (6.84 g; 37 mmol) and THF (80 cm^3) was cooled to –78 °C before *n*-BuLi (2.5 M in hexane, 14.8 cm^3) was added. The resulting solution was stirred for 1 h before [^{13}C]iodomethane (5.00 g; 35 mmol) was added. The mixture was stirred for 2 h then warmed to room temperature. THF and any unreacted [^{13}C]iodomethane were removed *in vacuo*, venting to a fume hood. The crude product was washed with brine (100 cm^3) and extracted into DCM (2 × 30 cm^3). The organic layer was dried over $MgSO_4$, filtered and concentrated *in vacuo*. The crude product was purified by vacuum distillation and 1[^{13}C],3,5-trimethylbenzene was obtained as a clear oil (2.95 g, 70 %).

Oxidation of 1[^{13}C],3,5-trimethylbenzene was achieved by a modified version of the procedure of Juršić.[2] To water (100 cm^3), cetyltrimethylammonium bromide (CTAB) (0.73 g; 2 mmol), 1[^{13}C],3,5-trimethylbenzene (1.25 g; 10 mmol) and

$KMnO_4$ (14.8 g; 94 mmol) were added; the resulting suspension was stirred vigorously and heated to 90-95 °C. After 6 h the suspension was cooled to room temperature and the reaction mixture filtered through celite to remove MnO_2. The filtrate was saturated with NaCl and extracted with DCM (2×30 cm^3) to remove any unreacted starting material. The aqueous layer was adjusted to pH 2 by addition of 5 M HCl. The resulting precipitate of benzene-1[^{13}C],3,5-tricarboxylic acid (0.96 g; 44 %) was filtered, washed with ice-cold water (3×10 cm^3) and dried at 110 °C.

4.3.1.2 [U-^{13}C]Benzene-1,3,5-tricarboxylic acid

As previously reported,[1] $AlCl_3$ (4.77 g; 35.8 mmol) was added to a three-necked flask equipped with a reflux condenser and a dropping funnel. The condenser was fitted with a gas absorption trap containing saturated aqueous $NaHCO_3$. The flask was cooled to 0 °C and bromoethane (4.70 cm^3; 62.5 mmol) was added dropwise over 10 min. A mixture of benzene (2.60 cm^3; 29.1 mmol) and [U-^{13}C]benzene (420 μl; 4.70 mmol) was added dropwise over 15 min. The mixture was stirred at 0 °C for 20 min. Bromoethane (3.10 cm^3; 42.2 mmol) was added dropwise over 10 min and the mixture was warmed to room temperature and stirred for 12 h. The mixture was poured carefully over ice (~50 g) and the aqueous layer extracted with Et_2O (2×50 cm^3). The combined organic layers were washed with H_2O (50 cm^3), 1 M NaOH (50 cm^3), dried over $MgSO_4$, filtered and evaporated under reduced pressure. A colourless liquid comprising 1,3,5-triethylbenzene and 1,3,5-triethyl-[U ^{13}C]benzene (5.35 g; 97%) was obtained and used without further purification. From the integrals of the solution-phase ^{1}H NMR spectrum, some unreacted bromoethane remained. This was removed during the work-up in the next stage of the reaction sequence.

A mixture of benzene-1,3,5-tricarboxylic acid and [U-^{13}C]benzene-1,3,5-tricarboxylic acid was obtained following oxidation of a mixture of 1,3,5-triethylbenzene and 1,3,5-triethyl-[U-^{13}C]benzene using a modified version of the procedure of Juršić.[2] A mixture of 1,3,5-triethylbenzene (711 mg; 4.38 mmol) and 1,3,5-triethyl[U-^{13}C]benzene (115 mg; 0.683 mmol) was added to H_2O (50 cm^3). CTAB (370 mg; 1.01 mmol) and $KMnO_4$ (8.00 g; 50.6 mmol) were added and the mixture was heated to 95 °C for 6 h. The mixture was cooled to room temperature, filtered through celite and the filter cake was washed with H_2O. The filtrate was

acidified to pH 2 with cold 5 M HCl and filtered. *n*-Butanol (10 vol%) was added and the aqueous layer was evaporated under reduced pressure. Benzene-1,3,5-tricarboxylic acid and [U-^{13}C]benzene-1,3,5-tricarboxylic acid were obtained as a pale yellow solid (0.35 g; 32.4 %).

4.3.1.3 2,4,6[$^2H_3$]Benzene-1,3,5-tricarboxylic acid

The synthesis of 2,4,6[$^2H_3$]benzene-1,3,5-tricarboxylic acid followed a modified version of the above synthesis of [U-^{13}C]benzene-1,3,5-tricarboxylic acid.[3] The benzene and [U-^{13}C]benzene were both replaced by C_6D_6 (98% enriched in ^{2}H), allowing installation of ~70% ^{2}H on the 2, 4 and 6 positions of the resulting 2,4,6[$^2H_3$]benzene-1,3,5-tricarboxylic acid. This deuteration level was increased to >90% by quenching the alkylation reaction with D_2O ice rather than H_2O ice.[3] The deuteration levels were determined from the relative integrated intensities of the signals from the CH_3CH_2 protons (at natural abundance) and the aromatic CH protons (depleted, owing to deuteration) in the solution-phase ^{1}H NMR spectrum.

4.3.1.4 HKUST-1

The synthesis of HKUST-1 was scaled up from the procedure of Xiao *et al.*[4] $Cu(NO_3)_2{\cdot}3(H_2O)$, (15.752 g; 66 mmol) and H_3btc (9.262 g; 44 mmol) were dissolved in H_2O/EtOH (50 : 50, 264 cm^3 total), homogenised, sealed in a 600 ml Teflon-lined autoclave and heated at 110 °C for 24 h before being filtered and washed with H_2O and finally air dried, yielding 15.66 g of HKUST-1.

4.3.1.5 STAM-1

Following the procedure of Mohideen *et al.*,[5] $Cu(NO_3)_2{\cdot}3(H_2O)$ (0.991 g; 4.1 mmol) and H_3btc (0.862 g; 4.1 mmol) were mixed with MeOH/H_2O (50 : 50, 20 cm^3 total) in a Teflon-lined steel autoclave. The mixture was stirred for 15 min then heated to 110 °C for 7 days. After cooling to room temperature, blue crystals of STAM-1 were isolated by suction filtration and dried in air.

4.3.1.6 ^{2}H(3)-HKUST-1

The synthesis of ^{2}H(3)-HKUST-1 followed the above procedure for HKUST-1, but was carried out on a smaller scale.[3] $Cu(NO_3)_2{\cdot}3(H_2O)$ (0.36 g; 1.4 mmol) and

2,4,6[$^2H_3$]-benzene-1,3,5-tricarboxylic acid (0.21 g; 1.0 mmol) were dissolved in H_2O/EtOH (50 : 50, 10 cm^3 total volume) and stirred for 15 min before being sealed in a Teflon-lined steel autoclave, heated at 110 °C for 1 day, cooled to room temperature, filtered, washed with H_2O and air dried, yielding 0.18 g ^{2}H(3)-HKUST-1. The abundance of ^{2}H at H3 was 70% (assuming complete retention of the level of enrichment of the parent acid).

4.3.1.7 ^{2}H(3,4)-STAM-1

The synthesis of ^{2}H(3,4)-STAM-1 followed the above procedure for STAM-1, but on a smaller scale.[3] $Cu(NO_3)_2 \cdot 3(H_2O)$ (0.50 g; 2.1 mmol) and 2,4,6[$^2H_3$]-benzene-1,3,5-tricarboxylic acid (0.43 g; 2.0 mmol) were dissolved in H_2O/MeOH (50 : 50, 10 cm^3 total volume) and stirred for 15 min before being sealed in a Teflon-lined steel autoclave, heated at 110 °C for 1 day, cooled to room temperature, filtered, washed with H_2O and air dried, yielding 0.28 g blue powder, which was determined to be a mixture of ^{2}H(3,4)-STAM-1 and ^{2}H(3)-HKUST-1. The abundance of ^{2}H at H3 and H4 was >90% (assuming complete retention of the level of enrichment of the parent acid).

4.3.1.8 ^{2}H(7)-STAM-1

As previously reported,[1] the synthesis of ^{2}H(7)-STAM-1 followed the above procedure (and scale) for the synthesis of STAM-1, but with CD_3OD (99.8 atom% ^{2}H) in place of CH_3OH. The abundance of ^{2}H at H7 was 99.8% (assuming complete retention of the level of enrichment of the methanol).

4.3.1.9 ^{13}C(2)-HKUST-1

As previously reported,[1] ^{13}C(2)-HKUST-1 was prepared following the above procedure for HKUST-1, but on a smaller scale. $Cu(NO_3)_2 \cdot 3(H_2O)$ (0.752 g; 3.0 mmol), H_3btc (0.210 g; 1.0 mmol) and benzene-1[^{13}C],3,5-tricarboxylic acid (0.210 g; 1.0 mmol) were dissolved in H_2O/EtOH (50 : 50, 20 cm^3 total volume) and stirred for 15 min before being sealed in a Teflon-lined steel autoclave, heated at 110 °C for 1 day, cooled to room temperature, filtered, washed with H_2O and air dried, yielding 0.75 g of ^{13}C(2)-HKUST-1. The abundance of ^{13}C at C2 was 17% (assuming complete retention of the level of enrichment of the parent acid).

4.3.1.10 ^{13}C(1,3)-HKUST-1

As previously reported,[1] ^{13}C(1,3)-HKUST-1 was prepared by dissolving $Cu(NO_3)_2 \cdot 3(H_2O)$ (0.362 g; 1.5 mmol), H_3btc (0.118 g; 0.6 mmol) and [U-^{13}C]benzene-1,3,5-tricarboxylic acid (0.092 g; 0.4 mmol) in 10 ml H_2O/EtOH (50 : 50). This solution was stirred for 15 min before being sealed in a Teflon-lined steel autoclave, heated at 110 °C for 1 day, cooled to room temperature, filtered, washed with H_2O and air dried, yielding 0.62 g of ^{13}C(1,3)-HKUST-1. The abundance of ^{13}C at C1 and C3 was 7% (assuming complete retention of the level of enrichment of the parent acid).

4.3.1.11 ^{13}C(2,6)-STAM-1

As previously reported,[1] ^{13}C(2,6)-STAM-1 was prepared by a modified version of the above procedure for STAM-1. $Cu(NO_3)_2 \cdot 3(H_2O)$ (0.496 g; 2.0 mmol), H_3btc (0.215 g; 1.0 mmol) and benzene-1[^{13}C],3,5-tricarboxylic acid (0.215 g; 1.0 mmol) were mixed with 10 ml of MeOH/H_2O (50 : 50) in a Teflon-lined steel autoclave. The mixture was stirred for 15 min before heating at 110 °C for 5 days. The autoclave was cooled to room temperature and blue crystals of ^{13}C(2,6)-STAM-1 were isolated by filtration and air dried, yielding 0.59 g of ^{13}C(2,6)-STAM-1 (containing ~10-15% ^{13}C(2)-HKUST-1 as an impurity). The abundance of ^{13}C at C2 and C6 was 17% (assuming complete retention of the level of enrichment of the parent acid).

4.3.1.12 ^{13}C(1,3,4,5)-STAM-1

As previously reported,[1] ^{13}C(1,3,4,5)-STAM-1 was prepared by dissolving $Cu(NO_3)_2 \cdot 3(H_2O)$ (0.496 g; 2.1 mmol), H_3btc (0.243 g; 1.2 mmol) and [U-^{13}C]benzene-1,3,5-tricarboxylic acid (0.188 g; 0.9 mmol) in MeOH/H_2O (50 : 50, 10 cm^3 total volume) in a Teflon-lined steel autoclave. The mixture was stirred for 15 min before heating at 110 °C for 6 days. The autoclave was cooled to room temperature, and blue crystals of ^{13}C(1,3,4,5)-STAM-1 (containing ~10-15 wt% ^{13}C(1,3)-HKUST-1 as an impurity) were isolated by filtration and dried in air, yielding 0.49 g ^{13}C(1,3,4,5)-STAM-1. The abundance of ^{13}C at C1, C3, C4 and C5 was 7% (assuming complete retention of the level of enrichment of the parent acid).

4.3.1.13 CPO-27-Mg

Following the procedure of Dietzel *et al.*,[6] H_4dhtp (149 mg; 0.75 mmol) was dissolved in 10 cm^3 THF in the Teflon liner of a steel autoclave. The linker was deprotonated by adding 1 M NaOH (3 cm^3) with stirring. $Mg(NO_3)_2 \cdot 6H_2O$ (384 mg; 1.7 mmol in 3 cm^3 H_2O) was added to the deprotonated linker and stirring was continued for 1 min. The autoclave was then sealed and placed in an oven at 110 °C for 60 h. After cooling, a yellow powder (dry mass 248 mg) was isolated by vacuum filtration and dried under air at 40 °C for 3 h. The synthesis was repeated three times and the product from each synthesis was kept separate until powder XRD (Appendix H) confirmed that all three samples yielded the same pattern, corresponding to CPO-27-Mg. The samples were then combined to give a total mass of 593 mg.

4.3.1.14 CPO-27-Mn

Following the procedure of Wu *et al.*,[7] $MnCl_2 \cdot 4H_2O$ (549 mg; 3.0 mmol) and H_4dhtp (167 mg; 0.84 mmol) were dissolved in 15 : 1 : 1 DMF : EtOH : H_2O (75 cm^3 total volume) and divided into three equal parts, each of which was sealed in a Teflon-lined steel autoclave and placed in an oven at 135 °C for 42 h. After cooling, a brown powder was isolated from each autoclave and dried under air at 40 °C for 3 h. The product from each autoclave was kept separate until powder XRD (Appendix H) confirmed that all three samples yielded the same pattern, corresponding to CPO-27-Mn. The samples were then combined to give a total mass of 88.5 mg.

4.3.1.15 CPO-27-Co

Following the procedure of Dietzel *et al.*,[8] $Co(OAc)_2 \cdot 4H_2O$ (1.152 g; 4.63 mmol in 30 cm^3 H_2O) was added to H_4dhtp (447 mg; 2.25 mmol in 30 cm^3 THF). The reaction mixture was stirred to ensure complete dissolution of reagents, then divided into three equal parts, each of which was sealed in a Teflon-lined steel autoclave and placed in an oven at 110 °C for 60 h. The autoclaves were allowed to cool and an orange powder was isolated by suction filtration. This solid was washed three times with H_2O and dried under air at approximately 40 °C for 3 h. The product from each autoclave was kept separate until powder XRD (Appendix H) confirmed that all three samples yielded the same pattern, corresponding to CPO-27-Co. The samples were then combined to give a total mass of 601 mg.

4.3.1.16 CPO-27-Ni

Using $Ni(OAc)_2 \cdot 4H_2O$ as the metal source, the same procedure was followed as for CPO-27-Co. The three samples of ochre powder yielded powder XRD patterns (Appendix H), corresponding to CPO-27-Ni. The combined mass was 744 mg.

4.3.1.17 CPO-27-Zn

Following the procedure of Rosi *et al.*,[9] $Zn(NO_3)_2 \cdot 6H_2O$ (5.0 g; 18.8 mmol) and H_4dhtp (1.25 g; 6.3 mmol) were dissolved, with stirring, in 250 cm^3 DMF. H_2O (12.5 cm^3) was added and the reaction mixture was transferred to a 500 cm^3 plastic screw-top jar and placed in an oven at 110 °C for 24 h. After this time, the reaction was cooled to room temperature and a dark yellow powder (dried mass of 2.62 g) was isolated by suction filtration. This solid was washed once with DMF, then twice with H_2O before being dried under air at approximately 40 °C for 3 h. The powder XRD pattern (Appendix H) of the product indicated that CPO-27-Zn had formed.

The DMF in the pores of as-synthesised CPO-27-Zn was removed by immersing a portion (approx. 2.2 g) of the material in MeOH and stirring gently for 24 h. The MOF was recovered by suction filtration and the solvent exchange was carried out twice more, resulting in 1.80 g of a pale yellow powder, the powder XRD pattern of which indicated CPO-27-Zn[MeOH] had been prepared (Appendix H).

4.3.1.18 La(btc)(dmu)$_2$

As described by Himeur *et al.*,[10] $La(btc)(dmu)_2$ was prepared by combining $La(NO_3)_3 \cdot 6H_2O$ (0.43 g; 1 mmol), H_3btc (0.21 g; 1.0 mmol), choline chloride (0.70 g; 5.0 mmol) and 1,3-dimethylurea (0.88 g; 10 mmol) in a Teflon-lined steel autoclave. The reaction vessel was sealed and heated at 110 °C for 6 days before being cooled to room temperature. Upon cooling, the products were filtered, washed with MeOH and dried in air for 24 h, giving colourless crystals of $La(btc)(dmu)_2$.

4.3.1.19 Nd(btc)(dmu)$_2$

As described by Himeur *et al.*,[10] $Nd(btc)(dmu)_2$ was prepared by combining $NdCl_3 \cdot 6H_2O$ (0.36 g; 1 mmol), H_3btc (0.21 g; 1.0 mmol), choline chloride (0.70 g; 5.0 mmol), 1,3-dimethylurea (0.88 g; 10 mmol) and HF (50 μl, 48 % in H_2O) in a

Teflon-lined steel autoclave. The reaction vessel was sealed and heated at 110 °C for 6 days before being cooled to room temperature. Upon cooling, the products were filtered, washed with MeOH and dried in air for 24 h, giving pale lilac crystals of $Nd(btc)(dmu)_2$. The addition of the HF is not necessary for the reaction to occur, but was observed to improve the crystallinity of the product.

4.3.2 Activation of MOFs

Flame-sealable vials containing small portions (up to ~200 mg) of the MOFs were heated at 120 °C under vacuum overnight, cooled and sealed under argon.

4.3.3 Guest Loading of MOFs

Portions of the dehydrated MOFs were exposed to either atmospheric moisture (H_2O-loaded) or liquid MeOH or EtOH (HKUST-1 only). Samples loaded with MeOH or EtOH were recovered by suction filtration. All samples were the typical bright turquoise colour of hydrated HKUST-1 or STAM-1.

Metronidazole (metro) loading was achieved by dissolving 100 mg of metro in 10 cm^3 dry methanol in a dried glass vial. A portion of activated MOF was added to the vial, which was sealed while the mixture stirred for 3 days.

NO loading was achieved by activating portions of the MOFs, either as described above, or at the lower temperature of 80 °C (metro-loaded HKUST-1). The MOFs were then cooled to room temperature and exposed to approximately 2 atm of dry NO for 30 min, evacuated, and exposed to dry argon. Evacuation and exposure to NO was repeated three times.

4.3.4 Solid-State NMR Spectroscopy

Solid-state NMR spectra reported in this chapter were recorded at 9.4 and 14.1 T (University of St Andrews) and 20.0 T (UK 850 MHz Solid-State NMR Facility). Relevant experimental details are given in the text, figure captions and Appendix A.

4.3.5 First-Principles DFT Calculations

First-principles calculations were carried out using the codes GAUSSIAN09[11] and CASTEP versions 4.3 and 6.[12, 13] The calculations using GAUSSIAN09 were carried

out at the B3LYP/6-311+G(2d,p) theory level. The calculations using CASTEP were carried out using a cut-off energy of 60 Ry. Sampling of the Brillouin zone used a Monk-Packhurst grid with a k-point spacing of 0.04 $Å^{-1}$. A reference shielding of 172.79 ppm was used for ^{13}C, obtained as described in Chapter 5.

4.3.6 X-Ray Crystallography

4.3.6.1 Powder XRD

For HKUST-1 and STAM-1, powdered samples were loaded into disks of 3 mm depth, and data were obtained using a Panalytical EMPYREAN diffractometer with a Cu $K_{\alpha1}$ radiation source of wavelength, λ = 1.5406 Å. All data were recorded at room temperature with a 1 h scan time and a 2θ range of 3-50°.

For the CPO-27 series, data for all samples except CPO-27-Co were acquired using a Stoe Stadip diffractometer with Cu $K_{\alpha1}$ radiation of wavelength, λ = 1.5406 Å. As CPO-27-Co exhibits autofluorescence when exposed to Cu $K_{\alpha1}$ radiation, a similar diffractometer equipped with a Fe $K_{\alpha1}$ radiation source with λ = 1.9360 Å was used for this material. All data were recorded at room temperature, typically with a 1 h scan time and a 2θ range of 5 to 70° (5 to 80° for Fe $K_{\alpha1}$).

4.4 Cu(II)-Based MOFs – HKUST-1 and STAM-1

4.4.1 Introduction

MOFs have a great diversity of structural and chemical features of interest to researchers aiming to develop new MOFs for many different target applications. Accurate and detailed characterisation techniques are, therefore, required in order to provide information on the structure of new frameworks, the behaviour of guests within the pores of the framework, ordering of metal ions or modified linkers doped into the structure, and chemical transformations occurring as a result of, *e.g.*, post-synthetic modification or catalytic activity. Solid-state NMR is ideally placed to complement crystallographic techniques, providing a detailed picture of the local environment of individual nuclei within the material, yielding information on, *e.g.*, crystallographic symmetry, chemical species present, ordering of dopant species or

binding modes of guest species. In MOFs, the most commonly-studied NMR-active nuclei are ^{1}H, ^{2}H and ^{13}C, owing to their presence in the organic constituents of all frameworks. Isotopes of nitrogen may also be present in some linkers, but their unfavourable nuclear magnetic properties (summarised in Table 1.1) can make them less amenable to study by NMR. In some cases, the metal species itself is both NMR active and NMR accessible. This is particularly true of ^{27}Al and ^{45}Sc, and NMR spectra of these nuclei can provide information on the SBUs present[14] and, in the case of the flexible framework, MIL-53, the conformation of the framework.[15, 16] The growing availability of higher-field spectrometers means that ^{25}Mg[17-19] and ^{67}Zn[20] have recently been used to provide additional characterisation of some new Mg- and Zn-based MOFs. Acquisition of the NMR spectra of ^{25}Mg and ^{67}Zn may require wide-line techniques and access to national or international high-field facilities, and is often too time-consuming to be considered routine. However, it is clear that ^{1}H and ^{13}C NMR spectra have the widest applicability to the routine characterisation of MOFs, owing to their ubiquitous presence both in the frameworks, and also in most guest species of interest (drugs, catalytic substrates, CO_2, CH_4, H_2, *etc.*).

In diamagnetic MOFs, ^{1}H and ^{13}C NMR experiments are straightforward, requiring only rapid MAS to provide reasonable resolution for ^{1}H, and cross-polarisation from ^{1}H to achieve reasonable sensitivity for ^{13}C. However, many of the most well-known and important MOFs contain paramagnetic metal centres. In such MOFs, interactions between the unpaired electrons and the nuclei of interest mean that the NMR experiments described above are not necessarily suitable. A summary of the main effects of the interactions with unpaired electrons on the NMR spectra of nuclei in paramagnetic samples is provided in Table 4.1 and a more detailed description of these interactions is provided in Section 2.3.

4.4.2 Acquisition of Complete ^{13}C NMR Spectra

HKUST-1 is a MOF consisting of copper "paddlewheel" dimers connected by benzene-1,3,5-tricarboxylate (btc or trimesate) linkers.[21] HKUST stands for Hong-Kong University of Science and Technology, where the material was first synthesised and reported in 1999, although it should be noted that the same material was also synthesised by the Yaghi group, and was called MOF-199,[22] although this

Table 4.1. Summary of the effects of the hyperfine (hf), transferred hyperfine (thf) and pseudocontact (pc) interactions on the NMR spectra of paramagnetic materials.

Effect	Source(s)	Maximum Magnitude
isotropic shift	(t)hf and pc interactions	0.1% (hf), tens of ppm (pc)
anisotropy	(t)hf and pc interactions, BMS	thousands of ppm
rapid relaxation	electronic relaxation	ms or μs timescale

name is less popular in the literature. The structure of HKUST-1 is shown in Figure 4.1(a), and the high symmetry (space group $Fm\bar{3}m$) means that there is one unique btc linker, with a C_3 symmetry axis through the centre of the ring, so that there are only three unique C atoms and one unique framework H atom within the structure, identified using the scheme in Figure 4.1(b). The structure of the copper paddlewheel dimer SBU is shown in Figure 4.1(c), and it can be seen that there is a molecule of H_2O occupying the axial position in the as-prepared material. The published crystal structure also contains a well-defined network of H_2O molecules within the pores of the MOF, although the locations of the water molecules are likely to be a consequence of an attempt to refine significant residual electron density within the pores (TGA indicates up to 4.33 molecules of H_2O per Cu centre[21]) in the presence of the high crystallographic symmetry imposed. Evidence of this comes from the solid-state ^{1}H NMR study of Gul-E-Noor *et al*., who reported rapid exchange of Cu-bound and pore H_2O on the NMR timescale.[23] All water within the structure can be removed by heating to temperatures above 100 °C in air,[21] yielding the "activated" material, shown in Figure 4.1(d),[21] which contains coordinatively unsaturated sites (CUSs) at the axial positions of the SBU, as shown in Figure 4.1(e), and has a pore diameter of 9.5 Å. However, owing to the very hygroscopic nature of the activated MOF, the material must be stored under a dry atmosphere in order to prevent essentially immediate rehydration. The presence of these large pores with a high concentration of active binding sites on their surface means that HKUST-1 has been investigated for a wide range of applications including gas flow purification/harmful gas capture,[22, 24] drug storage and delivery,[25, 26] hydrogen storage,[27] and catalysis.[28]

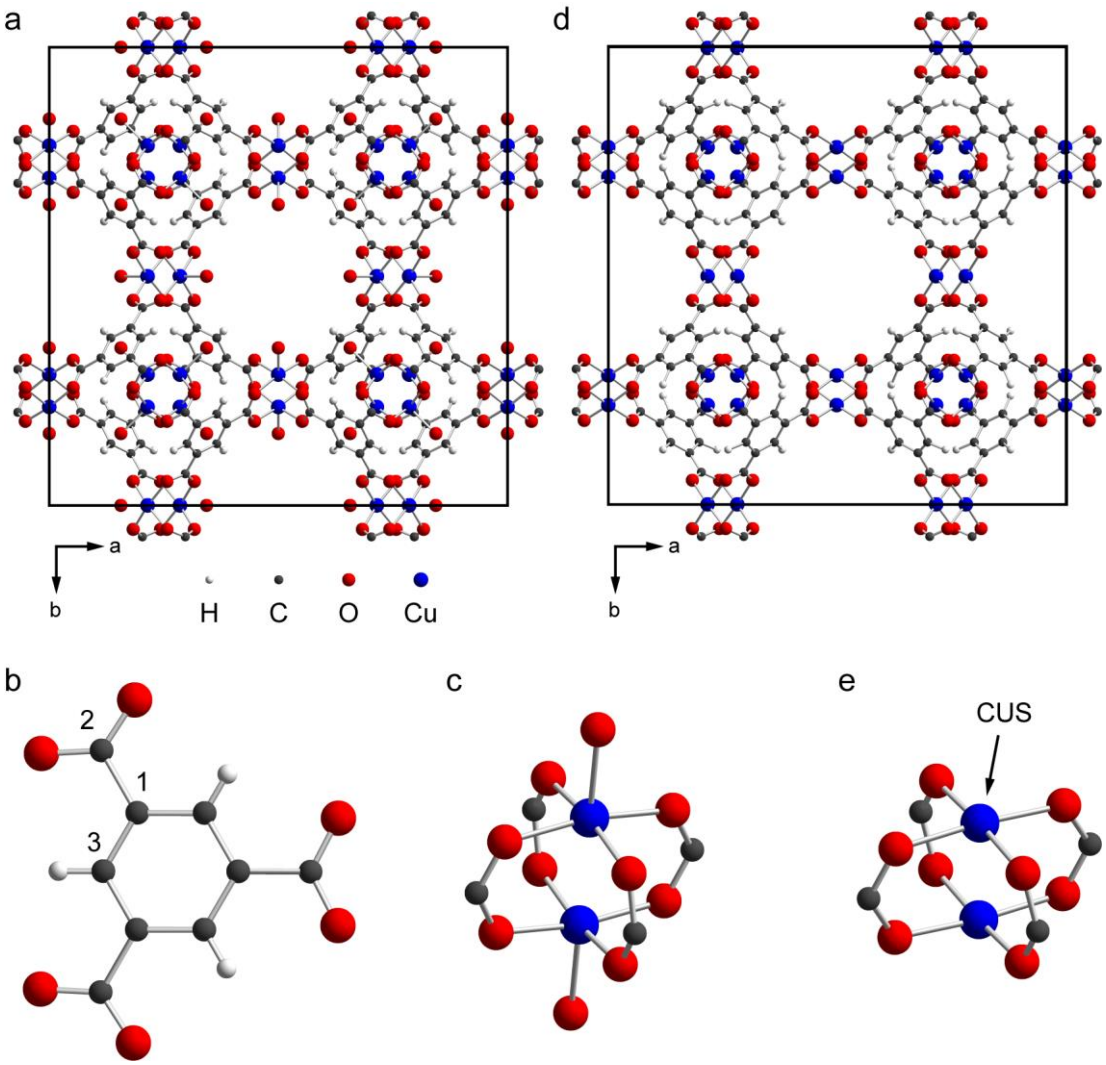

Figure 4.1. The crystal structures of (a) HKUST-1 with water molecules within the pore omitted for clarity, (b) the btc linker and the numbering scheme used in this work, (c) the copper paddlewheel dimer SBU (H atoms of the axial H_2O molecule were not located by diffraction), (d) dehydrated HKUST-1 and (e) the activated copper paddlewheel dimer, showing the location of the CUS.

Prior to the start of this work, the ^{13}C NMR spectrum of HKUST-1 had been reported by Peterson *et al.*,[24] although the spectrum was acquired with a one-pulse experiment and relatively slow MAS, resulting in a spectrum crowded with SSBs and with a background signal and baseline distortions of the same order of magnitude as the (natural abundance) signal from the MOF, as shown in Figure 4.2(a). Two resonances were identified as resulting from the MOF, with isotropic shifts of –78 and 228 ppm. The resonance at –78 ppm was assigned to C2 (the C species closest to

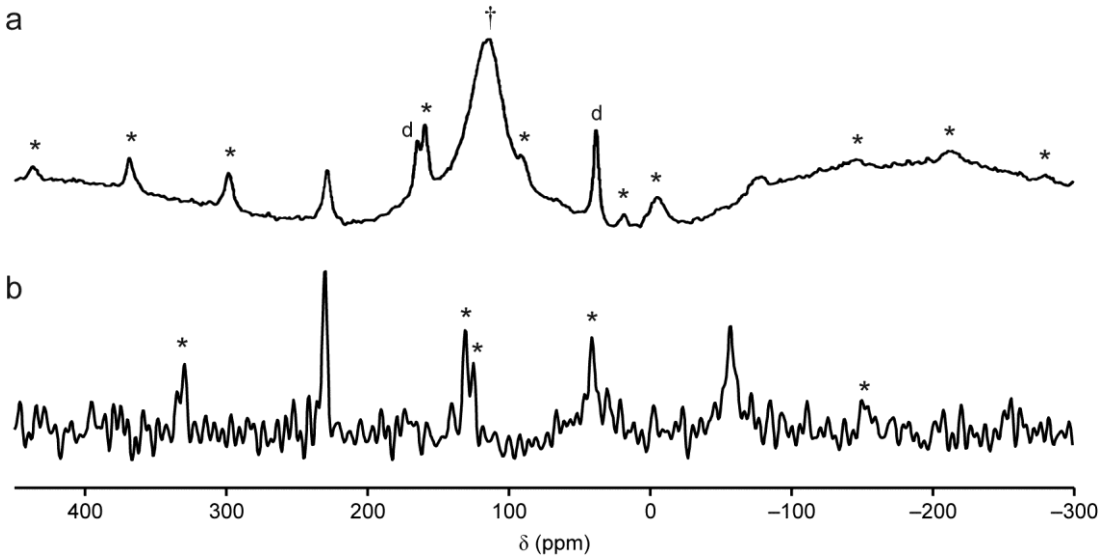

Figure 4.2. ^{13}C MAS NMR spectra of (a) "nominally dry" HKUST-1, adapted with permission from ref. 24 and (b) hydrated HKUST-1.[23] Asterisks denote SSBs, d denotes resonances arising from DMF and † denotes the background signal.

Cu^{2+}, and the resonance is the most shifted from the "normal" chemical shift range of ^{13}C). The other resonance was assigned to C1 and C3, although it was claimed that decoupling of ^{1}H led to the observation of resonances at 218 and 240 ppm, both of which were assigned to C1, despite C3 being the only directly-protonated C species. During the course of this work, a second report was published by Gul-E-Noor *et al.*, detailing changes in the ^{1}H and ^{13}C MAS NMR spectra during hydration.[23] Again, the spectra were acquired with relatively slow MAS, resulting in numerous SSBs, but the use of a DEPTH pulse sequence removed the probe background and baseline distortions of the earlier work, as shown in Figure 4.2(b). Again, two resonances were observed at 228 ppm and –86 ppm for the dehydrated material and 228 and –56 ppm for the hydrated material. The assignment was similar to that of Peterson *et al.*, but the resonances at 218 and 240 ppm were not observed at all. Work presented here adds considerably to the body of information regarding the NMR parameters of HKUST-1, including the first complete ^{13}C MAS NMR spectra of the material containing different guest molecules, as well as T_1 relaxation measurements and full assignment of the ^{1}H and ^{13}C MAS NMR spectra.[1]

STAM-1 (STAM = St Andrews MOF) is a MOF containing the same copper paddlewheel dimers as HKUST-1 but, linked by the monomethyl ester of btc

(mmbtc). This linker is formed by *in situ* esterification of btc in the reaction medium (1 : 1 MeOH : water) and the presence of the methyl ester leads to the formation of a double-barrelled material containing both hydrophobic and hydrophilic pores, as shown in Figure 4.3(a). The synthesis of STAM-1 was first reported by Mohideen *et al.* in 2011.[5] The structure has trigonal symmetry (space group $P\bar{3}m1$) and contains one unique mmbtc species, which has been refined with a C_2 axis of symmetry, giving rise to the seven unique C species and three unique framework H species shown in Figure 4.3(b). The symmetry of the structure requires disorder of the methyl group over two positions of equal occupancy, C7A and C7B, but it is unclear from the original work whether this is as a result of motional disorder of each ester group (*i.e.*, rapid (on the diffraction timescale) rotation about the C5-C6 bond) or static disorder (*i.e.*, the methyl groups are locked in position but the position is random). As shown in Figure 4.3(c), the ester groups occur in rings around the inside of the hydrophobic pore, with the C7A-C7B distance between neighbouring groups within a ring being 1.89 Å. This arrangement is unlikely on steric grounds, whereas the C7A-C7A (and the identical C7B-C7B) distance of 4.16 Å would avoid a steric clash. As such, for any one ring of esters, it seems likely that either C7A or C7B must be fully occupied but, as the shortest C7-C7 distance between different rings is 6.83 Å, it is unlikely that the orientation of the esters in one ring will affect that of another ring, and the overall distribution of methyl groups down a pore would likely be random. It is likely, therefore, that the "disorder" of the methyl group is a static ensemble average disorder, rather than a dynamic disorder, as the same steric interactions that would disfavour occupancy of adjacent C7A and C7B pairs would likely lead to hindrance of any C5-C6 rotation. However, one final scenario is a concerted motion, in which all of the methyl esters in a given ring reorient simultaneously and by rotation in the same direction. While perhaps unlikely, this would also lead to the apparent disorder of the methyl groups that is observed.

STAM-1 can also be activated by removal of H_2O to give CUSs on the axial position of the copper dimers. Upon activation, STAM-1 appears to undergo a large increase in disorder, linked to a collapse of the hydrophobic pores,[29] and relatively little is known about the structure of the activated phase. It can be seen from Figure 4.4 that, while HKUST-1 and STAM-1 are the same colour when first prepared (*i.e.*,

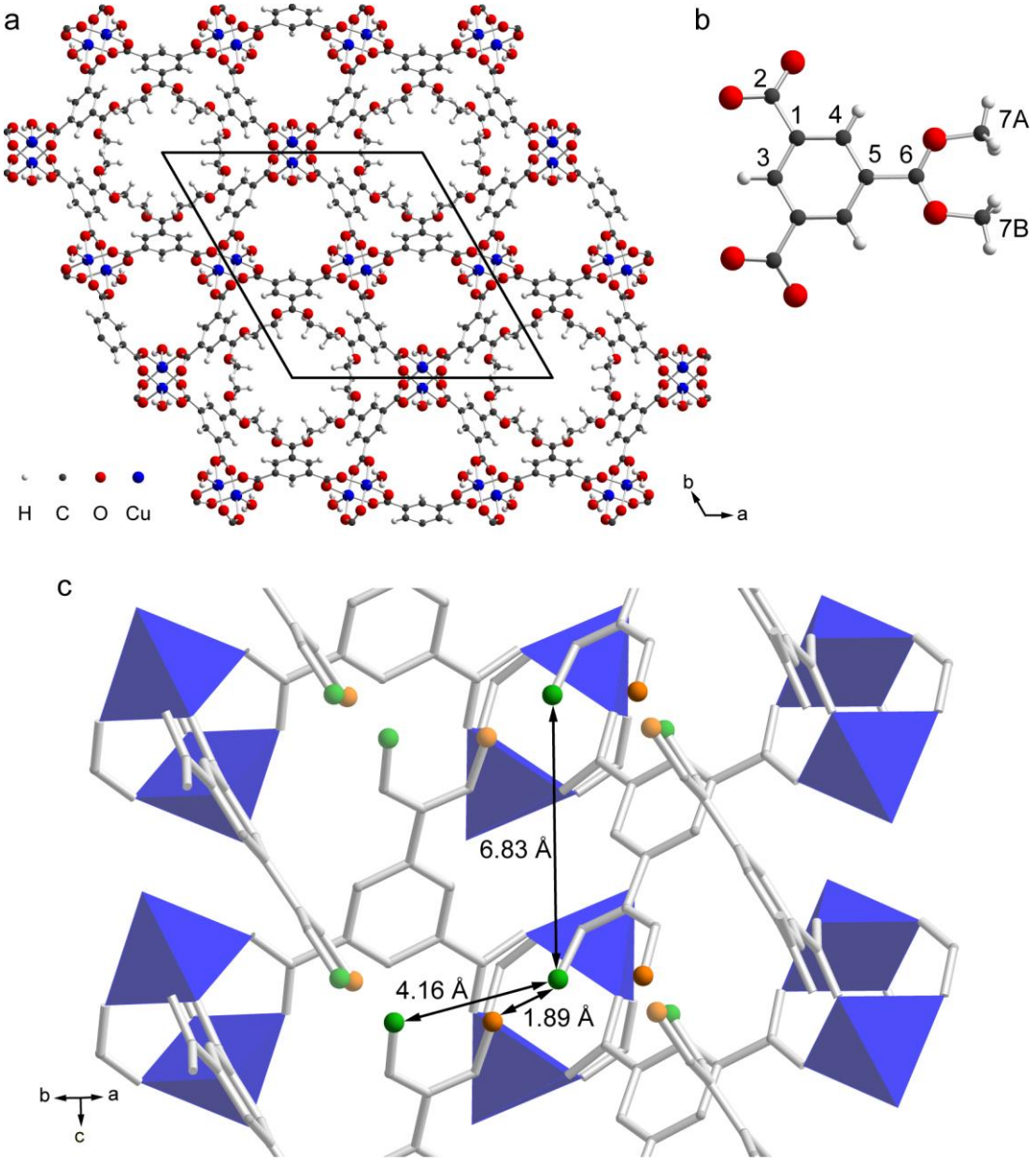

Figure 4.3. The crystal structures of (a) STAM-1,[5] (b) the mmbtc linker (including the disordered methyl group, C7A and C7B – the structure of mmbtc without disorder is given in Appendix B) and the numbering scheme used in this work, and (c) the rings of disordered methyl ester groups present within the hydrophobic pores of the MOF. CuO_5 units are shown as blue polyhedra, mmbtc is shown in grey, with C7A and C7B in orange and green, respectively. H atoms are omitted for clarity.

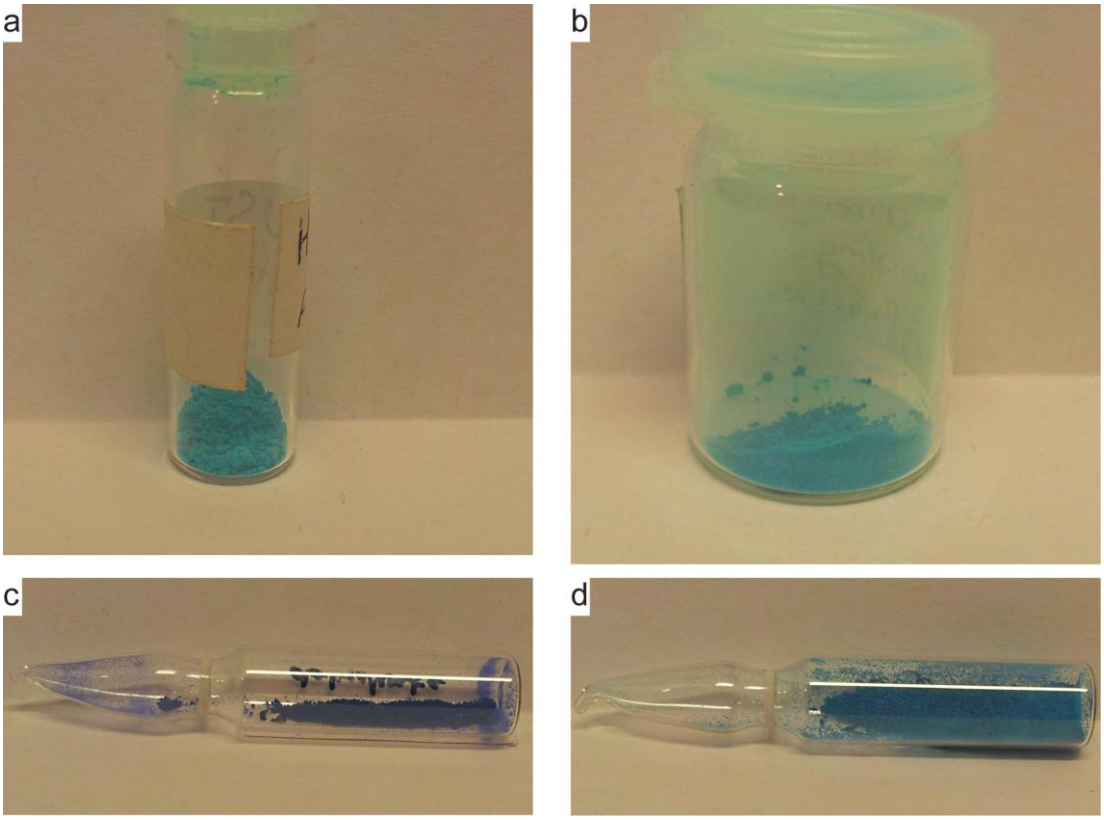

Figure 4.4. Photographs of (a) as-prepared HKUST-1, (b) as-prepared STAM-1, (c) activated HKUST-1 and (d) activated STAM-1.

the Cu^{2+} is in a similar environment in both cases), activation leads to two materials with significantly different colours, indicating that the Cu^{2+}, while nominally in the same activated state in both MOFs, may be in a different specific environment in the two cases. Mohideen *et al*. demonstrated that STAM-1 can be used to separate O_2 and N_2, and the MOF also exhibits unusual "pressure-gated" adsorption properties, which may be of use in sensing applications, as well as the separation of other mixtures of small molecules.[5] Mohideen *et al*. presented a partial ^{13}C CP MAS NMR spectrum of the material (Figure 4.5(a)) and assigned the resonance at 49 ppm to C7. However, as for HKUST-1, work presented here, and reported previously,[1] reveals that the earlier spectrum is incomplete. Complementary to solid-state NMR measurements of HKUST-1, STAM-1 has been studied by ^{1}H, ^{2}H and ^{13}C NMR, and the results of this investigation are presented herein.

As with many MOFs, STAM-1 and HKUST-1 are of interest for gas storage and drug delivery applications. Their potential to store the medically-important

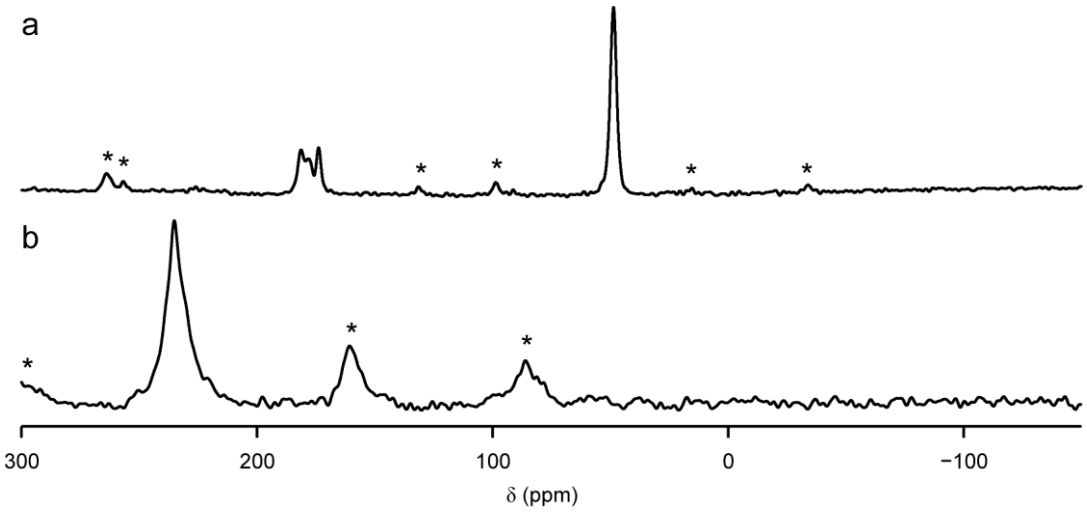

Figure 4.5. ^{13}C (14.1 T, 12.5 kHz CP MAS) NMR spectra of (a) STAM-1 and (b) HKUST-1.

guests, NO and metronidazole, and the ability of solid-state NMR to study these guests *in situ*, is investigated here.[25] The Cu^{2+} in the SBUs occupies a nominally 5-coordinate (square-based pyramidal) environment, with an unpaired electron present on each of the d^9 Cu^{2+} ions. However, the two Cu^{2+} within the SBU are in close proximity (2.63 Å in HKUST-1[21] and 2.62 Å in STAM-1[5]), allowing antiferromagnetic coupling (*i.e.*, partial bond formation) between the ion pairs at lower temperatures. Superconducting quantum interference device (SQUID) magnetometry of the two MOFs[29, 30] shows that there is a weak ferromagnetic coupling between adjacent SBUs. In both MOFs, this leads to a minimum magnetic susceptibility at ~70-80 K (although the Weiss constant for HKUST-1 is ~4.7 K[30]) and a maximum at ~250 K (corresponding to the Néel temperature). Despite this rather complex magnetic behaviour, at room temperature the materials will be in the "high temperature" paramagnetic regime, such that their magnetic susceptibility will be inversely proportional to T. However, at temperatures below ~0 °C (273 K), the magnetic susceptibility may deviate from this idealised behaviour as the Néel temperature is approached.

Given the many possible applications of HKUST-1 and STAM-1, and the fact that Bragg diffraction cannot locate accurately the guests within the pores, it was proposed that solid-state ^1H and, particularly, ^{13}C NMR spectroscopy might prove a

more useful probe of the local structure and position of guest molecules within the MOFs. However, in view of the paramagnetic nature of the frameworks, it was clear that the standard approaches to acquiring ^{13}C NMR spectra were unlikely to succeed and, therefore, the first goal of this work was to determine the conditions required for successful acquisition of the complete ^{13}C NMR spectra of the two MOFs and then to assign the spectra of the two as-prepared materials. Prior to the start of this work, only the C7 resonance of STAM-1 (at 48 ppm) had been identified by Mohideen *et al.*, and was used essentially just to confirm the presence of the methyl ester.[5] However, three resonances (assigned to the "aromatic carbons" by Mohideen *et al.*) were observed between 167 and 184 ppm, and their assignment was imperative for the extraction of useful information from the ^{13}C NMR spectra of STAM-1. Assignment of these resonances was not obvious, given that, as shown in Figures 4.1 and 4.3, the local structures of HKUST-1 and STAM-1 are (at least superficially) very similar, whereas Figure 4.5 shows that the ^{13}C CP MAS NMR spectra of the two MOFs are very different. The resonance at –50 ppm observed in the earlier (non-CP) ^{13}C NMR spectra of HKUST-1[23, 24] (Figure 4.2) is absent, and further discussion of this is provided below. Given the absence of this resonance from the CP MAS NMR spectrum of HKUST-1, it seemed plausible that there may also be resonances absent from the CP MAS NMR spectrum of STAM-1; a suggestion corroborated by the four resonances present (assuming no overlapped resonances) compared to the seven crystallographically-distinct C species.

In the (relatively) recent literature, NMR spectra have been acquired for many different types of paramagnetic systems, ranging from metalloproteins (low concentration of non-connected metal centres) to simple complexes of paramagnetic ions (high concentration of non-connected centres) to MOFs (high concentration of interconnected metal centres).[23, 24, 31-38] However, despite the diversity of the systems studied, a number of similarities and key features emerge for the successful acquisition of high-resolution ^{13}C NMR spectra of paramagnetic materials. Rapid MAS ($\geq$ 30 kHz) is usually required to remove large PSAs. An exception to this is for the case of low B_0 field strength (*e.g.*, 4.7 T), where line broadening of hundreds of ppm can be removed by MAS rates of only a few kHz, owing to the smaller Larmor frequencies achieved at lower field. However, the use of fast MAS comes

with the caveat that, should the MAS rate be insufficiently rapid, there is the chance that the linewidth of the individual spinning sidebands might exceed their spacing, leading to overlap of sidebands and no resolution enhancement.[39]

Decoupling of ^{1}H is generally not required for paramagnetic materials, especially if fast MAS is used, as this effectively removes much of the heteronuclear dipolar interaction, and the remaining contributions to the line broadening generally arise from the interactions with the unpaired electrons, rather than other nuclei.[37, 38] Peterson *et al*. did suggest that decoupling has an effect on the ^{13}C NMR spectrum of HKUST-1,[24] but this is not a general observation and this claim will be investigated in greater detail below. By avoiding decoupling during acquisition, the "duty factor" (*i.e.*, the proportion of the experimental time during which rf power is applied) is drastically reduced and wear to the probe is minimised.

Despite being the standard ^{13}C NMR experiment, CP from ^{1}H is generally inefficient as a result of the large PSAs (and corresponding off-resonance effects) for both ^{1}H and ^{13}C, the rapid $T_{1\rho}$ relaxation during the spin lock and the reduction in the dipolar coupling under fast MAS. It has been shown that the use of adiabatic pulses may allow more efficient inversion and spin-locking in paramagnetic samples.[40] However, it is unclear how these pulses actually act upon the spins in the fast MAS regime (where the rotor period may be significantly shorter than the pulse length).

Very rapid experimental repetition rates (up to hundreds of repetitions per second) may be possible for paramagnetic solids, occasionally limited by the data transfer rate or experimental duty factor rather than relaxation. This means that spectra may be acquired more rapidly than for diamagnetic materials. In order to maintain a low duty factor, such rapid repeat rates are only possible if the experiment employs a relatively small number of short pulses (*i.e.*, long spin-locking pulses and decoupling schemes are usually incompatible with this approach).[37, 38] However, this latter constraint is not a significant problem since, as discussed above, neither spin-locking pulses nor decoupling schemes are very effective in the fast MAS regime.

Owing to the linewidths often present, the baseline of the spectrum, as well as the intensities of broad resonances, may be severely distorted if a refocusing pulse

(*i.e.*, a spin echo) is not used.[24] The spin-echo experiment also has the advantage of removing the background signal, which can be especially prominent in natural-abundance ^{13}C NMR spectra of MOFs, as the signal from the sample is typically relatively weak and spread across the (often broad) SSB manifold. However, rapid transverse relaxation may lead to significant loss of signal during the spin echo and, consequently, the echo delay must be kept to a minimum. The use of rapid (30-80 kHz) MAS reduces the rotor period to ~12.5-33 μs, thereby minimising signal loss.

The large shift ranges often present mean that, in many cases, experiments such as variable-offset cumulative spectroscopy (VOCS) or spin-echo mapping (SEM)[41] are required. These techniques are required when the excitation bandwidth of the pulse (approximately the inverse of the pulse duration) is less than the width of the spectral region of interest. In such cases, the spectrum is acquired in a stepwise manner, with the transmitter frequency incremented by no more than half the excitation bandwidth of the pulse between steps. The intensities of these individual steps, or sub-spectra, are corrected for different relaxation rates at different frequencies (as T_2 typically decreases with increasing paramagnetic shift contribution), and then coadded to provide the final spectrum. This approach is often used to achieve uniform excitation of wide-line spectra (particularly for nuclei with spin quantum number $I > 1/2$ and subject to the quadrupolar interaction), but is not normally applied to ^{13}C.[36, 41, 42]

It is clear from the above discussion that a simple experimental approach is likely to be the most effective for the study of paramagnetic MOFs, with the length of time between creation of transverse magnetisation and observation being minimised to reduce relaxation-based signal losses. As such, the MAS NMR spectra of HKUST-1 and STAM-1 were acquired (at natural abundance) using a spin-echo pulse sequence, and are shown in Figure 4.6. The use of 1.3 mm rotors enabled rapid (60 kHz) MAS and a short (16.67 μs) rotor-synchronised delay in the spin echo. Owing to the small sample mass (> 5 mg) present, the signal per transient was low and extensive signal averaging (327,680 transients per spectrum) was required to ensure reasonable a SNR was achieved. However, by using a rapid experimental repeat interval of 20 ms, the total experimental time was only ~2 h.

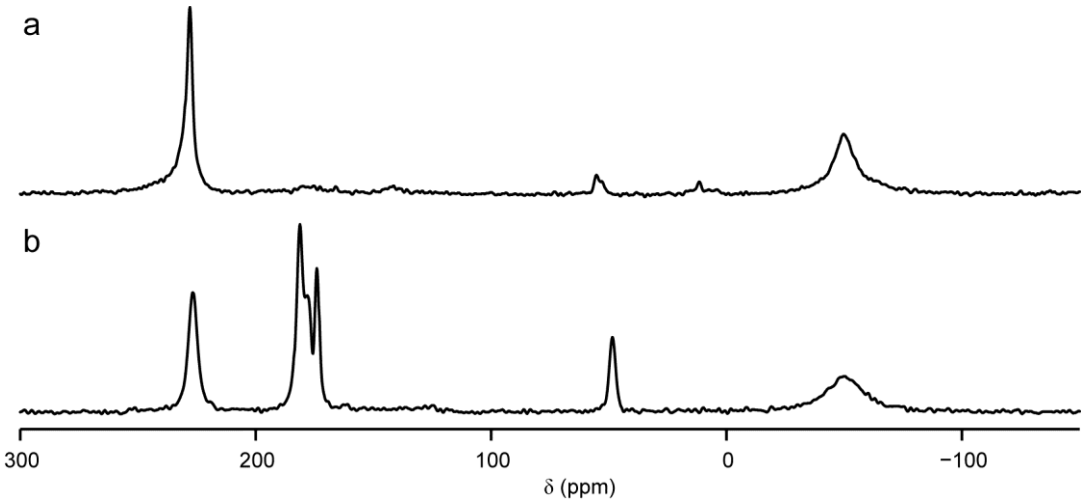

Figure 4.6. ^{13}C (14.1 T, 60 kHz MAS) spin-echo NMR spectra of as-prepared (a) HKUST-1 and (b) STAM-1.

For HKUST-1, the spectrum contains the resonances observed previously at 228 and −50 ppm. However, for STAM-1, in addition to the four resonances present in the CP MAS NMR spectrum in Figure 4.5, resonances are observed at 227 and –50 ppm, as shown in Figure 4.6(b). This supports the suggestion that the local environments of the C species are similar in both MOFs. From the literature assignment for HKUST-1,[23, 24] the resonance at −50 ppm can be assigned to C2 in STAM-1, while the resonance at 227 ppm can be assigned to C1 and C3 in STAM-1. However, assignment of the remaining resonances (174, 178 and 181 ppm) is not as clear, and the assignment of the resonance at 227/8 ppm as both C1 and C3 is unsatisfactory, as the species are chemically very different and it seems unlikely that they would coincidentally have the same isotropic shift. The full width of the spectrum shown in Figure 4.6(a) is shown in Figure 4.7(a). Inspection of the baseline reveals a low-intensity feature at ~850 ppm, which cannot be assigned as a SSB of either of the two resonances mentioned above. By moving the transmitter offset from 100 ppm to 850 ppm and signal averaging for 2,010,112 transients, the spectrum shown in Figure 4.7 (b) demonstrates that the relative intensity of this feature, which can be fitted as a single Lorentzian with an isotropic shift of 853 ppm, is greatly enhanced, suggesting that this resonance is genuine and that the spectrum of HKUST-1 must be recorded as at least two sub-spectra with different transmitter offsets. There is no evidence of a similar resonance at ~850 ppm in the baseline of

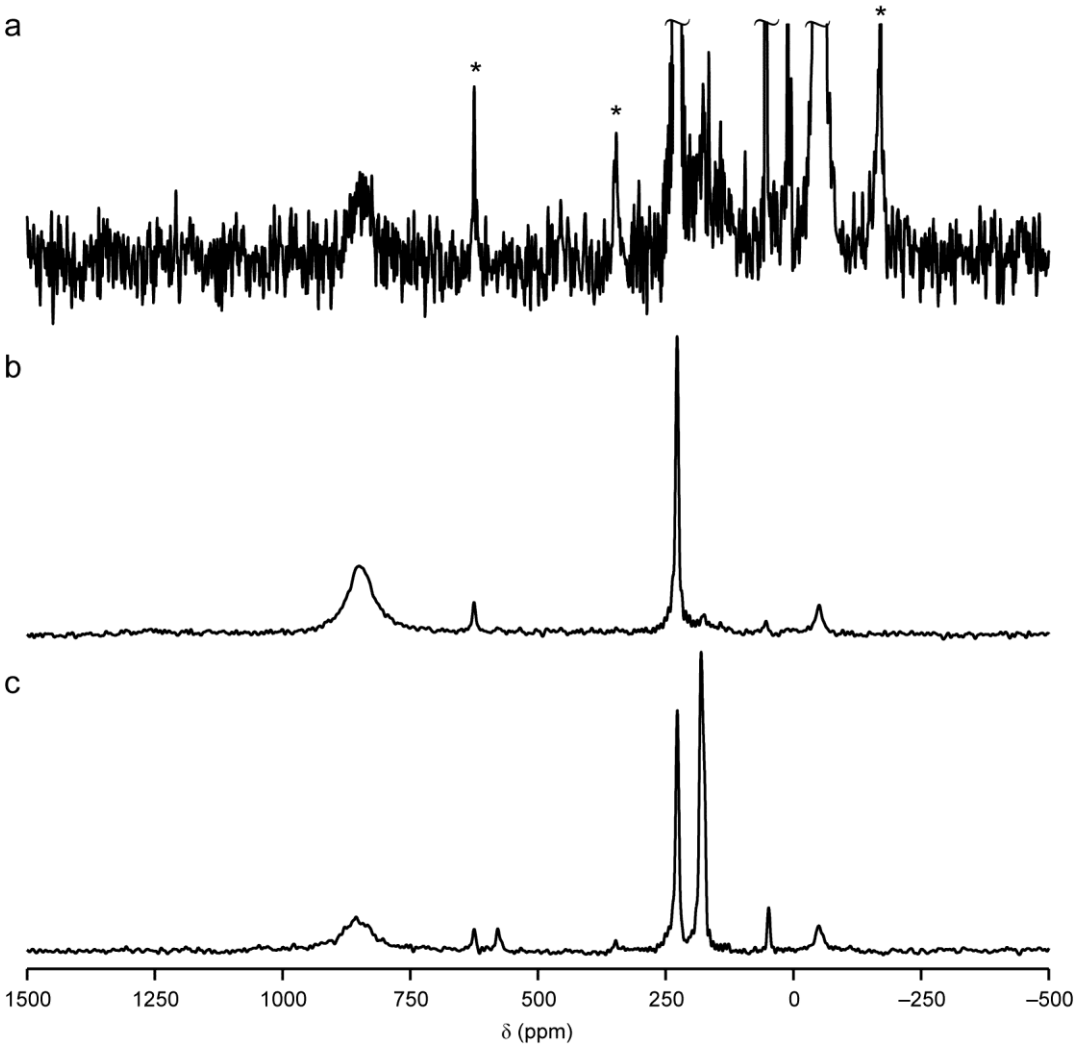

Figure 4.7. (a) Expansion of the baseline of a larger portion of the spectral width of the spectrum shown in Figure 4.6(a). (b) ^{13}C (14.1 T, 60 kHz MAS) spin-echo NMR spectrum of HKUST-1 acquired with the transmitter frequency at 850 ppm. (c) ^{13}C (14.1 T, 60 kHz MAS) spin-echo NMR spectrum of STAM-1 acquired with the transmitter frequency at 850 ppm. Spectra in (b) and (c) were processed with 500 Hz Lorentzian broadening.

the spectrum of STAM-1 in Figure 6.4(b), but, as shown in Figure 4.7(c), an experiment carried out with the transmitter offset at 850 ppm and signal averaging for 2,160,000 transients reveals a resonance with an isotropic shift of 853 ppm. However, this resonance is considerably broader and of lower intensity than the resonance in HKUST-1, which explains why it was not observed initially. The very unusual chemical shift of these resonances, and their low peak-height-to-noise ratio

(on account of the 5.0 and 9.4 kHz FWHH peak width for HKUST-1 and STAM-1, respectively) are the most likely reason that these resonances were not observed in previous NMR studies of either MOF. (In addition, the slower MAS rates, – comparable to the FWHH of the resonances – used in the earlier works, may have contributed to the broad resonances being overlooked.) However, it is also possible that such a resonance was not observed earlier owing to its origin in a contaminant within the probe or rotors used in this work. This possibility was excluded by ^{13}C isotopic labelling experiments, discussed below, and, more recently, in work by Gul-E-Noor *et al*.,[43] who report a similar resonance for a sample of Zn-doped HKUST-1, using a completely different probe and rotor.

The observation of the resonance at ~850 ppm for both MOFs means that the numbers of resonances observed matches the numbers of crystallographically-distinct C species. However, given that frequency-stepped acquisition had already revealed one additional resonance, the spectral region from −2000 to 2000 ppm was searched for further resonances in both MOFs, but no additional signals were observed. The spectra reported here are, therefore, assumed to be complete. In order to avoid the distorted relative intensities of the resonances, observed in Figure 4.7, the spectra were re-recorded in two steps, shown for HKUST-1 in Figure 4.8(a), each with signal averaging for 327,680 transients and the transmitter offset at 100 ppm for the first step, and 850 ppm for the second step. These sub-spectra were processed and then summed, with the resulting spectra shown in Figures 4.8(a and b). Given the presence of a previously unobserved resonance in the spectrum of HKUST-1 and three previously unobserved resonances for STAM-1, the earlier literature assignments for these MOFs cannot be correct, as they relate to incomplete spectra, and the above assignment must be discounted without further evidence.

4.4.3 Assignment of the ^{13}C NMR Spectra of HKUST-1 and STAM-1

Assignment of resonances in a ^{13}C NMR spectrum with shifts ranging from +850 to −50 ppm (*cf.* the shift range for most diamagnetic materials of 0 to 220 ppm) is a non-trivial task. Previous assignments have been made in the literature, based mainly on the assumption that nuclei closer to the unpaired electron (either through space or through a bonded pathway) will experience greater paramagnetic effects than more

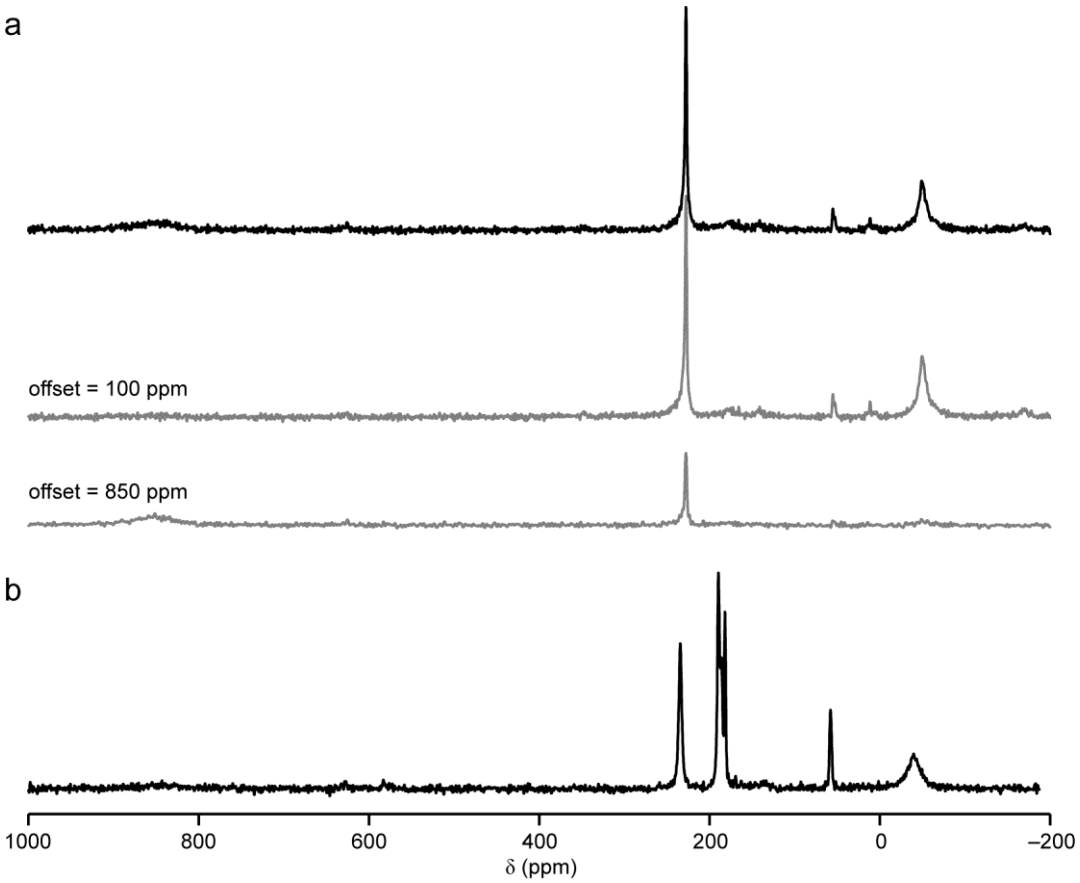

Figure 4.8. ^{13}C (14.1 T, 60 kHz MAS) NMR spectra of (a) HKUST-1 and (b) STAM-1. Each spectrum was recorded in two steps, each with signal averaging for 327,680 transients and the transmitter offset at 100 ppm for the first step, and 850 ppm for the second step. In (a), the individual sub-spectra are shown in grey below the summed spectrum (shown in black).

distant nuclei.[23, 31-33] This approach is intuitive and was, therefore, implemented for HKUST-1 and STAM-1. For each resonance in the MOF, the isotropic shift, linewidth (Δ*, as defined by Lesage *et al.*[44]) and T_1 relaxation constant were measured, and are reported in Table 4.2. Inversion recovery experiments were used to measure T_1 and, given the excitation bandwidth of the pulses (~100 kHz) was significantly smaller than the dispersion of the resonances in the spectrum (~150 kHz at 14.1 T), a separate experiment was carried out for each resonance. The transmitter frequency was offset to match the frequency of the resonance of interest for each experiment, in order to ensure complete inversion and accurate measurement of T_1. As the largest T_1 relaxation constant recorded was 18.4 ms, for the resonance at

Table 4.2. Summary of δ_{iso}, T_1, Δ* and tentative assignment of the ^{13}C NMR spectra of HKUST-1 and STAM-1.

δ_{iso} (ppm)	T_1 / ms	Δ* / kHz	Suggested Assignment
HKUST-1			
853	4.4	9.96	C2
–50	3.5	1.77	C1
228	10.8	0.66	C3
STAM-1			
853	3.6	9.44	C2
–50	1.3	2.97	C1
227	5.9	0.62	C3
181	7.7	0.45	C4, 5 or 6
174	18.3	0.29	C4, 5 or 6
178	15.2	0.40	C4, 5 or 6
49	18.4	0.44	C7

49 ppm for STAM-1, all subsequent spectra were (unless otherwise noted) recorded with a repeat interval of 100 ms. This interval (of > $5T_1$) was chosen to allow full longitudinal relaxation, leading to spectra that were, as far as possible, quantitative.

For comparison, the ^{13}C CP MAS NMR spectra of trimesic acid (H_3btc) and trimethyl trimesate (tmbtc) were also recorded, as these provide approximate diamagnetic analogues of the C environments of HKUST-1 and STAM-1, as shown in Scheme 4.1, where the numbering system has been chosen to emphasise the (local) structural similarities between HKUST-1, STAM-1, H_3btc and tmbtc. The ^{13}C CP MAS NMR spectra of the two diamagnetic materials are shown in Figures 4.9(a and b). The presence of crystallographic inequivalences in both structures leads to broadening and splitting of the resonances. The structure of H_3btc contains six distinct molecules (54 distinct C atoms)[45] and, while there is no published structure of tmbtc, it is clear that there are at least three distinct CH_3 species, giving rise to at least three distinct C4, C5 and C6 types, although only two resonances are observed

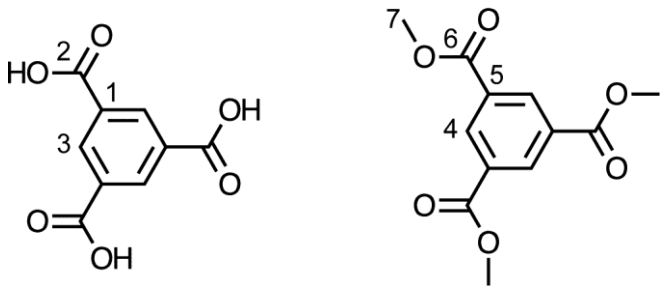

Scheme 4.1. The structures of H_3btc acid and tmbtc and numbering schemes used in this thesis.

for each of these chemical species, indicating that some resonances overlap. It is, therefore, clear that these species are poor diamagnetic analogues, as no single diamagnetic shift can be defined for each C species. Attempts were made to synthesise the (diamagnetic) Zn analogues of HKUST-1 and STAM-1,[46] using zinc nitrate as the metal source instead of copper nitrate, but the reactions yielded, instead, the material recently reported as "Zn-BTC".[47, 48] The ^{13}C NMR spectrum of

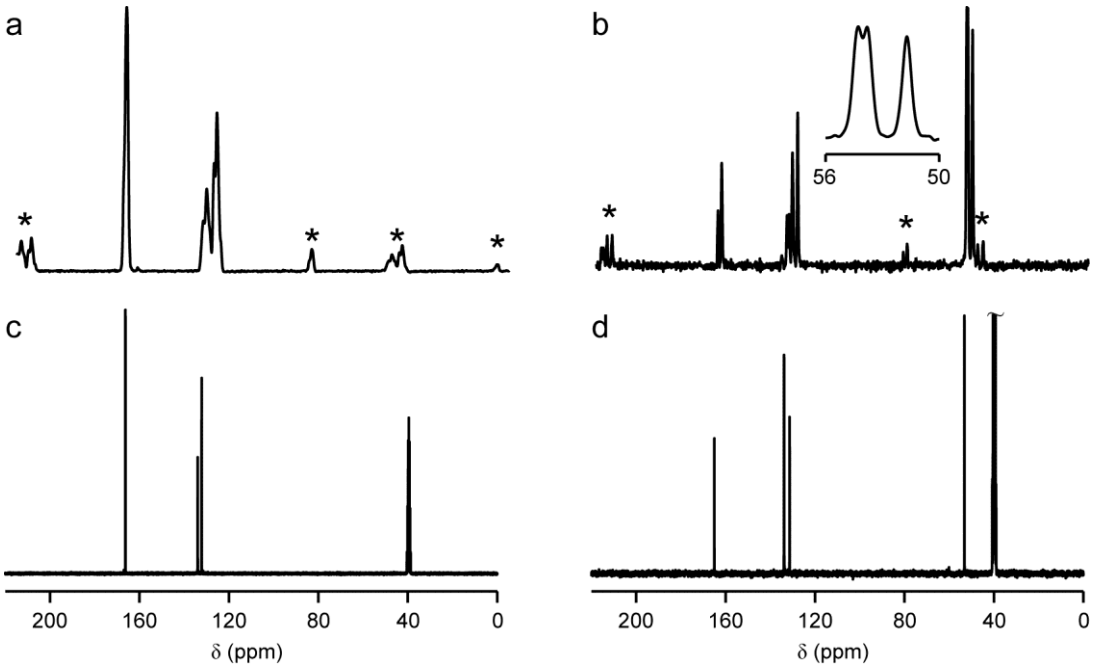

Figure 4.9. ^{13}C (14.1 T, 12.5 kHz CP MAS) NMR spectra of (a) H_3btc and (b) tmbtc. Solution-phase (7.05 T, $(CD_3)_2SO$) ^{13}C NMR spectra of (c) H_3btc and (d) tmbtc. In (c) and (d), the multiplet at 39.52 ppm arises from the solvent, and was used to reference the spectra.

this material has been reported as containing resonances between 131 and 138 ppm (aromatics) and 174-178 ppm (carboxylates) and similar resonances were observed in the ^{13}C CP MAS NMR spectrum of the material synthesised for this work, shown in Figure 4.10. Given the lack of a diamagnetic MOF analogue of HKUST-1 or STAM-1, the solution-phase ^{13}C NMR spectra of H_3btc and tmbtc (shown in Figures 4.9(c and d), with details given in Appendix I) were used to provide approximate diamagnetic chemical shifts for the C species in HKUST-1 and STAM-1. However, it must be remembered that these shifts will be subject to solvent effects, *etc*., which were not investigated for this work, but would be expected to contribute up to ~2-3 ppm to the chemical shifts recorded. The chemical shifts of these "analogous" compounds are given in Table 4.3.

According to the above approach to assignment, the ^{13}C NMR spectra of HKUST-1 and STAM-1 can be assigned as follows. On the basis of the very large isotropic shift, rapid T_1 relaxation and very broad line, the resonance at 850 ppm should be assigned to C2. The next most shifted and broadened resonance is that at −50 ppm, which has a slightly smaller T_1 relaxation constant than C2, suggesting its assignment as C1. In both MOFs, the assignment would be reversed if based purely on T_1, although the error in the inversion recovery measurements is of the order of 0.5 ms, so there is little practical difference between the T_1 values for these resonances, whereas the differences in δ_{iso} and Δ^* are much more significant. For HKUST-1, a process of elimination allows the resonance at 228 ppm to be assigned as C3, with the slower T_1 relaxation, isotropic shift closer to the expected chemical shift for aromatic CH (~120-125 ppm), and narrower linewidth all corroborating this assignment. Given the similarity of the chemical shifts, it is reasonable to assume that the resonance at 227 ppm in the ^{13}C NMR spectrum of STAM-1 can also be assigned as C3, although T_1 for this resonance is about half that of the corresponding resonance for HKUST-1. Following the earlier work of Mohideen *et al.*,[5] the resonance at 49 ppm can be assigned to C7, as its shift is similar to that of C7 in tmbtc (52.8 ppm). The remaining three resonances for STAM-1 must correspond to C4, C5 and C6. Based on T_1 and Δ^*, their assignment would be C4 (181 ppm), C5 (178 ppm) and C6 (174 ppm). This would give paramagnetic shift contributions, δ_{para}, of 47.6 ppm (C4), 47.1 ppm (C5) and 9.5 ppm (C6), relative to the shifts of the

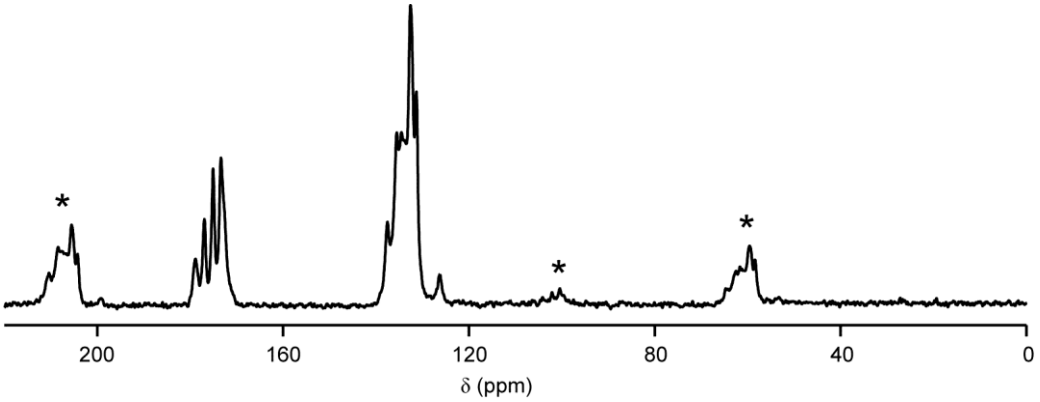

Figure 4.10. ^{13}C (14.1 T, 11 kHz CP MAS) NMR spectrum of Zn-BTC prepared in an attempt to synthesise Zn-HKUST-1.

diamagnetic analogues. While this is in the correct order (*i.e.*, C4 is closer to Cu and more shifted than C5, and both are closer and more shifted than C6), there is a very small difference in δ_{para} for C4 and C5, so it is possible that this assignment of the two resonances should be reversed. Additionally, as discussed above, the hydrophobic pore is lined with methyl ester groups and any disorder of these is likely to lead to a greater spread of chemical shifts (arising from slightly different local environments) for C6 than C5 or C4. Such a distribution of chemical shifts would contribute to Δ*, making this assignment tentative at best. Further evidence was, therefore, required in order to achieve a confident assignment.

As discussed above, ^{13}C CP MAS did not provide a complete ^{13}C NMR spectrum of either MOF. However, the three resonances for C4, C5 and C6 were observed, and it was hoped that further insight into their assignment might be obtained from their CP build-up behaviour. In order to refocus the signal from

Table 4.3. ^{13}C (7.05 T, $(CD_3)_2SO$) chemical shifts H_3btc and tmbtc.

Species	δ (ppm)	Species	δ (ppm)
H_3btc		tmbtc	
C1	132.1	C4	133.4
C2	166.1	C5	130.9
C3	133.8	C6	164.5
		C7	52.8

broader resonances, the CP experiment was modified by the addition of a rotor-synchronised spin echo between magnetisation transfer and acquisition. The experiments were also carried out under rapid (60 kHz) MAS, which will have reduced the efficiency of the magnetisation transfer during CP. The rapid MAS rate was chosen in order to achieve a short rotor-synchronised echo delay and to avoid heteronuclear decoupling during acquisition – this latter point allowed for more rapid signal averaging (although the addition of the spin-locking pulses meant that a repeat interval of 250 ms was chosen in order to protect the delicate coil of the 1.3 mm probe used) and offset the poorer sensitivity arising from the decreased efficiency of the magnetisation transfer.

Series of ^{13}C CP MAS NMR spectra were recorded for HKUST-1 and STAM-1 with contact times of 50-5000 μs. Build-up plots for each resonance observed are shown in Figure 4.11. The resonances assigned to C1 and C2 were not observed at any contact time, as these species do not have directly-bonded ^{1}H and have T_1 values on the same order of magnitude as the contact time. As such, T_{IS} is likely to be relatively slow, while $T_{1\rho}$ will be very rapid; causing a large reduction in signal relative to the non-CP experiment (*cf.* Figure 3.8). While the C2 resonance will not be efficiently refocused by a 180° pulse applied at a transmitter frequency of 100 ppm, a series of experiments with a ^{13}C transmitter frequency of 850 ppm did not show any transfer of magnetisation from ^{1}H to this resonance. For HKUST-1, the only resonance observed is at 228 ppm: consistent with its assignment as C3 (the only C species with a directly-bonded ^{1}H). As noted by Gul-E-Noor *et al*. (who carried out CP MAS experiments with 10 kHz MAS), the maximum signal intensity occurs with a very short contact time (~250 ms), indicative of rapid $T_{1\rho}$ relaxation.[23] For STAM-1, the resonance at 227 ppm has a very similar CP build-up behaviour to the resonance at 181 ppm, suggesting that these are C3 and C4, respectively. While C3 has a similar chemical shift in both MOFs, it is clear that the relaxation behaviour (both in terms of T_1 and $T_{1\rho}$) is different. The assignment of the resonance at 49 ppm as C7 is supported by the CP build-up curves, which show that this resonance has the slowest $T_{1\rho}$ relaxation and is, therefore, most likely to be furthest from the paramagnetic centres. The slower build up for C7 compared to C3 and C4 can be

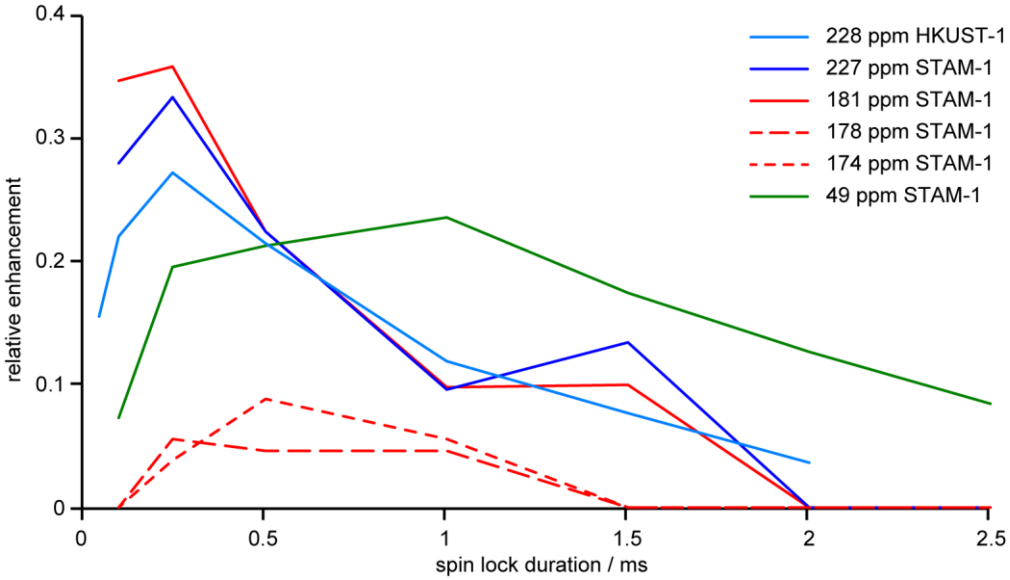

Figure 4.11. CP build-up plots for the ^{13}C resonances observed for HKUST-1 and STAM-1 (14.1 T, 60 kHz CP MAS). Intensities are plotted relative to spin-echo experiments carried out under comparable conditions.

attributed to the fact that H3 and H4 remain in a fixed orientation relative to C3 and C4, respectively, whereas rotation about the C7-O bond might reduce the H7-C7 dipolar coupling to some average value, making transfer of polarisation to C7 less efficient. The resonances assigned to C5 and C6 are observed, but only with very low intensity, and it is impossible to distinguish between these resonances by the CP MAS experiments carried out here. As such, using just the NMR experiments described above, a full and confident assignment of the ^{13}C NMR spectra for the two MOFs remains elusive and an alternative assignment strategy is required.

4.4.4 Specific ^{13}C Labelling of HKUST-1 and STAM-1

Given the somewhat unsatisfactory assignment of the ^{13}C NMR spectra of HKUST-1 and STAM-1, two specifically-^{13}C-labelled samples of H_3btc were prepared. Benzene-1[^{13}C],3,5-trimesic acid (**1**) was prepared by lithiation of 1-bromo-3,5-dimethylbenzene, followed by methylation with $^{13}CH_3I$. Oxidation of the resulting 1[^{13}C],3,5-trimethylbenzene gave **1** in ~44% overall yield, as shown in Scheme 4.2. The low temperature is essential during the methylation, as the reaction in Scheme 4.3 occurs with 100% conversion at room temperature. While $KMnO_4$ will oxidise 1-butyl-3,5-dimethylbenzene to H_3btc, the product will not contain the ^{13}C label.

[U-^{13}C]benzene-1,3,5-tricarboxylic acid (**2**) was prepared by the Friedel-Crafts ethylation of a 1 : 6.2 mixture of [U-^{13}C]-benzene and benzene, followed by oxidation of the resulting 1,3,5-triethyl[U-^{13}C]benzene (and 1,3,5-triethylbenzene) to yield **2**, as shown in Scheme 4.4. A more efficient oxidation (yields of ~70%) for the preparation of **2** has since been developed,[3] based on the process shown in Scheme 4.5. Future syntheses of enriched material are likely to use this oxidation route. This would require the use of bromo[1-^{13}C]ethane for the synthesis of H_3btc with the ^{13}C label installed on the acid groups, and would yield the triply-labelled benzene-1,3,5[$^{13}C_3$]-tricarboxylic acid rather than **1**.

^{13}C(2)-HKUST-1 and ^{13}C(2,6)-STAM-1 (where the number(s) in parentheses indicate ^{13}C-labelled positions) were prepared using a 1 : 1 mix of **1** and natural-abundance H_3btc, giving an average abundance of ^{13}C on the labelled positions of 17% (*cf.* 1.07% natural abundance), but with a maximum of one ^{13}C label per linker. ^{13}C(1,3)-HKUST-1 and ^{13}C(1,3,4,5)-STAM-1 were prepared using a ~6 : 4 mix of **2** and natural-abundance H_3btc, giving an average abundance of ^{13}C on the labelled positions of 7%, but with either zero or six ^{13}C labels per linker. By selectively enriching certain C species, the relative intensity of their resonances in the NMR spectrum will be increased. The ^{13}C NMR spectra of the four labelled MOFs are shown in Figure 4.12. Owing to the increased signal, spectra were recorded with 32768 (^{13}C(2)-HKUST-1 and ^{13}C(2,6)-STAM-1) and 40960 transients per sub-spectrum (^{13}C(1,3)-HKUST-1 and ^{13}C(1,3,4,5)-STAM-1). When **1** was included as the linker, the resonances corresponding to C2 (and C6 in STAM-1) were expected to increase in relative intensity, and it can immediately be seen from the ^{13}C NMR spectra in Figures 4.12(a and b) that the assignment of the resonance at 853 ppm in both MOFs as C2 is incorrect and the earlier literature assignment of the resonance at –50 ppm as C2 was, by chance, correct. As discussed above, the resonance at 174 ppm in the ^{13}C NMR spectrum of STAM-1 was tentatively assigned to C6 but, as can be seen in Figure 4.12(b), it is the resonance at 178 ppm that increases in relative intensity when C6 is labelled, indicating that the earlier assignment was incorrect.

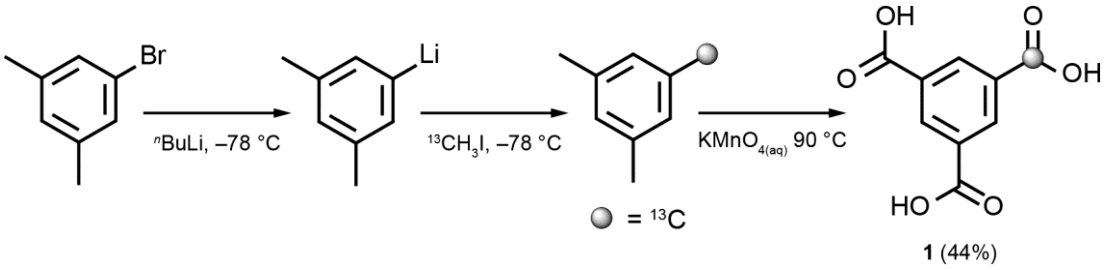

Scheme 4.2. Route to the preparation of benzene-1[^{13}C],3,5-trimesic acid (**1**).

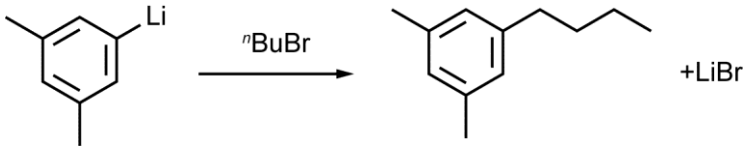

Scheme 4.3. Butylation of 1-lithium-3,5-dimethylbenzene.

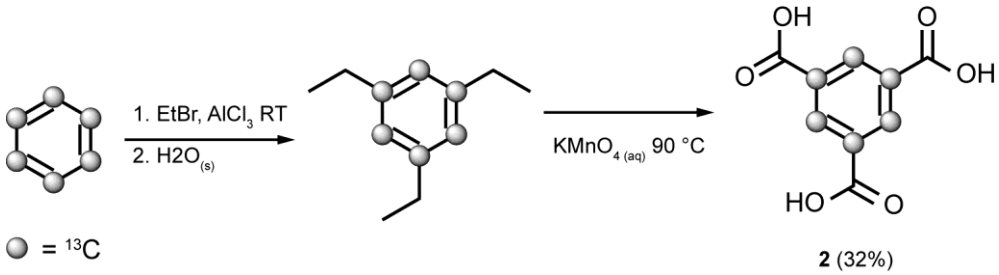

Scheme 4.4. Route to the preparation of [U-^{13}C]benzene-1,3,5-trimesic acid (**2**).

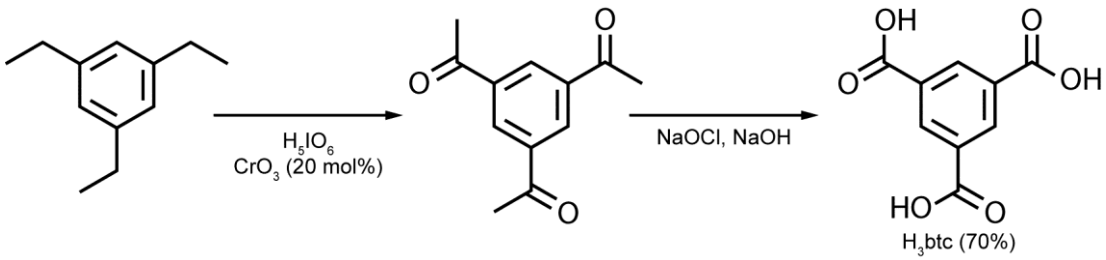

Scheme 4.5. Higher-yielding oxidation of 1,3,5-triethylbenzene to H_3btc.

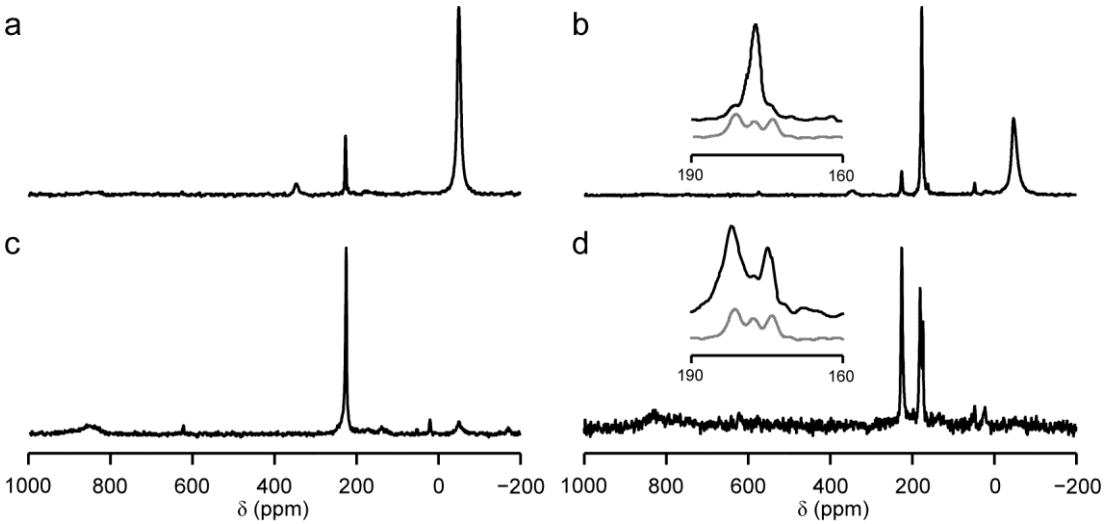

Figure 4.12. ^{13}C (14.1 T, 60 kHz MAS) NMR spectra of (a) ^{13}C(2)-HKUST-1, (b) ^{13}C(2,6)-STAM-1, (c) ^{13}C(1,3)-HKUST-1 and (d) ^{13}C(1,3,4,5)-STAM-1. The insets in (b and d) show the spectra of the labelled (black) and natural-abundance (grey) MOFs.

The assignment of the resonance at –50 ppm as C2 means that the origin of the resonance at 853 ppm must be questioned since, by a process of elimination for HKUST-1, C2 was assigned by isotopic labelling and C3 was assigned by CP build-up behaviour, meaning that this third resonance must arise from C1, an unidentified impurity phase, or the background, with the same assignment likely to apply to STAM-1, given the similar isotropic shifts. When **2** is used as the linker in both MOFs, the resonances at 227/8 ppm increase in intensity relative to C2, as shown in Figures 4.12(c and d), confirming their assignment as C3 (and possibly also C1). The resonances at 853 ppm also increase in intensity relative to C2, suggesting that they do not arise from background signal. For HKUST-1, the integrated intensity ratio of the resonances at 228 and 853 ppm in the natural-abundance material is 2.09 : 1 (where, if the resonance at 853 ppm can be assigned as C1, the deviation from the expected 1 : 1 ratio may be explained by the more rapid transverse relaxation of C1). In ^{13}C(1,3)-HKUST-1, the ratio of these two resonances is 2.05 : 1 and, as it is very unlikely that the ratio of product to impurity in two different syntheses would be so reproducible, this suggests that the resonance at 853 ppm can, indeed, be assigned to C1. The integrated intensity ratios of C1 and C3 for natural-abundance and ^{13}C(1,3,4,5)-STAM-1 are different in the two materials (2.64 : 1 and 4.02 : 1, respectively), owing to the ~10-15 wt% ^{13}C(1,3)-HKUST-1 present in the sample of

^{13}C(1,3,4,5)-STAM-1. The presence of the impurity phase was confirmed by powder XRD, shown in Figure 4.13, where low-intensity reflections from HKUST-1 can be identified. A small amount of ^{13}C(2)-HKUST-1 was also observed in ^{13}C(2,6)-STAM-1 and, again, is reflected in the relative intensities of C1 and C3 resonances in this sample (2.78 : 1). HKUST-1 is a common impurity phase in the synthesis of STAM-1,[29] and it was suggested that the labelling procedure may have been responsible for increasing the amount of HKUST-1 observed in the labelled samples of STAM-1 – a point that is discussed in greater detail below. The ^{13}C NMR spectrum of ^{13}C(1,3,4,5)-STAM-1 also confirms that the resonances at 174 and 181 ppm arise from C4 and C5 and, from the CP MAS experiments discussed above, the assignment is C4 (181 ppm) and C5 (174 ppm). The assignment of C4, C5 and C6 determined by isotopic labelling and CP MAS NMR experiments yields δ_{para} values of 47.6, 43.1 and 13.5 ppm for C4, C5 and C6, respectively, in agreement with C4 being closest to Cu and C6 being most distant. However, the T_1 and Δ^* measurements do not support this assignment, suggesting that, as discussed above, disorder or motion of C7 may contribute to the linewidth of these narrow resonances. As the resonance at 49 ppm does not increase in relative intensity in the spectra of the ^{13}C-labelled samples of STAM-1, its assignment as C7 (the only site that was not labelled in either MOF) is confirmed. The final assignment based on the evidence discussed above is given in Table 4.4. It can be assumed that the assignments are complete, as the number of resonances observed matches that predicted by crystallography. However, the assignments raise many questions, most prominently, the question of why C1 apparently experiences a far greater interaction with the unpaired electrons than C2, despite being more distant (both in terms of the bonded pathway and spatial proximity).

It should be noted that the ^{13}C resonances at 218 and 240 ppm, observed by Peterson *et al.* for HKUST-1,[24] were not observed in any of the isotopic labelling experiments, or by Gul-E-Noor *et al.*,[23] suggesting that their origin was some impurity or artefact in the original work, rather the HKUST-1 framework itself.

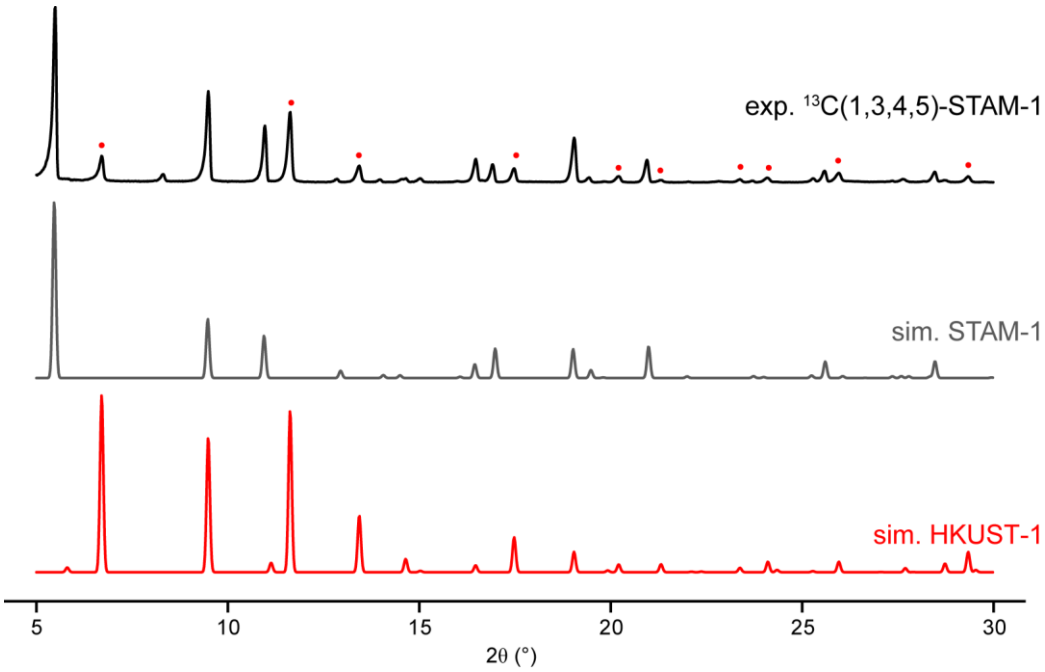

Figure 4.13. Experimental powder XRD pattern of ^{13}C(1,3,4,5)-STAM-1 (black) and simulated patterns for STAM-1 (grey) and HKUST-1 (red). Reflections in the experimental pattern arising only from HKUST-1 are indicated by red dots.

Table 4.4. Assignment of the ^{13}C MAS NMR spectra of HKUST-1 and STAM-1.

Species	δ_{iso} (ppm)	Species	δ_{iso} (ppm)
HKUST-1		STAM-1	
C1	853	C1	853
C2	–50	C2	–50
C3	228	C3	227
		C4	181
		C5	174
		C6	178
		C7	49

4.4.5 ^{1}H NMR Spectra of HKUST-1 and STAM-1

The ^{1}H MAS NMR spectrum of activated HKUST-1 was reported by Gul-E-Noor *et al.*,[23] and contains a single resonance at 8.3 ppm, assigned to H3. When the material was exposed to a low level of H_2O (up to 1.5 mol. equiv.), a resonance was observed at 11 ppm, assigned to Cu-bound H_2O and the H3 resonance moved to ~7 ppm. Upon increasing the water content to 5 mol. equiv., the H_2O resonance broadened and moved to 5.6 ppm, indicating a rapid (on the NMR timescale) exchange between the water molecules bound to Cu and those free in the pores, giving rise to only an average isotropic shift. The ^{1}H MAS NMR spectrum of HKUST-1 recorded for this work (Figure 4.14(a)) is in agreement with the work of Gul-E-Noor *et al.*, with a sharp (Δ* = 560 Hz) resonance observed at 7.1 ppm and a broad (Δ* = 1.45 kHz) resonance observed at 5.9 ppm (overlapped with the resonance at 7.1 ppm). No further ^{1}H resonances were observed between 650 and –650 ppm, indicating that the ^{1}H NMR spectrum reported by Gul-E-Noor *et al*. is complete and their assignment correct. As might be expected, the ^{1}H NMR spectrum of STAM-1 (Figure 4.14(b)) is more complicated to interpret than that of HKUST-1, owing to the relatively poor resolution of ^{1}H spectra (particularly of paramagnetic species), even with rapid MAS, and the greater number of distinct H species present in STAM-1.

In order to confirm the assignment of the ^{1}H NMR spectrum of HKUST-1, and to assign the ^{1}H NMR spectrum of STAM-1, 2D ^{1}H-^{13}C CP-HETCOR spectra were recorded. The pulse sequence was modified from that shown in Figure 3.13 by the addition of a spin echo for ^{13}C prior to acquisition of the FID. The spectrum for HKUST-1 (Figure 4.14(c)) contains a single ^{1}H-^{13}C correlation, (δ_C, δ_H) of (227 ppm, 6.9 ppm), corresponding to C3-H3 and confirming the assignment of these resonances. For STAM-1, the spectrum (Figure 4.14(d)) shows correlations at (49 ppm, –1.0 ppm), (174 ppm, 9.0 ppm), (181 ppm, 9.1 ppm) and (227 ppm, 8.8 ppm). Based on the assignment of the ^{13}C resonances, these correlations can be assigned to C7-H7, C5-H4, C4-H4 and C3-H3, respectively, allowing the assignment of the ^{1}H NMR resonances given in Table 4.5. The resonance observed at 4.8 ppm can be assigned to H_2O within the pores of the MOF, as it does not correlate with any of the ^{13}C resonances.

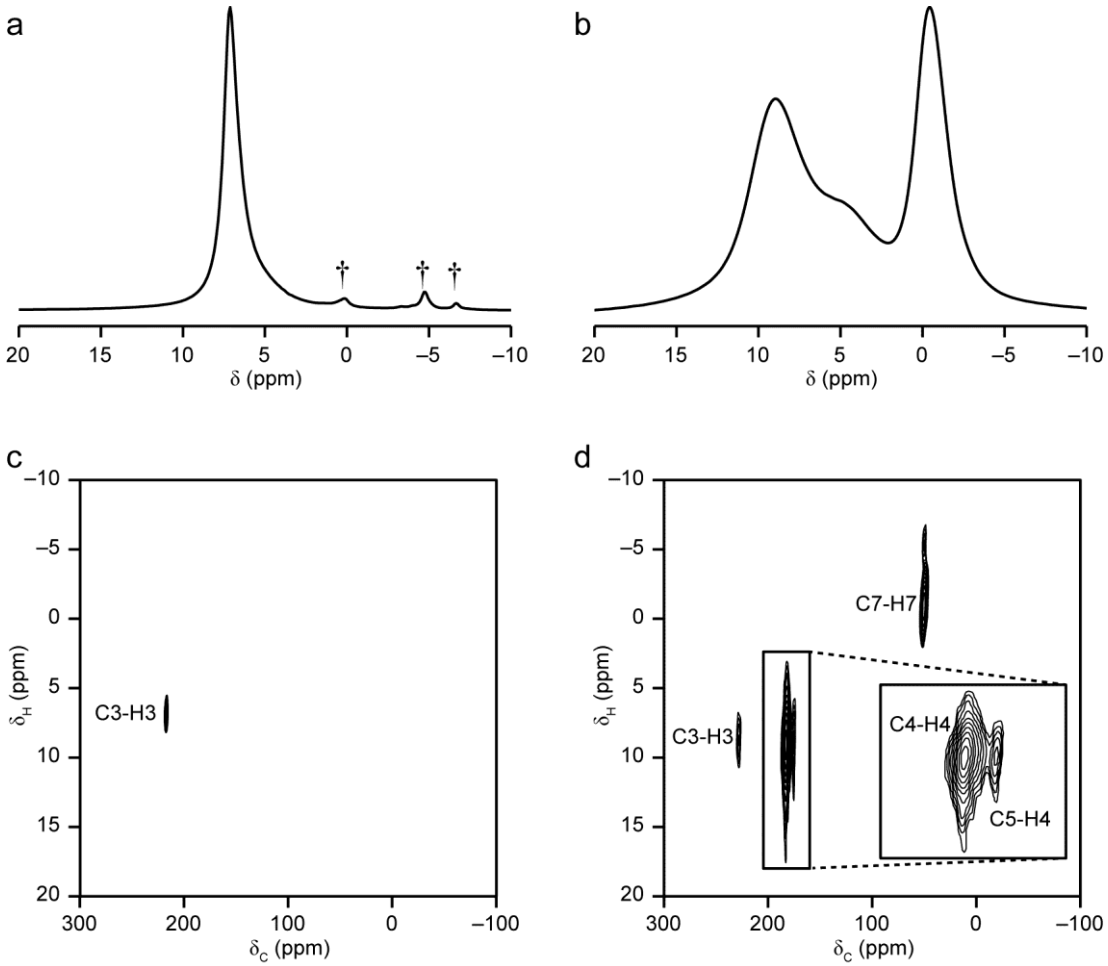

Figure 4.14. ^{1}H (14.1 T, 60 kHz MAS) NMR spectra of (a) HKUST-1 and (b) STAM-1. ^{1}H-^{13}C (14.1 T, 50 kHz MAS) CP-HETCOR spectra of (c) HKUST-1 and (d) STAM-1. In (a), resonances marked † are commonly observed in spectra recorded for samples packed in 1.3 mm rotors, where small amounts of contaminants in the rotor end caps can lead to moderately intense resonances.

Table 4.5. Assignment of the ^{1}H MAS NMR spectra of HKUST-1 and STAM-1.

Species	δ_{iso} (ppm)	Species	δ_{iso} (ppm)
HKUST-1		STAM-1	
H3	7.1	H3	8.8
H_2O	5.9	H4	9.1
		H7	–1.0
		H_2O	4.8

4.4.6 The Effects of Temperature and B_0 Field Strength

As it is well known that paramagnetic interactions are temperature dependent, one might expect the observed isotropic shifts also to be temperature dependent. If the magnitude of this temperature dependence were sufficiently large, it may be that C2 experiences a larger temperature-dependent paramagnetic shift than C1, and the resonances have simply "crossed over" at the temperature of the NMR experiments discussed above (~40 °C above room temperature, owing to frictional heating of the rotor), leading to the somewhat surprising assignment determined above.

The temperature dependence of the ^{1}H and ^{13}C NMR spectra of HKUST-1 and STAM-1 was investigated at the UK National 850 MHz Solid-State NMR Facility (B_0 = 20.0 T). It can be seen from Figure 4.15 that the high field does not lead to any significant differences in the ^{13}C NMR spectra of either MOF. (The effects of changing the B_0 field strength will be discussed in greater detail below.) Two series of variable-temperature experiments were carried out for HKUST-1 – the first of these explored the temperature range between 250 and 303 K while the shim coils were maintained at a constant temperature, whereas the second series explored the temperature range between 258 and 313 K, but with no control of the temperature of the shim coils. This is a possible source of error that will significantly affect the ^{1}H NMR spectra (owing to the small observed shift range of ^{1}H), and may also mask small shift differences for ^{13}C. Figure 4.16 shows plots of the ^{13}C chemical shifts for HKUST-1 as a function of the inverse of the absolute temperature, T. Owing to the limited time available at the national facility, and the difficulty of acquiring the broad C1 resonance in a short time, some temperature steps were omitted for this resonance. In the high temperature regime, the isotropic positions of resonances for paramagnetic species are proportional to 1/T, and it can be seen that this is the case for all three resonances in HKUST-1 for both series of data. It can be seen that the temperature-dependent change (proportional to the hyperfine coupling constant, $A/\hbar$) is greatest for C1 and least for C3. $A/\hbar$ can also be seen to have opposite sign for C2 relative to C1 and C3. It can be seen from Figure 4.16(d) that the ordering of the resonances observed for HKUST-1 will remain the same for all temperatures readily accessible in MAS NMR experiments, meaning that the suggestion that the resonances for C1 and C2 may have "crossed over" is incorrect. However, the

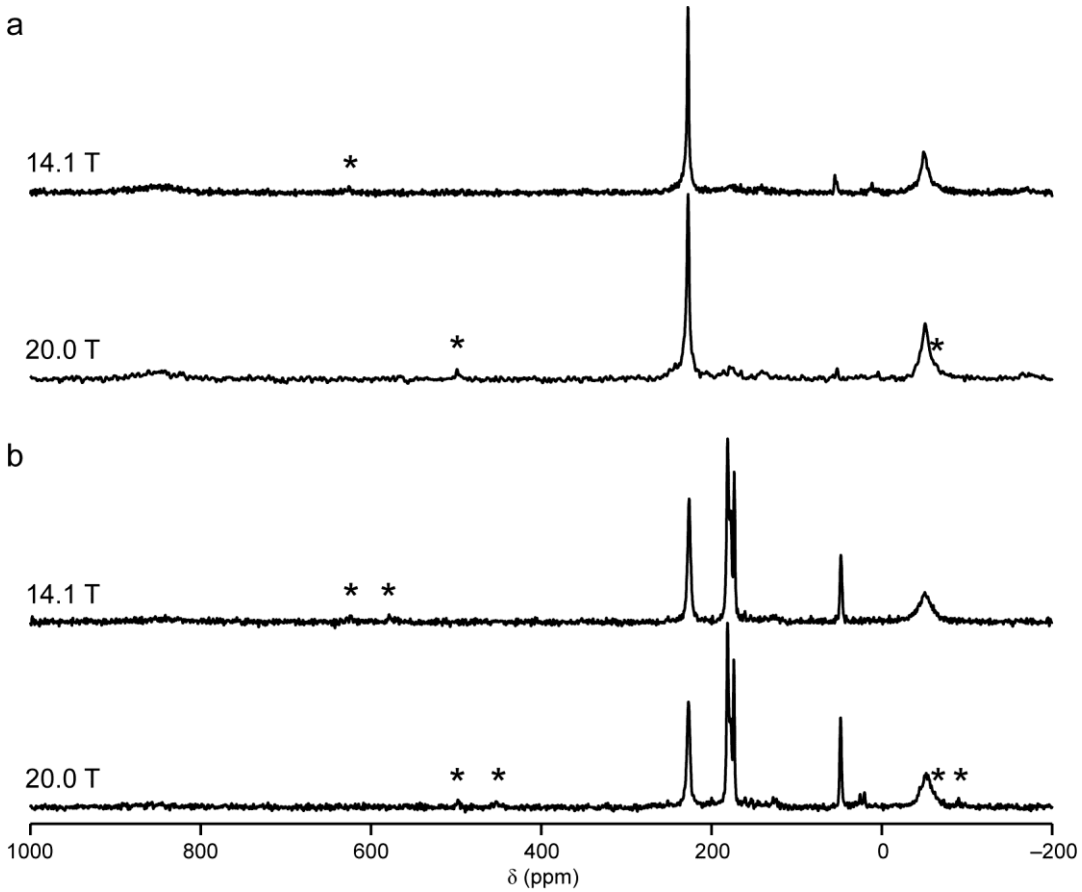

Figure 4.15. ^{13}C NMR spectra of (a) HKUST-1 and (b) STAM-1 recorded at B_0 field strengths of 14.1 T (60 kHz MAS, 327680 transients for each of 2 sub-spectra) and 20.0 T (58 kHz MAS, 65536 transients for each of 5 sub-spectra).

change in the sign of A/ħ between C2 and C1, observed by the sign of the gradient of the plot of δ_{iso} as a function of 1/T, explains the observed ordering of the resonances.

It is still unclear why the sign of A/ħ for C2 is opposite to that of C1 and C3, but an initial hypothesis is that the unpaired electron density occupies a relatively high-energy orbital of the btc, most likely the lowest unoccupied molecular orbital (LUMO). If the LUMO has a node (*i.e.*, a change in the sign) between C2 and C1, this would lead to a corresponding change in sign of A/ħ. Calculations using GAUSSIAN09 were carried out for a molecule of H_3btc in the gas phase, and the frontier orbitals (the highest occupied molecular orbital (HOMO), LUMO, and the two orbitals with next-lowest and next-highest energy, HOMO–1 and LUMO+1) are shown in Figure 4.17. It can be seen that the frontier orbitals appear to possess essentially bilateral symmetry, rather than the expected trilateral symmetry, meaning

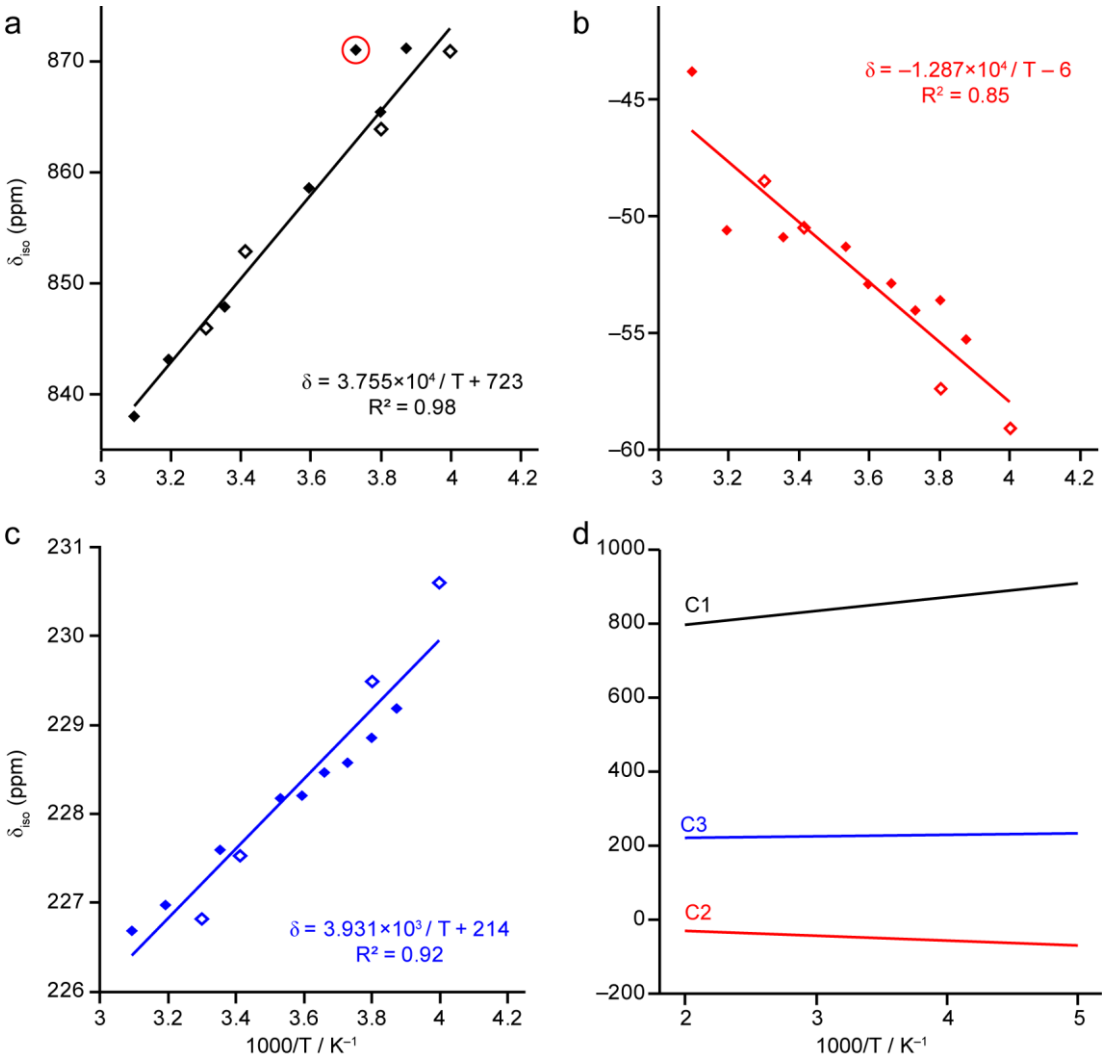

Figure 4.16. Plots of the isotropic positions of the resonances for (a) C1, (b) C2 and (c) C3 in HKUST-1 against 1000/T. Data from the two series of experiments are shown as open (shim temperature controlled) and filled (no shim temperature control) points. Trend lines are plotted for the combined data set. The point highlighted in part (a) was excluded from the calculation of the trend line for C1. (d) A plot of the trend lines for the position of each resonance as a function of 1000/T, over a much greater temperature range (200-500 K) than accessible experimentally.

that the three equivalent C species do not experience equal electron density in each of these orbitals. It is likely that this arises from the fact that the calculations were carried out for a single molecule of H_3btc in the gas phase (calculations for btc^{3-} in the gas phase yielded essentially identical results). These results cannot, of course, be applied directly to the MOF, where the presence of the Cu^{2+} ions and the infinite

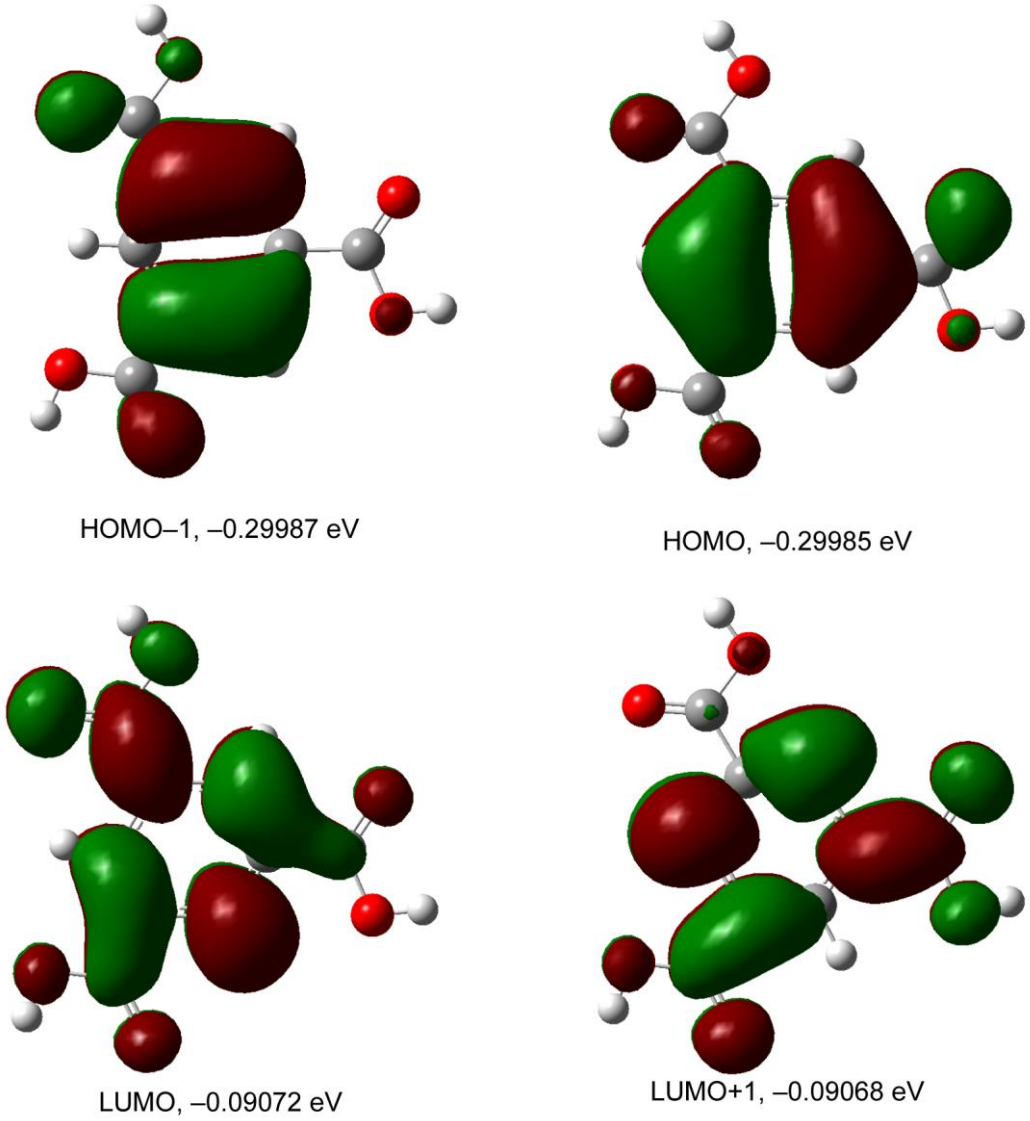

Figure 4.17. The frontier orbitals (HOMO–1, HOMO, LUMO and LUMO+1) of H_3btc in the gas phase, calculated using the B3LYP functional and the 6-311+G(2d,p) CGF basis set. Orbitals are plotted with an isovalue of 0.02, with green and red indicating the different phases.

periodic structure, mean that the electronic structure of the material is likely to be very different to that of a single linker molecule in the gas phase.

Calculations involving more realistic model clusters of HKUST-1, based on the copper benzoate structure with various axial ligands (*e.g.*, dimethylsulfoxide,[49] as shown in Figure 4.18), are currently underway, in collaboration with Professor Michael Bühl (University of St Andrews) and Professor Martin Kaupp (Technische

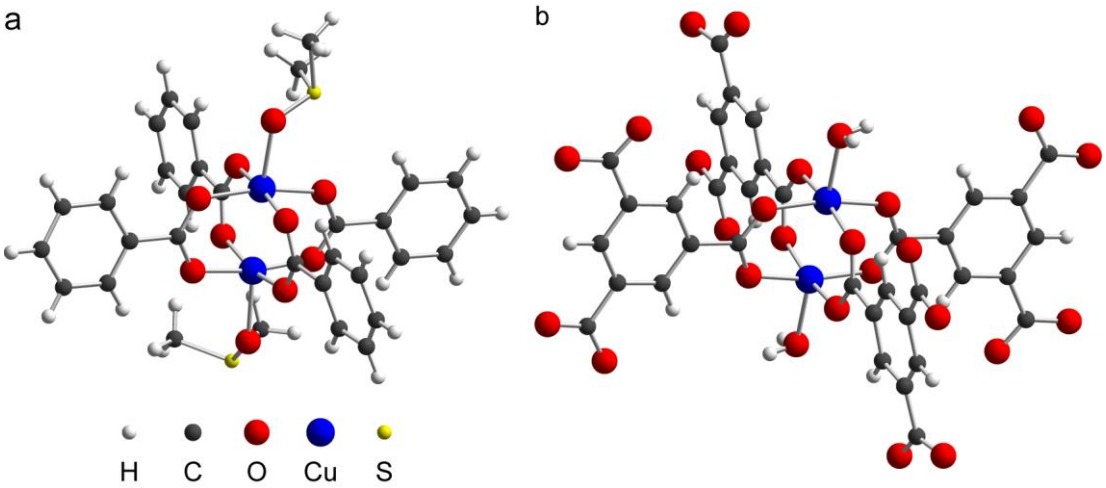

Figure 4.18. Comparison of the structure of (a) the dimethylsulfoxide adduct of copper benzoate[49] and (b) the copper paddlewheel dimer of HKUST-1.

Universität Berlin). Unfortunately, owing to the complexity of the calculation (the open-shell singlet ground state of the copper dimer is challenging to model computationally, and thermal effects must also be included in the calculations), the results of these calculations are not yet available.

The temperature-dependence of the positions of the ^{13}C resonances observed for STAM-1 was also investigated at the UK 850 MHz Solid-State NMR Facility. Spectra were recorded in the same two studies as those for HKUST-1, reported above; one exploring the temperature range between 250.15 and 303.15 K while the shim coils were maintained at a constant temperature, whereas the second series explored the temperature range between 258.15 and 313.15 K, but with no control of the temperature of the shim coils. Data were not recorded for C1, owing to the limited time available at the high-field facility and the difficulty of recording this very broad resonance in a suitably short experimental time. Plots of δ_{iso} against 1/T for all other ^{13}C resonances in STAM-1 are shown in Figure 4.19.

It can be seen that C2 in STAM-1 behaves in a similar manner to C2 in HKUST-1, with $d\delta_{iso}/d(1/T)$ of -1.287×10^7 ppm K^{-1} for HKUST-1 and -1.234×10^7 ppm K^{-1} for STAM-1. On the other hand, C3 of HKUST-1 has a temperature dependence of $d\delta_{iso}/d(1/T) = 3.931 \times 10^6$ ppm K^{-1}, whereas in STAM-1, C3 has a smaller $d\delta_{iso}/d(1/T)$ of 2.346×10^6 ppm K^{-1}, despite their very similar isotropic shifts

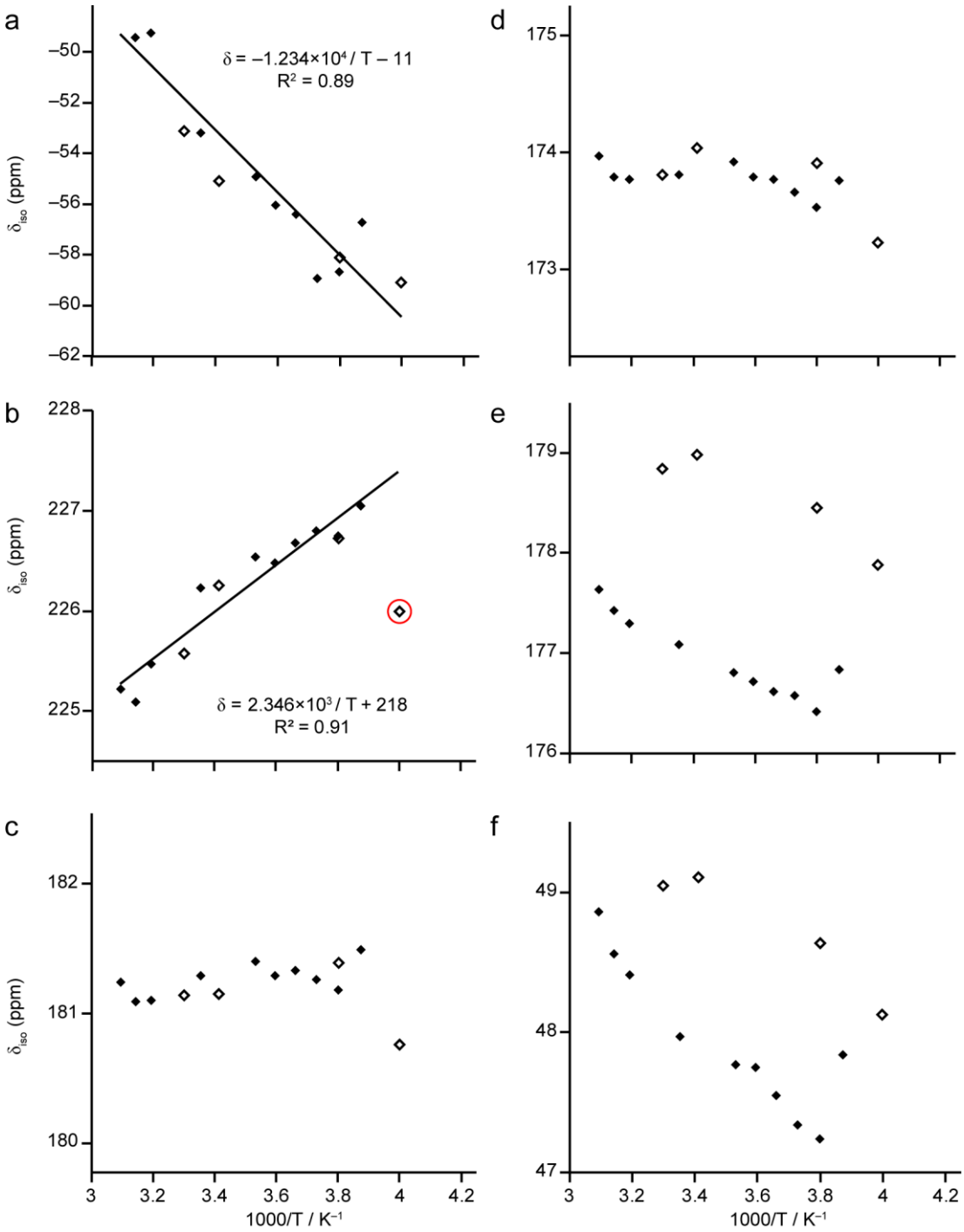

Figure 4.19. Plots of the isotropic positions of the resonances observed for (a) C2, (b) C3, (c) C4, (d) C5, (e) C6 and (f) C7 in STAM-1 against 1000/T. Data from the two series of experiments are shown as open (shim temperature controlled) and filled (no shim temperature control) points. In parts (a) and (b), trend lines are plotted for the combined data sets. The point highlighted in part (b) was excluded from the calculation of the trend line for C3.

in MAS experiments where the temperature is unregulated (*i.e.*, T ≈ 330 K). For the remaining four resonances, C4 and C5 do not appear to display a clear linear dependence on 1/T, most likely owing to relatively small A/ħ (reflected in the relatively small paramagnetic contributions to the isotropic shift), whereas C6 and C7 do appear to display a linear dependence on 1/T, but only for the series of measurements carried out with no shim temperature control. This suggests that the temperature of the shim coils may have an appreciable influence (on the scale of any genuine temperature-dependent shifts present for C4-C7) on the observed isotropic shift position. It is possible that motion of C7 in STAM-1 is more rapid at elevated temperatures, which may contribute to small differences in the positions of some ^{13}C resonances. The different motion of the water molecules within the pores of the two MOFs may also be partially responsible for the different temperature dependence of the ^{13}C resonances in the two MOFs. In order to investigate this possibility, variable-temperature ^{1}H NMR spectra were also recorded for both MOFs, again in the same two visits to the UK 850 MHz Solid-State NMR Facility as for the ^{13}C experiments described above. The ^{1}H MAS NMR spectra of HKUST-1 and STAM-1 recorded at different temperatures (from the second series of experiments, with no control of the temperature of the shim coils) are shown in Figures 4.20(a and b). The position of the resonance assigned to H3 in HKUST-1 displays a linear dependence on 1/T, as shown in Figure 4.20(c). However, the resonance assigned to H_2O displays significantly more complicated behaviour, shifting first from ~6.5 ppm (*i.e.*, the resonance overlaps with that from H3) to 10.5 ppm between –15 and 0 °C, and then shifting to ~5.5 ppm between 0 and 50 °C. This behaviour could relate to a difference in the exchange rate between the Cu-bound H_2O and the free H_2O within the pores, increased deprotonation of H_2O at increasing temperature, or the formation of a hydrogen-bonded network of H_2O at lower temperatures (it should be remembered, though, that the temperatures reported here are not the true sample temperature, which is likely to be ~30-40 °C above the reported temperature). Further investigation of this phenomenon – including variable-temperature T_1 measurements, deuteration of H_2O and molecular dynamics modelling – is required before an explanation can be provided for this observation. It is interesting that no such behaviour is observed in the ^{1}H NMR spectra of STAM-1. However, it is unclear

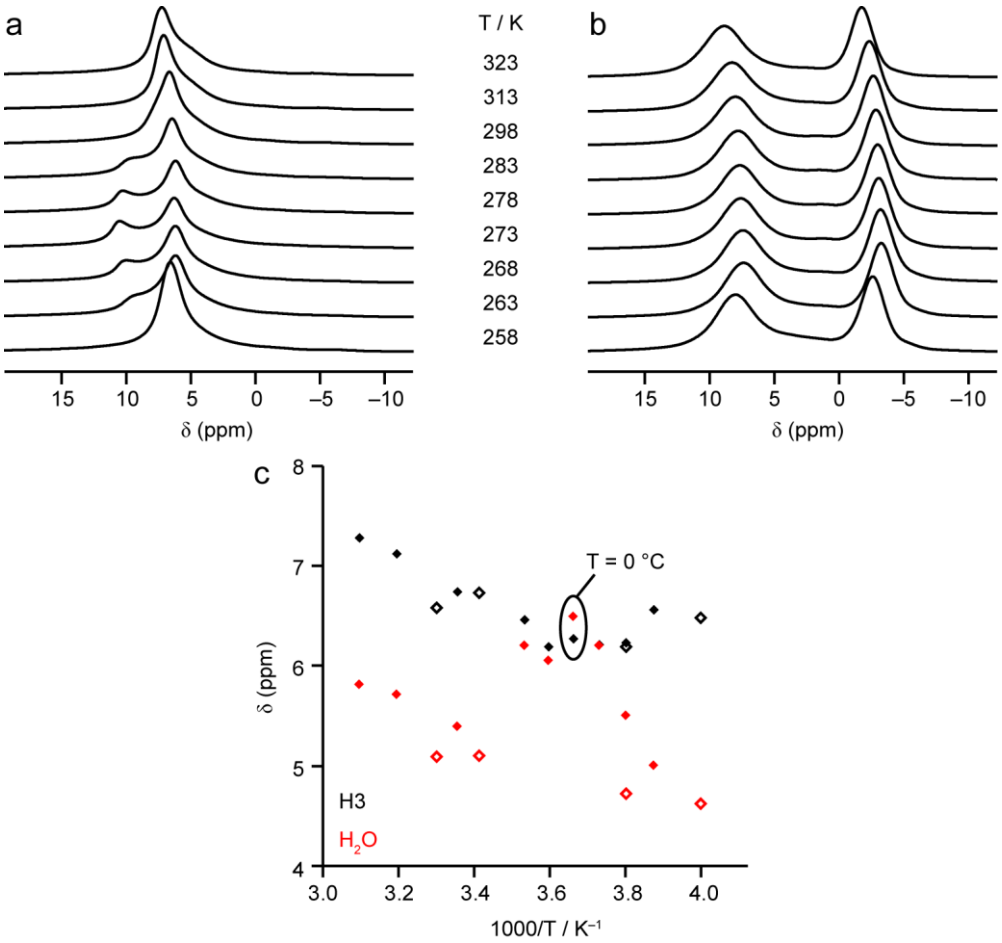

Figure 4.20. ^{1}H (20.0 T, 60 kHz MAS) NMR spectra of (a) HKUST-1 and (b) STAM-1 recorded at the indicated temperature. (c) Plot of the isotropic shifts of H3 in HKUST-1 against 1/T. Data from the two series of experiments are shown as open (shim temperature controlled) and filled (no shim temperature control) points.

whether the sample of STAM-1 used in the study is fully hydrated, as the resonance observed at 4.8 ppm in the spectrum in Figure 4.14 is absent from the spectra at all temperatures, as shown in Figure 4.20(b). These experiments would, therefore, need to be repeated with a second sample to determine whether the resonance at 4.8 ppm truly corresponds to H_2O within the material, or arose from an impurity or contaminant in the original spectrum.

The influence of B_0 field on the isotropic shifts and T_1 relaxation constants was investigated by measuring these values at B_0 = 20.0, 14.1 and 9.4 T. The isotropic shifts were measured from spin-echo spectra and the T_1 relaxation constant was measured by inversion recovery experiments. The MAS rates used were 14 kHz

(9.4 T), 60 kHz (14.1 T) and 58 kHz (20.0 T). Owing to the different MAS rates used, care must be taken in comparing the data directly, as the exact sample temperature is a function of MAS rate and rotor diameter. The data, reported in Table 4.6, appear to indicate a trend for more rapid T_1 relaxation at greater B_0 field strength (especially for C1, C2 and C3). However, the differences in measured values of T_1 are of the same order of magnitude as the errors in these values (and, indeed, the same order of magnitude as the smaller T_1 values). Data with reduced errors (*i.e.*, significantly increased signal to noise ratios) would be required to confirm these observations. At 9.4 T, the rapid relaxation and relatively long rotor-synchronised echo delay (71.4 μs) mean that no signal was observed for C1. Experiments using rapid MAS (currently impossible with the hardware available in house) would be required to make this measurement.

It can be seen from Table 4.6 that δ_{iso} is essentially independent of B_0, which is an important finding as access to national high-field facilities is limited to a few days per year and, being able to determine the positions of resonances using lower-field local facilities prior to visiting a national facility would be of great benefit, as this process would not need to be carried out at high field. Additionally, as the frequency dispersion of resonances is increased at higher B_0 field (*e.g.*, for ^{13}C, 1 ppm = 100.6 Hz at 9.4 T, but 213.8 Hz at 20.0 T), it is actually considerably more challenging to determine the positions of all resonances at higher B_0 fields, as frequency-stepped experiments will require more steps in order to achieve uniform excitation of the same spectral region (in ppm) than at lower field. The T_1 relaxation constant does not change dramatically (*e.g.*, by orders of magnitude) as the B_0 field strength is increased, either, meaning that the experimental parameters (*i.e.*, repeat interval, transmitter offsets and spectral regions of interest) can all be determined at low field and transferred directly to high-field experiments. A sensible strategy for minimising the overall experimental time required, therefore, would be to determine the positions of all resonances at the lowest available B_0 field strength, and then focus on resonances of interest at the higher-field national facilities.

Table 4.6. ^{13}C δ_{iso} and T_1 for HKUST-1 and STAM-1, measured at B_0 field strengths of 9.4, 14.1 and 20.0 T.

Species	δ_{iso} (ppm)			T_1 / ms		
	9.4 T	14.1 T	20.0 T	9.4 T	14.1 T	20.0 T
HKUST-1						
C1	850 (5)	853 (5)	851 (5)	8.0 (10)	4.4 (10)	5.6 (10)
C2	–51 (2)	–50 (1)	–51 (2)	4.2 (10)	3.5 (10)	2.6 (10)
C3	228 (1)	228 (1)	228 (1)	14.3 (10)	10.8 (10)	9.5 (10)
STAM-1						
C1		853 (5)	850 (10)		3.6 (10)	2.7 (10)
C2	–53(1)	–50 (1)	–52 (2)	2.3 (10)	1.4 (10)	1.3 (10)
C3	228 (1)	227 (1)	227 (1)	8.9 (10)	8.5 (10)	5.9 (10)
C4	181 (1)	181 (1)	181 (1)		7.5 (10)	7.7 (10)
C5	174 (1)	174 (1)	174 (1)	15.9 (10)	13.7 (10)	18.3 (10)
C6	178 (1)	178 (1)	178 (1)	17.9 (10)	15.1 (10)	15.2 (10)
C7	49 (1)	49 (1)	49 (1)	22.4 (10)	16.2 (10)	18.4 (10)

4.4.7 The Influence of CTAB on the Synthesis of STAM-1

The initial synthesis of $^{13}C(2,6)$-STAM-1 and $^{13}C(1,3,4,5)$-STAM-1 used labelled H_3btc, prepared by surfactant-assisted oxidation of the labelled alkylbenzenes. While attempts were made to remove the surfactant (CTAB, Scheme 4.6), resonances at 57, 49 and 38-20 ppm in the ^{13}C NMR spectra of $^{13}C(2,6)$-STAM-1 and $^{13}C(1,3,4,5)$-STAM-1 (Figures 4.12(b and d)) indicated that some CTAB remained in the samples. As CTAB is relatively large (compared to the other components of the reaction mixture) and has been used to direct the structures of a range of inorganic materials including mesoporous silicas,[50] metal and oxide nanoparticles[51] and, most pertinently, MOFs,[52] it is plausible that the presence of modest concentrations of CTAB may give rise to differences in the reaction mixture that would favour formation of HKUST-1 (or disfavour formation of STAM-1). In order to investigate this possibility, STAM-1 was synthesised with the addition of 6.25, 12.5, 25, 50, 75

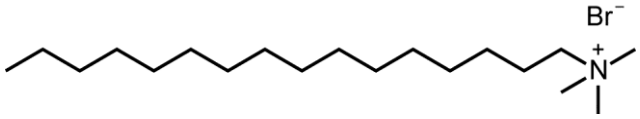

Scheme 4.6. The structure of CTAB.

and 100 mol% CTAB to the reaction mixture prior to mixing and, as can be seen by the powder XRD patterns shown in Figure 4.21(a), the presence of CTAB does, indeed, appear to influence the proportion of HKUST-1 formed. This can be seen more clearly from Figure 4.21(b), where the ratio of the heights of the two diffraction peaks at 5.4° 2θ ((100) peak, STAM-1) and 6.7° 2θ ((200) peak, HKUST-1), $R_{S/H}$, is plotted against the amount of CTAB added to the reaction. It can, therefore, be suggested that the small amounts of surfactant present in the synthesis of the ^{13}C-labelled MOFS is responsible for the presence of HKUST-1 in ^{13}C(2,6)-STAM-1 and ^{13}C(1,3,4,5)-STAM-1. It should be noted that a two-step oxidation process was subsequently developed, shown above in Scheme 4.5, involving the oxidation of 1,3,5-triethylbenzene to 1,3,5-triacetylbenzene with HIO_4/Cr(VI), followed by oxidation to benzene-1,3,5-trimesic acid *via* a haloform (typically chloroform) reaction.[3] This process was developed to avoid the use of the surfactant, but also has the advantage that the H_3btc is obtained with higher yield and purity.

The fact that HKUST-1 and STAM-1 can be formed in the presence of surfactants is itself of interest, as surfactants can, in principle, be used to control the size, morphology, and surface properties of MOF particles, suggesting that the unusual adsorption properties of STAM-1 could be modified and enhanced by a surfactant-assisted synthesis to give a range of materials with similar adsorption behaviour but different physical and chemical behaviour. However, in order to fully exploit this potentially interesting avenue of materials science, modifications to the synthetic process would be required in order to minimise the amount of HKUST-1 formed when CTAB is present in the reaction mixture.

4.4.8 Activation and Rehydration

The ^{13}C NMR spectra of many as-prepared MOFs are complicated by the presence of solvent molecules within the pores of the material. These molecules are rarely located by Bragg diffraction, as they are often disordered, mobile, or part of a mixed

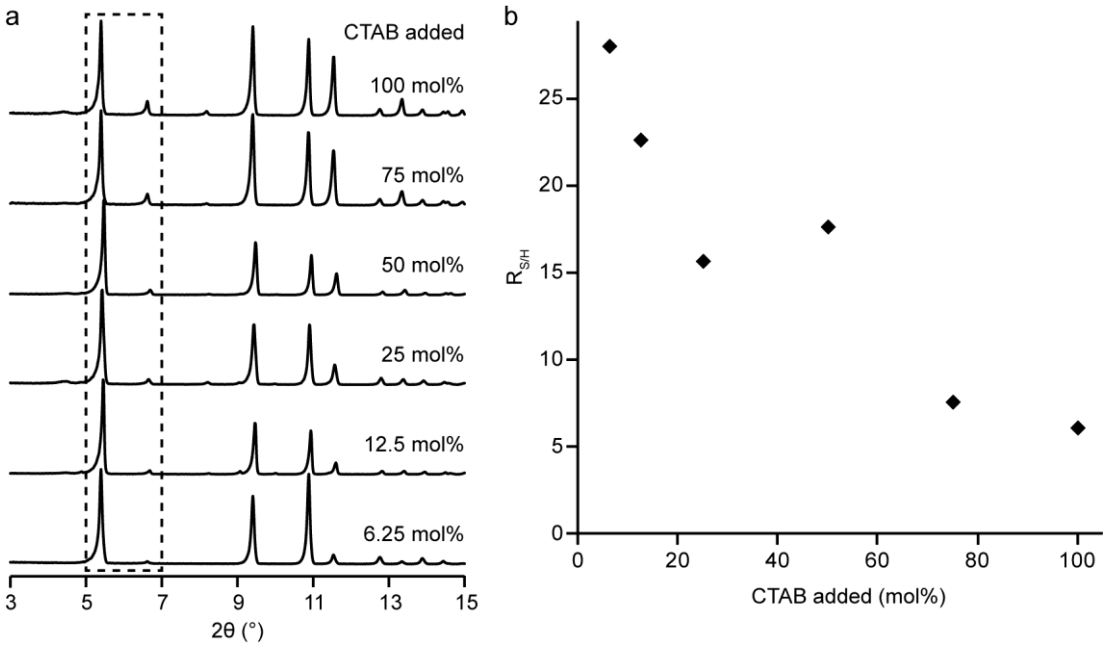

Figure 4.21. (a) Powder XRD patterns of STAM-1 synthesised in the presence of the indicated amount of CTAB. The region containing the (100) peak of STAM-1 and the (200) peak of HKUST-1 is highlighted by the dashed box. (b) Plot of $R_{S/H}$ from the diffraction patterns in (a) against the mol% CTAB present in the reaction media.

solvent system. In the ^{13}C NMR spectrum of HKUST-1 (Figure 4.6), four minor resonances are present at approximately 4.5, 11.2, 52.7 and 54.6 ppm. These shifts are similar to those of ethanol in the solution phase, indicating their origin is perhaps some residual molecules of ethanol from the synthesis solvent. However, another possibility would be a low level of esterification (*i.e.*, ethylation analogous to the methylation in STAM-1). Evacuation of HKUST-1 was carried out, resulting in the removal of all guest molecules (including residual ethanol). For comparison, a sample of STAM-1 was also evacuated in the same manner. The ^{13}C MAS NMR spectra of these evacuated forms of the MOFs (denoted dehydrated (deh-)) are shown in Figure 4.22, along with spectra for samples that were subsequently rehydrated by exposure to atmospheric moisture (denoted -[H_2O], where the brackets indicate the guest species within the pores of the MOF). No "ethyl" resonances were present for either deh-HKUST-1 or HKUST-1[H_2O], indicating that there are no ethyl esters present. However, it is interesting that two sets of resonances arising from ethanol (*i.e.*, two distinct types of ethanol) are observed for the as-prepared material, given that previous work by Gul-E-Noor *et al.*[23] demonstrated the existence of a rapid

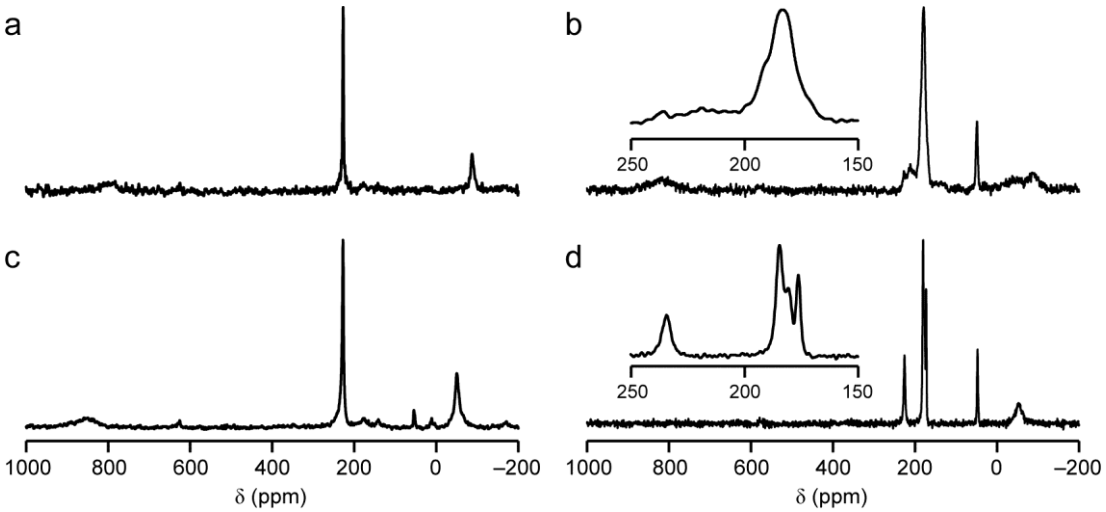

Figure 4.22. ^{13}C (14.1 T, 60 kHz MAS) NMR spectra of (a) deh-HKUST-1, (b) deh-STAM-1, (c) HKUST-1[H_2O] and (d) STAM-1[H_2O].

exchange between H_2O bound to Cu and bulk H_2O in the pores of HKUST-1[H_2O], leading to only one ^1H resonance being observed in the NMR spectrum. It is possible that the adsorption/desorption kinetics of ethanol may be slower, owing to its larger mass and bulk, or it may simply have a greater affinity for the Cu site.

In addition to the changes to the ethyl resonances, significant changes to the resonances arising from the linkers of both MOFs are observed upon activation. For HKUST-1, C3 has the same shift (228 ppm), whereas the C1 and C2 resonances both appear at significantly lower shifts (795 and –87 ppm, respectively). The shift of C2 is in agreement with that observed by Peterson *et al.*[24] and Gul-E-Noor *et al.*[23] Unlike HKUST-1, for which the structure of the dehydrated material is very similar to that of the hydrated material,[21] the structure of STAM-1 changes significantly upon dehydration, with the apparent partial collapse of the hydrophobic pores.[5, 29] This structural change is reflected in the differences observed in the ^{13}C NMR spectra between the dehydrated material (Figure 4.22(b)) and the rehydrated material (Figure 4.22(d)). It can be seen that the resonances corresponding to the C species closest to the hydrophobic pore (C4, C5, C6 and C7) are significantly broadened and overlap to contribute to a single, broad region of spectral intensity between 160 and 200 ppm, which cannot reliably be decomposed into Gaussian/Lorentzian functions in order to obtain isotropic shifts. Collapse of the hydrophobic pore leads to a decrease in the symmetry of the structure of deh-STAM-1,[29] evidence for which is

observed in the fact that the C3 resonance is split into two resonances at 212 and 227 ppm. The C2 resonance is also split into two resonances, at –45 and –90 ppm, and the C1 resonance has an asymmetric shape, which can be decomposed into two overlapping Lorentzian lineshapes with isotropic shifts of 854 and 817 ppm. Such an increase in the number of magnetically-distinct C species could be explained by an increase in the number of crystallographically-distinct species, which would require a lowering of the symmetry of the structure. However, as the resonances at 854, 227 and –45 ppm are very similar to those observed for as-prepared STAM-1, it is possible that some portion of the sample is hydrated, either owing to incomplete evacuation or to exposure to atmospheric moisture during packing into the rotor.

As the resonances in the ^{13}C NMR spectrum of deh-HKUST-1 are well defined and separated, it was possible to measure their T_1 relaxation constants and Δ^*. In addition, these parameters could reliably be obtained for C7 of deh-STAM-1. These values are given in Table 4.7, and it can be seen that, while the values have all changed between the as-prepared and activated MOFs, they are all approximately the same order of magnitude, regardless of whether there are guest species within the framework. This suggests that the experimental conditions required to observe the framework resonances will be similar for all guest-loaded (and activated) samples of HKUST-1 and STAM-1. The exception to this observation is C7 in deh-STAM-1, which behaves essentially like a diamagnetic CH_3 species (*cf.* T_1 of ~120 ms for (diamagnetic) L-alanine). Upon rehydration of the MOFs, the observed ^{13}C NMR spectra are essentially identical to those for the as-prepared MOFs. This confirms that the structural changes occurring on dehydration of STAM-1 are fully reversible.

4.4.9 Guest Loading

The observation of large differences in the isotropic positions of the ^{13}C resonances of hydrated and dehydrated MOFs indicates that the spin and electron density distribution of the MOF change significantly with changes in the coordination environment of the Cu^{2+} ions. This observation suggests that ^{13}C NMR spectra should be capable of detecting differences in the electronic structure of the MOFs arising from the binding of different guest species to the Cu^{2+} centres. As the ^{13}C NMR spectrum of HKUST-1 is the least crowded by resonances arising from the

Table 4.7. Isotropic shifts, δ_{iso} and, where measured, the longitudinal relaxation constants, T_1 and linewidths, Δ^*, of the ^{13}C resonances observed for deh-HKUST-1 and deh-STAM-1, recorded at 14.1 T, unless otherwise indicated.

Species	δ_{iso} (ppm)	T_1 / ms	Δ^* / kHz
deh-HKUST-1			
C1	795 (5)	3.9 (10)[a]	14.3 (2)
C2	–87 (1)	8.6 (10)[a]	2.3 (1)
C3	228 (1)	8.8 (10)[a]	0.33 (2)
deh-STAM-1			
C1[b]	815 (10), 845 (10)		7.5 (5), 4.2 (5)
C2[b]	–45 (5), –90 (2)		7.2 (10), 5.4 (5)
C3[b]	212 (2), 227 (2)		2.6 (5), 1.2 (2)
C4, C5, C6[c]	160-200		
C7	50 (1)	68.7 (10)	0.8 (5)

a. Experiments carried out with B_0 = 20.0 T.

b. Two resonances assigned to this C species are observed in the ^{13}C NMR spectrum of deh-STAM-1.

c. Reliable information on the resonances arising from these C species could not be obtained, owing to extensive overlap.

MOF, and the pores are larger than those of STAM-1, allowing adsorption of larger guests, the following discussion will focus exclusively on HKUST-1 loaded with different guest species. Samples of HKUST-1 were loaded with methanol (MeOH), ethanol (EtOH), nitric oxide (NO) and metronidazole (metro, Scheme 4.7). In addition, a sample of HKUST-1[metro] was loaded with NO, giving HKUST-1[metro+NO] and some of this material was exposed to ambient moisture to give HKUST-1[metro+H_2O], where the H_2O has displaced the NO.

Figure 4.23 shows ^{13}C NMR spectra of HKUST-1[H_2O], HKUST-1[MeOH] and HKUST-1[EtOH]. The isotropic shift of C3 of the MOF is essentially unchanged in all three samples (as might be expected, since this resonance was not sensitive to evacuation). However, the position of the C2 resonance exhibits small changes,

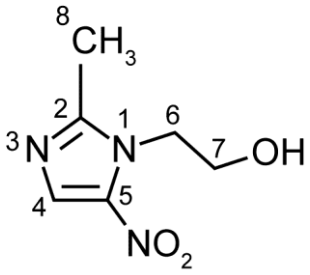

Scheme 4.7. The structure and numbering scheme for metronidazole (metro).

occurring at –50 ppm in HKUST-1[H_2O], –48 ppm in HKUST-1[MeOH] and –44 ppm in HKUST-1[EtOH]. It is challenging to phase spectra with sufficient accuracy to determine whether there are small isotropic shift differences for C1 when different guest species are present. However, the spectra shown in Figure 4.23 demonstrate two important points. First, the C2 resonance (which can be observed readily) is suitably sensitive to the nature of the Cu-bound guest species to act as a probe of

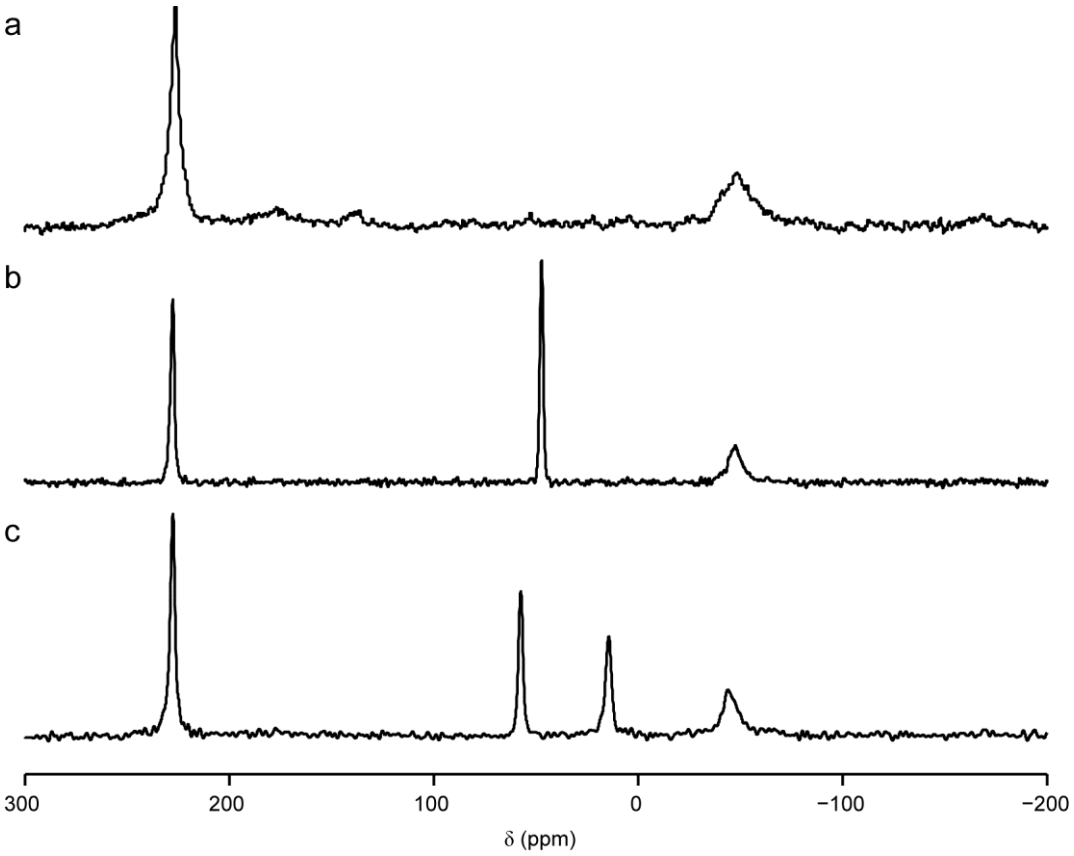

Figure 4.23. ^{13}C (14.1 T, 60 kHz MAS) NMR spectra of (a) HKUST-1[H_2O], (b) HKUST-1[MeOH] and (c) HKUST-1[EtOH].

guest binding and, secondly, the ^{13}C resonances arising from the guest species appear to be close to those of the pure guest species, so that a large spectral window is not required. In order to confirm that no resonances related to the guest species appeared outside the shown shift range, the range between 5000 and –5000 ppm was surveyed for HKUST-1[MeOH], but no sample-related resonances other than those shown in Figure 4.23 were observed under the conditions used here. Subsequently, only the spectral window between 300 and –200 ppm was studied for the guest-loaded samples, thereby reducing the total experimental time required. It should be noted that, in the ^{13}C NMR spectrum of HKUST-1[EtOH] (Figure 4.23(c)), there are only two resonances arising from the ethanol, at 14.6 and 57.6 ppm, rather than the four resonances discussed above. It would appear that, at higher ethanol concentrations, the ethanol within the pores may be in dynamic equilibrium with the ethanol bound to Cu, giving rise to a single weighted average isotropic shift rather than the two observed at lower ethanol concentrations (and higher water concentrations). The methanol within HKUST-1[MeOH] gives rise to a single ^{13}C resonance, at 47.3 ppm (Figure 4.23(b)), indicating that, like ethanol and water, the Cu-bound methanol is likely to be in rapid exchange with free methanol in the pores of the MOF. However, in order to prove these suggestions, variable-temperature and controlled loading experiments, analogous to those of Gul-E-Noor *et al*.[23] would be required.

Currently, there is much interest in the medical applications of MOFs, which include inherent antibacterial activity, drug storage and delivery, and MRI contrast enhancement.[25, 26, 53, 54] Of interest here is the storage of the antibacterial species, NO and metro in HKUST-1. NO has many biological functions, including vasodilation and neurotransmission, but is toxic at high concentrations, meaning that its controlled storage and release is of great benefit to medical applications.[54] NO was also of interest in the present work, as it exists as a radical with a doublet ground state, so its effects on the solid-state ^{13}C NMR spectrum of the NO-loaded MOF would be expected to be more pronounced than those of the diamagnetic guest species.

Figure 4.24(a) shows part of the ^{13}C NMR spectrum of HKUST-1[NO], which contains resonances at 795 (not shown), 228 and –87 ppm. These resonances are very similar to those of deh-HKUST-1, perhaps suggesting that there is no NO

present. However, as shown in Figure 4.24(b), NO release measurements carried out on the sample immediately after the NMR experiment confirmed the release of appreciable amounts of NO, indicating its presence during the NMR experiment. A second sample of HKUST-1[NO] was packed into a 4 mm MAS rotor (to maximise the sample mass present) and its ^{13}C NMR spectrum was recorded (shown in Figure 4.24(d)). The cap was then removed from the rotor, which was placed in a humid environment for a week to allow for complete release of NO and rehydration of the MOF. Over the course of the hydration, the sample was observed to change colour from the deep indigo of the evacuated/NO-loaded MOF to the bright blue of the hydrated MOF. The ^{13}C NMR spectrum of this rehydrated sample was recorded, and is shown in Figure 4.24(e). Despite being recorded with experimental conditions that were as close to identical as possible, the spectrum shown in Figure 4.24(e) contains approximately 30% more integrated spectral intensity than that of Figure 4.24(d), indicating that an appreciable proportion of the ^{13}C signal from the NO-loaded MOF is not present in the region between –300 and 1300 ppm. Therefore, the spectral region between 4000 and –3000 ppm was surveyed (with 60 kHz MAS) for any additional resonances, but no resonances, other than those already discussed, were observed under the conditions used. This indicates that the NO radical renders the framework species in its vicinity "invisible" to NMR, owing either to very extreme isotropic shifts, or to very rapid relaxation. A sample of STAM-1[NO] was also prepared, and its ^{13}C NMR spectrum (Figure 4.24(f)) is also essentially identical to that of the evacuated MOF. As such, solid-state NMR spectra cannot be used to determine directly the presence of paramagnetic NO within HKUST-1 or STAM-1.

Metronidazole (metro) is another antibiotic, used particularly against *Clostridium difficile*.[55] Metro has three functional groups that may interact with Cu^{2+}: a terminal alcohol, a nitro functionality, and N3 of the imidazole (N1 is too sterically hindered to interact significantly with Cu^{2+}). However, it is unclear which, if any, of these functional groups bind to Cu in HKUST-1. Figure 4.25 shows ^{13}C NMR spectra of HKUST-1[metro], HKUST-1[metro+NO] and HKUST-1[metro+H_2O]. For HKUST-1[metro], in addition to the three resonances from the MOF (856 ppm (C1, not shown), –45 ppm (C2) and 227 ppm (C3)), six resonances are observed for the six C species in metro, and an intense resonance at 47 ppm, which can be

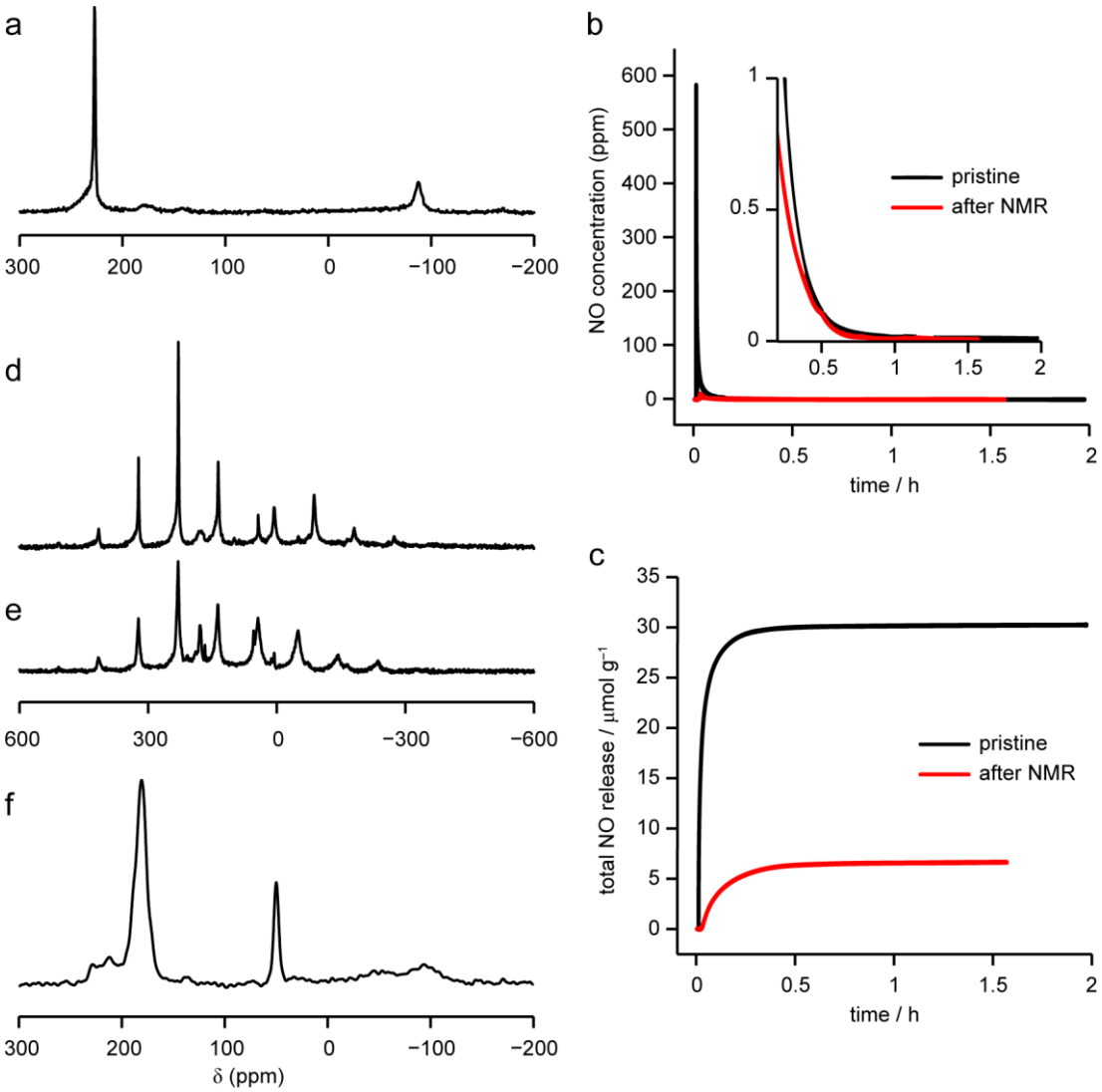

Figure 4.24. (a) ^{13}C (14.1 T, 60 kHz MAS) NMR spectrum of HKUST-1[NO]. (b) Instantaneous and (c) cumulative NO release from a pristine sample of HKUST-1[NO] and another sample after used for a ^{13}C NMR experiment. ^{13}C (14.1 T, 14 kHz MAS) NMR spectra of HKUST-1[NO] (d) before and (e) after exposure to moist air for a week. The spectra in parts (d and e) are plotted on the same vertical intensity scale. (f) ^{13}C (14.1 T, 60 kHz MAS) NMR spectrum of STAM-1[NO].

attributed to MeOH (*cf.* HKUST-1[MeOH]); a consequence of the loading procedure, in which the MOF is stirred in a methanolic solution of metro. The resonances observed for metro are broad and overlapping, preventing the measurement of accurate isotropic shifts. However, approximate isotropic shifts were obtained by decomposition of the spectrum using DMFit,[56] and are reported in Table 4.8. The solid-state ^{13}C NMR spectrum of pure metronidazole (Figure 4.25(d)) was

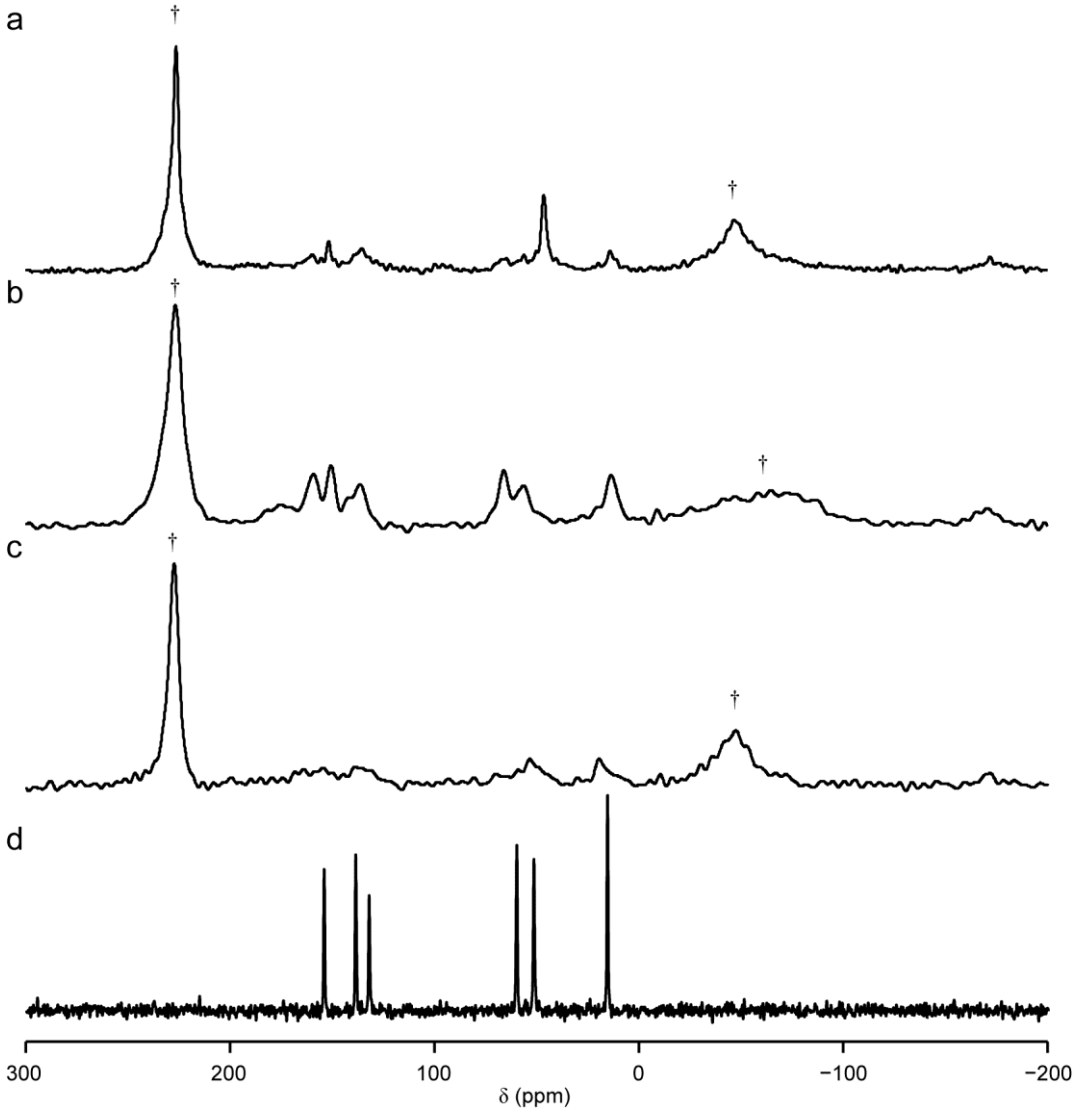

Figure 4.25. ^{13}C (14.1 T, 60 kHz MAS) NMR spectra of (a) HKUST-1[metro], (b) HKUST-1[metro+NO] and (c) HKUST-1[metro+H_2O]. (d) ^{13}C (14.1 T, 12.5 kHz CP MAS) NMR spectrum of solid metro. In parts (a-c), † denotes resonances arising from the MOF.

recorded and assigned by calculation of the NMR parameters for the structure of Blaton *et al.*[57] (after optimisation of the structure, including the G06 SEDC) using CASTEP 6. As a first approximation, it can be assumed that the order of the isotropic shifts of metro does not change between pure metro and HKUST-1[metro], suggesting the assignment given in Table 4.8. However, it should be stressed that the tentative assignment given here requires confirmation by more advanced assignment methods (*e.g.*, ^{13}C labelling and ^{1}H-^{13}C CP NMR experiments).

Table 4.8. The experimental ^{13}C δ_{iso} of pure metro (Scheme 4.7) and metro within various samples of HKUST-1. Calculated values for metro are also given.

Species	δ_{iso} (ppm)[a]				
	calculated	metro	HKUST-1 [metro]	HKUST-1 [metro+NO]	HKUST-1 [metro+H_2O]
C2	157.5	153.8(1)	161(5)	160(1)	166(2)
C4	137.7	131.8(1)	136(5)	137(1)	137(5)
C5	142.3	138.4(1)	152(1)	150(1)	155(2)
C6	50.6	51.3(1)	57(2)	56(1)	53(5)
C7	70.5	59.7(1)	67(2)	66(1)	68(2)
C8	14.4	15.4(1)	14(1)	14(1)	18(1)

a. It is assumed that the order of the resonances from metro remains the same in all four samples.

The large shift differences for the metro resonances suggest that the metro molecules are present within the pores of the MOF, rather than in crystals of bulk metro mixed with HKUST-1[MeOH]. This suggestion is confirmed by the fact that the short (50 ms) repeat interval used to record the spectrum would rapidly saturate any species with long T_1 relaxation times, such as would be expected for diamagnetic solid metro. Therefore, the observation of these resonances after the 782336 transients recorded for the spectrum indicates that the metro truly is within the MOF. The shift of C2 of HKUST-1 (–45 ppm) indicates that the most likely Cu-bound species is MeOH, although it is also possible that binding of the alcohol species of metro would yield a similar shift for C2. However, as the metro was presented to HKUST-1 as a methanolic solution, it is unsurprising that the smaller MeOH would enter the pores of the MOF first, with the bulkier metro entering more slowly. In a recent study, McKinlay *et al*. located metro within the pores of the MOF, CPO-27, using Bragg diffraction methods, and determined that metro was not bound to the CUSs on the metal sites present when the smaller and more polar H_2O was present, but also when the (essentially non-polar)[58] NO was present,[25] suggesting that metro may be a poor ligand for binding to CUSs in MOFs.

The MeOH can be removed from HKUST-1[metro] by gentle heating under vacuum (taking care not to remove the metro). Subsequent exposure of the MOF to NO yields HKUST-1[metro+NO]. The ^{13}C NMR spectrum of HKUST-1[metro+NO], shown in Figure 4.25(b), contains six resonances assigned to metro, as summarised in Table 4.8. The resonance arising from MeOH is absent, confirming its removal during the heating stage. The C2 resonance is broadened to between –10 and –100 ppm. As discussed above, isotropic shifts for C2 of HKUST-1 are typically around –40 to –50 ppm when simple alcohols and H_2O are bound to the Cu, and –87 ppm when the CUS is vacant. Therefore, it appears that HKUST-1[metro+NO] contains both vacant and occupied CUSs. While it is known from the work of McKinlay *et al*. that NO binds to the CUSs of MOFs,[25, 54] it was demonstrated above that regions of the MOF around the NO radical are most likely invisible to NMR, suggesting that the observed shifts for C2 arise from regions of the MOF containing either vacant CUSs, or CUSs occupied by a species other than NO. Therefore, it seems likely that metro can also bind to the Cu in the absence of other guests but some of the CUSs remain unoccupied. The origin of the unoccupied CUSs is likely to be either partial loss of metro as well as methanol upon heating HKUST-1[metro], or a result of the steric bulk of metro preventing eight molecules of metro from occupying each pore. Another possible explanation for the observation of C2 shifts around –50 ppm is that some methanol remains in HKUST-1[metro+NO], but is invisible to NMR. While this seems unlikely (Gul-E-Noor *et al*. observed the ^{1}H resonance of Cu-bound H_2O was not dramatically shifted from its diamagnetic position,[23] indicating that spin transfer to the axial ligand is not large), the prospect of "invisible" methanol cannot immediately be ruled out. Experiments such as combined thermogravimetric analysis and mass spectrometry (TGA-MS) would be able to investigate this possibility.

Exposure of HKUST-1[metro+NO] to air results in rapid release of the NO, which is displaced by H_2O, giving rise to HKUST-1[metro+H_2O]. The ^{13}C NMR spectrum for this material is shown in Figure 4.25(c) and, again, approximately six broad, overlapped resonances can be identified, arising from metro within the pores of the MOF. The approximate isotropic shifts of these resonances are given in Table 4.8. Hydration of the material results in a narrowing of the C2 resonance, with its isotropic shift (–46 ppm) indicating H_2O is bound to the Cu centres. It should be

noted that, in the spectra for both HKUST-1[metro] and HKUST-1[metro+H_2O] the resonances arising from metro are relatively broad (on the order of 1-2.5 kHz) whereas, in the case of HKUST-1[metro+NO], the resonances arising from metro are on the order of 0.5-1.5 kHz. This observation indicates a greater degree of disorder (either motional or static) in the two MOFs in which either MeOH or H_2O is bound to the Cu and the metro is believed to occupy the pore volume, whereas the metro is more ordered in the NO-containing system. This again suggests that, in the case of HKUST-1[metro+NO], it is the metro itself that is bound to the Cu centres

While there are many unanswered questions remaining in this study of guest species within the pores of paramagnetic MOFs, it can clearly be seen that solid-state ^{13}C NMR spectra of such materials have the potential to provide much relevant information. At its most basic, this information may be whether the guest species is within the pores of the MOF (experiencing paramagnetic relaxation) or simply present as a physical mixture with the MOF. However, it would appear that the technique has the potential to determine which guest species are bound to the CUSs of MOFs (and, hence, which guest species would be expected to be released or replaced by another guest species first) in complicated multiple-guest systems. This latter point suggests that the present study could be extended to study, *e.g.*, the catalysis of chemical reactions within paramagnetic MOFs – dynamic processes that cannot be probed well by Bragg diffraction techniques.

4.4.10 Further Isotopic Labelling Schemes for H_3btc and mmbtc

The isotopic ^{13}C labelling schemes discussed above have, in common with most isotopic enrichment procedures, the disadvantage of being relatively costly, with an estimated cost of £123 per gram of benzene-1[^{13}C],3,5-tricarboxylic acid, and £121 per gram of [U-^{13}C]benzene-1,3,5-tricarboxylic acid (at 33% and 13%, enrichment of the indicated sites, respectively). However, while this initial outlay is considerably more than for the natural-abundance linker (£0.37 per gram, Sigma-Aldrich), the labelling scheme need not be excessively expensive overall, as it was demonstrated by Mohideen[29] that mmbtc can be recovered in almost quantitative yield by careful alkaline hydrolysis of STAM-1. The solution-phase ^1H NMR spectrum of the organic material produced by alkaline hydrolysis of a sample of STAM-1 is shown in Figure

4.26, and it can be seen that the material is essentially pure mmbtc. The same approach was applied to ^{13}C(2,6)-STAM-1 and ^{13}C(1,3,4,5)-STAM-1, and the resulting organic matter analysed by solution-phase ^{1}H and ^{13}C NMR spectroscopy.[46] It can be seen from the spectra shown in Figure 4.26 that a mixture of labelled H_3btc and labelled H_2mmbtc was recovered in both cases but, as both MOFs were demonstrated to contain ^{13}C-labelled HKUST-1, it is unsurprising that the linker from this material was also recovered. The ability to recover the labelled linkers in high yield means that, in principle, they may be recycled several times, and only a small amount of labelled material may be required in order to prepare many ^{13}C-enriched MOFs.

In addition to reducing the cost of the synthesis of labelled MOFs, recovery of mmbtc with selective ^{13}C labels opens up the possibility for selectively-enriched dendritic polymers (dendrimers).[59] As the core of the dendrimers (which would be formed from ^{13}C-enriched mmbtc) makes up only a small proportion of the total C-containing mass of the material, ^{13}C enrichment would not be able to drastically improve the sensitivity of ^{13}C NMR experiments. However, many dendrimers are proposed for biological and medical applications and it is possible that the isotopic labelling schemes could be extended to include ^{14}C – a positron emitter suitable for use in positron emission tomography (PET) experiments. Furthermore, Mohideen synthesised several new MOF structures using recovered mmbtc,[29] some of which may benefit from further characterisation by solid-state ^{13}C NMR.

Another candidate for isotopic enrichment is deuterium (^{2}H or D), which provides essentially the same isotropic shift information as ^{1}H (with the inclusion of a small, typically negligible, isotropic quadrupolar shift). ^{2}H NMR spectra are typically of higher resolution than ^{1}H NMR spectra, when even moderate MAS rates are used, owing to the lower gyromagnetic ratio of, and subsequently reduced dipolar coupling to, ^{2}H. In addition, ^{2}H NMR spectra can also provide information on the EFG at the H location. Such information has been used by Mowat *et al*. to observe the reorientation of the deuterated bdc linkers in a scandium terephthalate MOF,[60] indicating that ^{2}H NMR spectroscopy should be able to provide additional information on the behaviour of guest species within the pores of MOFs. In addition,

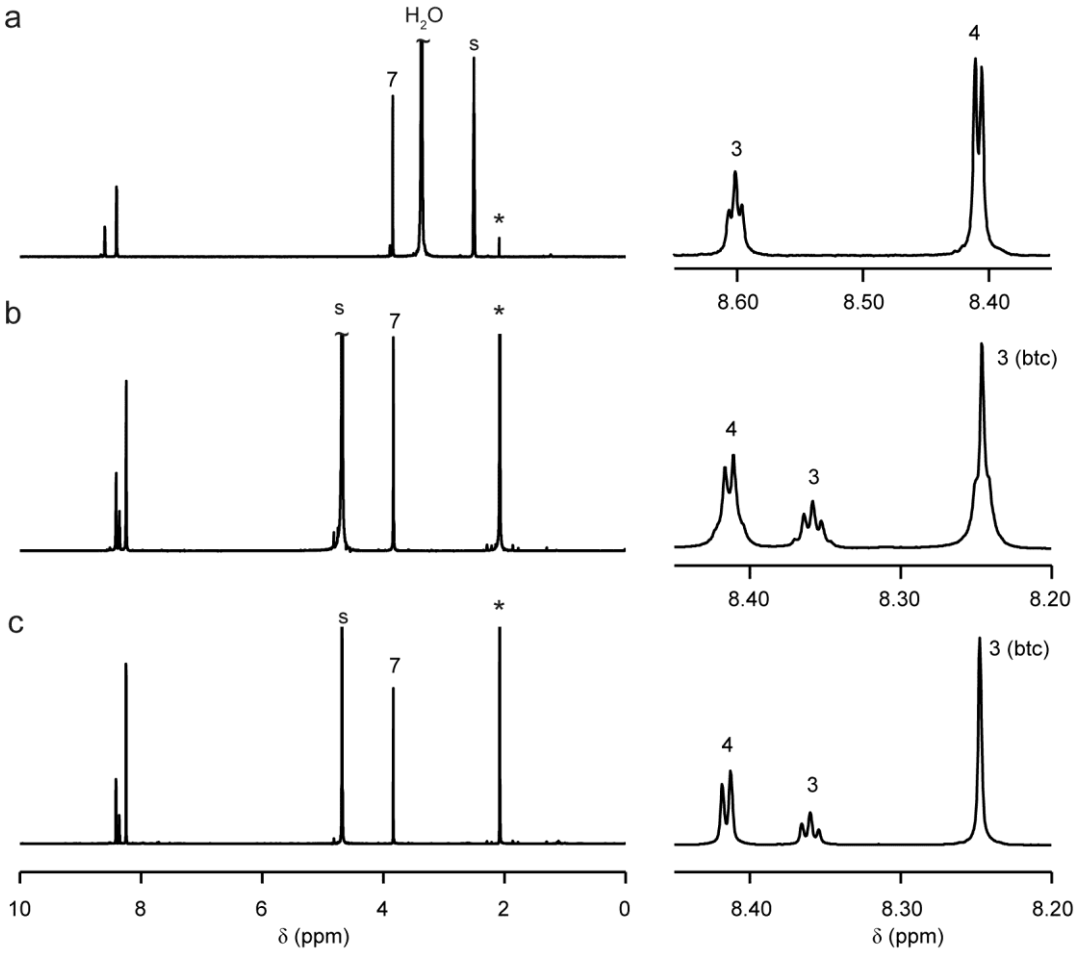

Figure 4.26. Solution-phase ^{1}H (7.05 T) NMR spectra of the organic material recovered by alkaline hydrolysis of (a) STAM-1, (b) ^{13}C(2,6)-STAM-1 and (c) ^{13}C(1,3,4,5)-STAM-1. The solvent, marked s in each spectrum, was (a) $(CD_3)_2SO$ or (b and c) D_2O. Asterisks denote resonances arising from trace acetone. Further spectral analysis is provided in Appendix I.

as γ of ^{2}H is a factor of ~6.5 less than that of ^{1}H, ^{2}H MAS NMR spectra (with MAS rates of ~10 kHz) are typically of much higher resolution than the corresponding ^{1}H spectra (with MAS rates of ~60 kHz), owing to the greatly reduced homonuclear dipolar interactions. The NMR spectrum of the residual ^{1}H in a (heavily) deuterated material is also of high resolution, as any remaining ^{1}H are surrounded by a network of ^{2}H rather than ^{1}H, and are not subject to homonuclear dipolar interactions with an infinite spin network. Deuteration can allow the crystallographic locations of H atoms to be determined by neutron diffraction experiments – potentially of great advantage in determining the structure of new MOFs.

Deuteration of the aromatic H can be achieved with the same reaction scheme used to prepare [U-^{13}C]benzene-1,3,5-tricarboxylic acid (Scheme 4.4), but starting with C_6D_6 rather than $^{13}C_6H_6$.[3] However, it was observed that, when starting from 99%-enriched C_6D_6, the overall enrichment level in the resulting 2,4,6[$^2H_3$]-benzene-1,3-5-tricarboxylic acid was only ~70 atom%. The level of ^{2}H labelling was determined from the integrated intensity ratios of the CH_3 and CH resonances in the solution-phase ^{1}H NMR spectra of the 1,3,5-triethyl-2,4,6[$^2H_3$]-benzene intermediate, shown in Figure 4.27. The reason for this loss of deuteration is that, during the quenching stage of the Friedel-Crafts reaction, the $AlCl_3$ remaining in the reaction mixture forms an adduct with H_2O, H[$AlCl_3OH$], which is a powerful acid and can introduce H atoms to the benzene ring according to Scheme 4.8.[61] To overcome such loss of labelling, the quench was performed using 98% D_2O ice instead of H_2O ice, resulting in >90% enrichment of ^{2}H in the final product.[3]

While quenching the reaction with D_2O slightly increases the cost of the procedure, it also suggests a more cost-effective route to partial labelling, as D[$AlCl_3OD$] could be prepared relatively easily, and mixed with natural-abundance 1,3,5-triethylbenzene. This would result in partial deuteration of the aromatic protons, to a level that would be suitable for solid-state NMR experiments, but probably not to the higher level required for neutron diffraction experiments. As D_2O is much cheaper than C_6D_6, such a labelling method would offer clear cost benefits. A preliminary attempt to model this procedure by mixing 1,3,5-triethylbenzene, $AlCl_3$ and D_2O ice was unsuccessful, although this approach did not truly mimic the species present at the end of the alkylation reaction, where significant quantities of $AlCl_{(3-x)}Br_x$ will be present. Further work is required to determine whether the process can give partial deuteration in a real reaction mixture, rather than a model.

A sample of ^{2}H(3)-HKUST-1 was prepared with 2,4,6[$^2H_3$]-benzene-1,3,5-tricarboxylic acid as the linker. An attempt to make ^{2}H(3,4)-STAM-1 by the same approach led to predominantly ^{2}H(3)-HKUST-1 containing ~25% ^{2}H(3,4)-STAM-1 (determined by ^{13}C MAS NMR), and that sample will not be discussed further (a repeat synthesis is planned for the future). The ^{2}H(3)-HKUST-1 was split into two portions, one which was retained as the as-prepared sample while the other was

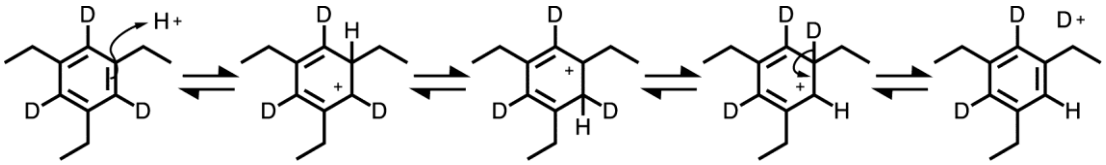

Scheme 4.8. Mechanism of H/D exchange during the quench of the Friedel-Crafts alkylation reaction of Scheme 4.4

dehydrated to yield deh-^{2}H(3)-HKUST-1. The ^{2}H NMR spectra of these samples are shown in Figure 4.28. For D3 in ^{2}H(3)-HKUST-1, the MAS NMR spectrum yielded δ_{iso} of 6.9 ppm, consistent with the value for ^{1}H, and fitting of the static lineshape yielded a C_Q of 180 kHz. It can be seen that both the height of the horns and the intensity of the steps are asymmetric, indicating the presence of a small but significant CSA-like (*i.e.*, PSA) contribution to the lineshape. However, fitting the static lineshape using a model that included anisotropic broadening from both the chemical shift and quadrupolar interactions did not provide a reliable set of parameters for the PSA tensor (*i.e.*, the intensities of the horns could be modelled,

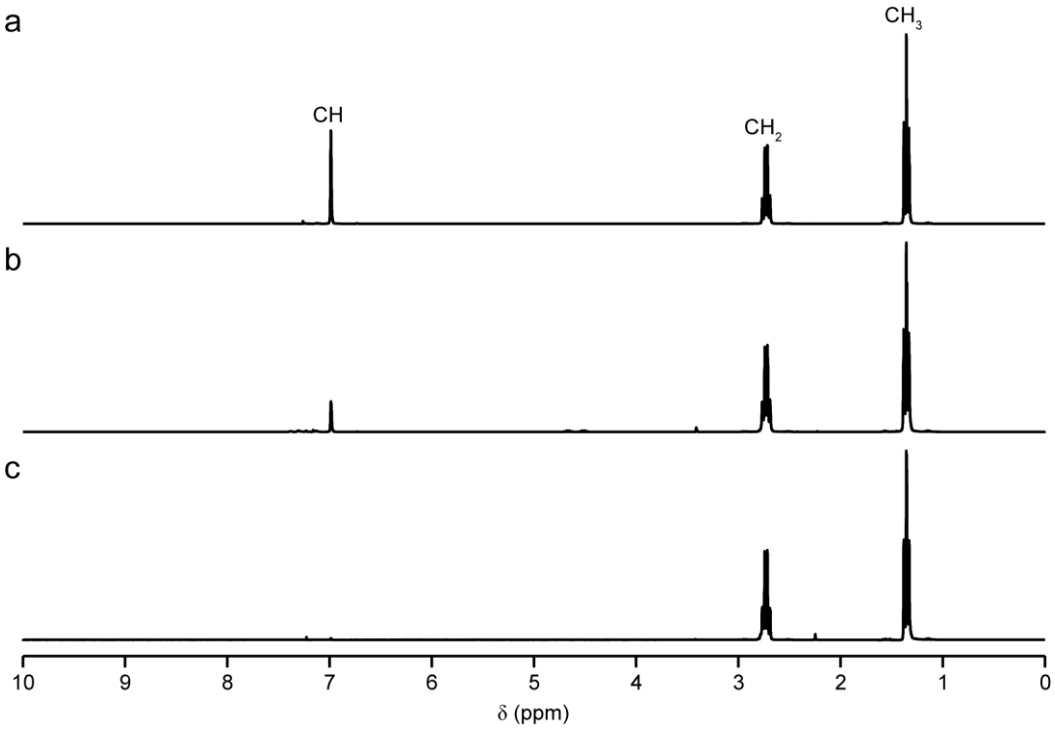

Figure 4.27. Solution-phase ^{1}H (7.05 T, $CDCl_3$) NMR spectra of (a) 1,3,5-triethylbenene and 2,4,6-[$^{2}H_3$]-triethylbenzene prepared from C_6D_6 by quenching the Friedel-Crafts reaction with (b) H_2O and (c) D_2O ice.

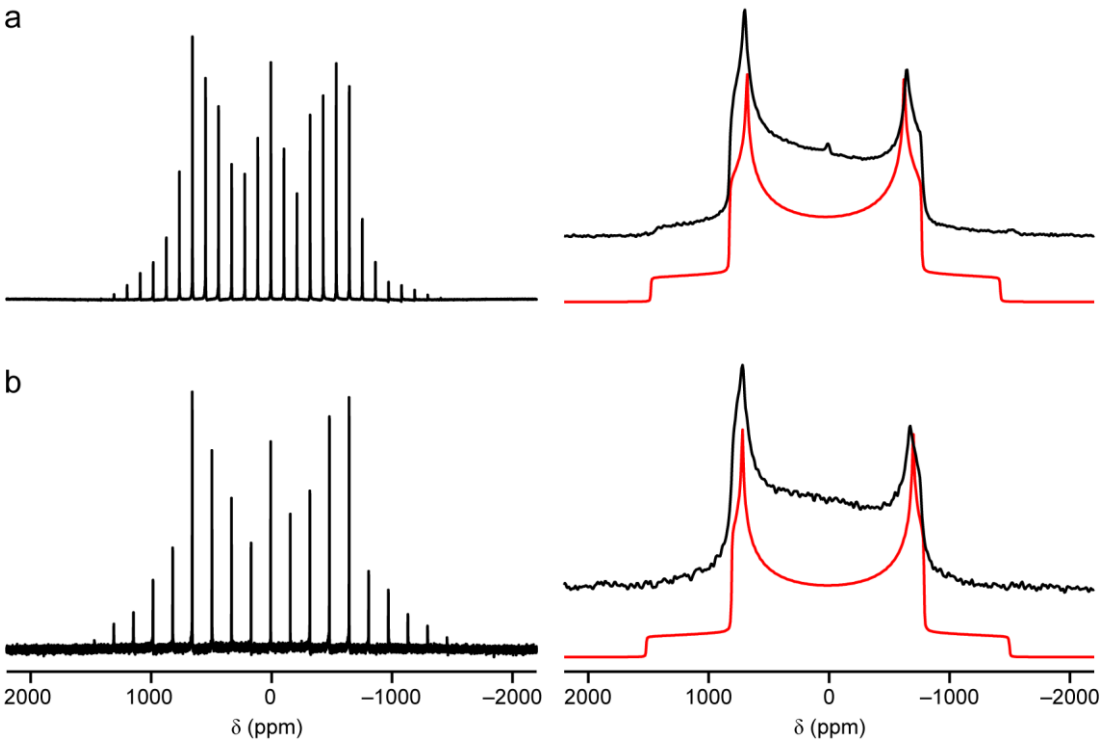

Figure 4.28. ^{2}H (14.1 T) NMR spectra of (a) ^{2}H(3)-HKUST-1 and (b) deh-^{2}H(3)-HKUST-1 recorded with (a) 10 or (b) 15 kHz MAS and static samples. Spectra simulated using the values in Table 4.9 (with δ_{iso} constrained) are shown in red.

but only with an isotropic shift of ~170 ppm, which is inconsistent with the MAS experiment). This issue requires further investigation at different B_0 field strengths in order to separate the PSA and quadrupolar contributions to the lineshape and achieve an unambiguous fit for both. Alternatively, the experimental approach of Antonijevic and Wimperis[62, 63] could be used to separate the PSA and quadrupolar contributions into two separate dimensions of a two-dimensional spectrum. Such an approach should allow the determination of both the magnitude (and asymmetry) of the two interaction tensors, and their relative orientations using a single experiment at a single B_0 field. The parameters providing the current best fit to the experimental ^{2}H NMR spectra of ^{2}H(3)-HKUST-1 are summarised in Table 4.9.

In the dehydrated sample, δ_{iso} of D3 was 8.3 ppm and fitting of the static lineshape yielded a C_Q of 185 kHz. The parameters providing the current best fit to the experimental ^{2}H NMR spectra of deh-^{2}H(3)-HKUST-1 are summarised in Table 4.9. As for the as-prepared MOF, it can be seen (Figure 4.28(b)) that the horns of the

Table 4.9. ^{2}H NMR parameters obtained from static and MAS NMR spectra of deuterated samples of HKUST-1 and STAM-1, where fits assumed only quadrupolar (*i.e.*, no CSA or PSA) contributions to the lineshape. For the static spectra, two fits were carried out; the first with δ_{iso} constrained to the value obtained from the MAS experiment, and the second with no constraints.

Species	MAS experiment			static experiment		
	δ_{iso} (ppm)	C_Q / kHz	η_Q	δ_{iso} (ppm)	C_Q / kHz	η_Q
^{2}H(3)-HKUST-1						
D3	6.6(3)	175(5)	0.10(5)	6.6[a]	177(5)[a]	0.09(5)[a]
				31.5[b]	179(5)[b]	0.10(5)[b]
deh-^{2}H(3)-HKUST-1						
D3	8.3(3)	201(5)	0.00(5)	8.3[a]	183(5)[a]	0.06(5)[a]
				13.5[b]	185(5)[b]	0.06(5)[b]
^{2}H(7)-STAM-1						
D7	0.8(3)	54(5)	0.11(5)	0.8[a]	53(5)[a]	0.07(5)[a]
				–4.3[b]	52(5)[b]	0.00(5)[b]

a. δ_{iso} constrained to the value obtained from the MAS experiment.

b. No constraint of δ_{iso}.

lineshape are asymmetric for the dehydrated MOF. However, the steps of the lineshape could not be observed, owing to the poorer signal-to-noise ratio in the spectrum (arising from the lower sample mass used). As above, fitting of the static lineshape using a model that included anisotropic broadening from both the chemical shift and quadrupolar interactions did not provide reliable PSA parameters.

One common reason for conducting ^{2}H NMR experiments is that the lineshape is typically sensitive to motion on the microseond timescale.[64] As there is no motion of the btc linkers in HKUST-1 (unlike the bdc linkers studied by Mowat *et al.*[60]), any motional effects observed for guest-loaded samples must arise from guest motion. It is hoped that future work will involve loading of ^{2}H(3)-HKUST-1 with different guest species and conducting a series of variable-temperature ^{2}H NMR experiments to evaluate the suitability of this approach to probing guest dynamics.

Deuteration of H7 in STAM-1 can be readily achieved, and a sample of ^{2}H(7)-STAM-1 was prepared by synthesis of the MOF in CD_3OD/H_2O. Figure 4.29 shows the MAS and static ^{2}H NMR spectra of this material. As summarised in Table 4.9, C_Q for D7 is smaller than for D3; an observation consistent with the rapid C_3 rotation of a CD_3 group leading to efficient partial averaging of the quadrupolar broadening. The horns and steps in the static ^{2}H NMR spectrum of ^{2}H(7)-STAM-1 are more symmetric than for ^{2}H(3)-HKUST-1, which is likely to arise from a combination of motional averaging of any PSA contribution to the lineshape for D7, and the smaller magnitude of this contribution, owing to the greater distance of D7 from the paramagnetic centres. The synthesis of ^{2}H(7)-STAM-1 paves the way for a variable-temperature ^{2}H NMR investigation of the dynamic behaviour of the CD_3 groups in the MOF, leading to the crystallographically-observed disorder of C7. The incorporation of the CD_3 group of the solvent into ^{2}H(7)-STAM-1 also provided definite proof that the formation of STAM-1 involves the proposed *in situ* esterification. While this may be the only obvious source of the CH_3 group of mmbtc, it remains surprising, as no such esterification is observed for HKUST-1.

4.4.11 Summary

The work presented in this study demonstrates that, while acquiring the solid-state NMR spectra of paramagnetic MOFs is initially somewhat more challenging (as there is currently no easy means of predicting the locations of all spectral resonances), the experimental techniques required are actually relatively straightforward. In addition, even with the low sensitivity of the experiment (the small rotors required for fast MAS restrict the sample mass to >5 mg), ^{13}C NMR spectra acquired at natural abundance can be recorded in approximately the same time as spectra for diamagnetic materials, owing to the far greater experimental repeat rates available for paramagnetic materials. Assignment of the ^{13}C NMR spectra of paramagnetic MOFs is considerably more challenging than for the diamagnetic case, as rapid relaxation limits the magnetisation-transfer experiments possible. Furthermore, assignments based on intuition (*i.e.*, that larger isotropic shifts, more rapid relaxation and greater Δ^* linewidths result from greater proximity to the paramagnetic centre) appear to be ambiguous, and selective ^{13}C isotopic

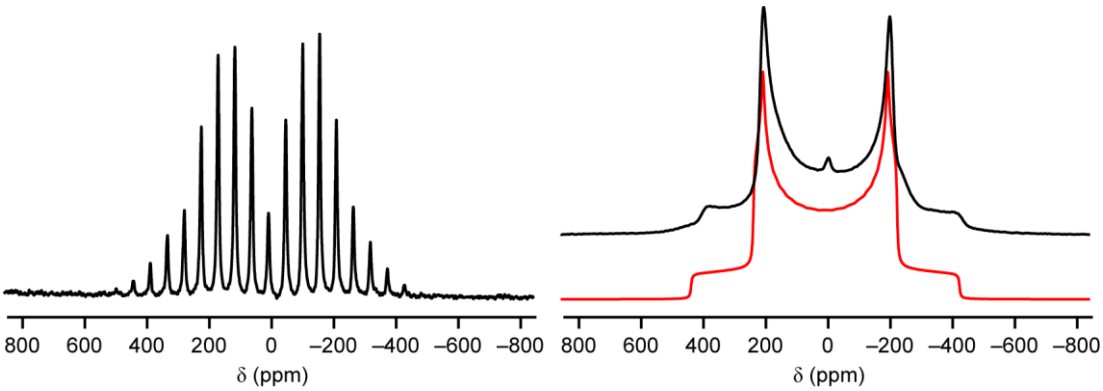

Figure 4.29. ^{2}H (14.1 T) NMR spectra of ^{2}H(7)-STAM-1, recorded with 5 kHz MAS (left) and a static sample (right). For the static spectrum, the red line indicates the spectrum simulated using the parameters given in Table 4.9.

enrichment was demonstrated to be necessary in order to achieve a confident assignment.[1] It is still unclear why the quaternary aromatic species, C1, exhibits a greater line-broadening and isotropic shift than the carboxylate species, C2, despite the latter being closer (both in terms of bonded pathway and through space) to the paramagnetic centre. Further work is required to explain this observation, involving the development of improved computational approaches such as the inclusion of paramagnetic interactions in periodic codes, such as CASTEP.

The ^{1}H NMR spectra of HKUST-1 and STAM-1 were recorded and assigned by comparison to the literature (HKUST-1 only) and using ^{1}H-^{13}C CP-HETCOR experiments. Despite the very large paramagnetic influences observed for ^{13}C, the ^{1}H resonances were all within ~2 ppm of their expected diamagnetic shifts.

The ^{13}C isotropic shifts, T_1 relaxation constants and Δ^* linewidths observed for both HKUST-1 and STAM-1 were shown to be essentially independent of B_0 field strength. This finding allows the spectrum of a paramagnetic material of interest to be "mapped" at low B_0 field strength, taking advantage of the reduced shift dispersion (in Hz) of the resonances. Specific regions of interest can then be studied in greater detail at higher B_0 field strengths, thereby taking advantage of the increased shift dispersion in more crowded spectral regions, and the improved sensitivity. The temperature dependence of the ^{1}H and ^{13}C shifts of HKUST-1 and STAM-1 was also investigated. For ^{13}C, it was found that the isotropic shifts of the

resonances for the C species closest to Cu^{2+} (C1, C2 and C3) displayed a clear linear variation with 1/T, proportional to the hyperfine coupling constant, A/ħ. When HKUST-1 was dehydrated, the sign of A/ħ was reversed for all resonances, indicating a change in the electronic structure of the MOF upon removal of the axial ligand of the copper dimer. As the variation in δ_{iso} with temperature is sufficiently large to be readily detected over a relatively narrow temperature range, this suggests that variable-temperature ^{13}C NMR experiments may be a very sensitive probe of the nature of the axial ligands bound to Cu. An unexpected observation was that the shifts of C1 and C3 increase with temperature (for the as-prepared MOFs), whereas the shift of C2 decreases with temperature, indicating that A/ħ has the opposite sign for C2. This observation requires further theoretical investigation before a full understanding is achieved. It is also clear from these variable-temperature experiments that care must be taken when interpreting isotropic shift values reported in the literature for paramagnetic materials, as these may vary significantly with the experimental conditions. The variable-temperature ^{1}H NMR spectra did not display quite such a clear linear relationship between the isotropic shift and 1/T. However, for HKUST-1, it was observed that an additional resonance, tentatively assigned to an ordered hydrogen-bonded network of H_2O, occurs over a temperature range of ~20 to 40 °C. Again, further work, including measurement of ^{1}H T_1 relaxation constants over this temperature range, is required in order to achieve a full understanding of this observation.

The ^{13}C MAS NMR spectra of both HKUST-1 and STAM-1 were demonstrated to be very sensitive to changes occurring in the local structure of the materials, enabling solid-state ^{13}C NMR spectroscopy to provide information on the loading of different guests within the pores. This information is of particular benefit when the guest species within the pores of the MOF cannot be located accurately by Bragg diffraction techniques, as demonstrated by the HKUST-1[metro+NO] system.[25]

A preliminary study into the information available from ^{2}H NMR spectra was somewhat inconclusive, but further experiments involving guest loading of deuterated HKUST-1 are planned. It is hoped that deuteration of the framework will

provide a cost-effective means of determining the dynamic behaviour of guest species within the pores of the MOF, as the deuterated linker (or, indeed, the MOF itself) may be recycled with different guest species, whereas using deuterated guests would require the (more costly) synthesis or purchase of many different deuterated compounds. Deuteration of H7 in STAM-1 was used as evidence that the formation of the MOF did involve *in situ* methylation of the btc linker by the methanol solvent.

In addition to the solid-state NMR spectroscopy, work presented here has led to the development of several isotopic labelling schemes, allowing the selective introduction of ^{13}C and ^{2}H labels into btc and mmbtc – molecules and strategies that may be of interest in the synthesis and characterisation of new MOFs, determining the location of guest species within known MOFs, and in the synthesis and development of dendrimers. It is believed that, with further optimisation of synthetic procedures, the synthesis of the isotopically enriched/labelled btc and mmbtc may be made more efficient and cost effective.

4.5 THE CPO-27-M (M = MG, MN, CO, NI, ZN) SERIES

4.5.1 Introduction

The MOF, CPO-27-M (CPO = Coordination Polymer of Oslo), has the framework formula M_2dhtp, (H_4dhtp = 2,5-dihydroxybenzene-1,4-dicarboxylic acid and M is a divalent metal cation). To date, CPO-27 has been prepared with M = Mg^{2+},[6] Mn^{2+},[7] Fe^{2+},[65] Co^{2+},[8] Ni^{2+} and Zn^{2+}.[9, 66] The structure of as-prepared CPO-27 comprises infinite one-dimensional chains of edge-sharing MO_6 octahedra, with five of the six O species donated by dhtp and the sixth from a molecule of coordinated H_2O (or DMF in CPO-27-Zn[9]). These inorganic chains are connected in a hexagonal "honeycomb" structure with one-dimensional channels of ~16 Å in diameter running parallel to the crystallographic c axis, as shown in Figure 4.30. Activation of the MOF can be achieved by heating under vacuum to remove the metal-coordinated guest species, giving rise to a CUS on each metal site (Figure 4.30(c)). As for HKUST-1 and STAM-1, the CUSs in CPO-27 can bind to a variety of guest species.

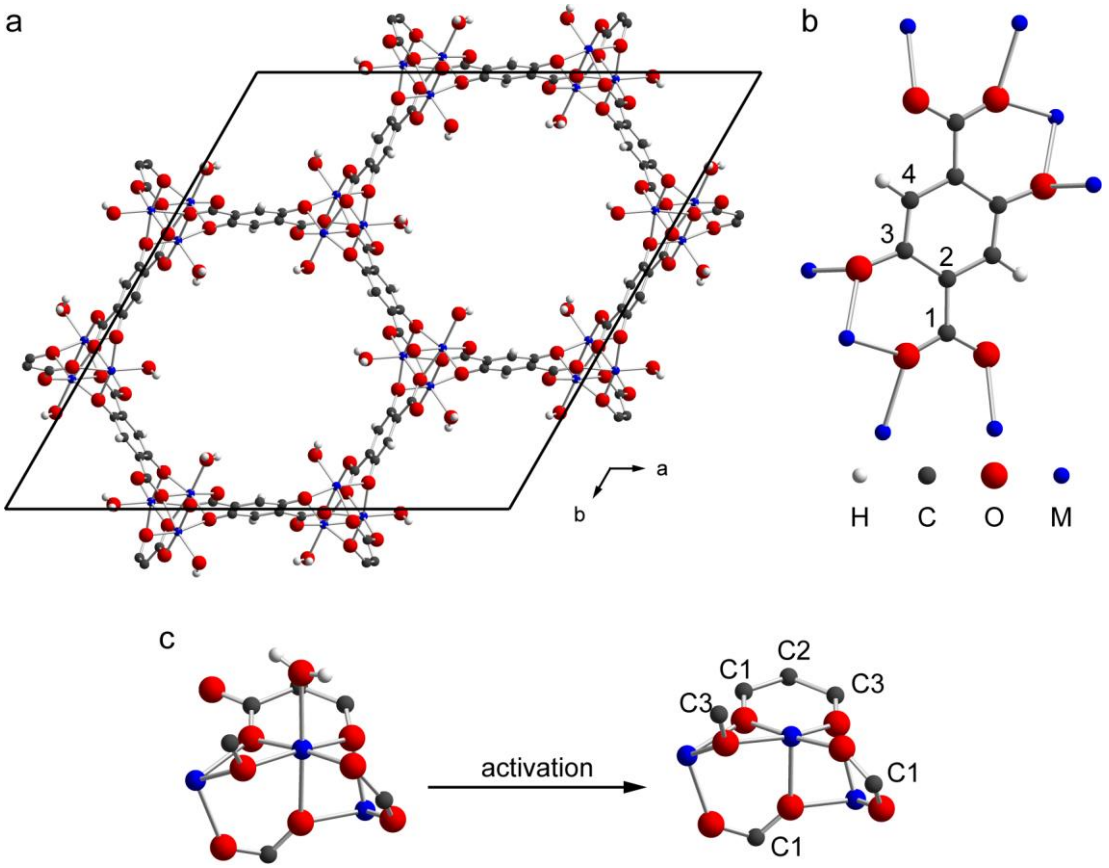

Figure 4.30. (a) The crystal structure of CPO-27-M (shown here for M = Co[8]), with free H_2O within the pores omitted for clarity. (b) The structure and coordination environment of the dhtp linker and the numbering scheme used in this work. (c) The coordination environment of the M^{2+} ions in the hydrated and activated MOF.

As the CPO-27 framework has good thermal stability (for a MOF) and the flexibility to incorporate several different metals into the same framework structure, much work has been carried out investigating its properties and applications. As the active sites within the MOF are the CUSs, it can be appreciated that changing the nature of the metal centres will change the adsorption characteristics of the MOF and, therefore, the applications possible. For example, Dietzel *et al*. have demonstrated that the Mg and Zn forms display favourable adsorption properties for CO_2,[67] Wu *et al*. showed that the Mn form can absorb important fuel gases (*e.g.*, CH_4 and H_2),[7] Bhattacharjee *et al*. investigated the catalytic behaviour of the Fe form in the oxidation of phenols[65] and McKinlay *et al*. used the Co and Ni forms for the storage and controlled release of medically-important quantities of NO gas.[54]

To date, no ^{1}H or ^{13}C NMR spectra of CPO-27 have been reported in the literature (although the ^{25}Mg and ^{17}O NMR spectra of the Mg form are known[18, 68]), possibly owing to the fact that the Mn, Fe, Co and Ni forms are paramagnetic. In a recent study on the dynamics of CO_2 in the diamagnetic CPO-27-Mg, Kong *et al*. used ^{13}C NMR spectra to determine the motion of the CO_2 molecules coordinated to the Mg ions.[69] However, as the CO_2 was enriched in ^{13}C and the spectra were recorded with static samples, the resonances arising from the framework were not observed. The aim of this study, then, was to acquire and assign the solid-state ^{13}C NMR spectra of the as-prepared MOFs, CPO-27-M (with the exception of CPO-27-Fe, which was first reported after the work here was carried out).

4.5.2 Diamagnetic CPO-27-M

Samples of the two diamagnetic forms of CPO-27-M (M = Mg and Zn) were synthesised as described in Section 4.3. The ^{13}C CP MAS NMR spectra of as-prepared CPO-27-Mg and CPO-27-Zn are shown in Figure 4.31. In both cases, there are four resonances that may be assigned to the distinct C species in the dhtp linker (Figure 4.30(b)), and in the case of CPO-27-Zn, three resonances, arising from the DMF, are also observed, confirming the presence of DMF within the pores of the MOF. A third sample, CPO-27-Zn[MeOH] was prepared by solvent exchange of the H_2O/DMF within the pores of the as-prepared sample for MeOH. The ^{13}C CP MAS NMR spectrum of this sample is also shown in Figure 4.31 and, again, there are four resonances that can be attributed to the framework, and one arising from the MeOH.

For CPO-27-Mg, the four resonances have chemical shifts of 174.6, 156.5, 127.2 and 126.8 ppm. Based on these shifts, the resonances at 174.6 and 156.5 ppm can be assigned to C1 and C3, respectively. The other two resonances can be assigned based on their CP build-up behaviour, shown in Figure 4.32. As C4 is directly bonded to ^{1}H, its build-up rate is likely to be more rapid than for the other three C species, suggesting the assignment of the resonance at 127.2 ppm to C4 and the remaining resonance to C2. In order to confirm this assignment, a ^{1}H-^{13}C INEPT experiment was carried out (Figure 4.33), and showed a single intense resonance with ^{1}H shift of 7.9 ppm and ^{13}C shift of 127.2 ppm. This is in agreement with the ^{1}H NMR spectrum of the MOF (Figure 4.33), which contains a single sharp resonance

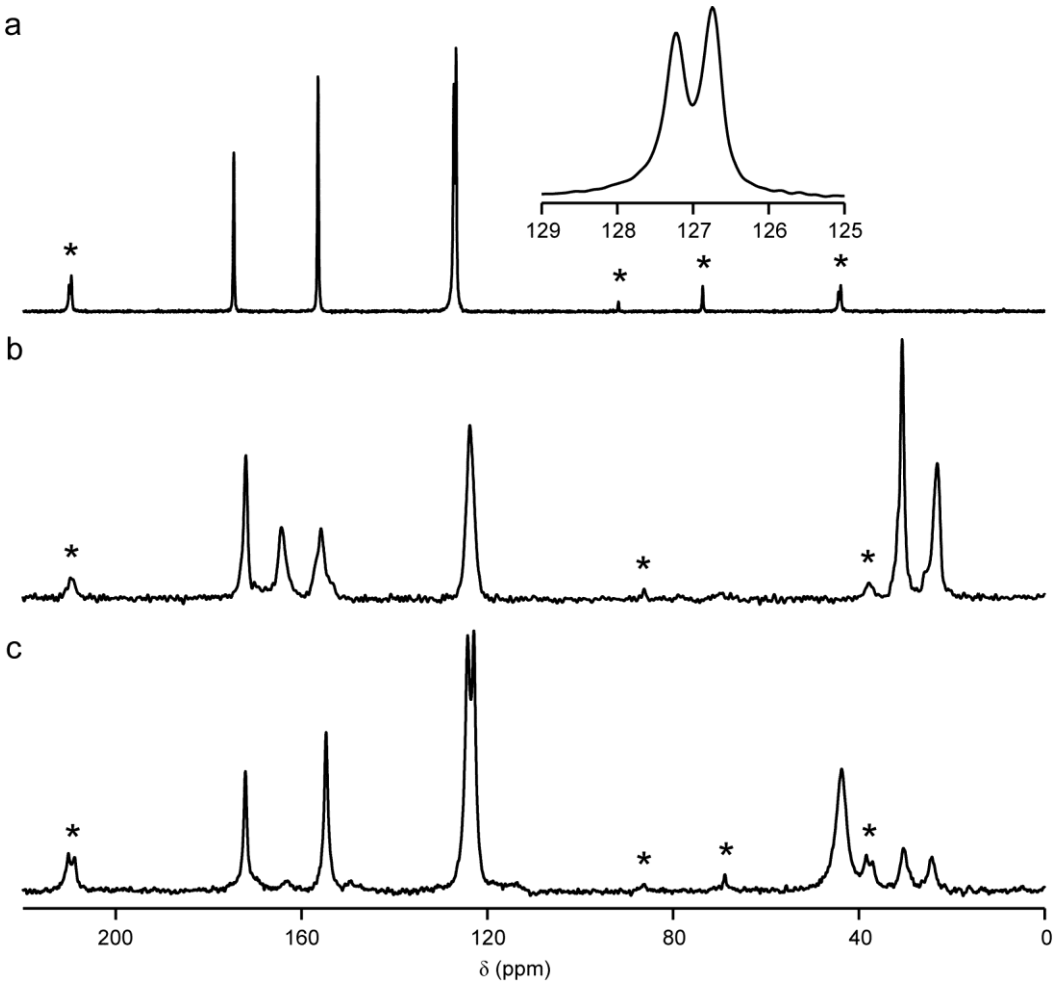

Figure 4.31. ^{13}C (14.1 T, 12.5 kHz CP MAS) NMR spectra of (a) CPO-27-Mg, (b) CPO-27-Zn and (c) CPO-27-Zn-[MeOH]. Asterisks denote SSBs.

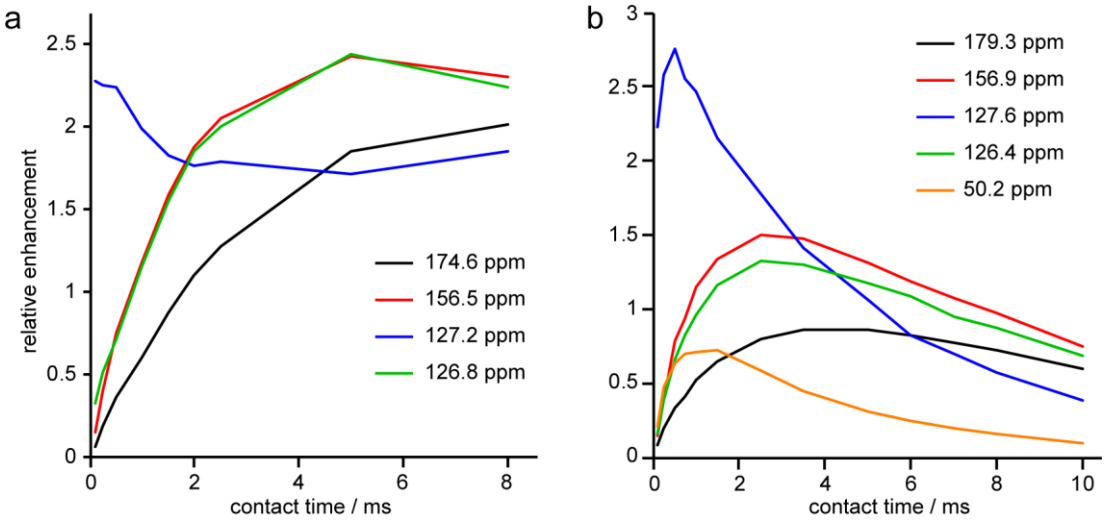

Figure 4.32. ^{13}C CP build-up behaviour for (a) CPO-27-Mg and (b) CPO-27-Zn.

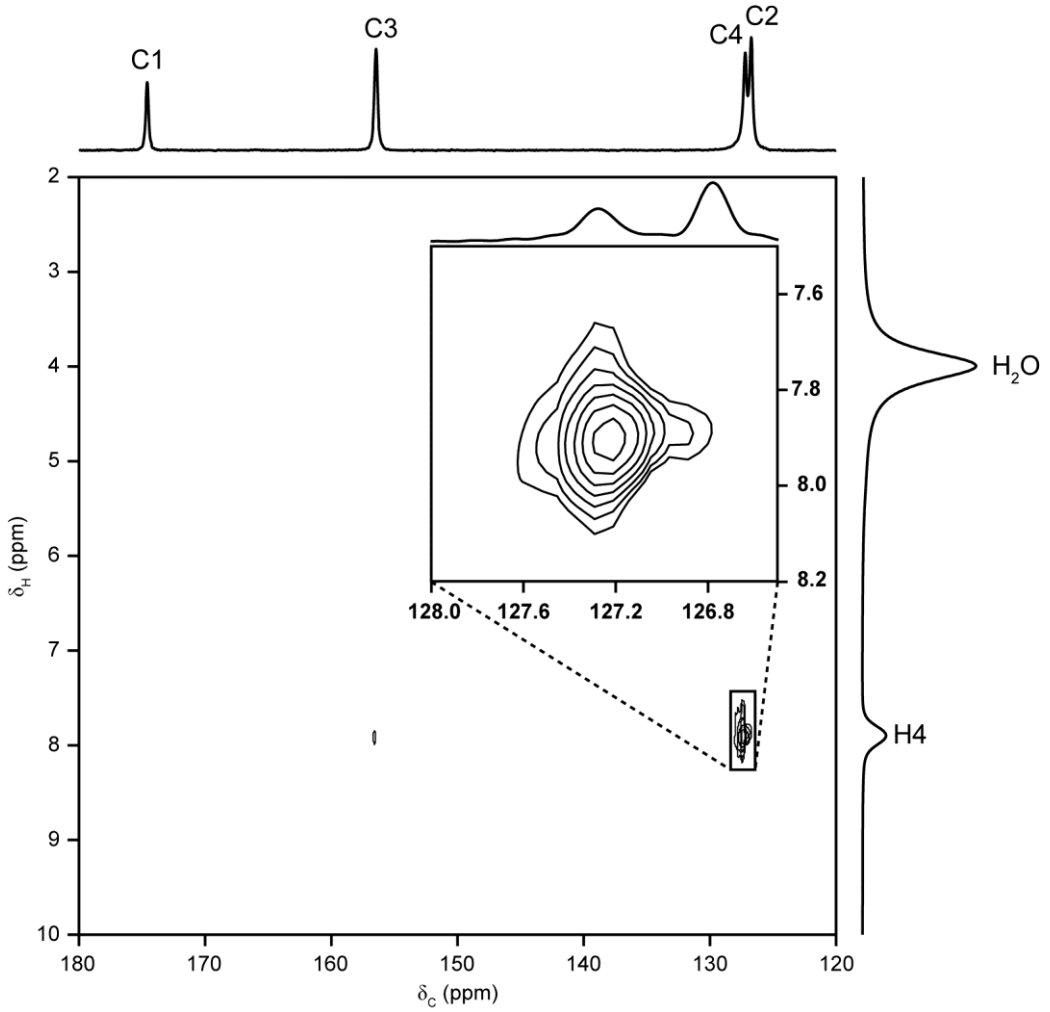

Figure 4.33. ^{1}H-^{13}C INEPT spectrum of CPO-27-Mg (14.1 T, 12.5 kHz MAS). The ^{13}C NMR spectrum shown along the δ_C axis is the same as in Figure 4.31(a) and the ^{1}H NMR spectrum shown along the δ_H axis was recorded at 14.1 T (60 kHz MAS).

at 7.9 ppm, and a broader resonance at 3.9 ppm, corresponding to H_2O. Two low-intensity resonances were also observed in the ^{1}H-^{13}C INEPT spectrum, with ^{1}H shifts of 7.9 ppm and ^{13}C shifts of 126.9 and 156.5 ppm, confirming that the resonance at 174.6 ppm corresponds to C1 (*i.e.*, three bonds from the nearest H4).

For the ^{13}C NMR spectrum of CPO-27-Zn, resonances are observed at 173.8, 166.3, 158.3, 127.2, 37.5 and 30.4 ppm. The resonances for the DMF can be identified at 166.3, 37.5 and 30.2 ppm, assigned to the CHO and two CH_3 groups, respectively.[70] Owing to the partial double-bond character of the amide C-N bond (shown in Figure 4.34(a)), free rotation about this bond is not possible and the two

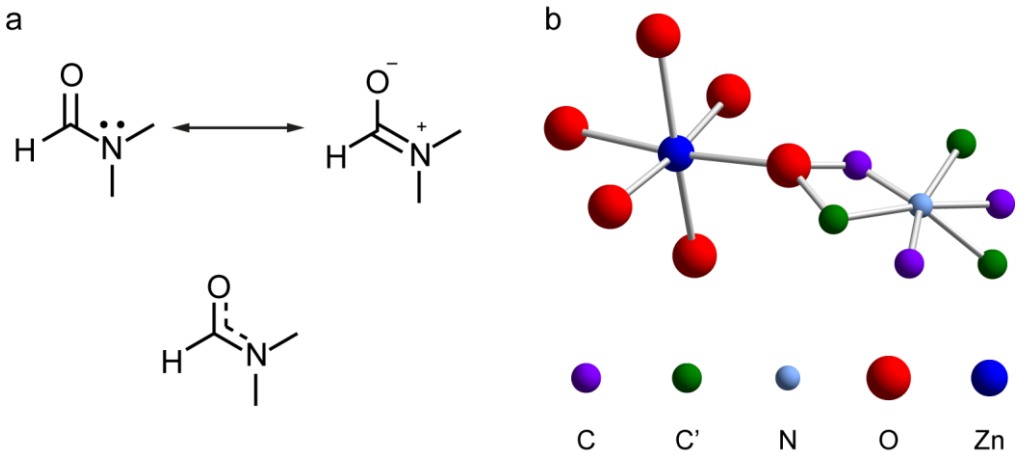

Figure 4.34. (a) The canonical forms and average structure of DMF. (b) The positions of DMF within the pores of CPO-27-Zn, determined by Bragg diffraction.[9] C atoms from the two different orientations are shown in purple and green. Owing to disorder, the H atoms of DMF were not located.

CH_3 groups are inequivalent. This inequivalence may be responsible for the observed difference in intensity of the two resonances, as the CP build-up dynamics may be expected to be different for the two species if they have different spatial proximities to, *e.g.*, C**H**O of nearby DMF or C**H** of the dhtp linkers. The assignment of the resonances from the dhtp may be assumed to be analogous to that for CPO-27-Mg, although the resonances for C2 and C4 cannot be resolved, owing to their significantly greater linewidths. The line broadening observed is likely to arise from motion of the DMF molecules bound to the Zn ions, which were identified by X-ray diffraction as being disordered, as shown in Figure 4.34.[9] It was recently shown by Kong *et al*. that CO_2 bound to Mg in CPO-27-Mg was dynamic,[69] suggesting that a similar case of dynamic disorder may be possible for DMF, although further experimental work would be required to confirm this.

In order to confirm that the assignment of the framework resonances was correct (*i.e.*, the resonance arising from the CHO of DMF had been correctly identified), the DMF and H_2O within the pores of the MOF were replaced with MeOH, giving CPO-27-Zn[MeOH]. It can be seen from the ^{13}C NMR spectrum of this sample (Figure 4.31(c)), that the CHO resonance was correctly identified, as there is no resonance at 166.4 ppm when the DMF is absent. Resonances are observed at 173.9, 156.9, 127.6, 126.4 and 50.2 ppm. The resonance at 50.2 ppm can

be assigned to methanol, and the remaining four can be assigned to the dhtp, as there is no significant difference between their chemical shifts and those of the DMF-containing CPO-27-Zn, although the resonances narrow significantly upon guest exchange. This narrowing is likely arises from the different timescale of the motions of MeOH and DMF, owing to the different sizes of the two species. However, variable-temperature NMR experiments would be required in order to confirm this suggestion by determining whether the linewidth is temperature dependent.

Assignment of the resonances observed in the ^{13}C CP MAS NMR spectrum of CPO-27-Zn[MeOH] was achieved based on their isotropic shifts and CP build-up behaviour, shown in Figure 4.32(b). The resonance at 127.6 ppm has a similarly rapid build-up rate to that at 127.2 ppm in CPO-27-Mg, indicating that it corresponds to C4, whereas the resonance at 126.4 ppm in CPO-27-Zn[MeOH] can be identified as C2. This assignment confirms that that both C2 and C4 have very similar shifts, whether the MOF contains Mg or Zn. The shifts of C1 and C3 are also relatively insensitive to the nature of the metal ions, despite having M-O-C linkages. The ^{13}C chemical shifts of all three diamagnetic samples of CPO-27-M are summarised in Table 4.10. It can be seen that neither changing the diamagnetic metal species nor the metal-bound guests has a significant effect on the ^{13}C chemical shifts of the MOF.

The ^{1}H MAS NMR spectra of CPO-27-Zn and CPO-27-Zn[MeOH] are shown in Figure 4.35. In both cases, the position of the resonance from H4 of the MOF is essentially unaffected by the nature of the guest species (8.0 ppm in both cases) and, by comparison to the ^{1}H NMR spectrum of CPO-27-Mg, it can be seen that the position of this resonance is affected very little by the different metal ions present. The remaining resonances in the ^{1}H NMR spectrum of CPO-27-Zn can be identified as arising from DMF (7.5 ppm (CH) and 2.5 and 1.5 ppm (CH_3)) by analogy to their shifts in solution (7.6, 2.4 and 1.9 ppm in C_6D_6, but generally at higher shift for all other solvents investigated by Gottlieb *et al.*[70]) and water (3.9 ppm). The remaining resonances in the ^{1}H NMR spectrum of CPO-27-Zn[MeOH] can be identified as MeOH (4.5 ppm (OH) and 2.5 ppm (CH_3)), although the asymmetry of the resonance at 4.5 ppm, and its intensity relative to that at 2.5 ppm (approximately 3.8 : 3) indicates that H_2O is also present.

Table 4.10. Assignment of the ^{13}C resonances arising from the dhtp linker in the diamagnetic forms of CPO-27 studied in this work.

Species	δ (ppm)		
	CPO-27-Mg	CPO-27-Zn	CPO-27-Zn[MeOH]
C1	174.6(1)	173.8(2)	173.9(1)
C2	126.8(1)	126.8(2)	126.4(1)
C3	156.5(1)	158.3(2)	156.9(1)
C4	127.2(1)	127.5(2)	127.6(1)

4.5.3 Paramagnetic CPO-27-M

As discussed in Section 4.4, recording the ^{13}C NMR spectra of paramagnetic MOFs requires a different experimental approach than for diamagnetic MOFs. For the paramagnetic CPO-27-M studied here (M = Ni, Co and Mn), ^{1}H and ^{13}C NMR spectra were acquired using a spin-echo, with rapid (60 kHz) MAS. Frequency-

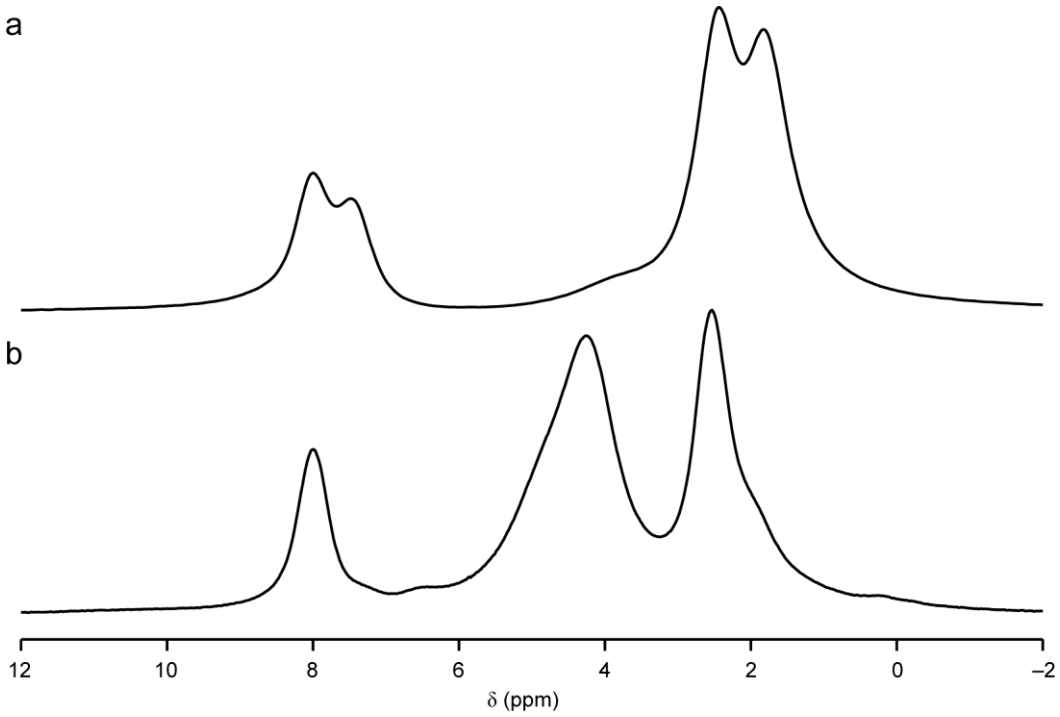

Figure 4.35. ^{1}H (14.1 T, 60 kHz MAS) NMR spectra of (a) CPO-27-Zn and (b) CPO-27-Zn[MeOH].

stepped acquisition was carried out for CPO-27-Ni. The spectra are shown in Figure 4.36 and, unlike the cases of HKUST-1 and STAM-1, the PSAs for ^{13}C in CPO-27 are very large, on the order of a few thousand ppm, and many SSBs remain. The same is true for ^{1}H, with the SSB manifolds broader than the excitation bandwidth of the pulses, necessitating the use of frequency stepping for both ^{1}H and ^{13}C.

Owing to the proliferation of SSBs in the ^{13}C NMR spectra, the first challenge is to identify the isotropic shifts of the four C species. This is generally achieved by altering the MAS rate, such that the positions of all spinning sidebands are changed while the isotropic peak remains in the same position. As the sensitivity of the spectra of CPO-27-Ni was greatest (owing to the narrower linewidths, discussed in more detail below), the identification of SSBs and isotropic resonances was first attempted for this MOF. However, this task proved challenging, owing to the temperature dependence of the isotropic shifts observed. Simply by changing the MAS rate from 60 to 50 kHz, the difference in frictional heating of the sample led to a change in the position of the (suspected) isotropic shift of up to 25 ppm. At the B_0 field strength of 14.1 T used for this work, 25 ppm is equivalent to 3.8 kHz, which is less than the expected change in position of the first- order SSBs (±10 kHz), and identification of isotropic positions was still possible. However, care must be taken in interpreting the isotropic shift information reported here, as the shifts will only be relevant for samples packed into 1.3 mm rotors and rotated at 60 kHz MAS. The ^{13}C MAS NMR spectra of CPO-27-Ni, recorded with 50 and 60 kHz MAS are shown in Figure 4.37, and isotropic resonances (at 60 kHz MAS) can tentatively be identified at 1027, 870, 679 and 235 ppm. Based on these shifts, an initial assignment can be suggested of C1 (1027 ppm), C3 (870 ppm), C2 (679 ppm) and C4 (235 ppm), given the number and length of the bonded pathways to the nearest Ni^{2+} ions for each C species. However, as was demonstrated for HKUST-1 and STAM-1, such "intuitive" assignments cannot be trusted completely, and selective ^{13}C labelling would be required in order to confirm the assignment.

The synthesis of ^{13}C-labelled (or even uniformly enriched) H_4dhtp has not yet been attempted, owing to the greater complexity of H_4dhtp, compared to H_3btc and the limited number of cost-effective ^{13}C-labelled starting materials available. Such

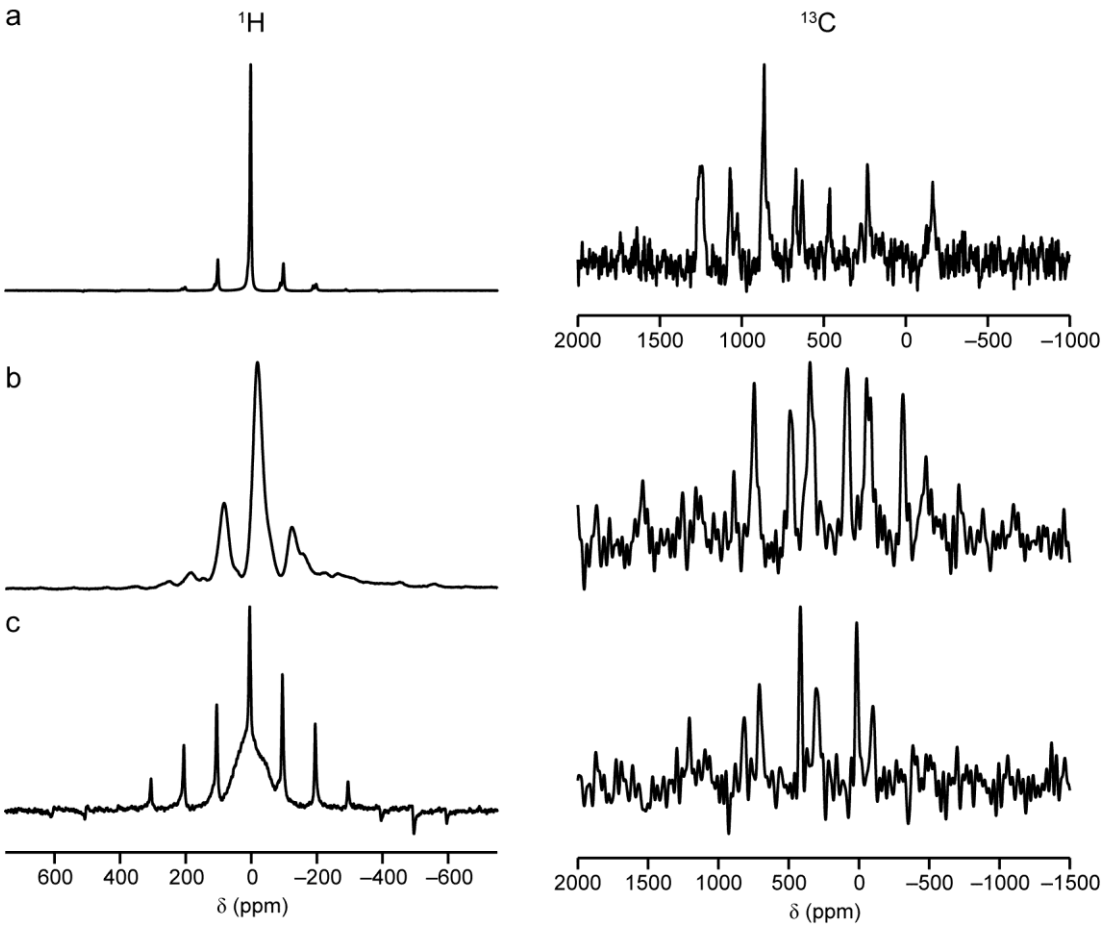

Figure 4.36. ^{1}H and ^{13}C (14.1 T, 60 kHz MAS) NMR spectra of (a) CPO-27-Ni, (b) CPO-27-Co and (c) CPO-27-Mn. ^{13}C NMR spectra were acquired with frequency stepping over 6 steps of 75 kHz (CPO-27-Ni) and with a single frequency step for CPO-27-Co and CPO-27-Mn.

labelled material will, however, be required in order to improve the sensitivity of the ^{13}C NMR experiments for CPO-27-Co and CPO-27-Mn. Such an enhancement in sensitivity is necessary, given the very poor SNR observed for the ^{13}C NMR spectra of both MOFs in Figure 4.36. The poor sensitivity for CPO-27-Co can be attributed to the very large ground-state magnetocrystalline anisotropy of Co^{2+}, which leads to a broadening of the resonances in NMR spectra. For the case of CPO-27-Mn, it would appear that the five nominally-unpaired electrons per metal centre (*i.e.*, for isolated high-spin octahedral Mn^{2+}) result in large relaxation-related signal losses, and overall poor sensitivity, despite each resonance being relatively narrow.

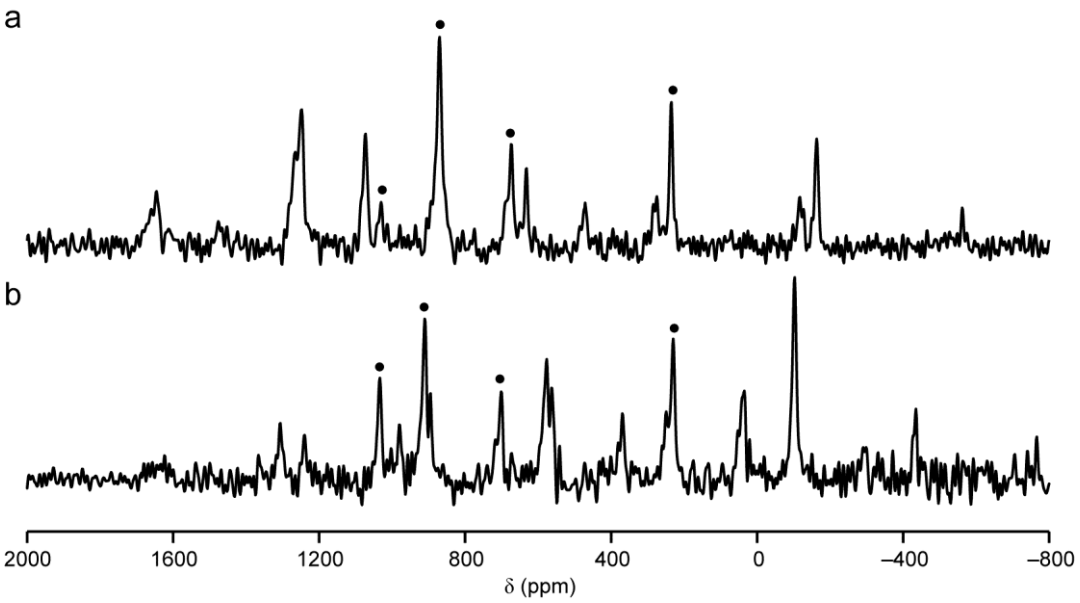

Figure 4.37. ^{13}C (14.1 T) NMR spectra of CPO-27-Ni acquired with (a) 60 kHz and (b) 50 kHz MAS. Dots indicate what are believed to be the isotropic resonances.

4.5.4 Summary

This study presented the solid-state ^{1}H and ^{13}C NMR spectra of the CPO-27-M series, with M = Mg, Mn, Co, Ni and Zn. The solid-state ^{13}C NMR spectra of the diamagnetic (M = Mg, Zn) MOFs were assigned using their CP build-up behaviour and ^{1}H-^{13}C correlation spectroscopy, and demonstrated that the isotropic chemical shifts of the resonances from the dhtp linkers are not sensitive to the nature of the metal ion or the metal-bound guest species. For the paramagnetic (M = Mn, Co, Ni) MOFs, both ^{1}H and ^{13}C NMR spectra were demonstrated to require frequency-stepped acquisition. It is believed that complete ^{1}H NMR spectra have been recorded for all members of the series, and that the ^{13}C NMR spectrum for CPO-27-Ni is also complete. The identification of isotropic ^{13}C resonances for CPO-27-Ni was challenging, owing to the temperature dependence of the isotropic shifts of all resonances, which complicated attempts to identify SSBs by changing the MAS rate.

The ^{13}C NMR spectra of the paramagnetic samples of CPO-27 were acquired using the experimental techniques developed for the study of HKUST-1 and STAM-1 (which have much smaller PSAs). While the spectra for the two Cu-based MOFs were acquired relatively readily with B_0 = 14.1 T, the spectra of the CPO-27-M samples were very challenging to acquire at this field strength. This emphasises the

conclusion of the earlier study, that mapping out of the whole NMR spectrum of a paramagnetic MOF requires not only rapid MAS to improve sensitivity, but also the lowest B_0 field strength available, to reduce the number of frequency steps required.

While this study could not provide complete spectra and assignments for all members of the CPO-27-M series studied here, it forms a useful starting point for further investigation of these systems. However, the first stage in any such investigation should be the synthesis of ^{13}C-labelled H_4dhtp, which will be a challenging task, given the constraints imposed (in terms of available starting materials and required efficiency of chemical transformations).

4.6 Ln(btc)(dmu)$_2$ (Ln = La, Nd)

4.6.1 Introduction

Lanthanide-based MOFs have many interesting applications, owing to their ability to combine the useful properties of MOFs with the intrinsic luminescence of many lanthanide ions.[71] In addition, owing to the unique coordination geometry of the lanthanides (*i.e.*, lanthanide ions favour higher coordination numbers than other metal ions), many MOF structures are only accessible when lanthanide ions are present. This study focuses on the material Ln(btc)(dmu)$_2$ (dmu = 1,3-dimethylurea, Ln = La, Nd), which was prepared by Himeur *et al*. using an ionothermal synthesis route.[10] The reaction was carried out in the deep eutectic solvent, *i.e.*, a mixture of two solids with high melting points that, when combined, experience a large depression in their melting point. In this case, the solvent was a mixture of dmu and choline chloride (cc), and some of the dmu is incorporated in the structure of the MOF. The structure of Ln(btc)(dmu)$_2$ is shown in Figure 4.38 and is composed of Ln_2 dimers, connected by btc, with two "bridging" carboxylate groups and two carboxylate groups doubly bonded to each Ln^{3+} ion. The Ln dimers are contained within Ln(btc) layers, with the carboxylate groups all bonded to the Ln^{3+} ions in the same plane. Two molecules of dmu are bonded to the metal centre, one above and one below the plane of the carboxylate groups, as shown in Figure 4.38(c). The dmu species are also hydrogen bond donors, and form two hydrogen bonds to two of the

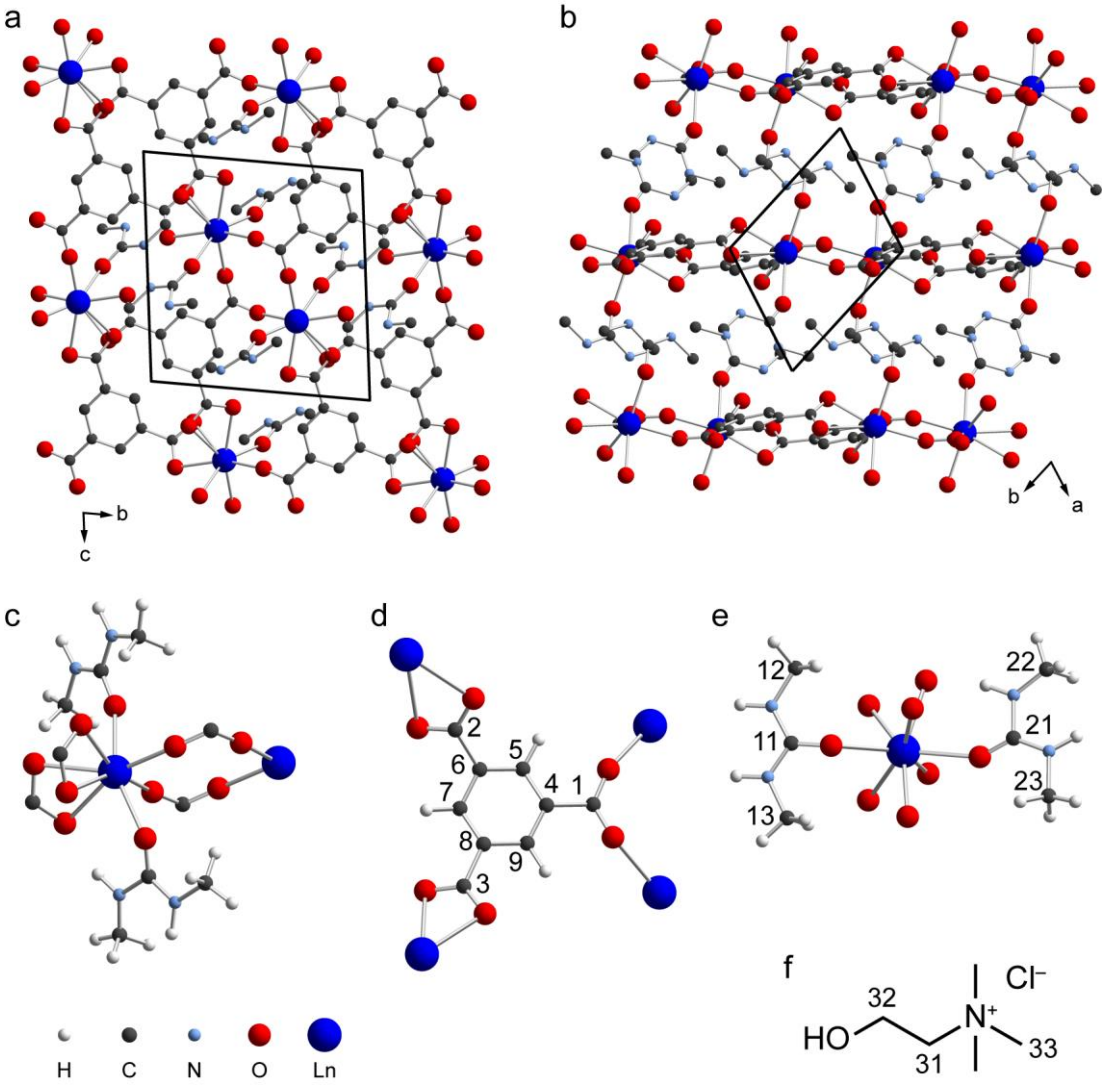

Figure 4.38. The crystal structure of Ln(btc)(dmu)$_2$, viewed down the crystallographic (a) a and (b) c axes. The coordination environments of (c) the Ln ions and (d) the btc linkers within the MOF, (e) the structure of the two crystallographically-distinct dmu species present and (f) the structure of cc. In parts (d-f), the numbering schemes used in this work are shown.

non-bridging carboxylate species in adjacent layers, leading to the formation of a three-dimensional structure. Owing to the low symmetry of the structure (space group $P\bar{1}$), there are nine inequivalent C species in the btc linker, and a further six inequivalent C species in the two molecules of dmu. The numbering schemes for the crystallographically- and chemically-distinct C species in the structure are shown in Figures 4.38(d, e and f). Given that this material contains the same btc linker as HKUST-1, and has both a diamagnetic (Ln^{3+}) and paramagnetic (Nd^{3+}) form, it was

seen as a suitable target structure for the extension of the NMR experimental techniques developed for the study of HKUST-1 and STAM-1. (The Eu^{3+} form of the MOF was also prepared by Himeur *et al.*, but not studied here).

4.6.2 La(btc)(dmu)$_2$

The ^{13}C CP MAS NMR spectrum of La(btc)(dmu)$_2$ is shown in Figure 4.39(a) and contains approximately 10 resonances (although the presence of shoulders and asymmetric lineshapes indicates that more than 10 magnetically-distinct species are present within the sample). These can be assigned tentatively on the basis of their chemical shifts, with resonances between 167 and 182 ppm assigned to CO_2La, the resonance at 160.8 ppm assigned to CO of dmu (161.2 ppm in $CDCl_3$[72]), resonances between 120 and 140 ppm assigned to aromatic C and CH of the btc linker, and the resonance at 27.5 ppm to CH_3 in dmu (26.8 ppm in solution). The remaining two resonances can be assigned to C31 (68.1 ppm) and C32 and C33 (55.6 ppm) of cc, which have shifts of 68.2, 56.3 and 54.7 ppm, respectively, in D_2O.[72]

In order to provide a more complete assignment, the ^{13}C NMR parameters were calculated (using CASTEP 6) for the structure of La(btc)(dmu)$_2$. Agreement between the spectrum simulated from the calculated parameters (Figure 4.39(b)) and experiment is poor. However, the forces upon some of the atoms exceeded 20 eV Å^{-1} (with a mean value for all atoms of 7.1 eV Å^{-1}), indicating that the structure required optimisation. Following optimisation (of the unit cell parameters and atomic positions, using CASTEP 4.3), the NMR parameters were calculated again (using CASTEP 6) and good agreement was obtained for all resonances, particularly the carboxylate and carbonyl species, as can be seen by the spectrum simulated using the calculated NMR parameters, shown in Figure 4.39(c). The NMR parameters calculated for the optimised structure were used to assign the ^{13}C NMR spectrum of La(btc)(dmu)$_2$, as summarised in Table 4.11. While it would have been of interest to optimise the structure using SEDC schemes to determine the importance of the intermolecular hydrogen bonding between the different layers of the structure, such calculations are not currently possible, as the SEDC schemes employed in the CASTEP code have not yet been parameterised for La. The cif file for the optimised structure is included in the electronic information supporting this thesis.

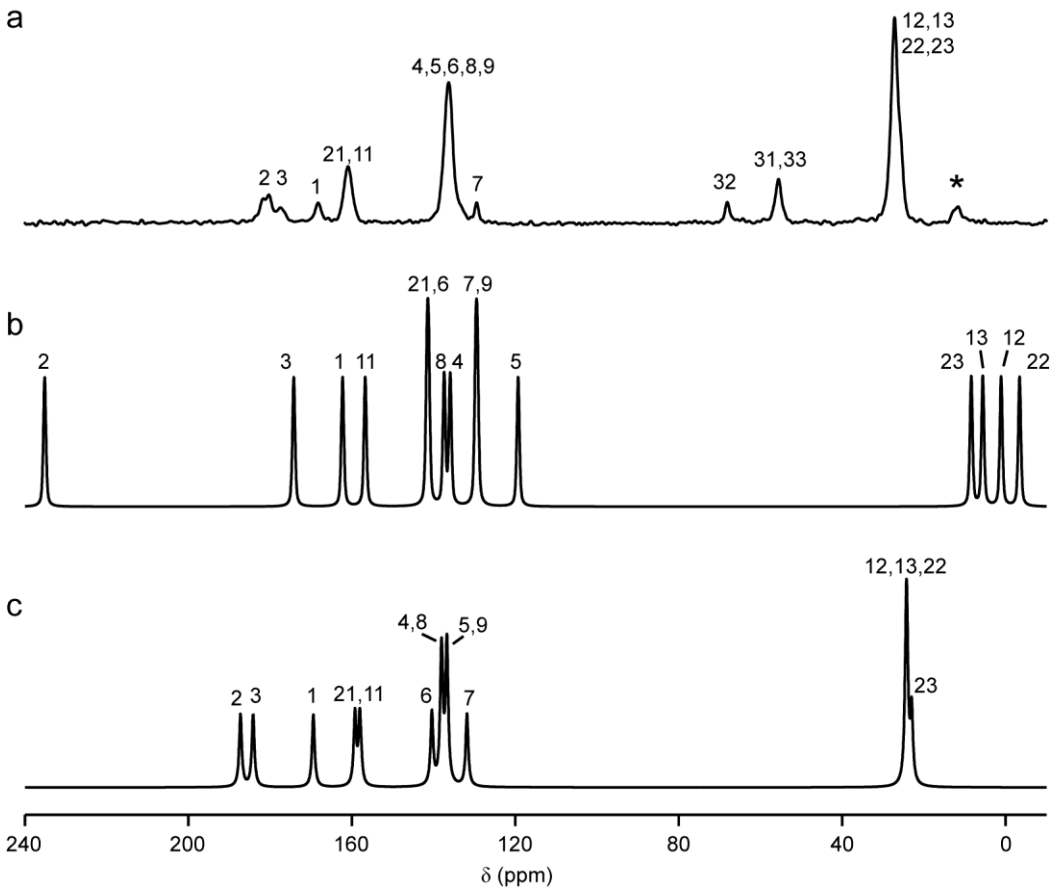

Figure 4.39. (a) ^{13}C (14.1 T, 12.5 kHz CP MAS) NMR spectrum of La(btc)(dmu)$_2$, acquired with a spin lock duration of 1 ms. ^{13}C NMR spectra for La(btc)(dmu)$_2$, simulated using parameters calculated (b) before and (c) after structural optimisation.

4.6.3 Nd(btc)(dmu)$_2$

The ^{13}C NMR spectrum of Nd(btc)(dmu)$_2$, shown in Figure 4.40, contains approximately 11 distinct resonances, with isotropic shifts of ~225, 207, 190, 164, 134, 117, 84, 55, 34, 25 and 19 ppm. However, the relative intensities and asymmetric shapes of these resonances indicate that there are additional resonances present, which are not resolved in the spectrum recorded at 14.1 T. In an attempt to improve the spectral resolution, the spectrum was recorded at 20.0 T, (Figure 4.40(b)), but there is little difference in resolution between the two spectra.

Interestingly, the observed isotropic shifts are all within the typical range for diamagnetic ^{13}C. There are two possible explanations for this; either that only H_3btc, dmu and cc that are not part of the MOF are observed in the ^{13}C NMR spectrum, or that there are no significant contact interactions between the Nd^{3+} and the ^{13}C nuclei,

Table 4.11. Experimental and calculated (CASTEP 6, after optimisation) ^{13}C isotropic shifts for La(btc)(dmu)$_2$.

Species	experimental δ_{iso} (ppm)	calculated δ_{iso} (ppm)
btc		
1	177.5	172.8
2	180.5	187.5
3	181.8	190.6
4	136.4	141.6
5	136.4	140.1
6	136.4	141.4
7	129.6	135.3
8	136.4	143.8
9	136.4	140.2
dmu1		
11	161.2	161.4
12	27.6	27.8
13	27.6	27.6
dmu2		
21	168.4	162.6
22	27.6	27.6
23	27.6	24.4
cc		
31	68.1	
32	55.6	
32	55.6	

with paramagnetic shifts being due solely to the pseudocontact interaction. The first option can be discounted owing to the short repeat interval (100 ms) used. Such a short interval would rapidly saturate any diamagnetic species, leading to very little spectral intensity being observed. In addition, the isotropic shifts observed do not

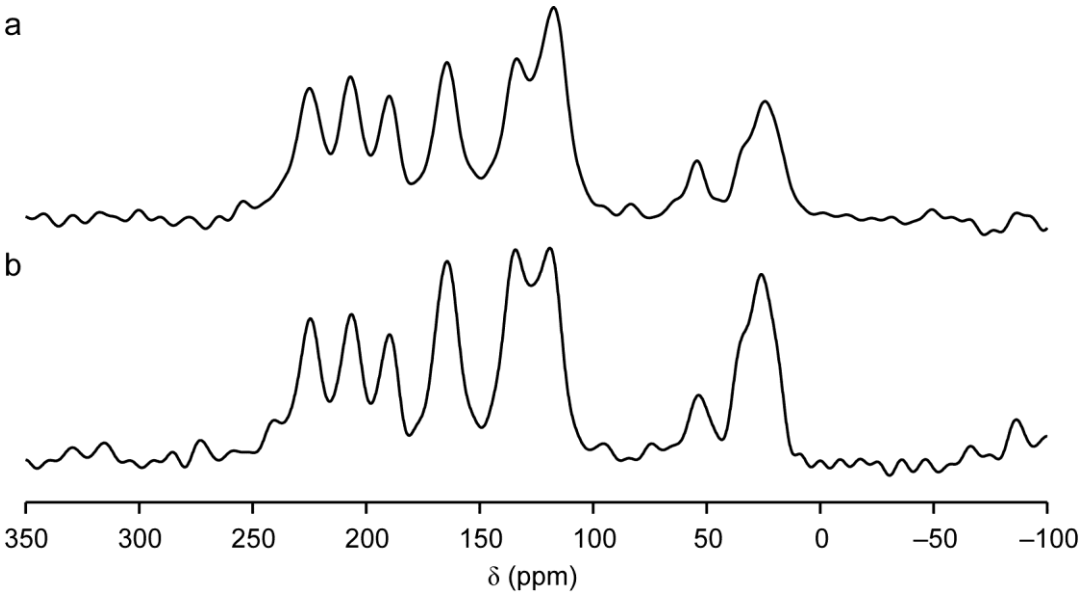

Figure 4.40. ^{13}C NMR spectra of Nd(btc)$(dmu)_2$, recorded at (a) 14.1 T with 60 kHz MAS and (b) 20.0 T with 62.5 kHz MAS.

agree with those expected for H_3btc (166.1, 133.8 and 132.1 ppm), dmu (161.2 and 26.8 ppm) and cc (68.1, 56.3 and 54.7 ppm). However, it is well known that the bonding between lanthanide ions and their ligands is predominantly electrostatic, owing to the fact that the f orbitals are relatively compact and typically do not interact with the ligand orbitals. This negligible covalency means that there will be little or no contact interaction between Nd^{3+} and ^{13}C and only the pseudocontact interaction will contribute significantly to the isotropic shifts of ^{13}C.

As demonstrated by Bertini *et al*. for a paramagnetic metalloprotein,[31] and by Brough *et al*. for lanthanide acetates,[32] the pseudocontact shifts in a crystalline material may be interpreted in geometrical manner. In such an approach, the contribution of each paramagnetic centre is determined, and all non-negligible contributions summed to give the total pseudocontact shift. However, this approach was not adopted here, owing to the complexity of the structure of the Ln(btc)$(dmu)_2$ MOF relative to the metalloprotein (which had a low concentration of metal ions, making analysis relatively straightforward) and the lanthanide acetates (the symmetry and structural simplicity of which simplified the analysis). Furthermore, it is unclear whether there will be any magnetic exchange between the two Nd^{3+} ions in Nd(btc)$(dmu)_2$, which would affect the "point charge" treatment assumed in the

geometry-based analysis. Further investigation of the magnetic properties of this MOF would be required before such analysis could be attempted.

Identification and assignment of the resonances arising from the btc linkers of the framework could be achieved by synthesis of ^{13}C-labeleld Nd(btc)(dmu)$_2$. Such an approach would also allow resonances arising from dmu and choline chloride to be identified and, through geometric analysis (which would be greatly simplified with a tentative assignment of resonances), a full assignment may be possible.

Although the assignment of the ^{13}C NMR spectrum of Nd(btc)(dmu)$_2$ has not been achieved here, the work carried out demonstrates that the experimental approached developed for the study of HKUST-1 and STAM-1 can be extended to MOFs containing lanthanide group metals. Furthermore, the ^{13}C NMR spectrum of Nd(btc)(dmu)$_2$ demonstrates that the extent of the paramagnetic effects on the NMR spectrum depend not just on the number of unpaired electrons per metal centre (Nd^{3+} has three nominally-unpaired electrons, whereas Cu^{2+} has only one), but also on the extent and type of interactions between the metal centre and the ^{13}C species.

4.6.4 Summary

The work presented here demonstrates that the experimental methodology developed for the study of paramagnetic MOFs can be extended to those based on lanthanide group metals. The ^{13}C NMR spectrum of Nd(btc)(dmu)$_2$ demonstrates that the extent of the paramagnetic effects on the NMR spectrum are strongly dependent on the extent of the covalent bonding between the metal centre and ^{13}C nuclei within the MOF. The study of this MOF by ^{13}C NMR would benefit from an extension of the isotopic labelling procedures for H_3btc, described in the study of HKUST-1 and STAM-1, as even a tentative assignment of the ^{13}C NMR spectrum is impossible at natural abundance. However, assignment of the ^{13}C NMR spectrum of the diamagnetic La(btc)(dmu)$_2$ was achieved by comparison of the experimental isotropic shifts with those calculated by CASTEP (after full structural optimisation).

4.7 CHAPTER SUMMARY

This chapter has presented studies of three paramagnetic MOF systems; the Cu-based HKUST-1 and STAM-1, the CPO-27-M series, (M = Mg, Mn, Co, Ni, Zn), and the lanthanide-based Ln(btc)$(dmu)_2$, (Ln = La, Nd). Initially, methods suitable for observing the ^{13}C NMR spectra of paramagnetic MOFs at natural abundance were investigated, and it was shown that a combination of rapid MAS and a spin-echo experiment was required. In addition, frequency-stepped acquisition was required in many cases, in order to observe all spectral resonances. It was shown that the use of lower B_0 field strengths assists this process of observing the complete spectrum.

Assignment of the ^{13}C NMR spectra of these paramagnetic MOFs was shown to be challenging, and isotopic labelling of ^{13}C provided the most reliable means of assignment, although useful information was also obtained from CP MAS spectra, allowing the identification of C species directly bonded to H. Two reasonably efficient and low-cost routes to the synthesis of ^{13}C labelled H_3btc were developed and have enabled complete and unambiguous assignment of the ^{13}C NMR spectra of HKUST-1 and STAM-1. This labelling approach could readily be applied to Nd(btc)$(dmu)_2$, which also contains the btc linker. However, labelling of the H_4dhtp required for the synthesis of CPO-27 was not attempted, owing to the difficulty of the synthesis of isotopically-enriched materials (*e.g.*, a limited number of available cost-effective starting materials and a desire to minimise the number of steps in the reaction while maximising the yield of each step).

It was demonstrated for HKUST-1 and STAM-1 that solid-state ^{13}C NMR spectra are very sensitive to dehydration of the MOF, particularly for STAM-1, which undergoes a reversible conformational change on dehydration. For HKUST-1, the ^{13}C NMR spectra were also shown to be sensitive to the chemical nature of the guest species. This sensitivity to different guest species is likely to be of great use as MOFs find ever more applications, particularly those involving loading of multiple guest species simultaneously. As an example, work on HKUST-1 loaded with both metronidazole and NO – a material shown to be a powerful antibiotic, was supported by the use of solid-state NMR spectroscopy.[25]

The differences between the ^{13}C NMR spectra of the three families of MOFs studied here demonstrates that the ease of acquiring the solid-state ^{13}C NMR spectrum of a MOF does not depend simply on whether the material contains nominally-unpaired electrons, but also on the interactions of those electrons with the ^{13}C nuclei. When this interaction is entirely through space (*i.e.*, pseudocontact), as in $Nd(btc)(dmu)_2$, it is relatively easy to observe the ^{13}C NMR spectrum, and frequency stepping may not be required (although assignment then becomes more challenging). However, when the interaction is through-bond (*i.e.*, contact), as in CPO-27-M (M = Mn, Co and Ni), the spectrum may be very challenging to record, with poor sensitivity and large anisotropies resulting in very long experimental times.

4.8 REFERENCES

1. D. M. Dawson, L. E. Jamieson, M. I. H. Mohideen, A. C. McKinlay, I. A. Smellie, R. Cadou, N. S. Keddie, R. E. Morris and S. E. Ashbrook, *Phys. Chem. Chem. Phys.*, **2013**, *15*, 919.

2. B. Juršić, *Can. J. Chem.*, **1989**, *67*, 1381.

3. H. A. Hopper, *MChem Thesis*, University of St Andrews, **2013**.

4. B. Xiao, P. S. Wheatley, X. Zhao, A. J. Fletcher, S. Fox, A. G. Rossi, I. L. Megson, S. Bordiga, L. Regli, K. M. Thomas and R. E. Morris, *J. Am. Chem. Soc.*, **2007**, *129*, 1203.

5. M. I. H. Mohideen, B. Xiao, P. S. Wheatley, A. C. McKinlay, Y. Li, A. M. Z. Slawin, D. W. Aldous, N. F. Cessford, T. Düren, X. Zhao, R. Gill, K. M. Thomas, J. M. Griffin, S. E. Ashbrook and R. E. Morris, *Nature Chem.*, **2011**, *3*, 304.

6. P. D. C. Dietzel, R. Blom and H. Fjellvåg, *Eur. J. Inorg. Chem.*, **2008**, 3624.

7. H. Wu, W. Zhou and T. Yildirim, *J. Am. Chem. Soc.*, **2009**, *131*, 4995.

8. P. D. C. Dietzel, Y. Morita, R. Blom and H. Fjellvåg, *Angew. Chem. Int. Ed.*, **2005**, *44*, 6354.

9. N. L. Rosi, J. Kim, M. Eddaoudi, B. L. Chen, M. O'Keeffe and O. M. Yaghi, *J. Am. Chem. Soc*, **2005**, *127*, 1504.

10. F. Himeur, I. Stein, D. S. Wragg, A. M. Z. Slawin, P. Lightfoot and R. E. Morris, *Solid State Sci.*, **2010**, *12*, 418.

11. GAUSSIAN 09, Revision A.02, M. J. Frisch, *et al.*, Gaussian, Inc., Wallingford, CT, **2009**.

12. M. D. Segall, P. J. D. Lindan, M. J. Probert, C. J. Pickard, P. J. Hasnip, S. J. Clark and M. C. Payne, *J. Phys. Cond. Matter*, **2002**, *14*, 2717.

13. S. J. Clark, M. D. Segall, C. J. Pickard, P. J. Hasnip, M. J. Probert, K. Refson and M. C. Payne, *Z. Kristallogr.*, **2005**, *220*, 567.

14. V. R. Seymour, *PhD Thesis*, University of St Andrews, 2013.

15. J. P. S. Mowat, V. R. Seymour, J. M. Griffin, S. P. Thompson, A. M. Z. Slawin, D. Fairen-Jimenez, T. Düren, S. E. Ashbrook and P. A. Wright, *Dalton Transact.*, **2012**, *41*, 3937.

16. T. Loiseau, C. Serre, C. Huguenard, G. Fink, F. Taulelle, M. Henry, T. Bataille and G. Férey, *Chem. Eur. J.*, **2004**, *10*, 1373.

17. M. Rangus, M. Mazaj, N. Z. Logar, G. Mali and V. Kaučič, 7th *Alpine Conference on Solid-State NMR*, Chamonix-Mont Blanc, France, **2011**.

18. J. Xu, V. V. Terskikh and Y. Huang, *J. Phys. Chem. Lett.*, **2013**, *4*, 7.

19. J. Xu, V. V. Terskikh and Y. Huang, *Chem. Eur. J.*, **2013**, *19*, 4432.

20. A. Sutrisno, V. V. Terskikh, Q. Shi, Z. Song, J. Dong, S. Y. Ding, W. Wang, B. R. Provost, T. D. Daff, T. K. Woo and Y. Huang, *Chem. Eur. J.*, **2012**, *18*, 12251.

21. S. S. Y. Chui, S. M. F. Lo, J. P. H. Charmant, A. G. Orpen and I. D. Williams, *Science*, **1999**, *283*, 1148.

22. D. Britt, D. Tranchemontagne and O. M. Yaghi, *Proc. Nat. Acad. Sci. USA*, **2008**, *105*, 11623.

23. F. Gul-E-Noor, B. Jee, A. Pöppl, M. Hartmann, D. Himsl and M. Bertmer, *Phys. Chem. Chem. Phys.*, **2011**, *13*, 7783.

24. G. W. Peterson, G. W. Wagner, A. Balboa, J. Mahle, T. Sewell and C. J. Karwacki, *J. Phys. Chem. C*, **2009**, *113*, 13906.

25. A. C. McKinlay, P. K. Allan, C. L. Renouf, M. J. Duncan, S. J. Warrender, D. M. Dawson, S. E. Ashbrook, B. Gil, B. Marszalek, T. Düren, J. J. Williams, C. Charrier, D. Mercer, S. J. Teat and R. E. Morris, *in preparation*.

26. P. Horcajada, R. Gref, T. Baati, P. K. Allan, G. Maurin, P. Couvreur, G. Férey, R. E. Morris and C. Serre, *Chem. Rev.*, **2012**, *112*,1232.

27. J. L. C. Rowsell and O. M. Yaghi, *Micropor. Mesopor. Mater.*, **2004**, *73*, 3.

28. J. Lee, O. K. Farha, J. Roberts, K. A. Scheidt, S. T. Nguyen and J. T. Hupp, *Chem. Soc. Rev.*, **2009**, *38*, 1450.

29. M. I. H. Mohideen, *PhD Thesis*, University of St Andrews, 2011.

30. X. X. Zhang, S. S. Y. Chui and I. D. Williams, *J. Appl. Phys.*, **2000**, *87*, 6007.

31. I. Bertini, L. Emsley, M. Lelli, C. Luchinat, J. Mao and G. Pintacuda, *J. Am. Chem. Soc.*, **2010**, *132*, 5558.

32. A. R. Brough, C. P. Grey and C. M. Dobson, *J. Am. Chem. Soc.*, **1993**, *115*, 7318.

33. G. de Combarieu, M. Morcrette, F. Millange, N. Guillou, J. Cabana, C. P. Grey, I. Margiolaki, G. Férey and J. M. Tarascon, *Chem. Mater.*, **2009**, *21*, 1602.

34. C. P. Grey, C. M. Dobson, A. K. Cheetham and R. J. B. Jakeman, *J. Am. Chem. Soc.*, **1989**, *111*, 505.

35. C. P. Grey, M. E. Smith, A. K. Cheetham, C. M. Dobson and R. Dupree, *J. Am. Chem. Soc.*, **1990**, *112*, 4670.

36. J. Kim, D. S. Middlemiss, N. A. Chernova, B. Y. X. Zhu, C. Masquelier and C. P. Grey, *J. Am. Chem. Soc.*, **2010**, *132*, 16825.

37. Y. Ishii, N. P. Wickramasinghe and S. Chimon, *J. Am. Chem. Soc.*, **2003**, *125*, 3438.

38. N. P. Wickramasinghe and Y. Ishii, *J. Magn. Reson.*, **2006**, *181*, 233.

39. K. Liu, D. Ryan, K. Nakanishi and A. McDermott, *J. Am. Chem. Soc.*, **1995**, *117*, 6897.

40. G. Kervern, G. Pintacuda and L. Emsley, *Chem. Phys. Lett.*, **2007**, *435*, 157.

41. Y. Y. Tong, *J. Magn. Reson. A*, **1996**, *119*, 22.

42. G. Mali, A. Ristić and V. Kaučič, *J. Phys. Chem. B*, **2005**, *109*, 10711.

43. F. Gul-E-Noor, B. Jee, M. Mendt, D. Himsl, A. Pöppl, M. Hartmann, J. Haase, H. Krautscheid and M. Bertmer, *J. Phys. Chem. C*, **2012**, *116*, 20866.

44. A. Lesage, M. Bardet and L. Emsley, *J. Am. Chem. Soc.*, **1999**, *121*, 10987.

45. D. J. Duchamp and R. E. Marsh, *Acta Crystallogr.*, **1969**, *B25*, 5.

46. L. E. Jamieson, *MChem Thesis*, University of St Andrews, **2012**.

47. T. Cendak, T. B. Čelič, M. Rangus, N. Z. Logar, G. Mali and V. Kaučič, *7th Alpine Conference on Solid-State NMR*, Chamonix-Mont Blanc, France, **2011**.

48. T. B. Čelič, M. Mazaj, N. Guillou, V. Kaučič and N. Logar, *3rd Croatian-Slovenan Symposium on Zeolites*, Zagreb, Croatia, **2010**.

49. M. Melník, M. Dunaj-Jurčo and M. Handlovič, *Inorg. Chim. Acta*, **1984**, *86*, 185.

50. M. M. Helmkamp and M. E. Davis, *Ann. Rev. Mater. Sci.*, **1995**, *25*, 161.

51. V. Uskoković and M. Drofenik, *Surf. Rev. Lett.*, **2005**, *12*, 239.

52. M. Ma, D. Zacher, X. N. Zhang, R. A. Fischer and N. Metzler-Nolte, *Cryst. Growth Des.*, **2011**, *11*, 185.

53. P. Horcajada, T. Chalati, C. Serre, B. Gillet, C. Sebrie, T. Baati, J. F. Eubank, D. Heurtaux, P. Clayette, C. Kreuz, J.-S. Chang, Y. K. Hwang, V. Marsaud, P.-N. Bories, L. Cynober, S. Gil, G. Férey, P. Couvreur and R. Gref, *Nature Mater.*, **2010**, *9*, 172.

54. A. C. McKinlay, B. Xiao, D. S. Wragg, P. S. Wheatley, I. L. Megson and R. E. Morris, *J. Am. Chem. Soc.*, **2008**, *130*, 10440.

55. O. M. Williams and R. C. Spencer, *Brit. Med. Bull.*, **2009**, *91*, 87.

56. D. Massiot, F. Fayon, M. Capron, I. King, S. Le Calve, B. Alonso, J. O. Durand, B. Bujoli, Z. H. Gan and G. Hoatson, *Magn. Reson. Chem.*, **2002**, *40*, 70.

57. N. M. Blaton, O. M. Peeters and C. J. Deranter, *Acta Crystallogr.*, **1979**, *B35*, 2465.

58. C. P. Smyth and K. B. McAlpine, *J. Chem. Phys.*, **1933**, *1*, 60.

59. S. M. Grayson and J. M. J. Fréchet, *Chem. Rev.*, **2001**, *101*, 3819.

60. J. P. S. Mowat, S. R. Miller, J. M. Griffin, V. R. Seymour, S. E. Ashbrook, S. P. Thompson, D. Fairen-Jimenez, A. M. Banu, T. Düren and P. A. Wright, *Inorg. Chem.*, **2011**, *50*, 10844.

61. G. A. Olah, M. W. Meyer and N. A. Overchuk, *J. Org. Chem.*, **1964**, *29*, 2313.

62. S. Antonijevic and S. Wimperis, *J. Magn. Reson.*, **2003**, *164*, 343.

63. S. Antonijevic and S. Wimperis, *J. Chem. Phys.*, **2005**, *122*, 044312.

64. L. S. Batchelder, "Deuterium NMR in Solids" in eMagRes, ed. R. K Harris, and R. Wasylishen, Wiley, **2007**.

65. S. Bhattacharjee, J.-S. Choi, S.-T. Yang, S. B. Choi, J. Kim and W.-S. Ahn, *J. Nanosci. Nanotechnol.*, **2010**, *10*, 135.

66. P. D. C. Dietzel, R. E. Johnsen, R. Blom and H. Fjellvåg, *Chem. Eur. J.*, **2008**, *14*, 2389.

67. P. D. C. Dietzel, V. Besikiotis and R. Blom, *J. Mater. Chem.*, **2009**, *19*, 7362.

68. P. He, J. Xu, V. V. Terskikh, A. Sutrisno, H.-Y. Nie and Y. Huang, *J. Phys. Chem. C*, **2013**, *117*, 16953.

69. X. Kong, E. Scott, W. Ding, J. A. Mason, J. R. Long and J. A. Reimer, *J. Am. Chem. Soc*, **2012**, *134*, 14341.

70. H. E. Gottlieb, V. Kotlyar and A. Nudelman, *J. Org. Chem.*, **1997**, *62*, 7512.

71. M. D. Allendorf, C. A. Bauer, R. K. Bhakta and R. J. T. Houk, *Chem. Soc. Rev.*, **2009**, *38*, 1330.

70. T. Yamaji, T. Saito, K. Hayamizu, M. Yanagisawa, O. Yamamoto, N. Wasada, K. Somento, S. Kinugasa, K. Tanabe, T. Tamura and J. Hiraishi, *Spectral Database for Organic Compounds*, http://sdbs.riodb.aist.go.jp/, Accessed March, **2013**.

5 ALUMINOPHOSPHATES

5.1 CHAPTER OVERVIEW

Aluminophosphate zeolites[1] (AlPOs) and their silicon- or metal-substituted analogues (SAPOs and M(e)APOs) are of interest in applications such as catalysis, gas storage and drug delivery. These systems contain a large number of NMR-active nuclei, including $^{1/2}$H, ^{13}C, $^{14/15}$N, ^{17}O, ^{19}F, ^{27}Al, ^{29}Si and ^{31}P, and solid-state NMR is capable of providing a large amount of useful information on the detailed local structure, disorder and dynamics present. The first part of this chapter explores the relationship between the local structure of AlPOs and their ^{27}Al and ^{31}P NMR parameters from a computational perspective, providing a link between the crystal structure of an AlPO and its ^{31}P, ^{27}Al and ^{17}O NMR spectra, and also highlighting the sensitivity of solid-state NMR to the structural parameters of AlPOs. The relationships determined are then used as the basis for a new code for the rapid calculation of approximate ^{27}Al and ^{31}P NMR parameters for calcined AlPOs. This code may find application in the rapid "validation" of crystallographic structures with respect to solid-state NMR spectra, as well as in high-throughput computational modelling approaches. The second part of the chapter uses a combination of multinuclear solid-state NMR spectroscopy and DFT calculations to investigate the AlPO-53 system, including the ambient hydration of JDF-2 to AlPO-53(A) and the ordering of methylammonium cations and H_2O in AlPO-53(A).

5.2 ACKNOWLEDGEMENTS

Work carried out and reported in this chapter would have been impossible without Professor Richard Walton and Dr Zoe Lethbridge (University of Warwick), who provided many of the samples studied. Professor David Bryce (University of Ottawa) is thanked for his helpful input on the calculations involving model clusters.

5.3 EXPERIMENTAL DETAILS

5.3.1 Syntheses

All samples studied in this chapter were provided by the group of Professor Richard Walton (University of Warwick). A brief summary of their syntheses is given here.

5.3.1.1 AlPO-53(A)

As previously reported,[2] AlPO-53(A) was synthesised according to the procedure of Kirchner *et al*.[3] $Al_2O_3 \cdot 1.9H_2O$ (1 g) was stirred into a solution of 1.7 g H_3PO_4 (85% in H_2O) in 4.7 g H_2O, followed by addition of 0.7 cm^3 methylamine solution (40% in H_2O), with stirring maintained throughout. The resulting gel was heated in a Teflon-lined autoclave at 150 °C for 7 days and then cooled to room temperature. A white solid was recovered by filtration, washed with water and dried in air at room temperature to yield AlPO-53(A). Other samples of AlPO-53(A) were prepared by exposing JDF-2 to air for up to 3 months or stirring JDF-2 in water for 7 days.

5.3.1.2 JDF-2

As previously reported,[2] the synthesis of JDF-2 followed the above procedure for the synthesis of AlPO-53(A). However, by drying the washed white solid at 70 °C rather than room temperature, the product obtained was the dehydrated JDF-2 rather than the hydrated AlPO-53(A). JDF-2 was also prepared by heating samples of AlPO-53(A) to temperatures of 100-110 °C overnight.

5.3.2 Solid-State NMR

All solid-state NMR spectra were recorded with B_0 field strengths of 9.4 or 14.1 T. Further details are given in the text, figure captions and Appendix A.

5.3.3 Monitoring of Ambient Conditions

The ambient conditions (temperature and relative humidity) were monitored using an ETI Therma-Hygrometer, accurate to within ± 1 °C and ± 3% relative humidity.

5.3.4 First-Principles DFT Calculations

First-principles calculations reported in Section 5.4 were carried out using the codes GAUSSIAN03 (revision D.01[4]) and CASTEP 4.3.[5, 6] Calculations for AlPO-53(A)

and related structures were carried out using CASTEP 6.[5, 6] All calculations using CASTEP were carried out using a cut-off energy of 60 Ry. Sampling of the Brillouin zone used a Monk-Packhurst grid with a k-point spacing of 0.04 $Å^{-1}$. CASTEP 6 calculations used reference shieldings of 22.84 ppm (^{1}H), 172.79 ppm (^{13}C), –156.55 ppm (^{15}N), 547.90 ppm (^{27}Al) and 277.91 ppm (^{31}P), obtained using the experimental NMR spectra of JDF-2. Calculated ^{1}H shieldings were scaled by a factor of 0.721, as described in Chapter 2. Scaling was not carried out for the other nuclei. For ^{27}Al, CASTEP calculates both the magnitude and sign of C_Q, but only the magnitude is reported here, owing to the difficulty of measuring the sign experimentally.

5.4 THEORETICAL STRUCTURE-PARAMETER RELATIONSHIPS IN ALPOS

5.4.1 Introduction

The structures of solids are often determined by a combination of Bragg diffraction, solid-state NMR and elemental analysis techniques. However, none of these techniques can provide a complete structural solution, and all provide slightly different aspects of the answer, with different sensitivity to structural features on different length- and timescales (as discussed briefly in Chapter 2). Therefore, it is essential to be able to relate the results of the different analytical techniques to each other to arrive at a more complete description of the material in question. This study focuses on the relationship between structures obtained by Bragg diffraction methods, which are sensitive to the long-range average structure and solid-state NMR, which is more sensitive to the local arrangement of atoms around individual nuclear species. The local structure of a tetrahedral atom, T, (T = Si or Al in aluminosilicates, and T = Al or P in AlPOs) in a zeolitic framework can be described in terms of the four T-O bond lengths and six O-T-O angles of the TO_4 tetrahedron and the four T-O-T′ bond angles connecting the TO_4 tetrahedron to its neighbouring $T'O_4$ tetrahedra. It can readily be appreciated that changes in these bond geometries are likely to lead to a change in atomic orbital overlap between T and O and, consequently, the electron distribution around the T atom will be influenced by these geometric parameters. As both the chemical shift interaction and the electric field gradient (and, hence, quadrupolar interaction) are influenced by the local electron

distribution, a change in the local bond geometry at a T atom is likely to cause a change to its NMR spectrum. There are many documented cases of next-nearest neighbour (NNN) effects on the NMR spectra of, *e.g.*, ^{29}Si in zeolites with different numbers of Si-O-Si and Si-O-Al linkages,[7, 8] ^{31}P in MgAPOs with different numbers of P-O-Mg and P-O-Al linkages,[9] and ^{31}P in a series of orthophosphates with different NNN cations.[10] Furthermore, the coordination number of Al has a major effect on the ^{27}Al chemical shift in such frameworks.[7, 8] However, the present study is concerned with calcined $AlPO_4$ frameworks, for which the NNN T′ atoms (T′ = Al if T = P, and *vice versa*) are all the same and all Al is tetrahedrally coordinated.

5.4.2 The Effect of Local Structure on ^{31}P NMR Parameters

In 1984 (*i.e.*, two years after AlPOs were first reported[1]), Müller *et al.* reported a relationship between the average P-O-Al bond angle, $\bar{\theta}_{POAl}$, and δ_{iso} for both ^{31}P and ^{27}Al in three dense $AlPO_4$ phases.[11] Surprisingly, the change in δ_{iso} with $\bar{\theta}_{POAl}$, $d\delta/d\bar{\theta}_{POAl}$, was reported as −0.51 ppm per degree for ^{31}P, ^{27}Al and ^{29}Si (the ^{29}Si data were for the SiO_2 analogues of the $AlPO_4$ phases studied). However, on closer inspection of the original work, different values of $d\delta/d\bar{\theta}_{POAl}$ are reported for ^{31}P and ^{27}Al, with the value of –0.51 ppm per degree being reported for a combined dataset. In addition, the study included only three dense $AlPO_4$ phases and their SiO_2 analogues; cristobalite, berlinite and tridymite, giving only three data points for each nucleus. Nevertheless, since its publication, this relationship has been widely used to assign the ^{31}P NMR spectra of many phosphate materials, including templated[12-27] and calcined[24, 26, 28, 29] AlPOs, AlPO-like clusters,[30, 31] SAPOs,[32, 33] GaPOs,[34, 35] a ZnPO[36] and several other relevant structures.[19, 37-39] The results of these assignments are plotted in Figure 5.1, showing that there is a general trend for increasing δ_{iso} with decreasing $\bar{\theta}_{POT'}$ (T′ = Al, Si, Ga, Zn, *etc.*) for all classes of material included in the plot. More recently, Kanehashi *et al.*[40] determined that, for ^{31}P, $d\delta/d\bar{\theta}_{POAl}$ was –1.25 ppm per degree, based on a series of AlPOs in the literature. This relationship is also plotted in Figure 5.1. It can be seen that $d\delta/d\bar{\theta}_{POAl}$ and the y-intercepts are different for each class of material. Furthermore, there is a large scatter in the data, and all of the assignments were based on the relationship of Müller *et al.*, meaning that they are

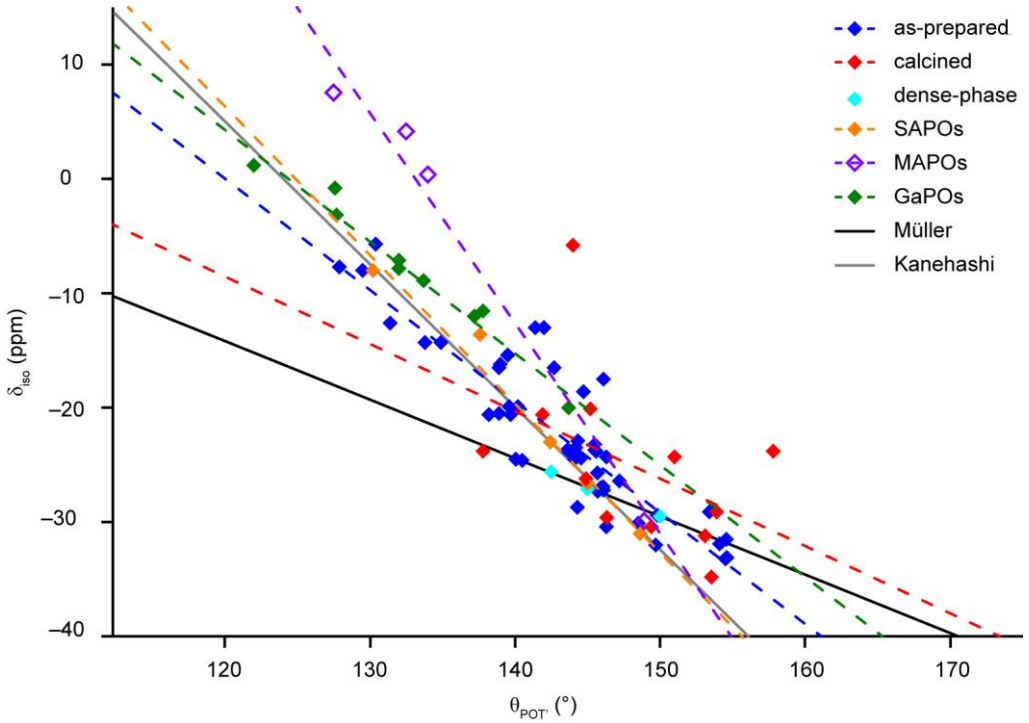

Figure 5.1. A plot of published experimental ^{31}P δ_{iso} against $\bar{\theta}_{POT'}$ (T′ = Al, Si, Ga or Zn) measured experimentally by Bragg diffraction for a range of AlPOs, SAPOs, GaPOs and other MAPOs, for which the Müller relationship was used to assign the resonances. The relationships published by Müller *et al.*[11] and Kanehashi *et al.*[40] are indicated. The broken lines indicate the lines of best fit for the datasets (the line of best fit for the dense phases is the relationship of Müller *et al.*).

inherently biased towards a trend for increasing δ_{iso} with decreasing $\bar{\theta}_{POT'}$. It should also be noted that the relationship of Müller *et al.* is in poor agreement with the experimental assignments, despite their basis in this relationship. These discrepancies may be partially explained by the fact that the values for both $\bar{\theta}_{POT'}$ and δ_{iso} are taken from experimental diffraction structures and NMR spectra, respectively, and so will be subject to inherent experimental errors. However, another possible explanation comes from work by Campomar,[41] which suggested that the mean P-O bond length, $\bar{r}_{PO}$, influenced the ^{31}P δ_{iso} in a series of phosphates and, if the works of Müller *et al.*, Kanehashi *et al.* and Campomar are to be believed, there must be at least two structural parameters influencing the chemical shifts of ^{31}P in metallophosphates.

In order to investigate the influence of $\bar{r}_{PO}$ and $\bar{\theta}_{POAl}$ on δ_{iso}, a series of model clusters of the formula $[P(OAl(OH)_3)_4]^{3-}$, shown in Figure 5.2 were considered. In

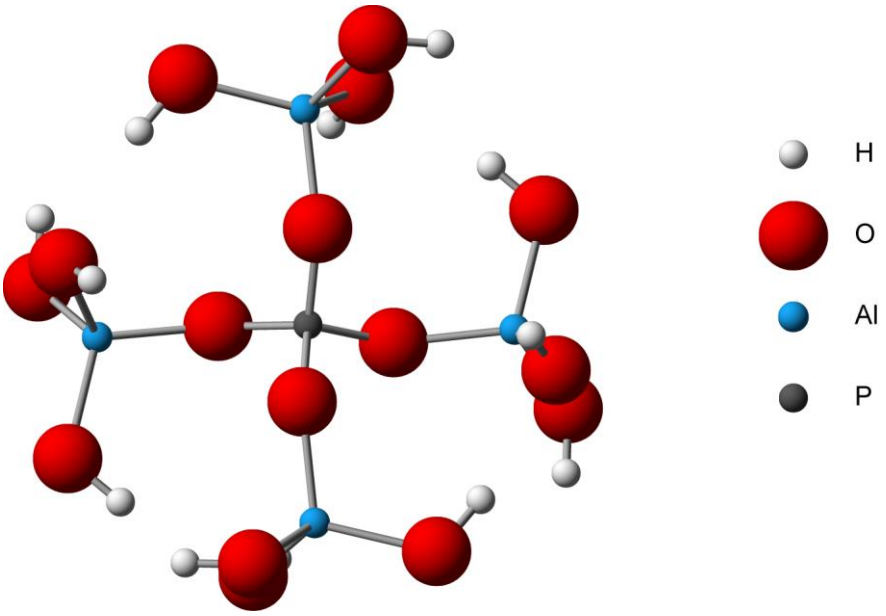

Figure 5.2. A $[P(OAl(OH)_3)_4]^{3-}$ cluster (series 1, n = 7) used as an analogue of the local environment of P in an AlPO framework.

the first set of clusters all P-O bond lengths and O-P-O bond angles were constrained to 1.52 Å and 109.47°, respectively, while $\bar{\theta}_{POAl}$ was varied according to Table 5.1. For each cluster, σ_{iso} for the central P was calculated with GAUSSIAN03,[4] and, as shown in Figure 5.3(a), when only $\bar{\theta}_{POAl}$ is varied (series 1), there is a strong linear correlation (R^2 = 0.995) between σ_{iso} and $\bar{\theta}_{POAl}$ with $d\sigma_{iso}/d\bar{\theta}_{POAl}$ = 1.05 ppm per degree. In series 2 and 3 (Figure 5.3(b)), $\bar{\theta}_{POAl}$ was kept constant at 140° while the maximum and minimum $\theta_{POAl(i)}$ (and, hence, the standard deviation, $\sigma(\theta_{POAl})$) were varied. There is a difference of up to 6.7 ppm (series 3, n = 7) in σ_{iso} relative to the corresponding point of series 1 (n = 7), in which $\bar{\theta}_{POAl}$ = 140 and $\sigma(\theta_{POAl})$ = 0, which indicates that the individual bond angles contribute to σ_{iso}, rather than just $\bar{\theta}_{POAl}$. Further evidence for this comes from series 4 (one angle varied systematically with the other three angles adjusted so that $\bar{\theta}_{POAl}$ = 140°), series 5 and 6 (maximum or minimum angle fixed, one angle varied systematically and the other two adjusted so that $\bar{\theta}_{POAl}$ = 140°), as shown in Figure 5.3(b), and series 7 (one angle varied systematically with the other three angles fixed at 140° so that $\bar{\theta}_{POAl}$ was also varied systematically), shown in Figure 5.3(a). In series 4, 5 and 6, there is a difference in

Table 5.1. The systematic variation of θ_{POAl} bond angles, in the series of model $[P(OAl(OH)_3)_4]^{3-}$ clusters (see Figure 5.2) studied here. The angles are expressed for the n^{th} member of the series, and the number of clusters in the series, N, is given.

Series	$\theta_{POAl(i)}$ (°)	N
1	$\theta_{POAl(1)} = \theta_{POAl(2)} = \theta_{POAl(3)} = \theta_{POAl(4)} = \bar{\theta}_{POAl} = 105 + 5n$	15
2	$\theta_{POAl(1)} = \theta_{POAl(2)} = 140$ $\theta_{POAl(3)} = 140 + 5n$ $\theta_{POAl(4)} = 140 - 5n$	7
3	$\theta_{POAl(1)} = \theta_{POAl(2)} = 140 + 5n$ $\theta_{POAl(3)} = \theta_{POAl(4)} = 140 - 5n$	7
4	$\theta_{POAl(1)} = 105 + 5n$ $\theta_{POAl(2)} = \theta_{POAl(3)} = \theta_{POAl(4)} = 140 + \left(\frac{140 - \theta_{POAl(1)}}{3}\right)$	14
5	$\theta_{POAl(1)} = 150$ $\theta_{POAl(2)} = 105 + 5n$ $\theta_{POAl(3)} = \theta_{POAl(4)} = \left(\frac{410 - \theta_{POAl(2)}}{2}\right)$	8
6	$\theta_{POAl(1)} = 120$ $\theta_{POAl(2)} = 175 - 5n$ $\theta_{POAl(3)} = \theta_{POAl(4)} = \left(\frac{440 - \theta_{POAl(2)}}{2}\right)$	11
7	$\theta_{POAl(1)} = 105 + 5n$ $\theta_{POAl(2)} = \theta_{POAl(3)} = \theta_{POAl(4)} = 140$	14
8	all angles randomly generated,[a] $115.58 \leq \theta_{POAl(i)} \leq 167.41$	20

a. For a full list of the angles used, see Appendix J.

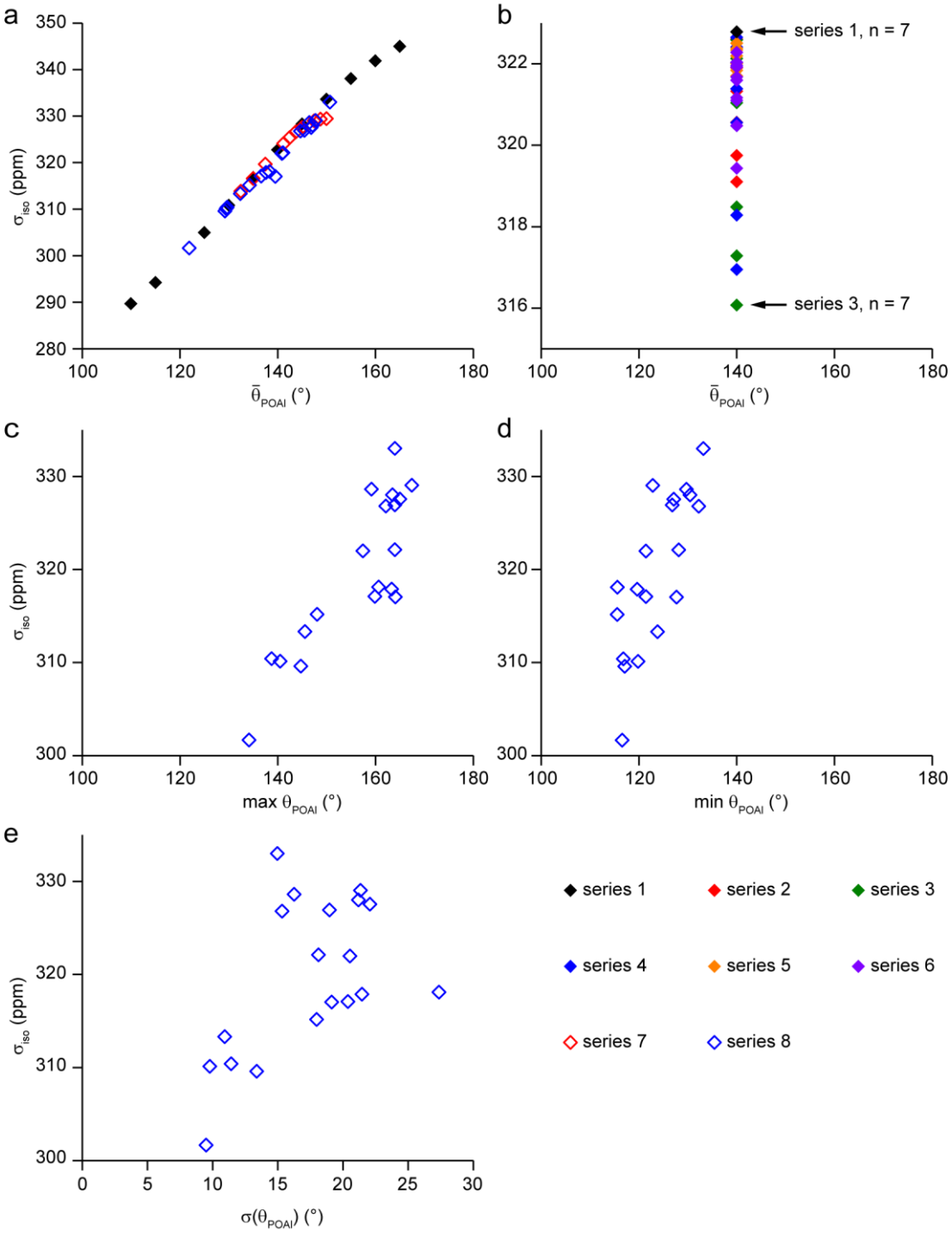

Figure 5.3. (a and b) Plots of calculated ^{31}P σ_{iso} against $\bar{\theta}_{POAl}$ for the series of model $[P(OAl(OH)_3)_4]^{3-}$ clusters detailed in Table 5.1. (c and d) Plots of calculated ^{31}P σ_{iso} against the (c) maximum and (d) minimum θ_{POAl} and (e) $\sigma(\theta_{POAl})$ for series 8.

σ_{iso} (of up to 5.79 ppm for series 4, n = 14) despite the constant $\bar{\theta}_{POAl}$. In series 7, where both $\bar{\theta}_{POAl}$ and $\sigma(\theta_{POAl})$ were varied, it can be seen that there is still a strong linear relationship for $n \leq 12$ ($\bar{\theta}_{POAl} \leq 147.5°$) but, at higher $\bar{\theta}_{POAl}$ (*i.e.*, when the maximum angle approaches 180° and $\sigma(\theta_{POAl})$ approaches a maximum of 20°), σ_{iso} is lower than expected, indicating that $\sigma(\theta_{POAl})$ contributes to σ_{iso}. In order to further investigate the contributions of $\bar{\theta}_{POAl}$ and $\sigma(\theta_{POAl})$ to σ_{iso}, another series of clusters, series 8, was studied, with randomly-generated $\theta_{POAl(i)}$ (with values between 115.58 and 167.41°). From Figure 5.3(a), it can be seen that series 1 and 8 have a very similar relationship between σ_{iso} and $\bar{\theta}_{POAl}$. The line of best fit for series 1,

$$\sigma_{iso} = 1.05\bar{\theta}_{POAl} + 174.5 \quad , \tag{5.1}$$

in excellent agreement with that for series 8,

$$\sigma_{iso} = 1.06\bar{\theta}_{POAl} + 172.4 \quad , \tag{5.2}$$

where σ_{iso} and the y intercept are in ppm, $\bar{\theta}_{POAl}$ in degrees and the gradient in ppm per degree. This similarity, combined with the high R^2 values (0.995 for series 1, 0.987 for series 8) suggests that, in more realistic cases, the $\bar{\theta}_{POAl}$ is actually a good predictor for σ_{iso}, despite the presence of $\sigma(\theta_{POAl})$ between 8.23 and 23.70° for series 8. This appears to confirm the work of Müller *et al*. and Kanehashi *et al*., although it should be noted that the gradients in Equations 5.1 and 5.2 are ~1.1 ppm per degree: between the value determined by Müller *et al*. (0.51 ppm per degree) and Kanehashi *et al*. (1.25 ppm per degree), but closer to the latter. The discrepancies between the three studies are likely to arise from the more limited size of the two experimental datasets – as can be seen from Figure 5.1, sampling of only three or four of the experimental data points could easily yield a wide range of gradients.

The results from series 8 would suggest that any contribution to σ_{iso} from $\sigma(\theta_{POAl})$ is minimal when compared to the contribution from $\bar{\theta}_{POAl}$. However, it is interesting to note that the change to σ_{iso} in series 2-7, relative to series 1 (n = 7) is always negative with increasing $\sigma(\theta_{POAl})$, which would appear to indicate that the minimum bond angle plays a more important role than the maximum bond angle in determining σ_{iso} (as a lower average bond angle leads to lower calculated shielding).

In order to investigate this, σ_{iso} for series 8 was plotted against the maximum and minimum θ_{POAl}, as shown in Figures 5.3(c and d). However, when all four bond angles are random, there is no clear difference between the relationships between σ_{iso} and the minimum or maximum θ_{POAl}, with both plots showing much more scatter than is present in Figure 5.3(a). As can be seen in Figure 5.3(e), $\sigma(\theta_{POAl})$ does not appear to have a significant linear correlation with σ_{iso} for series 8.

In a second set of structures, the effect of r_{PO} – suggested by Campomar[41] to influence δ_{iso} – was investigated. For this set of clusters, all O-P-O bond angles were constrained to 109.47°, P-O-Al angles were constrained to 140° and $\bar{r}_{PO}$ was varied systematically as given in Table 5.2. A further twenty clusters with randomly-generated bond lengths (between 1.45 and 1.57 Å) were also involved in the study. It can be seen from Figure 5.4(a) that, when only $\bar{r}_{PO}$ is allowed to vary and all other structural parameters are kept constant (series 9), σ_{iso} and $\bar{r}_{PO}$ are related by

$$\sigma_{iso} = -375.01\bar{r}_{PO} + 891.49 \quad , \tag{5.3}$$

with $R^2 = 0.9876$. However, the correlation is significantly improved ($R^2 = 1.0000$) by using a quadratic function of $\bar{r}_{PO}$:

$$\sigma_{iso} = -1158.9\bar{r}_{PO}^2 + 3166.2\bar{r}_{PO} - 1812.5 \quad . \tag{5.4}$$

In series 10 and 11, the maximum and minimum r_{PO} were varied while $\bar{r}_{PO}$ was kept constant at 1.52 Å, allowing investigation of the influence of the standard deviation of r_{PO}, $\sigma(r_{PO})$. Figure 5.4(b) shows that the difference in $\sigma(r_{PO})$ (of up to 0.058 Å for series 11, n = 5) led to a difference in σ_{iso} of just 0.18 ppm, relative to the structure with the $\bar{r}_{PO}$ = 1.52 Å but $\sigma(r_{PO}) = 0$ (series 9, n = 8). This indicates that $\sigma(r_{PO})$ has limited influence on σ_{iso}, although it may be that the range of $\sigma(r_{PO})$ considered here was too small to observe effects that would be more apparent with a greater distribution of r_{PO}. For series 12, both $\bar{r}_{PO}$ and $\sigma(r_{PO})$ were varied, with one bond length systematically increased while the other three were always 1.52 Å. As can be seen in Figure 5.4(a), a good linear relationship between σ_{iso} and $\bar{r}_{PO}$ was observed,

$$\sigma_{iso} = -352.37\bar{r}_{PO} + 858.37, \tag{5.5}$$

with $R^2 = 0.9993$, and a marginally stronger correlation ($R^2 = 0.9999$) for the

Table 5.2. The systematic variation of r_{PO} bond lengths in the series of model $[P(OAl(OH)_3)_4]^{3-}$ clusters (see Figure 5.2) studied here. The lengths are expressed for the n^{th} member of the series, and the number of clusters in the series, N, is given.

Series	$r_{PO(i)}$ / Å	N
9	$r_{PO(1)} = r_{PO(2)} = r_{PO(3)} = r_{PO(4)} = \bar{r}_{PO} = 1.44 + 0.01n$	14
10	$r_{PO(1)} = r_{PO(2)} = 1.52$ $r_{PO(3)} = 1.52 + 0.01n$ $r_{PO(4)} = 1.52 - 0.01n$	5
11	$r_{PO(1)} = r_{PO(2)} = 1.52 + 0.01n$ $r_{PO(3)} = r_{PO(4)} = 1.52 - 0.01n$	5
12	$r_{PO(1)} = 1.47 + 0.01n$ $r_{PO(2)} = r_{PO(3)} = r_{PO(4)} = 1.52$	9
13	all lengths randomly generated,[a] $1.45 \leq r_{PO(i)} \leq 1.57$	20

a. For a full list of the lengths used, see Appendix J.

quadratic relationship,

$$\sigma_{iso} = -1465.2\bar{r}_{PO}^2 + 4098.5\bar{r}_{PO} - 2521.6 \ . \quad (5.6)$$

The deviation in the coefficients of Equations 5.4 and 5.6, which may arise owing to the small, but apparently significant, contribution from $\sigma(r_{PO})$ observed for series 10 and 11. However, as was observed for series 1-8, the effect of $\sigma(\theta_{POAl})$ appeared to be artificially enhanced when the bond angles were varied systematically, compared to the random variation of bond angles used for series 8. This can again be seen with series 13, for which the best linear agreement ($R^2 = 0.9929$) was

$$\sigma_{iso} = -314.27\bar{r}_{PO} + 800.44 \ , \quad (5.7)$$

while the quadratic relationship,

$$\sigma_{iso} = -1189.7\bar{r}_{PO}^2 + 3288.6\bar{r}_{PO} - 1906.3 \ , \quad (5.8)$$

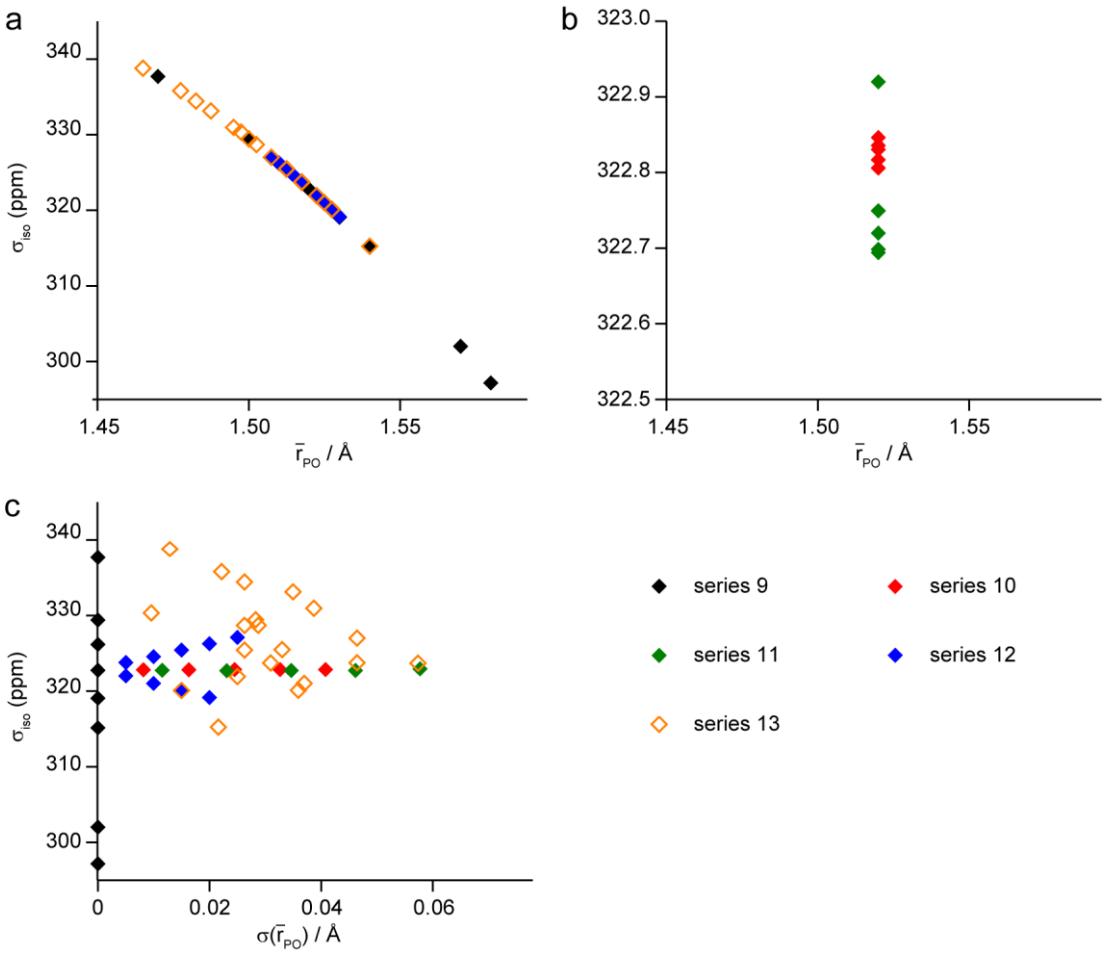

Figure 5.4. Plot of calculated ^{31}P σ_{iso} against (a and b) $\bar{r}_{PO}$ and (c) $\sigma(r_{PO})$ for the series of model $[P(OAl(OH)_3)_4]^{3-}$ clusters detailed in Table 5.2.

yielded $R^2 > 0.9999$. It can be seen that the coefficients in Equation 5.8 are similar to those of Equation 5.4, indicating that, when the P-O-Al bond angles are fixed, the quadratic relationship with $\bar{r}_{PO}$ dominates σ_{iso}, even in the presence of a non-zero $\sigma(r_{PO})$ (up to 0.057 Å for series 13).

The above studies suggest that both $\bar{\theta}_{POAl}$ and $\bar{r}_{PO}$ have a significant effect on the calculated ^{31}P σ_{iso} (and, therefore, presumably on the experimental δ_{iso}). This finding is relatively unsurprising when one considers that the shielding arises in part from the motion of electrons near to the P nucleus, which will be affected by the extent of overlap of the electronic orbitals of P and O, which will depend on both the bond length and angle. Therefore, while the works of Müller *et al.*,[11] Kanehashi *et al.*[40] and Campomar[41] all have some validity, the relationships reported do not fully

capture the relationship between σ_{iso} and the structure of AlPOs, owing to their assumption that the influence of one structural parameter dominates σ_{iso}.

In order to ascertain whether the results of the model cluster calculations could be applied to the periodic structures of AlPOs, it is necessary to compare the ^{31}P isotropic shifts of a series of calcined AlPOs with their crystal structures. However, such an approach suffers from two major issues. Firstly, there are several unreliable crystal structures for calcined AlPOs in the literature, as demonstrated by AlPO-14, for which NMR parameters calculated for the published crystal structure did not agree well with experiment but, once the structure was optimised using DFT, the agreement was considerably better,[28, 42] suggesting that the error lay with the original structure rather than the ability to calculate reliable NMR parameters (see, *e.g.*, Figure 2.18). Consequently, the equivalence of a reported structure of a material and the structure of the material actually present in the NMR experiment may not always be assumed. Secondly, given the existence of two conflicting chemical shift scales for ^{31}P,[10, 43] differing by 1.6 ppm (*i.e.*, on the order of the shift differences expected to arise from changes in the local structure), and the fact that resonances may be broadened and overlapped in the ^{31}P NMR spectra of calcined AlPOs, the reported experimental chemical shifts cannot always be assumed to be accurate, or reported to the same reference point (the reference point used is not always clear in the literature). Therefore, an alternative strategy was required to assess the relevance of the model cluster calculations. First-principles DFT calculations have been shown in the literature to give excellent agreement between experimental NMR parameters and those calculated for a crystal structure (when optimised, if required).[44, 45] The advantage of using theoretical rather than experimental data is that the NMR parameters obtained correspond exactly to the known structure, even if the structure and, hence, calculated NMR parameters do not match those of the corresponding material. The NMR parameters were calculated for 42 structures of calcined AlPOs, 31 of which were taken from the literature and used without further optimisation and 11 of which were optimised to an energy minimum prior to the calculation of NMR parameters (without the use of SEDC schemes, as these were not implemented in CASTEP 4.3, used for this work). In addition, the structures of the dense $AlPO_4$ phases, quartz and cristobalite, were used without further optimisation and the

structures of these two dense phases, as well as that of tridymite, were optimised and included in the study. The published structure of tridymite[46] was not included, owing to the presence of 180° P-O-Al bond angles, which are unrealistic (arising from the average position of the O atoms) and caused problems with some of the calculations discussed below. A full list of structures used appears in Appendix K. The calculated isotropic shieldings of the 159 crystallographically-distinct P species are plotted against $\bar{\theta}_{POAl}$ or $\bar{r}_{PO}$ in Figure 5.5, and it can be seen that the lines of best fit for each parameter do not adequately describe the data, with R^2 of 0.3315 for the relationship with $\bar{\theta}_{POAl}$ and 0.8501 for the relationship with $\bar{r}_{PO}$ and MAEs of 7.1 and 4.2 ppm, respectively. The best-fit quadratic function of $\bar{r}_{PO}$ is also a poor description of the data (R^2 = 0.8614, MAE = 3.9 ppm). Particularly poor agreement is observed for the P species arising from the structure of AlPO-5 reported by Ikeda *et al.*,[47] which contains unusually long P-O bonds, up to 1.682 Å. This is particularly noticeable in the plot in Figure 5.5(a), where these points are highlighted.

The results shown in Figure 5.5 are not surprising, given that both $\bar{\theta}_{POAl}$ and $\bar{r}_{PO}$ were shown above to affect σ_{iso}, such that either parameter on its own will be unable to explain fully the value of σ_{iso}. Multivariate linear regression (described in further detail in Appendix L) was carried out in order to determine the best-fit function of σ_{iso} to $\bar{\theta}_{POAl}$, $\bar{r}_{PO}$ and $\bar{r}_{PO}^2$. In order to assess the validity of this function, the 159 P species were split into a training set (to which the function would be fitted) of 150 values, and a test set (against which the function would be validated) of 9 values. The best fit function for the training set was determined to be

$$\sigma_{iso}\left(\bar{\theta}_{POAl},\bar{r}_{OP}\right) = 0.8978\bar{\theta}_{POAl} - 1189\bar{r}_{PO}^2 + 3322\bar{r}_{PO} - 2124 \ , \qquad (5.9)$$

where all coefficients are reported to 4 s.f.. The plot of the calculated σ_{iso} against predicted $\sigma_{iso}\left(\bar{\theta}_{POAl},\bar{r}_{OP}\right)$ in Figure 5.6 shows that this model is a vast improvement upon attempting to predict the ^{31}P σ_{iso} from $\bar{\theta}_{POAl}$ or $\bar{r}_{PO}$ alone. For the training set, R^2 = 0.9746 and MAE = 1.60 ppm and, for the test set, R^2 = 0.9910 and MAE = 0.49 ppm. While the results for the test set appear better than those for the training set, the training set contains the structure of AlPO-5 reported by Ikeda *et al.*, to include the greatest range of σ_{iso} and $\bar{r}_{PO}$ possible. Therefore, the apparent improvement in the

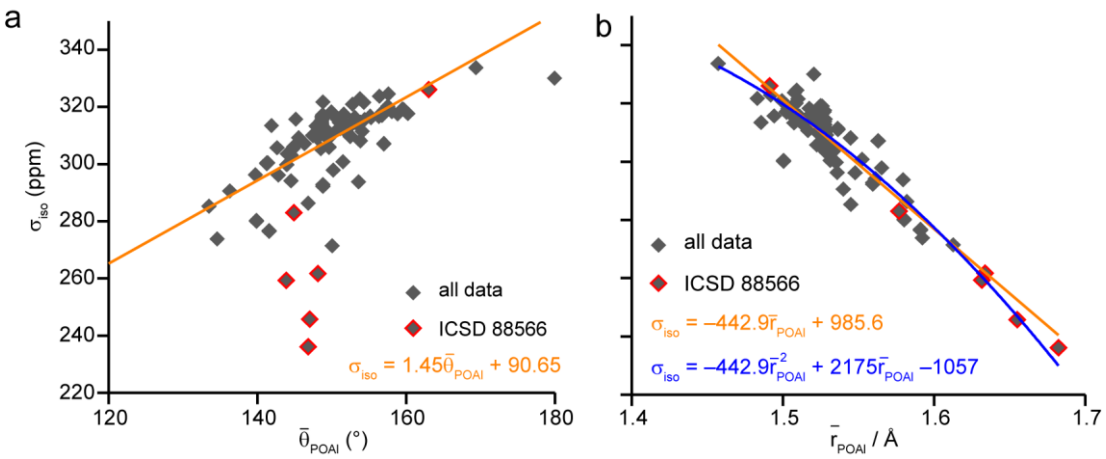

Figure 5.5. Plots of calculated ^{31}P σ_{iso} for 42 calcined and dense $AlPO_4$ phases, as a function of (a) $\bar{\theta}_{POAl}$ and (b) $\bar{r}_{PO}$. The best fit linear (and quadratic, in (b)) functions are shown and the points arising from the structure of AlPO-5 determined by Ikeda *et al*. (ISCD entry 88566)[47] are highlighted in red.

predictive power of the model for the test set may, perhaps, be attributed to the test set sampling a smaller number P species with more "normal" structural parameters that will be better described by the model. Interestingly, the largest deviation between the calculated σ_{iso} and $\sigma_{iso}(\bar{\theta}_{POAl},\bar{r}_{OP})$ is 9.95 ppm for P3 of AlPO-11 (prior to optimisation). This species has a relatively short $\bar{r}_{PO}$ of 1.457 Å, as well as a relatively large $\bar{\theta}_{POAl}$ of 169.4° and, although these values are not the extremes of $\bar{r}_{PO}$ and $\bar{\theta}_{POAl}$, it appears that their combination leads to a large deviation between the calculated and predicted σ_{iso}. However, the MAE for this model is now of the same order of magnitude as the differences between the experimental chemical shifts of ^{31}P in most AlPOs, and its predictive power is good (*i.e.*, the model describes equally well the test and training sets). Therefore, this model is likely to be significantly more useful than any of the single-parameter models found in the literature.

5.4.2.1 Improving the Model

In the ^{31}P NMR spectra of many calcined AlPOs, the shift difference between two resonances is small relative to the MAE of the model for σ_{iso} derived above. For example, in calcined AlPO-14 (Figure 2.18) δ_{iso} values for P2 and P4 differ by just 0.7 ppm. Therefore, while it would be possible to assign the spectrum using

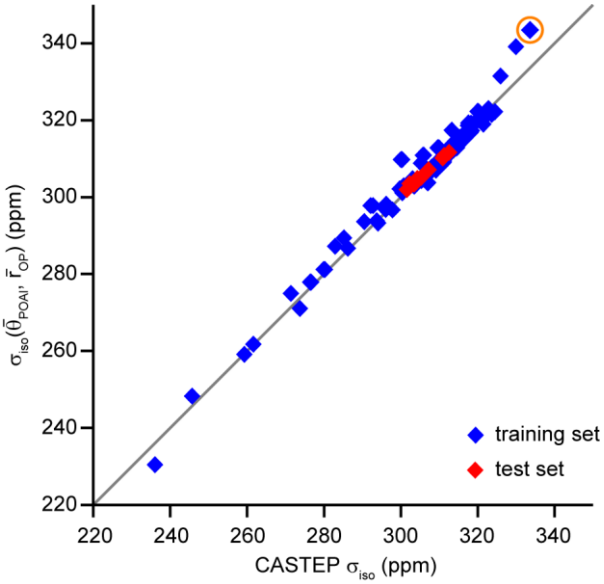

Figure 5.6. Plot of $\sigma_{iso}(\bar{\theta}_{POAl},\bar{r}_{OP})$ against calculated ^{31}P σ_{iso}. The point for P3 of AlPO-11 (prior to optimisation) is highlighted in orange and the ideal 1:1 correspondence is indicated in grey.

$\sigma_{iso}(\bar{\theta}_{POAl},\bar{r}_{OP})$, which predicts a shift difference of 1.06 ppm for the optimised structure (*cf.* 1.15 ppm predicted by CASTEP), the assignment would not be confident without further experimental confirmation, such as heteronuclear correlation experiments. As such, it would be desirable to reduce the MAE and improve confidence in any assignments made on the basis of the local structure. The most obvious way to achieve this would be to extend the number of parameters describing the local structure, as it would be naïve to assume that the full electronic structure of an AlPO, which gives rise to σ_{iso}, can adequately be described by one average bond length and one average bond angle.

Various parameters have been introduced in the literature in order to describe the coordination environment. These distortion parameters typically describe the deviation from either the mean or some "ideal" value (*e.g.*, of bond lengths or angles). The first of these is standard deviation:

$$\sigma(x) = \frac{1}{\sqrt{n}}\sqrt{\sum_{i=1}^{n}(x_i - \bar{x})^2} \quad , \tag{5.10}$$

where x is the structural parameter (bond lengths or angles) in question and n is the number of these parameters. The square root of the bias-corrected variance is also colloquially referred to as the standard deviation (and is returned when the STDEV() function is called in Microsoft Excel), but is defined as:

$$\sigma'(x) = \sqrt{\frac{1}{n-1}}\sqrt{\sum_{i=1}^{n}(x_i - \bar{x})^2} = \sqrt{\frac{n-1}{n}}\sigma(x) \ . \tag{5.11}$$

The remainder of this thesis uses the definition of Equation 5.10 for the standard deviation. Deviation from the mean value can also be described by the deviation parameter, $\Delta(x)$,

$$\Delta(x) = \frac{1}{n}\sum_{i=1}^{n}\left(\frac{x_i - \bar{x}}{\bar{x}}\right)^2 \ . \tag{5.12}$$

Deviation from ideality requires first the definition of the "ideal" coordination environment, which, for a tetrahedron, is defined by the ideal tetrahedral angle,

$$\theta_0 = \cos^{-1}(-1/3) = 109.47° \ , \tag{5.13}$$

between the T-O bonds, and the ideal bond length, r_0. The ideal bond length can be expressed in terms of the volume, V, of the tetrahedron

$$r_0 = \frac{\sqrt{6}}{4}\sqrt[3]{\frac{12V}{\sqrt{2}}} \ , \tag{5.14}$$

where

$$V = \frac{1}{6}\begin{vmatrix}(x_2 - x_1) & (y_2 - y_1) & (z_2 - z_1)\\ (x_3 - x_1) & (y_3 - y_1) & (z_3 - z_1)\\ (x_4 - x_1) & (y_4 - y_1) & (z_4 - z_1)\end{vmatrix} \ , \tag{5.15}$$

and x_i, y_i and z_i are the Cartesian coordinates of the i^{th} O atom, with one O atom (i = 1) arbitrarily chosen as the origin. This definition of r_0 yields the ideal bond length of a regular tetrahedron with the same volume as the distorted one under consideration. In the literature, $\Delta(x)$ is typically applied only to the deviation from ideality of the bond lengths, with deviation from the ideal bond angle characterised by the shear

strain parameter, $|\Psi|$,

$$|\Psi| = \sum_{i=1}^{n} |\tan(\theta_i - \theta_0)| \ , \tag{5.16}$$

where θ_i is the i^{th} O-T-O bond angle.[48] Alternatively, the parameter, R, defined as[49]

$$R = \frac{\sum_{i=1}^{n} |\theta_i - \theta_0|}{\sum_{i=1}^{n} \theta_i} \ , \tag{5.17}$$

the bond angle variance, $(\sigma_\theta)^2$, defined for a tetrahedron as[50, 51]

$$(\sigma_\theta)^2 = \sum_{i=1}^{n} \frac{(\theta_i - \theta_0)^2}{5} \ , \tag{5.18}$$

and the distortion index, D,[7]

$$D = \left|\theta_0 - \bar{\theta}\right| \ , \tag{5.19}$$

describe the deviation from an ideal bond angle. For calcined AlPOs, $|\Psi|$ and R are linearly related, and $(\sigma_\theta)^2$ measures the same structural distortion, so the following discussion considers only $|\Psi|$, which is most widely used in the literature. D is linearly related to the mean O-P-O angle, $\bar{\theta}_{OPO}$, and is not considered further. Deviation from an ideal bond length can be described by the longitudinal strain, $|\alpha|$,[48]

$$|\alpha| = \sum_{i=1}^{n} \left|\ln\left(\frac{r_i}{r_0}\right)\right| \ , \tag{5.20}$$

or the elongation, λ_r,[51]

$$\lambda_r = \frac{1}{n}\sum_{i=1}^{n} \left(\frac{r_i}{r_0}\right)^2 \ , \tag{5.21}$$

where r_i is the i^{th} T-O bond length. As λ_r measures the same distortion as $|\alpha|$, the following discussion considers only $|\alpha|$, which is used more often in the literature. Finally, the bond lengths and angles can be combined in the displacement parameter, $\mathbf{r}_{TO}$, given by the sum of the individual T-O bond vectors,

$$\mathbf{r}_{TO} = \sum_{i=1}^{n} \mathbf{r}_{TO(i)} \ , \tag{5.22}$$

which can be considered as the displacement of the T atom from the centre of gravity of the TO_4 tetrahedron. However, the direction of $\mathbf{r}_{TO}$ is meaningless and the following discussion considers only the magnitude of the displacement, $|\mathbf{r}_{TO}|$. There have been many reports of the use of these distortion parameters to assign NMR spectra and interpret trends in the NMR parameters of related compounds in the literature, and the main conclusions of these reports are summarised in Table 5.3. Given the use of these parameters in the literature, the DIStortion analysis COde (DISCO) was written in FORTRAN90 to calculate these parameters for the structures of calcined AlPOs, so that their relevance to the current study could be assessed. The source code for DISCO is included in the electronic information accompanying this thesis. DISCO, which will be described in greater detail below, calculates the distortion parameters introduced above for all P and Al species in the unit cells of calcined AlPOs, given their unit cell parameters and atomic coordinates.

In order to assess the relevance of all parameters simultaneously, the multivariate linear regression procedure was modified to include feature selection, where parameters with an insignificant correlation with σ_{iso} were discarded and the linear regression with feature selection (LRFS) process was repeated iteratively until only significant parameters remained. Further details of LRFS are given in Appendix L. In addition to the parameters discussed above, the maximum, minimum and standard deviation of the P-O bond lengths, O-P-O and P-O-Al bond angles were considered. NNN effects were taken into account by calculating the distortion parameters for the (non-bonded) PAl_4 tetrahedron around P.

The predicted isotropic shielding as a function of the structural parameters described above, σ_{iso}(structure), was determined by LRFS to be

$$\begin{aligned}\sigma_{iso}(\text{structure}) \;=\; & 23.19\max(r_{PO}) - 47.12\min(r_{PO}) + 2307\bar{r}_{PO} - 845.1\bar{r}_{PO}^2 \\ & - 278.5\Delta(r_{PO}) - 39.13|\alpha_{PO}| + 0.1408\min(\theta_{OPO}) + 0.1701\bar{\theta}_{OPO} + 0.2413\min(\theta_{POAl}) \\ & - 0.2357\max(\theta_{POAl}) + 0.9258\bar{\theta}_{POAl} + 0.4429\sigma(\theta_{POAl}) - 56.91\min(r_{PAl}) \\ & + 23.37\max(r_{PAl}) + 720.7\bar{r}_{PAl} - 109.7\bar{r}_{PAl}^2 - 102.5\sigma(r_{PAl}) - 22.95|\alpha_{PAl}| \\ & + 0.1669\min\theta_{AlPAl} - 0.1496\max(\theta_{AlPAl}) + 1.767\sigma(\theta_{AlPAl}) - 7.429|\Psi_{AlPAl}| \\ & - 2628 \;, \end{aligned} \qquad (5.23)$$

Table 5.3. A summary of some of the relationships between various structural distortion parameters and NMR parameters reported in the literature. Relationships for ^{29}Si are included owing to the similarity between the local environment of Si in SiO_2 polymorphs or zeolites and Al/P in AlPOs.

Structural Parameter	Linear relationship with	Reference
$\bar{r}_{SiO}$	^{29}Si δ_{iso} in silicas and silicates	52-57
$\bar{\theta}_{SiOT}$ (T = Si, Al)	^{29}Si δ_{iso} in silicas, silicates and zeolites	53, 58-64
$\frac{1}{4}\sum_{i=1}^{4} \sec\theta_{TOT(i)}$	^{29}Si δ_{iso} in silicas, silicates and aluminosilicates	52, 53, 59, 61, 65
$\bar{\theta}_{POAl}$	^{31}P δ_{iso} in AlPOs	11, 40
$\bar{\theta}_{POAl}$	^{17}O δ_{iso} in AlPOs	66
$\bar{r}_{PO}$	^{31}P δ_{iso} in phosphates	41
$\bar{r}_{PO}$	^{31}P CSA in phosphoryl and phosphate compounds	10, 67
$\bar{r}_{OT}$	^{17}O δ_{iso} and $\lvert C_Q \rvert$ in aluminophosphates	66
D_{OPO} (*i.e.*, $\bar{\theta}_{OPO}$)	^{31}P CSA in phosphates	10
$\bar{\theta}_{AlOT}$ (T = Si, Al)	^{27}Al δ_{iso} in aluminosilicates and aluminates	62, 68-72
$\bar{r}_{AlSi}$	^{27}Al δ_{iso} in aluminosilicates	62
$\lvert\alpha_{AlO}\rvert$	^{27}Al C_Q for AlO_6	48
$\lvert\Psi_{AlO}\rvert$	^{27}Al C_Q for AlO_4	48, 72
R_{OAlO}	^{27}Al δ_{iso} for AlO_5	73
D_{OAlO} (*i.e.*, $\bar{\theta}_{OAlO}$)	^{27}Al C_Q in cements	74

where all coefficients are reported to 4 s.f. and max(x) and min(x) denote, respectively, the maximum and minimum values of the parameter, x. Units (or scaling factors, where appropriate) for the coefficients are ppm per Å (lengths, in Å), ppm per degree (angles, in °) and ppm (dimensionless distortion parameters, and the intercept), giving σ_{iso}(structure) in ppm. As shown in Figure 5.7(a), this model for σ_{iso} yielded generally good agreement for the training set (R^2 = 0.9947, MAE = 0.76 ppm) and the test set (R^2 = 0.9646, MAE = 1.10 ppm). However, the marginally

improved agreement with the training set, at the expense of predictive ability for the test set, may be seen as evidence of overparameterisation (*i.e.*, the model describes in great detail small rounding or computing errors in the training set, rather than the more generally transferrable trends). From Equation 5.23, it is clear that many parameters affect σ_{iso}(structure), although it is unclear to what extent each parameter is important. Figure 5.8 plots the product of the coefficients given in Equation 5.23 and the mean value for the relevant parameter (note the logarithmic scale). It can be seen that, while $\Delta(r_{PO})$ has the relatively large coefficient of 278.5, its mean value of 5.923×10^{-4} means that its total contribution is ~0.16 ppm. In addition, the parameters with the greatest absolute contributions to σ_{iso}(structure), $\bar{r}_{PO}$, $\bar{r}^2_{PO}$, $\bar{r}_{PAl}$ and $\bar{r}^2_{PAl}$, appear to come in pairs with, for example, the large positive contribution from $\bar{r}$ partially cancelled by the negative contribution from $\bar{r}^2$.

Owing to the rapid and automated fashion in which the LRFS approach determines the relationships between various structural parameters and a given NMR parameter, extension of the approach to the full anisotropic shielding tensor (also calculated by CASTEP), rather than just the isotropic shielding, is facile. Using LRFS, σ_{11}(structure), σ_{22}(structure) and σ_{33}(structure) were determined to be

$$\begin{aligned}\sigma_{11}(\text{structure}) \;=\; & 278.1\max(r_{PO}) - 317.3\min(r_{PO}) + 2881\bar{r}_{PO} - 1001\bar{r}^2_{PO} - 539.6\sigma(r_{PO}) \\ & - 33.84|\alpha_{PO}| + 50.24|\mathbf{r}_{PO}| - 0.4628\min(\theta_{OPO}) + 20.80\bar{\theta}_{OPO} - 2.116\sigma(\theta_{OPO}) \\ & + 0.6541\min(\theta_{POAl}) - 0.5400\max(\theta_{POAl}) + 1.579\bar{\theta}_{POAl} + 0.8840\sigma(\theta_{POAl}) \\ & - 135.4\min(r_{PAl}) + 147.3\max(r_{PAl}) + 1808\bar{r}_{PAl} - 300.0\bar{r}^2_{PAl} - 139.9\sigma(r_{PAl}) \\ & - 7292\Delta(r_{PAl}) - 18.24|\alpha_{PAl}| - 3.524|\mathbf{r}_{PAl}| + 1.467\min\theta_{AlPAl} - 1.010\max(\theta_{AlPAl}) \\ & - 4.491\bar{\theta}_{AlPAl} + 9.928\sigma(\theta_{AlPAl}) - 53.95|\Psi_{AlPAl}| - 6505 \;, \end{aligned} \tag{5.24}$$

$$\begin{aligned}\sigma_{22}(\text{structure}) \;=\; & -76.45\max(r_{PO}) + 96.34\min(r_{PO}) + 3234\bar{r}_{PO} - 1170\bar{r}^2_{PO} \\ & + 847.0\sigma(r_{PO}) - 304.3|\alpha_{PO}| - 30.86|\mathbf{r}_{PO}| - 0.9338\min(\theta_{OPO}) - 7.195\bar{\theta}_{OPO} \\ & + 0.4196\max(\theta_{OPO}) - 6.551\sigma(\theta_{OPO}) + 68.71|\Psi_{OPO}| + 0.5125\min(\theta_{POAl}) \\ & - 0.7626\max(\theta_{POAl}) + 1.157\bar{\theta}_{POAl} + 1.405\sigma(\theta_{POAl}) - 64.21\min(r_{PAl}) \\ & + 35.41\max(r_{PAl}) + 5836\bar{r}_{PAl} - 932.8\bar{r}^2_{PAl} - 110.7\sigma(r_{PAl}) - 756.2\Delta(r_{PAl}) \\ & + 6.931|\alpha_{PAl}| + 3.802|\mathbf{r}_{PAl}| + 0.1877\min\theta_{AlPAl} - 0.1529\max(\theta_{AlPAl}) \\ & + 0.3090\bar{\theta}_{AlPAl} + 0.7314\sigma(\theta_{AlPAl}) - 9.362|\Psi_{AlPAl}| - 10290 \;, \end{aligned} \tag{5.25}$$

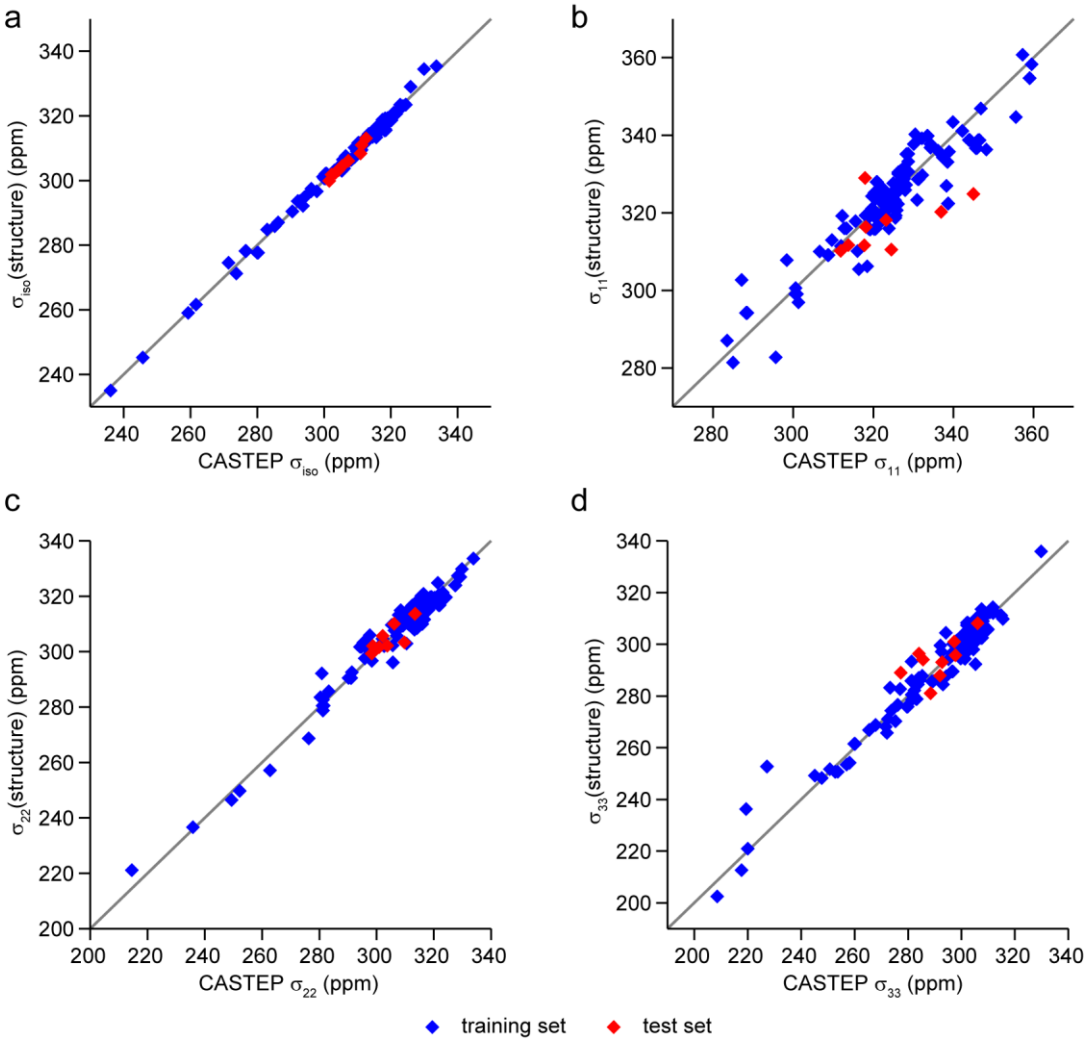

Figure 5.7. Plots of (a) σ_{iso}(structure) and (b-d) σ_{ii}(structure) against the values calculated by CASTEP. The ideal 1:1 correspondence is indicated in grey.

and

$$\begin{aligned}\sigma_{33}(\text{structure}) = {} & -99.91\max(r_{PO}) + 55.49\min(r_{PO}) + 962.7\bar{r}_{PO} - 416.4\bar{r}^2_{PO} \\ & + 512.5\sigma(r_{PO}) - 849.7\Delta(r_{PO}) + 278.1|\alpha_{PO}| - 14.87|\mathbf{r}_{PO}| + 1.745\min(\theta_{OPO}) \\ & - 0.3109\max(\theta_{OPO}) - 7.924\bar{\theta}_{OPO} + 9.100\sigma(\theta_{OPO}) - 79.28|\Psi_{OPO}| \\ & - 0.4430\min(\theta_{POAl}) + 0.6084\max(\theta_{POAl}) + 0.03448\bar{\theta}_{POAl} - 0.9501\sigma(\theta_{POAl}) \\ & + 30.01\min(r_{PAl}) - 115.1\max(r_{PAl}) - 5730\bar{r}_{PAl} + 943.5\bar{r}^2_{PAl} - 70.51\sigma(r_{PAl}) \\ & + 8895\Delta(r_{PAl}) - 56.79|\alpha_{PAl}| - 1.107\min\theta_{AlPAl} + 0.6607\max(\theta_{AlPAl}) \\ & + 4.147\bar{\theta}_{AlPAl} - 5.058\sigma(\theta_{AlPAl}) - 39.36|\Psi_{AlPAl}| + 9106\ , \end{aligned} \quad (5.26)$$

where all coefficients are reported to 4 s.f. and scaled to give σ_{ii} in ppm. However,

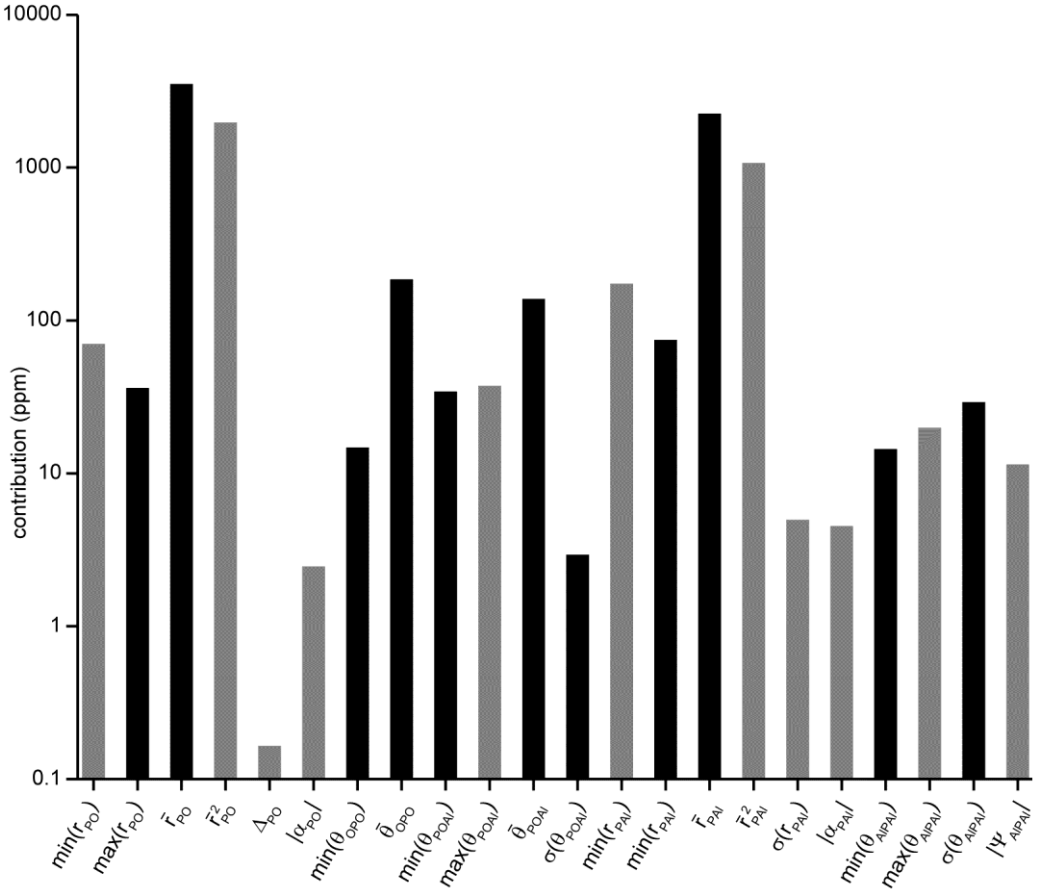

Figure 5.8. The magnitude of the mean contribution of each term in equation 5.23, plotted with a logarithmic vertical scale. Positive contributions are black and negative contributions grey.

the relationships given in Equations 5.24-26 yield relatively poor R^2 values (0.8746, 0.9583 and 0.9503, respectively) and high MAEs (3.89, 2.65 and 3.21 ppm, respectively) even for the training set. Nevertheless, as shown in Figures 5.7(b-d), σ_{ii}(structure) for the test set, while displaying apparently poor R^2 and greater deviation of the trendline from the ideal gradient of 1, actually fall within the scatter of the points for the training set, suggesting that these models could be used to predict the principal components of the ^{31}P shielding tensors in AlPOs, albeit with a random error of a few ppm. The value of this prediction is limited by the fact that spans (*i.e.*, $\sigma_{11} - \sigma_{33}$) for ^{31}P shielding tensors in calcined AlPOs are small, typically <30 ppm in calcined AlPOs.[75] It is, therefore, clear that the models for σ_{ii}(structure) determined here cannot adequately predict the chemical shift (or shielding) anisotropy of calcined AlPOs. This is perhaps not surprising as, according to

MacKenzie and Smith, the anisotropic component of the ^{31}P shielding tensor in phosphates arises predominantly from back bonding into the antibonding orbitals of P, the geometry of which may not be easily related to the bonding geometry present.[7] However, further theoretical investigation of this phenomenon would be required in order to determine whether there is truly no way of accurately determining σ_{ii} for ^{31}P.

Despite the relatively poor agreement between σ_{ii}(structure) and the calculated σ_{ii}, the coefficients for σ_{iso}(structure), determined as the average of the coefficients for each structural parameter in Equations 5.24-26, are in very good agreement with the coefficients for σ_{iso}(structure) determined using LRFS. This is demonstrated in Figure 5.9, where σ_{iso}(structure), determined using either LRFS or the average of the coefficients from Equations 5.24-26 is plotted against the calculated σ_{iso}. It can be seen that there is relatively little difference between the two plots. This observation is interesting, since it means that, although there is a relatively large error in all three of the predicted σ_{ii}(structure) values, the behaviour of the three predicted components of the shielding tensor is still close to the expected physical behaviour of the shielding tensor.

One obvious concern about the LRFS approach is that there are, in this case, 35 structural "predictor" parameters, meaning that it may be relatively easy to fit any set of "response" values to a model, without any physical meaning. This can be tested by adding random noise, N, with a maximum amplitude, A_N, to the calculated σ_{iso} values, to give $\sigma_{iso} \pm N$ and attempting to reparameterise the model to give $[\sigma_{iso} + N]$(structure). There are two limiting cases for the outcome of this test – firstly, the noise may be parameterised by the model, yielding good agreement for the training set but poor agreement for the test set, indicating that caution must be exercised when interpreting the above results. Alternatively, the noise may be ignored by the model, indicating that the LRFS approach can distinguish between structure-related changes in σ_{iso} and the random noise, which should not correlate with any structural features. These two scenarios can be described mathematically as yielding either

$$[\sigma_{iso} + N](\text{structure}) = \sigma_{iso}(\text{structure}) + N(\text{structure}) \quad , \qquad (5.27)$$

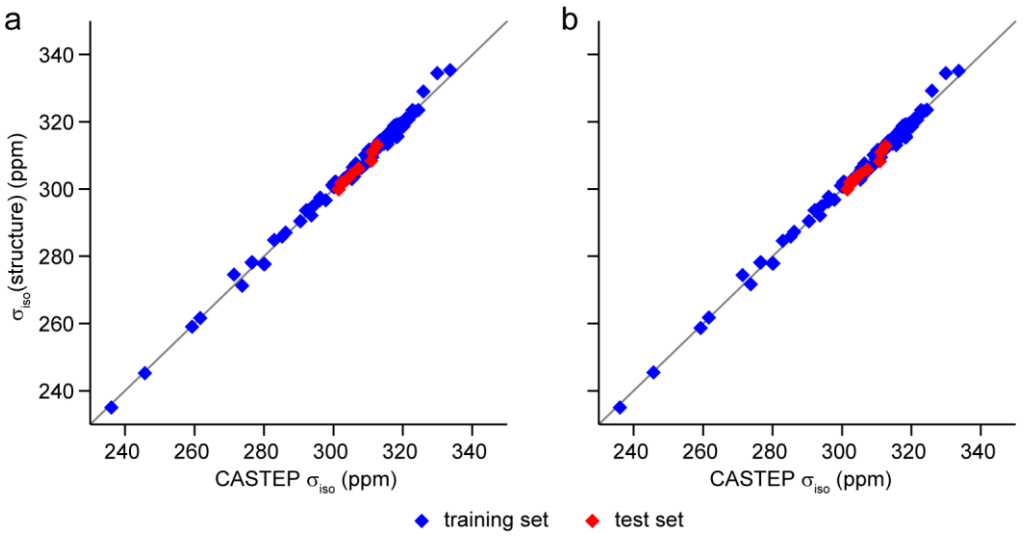

Figure 5.9. Plots of σ_{iso}(structure) against the value of σ_{iso} calculated by CASTEP where the coefficients for σ_{iso}(structure) were determined (a) using LRFS and (b) from the average of the values reported in Equations 5.24-26. The ideal 1:1 correspondence is shown in grey.

in the first case, or

$$[\sigma_{iso} + N](\text{structure}) = \sigma_{iso}(\text{structure}) + N \,, \qquad (5.28)$$

in the second case. The results of adding random noise with A_N = 0.1, 1 and 10 ppm (to both the test and training sets) are summarised in Table 5.4. It can be seen that the addition of a small amount of random noise (A_N = 0.1 ppm) does not appear to affect the model significantly, meaning that the model for σ_{iso}(structure) should be relatively insensitive to any small rounding and numerical errors that may have arisen during the calculation of the structural parameters or σ_{iso}. Most importantly, when A_N = 0.1, the same structural parameters are selected as significant as in the case where A_N = 0 (Equation 5.23). When a moderate amount of noise (A_N = 1) is added, the quality of the model can be seen to decrease, particularly in terms of its predictive power, and closer inspection of the model reveals that two additional structural parameters have been selected as significant, in this case, $\sigma(\theta_{OPO})$ and $\bar{\theta}_{AlPAl}$, with mean contributions (the product of the coefficient and the mean value of parameter) of ~0.07 ppm each, indicating that LRFS has determined some spurious dependence of the noise on the structure. With a large amount of noise applied, it can

Table 5.4. Summary of the gradients and R^2, of plots of [σ_{iso} + N](structure) against calculated σ_{iso}, and the MAE for the model when random noise, N, of amplitude A_N, is added to the calculated σ_{iso} for both the training and test sets.

A_N (ppm)	gradient		R^2		MAE (ppm)	
	training	test	training	test	training	test
0	0.9947	1.004	0.9947	0.9646	0.76	1.10
0.1	0.9946	1.042	0.9946	0.9642	0.77	1.10
1	0.9933	1.014	0.9933	0.9421	0.90	1.18
10	0.8632	0.3095	0.8362	0.3048	4.88	4.72

be seen that the resulting model does not describe the training set well, and its predictive power is very poor. In addition, all 30 structural parameters were selected as significant for this model, indicating that a large random error in the values used for the training set would lead to the LRFS approach determining a significant structural contribution to the error. It can, therefore, be seen that, with low levels of noise, the outcome of the LRFS approach most resembles Equation 5.28, whereas at higher levels of noise, Equation 5.27 is more relevant.

5.4.3 The Effect of Local Structure on ^{27}Al NMR Parameters

Given that there is some evidence for the validity of the application of the work of Müller *et al.*[11] for assigning the ^{31}P NMR spectra of AlPOs, the reported relationship between the ^{27}Al δ_{iso} and the mean Al-O-P bond angle, $\bar{\theta}_{AlOP}$, was also investigated here. As for ^{31}P, $d\delta/d\bar{\theta}_{AlOP}$, was reported by Müller *et al.* as −0.51 ppm per degree, although an alternative value of $d\delta/d\bar{\theta}_{AlOP}$ = –0.61 ppm per degree was reported for the dataset for ^{27}Al δ_{iso} alone. However, as discussed above, the accuracy of this value must be questioned, owing to the limited nature of the original study. In addition, the positions of ^{27}Al (I = 5/2) lineshapes in an MAS NMR spectrum are determined by both δ_{iso} and the quadrupolar shift, δ_Q. Determining δ_{iso} itself, rather than just the resonance position, δ, can be challenging, particularly with the low-field spectrometers (^{27}Al ν_0 of 9 and 70.4 MHz) used by Muller *et al.*,[11] and it is likely that

there is a significant uncertainty in both the structural and NMR parameters reported. The large contributions to the lineshape (and δ) from the quadrupolar interaction, combined with the fact that, in as-prepared AlPOs, the ^{27}Al δ_{iso} is dominated by the coordination number,[7] may explain why any relationship between δ_{iso} and $\bar{\theta}_{AlOP}$ has not gained the same popularity as the corresponding relationship for ^{31}P for assigning ^{27}Al NMR spectra. Given the lack of experimental studies investigating (or even using) the relationship between δ_{iso} and $\bar{\theta}_{AlOP}$ in the literature, it is unclear whether the relationship can be applied more generally than to just the three dense $AlPO_4$ phases originally studied.[11] Therefore, as for ^{31}P, a series of model clusters of the formula $[Al(OP(OH)_3)_4]^{3+}$, such as that shown in Figure 5.10 were considered.

In the first set of structures all Al-O bond lengths were constrained to 1.746 Å, O-Al-O bond angles were constrained to 109.47° and $\bar{\theta}_{AlOP}$ was varied systematically according to Table 5.5. The ^{27}Al δ_{iso} for the central Al was calculated using GAUSSIAN 03,[4] using the *aug*-pcS-3 basis set of Jensen,[76] and as seen in Figure 5.11(a), when only $\bar{\theta}_{AlOP}$ is allowed to vary and all other structural parameters are kept constant (series 14), there is a very strong linear correlation (R^2 = 0.9945) between σ_{iso} and $\bar{\theta}_{AlOP}$ with $d\sigma_{iso}/d\bar{\theta}_{AlOP}$ = 1.11 ppm per degree when $\bar{\theta}_{AlOP} \leq 165°$, although the gradient of the line can be seen to decrease to higher values of $\bar{\theta}_{AlOP}$. In series 15 and 16 (Figure 5.11(b)), $\bar{\theta}_{AlOP}$ was kept constant at 140° while the maximum and minimum values of $\theta_{AlOP(i)}$ (and, hence, the standard deviation, $\sigma(\theta_{AlOP})$) were varied. A difference was observed of up to 7.88 ppm (series 16, n = 7) in σ_{iso} relative to the corresponding point of series 14 (n = 7), in which $\bar{\theta}_{AlOP}$ is the same, while $\sigma(\theta_{AlOP})$ = 0. This indicates that the individual bond angles have a contribution to σ_{iso}, rather than just the average angle. Further evidence of this is shown in Figure 5.11(b) for series 17 (one angle varied systematically with the other three angles adjusted so $\bar{\theta}_{AlOP}$ = 140°), series 18 and 19 (maximum or minimum angle fixed, one angle varied systematically and the other two angles adjusted so $\bar{\theta}_{AlOP}$ = 140°) and series 20 (one angle varied systematically with the other three angles fixed at 140° so that $\bar{\theta}_{AlOP}$ was also varied systematically). In series 17, 18 and 19, there is also a difference in σ_{iso} (of up to 4.78 ppm for series 17, n = 13) despite the constant $\bar{\theta}_{AlOP}$. In series 20 (Figure 5.11(a)), where both $\bar{\theta}_{AlOP}$ and

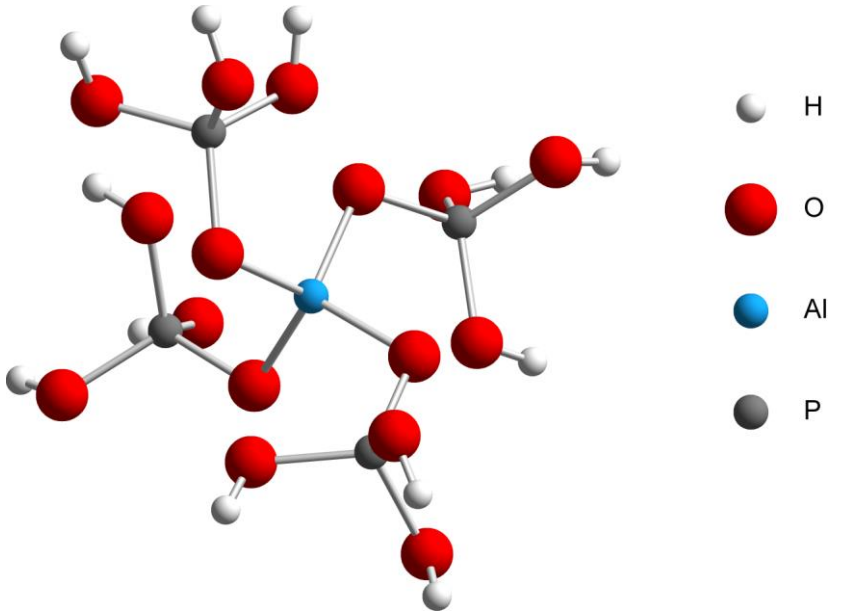

Figure 5.10. A $[Al(OP(OH)_3)_4]^{3+}$ cluster (series 14, n = 7) used as an analogue of the local environment of Al in an AlPO framework.

$\sigma(\theta_{AlOP})$ were varied, it can be seen that there is still a strong linear relationship for $n \leq 11$ ($\bar{\theta}_{AlOP} \leq 146.25°$) but, at higher $\bar{\theta}_{AlOP}$, σ_{iso} is lower than would be expected (from series 14), indicating that the large $\sigma(\theta_{AlOP})$ must also be taken into account. In order to further investigate the different contributions of $\bar{\theta}_{AlOP}$ and $\sigma(\theta_{AlOP})$ to σ_{iso}, a further series of $[Al(OP(OH)_3)_4]^{3+}$ clusters, series 21, was generated with four randomly-generated Al-O-P bond angles (constrained to the range 110 to 175°, with actual generated values between 124.1 and 168.8°). From Figure 5.11(c), it can be seen that the line of best fit for series 14 ($1 \leq n \leq 12$ only),

$$\sigma_{iso} = 1.11\bar{\theta}_{AlOP} + 363.47 \quad , \tag{5.29}$$

is in good agreement with the line of best fit for series 21,

$$\sigma_{iso} = 1.03\bar{\theta}_{AlOP} + 373.46 \quad . \tag{5.30}$$

This similarity, combined with the high R^2 (0.9945 for series 14 and 0.9682 for series 21), suggests that, as was observed for ^{31}P, σ_{iso} for ^{27}Al depends strongly on $\bar{\theta}_{AlOP}$. However, it appears that, for ^{27}Al, $\sigma(\theta_{AlOP})$ is much more significant than for ^{31}P. The results of the calculations reported here appear to support the work of Müller *et al.*, although it should be noted that the gradients in Equations 5.29 and 5.30 are

Table 5.5. The systematic variation of θ_{AlOP} bond angles, in the series of model $[Al(OP(OH)_3)_4]^{3+}$ clusters (see Figure 5.10) studied here. The angles are expressed for the n^{th} member of the series, and the number of clusters in the series, N, is given.

Series	$\theta_{AlOP(i)}$ (°)	N
14	$\theta_{AlOP(1)} = \theta_{AlOP(2)} = \theta_{AlOP(3)} = \theta_{AlOP(4)} = \bar{\theta}_{AlOP} = 105 + 5n$	15
15	$\theta_{AlOP(1)} = \theta_{AlOP(2)} = 140$ $\theta_{AlOP(3)} = 140 + 5n$ $\theta_{AlOP(4)} = 140 - 5n$	7
16	$\theta_{AlOP(1)} = \theta_{AlOP(2)} = 140 + 5n$ $\theta_{AlOP(3)} = \theta_{AlOP(4)} = 140 - 5n$	7
17	$\theta_{AlOP(1)} = 105 + 5n$ $\theta_{AlOP(2)} = \theta_{AlOP(3)} = \theta_{AlOP(4)} = 140 + \left(\frac{140 - \theta_{AlOP(1)}}{3}\right)$	14
18	$\theta_{AlOP(1)} = 150$ $\theta_{AlOP(2)} = 105 + 5n$ $\theta_{AlOP(3)} = \theta_{AlOP(4)} = \left(\frac{410 - \theta_{AlOP(2)}}{2}\right)$	8
19	$\theta_{AlOP(1)} = 120$ $\theta_{AlOP(2)} = 175 - 5n$ $\theta_{AlOP(3)} = \theta_{AlOP(4)} = \left(\frac{440 - \theta_{AlOP(2)}}{2}\right)$	11
20	$\theta_{AlOP(1)} = 105 + 5n$ $\theta_{AlOP(2)} = \theta_{AlOP(3)} = \theta_{AlOP(4)} = 140$	14
21	all angles randomly generated,[a] $124.1 \leq \theta_{AlOP(i)} \leq 168.8$	20

a. For a full list of the angles used, see Appendix J.

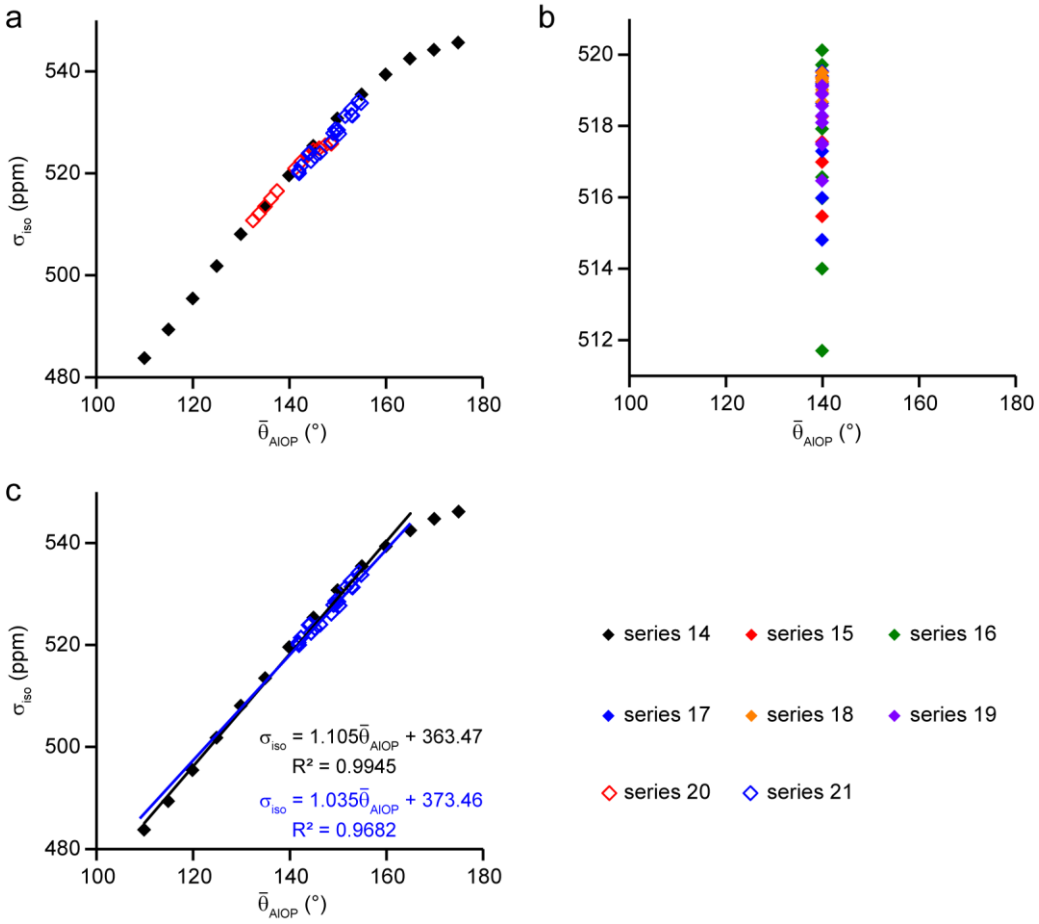

Figure 5.11. Plots of calculated ^{27}Al σ_{iso} against $\bar{\theta}_{AlOP}$ for (a and b) all series of model $[Al(OP(OH)_3)_4]^{3+}$ clusters detailed in Table 5.5 and (c) series 14 only, showing the line of best fit for points $1 \leq n \leq 12$).

approximately twice the values determined in the earlier work (although, interestingly, very similar to the gradients determined earlier for ^{31}P in Equations 5.1 and 5.2, as was suggested in the work of Müller *et al*.).

The mean T-O bond length (*i.e.*, $\bar{r}_{AlO}$ for ^{27}Al) was observed to contribute significantly to σ_{iso} for ^{31}P, and its effect on σ_{iso} of ^{27}Al was, therefore, investigated here, despite the lack of previous literature investigation of this potential relationship. In a second set of $[Al(OP(OH)_3)_4]^{3+}$ clusters, all O-Al-O and Al-O-P angles were constrained to 109.47° and 140.00°, respectively, while $\bar{r}_{AlO}$ was varied systematically as shown in Table 5.6. A further 20 clusters with randomly-generated bond lengths (between 1.68 and 1.82 Å) were also studied. It can be seen from

Figure 5.12 that, when only $\bar{r}_{AlO}$ is allowed to vary and all other structural parameters are kept constant (series 22), there is a strong linear correlation between σ_{iso} and $\bar{r}_{AlO}$,

$$\sigma_{iso} = -223.30\bar{r}_{AlO} + 129.06 \ , \quad (5.31)$$

with $R^2 = 0.9969$. However, as with ^{31}P, the correlation is improved ($R^2 = 1$) by using a quadratic function of $\bar{r}_{PO}$,

$$\sigma_{iso} = -324.36\bar{r}_{AlO}^2 + 1358.6\bar{r}_{AlO} - 863.69 \ . \quad (5.32)$$

It should be noted that, whereas for ^{31}P, increasing bond length led to a decrease in σ_{iso}, for ^{27}Al, σ_{iso} increases with bond length. In series 23 and 24, the maximum and minimum r_{AlO} were varied while $\bar{r}_{AlO}$ was kept constant at 1.74 Å, allowing the influence of $\sigma(r_{AlO})$ on σ_{iso} to be investigated. It can be seen from Figure 5.12 that the difference in $\sigma(r_{AlO})$ (of up to 0.081 Å for series 24, n = 5) led to a difference in σ_{iso} of 2.03 ppm, relative to the structure with the same $\bar{r}_{AlO}$ but $\sigma(r_{AlO}) = 0$ (series 22, n = 7). This indicates that $\sigma(r_{AlO})$ has a much more significant effect on σ_{iso} for ^{27}Al than ^{31}P. For series 25, both $\bar{r}_{AlO}$ and $\sigma(r_{AlO})$ were varied, with one bond length systematically increased while the other three were 1.74 Å. As with series 22, there was a good linear relationship between σ_{iso} and $\bar{r}_{AlO}$, given by

$$\sigma_{iso} = 221.45\bar{r}_{AlO} + 132.62 \ , \quad (5.33)$$

with $R^2 = 0.9954$, and a slightly stronger correlation ($R^2 = 0.9999$) for the quadratic relationship,

$$\sigma_{iso} = -1702.8\bar{r}_{AlO}^2 + 6155.7\bar{r}_{AlO} - 5037.4 \ . \quad (5.34)$$

However, it can be seen that there is a deviation in the coefficients of Equations 5.32 and 5.34, implying that the contribution from $\sigma(r_{AlO})$ observed for series 23 and 24 is, indeed, significant. However, as was suggested above for ^{31}P, the effect of $\sigma(\theta_{POAl})$ appeared to be artificially enhanced when the bond angles were varied systematically, compared to the random variation of bond angles (series 8). For series 26, the Al-O bond lengths were randomly varied, yielding a range of $\bar{r}_{AlO}$ and $\sigma(r_{AlO})$. For this series, the best linear relationship ($R^2 = 0.9961$) with $\bar{r}_{AlO}$ was

$$\sigma_{iso} = -226.21\bar{r}_{AlO} + 123.96 \ , \quad (5.35)$$

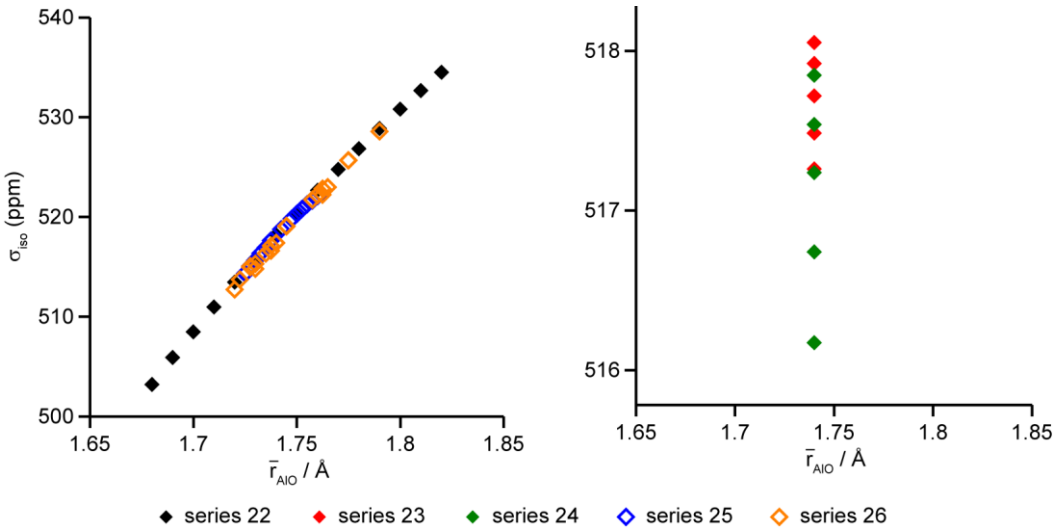

Figure 5.12. Plots of calculated ^{27}Al σ_{iso} against $\bar{r}_{AlO}$ for the series of model $[Al(OP(OH)_3)_4]^{3+}$ clusters detailed in Table 5.6.

Table 5.6. The systematic variation of r_{AlO} bond lengths, in the series of model $[Al(OP(OH)_3)_4]^{3+}$ clusters (see Figure 5.10) studied here. The lengths are expressed for the nth member of the series, and the number of clusters in the series, N, is given.

Series	$r_{AlO(i)}$ / Å	N
22	$r_{AlO(1)} = r_{AlO(2)} = r_{AlO(3)} = r_{AlO(4)} = \bar{r}_{AlO} = 1.67 + 0.01n$	15
23	$r_{AlO(1)} = r_{AlO(2)} = 1.74$ $r_{AlO(3)} = 1.75 + 0.01n$ $r_{AlO(4)} = 1.73 - 0.01n$	5
24	$r_{AlO(1)} = r_{AlO(2)} = 1.76 + 0.01n$ $r_{AlO(3)} = r_{AlO(4)} = 1.72 - 0.01n$	5
25	$r_{AlO(1)} = 1.67 + 0.01n$ $r_{AlO(2)} = r_{AlO(3)} = r_{AlO(4)} = 1.74$	14
26	all lengths randomly generated,[a] $1.68 \leq r_{AlO(i)} \leq 1.82$	20

a. For a full list of the lengths used, see Appendix J.

while the quadratic relationship,

$$\sigma_{iso} = -171.02\bar{r}_{AlO}^2 + 825.47\bar{r}_{AlO} - 400.92 \quad , \qquad (5.36)$$

yielded an essentially unchanged R^2 of 0.9963. Again, the coefficients in Equation 5.36 are different to those of Equation 5.32, indicating that consideration of both $\bar{r}_{AlO}$ and $\sigma(r_{AlO})$ is required in order to obtain a generalised relationship between ^{27}Al σ_{iso} and r_{AlO}. From the above studies, it would appear that both $\bar{\theta}_{AlOP}$ and $\bar{r}_{AlO}$ and, to some extent, $\sigma(\theta_{AlOP})$ and $\sigma(r_{AlO})$, have a significant effect on the calculated ^{27}Al σ_{iso}.

In ^{27}Al NMR spectra, the second-order quadrupolar broadening tends to be of the order of hundreds of Hz (up to tens of ppm at typical B_0 field strengths) and, for the tetrahedral Al in calcined AlPOs, may be of the same order of magnitude as the expected isotropic shift range (~35 to 40 ppm). Therefore, in addition to σ_{iso}, it is important to know whether it is possible to relate the quadrupolar coupling constant, C_Q, to the local structure. Many previous attempts have been made in the literature to relate C_Q to structural parameters although, as shown in Table 5.3, the majority of these are composite distortion parameters rather than simple geometric measurements of bond lengths or angles. The GAUSSIAN calculations described above also calculated the principal components of the ^{27}Al EFG tensor, V_{xx}, V_{yy} and V_{zz}. The calculations yield both sign and magnitude information for V_{ii} but, as the sign information is very challenging to measure experimentally, only the absolute value of V_{zz} and, hence C_Q, is reported here.

It can be seen from Figures 5.13(a and b) that, while $|C_Q|$ appears to decrease as $\bar{\theta}_{AlOP}$ increases (series 14), this is not true for series 21, in which there is a random distribution of both $\bar{\theta}_{AlOP}$ and $\sigma(\theta_{AlOP})$, indicating that, as one might expect, the EFG depends not on the average local geometry, but on the precise locations of the atoms around Al. This conclusion is supported by the results shown in Figures 5.13(c and d), where similar plots for series 22 and 26 show that, while $|C_Q|$ decreases as $\bar{r}_{AlO}$ increases for series 22, there is no such trend when $\sigma(r_{AlO} \neq 0)$, as for series 26. However, an additional caveat when interpreting these results is that the clusters are terminated with OH groups, the positions of which were freely optimised prior to calculating the NMR parameters, to ensure that there were no unrealistically close

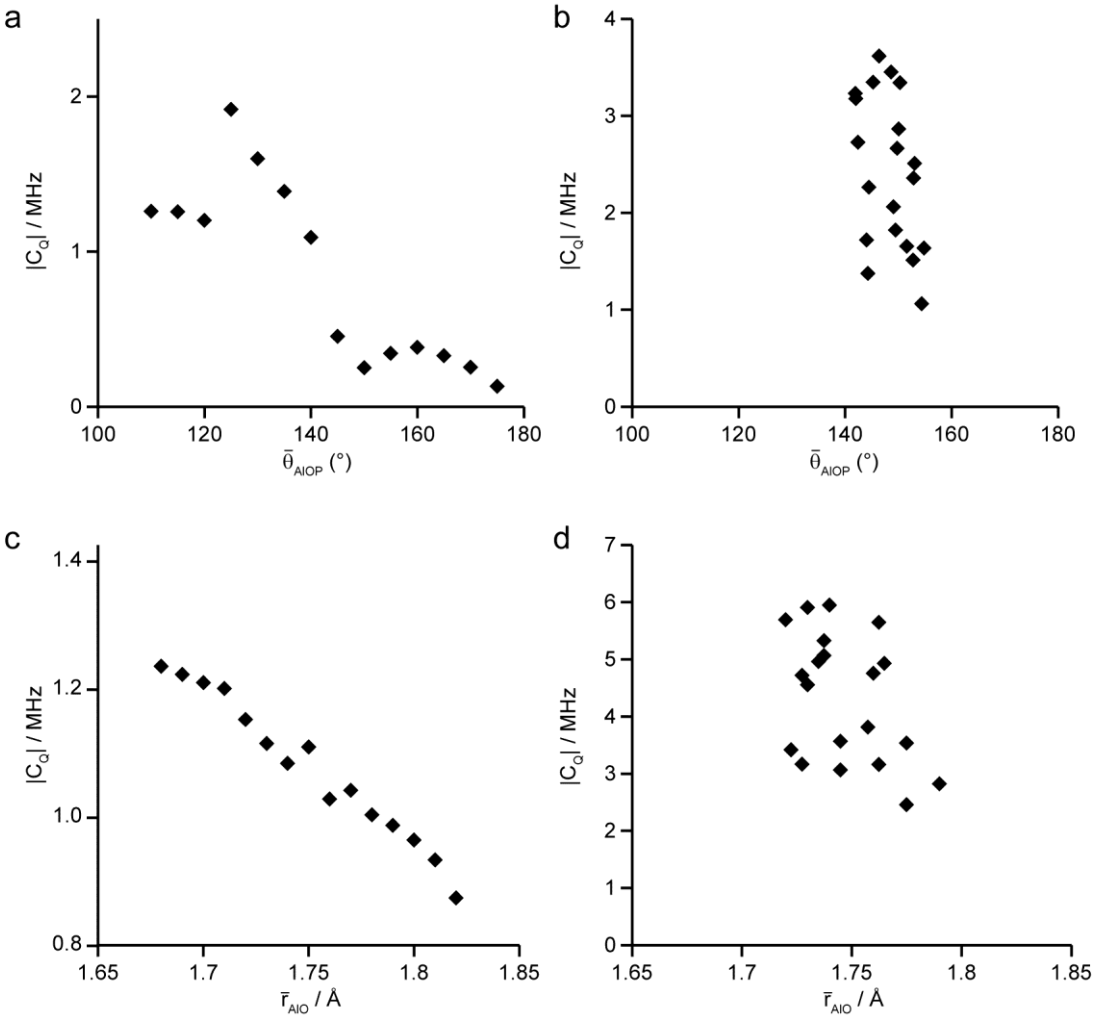

Figure 5.13. Plots of calculated ^{27}Al $|C_Q|$ against (a and b) $\bar{\theta}_{AlOP}$ and (c and d) $\bar{r}_{AlO}$ for (a) series 14, (b) series 21, (c) series 22 and (d) series 26.

contacts between the $P(OH)_3$ groups. While the locations of these OH groups could be disregarded (at least as a first approximation) when considering σ_{iso}, this is not possible when considering $|C_Q|$, owing to the longer-range nature of the EFG. It is possible that the influence of the positions of the OH groups is responsible for the deviation from a straight line observed in Figures 5.13(a and c). However, in-depth analysis was not attempted here, as there are no OH groups in calcined AlPOs.

The asymmetry of the EFG, η_Q, can be determined from the calculated V_{ii}. As η_Q is linked to the local symmetry of the Al environment, its experimental measurement can aid spectral assignment. It can be seen from Figure 5.14(a) that, when $\bar{\theta}_{AlOP}$ is increased systematically with $\sigma(\theta_{AlOP}) = 0$, there is no obvious

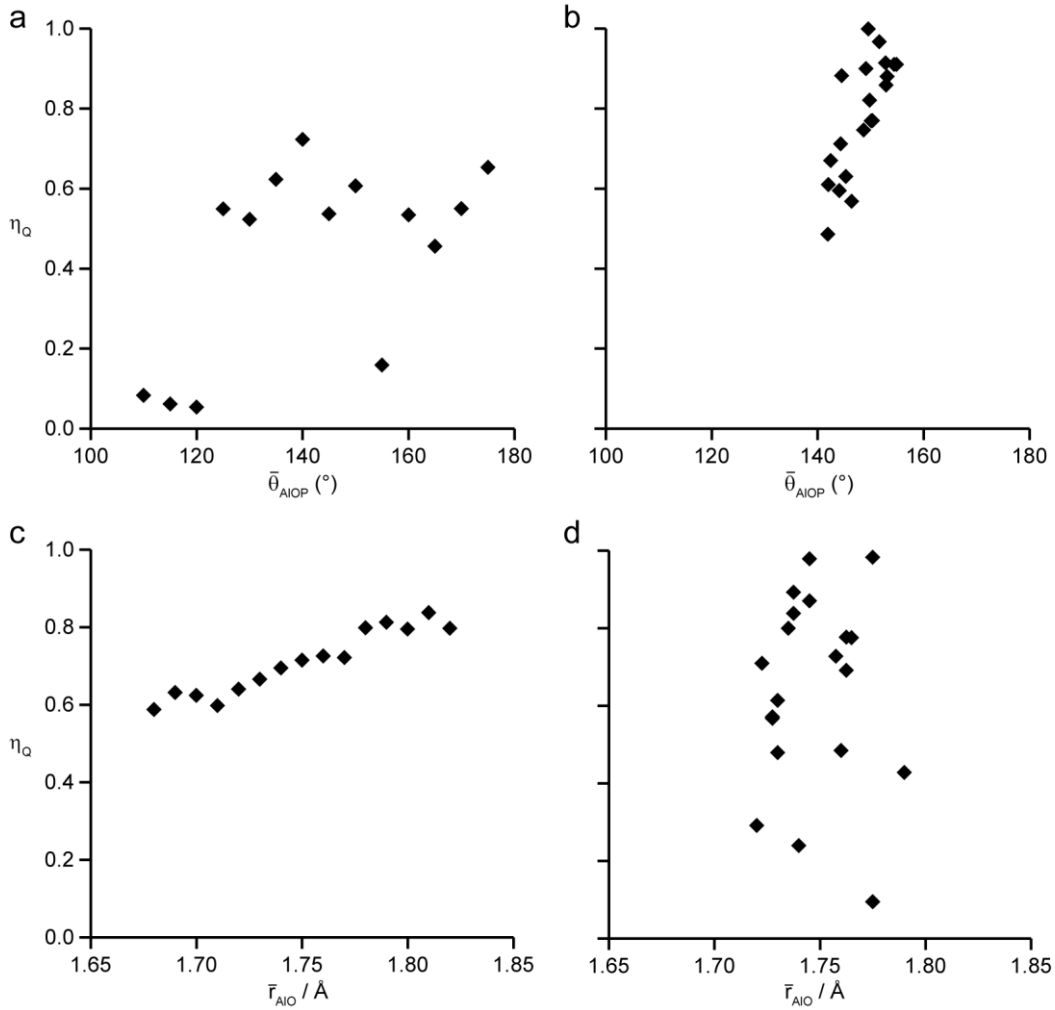

Figure 5.14. Plots of calculated ^{27}Al η_Q against (a and b) $\bar{\theta}_{AlOP}$ and (c and d) $\bar{r}_{AlO}$ for (a) series 14, (b) series 21, (c) series 22 and (d) series 26.

correlation between $\bar{\theta}_{AlOP}$ and η_Q. However, as shown in Figure 5.14(b), when both $\bar{\theta}_{AlOP}$ and $\sigma(\theta_{AlOP})$ are randomly generated, there seems to be a weak positive correlation between $\bar{\theta}_{AlOP}$ and η_Q. The reason for this is not immediately clear, and further randomly-generated values of $\bar{\theta}_{AlOP}$ would be required to ensure that this apparent relationship was not just chance. The situation is the opposite in Figures 5.14(c and d), where similar plots for series 22 and 26 show that while η_Q increases with increasing $\bar{r}_{AlO}$ for series 22, there is no such trend observable when $\sigma(r_{AlO}) \neq 0$, as is the case for series 26. These observations indicate that any relationships between η_Q and the local structure of AlPOs are unlikely to be applicable in all cases, owing to the longer-range nature of the EFG and the fact that η_Q depends on all three components of the EFG tensor.

5.4.3.1 Improving the Models

Given the success of LRFS for ^{31}P, and the model cluster results above that suggest that the ^{27}Al NMR parameters may also be related to structural features, LRFS was extended to ^{27}Al NMR parameters. The structures of the calcined AlPOs used were those described in Appendix K, and the same distortion parameters (here relating to the AlO_4 and AlP_4 tetrahedra), were used to describe the local structure. In addition, it is well known that an approximate EFG may be calculated using the point-charge model,[77] where atoms surrounding the nucleus of interest are treated as point charges and the EFG contributions from each individual charge are summed to give the overall tensor, $\mathbf{V}^{PC}$, where PC denotes the use of the point-charge model. The contribution to the components of $\mathbf{V}^{PC}$, V_{ij}^{PC}, (where i = x, y or z and j = x, y or z), for a point charge of magnitude ne, where e is the electronic charge, located at a distance r from the nucleus of interest, are

$$V_{ij}^{PC} = \frac{ne\left(3i^2 - r^2\right)}{r^5} , \tag{5.37}$$

when i = j, and

$$V_{ij}^{PC} = \frac{ne(3ij)}{r^5} , \tag{5.38}$$

when $i \neq j$. Diagonalisation of $\mathbf{V}^{PC}$ produces the three principal components of $\mathbf{V}^{PC(PAS)}$, V_{xx}^{PC}, V_{yy}^{PC} and V_{zz}^{PC}, where, for simplicity, the superscript (PAS), denoting the principal axes system, has been omitted, and all further mention of V_{ii}^{PC} refers to the principal components of $\mathbf{V}^{PC(PAS)}$. DISCO calculates the point-charge EFG tensor for each Al, assuming that, for Al, n = +3, for P, n = +5 and, for O, n = –2. Clearly, as the structures of AlPOs are covalent networks, rather than ionic solids, these values of n are unrealistic, but it was hoped that they would still provide a reasonable approximation of the relative, if not absolute, magnitudes of $\mathbf{V}^{PC}$. It is important to ensure that the values of V_{ii}^{PC} are converged with respect to the cut-off radius, r_{max}, *i.e.*, including charges more distant than r_{max} in the calculation does not significantly change V_{ii}^{PC} . In the DISCO input file, r_{max} is set by the keyword `efg_cutoff_radius`, followed by the value (in Å). Figure 5.15 shows the values of V_{ii}^{PC} obtained with r_{max} between 0 and 120 Å for Al in $AlPO_4$ berlinite.

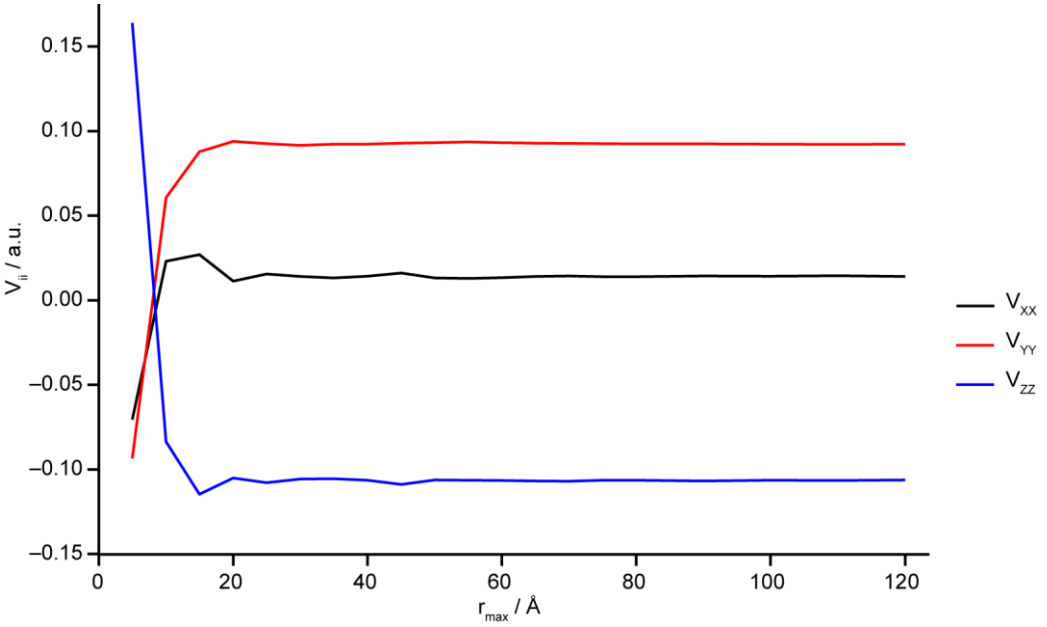

Figure 5.15. Plots of V_{ii}^{PC} (in atomic units) obtained for Al in $AlPO_4$ berlinite with different values of r_{max}.

Convergence to within $\pm 5 \times 10^{-4}$ atomic units is achieved when $r_{max} > 60$ Å, so this value was used for subsequent calculations of $\mathbf{V}^{PC}$.

The structural parameters for the Al species in the test and training sets (discussed above) were calculated using DISCO, and models for σ_{iso}(structure), σ_{ii}(structure), C_Q(structure), $|C_Q|$(structure) and η_Q(structure) were determined using LRFS. $\mathbf{V}^{PC}$ was included as V_{zz}^{PC} (for C_Q(structure)), $\left|V_{zz}^{PC}\right|$ (for $|C_Q|$(structure)) and η_Q^{PC}, calculated from the components of $\mathbf{V}^{PC}$ according to Equation 2.60 (for η_Q(structure)).

The model for σ_{iso}(structure) was determined to be

$$\begin{aligned}\sigma_{iso}(\text{structure}) \;=\; & -25.80\min(r_{AlO}) + 252.6\bar{r}_{AlO} - 2022\Delta(r_{AlO}) - 3.165|\mathbf{r}_{AlO}| \\ & + 0.3000\min(\theta_{OAlO}) - 0.2571\max(\theta_{OAlO}) + 2.131\sigma(\theta_{OAlO}) - 15.54|\Psi_{OAlO}| \\ & + 0.3336\min(\theta_{AlOP}) - 0.4918\max(\theta_{AlOP}) + 0.9338\bar{\theta}_{AlOP} + 0.9215\sigma(\theta_{AlOP}) \\ & + 5.713\min(r_{AlP}) + 15.97\max(r_{AlP}) + 1058\bar{r}_{AlP} - 172.6\bar{r}_{AlP}^2 - 818.7\Delta(r_{AlP}) \\ & - 15.93\,|\alpha_{AlP}| + 3.700|\mathbf{r}_{AlP}| - 0.08373\min(\theta_{PAlP}) - 0.02923\max(\theta_{PAlP}) \\ & + 1.883\bar{\theta}_{PAlP} - 1880\ , \end{aligned} \qquad (5.39)$$

where all coefficients are reported to 4 s.f.. As shown in Figure 5.16, this model

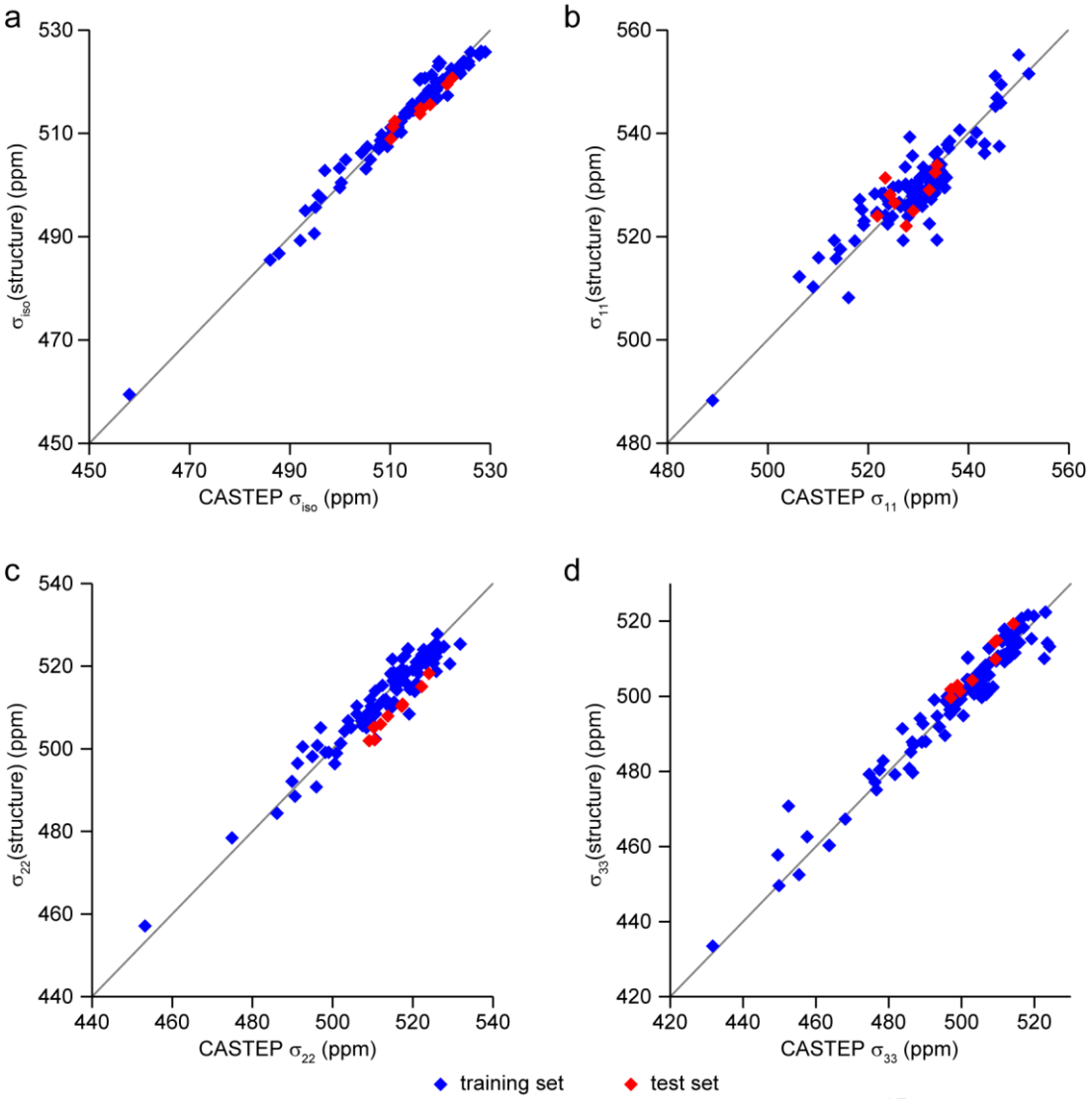

Figure 5.16. Plots of (a) σ_{iso}(structure) and (b-d) σ_{ii}(structure) for ^{27}Al against the values calculated by CASTEP for the training and test sets.

yielded reasonable agreement for the training set (R^2 = 0.9704, MAE = 1.09 ppm) and the test set (R^2 = 0.9368, MAE = 1.56 ppm). It is interesting to note that, unlike in the model cluster calculations, there does not appear to be any dependence on r^2_{AlO} or $\sigma(r_{AlO})$. This suggests that, unlike for ^{31}P, for some reason the model cluster results cannot be applied directly to those for the periodic structures for ^{27}Al. It is possible that this difference arises from a difference in the suitability of the calculation parameters (either the basis set used for the cluster calculations or the pseudopotential and/or energy cut off for the periodic calculations) for Al and P.

The models for the principal components of the shielding tensor, σ_{11}(structure), σ_{22}(structure) and σ_{33}(structure) were determined to be

$$\begin{aligned}\sigma_{11}(\text{structure}) = {} & 57.84\max(r_{AlO}) - 75.80\min(r_{AlO}) + 113.6\bar{r}^2_{AlO} - 288.7\sigma(r_{AlO}) \\ & - 1535\Delta(r_{AlO}) + 173.5|\alpha_{AlO}| + 56.39|\mathbf{r}_{AlO}| + 4.391\min(\theta_{OAlO}) - 5.071\max(\theta_{OAlO}) \\ & + 18.40\bar{\theta}_{OAlO} - 21.93\sigma(\theta_{OAlO}) - 110.0|\Psi_{OAlO}| - 0.2319\min(\theta_{AlOP}) \\ & - 0.4882\max(\theta_{AlOP}) + 1.817\bar{\theta}_{AlOP} + 0.2385\sigma(\theta_{AlOP}) - 14.43\min(r_{AlP}) \\ & + 53.72\max(r_{AlP}) + 2648\bar{r}_{AlP} - 441.5\bar{r}^2_{AlP} - 78.94\sigma(r_{AlP}) - 518.1\Delta(r_{AlP}) \\ & - 38.34|\alpha_{AlP}| - 15.09|\mathbf{r}_{AlP}| + 0.5171\min\theta_{PAlP} - 0.4374\max(\theta_{PAlP}) \\ & - 6.069\bar{\theta}_{PAlP} + 3.321\sigma(\theta_{PAlP}) - 16.59|\Psi_{PAlP}| - 6555 \quad , \end{aligned} \tag{5.40}$$

$$\begin{aligned}\sigma_{22}(\text{structure}) = {} & 151.6\max(r_{AlO}) + 7.418\min(r_{AlO}) + 3.193\bar{r}^2_{AlO} - 89.71\sigma(r_{AlO}) \\ & + 3072\Delta(r_{AlO}) - 21.98|\mathbf{r}_{AlO}| - 0.2244\min(\theta_{OAlO}) + 1.056\max(\theta_{OAlO}) \\ & - 12.43\bar{\theta}_{OAlO} - 2.751\sigma(\theta_{OAlO}) + 10.47|\Psi_{OAlO}| + 0.2009\min(\theta_{AlOP}) \\ & - 0.6797\max(\theta_{AlOP}) + 1.024\bar{\theta}_{AlOP} + 1.043\sigma(\theta_{AlOP}) + 14.87\min(r_{AlP}) \\ & + 59.85\max(r_{AlP}) + 419.5\bar{r}_{AlP} - 72.01\bar{r}^2_{AlP} - 44.76\sigma(r_{AlP}) - 3394\Delta(r_{AlP}) \\ & + 67.53|\alpha_{AlP}| + 5.704|\mathbf{r}_{AlP}| - 0.2604\min\theta_{PAlP} - 0.1796\max(\theta_{PAlP}) \\ & + 1.891\bar{\theta}_{PAlP} - 0.9535\sigma(\theta_{PAlP}) - 3.081|\Psi_{PAlP}| + 419.3 \quad , \end{aligned} \tag{5.41}$$

and

$$\begin{aligned}\sigma_{33}(\text{structure}) = {} & -184.8\max(r_{AlO}) + 63.49\min(r_{AlO}) + 1308\bar{r}_{AlO} - 275.0\bar{r}^2_{AlO} \\ & + 623.2\sigma(r_{AlO}) - 891.9\Delta(r_{AlO}) - 198.9|\alpha_{AlO}| - 44.55|\mathbf{r}_{AlO}| - 3.293\min(\theta_{OAlO}) \\ & + 3.353\max(\theta_{OAlO}) - 4.939\bar{\theta}_{OAlO} - 12.73\sigma(\theta_{OAlO}) + 51.31|\Psi_{OAlO}| \\ & + 0.9341\min(\theta_{AlOP}) - 0.2216\max(\theta_{AlOP}) - 0.004154\bar{\theta}_{AlOP} + 1.277\sigma(\theta_{AlOP}) \\ & - 16.91\min(r_{AlOP}) - 53.18\max(r_{AlP}) + 399.1\bar{r}_{AlP} - 52.00\bar{r}^2_{AlP} + 83.05\sigma(r_{AlP}) \\ & + 849.4\Delta(r_{AlP}) - 60.62|\alpha_{AlP}| - 9.115|\mathbf{r}_{AlP}| - 0.8598\min\theta_{PAlP} + 0.8202\max(\theta_{PAlP}) \\ & - 2.050\bar{\theta}_{PAlP} - 4.484\sigma(\theta_{PAlP}) + 30.04|\Psi_{PAlP}| - 570.8 \quad , \end{aligned} \tag{5.42}$$

where all coefficients are reported to 4 s.f.. However, as observed for ^{31}P, the models for σ_{ii}(structure) given in Equations 5.40-42 yield relatively poor R^2 (0.8420, 0.9260 and 0.9354, respectively) and high MAEs (2.86, 2.12 and 2.66 ppm, respectively), even for the training set. As shown in Figure 5.16, the σ_{ii}(structure) for the test set display poor correlation with the calculated σ_{ii}, as was observed for ^{31}P. However,

the predicted values still fall within the scatter of the points for the training set, again suggesting that there is some predictive power in these models, although their worth will be limited by the error of a few ppm, which is large compared to the typical calculated span of the ^{27}Al shielding tensor (~30 ppm here). Accurate prediction of the CSA parameters for ^{27}Al may well be of limited practical use, as ^{27}Al NMR spectra are typically (except at very high field) dominated by the second-order quadrupolar broadening, making measurement of the small CSA very difficult.

Unlike the case of ^{31}P, for ^{27}Al, the coefficients for σ_{iso}(structure), determined as the average of the coefficients for each parameter in Equations 5.40-42, do not agree with the coefficients for σ_{iso}(structure) determined by LRFS. However, as is shown in Figure 5.17, where σ_{iso}(structure), determined using either LRFS or the average of the coefficients from Equations 5.40-42 is plotted against the calculated σ_{iso}, both models provide an equally good description (R^2 = 0.9704, MAE = 1.09 ppm). In addition, the predictive power of σ_{iso}(structure) determined as the average of σ_{ii}(structure) for the test set is improved (R^2 = 0.9406 compared to 0.9368, MAE = 1.54 ppm, compared to 1.60 ppm). As the two models yield similar results, despite the differences in the coefficients (shown graphically in Figure 5.18), some caution must be taken when using the values reported in Equation 5.39, as these probably do not represent a unique solution to the parameterisation of σ_{iso}(structure).

Of course, for ^{27}Al, it is usually of more interest to consider the quadrupolar interaction, described by C_Q and η_Q. When determining the models, C_Q(structure), $|C_Q|$(structure) and η_Q(structure), the structural parameters were extended to include V_{zz}^{PC}, $|V_{zz}^{PC}|$ and η_Q^{PC}, respectively, yielding

$$\begin{aligned} C_Q(\text{structure}) \;=\; & 371.0\max(r_{AlO}) + 132.3\min(r_{AlO}) - 1627\bar{r}_{AlO} + 332.3\bar{r}_{AlO}^2 \\ & - 904.9\sigma(r_{AlO}) + 4854\Delta(r_{AlO}) + 250.6|\alpha_{AlO}| - 18.91|\mathbf{r}_{AlO}| - 4.363\min(\theta_{OAlO}) \\ & + 4.442\max(\theta_{OAlO}) - 18.67\bar{\theta}_{OAlO} - 21.38\sigma(\theta_{OAlO}) + 86.85|\Psi_{OAlO}| \\ & + 1.182\min(\theta_{AlOP}) - 1.426\max(\theta_{AlOP}) - 0.08200\bar{\theta}_{AlOP} + 3.739\sigma(\theta_{AlOP}) \\ & - 199.1\min(r_{AlOP}) + 134.5\max(r_{AlP}) + 2602\bar{r}_{AlP} - 403.2\bar{r}_{AlP}^2 - 517.6\sigma(r_{AlP}) \\ & + 3209\Delta(r_{AlP}) - 63.27|\alpha_{AlP}| - 0.9246|\mathbf{r}_{AlP}| + 0.08789\min\theta_{PAlP} - 1.750\bar{\theta}_{PAlP} \\ & - 0.3664\sigma(\theta_{PAlP}) - 5.819|\Psi_{PAlP}| - 1.799V_{zz}^{PC} - 570.8\ , \end{aligned} \qquad (5.43)$$

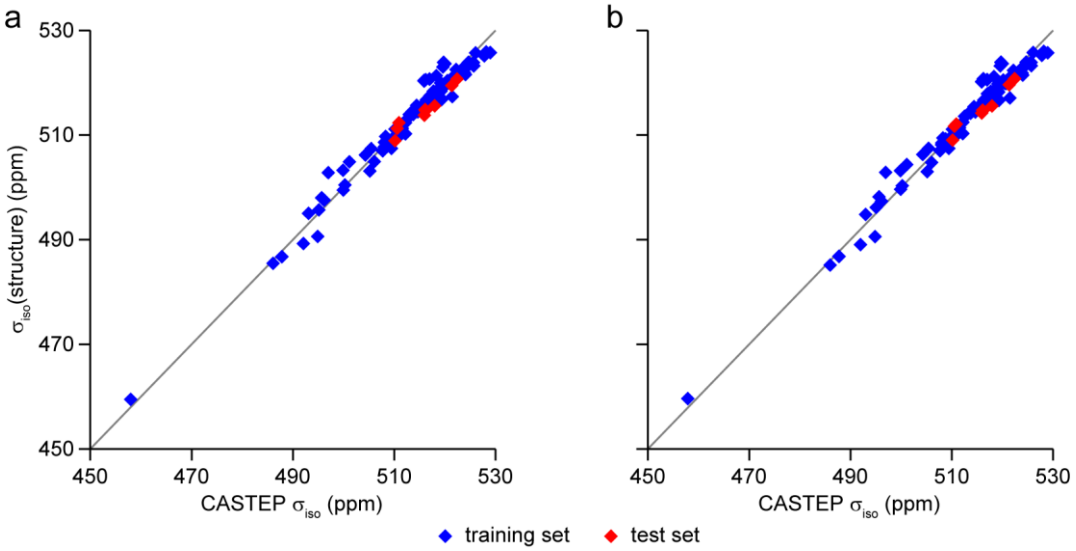

Figure 5.17. Plots of ^{27}Al σ_{iso}(structure) against the value of σ_{iso} calculated by CASTEP, where the coefficients for σ_{iso}(structure) were determined (a) using LRFS and (b) from the average of the values reported in Equations 5.40-42. The ideal 1:1 correspondence is indicated in grey in both parts.

$$\begin{aligned}|C_Q|(\text{structure}) \;=\; & -26.18\max(r_{AlO}) - 10.26\min(r_{AlO}) + 906.9\Delta(r_{AlO}) + 41.65|\alpha_{AlO}| \\ & + 19.30|\mathbf{r}_{AlO}| + 1.173\min(\theta_{OAlO}) - 1.368\max(\theta_{OAlO}) - 4.220\bar{\theta}_{OAlO} \\ & + 5.350\sigma(\theta_{OAlO}) - 25.43|\Psi_{OAlO}| - 0.08757\min(\theta_{AlOP}) - 0.1035\max(\theta_{AlOP}) \\ & + 0.1309\bar{\theta}_{AlOP} + 23.64\min(r_{AlOP}) - 0.9860\max(r_{AlP}) + 1276\Delta(r_{AlP}) + 13.01\,|\alpha_{AlP}| \\ & + 0.3315\min\theta_{PAlP} - 0.2150\max(\theta_{PAlP}) + 1.874\sigma(\theta_{PAlP}) - 11.74|\Psi_{PAlP}| \\ & - 452.0 \quad , \end{aligned} \tag{5.44}$$

and

$$\eta_Q(\text{structure}) \;=\; 0.6642 \quad , \tag{5.45}$$

where all coefficients are reported to 4 s.f.. Equation 5.45 merely represents the average calculated value of η_Q for the training set. This is likely owing to the inherently larger error in η_Q, which depends on the errors in all three V_{ii}. However, in many cases, η_Q is challenging to measure experimentally, and is often reported with an error of ~0.1, so while the accurate prediction of η_Q is desirable, it is not as important as the prediction of C_Q or $|C_Q|$. Disappointingly, as shown in Figure 5.19, both C_Q(structure) and $|C_Q|$(structure) yield relatively poor agreement between the

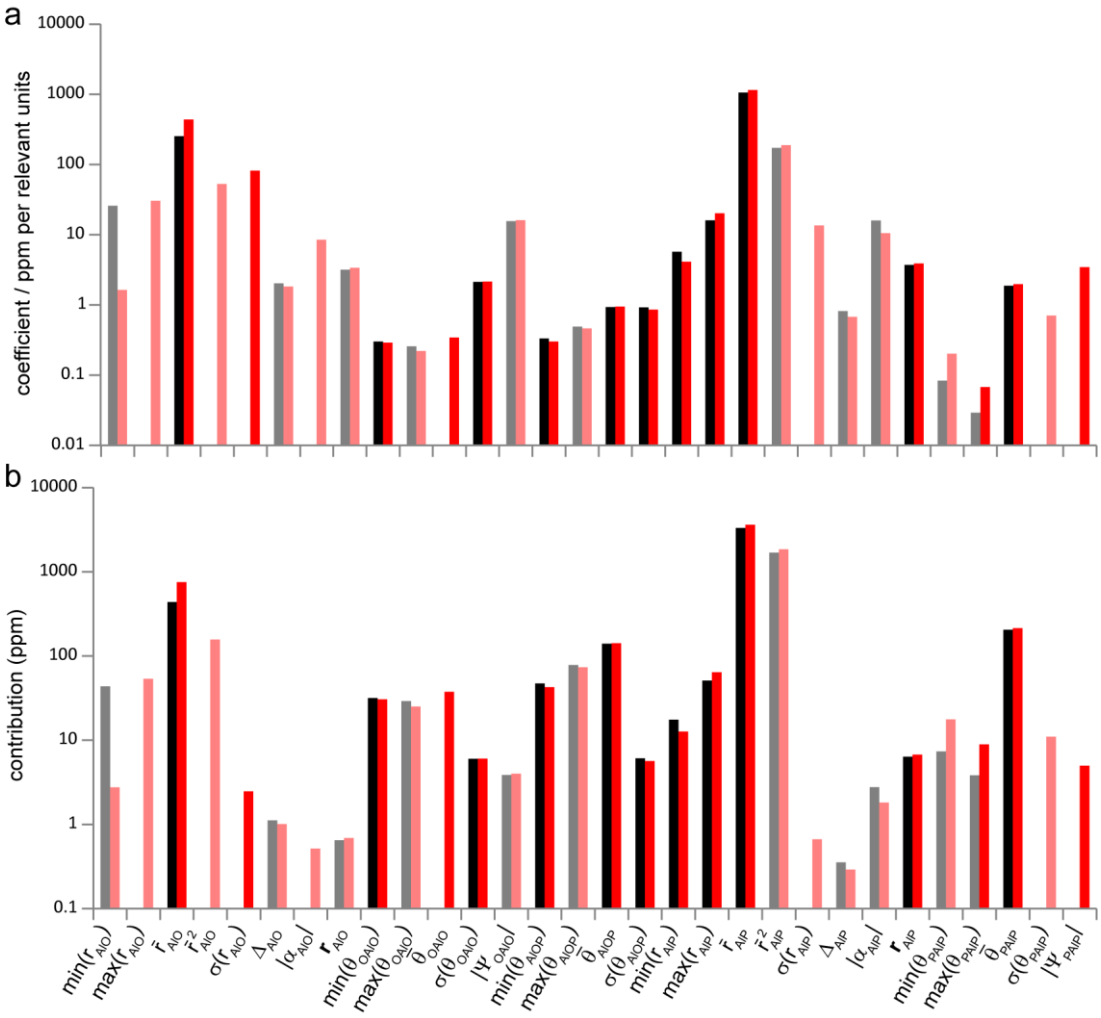

Figure 5.18. Plots of (a) the coefficients and (b) the average contribution of the structural parameters (the product of the coefficient and average value of the given parameter) in σ_{iso}(structure) determined by LRFS (black/grey) and as the average of σ_{ii}(structure) (red/pink) for ^{27}Al. Pale colours represent negative values

calculated and predicted values, and $|C_Q|$(structure) is not dependent on $\left|V_{zz}^{PC}\right|$, as was initially expected. This, combined with the poor η_Q(structure) model suggests that, as discussed above, the point-charge model provides an inadequate description of the atomic charges in the covalent $AlPO_4$ framework. A more accurate description of the charges may be obtained from the Mulliken charges, generated by CASTEP. In the test and training sets, the Mulliken charges of Al, P and O ranged from 2.07 to 2.42, 2.02 to 2.69 and –0.97 to –1.30, respectively, with respective mean values of 2.18, 2.46 and –1.16. The large discrepancies between the Mulliken and ionic charges assumed above suggest that repeating the calculation of $\mathbf{V}^{PC}$ with the mean Mulliken

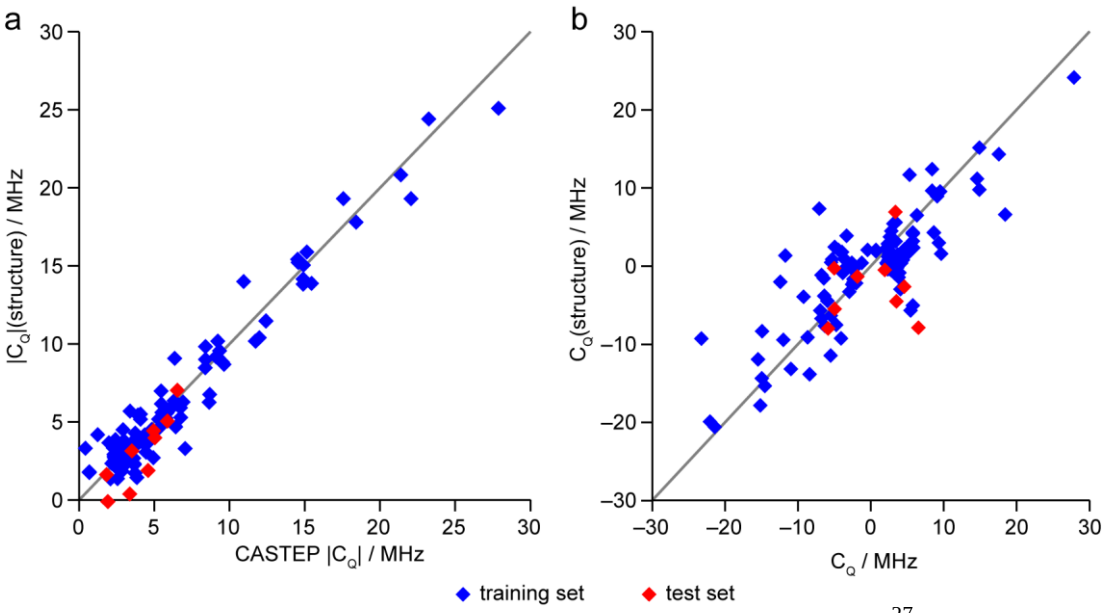

Figure 5.19. Plots of (a) C_Q(structure) and (b) $|C_Q|$(structure) for ^{27}Al against the values calculated by CASTEP, for the test and training sets. $\mathbf{V}^{PC}$ was determined assuming full ionic charges. The ideal 1:1 correspondence is indicated in grey.

charges assumed for Al, O and P, may yield more accurate EFG tensors. However, when the EFG tensors (and $\left|V_{zz}^{PC}\right|$ and η_Q^{PC}) were recalculated using the mean Mulliken charges, there was no change to the coefficients for $|C_Q|$(structure) and η_Q(structure) and, while there was a small change in for C_Q(structure), the agreement of this model with the calculated C_Q was not improved and the model is not shown here. While it would have been possible to include the calculated Mulliken charges for every atom, rather than a mean value, this option was not explored, owing to the unattractive requirement for calculation (using CASTEP) of the Mulliken charges for every AlPO structure for which NMR parameters were to be predicted. This removes the independence from DFT that was the original aim of the predictive model.

Covalency may be introduced into a point-charge model using the method of Brown and Shannon,[78] which relates the i^{th} X-O bond length, r_i, to its strength, s_i,

$$s_i = s_0 \left(\frac{r_i}{r_0}\right)^{-c} , \qquad (5.46)$$

where s_0 is the bond strength associated with the "ideal" bond of length, r_0, and c is a constant specific to a given X cation. Brown and Shannon determined the values of s_0, r_0 and c for a range of elements using several approaches, discussed in detail in

the original work. Here, the bond strengths were calculated using the parameters in Table 3 of the original work;[78] s_0 = 0.5 valence units (v.u.), r_0 = 1.888 Å and c = 4.6. The sum of the strengths of the bonds to an atom should, ideally, equal the valence, Z, of the atom, (where Z = +3 for Al). The covalence, f_i, of a bond can be defined as

$$f_i = a\, s_i^M \ , \tag{5.47}$$

where a and M are fitted parameters, tabulated by Brown and Shannon (see Table 6 of the original work). For Al, a = 0.54 v.u. and M = 1.64. The atomic charge, q, of Al in a tetrahedral AlO_4 environment is then given as

$$q = Z - \sum_{i=1}^{4} f_i \ . \tag{5.48}$$

In order to assess the suitability of the Brown-Shannon model for calculating the atomic charges, DISCO was modified to calculate the charge of every Al, O and P species by this method (using s_0 = 1.25 v.u., r_0 = 1.525 Å, N = 3.2, a = 0.54 and M = 1.64 for P-O bonds) and the overall charge of the unit cell determined. The unit cell charge was typically between 0 and –2, (with the exception of the structure of AlPO-5 published by Ikeda *et al.*,[47] which had a unit cell charge of +0.82) suggesting that the Brown-Shannon model systematically underestimates the atomic charges. When the number of atoms per unit cell was taken into account, the charge was typically underestimated by 0.008(2) per atom. This suggests that the Brown-Shannon model may provide a reasonably accurate description of the charge distribution in the unit cell, although with some small error (arising from the empirically-fitted nature of the parameters used to determine f_i). When the Brown-Shannon charges were used to determine $\mathbf{V}^{PC}$, C_Q(structure), $|C_Q|$(structure) and η_Q(structure) were determined to be

$$\begin{aligned} C_Q(\text{structure}) \ = \ & 390.1\max(r_{AlO}) + 127.7\min(r_{AlO}) - 1793\bar{r}_{AlO} + 377.5\bar{r}^2_{AlO} \\ & - 944.3\sigma(r_{AlO}) + 4967\Delta(r_{AlO}) + 251.3|\alpha_{AlO}| - 21.65|\mathbf{r}_{AlO}| - 4.952\min(\theta_{OAlO}) \\ & + 5.433\max(\theta_{OAlO}) - 23.45\bar{\theta}_{OAlO} - 25.67\sigma(\theta_{OAlO}) + 110.9|\Psi_{OAlO}| \\ & + 1.247\min(\theta_{AlOP}) - 1.406\max(\theta_{AlOP}) - 0.1247\bar{\theta}_{AlOP} + 3.791\sigma(\theta_{AlOP}) \\ & - 214.5\min(r_{AlOP}) + 128.5\max(r_{AlP}) + 2697\bar{r}_{AlP} - 416.6\bar{r}^2_{AlP} - 557.3\sigma(r_{AlP}) \\ & + 4536\Delta(r_{AlP}) - 65.96\,|\alpha_{AlP}| - 0.9060|\mathbf{r}_{AlP}| - 1.908\bar{\theta}_{PAlP} - 0.5927\sigma(\theta_{PAlP}) \\ & - 5.019|\Psi_{PAlP}| - 8.956V^{PC}_{zz} - 237.7 \ , \end{aligned} \tag{5.49}$$

$$
\begin{aligned}
|C_Q|(\text{structure}) \;=\; & -33.28\min(r_{AlO}) - 94.98\sigma(r_{AlO}) + 946.3\Delta(r_{AlO}) + 58.83|\alpha_{AlO}| \\
& + 17.46|\mathbf{r}_{AlO}| + 0.9633\min(\theta_{OAlO}) - 1.179\max(\theta_{OAlO}) - 4.477\bar{\theta}_{OAlO} \\
& + 4.652\sigma(\theta_{OAlO}) - 23.00|\Psi_{OAlO}| - 0.07720\min(\theta_{AlOP}) - 0.07998\max(\theta_{AlOP}) \\
& + 0.1133\bar{\theta}_{AlOP} + 20.04\min(r_{AlOP}) - 21.01\sigma(r_{AlP}) + 1923\Delta(r_{AlP}) + 19.64\,|\alpha_{AlP}| \\
& - 0.03647\max(\theta_{PAlP}) - 1.917|\Psi_{PAlP}| - 2.608\left|V_{zz}^{PC}\right| - 476.0 \;, \qquad (5.50)
\end{aligned}
$$

and

$$\eta_Q(\text{structure}) \;=\; 0.6642 \;. \qquad (5.51)$$

Figure 5.20(a) shows that C_Q(structure) still cannot reliably predict the sign or magnitude of C_Q. For $|C_Q|$(structure), the model is now dependent on $\left|V_{zz}^{PC}\right|$, as expected. However, Figure 5.20(b) demonstrates that the model has not improved significantly from that given in Equation 5.44. The model for η_Q(structure) still cannot be used for the prediction of η_Q. This suggests that the purely ionic model investigated above is as good for prediction of $|C_Q|$ as any model investigated here, despite its simplicity. However, it would be highly beneficial to achieve a more accurate prediction of the quadrupolar parameters for ^{27}Al. The fact that these quadrupolar parameters are not easy to relate to simple geometrical structural features indicates that the EFGs in AlPOs are dependent on factors other than the positions of atomic nuclei, and it is highly likely that some inclusion of the charge present in the bonds (*i.e.*, a more diffuse, less point-like distribution of charge within an atom) would allow more accurate prediction of the EFG parameters. However, such a model would require DFT, which is contrary to the original aims of this project.

5.4.4 The Effect of Local Structure on ^{17}O NMR Parameters

The O atoms of AlPOs are located in bent Al-O-P linkages, as shown in Figure 5.21. The most obvious parameters describing the local environment of O are, therefore, the O-Al bond length, r_{OAl}, the O-P bond length, r_{OP}, and the Al-O-P bond angle, θ_{AlOP}. Alternatively, the average O-T (T = Al, P) bond length, $\bar{r}_{OT}$, may be used to describe the local structure, rather than the individual bond lengths.[66] Owing to the apparent simplicity of the local environment of O, compared to Al and P, no model clusters were studied here. The calculated NMR parameters were taken from the

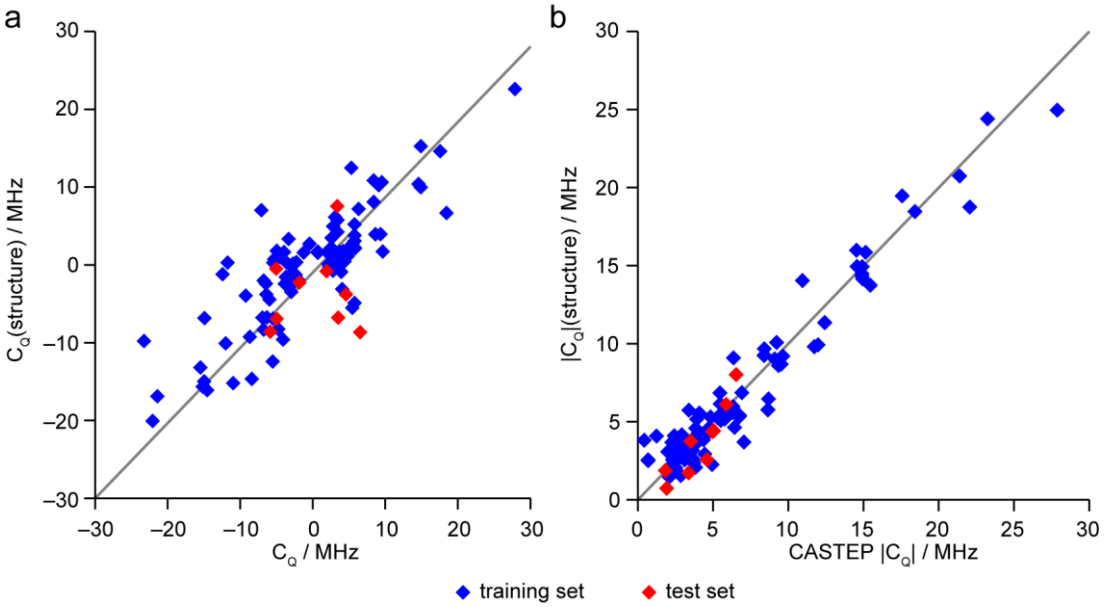

Figure 5.20. Plots of (a) C_Q(structure) and (b) $|C_Q|$(structure) for ^{27}Al against the values calculated by CASTEP, for the test and training sets. $\mathbf{V}^{PC}$ was determined using Brown-Shannon charges. The ideal 1:1 correspondence is indicated in grey.

CASTEP calculations described above and analysis of the local structure was performed by DISCO.

As for ^{27}Al, ^{17}O is quadrupolar (I = 5/2) and the most important parameters commonly influencing ^{17}O NMR spectra are σ_{iso}, C_Q and η_Q. It was assumed that, as was observed for ^{31}P and, to some extent, ^{27}Al, the relationship between the ^{17}O NMR parameters and $\bar{r}_{OT}$ (or r_{PO} and r_{Al}) might be quadratic, and the LRFS approach was used to determine relationships between the ^{17}O NMR parameters and either $\bar{\theta}_{AlOP}$ and $\bar{r}_{OT}$ or $\bar{\theta}_{AlOP}$, r_{OP} and r_{OAl}. It was found that, for ^{17}O,

$$\sigma_{iso}(\bar{r}_{OT},\bar{\theta}_{AlOP}) = 694.0 - 328.9\bar{r}_{OT} + 0.2499\bar{\theta}_{AlOP} \quad , \qquad (5.52)$$

and

$$\sigma_{iso}(r_{OAl},r_{OP},\bar{\theta}_{AlOP}) = 5319r_{OP} - 1822r_{OP}^2 + 713.1r_{OAl} - 222.8r_{OAl}^2 - 0.0624\theta_{AlOP} - 4238 \quad . \qquad (5.53)$$

However, the calculated σ_{iso} for many of the O species in the structure of AlPO-5 of Ikeda *et al.*[47] are very different from all of the other σ_{iso} values, owing to the unrealistic O-Al and O-P bond lengths discussed above, and it is possible that these

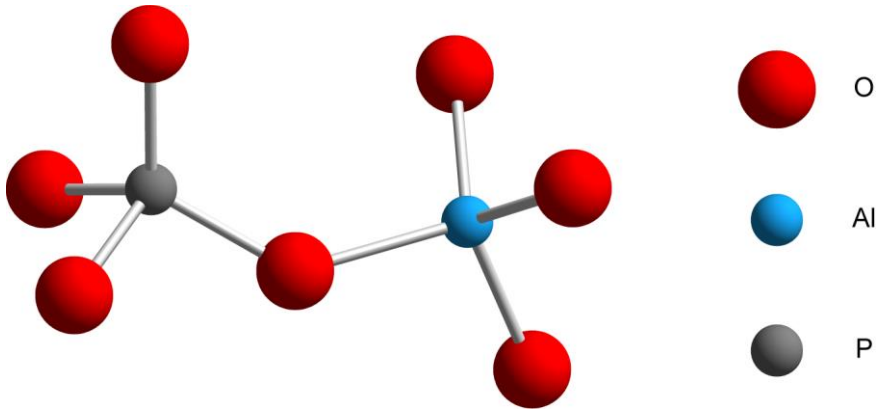

Figure 5.21. The typical local environment of O atoms in AlPOs.

data points distort the outcome of the LRFS process, leading to the poor overall agreement between σ_{iso} and the models in Equations 5.52 and 5.53 shown in Figure 5.22(a). For the remainder of the discussion of ^{17}O NMR parameters, this structure has been omitted from the data sets. Repeating LRFS for σ_{iso} with the values for this structure omitted gives

$$\sigma_{iso}\left(\bar{r}_{OT},\bar{\theta}_{AlOP}\right) = 547.2 - 237.0\bar{r}_{OT} + 0.2522\bar{\theta}_{AlOP} \quad , \tag{5.54}$$

and

$$\sigma_{iso}\left(r_{OAl},r_{OP},\bar{\theta}_{AlOP}\right) = 3488r_{OP} - 1209r_{OP}^2 + 1029r_{OAl} - 311.4r_{OAl}^2 + 0.2239\theta_{AlOP} - 3187 \quad . \tag{5.55}$$

Figure 5.22(b) shows that the agreement between the calculated σ_{iso} and σ_{iso} predicted from Equations 5.54 and 5.55 is somewhat improved, although further improvement is required in order to achieve prediction of ^{17}O σ_{iso} to within a useful margin of error. Describing in greater detail the environment of the O species (perhaps including the next coordination shell of O) may lead to this improvement. Such a study is planned for the future, but is beyond the scope of this thesis.

For the models predicting $|C_Q|$ and η_Q, the parameters, $\left|V_{zz}^{PC}\right|$ and η_Q^{PC}, respectively, were included in the LRFS process. Prediction of C_Q was not included here since, without exception, the signs of all calculated ^{17}O quadrupolar coupling constants were negative, meaning that a simple 1 : –1 correspondence would be expected between $|C_Q|$(structure) and C_Q(structure). When $\mathbf{V}^{PC}$ was calculated using

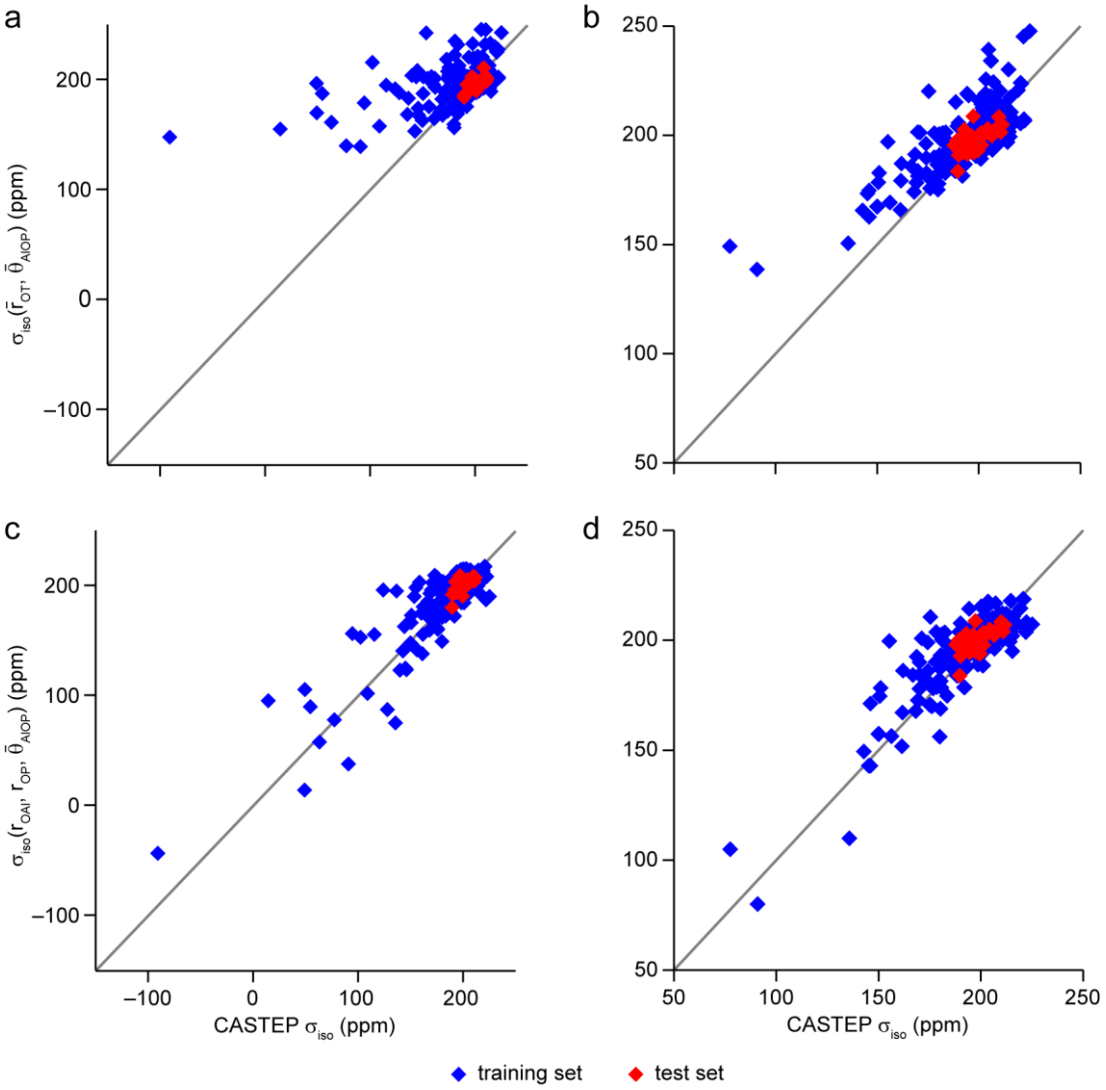

Figure 5.22. Plots of (a and b) $\sigma_{iso}(\bar{r}_{OT},\bar{\theta}_{AlOP})$ and (c and d) $\sigma_{iso}(r_{OAl},r_{OP},\bar{\theta}_{AlOP})$ for ^{17}O, where the models were parameterised using a training set that (a and c) included the structure of AlPO-5 of Ikeda *et al.*,[47] and (b and d) excluded this structure. The ideal 1:1 correspondence is indicated in grey.

ionic charges, this yielded

$$|C_Q|(\text{structure}) = 82.79r_{OP} - 20.18r_{OP}^2 + 40.24r_{OAl} - 10.06r_{OAl}^2 + 1.596\times10^{-3}\theta_{AlOP} + 1.308|V_{zz}^{PC}| - 116.9 \ , \quad (5.56)$$

or

$$|C_Q|(\text{structure}) = 6.381\bar{r}_{OT} + 0.04708\theta_{AlOP} - 1.622|V_{zz}^{PC}| - 6.158 \ , \quad (5.57)$$

depending on whether the individual O-P and O-Al bond lengths or the mean O-T bond length were considered, and, regardless of this consideration,

$$\eta_Q(\text{structure}) = 0.01462 + 1.1618\eta_Q^{PC} \quad . \tag{5.58}$$

Interestingly, as shown in Figure 5.23, unlike the case of ^{27}Al, where this very crude ionic model for the charge distribution in AlPOs was unsuccessful in generating EFG parameters correlated with the calculated ^{27}Al C_Q, for ^{17}O, the ionic model appears to work well, yielding, for $|C_Q|$, MAEs of 121 and 243 kHz for Equations 5.56 and 5.57, respectively and, for η_Q, MAE = 0.04. For the test set, the corresponding MAEs were, for $|C_Q|$, 80 and 147 kHz, for Equations 5.56 and 5.57, respectively, and, for η_Q, 0.04. This indicates a genuine predictive power for the models, especially when the individual O-P and O-Al bond lengths are considered. While the R^2 values (see Figure 5.23) are not as good as some of those achieved above for ^{31}P, the MAEs are of the order of the typical experimental error for both C_Q (typically quoted with errors of at least ±100 kHz, particularly in systems such as AlPOs where there are numerous O species whose resonances may overlap, even in high-resolution spectra) and η_Q (typically determined to within ±0.1), indicating that, while improvement to the model would be desirable from a theoretical standpoint, such improvement is not required for the models to be experimentally useful.

5.4.5 Analysis of Structural Stability

It was seen above that many of the distortion parameters calculated by DISCO were not relevant for the prediction of the NMR parameters of ^{17}O, ^{27}Al or ^{31}P in calcined AlPOs. However, since the parameters had been generated for all of the published crystal structures, and also for some of the same structures after optimisation (see Appendix K), it was possible to investigate whether any of these parameters could be used as an indicator for the "stability" of a structure, *i.e.*, whether a structure would be expected to change significantly on optimisation, or whether it was already close to an energetic minimum (at 0 K). Whereas most parameters showed no clear trends upon optimisation (*e.g.*, $\bar{\theta}_{TOT'}$ was equally likely to increase or decrease, and did not appear to have an "ideal" value common to all optimised structures, as shown in Figure 5.24(a)), it was observed that most of the parameters describing the TO_4 tetrahedron would decrease to a value consistent with a more symmetric (less

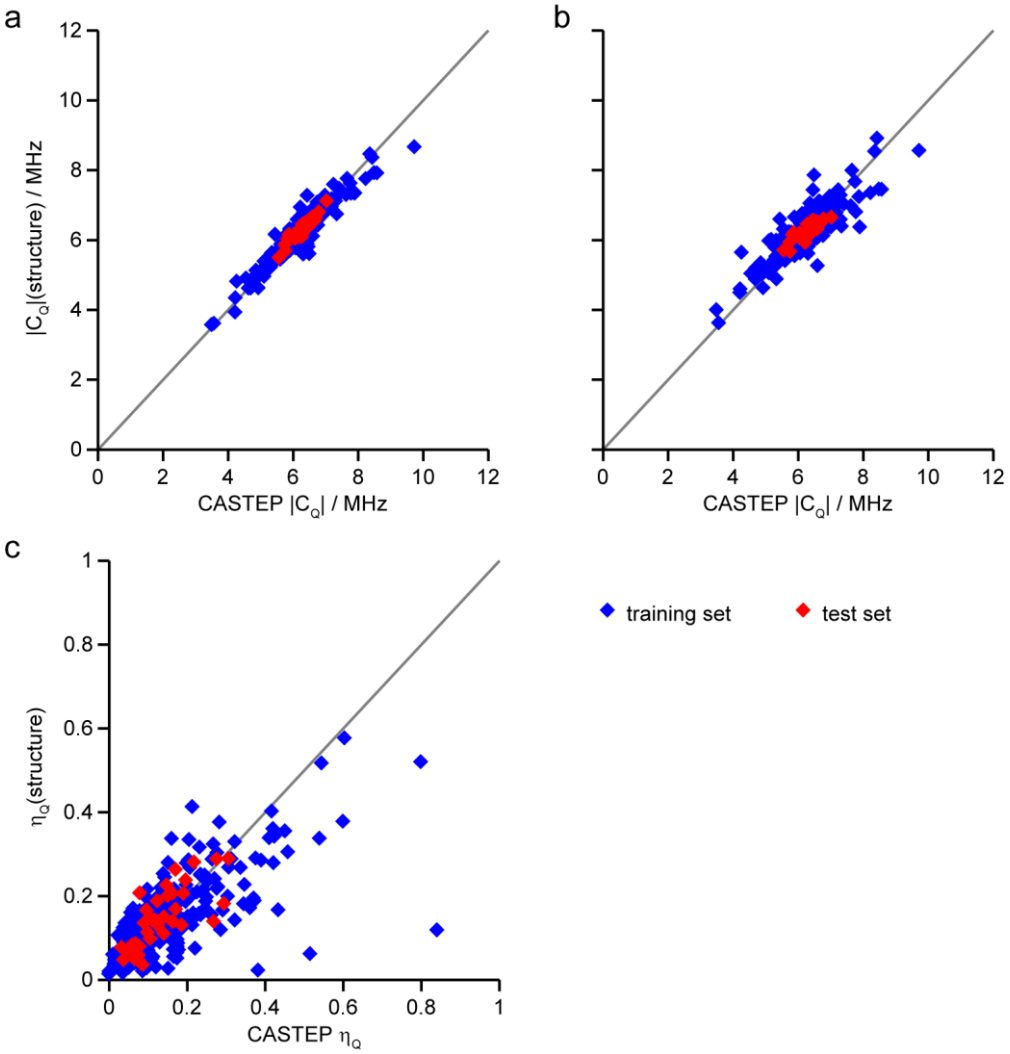

Figure 5.23. Plots of (a and b) $|C_Q|$(structure) using (a) Equation 5.56 and (b) Equation 5.57, and (c) η_Q(structure) for ^{17}O against the values calculated by CASTEP, for the test and training sets. $\mathbf{V}^{PC}$ was determined using ionic charges for Al (+3), O (–2) and P (+5). The ideal 1:1 correspondence is indicated in grey.

distorted) tetrahedron upon optimisation, unless the tetrahedral distortion was already low. Examples of this are shown in Figures 5.24(b and c), where the published and optimised values of $\bar{r}_{PO}$ and $\bar{r}_{AlO}$ are plotted. Tables 5.7 and 5.8 summarise the optimum ranges for the other parameters used to describe the TO_4 tetrahedra and, for ^{27}Al, the EFG parameters (calculated using the ionic model). In all optimisations, when the starting structural parameter was already within the optimum range, it remained within that range upon optimisation, whereas, when the structural parameter was outside the range, it was optimised to fall into the range. This suggests

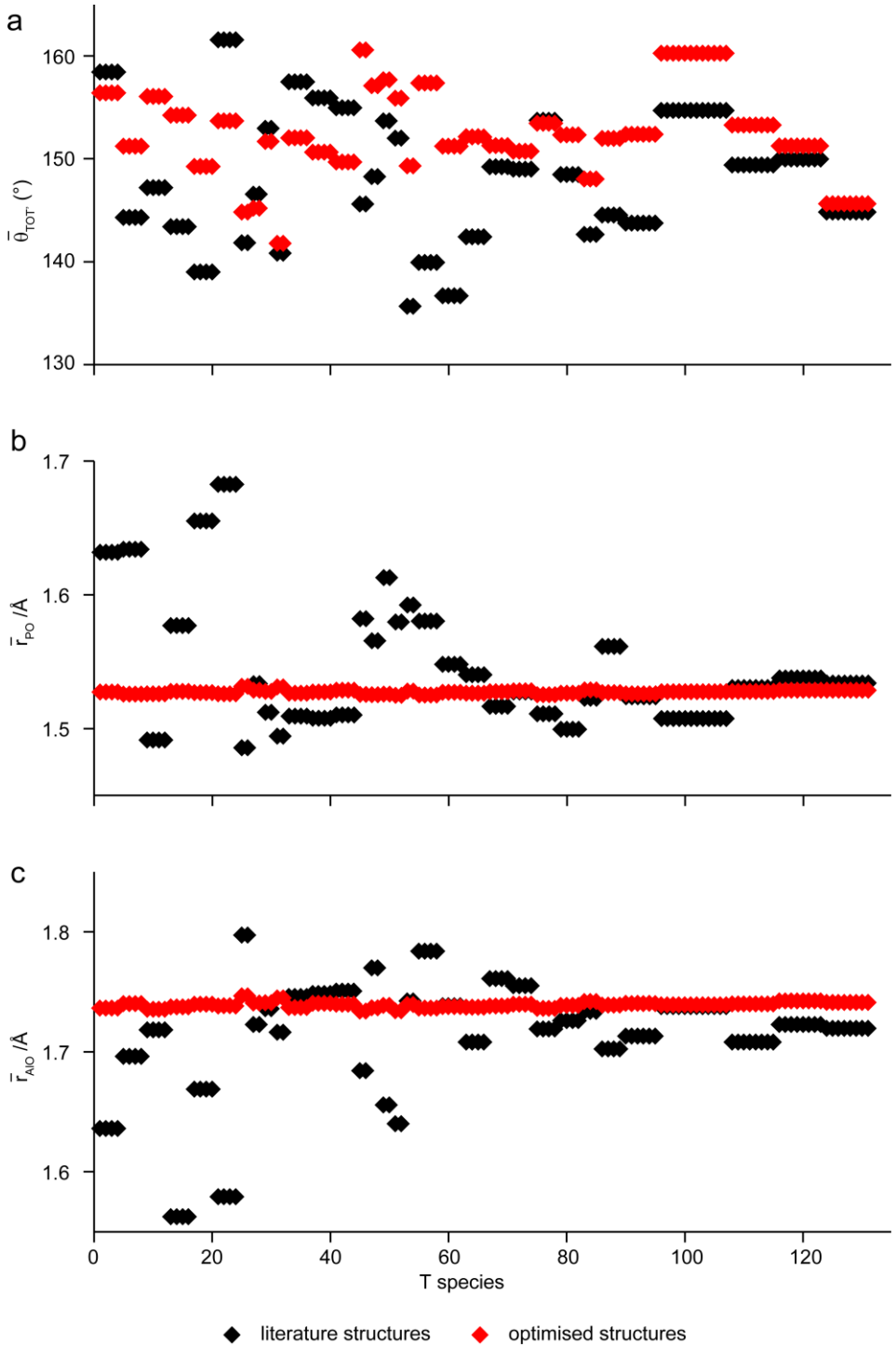

Figure 5.24. Plots of (a) $\bar{\theta}_{TOT'}$, (b) $\bar{r}_{PO}$ and (c) $\bar{r}_{AlO}$ before and after optimisation for the some calcined AlPOs.

Table 5.7. Ranges of structural parameters describing the PO_4 tetrahedra in calcined AlPOs before and after optimisation (see Appendix K for a list of structures used).

Parameter	Before Optimisation	After Optimisation
$\bar{r}_{TO}$ / Å	1.486 – 1.682	1.525 – 1.531
$\sigma(r_{TO})$ / pm	0.0907 – 14.00	0.0479 – 0.784
$\Delta(r_{TO}) \times 10^6$	0.338 – 7940	0.098 – 26.4
$\lvert\alpha_{TO}\rvert \times 10^3$	2.32 – 407	1.25 – 19.5
$\lvert\mathbf{r}_{TO}\rvert$ / pm	0.00 – 134	0.769 – 4.43
$\bar{\theta}_{OTO}$ (°)	107.665 – 109.974	109.468 – 109.474
$\sigma(\theta_{OTO})$ (°)	0.0392 – 18.7	0.406 – 1.21
$\lvert\Psi_{OTO}\rvert$	0.00374 – 1.94	0.0374 – 0.109

Table 5.8. Ranges of structural parameters describing the AlO_4 tetrahedra in calcined AlPOs before and after optimisation (see Appendix K for a list of structures used)..

Parameter	Before Optimisation	After Optimisation
$\bar{r}_{TO}$ / Å	1.563 – 1.797	1.739 –1.755
$\sigma(r_{TO})$ / pm	0.0904 – 11.3	0.0610 – 1.23
$\Delta(r_{TO}) \times 10^6$	0.282 – 5120	0.123 – 49.8
$\lvert\alpha_{TO}\rvert \times 10^3$	4.42 – 282	1.83 – 30.0
$\lvert\mathbf{r}_{TO}\rvert$ / pm	8.80 – 82.8	0.137 – 25.1
$\bar{\theta}_{OTO}$ (°)	108.755 – 109.781	109.448 – 109.506
$\sigma(\theta_{OTO})$ (°)	1.13 – 15.5	0.382 –6.70
$\lvert\Psi_{OTO}\rvert$	0.102 – 1.44	0.0354 – 0.600
V_{xx}^{PC} / a.u.	–0.181 – 0.167	–0.0745 – 0.0684
V_{yy}^{PC} / a.u.	–0.876 – 0.453	–0.191 – 0.191
V_{zz}^{PC} / a.u.	–0.605 – 0.945	–0.232 – 0.211

that the distortions of the TO_4 tetrahedra – particularly $\bar{\theta}_{OTO}$, which is confined to a very narrow range when optimised – can act as reliable indicator of the need to optimise a structure, and also indicates that almost all of the structures included in this study would change significantly on optimisation. (This issue may be responsible for much of the scatter observed in Figure 5.1.) It should be noted that the structural parameters that describe the longer-range structure (T-O-T′ linkages and TT'_4 tetrahedra) do not optimise to a well-defined range. However, this is not particularly surprising, as these structural features will depend more on the topology of the zeolitic framework (*i.e.*, 4MR SBUs and D4R and D6R CBUs must, by necessity, contain T′-T-T′ angles of ~90°, whereas these angles will be larger in most other cases). However, the local TO_4 environment is somewhat less linked to the overall zeolitic framework topology and can, therefore, attempt to adopt the same favourable coordination geometry in all calcined AlPOs.

The above observations suggest that a structure obtained by Bragg diffraction methods could be checked to determine whether it would change significantly on optimisation, and then modified at this early stage in the structural determination process, rather than during a structural optimisation calculation carried out using, *e.g.*, CASTEP, which can take days to run, compared to the minutes or hours required to modify a structure during the crystallographic structure refinement. However, one important caveat is that the structure calculated by CASTEP will only represent the ground-state energy minimum at 0 K, and recent observations by Sneddon *et al*. have shown that, particularly for calcined AlPOs, negative thermal expansion can lead to a significant discrepancy between the 0 K DFT structure and the finite-temperature diffraction structure.[79] Therefore, further investigation, including experimental verification, is required before preliminary screening of experimental structures to match DFT optimisations could be considered routine.

5.4.6 DISCO and NMR-DISCO

DISCO was introduced above as a useful tool for the calculation of structural parameters of calcined AlPOs. This section describes in greater detail the usage and performance of both DISCO and its extension to calculating NMR parameters, NMR-DISCO. NMR-DISCO simply uses the relationships (determined above)

between the local structural parameters generated by DISCO and the NMR parameters calculated by CASTEP, to predict the NMR parameters that would be calculated by CASTEP for a given structure.

5.4.6.1 Input and Output

The DISCO input file, disco.in, contains keywords that control the way the program operates. DISCO has two operation modes, single structure or batch job. For a single structure calculation, disco.in contains the structural data, using the `cell_abc` and `cell_abg` keywords to define the unit cell parameters and the `atoms_list_fract` and `end_atoms_list_fract` keywords to list the fractional coordinates of the atoms. For example, the unit cell of berlinite[80] is defined by

```
cell_abc   4.94300  4.94300  10.94800
cell_abg   90.0000  90.0000  120.0000
```

where a, b and c have units of Å and α, β and γ are in degrees. The atomic coordinates (of each atom in the unit cell, not just the inequivalent positions) are defined by the lines

```
atoms_list_fract
Al      0.466000    0.000000    0.333330
Al      0.000000    0.466000    0.666663
Al      0.534000    0.534000    0.000000
O       0.422000    0.296000    0.396500
O       0.126000    0.704000    0.270167
O       0.704000    0.126000    0.729833
O       0.874000    0.578000    0.063167
O       0.296000    0.422000    0.603500
O       0.578000    0.874000    0.936833
O       0.409000    0.252000    0.885800
O       0.157000    0.748000    0.780867
O       0.748000    0.157000    0.219133
O       0.843000    0.591000    0.552467
O       0.252000    0.409000    0.114200
O       0.591000    0.843000    0.447533
```

```
P       0.467500    0.000000    0.833330
P       0.000000    0.467500    0.166663
P       0.532500    0.532500    0.499997
end_atoms_list_fract
```

Many cif files report fractional coordinates of 1/3 and 2/3 as “0.33330” and “0.66670” (or, in the above example, 0.333330 and 0.666663), respectively. This small error will not cause problems to a human reading the file, but breaks the formal symmetry of the system, giving small spurious contributions to bond lengths and EFGs. In such cases, the input file should be changed so that 1/3 is defined as “0.33333” or even to higher precision, if desired. Once read by DISCO, numbers are treated with precision to at least 10 decimal places to prevent further errors. The input file may also contain additional keywords, detailed in Appendix M, and comment lines, which are ignored by the code, and must start with the “+” symbol.

In batch job mode, disco.in must contain as its first line, the keyword “batch_job_list” and, as its final line, the keyword “end_batch_job_list”. Between these two keywords appears a list of file names for single-structure calculations (without the .in extension). For example, to run calculations on both the published and optimised structures of berlinite, disco.in would contain the lines,

```
batch_job_list
berlinite_icsd
berlinite_opt
end_batch_job_list
```

where the files berlinite_icsd.in and berlinite_opt.in are in the single-structure calculation input format.

DISCO generates multiple output files for each job, (i) a .log file, which records the progress of the calculation and is primarily of use for debugging, (ii) the .struct file, which reports all of the structural parameters calculated (the notation for reporting these is described in further detail in Appendix M) and (iii) the .nmr file, which reports NMR parameters calculated using NMR-DISCO. If there is a fatal error detected within the calculation, which prevents the determination of a structural parameter, a .err file will also be generated, containing further information.

5.4.6.2 Performance and Limitations

As the calculations carried out by DISCO are geometric rather than quantum-mechanical, the code is very rapid, with calculation times on the order of 50-1150 ms for all of the structures included in the present study. In addition, the calculation time appears to scale linearly with the number of atoms present in the system, with a computational cost of around 4.7 ms per atom, as shown in Figure 5.25. This indicates that DISCO could readily be applied to very large systems, with predicted calculation times of ~5 s for systems containing 1000 atoms. Such systems are currently too large for DFT codes such as CASTEP to handle on readily-available local computing hardware, meaning that even the approximate prediction of NMR parameters in this way may be a significant aid to the assignment of the NMR spectra of such systems. However, it must be borne in mind that the accuracy of the results produced by NMR-DISCO are limited both by the simplicity of the models used and by the validity of the input structure. However, given that DISCO already calculates the structural parameters that were shown above to minimise upon optimisation, there is the potential for the code to highlight or rectify problems with the input structure, either by printing a warning message that the structure is unlikely to represent an energy minimum, or by iterative minimisation of relevant structural parameters, using any available experimental NMR and diffraction data as constraints. However, neither of these features is currently included in the program.

The ability to rapidly determine approximate NMR parameters for a system containing many hundreds or thousands of atoms means that one potential application of NMR-DISCO could be to generate NMR parameters from the results of molecular dynamics (MD) calculations. Such calculations employ relatively simple mechanical approximations about the behaviour of atoms and molecules, rather than the more rigorous approaches of DFT calculations, allowing MD to calculate the evolution (or trajectory) of a system over time periods on the order of ps to ns (depending on the computational power available). The output of an MD calculation is a series of structures, corresponding to the individual time increments in the trajectory. Typically, in order to model motion of, *e.g.*, a guest molecule from a pore in one unit cell to an adjacent pore in another unit cell, the structure used in the MD calculation is a relatively large supercell of the parent crystal structure,

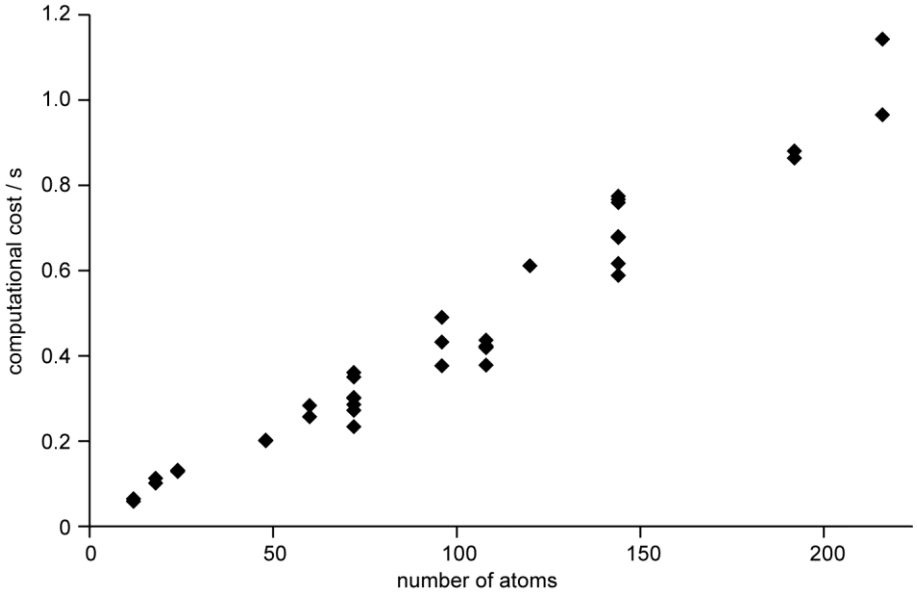

Figure 5.25. A plot of the DISCO calculation time against the number of atoms present in the input file for the series of calcined AlPOs detailed in Appendix K.

meaning that the output from an MD calculation contains (typically) thousands of structures, each containing hundreds or thousands of atoms. Clearly, calculating NMR parameters for all of these structures using DFT would be impractical, and is unlikely ever to be a reasonable prospect with conventional computing technology. However, if the calculation time for the NMR parameters can be reduced to the timescale of a few seconds per structure using NMR-DISCO, then calculating the NMR parameters for every structure in even a very large MD run would take only a few hours in total. This would mean that there could be a direct (although approximate) link between the MD simulation of, *e.g.*, a catalytic process occurring within the pores of an AlPO, and experimental NMR characterisation of the same system. It can be envisaged that such a link would allow for the investigation of possible reaction pathways and the identification of reaction intermediates in catalytic processes, or the determination of binding modes of guest species in applications such as drug storage and delivery.

5.4.7 Future Extensions

This study has so far been restricted to calcined AlPOs – a fair initial approximation, given that one can assume that the distortions of the $AlPO_4$ framework of most AlPOs will dominate the chemical shifts of ^{27}Al and ^{31}P. However, in as-prepared

AlPOs, species such as extraframework anions and molecular H_2O can bind to Al, leading to an increase in its coordination number to five or six. This can be seen to have a large influence on the ^{27}Al chemical shift, and consequent distortions in the Al-O-P bond angles also lead to changes in the ^{31}P chemical shifts. In addition, the EFG at the ^{27}Al nucleus will change significantly. Therefore, in order to make this study truly useful to synthetic chemists, who typically wish to study the as-prepared or guest-loaded materials, the above models must be validated for AlPOs containing higher-coordinate Al and a range of guest species. Such an extension of the study would also allow NMR-DISCO to be used in conjunction with *e.g., in situ* studies of catalytic processes occurring within AlPOs and MD models of the system, as mentioned above.

As demonstrated in Figure 5.1, most phosphate-based framework materials have similar relationships between the ^{31}P isotropic shift and the structure. It should, therefore, be possible to generalise the models presented above, to take into account structures such as SAPOs, MAPOs and GaPOs. While such generalisation would require a large computational expenditure for validation, it is likely to be worthwhile, particularly in the case of SAPOs, MAPOs and aluminosilicates, which are of greater interest to catalytic applications owing to the presence of framework acidity.

5.4.8 Conclusions

This work has demonstrated that the NMR parameters for ^{17}O, ^{27}Al and ^{31}P in calcined AlPOs can, in most cases, be related to the local structure. For all three nuclei, previous literature studies have indicated the presence of such relationships, but using either small datasets or comparing the experimental NMR parameters with the experimentally-determined structure, both of which may be subject to significant experimental errors. However, this study used a completely theoretical approach, comparing calculated NMR parameters with their corresponding structures, thereby vastly reducing the uncertainty involved in assuming that the crystal structure is a fair description of the sample studied by NMR experiment.

For ^{27}Al and ^{31}P, the initial investigation utilised a model cluster approach, using the GAUSSIAN03 code to calculate the NMR parameters for the central Al or

P atom of a $[Al(OP(OH)_3)_4)]^{3+}$ or $[P(OAl(OH)_3)_4]^{3-}$ cluster while the T-O bond lengths and T-O-T′ bond angles were varied systematically. The calculations revealed that there were clear relationships between σ_{iso} and these two structural parameters, for both ^{27}Al and ^{31}P. Although these relationships could not be applied directly to calcined AlPOs owing to the truncated structure necessitated by the model cluster approach, it was shown that, for a series of periodic calculations (carried out using the CASTEP code) for crystal structures of calcined AlPOs, there are also clear relationships between σ_{iso} and the T-O bond length and the T-O-T′ bond angles. More detailed analysis of the local structure of calcined AlPOs was achieved using the DIStortion analysis COde (DISCO), which can rapidly calculate a large number of local structural parameters for Al, P and O. Using a linear regression with feature selection (LRFS) approach, the relevant structural parameters were selected for each NMR parameter, and the overall models relating the local structure to the NMR parameters were generated. For the ^{27}Al and ^{31}P σ_{iso} and the ^{17}O C_Q, the models yielded good predictive power, suggesting that there are genuine links between the local structure and the NMR parameters of all three nuclei. However, for most of the other NMR parameters, the models determined did not yield adequate predictive power to enable a full assignment of an experimental NMR spectrum, although even the approximate values predicted by these models may be of use in some cases (*e.g.*, when a structure is too large to subject to DFT calculations to determine more accurate NMR parameters).

As many of the structures of the calcined AlPOs were optimised to an energy minimum, it was possible to compare the local distortion parameters of the initial (experimentally-determined) and optimised structures, to investigate whether the need for optimisation could be determined by inspection of the initial structure. It was shown that the TO_4 tetrahedron will always optimise to as close to an ideal tetrahedron with bond lengths of 1.525 – 1.531 for PO_4 and 1.739 –1.755 for AlO_4. However, there is no optimum value for the Al-O-P bond angles, and the AlP_4 and PAl_4 tetrahedra do not optimise to idealised tetrahedral geometry, as these three structural features are much more closely linked to the longer range zeolitic topology of the AlPO than its atomic-scale structure. Therefore, it was demonstrated that it is possible to determine whether a structure requires optimisation or not, simply by

inspection of the T-O bond lengths and O-T-O bond angles. It can also be seen that every structure included in the present study was in need of some optimisation.

Unfortunately, owing to the multivariate nature of the relationships determined here, it would be impossible to work "backwards"; determining the structure of a material from its NMR parameters. However, it may be possible, owing to the ability of DISCO to calculate NMR parameters very rapidly, to carry out an iterative structural optimisation using experimental NMR parameters and the optimal bond lengths and angles as constraints.

The ability to predict approximate NMR parameters in cases where the more accurate DFT calculations would be unfeasible (owing to the size of the system or the number of structures to consider) may mean that DISCO has many applications in areas such as combined NMR and MD or MC studies, where the MD and MC calculations output typically thousands of structures, for which calculation of NMR parameters would be required. Such a task would take years of computational time with DFT, but may only take a few hours or days with DISCO (*i.e.*, negligible time compared to the length of the MD or MC calculation). Such a time saving would be particularly useful for studying, *e.g.*, the mechanism of AlPO-catalysed reactions and the adsorption and dynamics of guests within the pores of AlPOs.

5.5 AlPO-53(A) and JDF-2

5.5.1 Introduction

The hydrothermal synthesis of AlPOs in the presence of methylammonium hydroxide has led to two distinct phases, known as AlPO-53(A)[3] and JDF-2[81, 82] (JDF = Jilin-Davy-Faraday, after the two labs where the material was discovered). JDF-2 has the formula $Al_3P_3O_{12}(CH_3NH_3OH)$. Its structure comprises a charge-neutral AlPO framework with the AEN topology,[83] with HO^- bridging two of the three crystallographic Al species (Al1 and Al2, in the nomenclature of Chippindale *et al.*,[82]), which are, consequently, five-coordinate and methylammonium (MA) located within the two-dimensional network of pores. Despite the presence of the MA within

its pores, JDF-2 reversibly hydrates under ambient conditions[2] to give the closely-related AlPO-53(A), with reported formula $Al_6P_6O_{24}(CH_3NH_3OH)_2(H_2O)_2$. The presence of the H_2O causes a lowering of the crystallographic symmetry (from *Pbca* to $P2_12_12_1$), giving rise to six crystallographically-distinct Al and P species, two distinct MA and HO^- species, and two distinct H_2O molecules.[3] The crystal structures of JDF-2 and AlPO-53(A) are shown in Figure 5.26, with the crystallographically-distinct Al, P, MA, HO^- and H_2O species identified. Kirchner *et al*., have also reported the direct synthesis of AlPO-53(A).[3]

Both AlPO-53(A) and JDF-2 can be calcined at 300 - 400 °C to give the AEN-type AlPO-53(B). Chippindale *et al*.[82] reported that JDF-2 became amorphous at ~350 °C, but Ashbrook *et al*.[2] demonstrated that the conversion of JDF-2 to AlPO-53(A) (which remains crystalline when calcined[2,3]) occurs at 20 - 80 °C, suggesting that the bulk sample involved in the single-crystal diffraction study of Chippindale *et al.* may have been of low starting crystallinity or purity. Heating AlPO-53(B) to 700 °C leads to a rearrangement of the Al-O-P linkages in the framework, giving the denser phase, AlPO-53(C). The AlPO-53(C) prepared by Kirchner *et al*.[3] was contained significant quantities of the dense phase $AlPO_4$ tridymite, indicating that prolonged heating at such elevated temperatures may lead to complete loss of the open framework structure.

Two aspects of the AlPO-53 series of materials are investigated in greater detail here. Firstly, there are few reports in the literature of adsorption of atmospheric moisture by AlPOs whose pores already contain guest species. Such an occurrence in the case of JDF-2 → AlPO-53(A), therefore, warrants further investigation, in order to understand why both AlPOs are stable, as well as to gain insight into the interactions of guest species in the confined spaces present in microporous materials. Ashbrook *et al.* previously observed that the hydration was facile, but relatively slow (on the timescale of weeks) under ambient conditions.[2] This section presents a more detailed investigation of the hydration process, using ^{31}P MAS NMR to follow the transformation of JDF-2 to AlPO-53(A) under ambient conditions. Following this investigation, discrepancies between the published crystal structure and experimental NMR results for AlPO-53(A) are investigated in a combined NMR and DFT study.

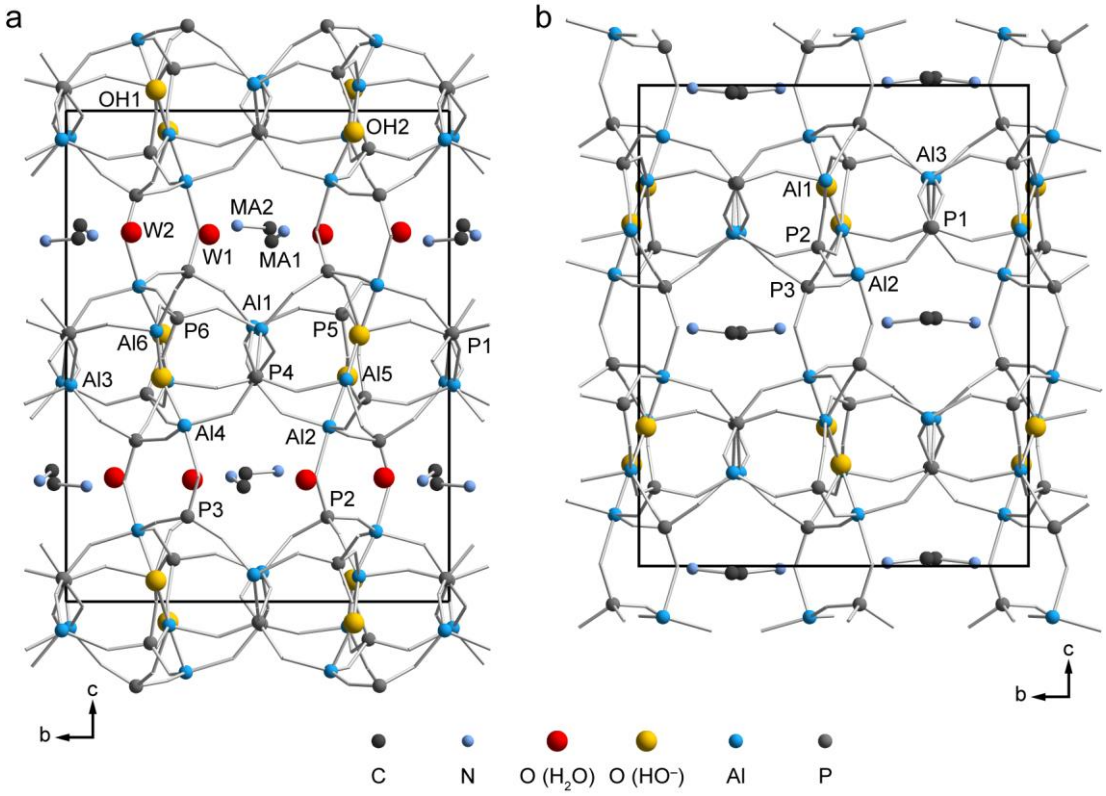

Figure 5.26. The published crystal structures of (a) AlPO-53(A)[3] and (b) JDF-2.[82] Crystallographically-distinct Al, P, MA, HO^- and H_2O species are indicated and H atoms are omitted for clarity.

5.5.2 Ambient Hydration of JDF-2 to AlPO-53(A)

The ambient hydration of AlPOs, whose pores already contain a SDA is unusual – indeed, the transformation of JDF-2 to AlPO-53(A) is the only such transformation reported in detail in the literature[2] (although the loss of H_2O – the reverse of this process – is often observed by thermogravimetry). Ashbrook *et al.*[2] confirmed that JDF-2 and AlPO-53(A) interconvert under conditions close to ambient (*i.e.*, atmospheric moisture for hydration and gentle heating for dehydration) over a period of several weeks. However, the present work aimed to carry out a more systematic investigation. The interconversion was followed by ^{31}P MAS NMR, since, as shown in Figure 5.27, despite the overlap of some resonances from JDF-2 and AlPO-53(A), the P5 and P2+P3 resonances of AlPO-53(A) (using the assignment of Ashbrook *et al.*, summarised in Table 5.9) do not overlap with any resonances from JDF-2.

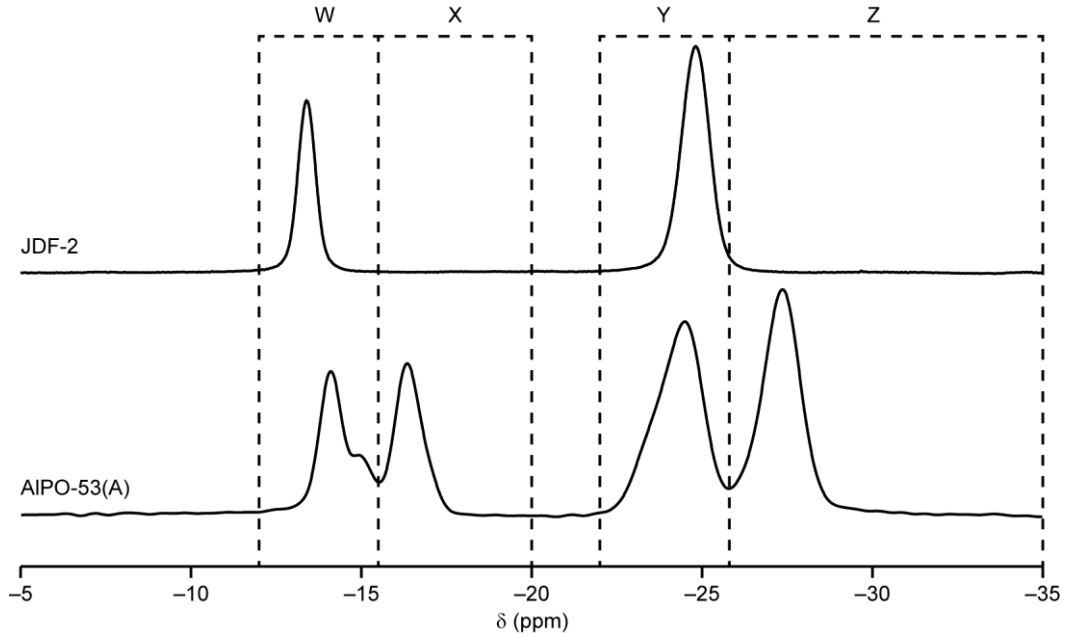

Figure 5.27. ^{31}P (14.1 T, 12.5 kHz MAS) NMR spectra of JDF-2 and AlPO-53(A). The distinct regions of spectral intensity used to determine the composition of mixtures of JDF-2 and AlPO-53(A) are indicated.

Table 5.9. Assignment of the ^{31}P NMR spectra of AlPO-53(A) and JDF-2, according to Ashbrook *et al*.[2] The shifts reported in the original work differ from those reported here by ~0.5 ppm, owing to a difference in the secondary reference frequency used for the spectra. The present spectra were referenced as detailed in Appendix D.

Species	δ_{iso} (ppm)	
	Ashbrook *et al*.	this work
	JDF-2	
P1 + P3	–25.3	–24.8
P2	–13.9	–13.4
	AlPO-53(A)	
P1 + P4	–25.1	–24.5
P2 + P3	–27.8	–27.4
P5	–16.9	–16.4
P6	–14.5	–14.2

Considering the ^{31}P MAS NMR spectrum of a mixture of JDF-2 and AlPO-53(A) of composition x_J JDF-2 + x_A AlPO-53(A), where

$$x_J + x_A = 1 \ , \tag{5.59}$$

the spectrum can be separated into four distinct regions, W, X, Y and Z, as shown in Figure 5.27. Region W (–12.0 to –15.5 ppm) has intensity I_W and contains resonances from P2 of JDF-2 and P6 of AlPO-53(A). Region X (–15.5 to –20.0 ppm) has intensity I_X and contains only the P5 resonance of AlPO-53(A). Region Y (–22 to –25.8 ppm) has intensity I_Y, and contains resonances from P1 and P3 of JDF-2 and P1 and P4 of AlPO-53(A). Region Z (–25.8 to –35 ppm) has intensity I_Z and contains the P2 and P3 resonances of AlPO-53(A). Using the notation I_{nM}, where n = the crystallographic P species and M = J or A (denoting JDF-2 or AlPO-53(A), respectively), the intensities of the regions are

$$I_W = I_{2J} + I_{6A} \ , \tag{5.60}$$

$$I_X = I_{5A} \ , \tag{5.61}$$

$$I_Y = I_{1J} + I_{3J} + I_{1A} + I_{4A} \ , \tag{5.62}$$

and

$$I_Z = I_{2A} + I_{3A} \ . \tag{5.63}$$

Given that all P species have equal occupancy in the crystal structures of JDF-2 and AlPO-53(A), and expressing I_W, I_X, I_Y and I_Z as a fraction of the total spectral intensity, Equations 5.60-63 can be rewritten in terms of x_A, giving

$$I_W = \frac{1}{3}\left(1 - \frac{x_A}{2}\right) \ , \tag{5.64}$$

$$I_X = \frac{x_A}{6} \ , \tag{5.65}$$

$$I_Y = \frac{2}{3}\left(1 - \frac{x_A}{2}\right) \ , \tag{5.66}$$

and

$$I_Z = \frac{x_A}{3} \ . \tag{5.67}$$

The value of x_A can, therefore, be determined by integration of the ^{31}P MAS NMR spectrum (including first-order SSBs) of a sample of JDF-2 exposed to ambient moisture for a given time period. The intensities of all four regions can be obtained from one spectrum, allowing four values of x_A to be determined and providing some indication of the error associated with this approach. In order to ensure that the spectra were quantitative, an experimental repeat interval of 20 minutes was used, with signal averaging over just two transients to ensure that the overall experimental time remained short (to minimise dehydration induced by frictional heating of the rotor during MAS). A portion of JDF-2 was dried at 110 °C for 72 h prior to the study. The sample was packed into a rotor under air, while hot, and the spectrum recorded immediately (t = 0). Spectra were then recorded after 1, 2, 3, 16, 21, 29, 42, 46, 64, 66 and 89 days of exposure to ambient moisture. Between recording NMR spectra, the sample was placed in a vial covered with punctured sealing film, allowing free access to air. During the experiment, the temperature of the air-conditioned room was maintained at 19.0(2) °C, while the relative humidity varied between 23 and 43%, dependent on external weather conditions.

The conversion of JDF-2 to AlPO-53(A), expressed as the mean x_A is plotted in Figure 5.28. The hydration initially proceeds rapidly with x_A = 0.26(5) after one day, but requires almost three months to near completion (x_A = 0.988(5)). This means that any samples of JDF-2 must be dried prior to study, as even brief exposure to atmospheric moisture will result in appreciable conversion to AlPO-53(A). However, JDF-2 that has been exposed to ambient conditions, even for several weeks, cannot be considered to have converted fully to AlPO-53(A). Indeed, it is likely that, with the relatively low relative humidity present in the experiment, JDF-2 and AlPO-53(A) will be in equilibrium, and JDF-2 will never fully hydrate when exposed to ambient moisture. Owing to the variation in the relative humidity (*i.e.*, the concentration of free water present), no more detailed kinetic analysis could be carried out. An important point to note is that, as shown in Figure 5.28(b), at all stages during the hydration experiment, the ^{31}P NMR spectra showed only resonances from JDF-2 and AlPO-53(A), indicating that there is no formation of an intermediate phase (in appreciable concentrations). As the reaction occurs in a solid, the diffusion of H_2O through the pores of the AlPO, into the core of each crystallite,

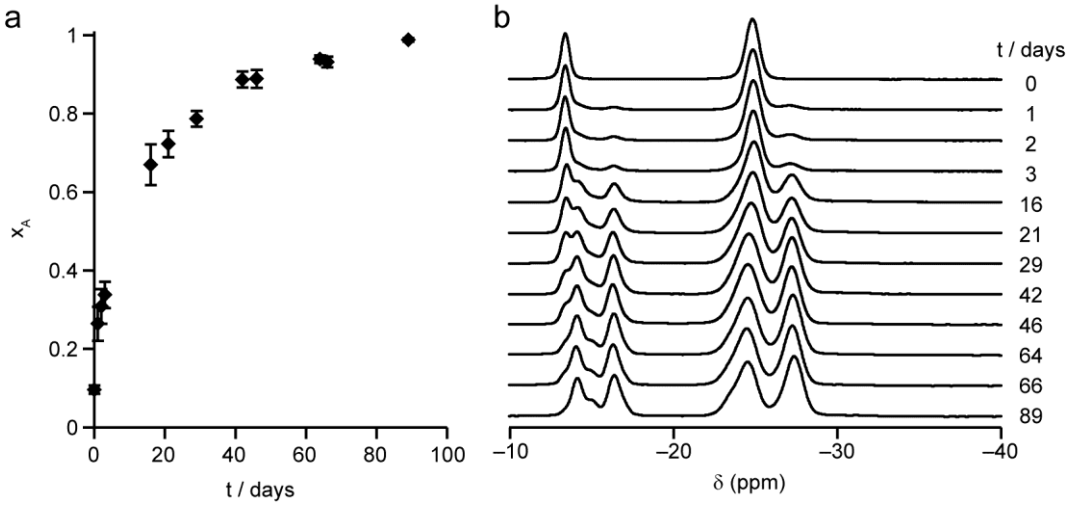

Figure 5.28. (a) The conversion of JDF-2 to AlPO-53(A), expressed as x_A, against time. (b) ^{31}P (14.1 T, 12.5 kHz MAS) NMR spectra of the mixture of JDF-2 and AlPO-53(A) obtained after hydration of JDF-2 for the indicated time.

will play a role in the overall kinetics of the hydration[84] and will depend on the crystallite size and size distribution.

Closer inspection of the ^{31}P NMR spectrum of AlPO-53(A) reveals several regions of spectral intensity (highlighted in Figure 5.29) that would not be expected, given the six distinct P species in the structure of Kirchner *et al.*[3] In order to ensure that these resonances were associated with pure AlPO-53(A), a sample of JDF-2 was stirred in water for 7 days to give fully-hydrated AlPO-53(A). Figure 5.29(b) shows that the additional regions of spectral intensity are still present, although with slightly different intensities, indicating that they do, indeed, arise from AlPO-53(A). However, the different relative intensities indicate that, as suggested above, "AlPO-53(A)" stored under ambient conditions may be slightly dehydrated.

5.5.3 Disorder in AlPO-53(A)

As discussed above, while the initial rate of hydration of JDF-2 to AlPO-53(A) can readily be followed by ^{31}P NMR, interpretation of NMR spectra obtained in the later stages of the hydration, *i.e.*, once the spectrum is dominated by the resonances assigned to AlPO-53(A), is complicated by the presence of resonances that can clearly be seen to result from AlPO-53(A), but which cannot be assigned directly to a species in the published crystal structure.[3] This discrepancy was observed previously

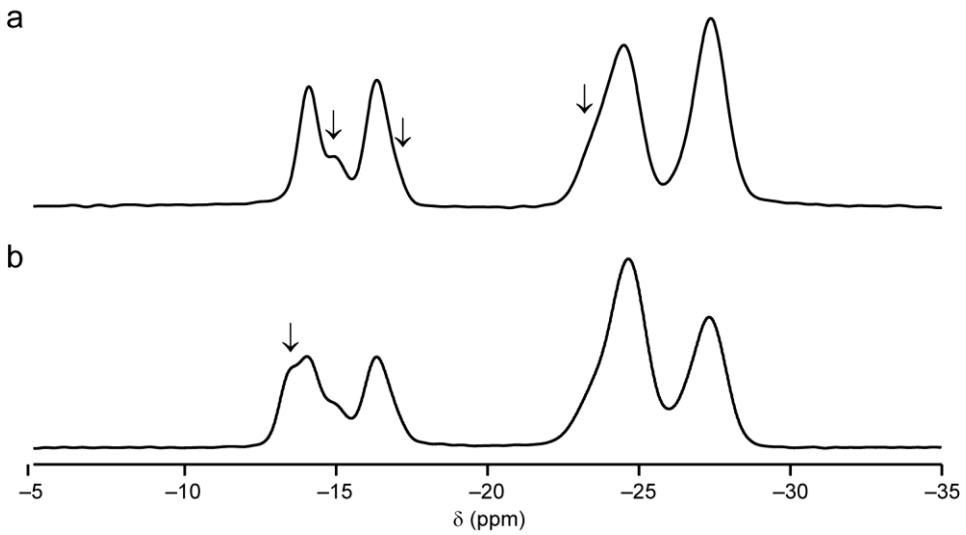

Figure 5.29. ^{31}P (14.1 T, 12.5 kHz MAS) NMR spectra of (a) as-prepared AlPO-53(A), (b) AlPO-53(A) prepared by submerging JDF-2 in water for 7 days. Resonances not expected from the given crystal structure of AlPO-53(A) are indicated by arrows.

by Ashbrook *et al.*,[2] but no detailed explanation was provided for the observation. This section aims to use a combination of solid-state NMR spectroscopy and DFT calculations to understand features of the local structure of AlPO-53(A) that may give rise to discrepancies between the diffraction and solid-state NMR experimental results.

The structure of AlPO-53(A) reported by Kirchner *et al.* has six distinct P species, six distinct Al species and 24 distinct O species within the framework, with two distinct MA and two distinct H_2O in the pores and two distinct OH^-, bridging Al4-Al6 and Al2-Al5. The structure of JDF-2, which will be studied here for comparison with AlPO-53(A), contains three distinct P species, three distinct Al species and 12 distinct O species within the framework, with one distinct MA species in the pores and one distinct OH^- species bridging Al1-Al2.[82] The two AlPOs were investigated by solid-state ^{1}H, ^{13}C, ^{15}N, ^{27}Al and ^{31}P NMR spectroscopy. Figure 5.30 shows the ^{1}H, ^{13}C, ^{15}N and ^{27}Al NMR spectra of JDF-2 (for the ^{31}P spectrum, see Figure 5.27). As expected from the structure of JDF-2, a single resonance is observed for ^{13}C (δ = 28.3 ppm) and ^{15}N (δ = –361.3 ppm), confirming a single type of MA is present. The ^{1}H MAS NMR spectrum confirms that the SDA is protonated MA, as

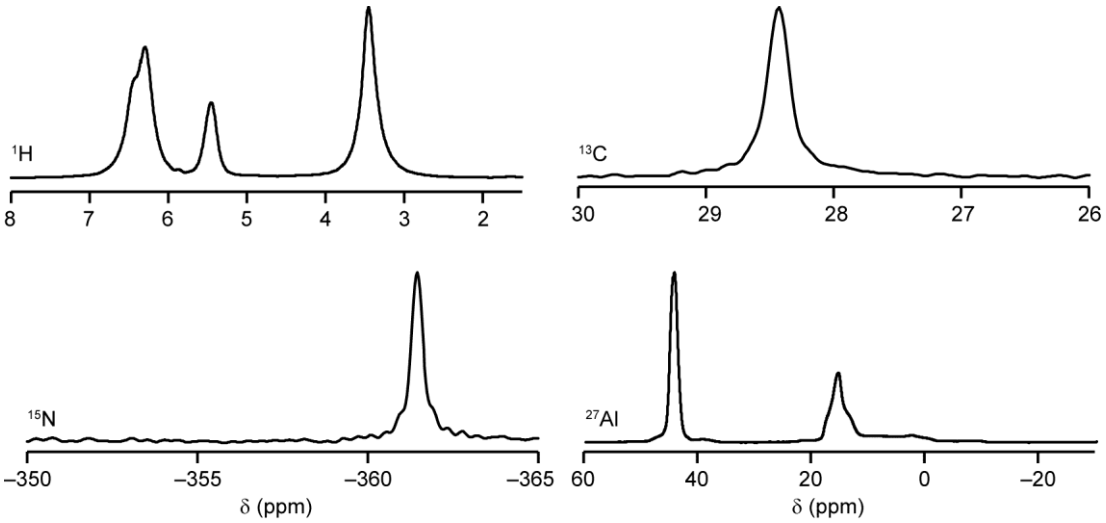

Figure 5.30. ^{1}H (14.1 T, 60 kHz MAS), ^{13}C (14.1 T, 12.5 kHz CP MAS), ^{15}N (9.4 T, 5 kHz CP MAS) and ^{27}Al (14.1 T, 14 kHz MAS) NMR spectra of JDF-2.

the integrated intensity of the resonance at ~6.3 ppm (assigned to N**H**$_x$) is equal to that of the resonance at 3.1 ppm (assigned to C**H**$_3$). The resonance at 5.3 ppm can, therefore, be assigned to O**H**$^-$, and has an integrated intensity one third that of the other two resonances, confirming the expected stoichiometry of JDF-2. The use of very fast (60 kHz) MAS affords significantly greater resolution than achieved in the earlier work of Ashbrook *et al.*,[2] who used 30 kHz MAS. This gain in resolution allows accurate integration of the ^{1}H resonances, the bases of which were overlapped in the earlier work. In addition, it is possible to observe a shoulder on the N**H**$_3$ resonance and, upon deconvolution, the resonance can be seen to be composed of two Lorentzian lines, with isotropic shifts of 6.33 and 6.16 ppm and a 1 : 2 intensity ratio, suggesting that there is some restricted motion of the NH_3 group (*i.e.*, the C_3 rotation about the C-N bond, which would normally be expected to be rapid enough to render all three N**H**$_3$ protons equivalent, must be hindered in some way). Assignment of the ^{1}H resonances was confirmed by a ^{1}H DQMAS NMR experiment, where DQCs were created using one block of BABA pulses. The spectrum, shown in Figure 5.31, contains only one pair of off-diagonal resonances, with shifts of (3.0, 9.1) and (6.1, 9.1) ppm, confirming the close spatial proximity of the two H species with shifts of 3.0 and 6.1 ppm, previously assigned to C**H**$_3$ and N**H**$_3$, respectively. On-diagonal resonances are also observed at (3.0, 6.0) and (6.1, 12.2) ppm, as would be expected for both C**H**$_3$ and N**H**$_3$. The resonance at 5.3 ppm, assigned to O**H**$^-$

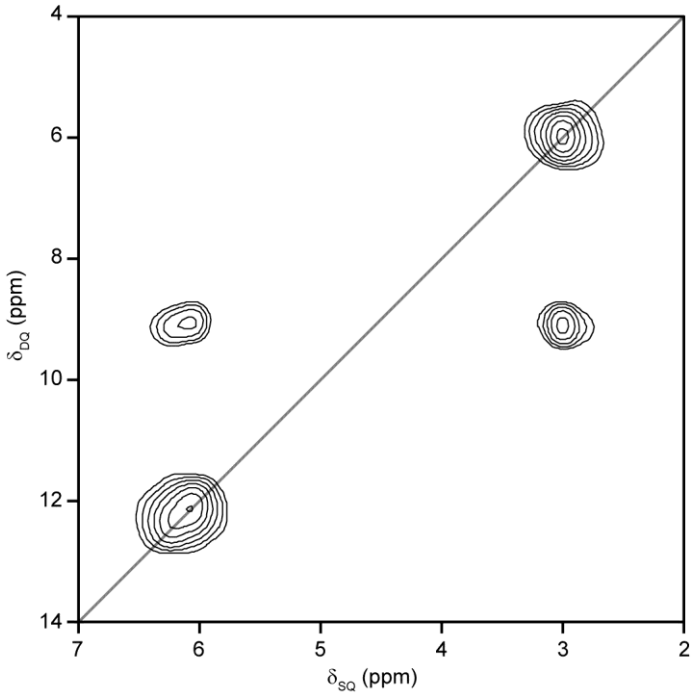

Figure 5.31. ^{1}H (14.1 T, 60 kHz DQMAS) NMR spectrum of JDF-2. The $\delta_{DQ} = 2\delta_{SQ}$ diagonal is indicated in grey.

above, does not appear in the DQMAS NMR spectrum, confirming that this resonance arises from spatially isolated ^{1}H nuclei, as would be expected from the structure of JDF-2, where the MA species occupy the pores and the HO^{-} species are located within small cages in the framework (see Figure 5.26).

In order to assign the ^{27}Al and ^{31}P NMR spectra of JDF-2, the NMR the structure reported by Chippindale *et al.*[82] was optimised (using CASTEP 6[5, 6] to relax all atomic coordinates and unit cell parameters using the G06 SEDC scheme[85, 86]) and the NMR parameters calculated for the optimised structure, as reported in Table 5.10. Assignment of the ^{31}P resonances was made by comparison of the isotropic shifts; P1 and P3 are predicted to have similar δ_{iso}, whereas P2 is predicted to be 13.6 ppm downfield from their centre of gravity. The ^{31}P MAS NMR spectrum of JDF-2 (Figure 5.27) contains two resonances at –13.4 and –24.8 ppm, with a 1 : 2 integrated intensity ratio. Therefore, the resonance at –24.8 ppm can be assigned to P1 and P3 and the resonance at –13.4 ppm to P2. For ^{27}Al, the assignment made use of δ_{iso} and C_Q. Fitting extracted cross sections for the lineshapes observed in the 3QMAS NMR spectrum, shown in Figure 5.32, allowed both parameters (and η_Q) to be obtained for

Table 5.10. (a) Experimental and (b) calculated (using CASTEP, after full structural optimisation) NMR parameters for JDF-2.

Species	δ_{iso} (ppm)		C_Q / MHz		η_Q	
	a	b	a	b	a	b
C**H**$_3$[i]	3.1(1)	3.2				
O**H**	5.3(1)	5.4				
N**H**$_3$	6.2(1), 6.3(1)	6.1[ii]				
C	28.5(1)	28.5[iii]				
N	–361.4(1)	–361.4[iii]				
Al1	18.2(3)	20.7	6.7(2)	7.55	0.2(1)	0.90
Al2	18.1(1)	19.5	2.8(2)	3.43	0.8(1)	0.27
Al3	45.2(2)	49.4	1.7(2)	1.74	0.5(1)	1.00
P1	–24.8(2)	–25.2				
P2	–13.4(1)	–11.2				
P3	–24.8(2)	–24.5				

i. The average δ_{iso} for the three C**H** species is reported, as rapid C_3 rotation about the C-N bond will make all three species equivalent, despite their inequivalence in the (static) crystal structure.

ii. While one of the three N**H**$_3$ appeared different in the NMR spectrum, the similarity of the experimental chemical shifts prevents more detailed assignment and only the calculated position of the centre of gravity of the N**H**$_3$ resonance is given here.

iii. These values were used as chemical shift references.

each of the three resonances, as reported in Table 5.10. As Al3 is the only Al(IV) species present, the narrow resonance with δ_{iso} = 45.2 ppm can be assigned as this species. The other two resonances can be assigned based on the calculated C_Q, which is large (7.55 MHz) for Al1 and smaller (3.43 MHz) for Al2. The resonance with δ_{iso} = 18.2 ppm has C_Q = 6.7 MHz, whereas the third resonance, at δ_{iso} = 18.1 ppm has a smaller C_Q of 2.8 MHz, indicating the assignment of these two resonances as Al1 and Al2, respectively. It should be noted that, for all three Al species, the experimental and calculated η_Q are in poor agreement. These assignments for ^{31}P and ^{27}Al are in agreement with the earlier assignment of Ashbrook *et al*., with only small differences in the calculated parameters, arising from the different versions of

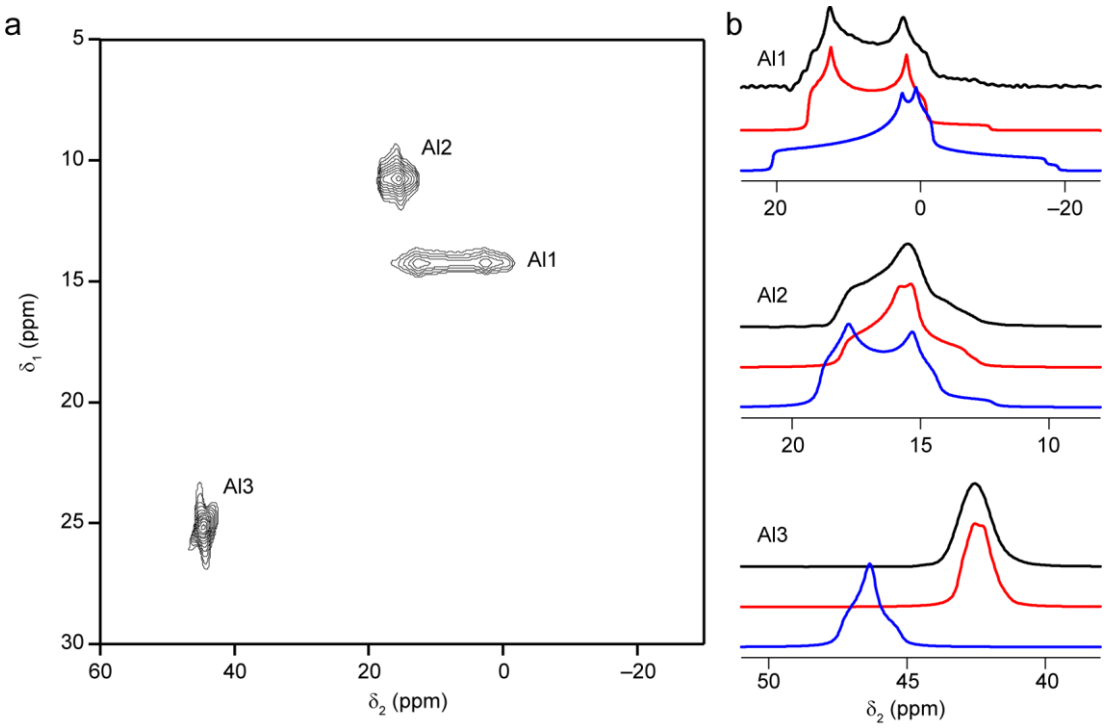

Figure 5.32. ^{27}Al (14.1 T, 14 kHz 3QMAS) NMR spectrum of JDF-2, with extracted cross sections (black) and corresponding fitted (red) and simulated (using the values in Table 5.10(b)) (blue) lineshapes for each resonance. Non-experimental spectra have 50 Hz Lorentzian broadening applied.

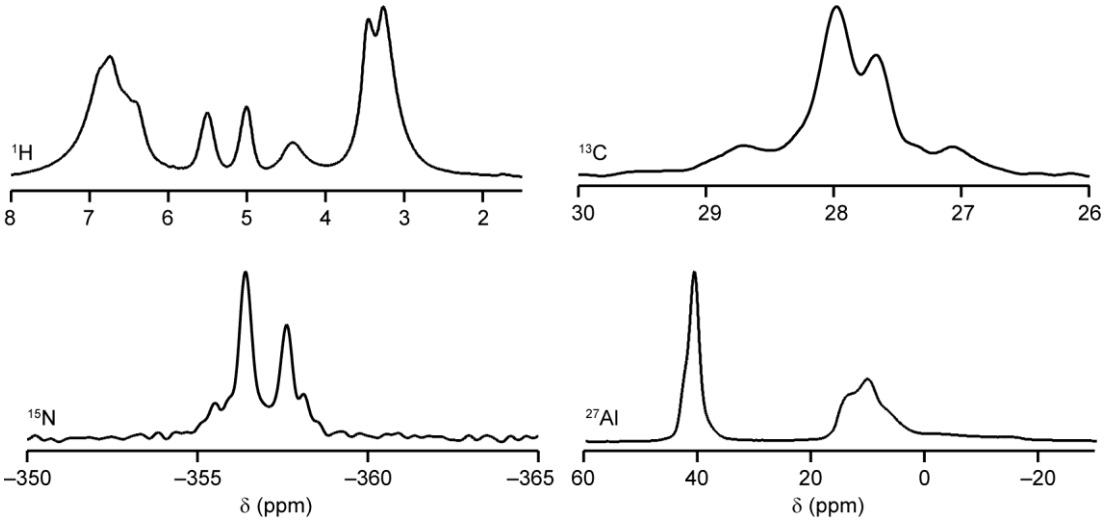

Figure 5.33. ^{1}H (14.1 T, 60 kHz MAS), ^{13}C (14.1 T, 12.5 kHz CP MAS), ^{15}N (9.4 T, 5 kHz CP MAS) and ^{27}Al (14.1 T, 14 kHz MAS) NMR spectra of AlPO-53(A).

CASTEP used. It can be seen from the calculated ^{1}H isotropic shifts in Table 5.10 that good agreement with experiment is achieved, but only when the calculated shieldings are scaled by a factor of 0.72. The calculation does suggest that the N**H**$_3$ signal should be split into two resonances, at ~6.3 and 5.8 ppm, but with a 2 : 1 intensity ratio, rather than the experimentally-observed 1 : 2 ratio, (and experimentally-observed shifts of 6.3 and 6.2 ppm), so it is unlikely that the calculation can provide any definite structural insight into the origins of the observed shoulder on the N**H**$_3$ resonance.

Figure 5.33 shows the ^{1}H, ^{13}C, ^{15}N and ^{27}Al NMR spectra of AlPO-53(A) (for ^{31}P, see Figure 5.27). The ^{1}H MAS NMR spectrum (recorded with 60 kHz MAS) has sufficient resolution to reveal two distinct C**H**$_3$ resonances (2.8 and 3.0 ppm) and distinct **H**O$^-$ resonances (4.7 and 5.2 ppm). However, only one broadened **H**$_2$O resonance (4.1 ppm) is observed (rather than two expected from the crystal structure) and the N**H**$_3$ resonance (~6.0 to 7.1 ppm) is broadened asymmetrically, suggesting a range of environments for this species. The resolution afforded by the rapid MAS allowed assignment of the ^{1}H resonances using a ^{1}H DQMAS NMR experiment, where DQCs were created by one block of BABA pulses (Figure 5.34). The spectrum contains sets of on-and off-diagonal resonances that can be traced out to give isotropic C**H**$_3$ and N**H**$_3$ shifts of 2.8 and 6.6 ppm for one MA and 3.0 and 6.3 ppm for the other, as indicated. A tentative assignment is possible as DQCs are observed at (5.2, 8.0) and (2.8, 8.0) ppm, corresponding to a close CH_3-HO$^-$ distance. The shortest such distance is 4.62 Å for C1-OH2, whereas for C2, the shortest distance is 5.34 Å. The C**H**$_3$ resonance at 2.8 ppm can, thus, be assigned to MA1 (in the nomenclature of Figure 5.26), allowing assignment of all observed ^{1}H resonances, as summarised in Table 5.11. There is also a weak correlation between **H**$_2$O and N**H**$_3$ of MA1 and MA2 (although only one of the pair of expected DQCs is observed in each case), consistent with the relatively short O-N separations between H_2O and N1 and N2, of 2.84 and 3.67 Å, respectively. However, the observation of a single broad resonance for H_2O indicates that there may be some motional averaging of the position of the H_2O in AlPO-53(A). Such motional averaging would not be surprising, since H_2O can diffuse throughout the structure of AlPO-53(A)/JDF-2.

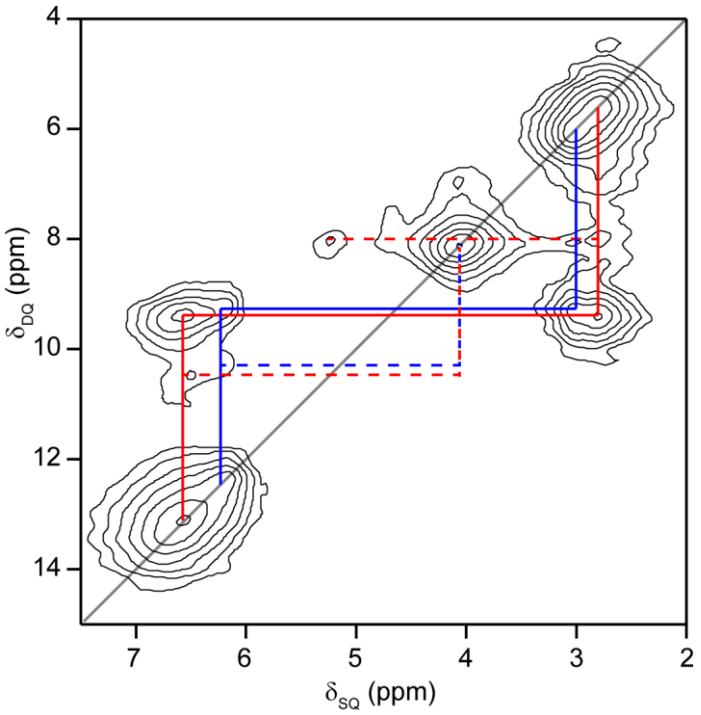

Figure 5.34. ^{1}H (14.1 T, 60 kHz DQMAS) NMR spectrum of AlPO-53(A). Sets of resonances arising from the same MA species are indicated with red and blue lines. C**H**$_3$-O**H** and N**H**$_3$-**H**$_2$O correlations are indicated with broken lines.

The two O atoms of H_2O also have unusually large thermal displacement parameters in the published structure,[3] indicative of some positional uncertainty.

Ashbrook *et al*. observed that the ^{13}C NMR spectrum of AlPO-53(A) contains four resonances (at 27.1, 27.7, 28.0 and 28.7 ppm), rather than the two expected from crystallography;[2] an observation that was repeated in the present work (Figure 5.33). While the CP MAS experiment used to record the ^{13}C NMR spectrum will not be truly quantitative, it can be assumed that all four resonances arise from CH_3 in MA (owing to their similar chemical shifts) and that these will have similar CP behaviour, meaning that the spectrum will be approximately quantitative. The integrated intensities of the resonances are 1.6 : 5.2 : 2.7 : 1.0, or, when the intensities of the three least intense resonances are combined, 5.3 : 5.2. This suggests that one of the MA species may be disordered, with three possible environments, while the other appears more ordered, giving just one resonance. The ^{1}H-^{13}C J-transferred INEPT experiment, shown in Figure 5.35, appears to support this suggestion, as the three least intense ^{13}C resonances all correlate to ^{1}H at 3.0 ppm

Table 5.11. Experimental NMR parameters for AlPO-53(A). Roman numerals are used where resonances have not yet been assigned to a crystallographic species.

Species	δ_{iso} (ppm)	P_Q / MHz
C**H**$_3$(1)	2.8(1)	
C**H**$_3$(2)	3.0(1)	
H$_2$O	4.1(1)	
O**H**(1)	4.7(1)	
O**H**(2)	5.2(1)	
N**H**$_3$(1)	6.6(1)	
N**H**$_3$(2)	6.3(1)	
C1	27.7(1)	
C2	27.1(1), 28.0(1), 28.7(1)	
N(i)	–355.5(1)	
N(ii)	–356.4(1)	
N(iii)	–357.6(1)	
N(iv)	–358.2(1)	
Al(i)	44(1)	2.6(2)
Al(ii)	42(1)	1.9(2)
Al(iii)	17(1)	9.1(5)
Al(iv)	17(1)	6.4(3)
Al(v, vi)	17(1)	4.1(2)
P(i)	–14.0(3)	
P(ii)	–15.0(3)	
P(iii)	–16.4(3)	
P(iv)	–18.0(5) to –20.0(5)	
P(v)	–24.4(3)	
P(vi)	–27.3(3)	
P(vii)	–29.0(5) to –33.0(5)	

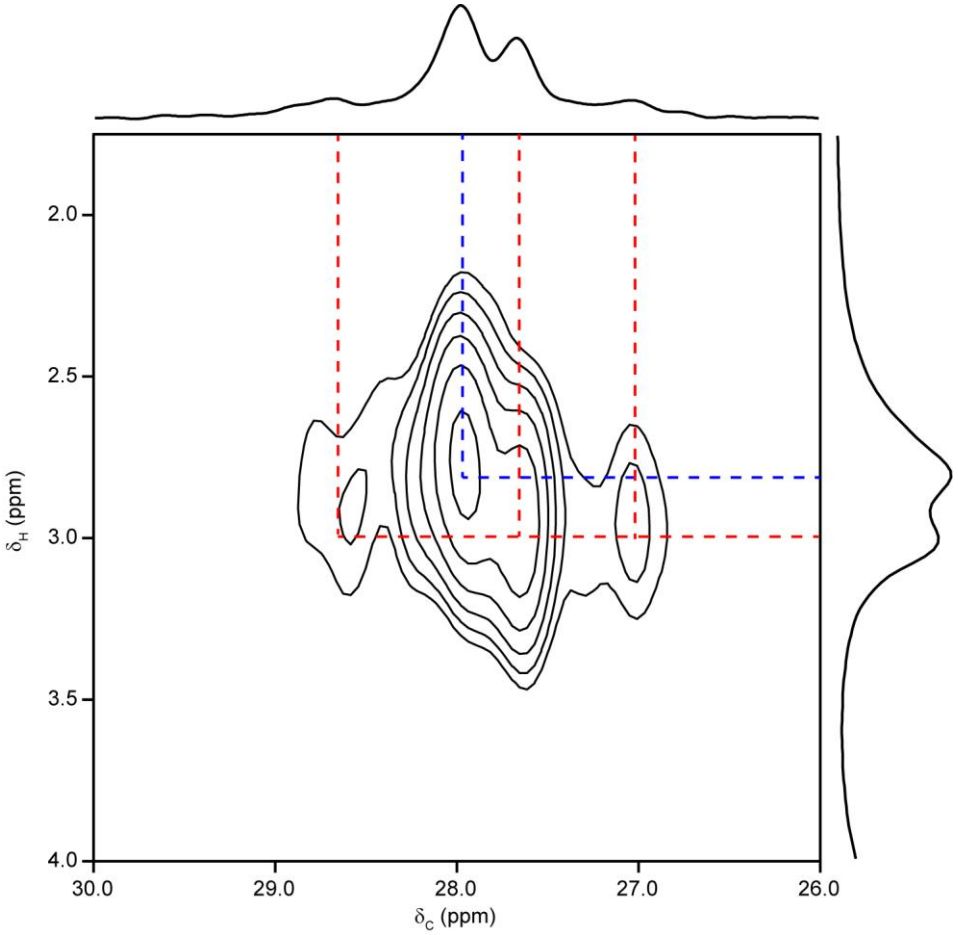

Figure 5.35. ^{1}H-^{13}C (14.1 T, 12.5 kHz MAS) J-transferred INEPT spectrum of AlPO-53(A). The ^{1}H (14.1 T, 60 kHz MAS) and ^{13}C (14.1 T, 12.5 kHz CP MAS) NMR spectra from Figure 5.34, are shown along δ_H and δ_C, respectively. Blue and red broken lines indicate correlations between ^{13}C and the ^{1}H resonances at 2.8 and 3.0 ppm, respectively.

(identified above as MA2) and the most intense ^{13}C resonance correlates to ^{1}H at 2.8 ppm, identified above as MA1. It would appear that any disorder affecting the chemical shift of ^{13}C does not produce a large enough shift difference to be observed at the currently-available resolution for ^{1}H.

The ^{15}N CP MAS NMR spectrum of AlPO-53(A), shown in Figure 5.33, appears similar to the ^{13}C NMR spectrum. The spectrum can be decomposed into four Lorentzian lineshapes with δ_{iso} of –355.5, –356.4, –357.6 and –358.2 ppm, with an integrated intensity ratio of 1.5 : 8.1 : 5.1 : 1.0, or 7.6 : 8.1 when the intensities of

the three least intense resonances are combined. While the ratio of the three least intense resonances to the most intense resonance is still approximately 1: 1, as was observed for ^{13}C, the relative intensities of the three least intense resonances are very different from those observed for ^{13}C. While this difference may simply be a consequence of the different dynamics of the NH_3 and CH_3 species, it might also suggest that the disorder present is more complicated than the three-environment model proposed above, with many different environments coincidentally giving rise to three groups of very similar ^{13}C and ^{15}N isotropic shifts, but with no direct correspondence between the ^{13}C and ^{15}N shift for the different environments (*i.e.*, two environments may yield similar ^{15}N shifts, but different ^{13}C shifts, or *vice versa*). However, as it is known that the H_2O within AlPO-53(A) is relatively mobile and can be lost to the air, it is possible that the hydration state of the material had changed owing to, *e.g.*, a change in the atmospheric moisture content between recording the ^{13}C and ^{15}N spectra, or heating arising from the 61.4 ms high-power decoupling of ^{1}H applied during the ^{15}N experiment. Owing to the natural abundances of both ^{13}C and ^{15}N, a ^{13}C-^{15}N correlation experiment was not possible. However, such an experiment (on an isotopically-enriched sample) would be particularly useful for shedding light on the disorder of MA in AlPO-53(A).

The ^{27}Al MAS NMR spectrum of AlPO-53(A), shown in Figure 5.33, contains two regions of intensity, in a 1 : 2 ratio, corresponding to Al(IV) and Al(V). The ^{27}Al 3QMAS NMR spectrum, shown in Figure 5.36, reveals five isotropic resonances, two corresponding to Al(IV) and three to Al(V). However, the intensities of the Al(V) resonances indicate that two resonances overlap, giving the expected total of four Al(V) species. The centres of gravity of the resonances observed in the 3QMAS NMR spectrum allow approximate δ_{iso} and P_Q to be determined for all five resonances, as summarised in Table 5.11. The ^{31}P MAS NMR spectrum of AlPO-53(A), shown in Figure 5.27, contains four intense resonances at –14.0, –16.4, –24.4 and –27.3 ppm, with integrated intensities of approximately 2 : 3 : 4 : 4. This ratio is reasonably close to the 1 : 1 : 2 : 2 ratio that would be expected if two pairs of the expected six ^{31}P resonances overlapped. Ashbrook *et al*. assigned the ^{31}P resonances

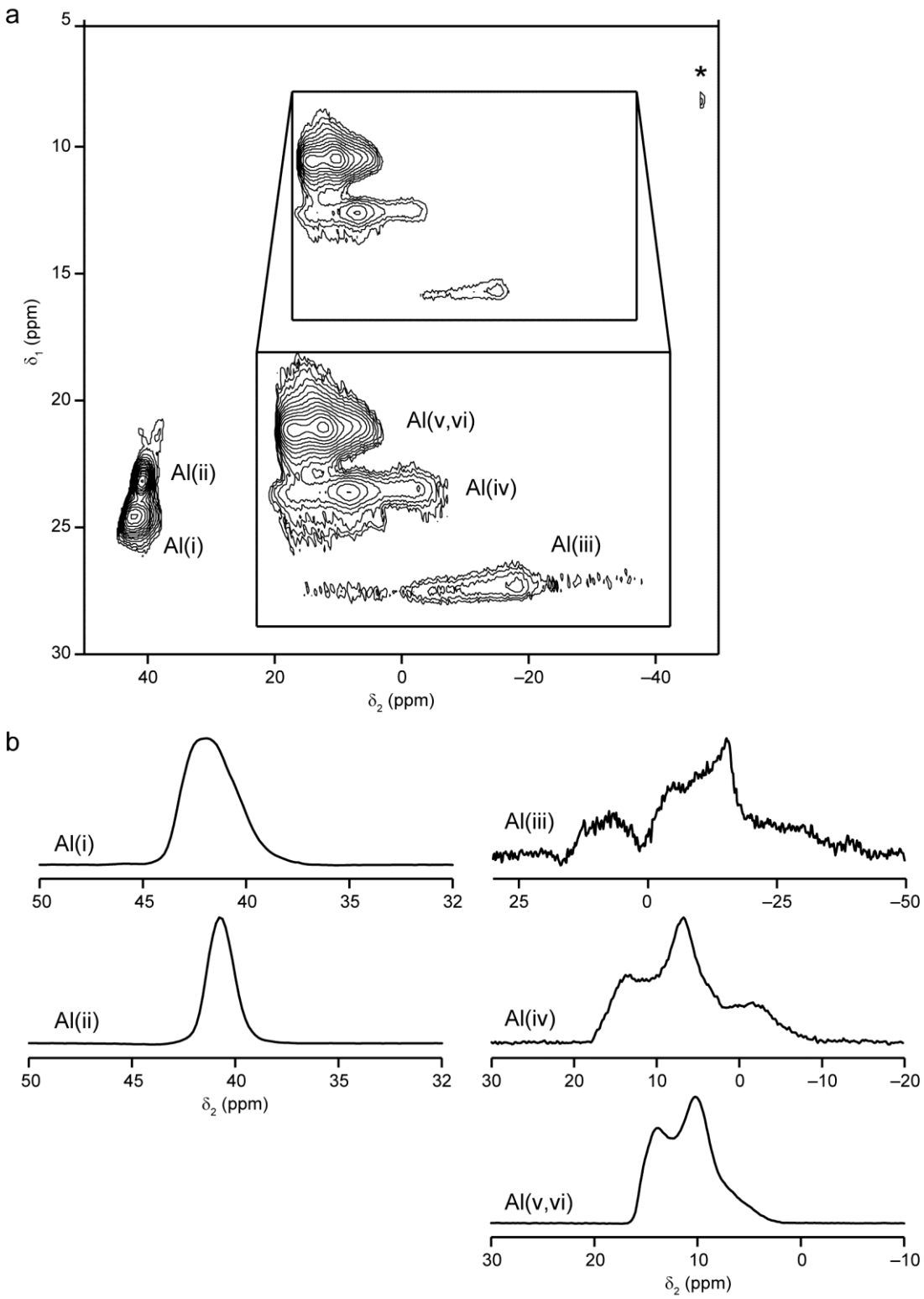

Figure 5.36. (a) ^{27}Al (14.1 T, 14 kHz 3QMAS) NMR spectrum of AlPO-53(A). The asterisk denotes a SSB and the inset shows the Al(V) region with the vertical scale of the contours increased by a factor of 2 relative to the main spectrum. (b) Lineshapes extracted parallel to δ_2.

based on CASTEP calculations, as summarised in Table 5.9. However, as mentioned above, additional resonances with lower intensity are observed at –15.0, –18 to –20 and –29 to –33 ppm. These resonances were shown to be a genuine feature of AlPO-53(A) and presumably relate to the disorder observed in the ^{13}C and ^{15}N NMR spectra. It seems likely that these resonances are responsible for the deviation of the integrated intensity ratio of the four most intense resonances from the idealised value. In order to ascertain whether these resonances truly arise from AlPO-53(A), a ^{31}P homonuclear DQMAS experiment was carried out, using POST-C7 recoupling to excite and convert the DQCs. The ^{31}P DQMAS NMR spectrum, shown in Figure 5.37, contains cross peaks between the four main resonances and, on closer inspection, further cross peaks also connect the resonances at –15.0 and between –18 and –20 ppm to the main resonances. This observation suggests that the low-intensity resonances arise from P species in close spatial proximity to the bulk of the AlPO-53(A) framework. No such DQCs were observed for the resonance between –29 and –33 ppm, although the broad nature of this resonance may mean that any DQCs present were not observed owing to their low intensity. This is assumed to be more likely than the resonance arising from an impurity, as it was previously shown to originate from AlPO-53(A) (*i.e.*, it appears and disappears reversibly when JDF-2 and AlPO-53(A) are interconverted). The evidence from the ^{31}P DQMAS NMR spectrum suggests that the additional resonances arise from P species within the same crystals as the "bulk" resonances, suggesting that any disorder present will be localised defects, rather than a second crystallographic phase. This would be consistent with the fact that no separate phase was observed by Kirchner *et al*. in their original study of AlPO-53(A).[3]

It is apparent from the ^{13}C and ^{15}N CP MAS NMR spectra of AlPO-53(A) that there are at least four distinguishable MA species within the material, with the similarity of their chemical shifts indicating that the differences between them arise from differences in the surroundings, rather than major changes to the molecules themselves, *e.g.*, deprotonation or coordination to a framework species.

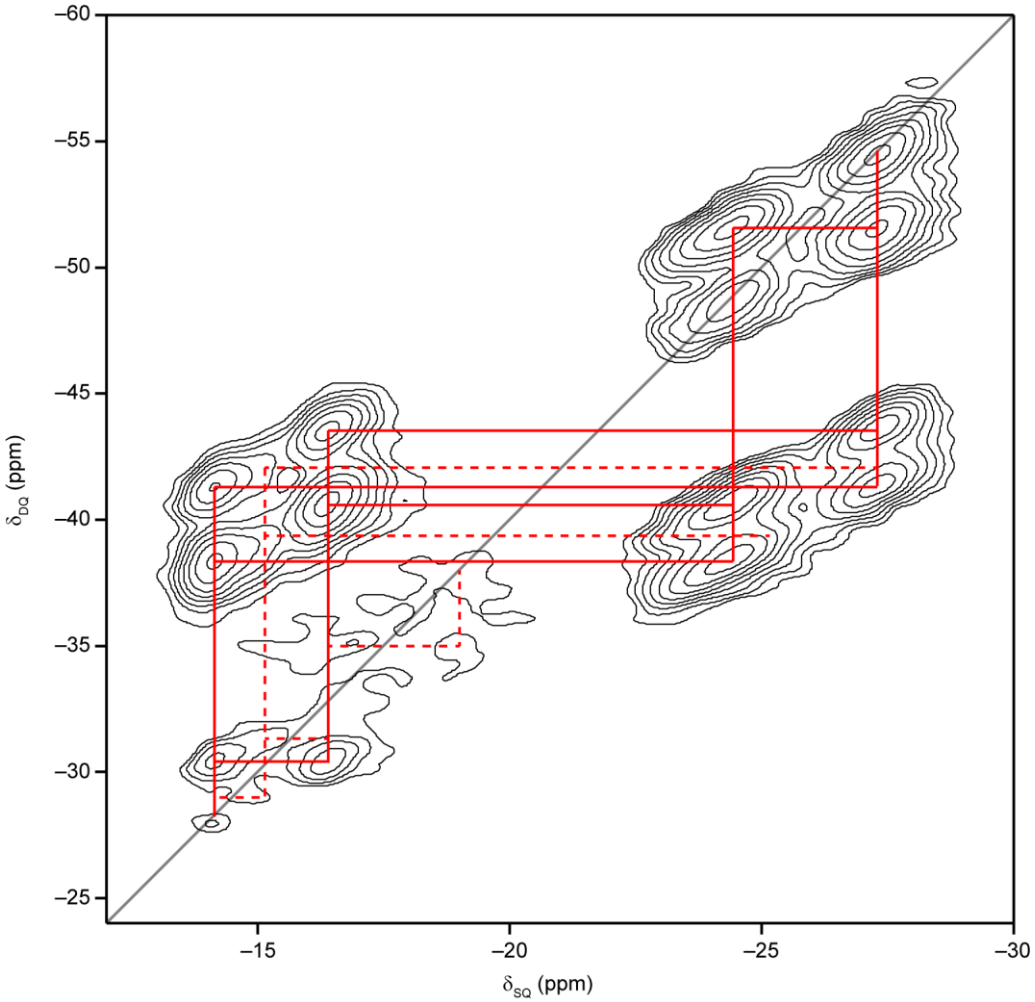

Figure 5.37. ^{31}P (14.1 T, 10 kHz DQMAS) NMR spectrum of AlPO-53(A). Correlations between the four main resonances are indicated by solid red lines and between the main resonances and those at –15.0 and –18 to –20 ppm are indicated with broken lines. The $\delta_{DQ} = 2\delta_{SQ}$ diagonal is indicated in grey.

5.5.3.1 DFT Investigation of Models of Disorder in AlPO-53(A)

Before considering modifications to the structure of AlPO-53(A) that may give rise to the additional resonances observed in the ^{13}C, ^{15}N and ^{31}P NMR spectra, it is necessary first to consider in greater detail the published crystal structure of the material. The structure of AlPO-53(A) can be considered as alternating layers of anionic (OH-bearing) $AlPO_4$ framework and cationic (MA-bearing) guests, as shown in Figure 5.38(a). The framework layers are connected by Al2-O-P2 and Al4-O-P3 bridges, *i.e.*, the term "layer" is intended merely as a means of viewing the structure,

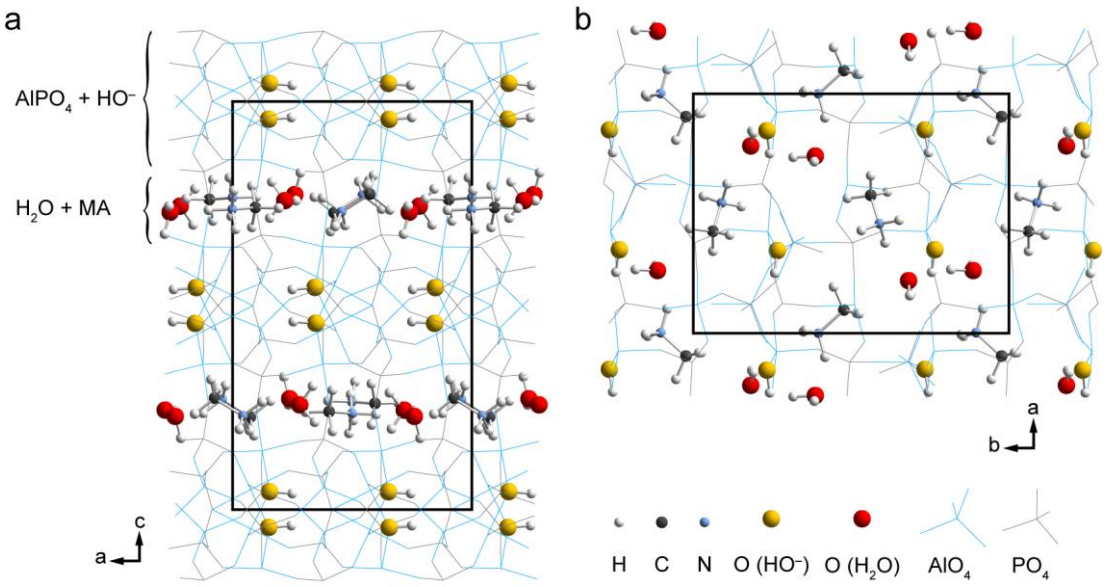

Figure 5.38. (a) The "layered" structure of AlPO-53(A). (b) One layer pair viewed along the crystallographic c axis.

rather than implying that the structure is genuinely lamellar. One pair of cationic and anionic layers is shown in Figure 5.38(b), viewed down the crystallographic c axis. It can be seen that the HO^- is located within the anionic layer, rather than at its surface. Therefore, the main interaction between the MA and HO^- is going to be electrostatic (charge balancing) rather than hydrogen bonding, as the closest **N**H...O contact between these ion pairs is 5.00 Å for MA1-HO2, and 4.78 Å for MA2-HO1. In the cationic layers, there are two water molecules (W) per MA pair, located between the two N atoms, with N-O distances for MA1 of 2.80 and 4.57 Å and for MA2 of 2.69 and 3.68 Å (*i.e.*, one length within the range expected for hydrogen bonding, and one longer). MA1 has a N-H···O hydrogen bond angle of 104.4°, and the corresponding angle for MA2 is 123.1° (angles are quoted for the published literature structure with the positions of the H atoms optimised as discussed below). Some constraints on possible modifications to the structure can be imposed, given that the AEN topology of the framework is retained to above 300 °C, and that the NMR parameters calculated from the (optimised) published crystal structure of JDF-2 give good agreement with the experimentally-measured parameters. These observations suggest that framework rearrangement and loss of MA/HO^- ions are unlikely to occur. Therefore, the most logical modifications of the structure to give rise to the

additional MA species observed by solid-state NMR are either the reversal of one or another of the MA species, or water vacancies resulting from incomplete hydration. Both of these would be difficult to observe by Bragg diffraction techniques, since it is unlikely that the diffraction experiment can distinguish confidently between $-CH_3$ and $-NH_3^+$, and non-periodic partial hydration would either pass unobserved, or be refined as fractional occupancy (indeed, there does appear to be some uncertainty over the precise water content of AlPO-53(A) in the work of Kirchner *et al*.[3]). The scenario of MA reorientation is, however, constrained by the lack of any observable disorder in the NMR spectra of JDF-2, meaning that any such reorientation must be either periodic or fully reversible on dehydration.

The position of the H atoms added manually[2] to the published structure of Kirchner *et al*. are somewhat unrealistic, especially for the hydroxide species, as shown for HO1 in Figure 5.39(a). As the atomic forces (calculated by DFT) acting on the H atoms were all between 5.8 and 11.2 eV $Å^{-1}$, full optimisation of this structure of AlPO-53(A) led to significant distortions of the framework, including reorientation of the OH, as shown in Figure 5.39(b), and changes of –0.18, +0.62 and –0.53 Å (–1.8, +4.6 and –3.0%) in the unit cell lengths, a, b and c. This poor agreement with the experimental diffraction structure indicated that the optimised structures, while lower in energy, was not a realistic representation of AlPO-53(A). Therefore, the positions of the H atoms were optimised while all other atomic coordinates and the unit cell parameters were fixed. The geometry of the hydroxide species after this optimisation is shown in Figure 5.39(c). Based on this more realistic structural model (maximum forces of 0.013, 2.0, 2.9, 4.0, 1.0 and 3.3 eV $Å^{-1}$ for H, C, N, O, Al and P, respectively), the modifications discussed above could be considered. A series of model structures was generated from the partially-optimised structure of AlPO-53(A), as summarised in Table 5.12 and with the structures of the cationic guest layer structures shown in Figures 5.40 and 5.41. All structural models (including 0) were optimised as far as possible within time constraints, with variation of all atomic coordinates and the unit cell parameters and dispersion interactions accounted for by the G06 SEDC scheme.[85, 86] For models including "point" defects (single MA reorientations (1ma and 3ma) or water vacancies (1w and 3w)) the centre of mass of the unit cell was not constrained during the optimisations. The final

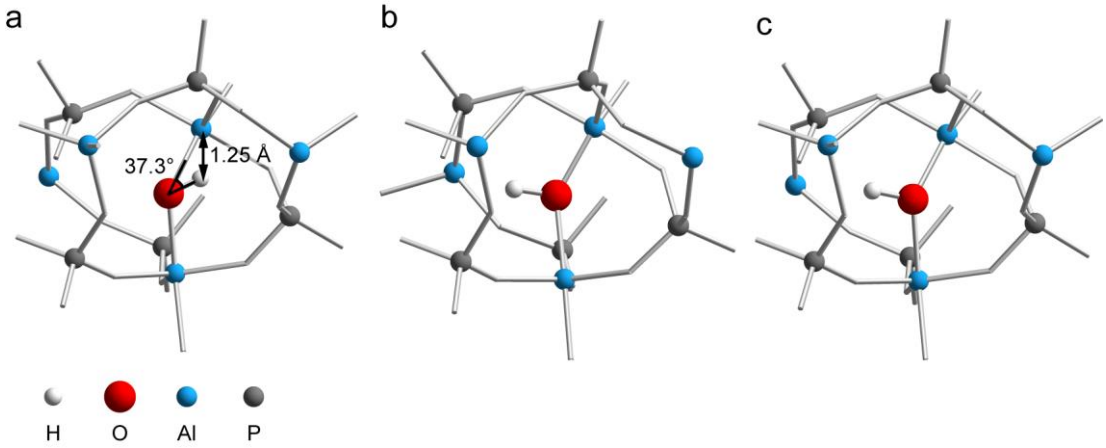

Figure 5.39. The local environment of the hydroxide species in AlPO-53(A) with (a) the H atoms added manually,[2] (b) full optimisation of the structure and (c) optimisation of only the H atoms. Framework O atoms are omitted for clarity

dispersion-corrected total energies of the structural models are reported in Table 5.12 (relative energies are not quoted as many models contain different numbers of atoms, making such a comparison meaningless).

It can be seen from Table 5.12 that reversing the orientation of one MA1 (model 1ma) is energetically favoured over model 0, while reversing the orientations of all MA1 (model 2ma) is energetically disfavoured. This can be rationalised by considering the hydrogen bonding present in the modified cation layers. In model 1ma, there is a hydrophobic arrangement of MA around one H_2O pair, highlighted in Figure 5.42(a), which is apparently offset by the hydrophilic arrangement of MA around the other H_2O pair in the layer. However, in model 2ma, all MA1 have been reoriented and such highly hydrophilic arrangements no longer exist. Instead, one of each H_2O pair is in a hydrophobic environment and can only hydrogen bond to the neighbouring H_2O, while the other is in a hydrophilic environment and can potentially hydrogen bond to two adjacent NH_3 groups, as shown in Figure 5.42(b). However, the reorientation of MA1 leads to a more favourable (shorter N-O distance, angle closer to 180°) hydrogen bond between N1 and H_2O. Therefore, it appears unlikely that all MA1 would reorient, but isolated MA1 reorientations may occur. The same is not true for reorientation of MA2, with both models 3ma and 4ma energetically favoured over model 0 (even with incomplete structural optimisations).

Table 5.12. Summary of the structural models used to describe possible scenarios for disorder in AlPO-53(A). The calculated dispersion-corrected total energy of each model (after optimisation) is also reported.

Model	Description	Total Energy / eV
0	published literature structure of AlPO-53(A)[3]	–60774.299
1ma	reorientation of a single MA1	–60774.399
2ma	reorientation of all MA1	–60773.980
3ma	reorientation of a single MA2	–60774.800
4ma	reorientation of all MA2	–60774.687[a]
5ma	reorientation of all MA1 and MA2	–60774.802
1w	removal of a single W1	–60301.173
2w	removal of all W1	–58879.878
3w	removal of a single W2	–60301.337[b]
4w	removal of all W2	–58879.566
5w	removal of all W1 and W2	–56984.336
1j	published literature structure of JDF-2[82]	–56985.176
2j	reorientation of a single MA in JDF-2	–56985.009
3j	reorientation of all MA in JDF-2	–56983.203[c]

a. 4ma was optimised for 395 iterations, rather than to an energy minimum, owing to time constraints.

b. 3w was optimised for 551 iterations, rather than to an energy minimum, owing to time constraints.

c. 3j was optimised for 519 iterations, rather than to an energy minimum, owing to time constraints.

This is in agreement with the assignment of the ^{1}H and ^{13}C NMR spectra discussed above, which indicated that MA1 was ordered (*i.e.*, unfavourable to reorient), whereas MA2 was disordered (*i.e.*, can be more readily reoriented). As shown in Figure 5.43, this stabilisation mainly arises from the more favourable hydrogen bonds that form between the reoriented MA2 and H_2O in both cases. It would appear that reorientation of MA2 causes an out-of-plane tilting, shown in Figure 5.43(c and d) (*cf.* model 0, shown in Figure 5.38(a)), which leads to hydrogen bond angles much closer to 180°. This tilting is of particular interest, since it shows that there is sufficient space for such motion of MA2 within the pores of AlPO-53(A), indicating that reorientation of MA2 may be kinetically accessible as well as

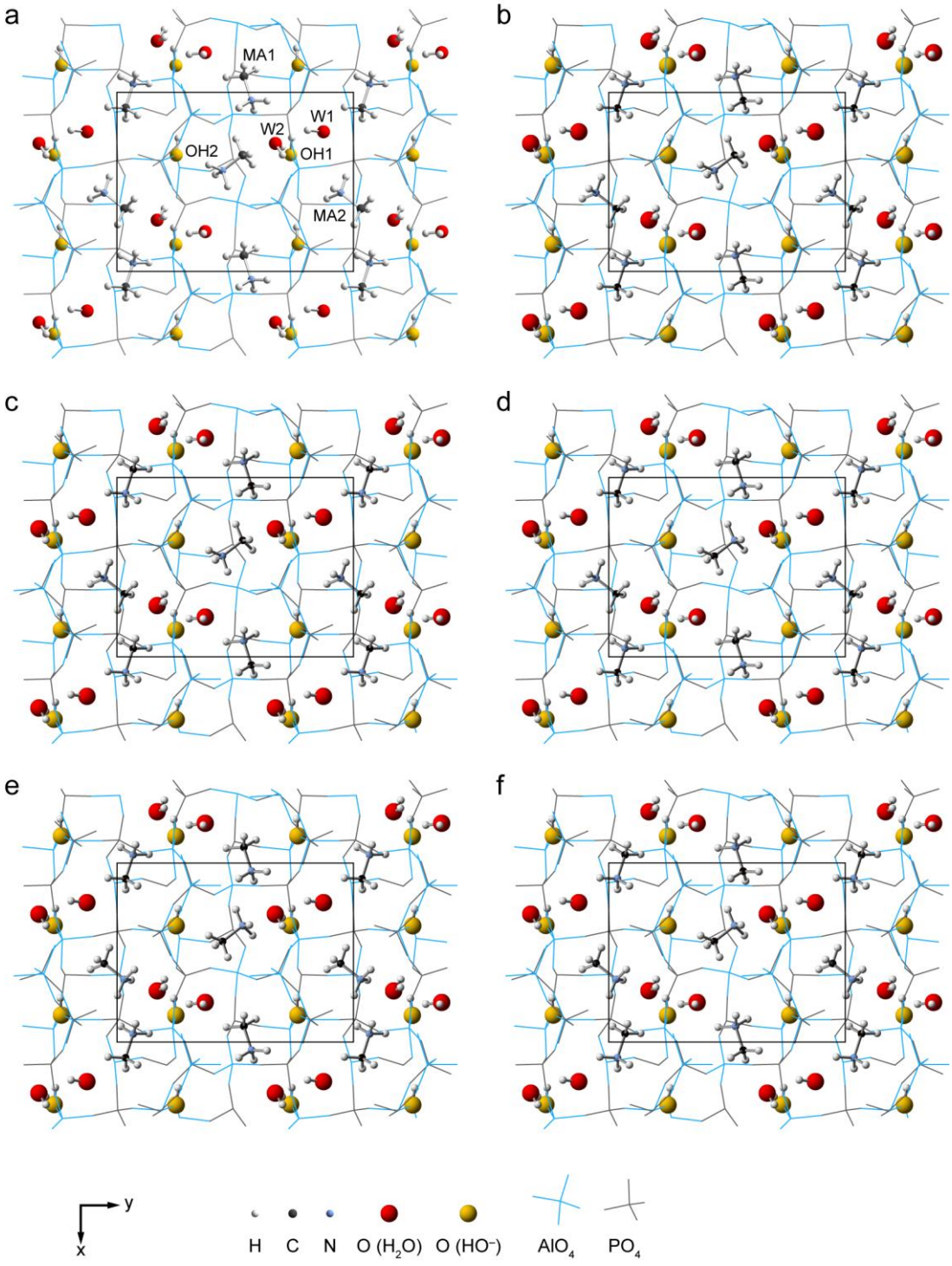

Figure 5.40. The structures (prior to optimisation) of the guest layers in the structural models, 0, 1ma, 2ma, 3ma, 4ma and 5ma, described in Table 5.12.

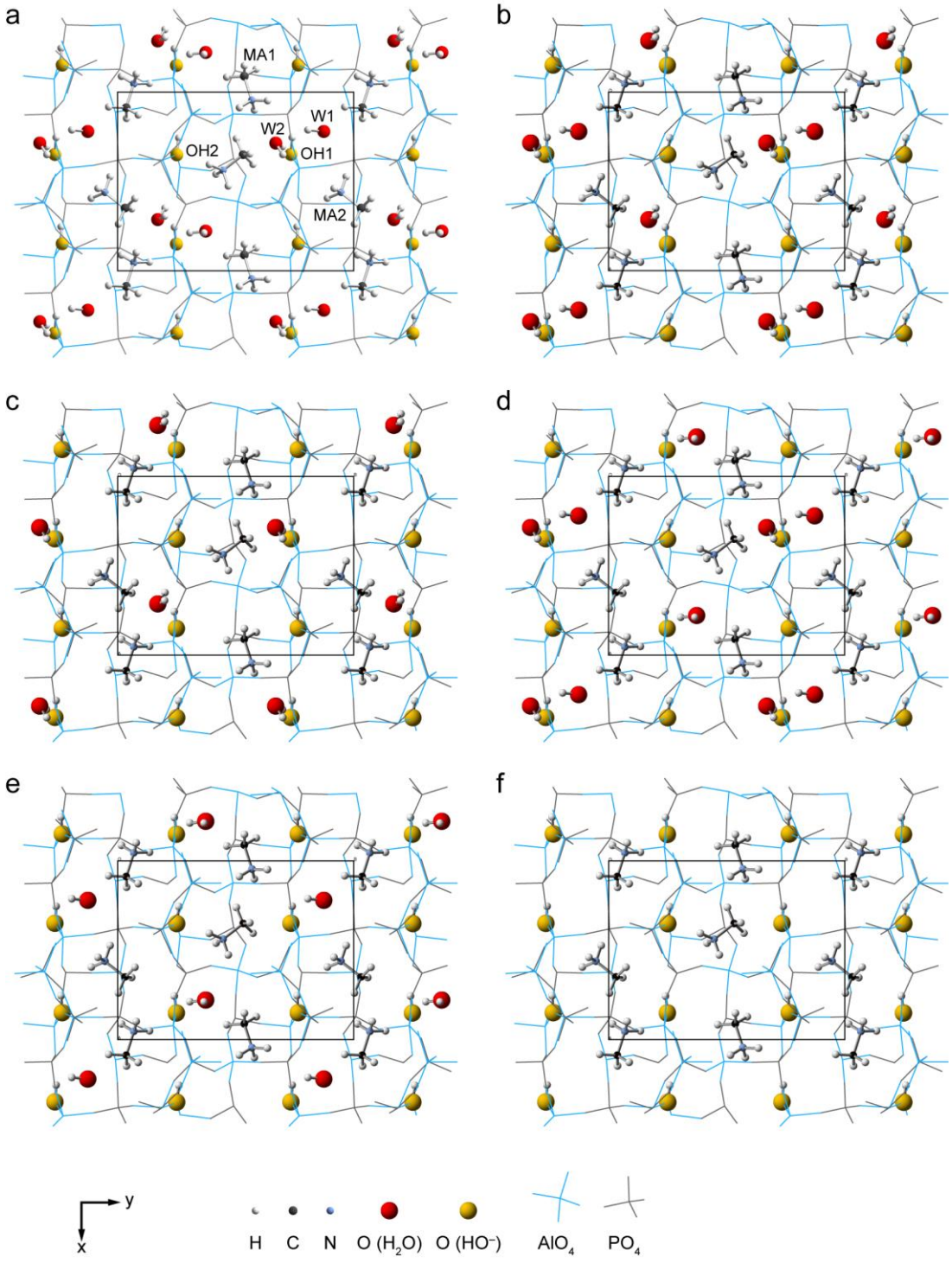

Figure 5.41. The structures (prior to optimisation) of the guest layers in the structural models, 0, 1w, 2w, 3w, 4w and 5w, described in Table 5.12.

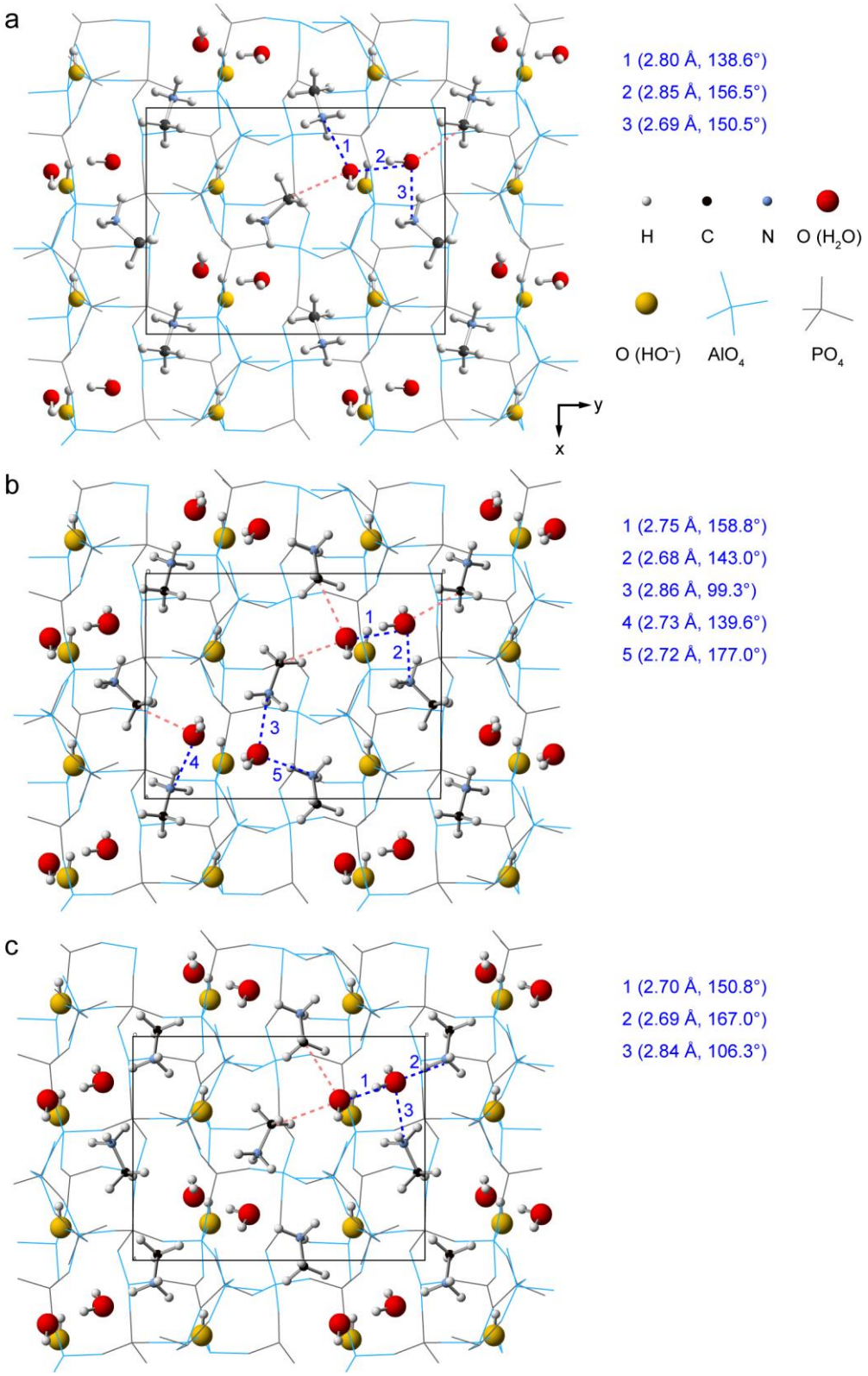

Figure 5.42. Optimised structures of the guest layers in models (a) 0, (b) 1ma and (c) 2ma. Hydrophobic interactions are indicated in pink and hydrogen bonds in blue, with the O-N or O-O distance and O-H-N or O-H-O angle given in the parentheses.

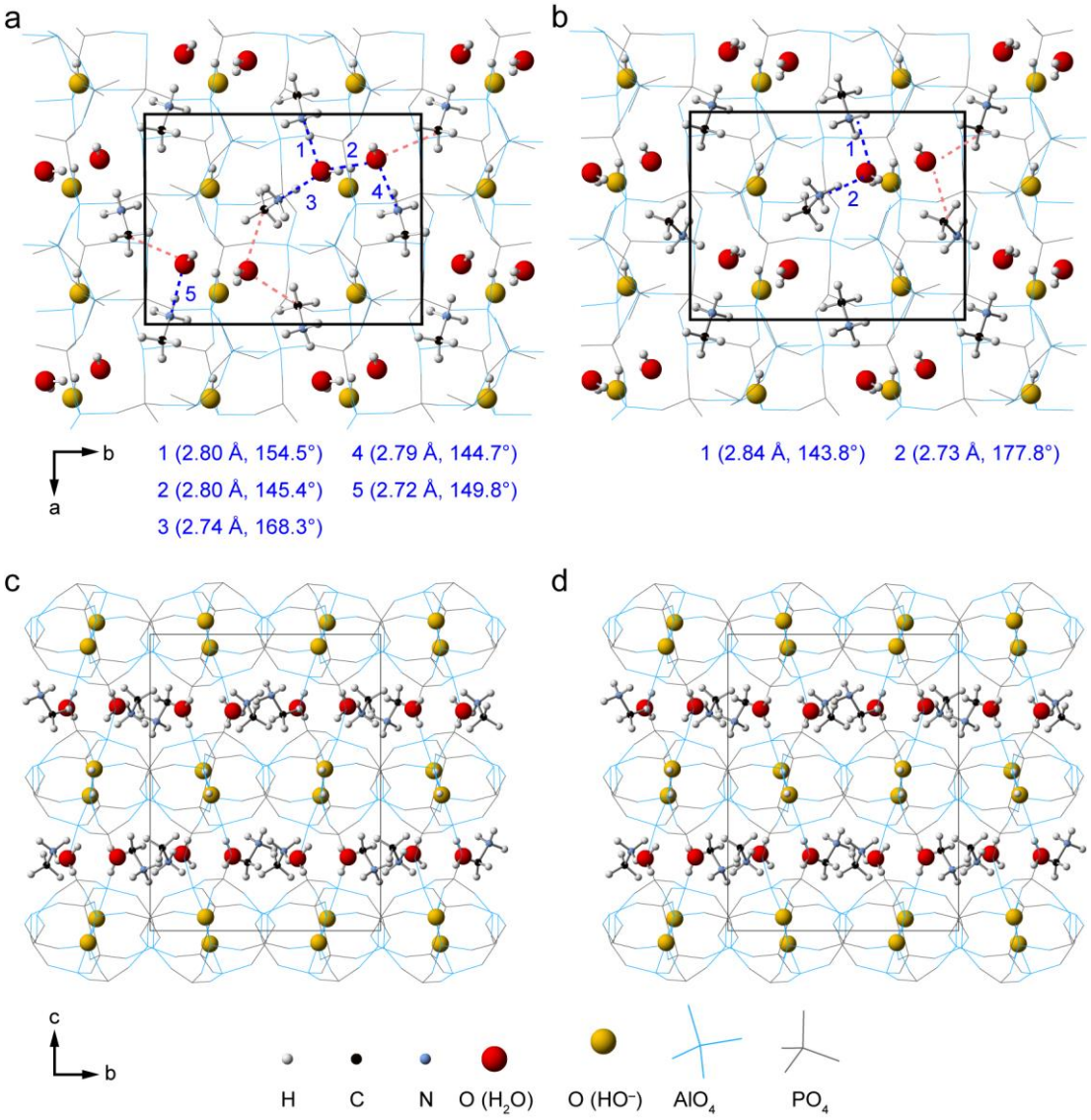

Figure 5.43. The optimised structures of the guest layers in models (a and c) 3ma and (b and d) 4ma, viewed (a and b) down the c axis and (c and d) down the a axis. In (a and b), hydrophobic interactions are indicated in pink and hydrogen bonds are indicated in blue, with the O-N or O-O distance and O-H-N or O-H-O angle given in the parentheses.

thermodynamically favoured. The fact that both of the models with reoriented MA2 are more energetically favoured than model 0 suggests that, in fact, the orientation of MA2 may be incorrect in the original structure. This idea may also appear to be supported by the fact that model 5ma (reorientation of all MA1 and MA2) is also lower in energy than any of the models with MA2 in its original orientation, despite the fact that model 2ma showed that reorientation of all MA1 was unfavourable.

However, it can be seen from Figure 5.44 that reorientation of all MA1 and MA2 actually leads to a hydrogen bonding situation that is superficially similar to model 0, with both H_2O in each water pair hydrogen bonded to one MA. However, closer inspection of the hydrogen bonding in model 5ma reveals that the reoriented MA are in a much better orientation to form strong hydrogen bonds (shorter N-O distances and angles very close to 180°) to the H_2O, and furthermore, the hydrophobic C-O distances have increased. This suggests that, in fact, reorientation of all MA may be energetically favoured over the published crystal structure.

It is more challenging to interpret the energies of structures with H_2O vacancies, as the number of atoms in the structure has changed and, therefore, the energy of the released H_2O must somehow be taken into account. The energy of a molecule of H_2O was calculated using the same computational parameters as for the structural models. A molecule of H_2O was placed in a unit cell the same size as the initial unit cell of model 0 and its structure was optimised. The final (dispersion-corrected) total energy was –473.072 eV. The approximate total energies of models including H_2O vacancies, corrected for the "lost" H_2O, are given in Table 5.13 and indicate that, in all cases, H_2O vacancies are disfavoured, with loss of W1 favoured over loss of W2. However, the H_2O vacancy models considered were based on model 0, and using one of the models with reoriented MA as the starting point for H_2O vacancies may yield a different result. For example, the hydrophobic W2 locations in model 2ma may be more favourable in conjunction with a W2 vacancy. The consideration of such permutations would be required for completeness, but was not included in the present work owing to the time and computational resources required (typically greater than a fortnight per structural optimisation, using 96 processors).

It can be seen from the energies of models 1j, 2j and 3j that reorientation of MA is energetically disfavoured (although time constraints prevented model 2j from being optimised to an energy minimum), suggesting that reorientation of MA is unlikely in JDF-2. The H_2O-corrected total energies of the models for JDF-2 and AlPO-53(A) confirm that JDF-2 + $8H_2O$ → AlPO-53(A) will be favourable (at 0 K), as all of the models for AlPO-53(A) are lower in energy than the models for JDF-2.

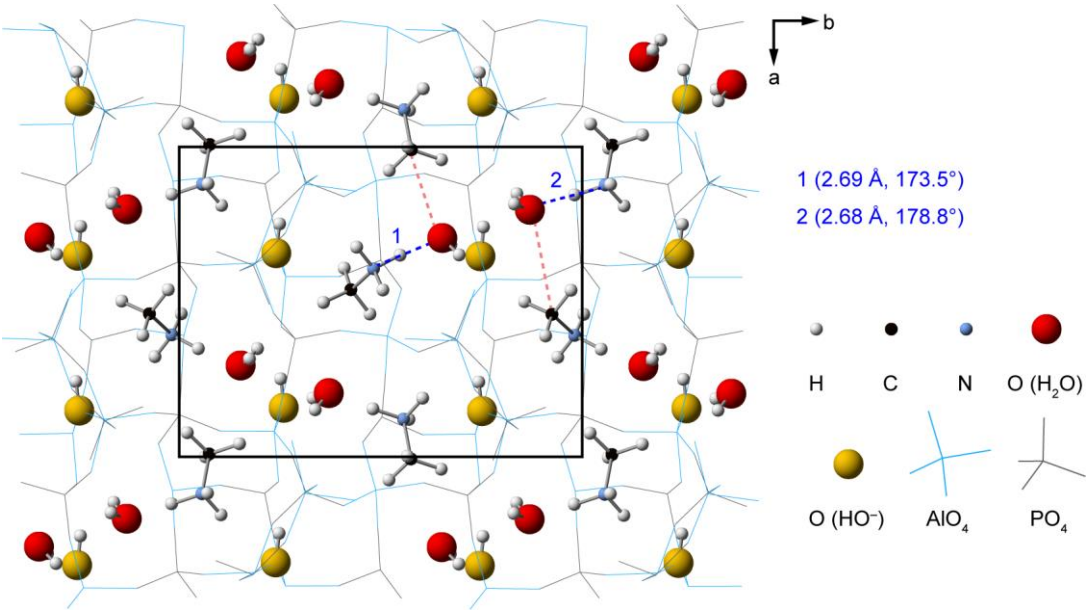

Figure 5.44. The optimised structure of the guest layer in model 5ma. Hydrophobic interactions are indicated in pink and hydrogen bonds are indicated in blue, with the O-N or O-O distance and O-H-N or O-H-O angle given in the parentheses.

The exception to this is model 5w, in which the MA occupies a slightly different and apparently less favourable, orientation than in model 1j, as shown in Figure 5.45.

The above results revealed that the published structure of AlPO-53(A) contains the second least stable orientation of MA, whereas the published structure of JDF-2 contains the most stable orientation of MA. Naturally, this raises the question

Table 5.13. Approximate water- and dispersion-corrected total energy, calculated using CASTEP 6, of models including H_2O vacancies. The contribution of one molecule of gaseous H_2O under the computational conditions used was –473.072 eV.

Model	Total Energy / eV	Model	Total Energy / eV
1w	–60774.245	5w	–60768.912
2w	–60772.166	1j	–60769.811
3w	–60774.112	2j	–60769.585
4w	–60771.854	3j	–60767.838

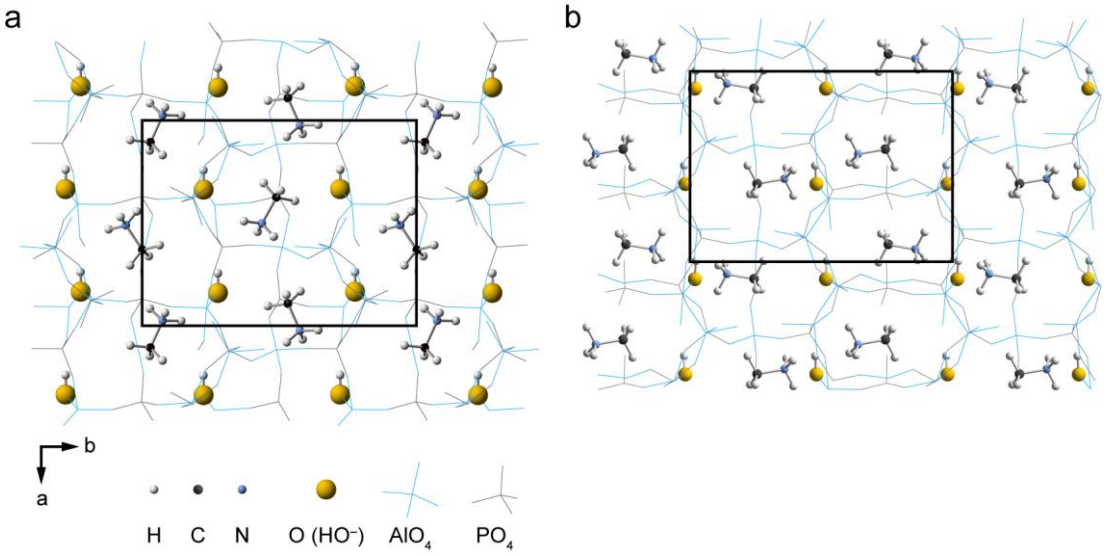

Figure 5.45. The optimised structures of the guest layers in models (a) 5w and (b) 1j.

of which orientation of MA in AlPO-53(A) would be expected from the published structure of JDF-2 – *i.e.*, is the energetically-favoured 5ma model of AlPO-53(A) likely to be kinetically accessible, starting from JDF-2? From the comparison of the published structures of JDF-2 and AlPO-53(A) shown in Figure 5.46, it can be seen that all MA are oriented with the CH_3 facing toward the centre of the pore in both cases, indicating that the orientation of all MA in the two structures is the same. Therefore, if the energetically favoured 5ma structure is to occur in reality, some mechanism must exist to achieve the observed reorientation of all MA. This could occur within the confined space of the pores of JDF-2 to give AlPO-53(A) either by complete rotation of the MA about an axis perpendicular to the C-N bond, followed by insertion of water, or a water-induced (*i.e.*, hydrophobic repulsion) translation of MA along the C-N bond, moving the C towards the outside of the pore, followed by a tilt, as was observed in the optimised 3ma, 4ma and 5ma structures. However, much more theoretical modelling would be required before any reliable comment could be made on the mechanism of MA reorientation, if such truly occurs.

While the average structure of AlPO-53(A) may resemble that of 5ma, it is clear from the experimental NMR spectra, reported above, that there must be some local disorder, such as that described by models 1ma, 3ma, 1w and 3w (although these are defects within the model 0 structure, rather than the apparently more

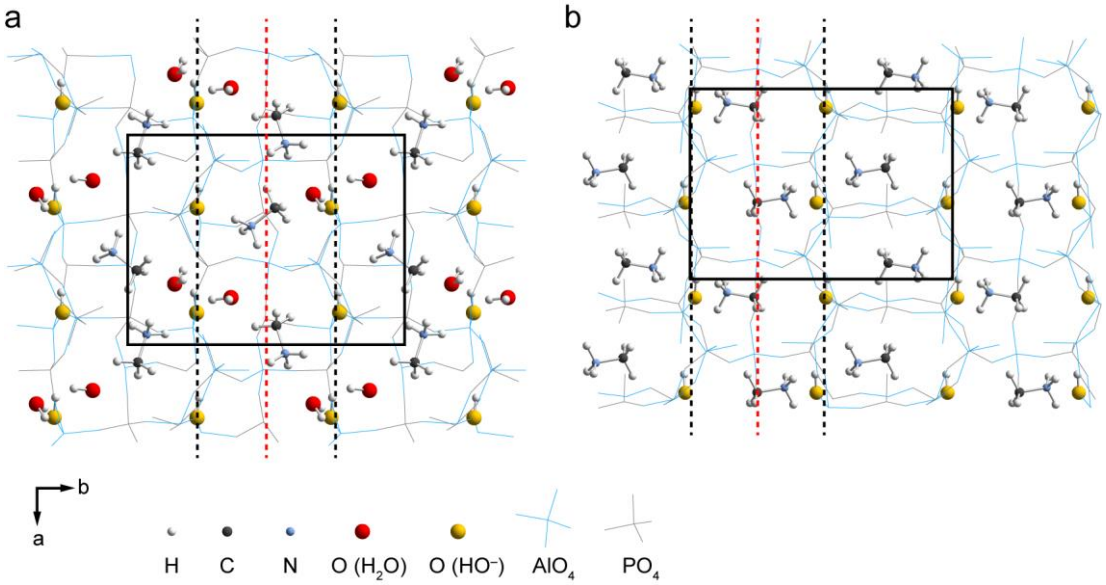

Figure 5.46. Representations of the guest layers in the published crystal structures of (a) AlPO-53(A)[3] and (b) JDF-2.[82]

favourable 5ma structure). Calculation of the NMR parameters of the optimised models was carried out in order to determine whether any of the structural defects considered here could be responsible for the additional resonances observed experimentally. Figure 5.47 shows the experimental ^{13}C and ^{15}N NMR spectra of AlPO-53(A) and JDF-2, along with the calculated chemical shifts for each of the models described above. At first sight, there is poor agreement with both the ^{13}C and ^{15}N isotropic shifts for all models (except 1j, which was used as the reference point). However, given that a reasonable error for CASTEP is ~1% of the experimental shift range (~2 ppm for ^{13}C and ~9 ppm for ^{15}N), it is, perhaps, not surprising that calculated spreads of shifts of 8.6 ppm and 13.5 ppm are observed for ^{13}C and ^{15}N, respectively, given that the experimentally observed spreads of shifts are 2.6 and 7.0 ppm, respectively. Unfortunately, this precludes the use of calculated shifts of either nucleus as a sensitive probe of the local structure in AlPO-53(A), despite the clear sensitivity observed experimentally. However, ^{31}P has an expected error in the calculated shifts of ~4 ppm, and an experimentally-observed shift range of ~23 ppm in AlPO-53(A), meaning that it may be a more reliable probe of local structure, despite the P atoms not being directly involved in the defects considered. As shown in Figure 5.48, however, the calculated ^{31}P isotropic shifts do not allow confident

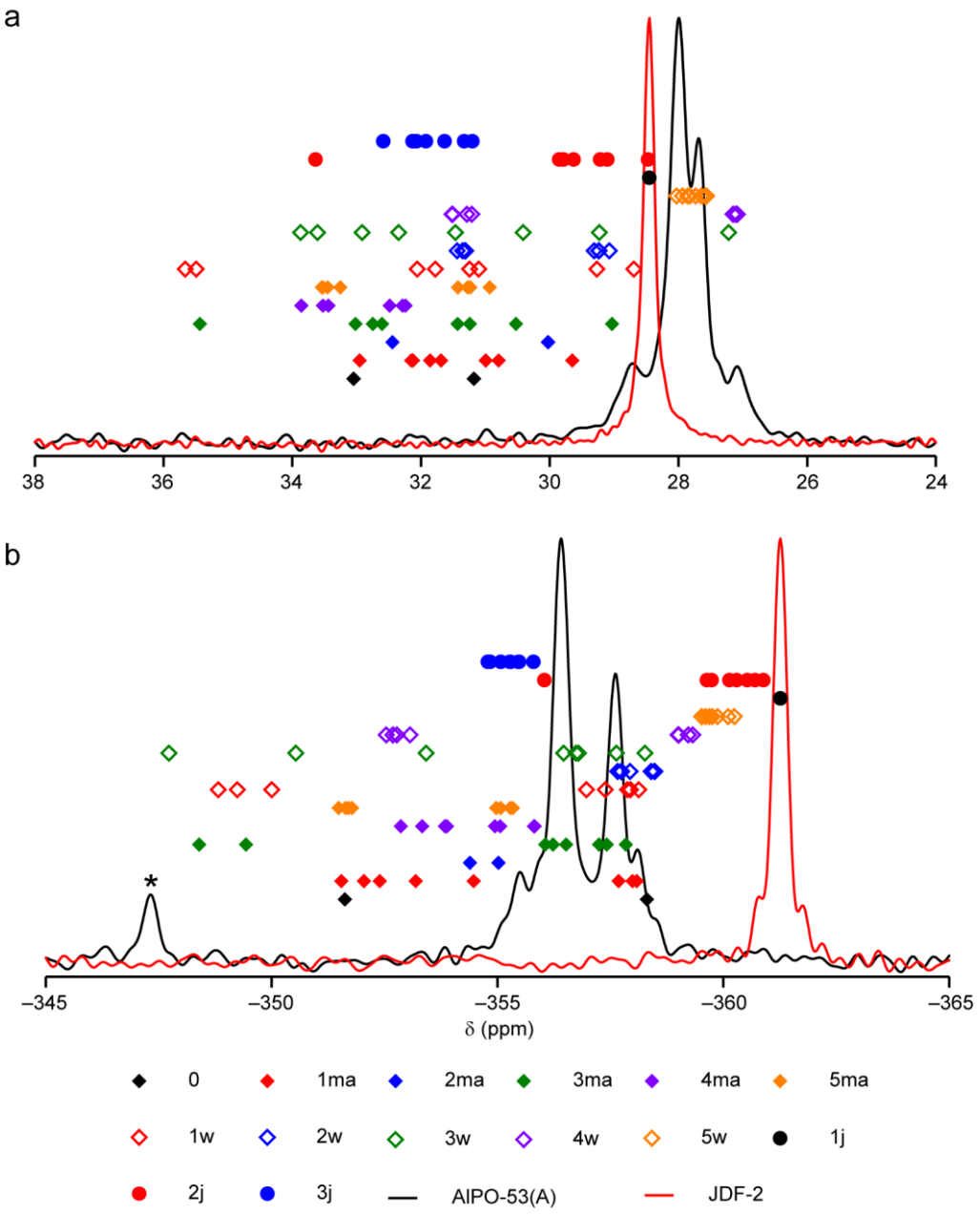

Figure 5.47. Experimental (a) ^{13}C and (b) ^{15}N NMR spectra of AlPO-53(A) (black) and JDF-2 (red), overlaid with data points representing the calculated isotropic chemical shifts for each nucleus in the structural models discussed in the text. The asterisk indicates a resonance assigned to a trace of the ^{15}N-enriched glycine used as the reference material.

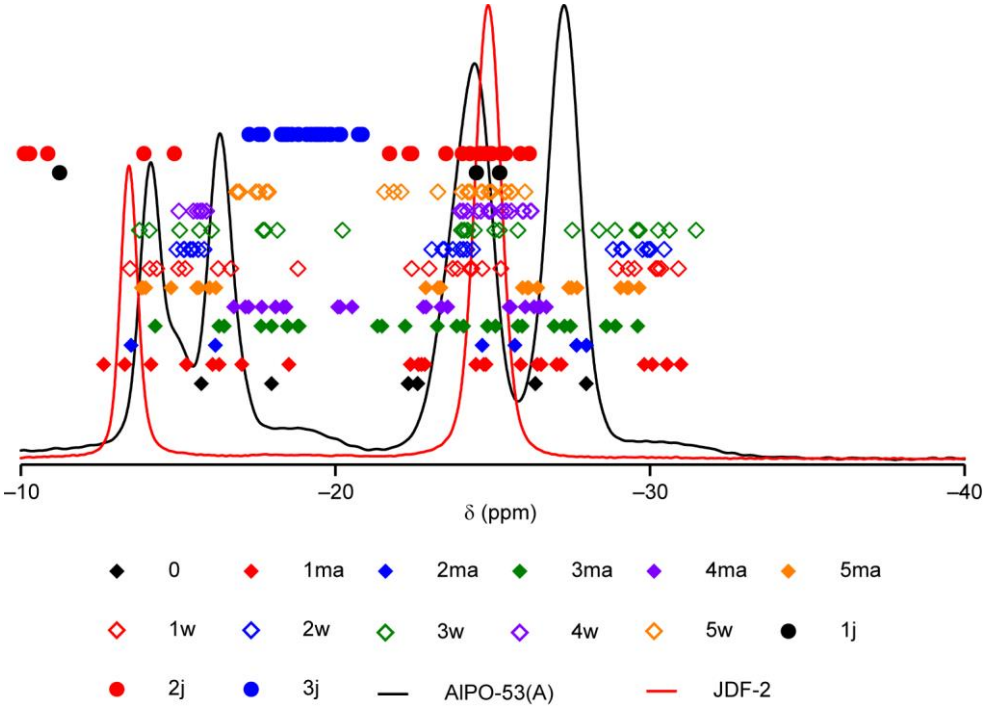

Figure 5.48. Experimental ^{31}P NMR spectra of AlPO-53(A) (black) and JDF-2 (red), overlaid with data points representing the calculated isotropic chemical shifts for the structural models discussed in the text.

conclusions to be drawn on which models, if any, describe the disorder present in AlPO-53(A), although it can be seen that there is very poor agreement for model 3j, confirming that model 1j is the more likely structure of JDF-2. While the calculated ^{27}Al NMR parameters were not analysed in detail here (the lineshapes and positions are a combination of three calculated NMR parameters, and so would carry an additional uncertainty) it is possible that they could be used to simulate ^{27}Al-^{31}P HETCOR spectra, which, in conjunction with experimental data, might be more informative than the 1D spectra alone. Such an approach was recently demonstrated, by Seymour *et al.*, to be highly effective as an aid to the identification of likely arrangements of HO^- in the AlPO, STA-2.[87]

The models considered here represent just a small subset of the possible structural models for defects in AlPO-53(A), which include numerous combinations of MA reorientations and H_2O vacancies, as well as defects not considered here, such as MA vacancies or H_2O occupying sites other than those identified by crystallography. As such, it is not surprising that comparison of the experimental and

calculated NMR parameters do not show a clearly preferable model for the disorder in AlPO-53(A). Therefore, before a detailed description of the local structure can be obtained, calculations sampling many more different defects are required. The *ab-initio* random structure searching (AIRSS) approach of Pickard and Needs[88] may be of assistance here, as it can rapidly generate thousands of initial structural models, without a requirement for crystallographically-identified locations (*e.g.*, for H_2O) or the "chemical intuition" inherent in human-generated structural models. It would also be advantageous to carry out supercell calculations to "dilute" the defects since, currently, reorientation of one MA in the unit cell affects one eighth of all MA in the structure. However, the computational cost of such an approach would be extremely high, and is not currently a feasible prospect. Further NMR experiments are also planned, including variable-temperature studies, ^{27}Al-^{31}P HETCOR and, if possible, ^{13}C-^{15}N HETCOR experiments on a partially-enriched sample. The crystallographic data should also be revisited, particularly in light of more recent techniques such as pair distribution function (PDF) analysis,[89] which can provide more detailed information on the local structure than Bragg diffraction alone.

5.5.4 Conclusions

The ambient hydration of JDF-2 to AlPO-53(A) was investigated in a more systematic fashion than the earlier study by Ashbrook *et al.*,[2] and it was shown that the hydration is initially rapid, achieving ~25% conversion within 24 h, as the JDF-2 on the surfaces of the crystallites is hydrated. However, complete conversion was not achieved, even after ~3 months, suggesting that diffusion of H_2O into the cores of the crystallites is slow and, perhaps, that JDF-2 and AlPO-53(A) are in equilibrium under ambient conditions.

It was observed that the solid-state NMR spectra of AlPO-53(A) contain more resonances than would be expected from the published crystal structure, suggesting some disorder is present within the material. A ^{1}H-^{13}C correlation spectrum of the material suggested that one of the two crystallographically-distinct MA species, MA2, is disordered with at least three orientations (as three ^{13}C resonances could be attributed to this species) while the other, MA1, is ordered and gives rise to only a single ^{13}C resonance. Additional resonances were also observed

for ^{15}N, and ^{31}P, but not for ^{1}H or ^{27}Al, owing to the inherently poorer resolution of MAS NMR spectra of the latter two nuclei. In an attempt to determine the nature of the disorder, a series of structural models for potential point and periodic defects was generated, based on MA reorientations and H_2O vacancies. DFT was used to optimise structures as far as possible, and then to calculate the NMR parameters of the (partially) optimised structures. It was shown that (at 0 K), the orientations of the MA in the published crystal structure of AlPO-53(A) are energetically disfavoured over reorientation of all MA. This suggests that future work should consider further models of MA reorientation and water vacancies, based on the lower-energy orientation of all MA, rather than the published structure. The NMR parameters of the structural models were also calculated by DFT, and it was shown that there was relatively poor agreement between the experimental and calculated ^{13}C, ^{15}N and ^{31}P isotropic chemical shifts for all of the models, with no model giving rise to good agreement for all three nuclei. However, this is likely to be owing to the fact that the models sampled a very small number of possible models of disorder in AlPO-53(A), and further work will be required to sample a greater number of possible models, possibly using the AIRSS approach to automate the sampling.

5.6 CHAPTER SUMMARY

Work presented at the start of this chapter showed that the NMR parameters for ^{17}O, ^{27}Al and ^{31}P in calcined AlPOs, particularly the ^{17}O C_Q, ^{27}Al σ_{iso} and ^{31}P σ_{iso}, can be related to the local structure by a series of relatively simple linear relationships. DISCO was written to automate the prediction of NMR parameters based on input crystal structures, and can rapidly (on the timescale of a few ms per atom) predict the NMR parameters for a given crystal structure. This is in contrast to DFT calculations, which are slower (hours timescale) and limited to systems containing fewer than ~250 atoms (when carried out using most readily-available hardware). The speed of DISCO, combined with its ability to accept systems of almost infinite size (up to tens of thousands of atoms) means that it may find applications in generating NMR parameters for each step of large molecular dynamics, *etc*. calculations.

In many cases, published crystal structures require optimisation to an energy minimum prior to the calculation of NMR parameters. It was demonstrated that some structural parameters (particularly T-O bond lengths and O-T-O bond angles) will consistently fall within a given range once optimised (at an effective temperature of 0 K), suggesting that these parameters may be used as predictors of whether a given structure requires further optimisation, or whether it is close to an energy minimum.

The ambient hydration of JDF-2 to AlPO-53(A) was also investigated. It was shown that the hydration initially occurs rapidly, owing to the hydration of JDF-2 on the surfaces of crystallites. However, complete conversion was not achieved under ambient conditions after almost three months, owing to the apparently very slow diffusion of H_2O into the cores of the crystallites. The structure of AlPO-53(A) was investigated in greater depth using multinuclear solid-state NMR experiments, which indicated that the material was disordered, with one of the two crystallographically-distinct methylammonium (MA) species apparently giving rise to at least three ^{13}C and ^{15}N resonances. Unexpected resonances were also observed for ^{31}P, but not for ^{1}H (possibly owing to the lower resolution of ^{1}H MAS NMR) or ^{27}Al (possibly owing to the second-order quadrupolar broadening in the MAS experiments and the lower sensitivity of the high-resolution 3QMAS experiments used). The nature of the disorder was investigated using DFT to optimise various structural models including reorientation of MA or loss of water, and it was shown that the orientations of the MA in the published crystal structure of AlPO-53(A) was energetically disfavoured over reorientation of all MA. This suggests that future work should consider further models of MA reorientation and water vacancies, based on the lower-energy orientation of all MA, rather than the published structure. The NMR parameters calculated for all of the structural models gave poor agreement with the experimental parameters. None of the models showed good agreement for the isotropic shifts of all three nuclei studied here (^{13}C, ^{15}N and ^{31}P δ_{iso}). Further experimental and computational work will, therefore, be required to investigate more potential models of disorder of AlPO-53(A).

5.7 REFERENCES

1. S. T. Wilson, B. M. Lok, C. A. Messina, T. R. Cannan and E. M. Flanigen, *J. Am. Chem. Soc.*, **1982**, *104*, 1146.

2. S. E. Ashbrook, M. Cutajar, J. M. Griffin, Z. A. D. Lethbridge, R. I. Walton and S. Wimperis, *J. Phys. Chem. C*, **2009**, *113*, 10780.

3. R. M. Kirchner, R. W. Grosse-Kunstleve, J. J. Pluth, S. T. Wilson, R. W. Broach and J. V. Smith, *Micropor. Mesopor. Mater.*, **2000**, *39*, 319.

4. GAUSSIAN03, revision D.01, M. J. Frisch *et al.*, Gaussian, Inc., Wallingford, CT, **2004**.

5. S. J. Clark, M. D. Segall, C. J. Pickard, P. J. Hasnip, M. J. Probert, K. Refson and M. C. Payne, *Z. Kristallogr.*, **2005**, *220*, 567.

6. M. D. Segall, P. J. D. Lindan, M. J. Probert, C. J. Pickard, P. J. Hasnip, S. J. Clark and M. C. Payne, *J. Phys.: Condens. Matter*, **2002**, *14*, 2717.

7. K. J. D. MacKenzie and M. E. Smith, *Multinuclear Solid-State NMR of Inorganic Materials*, 1st edn., Elsevier Science Ltd, Oxford, UK, 2002.

8. P. A. Wright, *Microporous Framework Solids*, 1st edn., The Royal Society of Chemistry, Cambridge, UK, 2008.

9. P. J. Barrie and J. Klinowski, *J. Phys. Chem.*, **1989**, *93*, 5972.

10. G. L. Turner, K. A. Smith, R. J. Kirkpatrick and E. Oldfield, *J. Magn. Reson.*, **1986**, *70*, 408.

11. D. Müller, E. Jahn, G. Ladwig and U. Haubenreisser, *Chem. Phys. Lett.*, **1984**, *109*, 332.

12. M. Soulard, J. Patarin and B. Marler, *Solid State Sci.*, **1999**, *1*, 37.

13. M. Hartmann, A. M. Prakash and L. Kevan, *J. Chem. Soc. Faraday Transact.*, **1998**, *94*, 723.

14. H. Y. He and J. Klinowski, *J. Phys. Chem.*, **1993**, *97*, 10985.

15. N. Z. Logar, G. Mali, N. Rajic, S. Jevtic, M. Rangus, A. Golobic and V. Kaucic, *J. Solid State Chem.*, **2010**, *183*, 1055.

16. P. J. Byrne, J. E. Warren, R. E. Morris and S. E. Ashbrook, *Solid State Sci.*, **2009**, *11*, 1001.

17. H. Fjellvåg, D. E. Akporiaye, E. N. Halvorsen, A. Karlsson, K. O. Kongshaug and K. P. Lillerud, *Solid State Sci.*, **2001**, *3*, 603.

18. J. L. Paillaud, P. Caullet, L. Schreyeck and B. Marler, *Micropor. Mesopor. Mater.*, **2001**, *42*, 177.

19. A. Tuel, V. Gramlich and C. Baerlocher, *Micropor. Mesopor. Mater.*, **2001**, *47*, 217.

20. K. Maeda, A. Tuel, S. Caldarelli and C. Baerlocher, *Micropor. Mesopor. Mater.*, **2000**, *39*, 465.

21. K. O. Kongshaug, H. Fjellvåg, B. Klewe and K. P. Lillerud, *Micropor. Mesopor. Mater.*, **2000**, *39*, 333.

22. L. Canesson, I. Arcon, S. Caldarelli and A. Tuel, *Micropor. Mesopor. Mater.*, **1998**, *26*, 117.

23. C. A. Fyfe, H. M. Z. Altenschildesche, K. C. Wong-Moon, H. Grondey and J. M. Chezeau, *Solid State Nucl. Magn. Reson.*, **1997**, *9*, 97.

24. D. E. Akporiaye, H. Fjellvåg, E. N. Halvorsen, J. Hustveit, A. Karlsson and K. P. Lillerud, *J. Phys. Chem.*, **1996**, *100*, 16641.

25. G. Engelhardt and W. Veeman, *J. Chem. Soc. Chem. Commun.*, **1993**, 622.

26. H. X. Li and M. E. Davis, *J. Chem. Soc. Faraday Transact.*, **1993**, *89*, 951.

27. H. X. Li and M. E. Davis, *J. Chem. Soc. Faraday Transact.*, **1993**, *89*, 957.

28. S. E. Ashbrook, M. Cutajar, C. J. Pickard, R. I. Walton and S. Wimperis, *Phys. Chem. Chem. Phys.*, **2008**, *10*, 5754.

29. V. R. Seymour, *PhD. Thesis*, University of St Andrews, 2013.

30. J. Pinkas, J. Lobl, D. Dastych, M. Necas and H. W. Roesky, *Inorg. Chem.*, **2002**, *41*, 6914.

31. Y. Yang, J. Pinkas, M. Schafer and H. W. Roesky, *Angew. Chem. Int. Ed.*, **1998**, *37*, 2650.

32. Z. Yan, B. Chen and Y. Huang, *Solid State Nucl. Magn. Reson.*, **2009**, *35*, 49.

33. B. Herreros and J. Klinowski, *J. Phys. Chem.*, **1995**, *99*, 9514

34. M. Amri, S. E. Ashbrook, D. M. Dawson, J. M. Griffin, R. I. Walton and S. Wimperis, *J. Phys. Chem. C*, **2012**, *116*, 15048.

35. L. Beitone, J. Marrot, T. Loiseau, G. Ferey, M. Henry, C. Huguenard, A. Gansmuller and F. Taulelle, *J. Am. Chem. Soc.*, **2003**, *125*, 1921.

36. K. O. Kongshaug, H. Fjellvåg and K. P. Lillerud, *J. Mater. Chem.*, **1999**, *9*, 3119.

37. D. E. Akporiaye, A. Andersen, I. M. Dahl, H. B. Mostad and R. Wendelbo, *J. Phys. Chem.*, **1995**, *99*, 14142.

38. A. Tuel, C. Lorentz, V. Gramlich and C. Baerlocher, *J. Solid State Chem.*, **2005**, *178*, 2322.
39. K. Maeda, Y. Kiyozumi and F. Mizukami, *J. Phys. Chem. B*, **1997**, *101*, 4402.
40. K. Kanehashi, T. Nemoto and K. Saito, *J. Non-Cryst. Solids*, **2007**, *353*, 4227.
41. V. Campomar, *PhD. Thesis*, Université P. et M. Curie, 1990.
42. S. E. Ashbrook and D. M. Dawson, *Acc. Chem. Res.*, **2013**, *46*, 1964.
43. J. F. Ducel, J. J. Videau, K. S. Suh and J. Senegas, *Phys. Chem. Glasses*, **1994**, *35*, 10.
44. C. Bonhomme, C. Gervais, F. Babonneau, C. Coelho, F. Pourpoint, T. Azais, S. E. Ashbrook, J. M. Griffin, J. R. Yates, F. Mauri and C. J. Pickard, *Chem. Rev.*, **2012**, *112*, 5733.
45. T. Charpentier, *Solid State Nucl. Magn. Reson.*, **2011**, *40*, 1.
46. H. A. Graetsch, *Acta Crystallogr.*, **2001**, *C57*, 665.
47. T. Ikeda, K. Miyazawa, F. Izumi, Q. Huang and A. Santoro, *J. Phys. Chem. Solids*, **1999**, *60*, 1531.
48. S. Ghose and T. Tsang, *Am. Mineral.*, **1973**, *58*, 748.
49. J. Zemann, *Z. Anorg. Allg. Chem.*, **1963**, *324*, 241.
50. M. Roux, C. Marichal, J. M. Le Meins, C. Baerlocher and J. M. Chezeau, *Micropor. Mesopor. Mater.*, **2003**, *63*, 163.
51. K. Robinson, G. V. Gibbs and P. H. Ribbe, *Science*, **1971**, *172*, 567.
52. J. V. Smith and C. S. Blackwell, *Nature*, **1983**, *303*, 223.
53. J. V. Smith, C. S. Blackwell and G. L. Hovis, *Nature*, **1984**, *309*, 140.
54. A. R. Grimmer, *Chem. Phys. Lett.*, **1985**, *119*, 416.
55. J. B. Higgins and D. E. Woessner, *Eos T. Am. Geophys. Un.*, **1982**, *63*, 1139.
56. A. R. Grimmer and R. Radeglia, *Chem. Phys. Lett.*, **1984**, *106*, 262.
57. N. Weiden and H. Rager, *Z. Naturforsch.*, **1985**, *A**40***, 126.
58. G. Engelhardt and R. Radeglia, *Chem. Phys. Lett.*, **1984**, *108*, 271.
59. J. M. Newsam, *J. Phys. Chem.*, **1987**, *91*, 1259.
60. J. M. Thomas, J. Klinowski, S. Ramdas, B. K. Hunter and D. T. B. Tennakoon, *Chem. Phys. Lett.*, **1983**, *102*, 158.
61. M. G. Mortuza, R. Dupree and D. Holland, *J. Mater. Sci.*, **1998**, *33*, 3737.
62. S. C. Kohn, C. M. B. Henderson and R. Dupree, *Am. Mineral.*, **1997**, *82*, 1133.

63. G. Engelhardt, in *Solid-State NMR Spectroscopy of Inorganic Materials*, ed. J. J. Fitzgerald, American Chemical Society, Washington, D.C., 1999.

64. C. Sivadinarayana, V. R. Choudhary, R. Vetrivel and S. Ganapathy, *Solid State Nucl. Magn. Reson.*, **1998**, *13*, 175.

65. K. J. D. Mackenzie, I. W. M. Brown, R. H. Meinhold and M. E. Bowden, *J. Am. Ceram. Soc.*, **1985**, *68*, 266.

66. J. M. Griffin, L. Clark, V. R. Seymour, D. W. Aldous, D. M. Dawson, D. Iuga, R. E. Morris and S. E. Ashbrook, *Chem. Sci.*, **2012**, *3*, 2293.

67. A. R. Grimmer, *Spectrochim. Acta*, **1978**, *A34*, 941.

68. E. Lippmaa, A. Samoson and M. Magi, *J. Am. Chem. Soc.*, **1986**, *108*, 1730.

69. G. L. Hovis, D. R. Spearing, J. F. Stebbins, J. Roux and A. Clare, *Am. Mineral.*, **1992**, *77*, 19.

70. B. L. Phillips, R. J. Kirkpatrick and A. Putnis, *Phys. Chem. Miner.*, **1989**, *16*, 591.

71. B. L. Phillips and R. J. Kirkpatrick, *Am. Mineral.*, **1994**, *79*, 1025.

72. M. T. Weller, M. E. Brenchley, D. C. Apperley and N. A. Davies, *Solid State Nucl. Magn. Reson.*, **1994**, *3*, 103.

73. S. R. Jansen, H. T. Hintzen, R. Metselaar, J. W. de Haan, L. J. M. van de Ven, A. P. M. Kentgens and G. H. Nachtegaal, *J. Phys. Chem. B*, **1998**, *102*, 5969.

74. J. Skibsted, E. Henderson and H. J. Jakobsen, *Inorg. Chem.*, **1993**, *32*, 1013.

75. S. Sneddon, *Unpublished Work*, 2012.

76. F. Jensen, *J. Chem. Theor. Comput.*, **2008**, *4*, 719.

77. H. Koller, G. Engelhardt, A. P. M. Kentgens and J. Sauer, *J. Phys. Chem.*, **1994**, *98*, 1544.

78. I. D. Brown and R. D. Shannon, *Acta Crystallogr.*, **1973**, *A29*, 266.

79. S. Sneddon, D. M. Dawson, C. J. Pickard and S. E. Ashbrook, *Phys. Chem. Chem. Phys.*, **2014**, *16*, 2660.

80. H. N. Ng and C. Calvo, *Can. J. Phys.*, **1976**, *54*, 638.

81. P. L. Gai-Boyes, J. M. Thomas, P. A. Wright, R. H. Jones, S. Natarajan, J. S. Chen and R. R. Xu, *J. Phys. Chem.*, **1992**, *96*, 8206.

82. A. M. Chippindale, A. V. Powell, R. H. Jones, J. M. Thomas, A. K. Cheetham, Q. S. Huo and R. R. Xu, *Acta Crystallogr.*, **1994**, *C50*, 1537.

83. J. B. Parise, *Stud. Surf. Sci. Catal.*, **1985**, *24*, 271.

84. E. Boldyreva and V. Boldyrev, *Reactivity of Molecular Solids*, 1st edn., John Wiley and Sons Ltd, Chichester, UK, 1999.

85. S. Grimme, *J. Comput. Chem.*, **2006**, *27*, 1789.

86. E. R. McNellis, J. Meyer and K. Reuter, *Phys. Rev. B*, **2009**, *80*, 205414.

87. V. R. Seymour, E. C. V. Eschenroeder, M. Castro, P. A. Wright and S. E. Ashbrook, *Cryst. Eng. Commun.* , **2013**, *15*, 8668.

88. C. J. Pickard and R. J. Needs, *J. Phys. Condens. Mat.*, **2011**, *23*, 053201.

89. S. J. L. Billinge and M. G. Kanatzidis, *Chem. Commun.*, **2004**, 749.

6 GALLOPHOSPHATES

6.1 CHAPTER OVERVIEW

The previous chapter demonstrated some of the information available from solid-state NMR spectra of AlPOs, particularly when carried out in conjunction with theoretical calculations and modelling. Gallophosphate zeotypes (GaPOs) are closely related to AlPOs and contain many NMR-active nuclei in their structures, as summarised in Table 1.1. Therefore, it is natural to assume that solid-state NMR will also offer much insight for these systems.

This chapter explores the GaPO, GaPO-34, which can be prepared with either pyridinium fluoride (pyHF) or 1-methylimidazolium fluoride (miHF) in the pores. GaPO-34[miHF] exhibits a low-temperature dehydrofluorination (loss of HF) at ~330 °C, before full calcination at ~375 °C. While a phase transition at ~330 °C was previously detected by TGA in the literature,[1] the phase formed was not identified (although its powder XRD pattern was recorded). Work presented here provides clear evidence of dehydrofluorination, and possible structures for dehydrofluorinated GaPO-34[mi] (mi = 1-methylimidazole) are discussed. Complete calcination of GaPO-34[pyHF] or GaPO-34[miHF] yields GaPO-34(calcined), which is shown to hydrate rapidly in air, giving GaPO-34(calcined, hydrated). The similarities and differences between GaPO-34(calcined, hydrated) and the analogous AlPO, AlPO-34 are then discussed. The structure of GaPO-34(calcined, hydrated) appears to be more complicated than that of AlPO-34, and complete structural characterisation was not possible. Unlike AlPO-34, which can be reversibly dried by heating, GaPO-34(calcined, hydrated) is shown to decompose, yielding GaPO-34(collapsed) when heated. In order to avoid decomposition, dehydration by gentle heating or evacuation at room temperature are investigated as a means of recovering GaPO-34(calcined) from GaPO-34(calcined, hydrated). Some success was obtained with this approach; a finding that may be of use both in drying GaPO-34 (allowing its application in industry) and in drying other moisture-sensitive GaPOs. In addition, two common impurity phases formed during the synthesis of GaPO-34, $GaPO_4$ berlinite and an unidentified GaPO phase are characterised by multinuclear solid-state NMR.

6.2 ACKNOWLEDGEMENTS

Work carried out and reported in this chapter would have been impossible without the group of Professor Richard Walton (University of Warwick), who provided many of the samples studied and carried out the TGA/DSC and *in-situ* powder XRD experiments; the group of Professor Stephen Wimperis (University of Glasgow), who recorded some of the high-field NMR spectra of GaPO-34; Dr John Griffin, who recorded some of the NMR spectra at 20.0 and 14.1 T, and Miss Emily McHale and Miss Laurie MacFarlane, both of whom carried out syntheses, calculations and NMR experiments as part of their undergraduate research projects at the University of St Andrews. Dr Magdalena Lozinska (University of St Andrews) is thanked for assistance with the capillary XRD experiment.

6.3 EXPERIMENTAL DETAILS

6.3.1 Synthesis

6.3.1.1 GaPO-34[pyHF]

GaPO-34[pyHF] was prepared as previously reported.[2] Briefly, a Ga source (nominally, amorphous Ga_2O_3) was prepared by decomposition of gallium nitrate hydrate in air at 250 °C for 24 h. 0.5 g of this material was combined with 85 wt% aqueous H_3PO_4, 40 wt% aqueous HF and pyridine to give a gel of composition Ga_2O_3 : P_2O_5 : HF : 70 H_2O : 1.7 pyridine (py). The gel was stirred at room temperature for 2 h, sealed in a Teflon autoclave liner and heated at 170 °C for 24 h. The reaction was then cooled to room temperature and GaPO-34[pyHF] was isolated by filtration and washed with H_2O.

6.3.1.2 GaPO-34[miHF]

GaPO-34[miHF] was prepared as described in the literature,[2] starting with a gel of composition Ga_2O_3 : P_2O_5 : HF : 70 H_2O : 1.7 mi. All other conditions were the same as for GaPO-34[pyHF]. Three further samples were prepared following the same synthetic procedure. As previously noted in the literature,[1, 2] this synthetic method can be hard to reproduce, and many other synthetic attempts formed mixtures of

$GaPO_4$ berlinite, GaPO-34[miHF] and a poorly-understood impurity phase discussed in greater detail below. An attempt to replace the gallium oxide starting material with gallium nitrate hydrate yielded predominantly $GaPO_4$ berlinite.

6.3.1.3 GaPO-34[mi]

GaPO-34[mi] was prepared by heating a portion of GaPO-34[miHF] to 330 °C at a rate of 10 °C min^{-1} in a tube furnace open to air. The sample was held at this temperature for 2 h, cooled to ~300 °C and transferred under air to a sample vial. The vial was immediately sealed and the sample was cooled to ambient temperature. Analysis by solid-state NMR spectroscopy (see below) revealed that the material was a mixture of GaPO-34[mi] and GaPO-34(calcined), although the latter rapidly hydrated upon exposure to ambient conditions.

6.3.1.4 GaPO-34(calcined)

GaPO-34(calcined) was prepared by calcining GaPO-34[miHF] under air at 425 °C as previously reported.[2] A portion of the sample was immediately packed into a 2.5 mm NMR rotor with CaO packed above and below the sample to absorb ambient moisture. A second sample was prepared in a similar manner by heating the material to 500 °C for 2 h. The material was then cooled to 330 °C and sealed into a glass vial while hot. The material was then rapidly packed into a 2.5 mm NMR rotor after storage in the sealed vial overnight.

6.3.1.5 GaPO-34(calcined, hydrated)

GaPO-34(calcined, hydrated) was prepared from GaPO-34(calcined) by exposing the calcined material to ambient conditions. As described in the literature, the material hydrates rapidly and exposure to ambient conditions for under an hour was generally sufficient for full hydration.[2]

6.3.1.6 GaPO-34(collapsed)

GaPO-34(collapsed) was prepared from GaPO-34(calcined, hydrated) by heating the hydrated material to 200 °C, as described in the literature.[2] The material was also prepared by heating at lower temperatures (80-110 °C) for periods of 1-2 days.

6.3.1.7 Unidentified Impurity Phases: GaPO-X[miHF] and GaPO-X[pyHF]

As noted above, the synthesis of GaPO-34 is challenging to reproduce and Schott-Darie *et al*. reported the presence of an impurity phase containing the hydrofluorinated SDA.[1] For the purposes of this thesis, the impurity phase, the structure of which is not yet known, will be termed GaPO-X.

A relatively pure sample of the miHF form of GaPO-X, GaPO-X[miHF], was prepared following the synthetic method outlined in Section 6.3.1.2. The sample was observed to consist of GaPO-X[miHF] and a trace of $GaPO_4$ berlinite. Small amounts of this material were also observed in most other samples of GaPO-34[miHF].

A relatively pure sample of the pyHF form of GaPO-X, GaPO-X[pyHF], was prepared following the method for the synthesis of GaPO-34[pyHF].[1, 2] The sample contains an as-yet unidentified F-containing phase.

6.3.1.8 $GaPO_4$ Berlinite

$GaPO_4$ berlinite was prepared by mixing $Ga_2(SO_4)_3$ (0.5 g), 85 wt% aqueous H_3PO_4 (0.2 ml), H_2O (0.8 ml) and 40 wt% aqueous methylammonium hydroxide (0.2 ml) in a Teflon autoclave liner, stirring for 15 minutes at room temperature and then heating at 150 °C for 5 days. $GaPO_4$ berlinite was isolated by suction filtration, washed with water and dried in air overnight. It should be noted that this was the result of a (repeatably) unsuccessful attempt to synthesise GaPO-M2,[3, 4] and the above method is not the best means of preparing $GaPO_4$ berlinite. $GaPO_4$ berlinite was also obtained as an impurity in a number of other GaPO samples.

6.3.2 Solid-State NMR Spectroscopy

Solid-state NMR spectra reported in this chapter were recorded at 9.4 and 14.1 T (University of St Andrews) and 20.0 T (UK 850 MHz Solid-State NMR Facility, University of Warwick). Relevant experimental details can be found in the text, figure captions and extended figure captions in Appendix A.

6.3.3 First-Principles DFT Calculations

Calculations reported in this chapter were carried out using CASTEP 5.5.2 and CASTEP 6. Prior to calculation of the NMR parameters, the structural model was

optimised either to an energy minimum or for the specified number of iterations, with the atomic positions and unit cell parameters allowed to vary as described in the text. In addition, for calculations carried out using CASTEP 6, the structural optimisations were carried out with dispersion interactions described by the G06 SEDC scheme.[5, 6] The calculations were carried out using a planewave cut-off energy of 60 Ry and a k-point spacing of 0.04 $Å^{-1}$. For CASTEP 5.5.2, chemical shifts were referenced using values for σ_{ref} of 282.1 ppm (^{31}P) and 1704.4 ppm (^{71}Ga),[2] whereas values 275.0 ppm (^{31}P) and 1681.1 ppm (^{71}Ga) were used for the CASTEP 6.

Calculations for free 1-methylimidazole and 1-methylimidazolium were carried out using GAUSSIAN09.[7] The structural optimisations and calculation of the NMR parameters were carried out at the B3LYP/6-311+G(d,p) theory level with the CSGT method used in calculation of the NMR parameters. The calculated shifts were referenced using the calculated shielding values for miH^+ and the experimental shift values for GaPO-34[miHF], giving σ_{ref} = 177.9 ppm.

6.3.4 X-Ray Crystallography

A Bruker D8 diffractometer operating with Cu $K_{\alpha 1/2}$ radiation was used for variable temperature powder XRD experiments. The samples were packed into a ceramic holder and data measured in θ-θ geometry using a VÅNTEC solid-state detector, which permitted a typical diffraction pattern to be accumulated in around 3 minutes. The diffractometer was equipped with an Anton Parr XRK 900 reactor chamber, which allowed the sample to be heated above room temperature. Before each data collection the temperature was allowed to equilibrate for 5 min.

A Mettler-Toledo TGA/DSC 1 Thermogravimetric Analyser was used to measure TGA and differential scanning calorimetry (DSC, not reported) simultaneously. Approximately 10 mg of powdered sample was placed in an aluminium pan and its mass monitored in static air upon heating to 1000 °C at a rate of 10 °C min^{-1}. For samples of GaPO-X, the temperature was held at 1000 °C until mass loss reached a minimum.

A powdered sample of GaPO-34(calcined, hydrated) was packed into a 0.5 mm glass capillary and data were obtained using a Stoe Stadip diffractometer with

Cu $K_{\alpha 1}$ radiation of wavelength, λ = 1.5406 Å. The pattern was recorded at room temperature with a 2 h scan time and a 2θ range of 3-50°.

A powdered sample of GaPO-X[miHF] was loaded into a disk of 3 mm depth, and data were obtained using a Panalytical EMPYREAN diffractometer with a Cu $K_{\alpha 1}$ radiation source of wavelength, λ = 1.5406 Å. The pattern was recorded at room temperature with a 1 h scan time and a 2θ range of 3-50°.

6.4 PHASES AND PHASE TRANSFORMATIONS OF GAPO-34

6.4.1 As-Prepared Phases

The GaPO form of the CHA framework is GaPO-34, which can be prepared hydrothermally with either mi or py as the SDA and HF as the mineraliser.[1] Both as-prepared forms of GaPO-34, GaPO-34[miHF] and GaPO-34[pyHF] crystallise with triclinic symmetry (space group $P\bar{1}$). The structure of GaPO-34[miHF], shown in Figure 6.1, contains 3 crystallographically-distinct Ga and P species, one distinct F species, bridging between two Ga1, and one crystallographically-distinct 1-methylimidazolium (miH^+) cation. In addition, there is a molecule of H_2O within the unit cell, which may occupy one of two equivalent positions. While there is no published crystal structure of GaPO-34[pyHF] (possibly owing to orientational disorder of the pyridinium (pyH^+) cations), its structure can be assumed to be very similar to that of the miHF analogue, as evidenced by solid-state NMR spectroscopy.[2] The ^{31}P and ^{71}Ga MAS NMR spectra of the two materials are shown in Figures 6.2(a and b), and reveal the presence of three distinct P species and both Ga(IV) and Ga(VI) species in both cases. While the ^{71}Ga resonances for the two expected Ga(IV) are overlapped, even at high field (Figure 6.2(c)), 3QMAS NMR experiments carried out at 20.0 T (Figure 6.2(d)) demonstrated that, in both cases, two distinct Ga(IV) species were present, and one distinct Ga(VI) species, as expected from the published crystal structure. The ^{71}Ga MAS NMR spectrum of GaPO-34[pyHF] contains asymmetric broadening of the lineshapes, typical of the presence of a small distribution of NMR parameters. In Figure 6.2(d) the ridges for

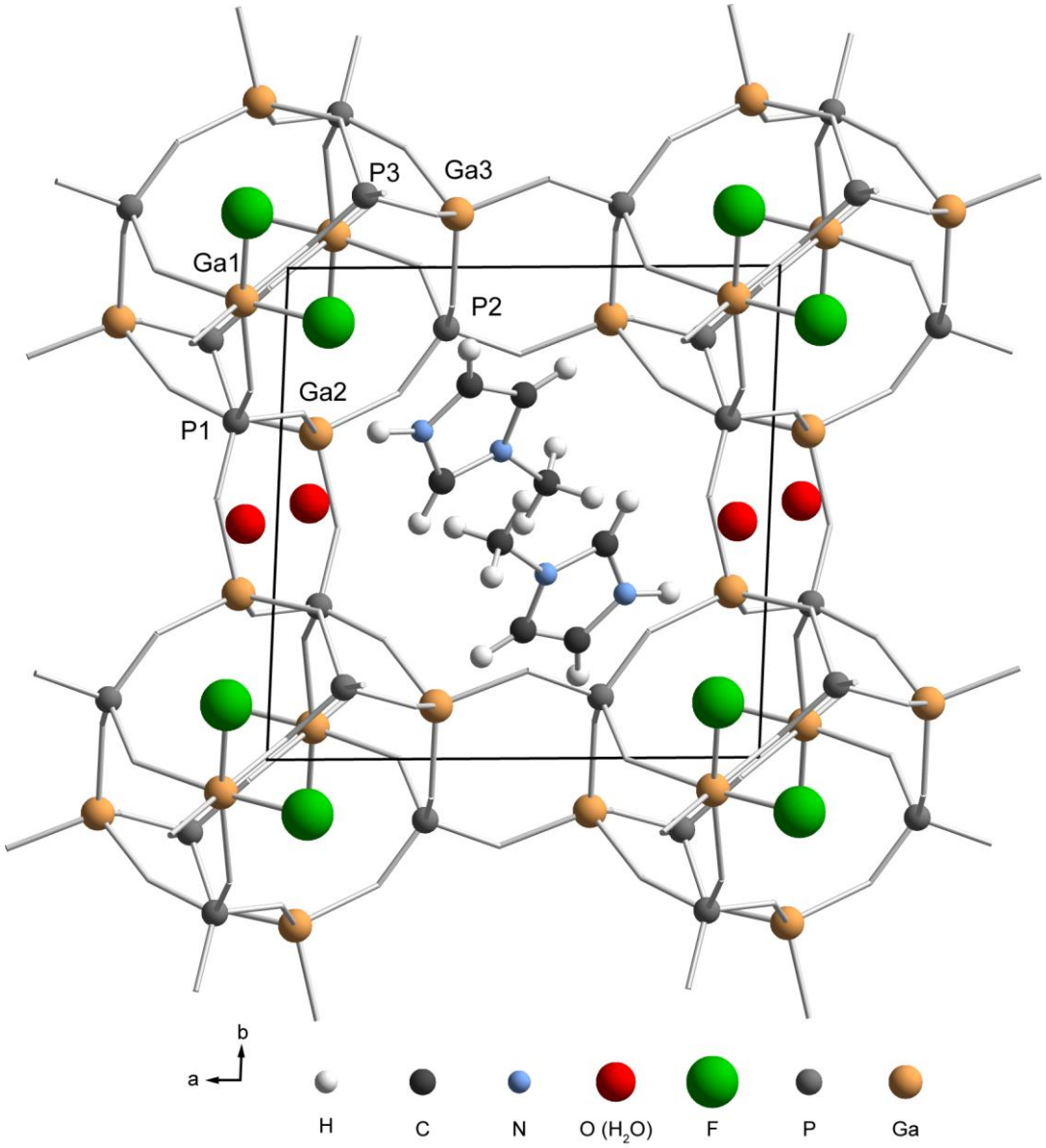

Figure 6.1. The crystal structure of GaPO-34[miHF], with crystallographically-distinct Ga and P species indicated. O atoms in the framework and H atoms are omitted for clarity.

Ga(IV) in the ^{71}Ga MQMAS NMR spectrum of GaPO-34[pyHF] are essentially perpendicular to δ_1, whereas the lineshape for Ga(VI) exhibits broadening indicative of a distribution of both chemical shifts and quadrupolar parameters. Such broadening implies the presence of disorder, most likely of the pyH^+ cations although, as discussed below, the structure contains H_2O, which is likely to be disordered. Nevertheless, average ^{71}Ga NMR parameters could be obtained for this

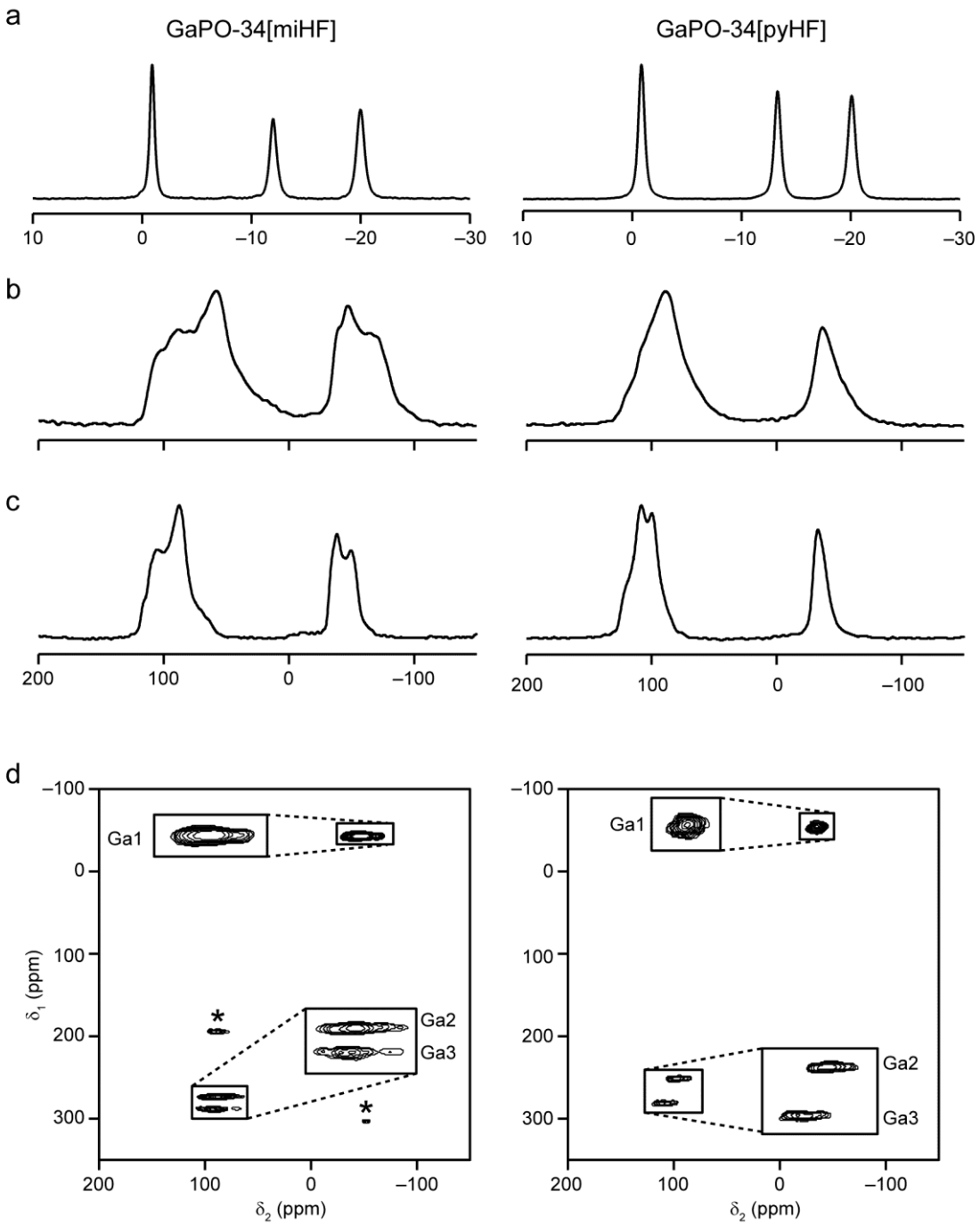

Figure 6.2. (a) ^{31}P (14.1 T, 25 kHz MAS), (b) ^{71}Ga (14.1 T, 28 kHz MAS), (c) ^{71}Ga (20.0 T, 30 kHz MAS) and (d) ^{71}Ga (20.0 T, 30 kHz MAS) sheared z-filtered 3QMAS NMR spectra of GaPO-34[miHF] and GapO-34[pyHF].

material by the fitting of several different ^{71}Ga MAS and MQMAS NMR spectra obtained at both 20.0 and 14.1 T. The experimental ^{31}P and ^{71}Ga NMR parameters for both materials are summarised in Table 6.1.

Table 6.1. Experimental ^{31}P and ^{71}Ga NMR parameters for GaPO-34[miHF] and GaPO-34[pyHF].

species	δ_{iso} (ppm)	C_Q / MHz	η_Q
GaPO-34[miHF]			
P1	–20.0(1)		
P2	–12.0(1)		
P3	–0.8(1)		
Ga1	–29(1)	6.3(2)	0.30(5)
Ga2	111(3)	7.0(4)	0.9(1)
Ga3	121(1)	7.9(2)	0.35(5)
GaPO-34[pyHF][a]			
P1	–20.1(1)		
P2	–13.3(1)		
P3	–0.9(1)		
Ga1	–27(3)	4.4(4)	0.3(2)
Ga2	112(4)	5.5(6)	0.6(3)
Ga3	126(3)	6.1(9)	0.6(3)

a. Resonances for GaPO-34[pyHF] are assigned based on the similarity of their chemical shifts to those for GaPO-34[miHF] and do not correspond to any crystallographic nomenclature (as no crystallographic structure exists). The ^{71}Ga NMR parameters reported are average values, as significant disorder is present.

In order to assign the NMR spectra, DFT calculations were carried out using CASTEP 5.5.2.[2] These calculations were complicated by the presence of the disordered water molecule since, although the two positions for this molecule are equivalent, when the molecule is present in one of these locations and not the other (as would happen in a real unit cell, rather than the average crystallographic unit cell), the local symmetry is broken and there are six inequivalent Ga and P species present. The two H_2O locations are close (O-O separation of 1.261 Å in the published structure), but it was observed that, when the O atom of the water molecule was placed at the average of the two crystallographically-observed locations, the molecule moved towards one of the original positions upon optimisation, suggesting that these

positions are close to energy minima.[2] The water molecules may exhibit either static disorder (*i.e.*, occupying a random one of the two equivalent positions in each unit cell), or "hop" rapidly between the two sites. The nature of this disorder could be probed by, *e.g.*, variable-temperature ^{2}H NMR experiments on a deuterated sample. Hopping of the H_2O would be expected to yield time-averaged NMR parameters so that, while P1 and P1′ may have different calculated NMR parameters, only a single P1 resonance will be observed experimentally, at the average chemical shift of P1 and P1′. Calculations were carried out with the H_2O occupying either of the two locations and the average ^{31}P and ^{71}Ga NMR parameters for all four "equivalent" species (*e.g.*, P1 and P1′ with the H_2O in one position, and P1 and P1′ with the H_2O in the other position) are reported in Table 6.2. Prior to calculation of the NMR parameters, the structures were optimised to account for the fact that a specific unit cell was considered, rather than the average crystallographic unit cell. In the published work,[2] the structures were optimised by relaxing the unit cell and atomic coordinates without an SEDC scheme. The calculations were, therefore, repeated more recently using CASTEP 6, with relaxation of the unit cell and atomic coordinates, and with application of the G06 SEDC scheme. The average ^{31}P and ^{71}Ga NMR parameters obtained from these calculations are given in Table 6.2, with parameters for individual calculations given in Appendix N. It can be seen that similar agreement between the experimental and calculated ^{31}P δ_{iso} is achieved using both methods, although it appears that the choice of ^{71}Ga σ_{ref} for the CASTEP 6 calculations led to a systematic ~10 ppm upfield shift, relative to the CASTEP 5.5.2 calculations. Inclusion of the SEDC appears to have had an adverse effect on the agreement between calculated and experimental quadrupolar parameters, particularly for C_Q of Ga2 and Ga3 (the calculated C_Q for Ga2 had a range from –2.5 to +6.2 MHz, suggesting that this parameter is very sensitive to the precise locations of the water and miH^+ within the pore). It is clear that no single structural model can fully describe the local structure of GaPO-34[miHF], and even the averaged parameters in Table 6.2 do not provide particularly satisfactory agreement with experiment. Nevertheless, based on the relative order of the calculated δ_{iso}, both the ^{31}P and ^{71}Ga NMR spectra can be assigned, as reported in Table 6.1.[2] As both materials appear disordered, it was beneficial to confirm the extent of the broadening of the ^{71}Ga resonances using

Table 6.2. NMR parameters calculated for GaPO-34[miHF] using (a) CASTEP 5.5.2[2] (with no SEDC scheme) and (b) CASTEP 6 (including G06 SEDC scheme). The parameters reported are the average of the "equivalent" P and Ga species in the two considered models of GaPO-34[miHF] discussed in the text.

	δ_{iso} (ppm)		$\lvert C_Q \rvert^{\dagger}$ / MHz		η_Q	
species	a	b	a	b	a	b
P1	–18.0	–13.0				
P2	–8.9	–11.3				
P3	4.6	–0.7				
Ga1	–37.9	–52.6*	5.9	5.5	0.7	0.4
Ga2	111.5	100.6*	6.6	4.3	0.6	0.7
Ga3	122.6	113.6*	5.9	10.6	0.6	0.9

†. Owing to the range of positive and negative values of C_Q calculated for Ga2 using CASTEP 6 (discussed in the main text), the mean absolute value of C_Q, $|C_Q|$, is reported here.

high-field (20.0 T) ^{69}Ga MAS NMR spectra. These spectra, shown in Figure 6.3, were obtained using a spin-echo pulse sequence to minimise the significant distortion of the lineshapes observed otherwise (not shown). As the nuclear quadrupole moment of ^{69}Ga is ~1.6 times greater than that of ^{71}Ga,[8] the resonances are significantly more overlapped than for the ^{71}Ga NMR spectra, even at high field. However, it can be seen that ^{69}Ga MAS NMR spectra simulated using the parameters given for ^{71}Ga in Table 6.1 (with the C_Q scaled by a factor of 1.6, and excluding any explicit treatment of disorder) are in good agreement with the experimental ^{69}Ga MAS NMR spectra, increasing confidence in the values quoted, particularly for GaPO-34[miHF]. While the broadening of the resonance for GaPO-34[pyHF] means that some of the features of the simulated spectrum are not observed experimentally, the widths of the lines are similar, indicating that there is a small distribution of quadrupolar and chemical shift parameters.

In order to fully characterise the two as-prepared forms of GaPO-34, the ^{1}H, ^{13}C and ^{19}F NMR spectra of these materials were acquired ($^{14/15}$N NMR spectra were not acquired owing to the unfavourable NMR properties of both isotopes (at natural

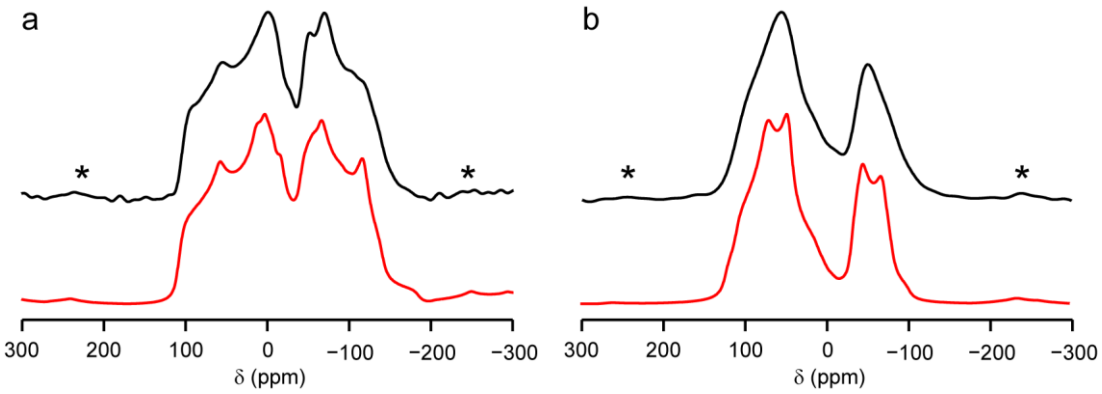

Figure 6.3. Experimental ^{69}Ga (20.0 T, 62.5 kHz MAS) NMR spectra (black) and ^{69}Ga NMR spectra simulated using the parameters given in Table 6.1 (red), for (a) GaPO-34[miHF] and (b) GaPO-34[pyHF]. Asterisks denote SSBs.

abundance) and the limited mass of samples available), and are shown in Figure 6.4. From the ^{1}H MAS NMR spectra, N**H** can clearly be identified at 12.3 ppm (GaPO-34[miHF]) and 14.4 ppm (GaPO-34[pyHF]). The remaining resonances can be

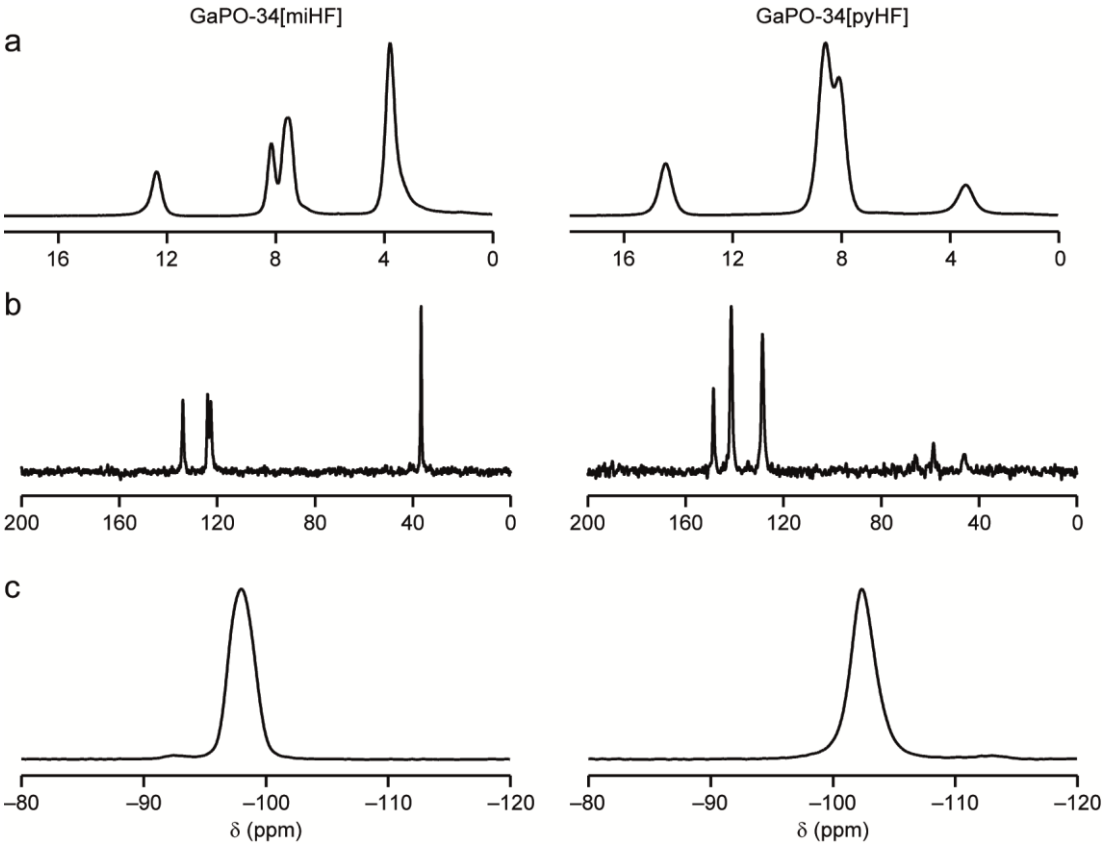

Figure 6.4. (a) ^{1}H (14.1 T, 60 kHz MAS) (b) ^{13}C (14.1 T, 12.5 kHz CP MAS) and (c) ^{19}F (14.1 T, 55 kHz MAS) NMR spectra of GaPO-34[miHF] and GaPO-34[pyHF].

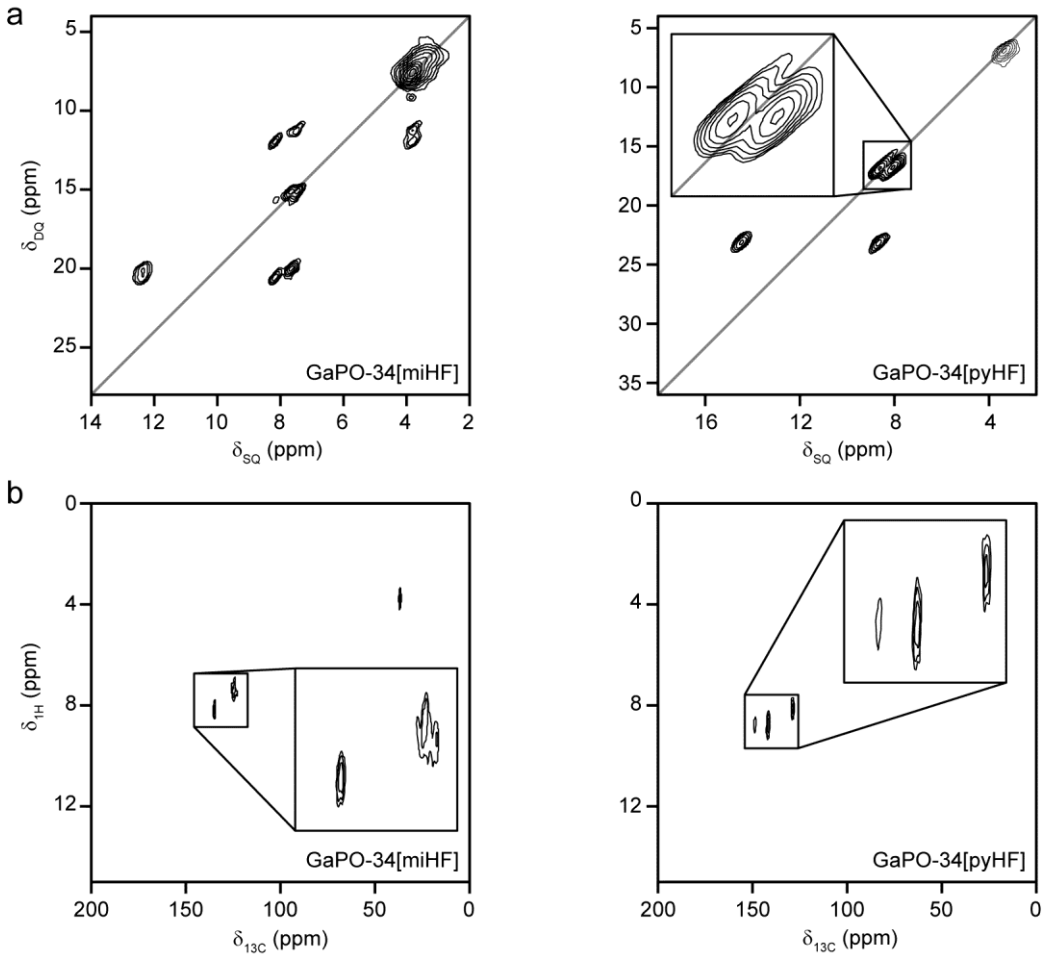

Figure 6.5. (a) ^{1}H (14.1 T, 60 kHz DQMAS) NMR spectra of GaPO-34[miHF] and GaPO-34[pyHF]. The $\delta_{DQ} = 2\delta_{SQ}$ diagonal is indicated in grey. (b) ^{1}H-^{13}C (14.1 T, 50 kHz MAS) CP HETCOR NMR spectra of GaPO-34[miHF] and GaPO-34[pyHF].

assigned using the ^{1}H DQMAS spectra shown in Figure 6.5(a). For GaPO-34[miHF],the protons with δ_{SQ} = 3.4 ppm are close in space, with an intense diagonal resonance at δ_{DQ} = 6.8 ppm. However, no DQCs are observed between these protons and any others in the material, as would be expected for H_2O, which typically undergoes rapid rotation, effectively "decoupling" any intermolecular dipolar interactions, whilst retaining the intramolecular dipolar interaction. The CH_3 resonance (H6, δ_{SQ} = 3.8 ppm) has an intense diagonal resonance, but also exhibits interactions with protons with δ_{SQ} of 7.4 and 8.2 ppm. From Scheme 6.1 H6 is spatially close to H2 and H5. The assignment of these resonances as H2 (δ_{SQ} = 8.2 ppm) and H5 (δ_{SQ} = 7.4 ppm), is confirmed by the DQC observed between H2 and

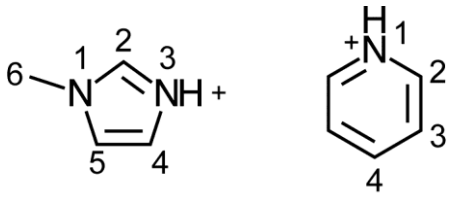

Scheme 6.1. Labeling scheme used for 1-methylimidazolium and pyridinium cations.

H3 (δ_{DQ} = 20.5 (= 8.2 + 12.3) ppm). Similarly, a DQC is observed between H5 and H4 (δ_{DQ} = 15.0 (= 7.4 + 7.7) ppm) and also between H4 and H3 (δ_{DQ} = 19.9 (= 7.7 + 12.3) ppm). In a similar manner, the DQCs observed for GaPO-34[pyHF] can be analysed. The resonance at δ_{SQ} = 3.3 ppm can identified as H_2O using the same arguments as above. The structure of pyH^+ (Scheme 6.1) contains three aromatic H species, but only two ^{1}H resonances are observed in the aromatic region of the ^{1}H MAS NMR spectrum shown in Figure 6.4(a). These resonances, at δ_{SQ} = 8.6 and 8.1 ppm have an intensity ratio of 3:2, suggesting that two of the aromatic H environments have overlapping chemical shifts. Possible assignments are, therefore, H2 and H4 with δ_{SQ} = 8.6 ppm, and H3 with δ_{SQ} = 8.1 ppm, or H3 and H4 with δ_{SQ} = 8.6 ppm and H2 with δ_{SQ} = 8.1 ppm. The presence of strong off-diagonal resonances and the absence of a diagonal resonance (Figure 6.5(a) expansion) suggest the former assignment, as an on-diagonal resonance would indicate the presence of two adjacent ^{1}H with the same isotropic shift. This is confirmed by the DQC occurring at δ_{DQ} = 23.1 (≈ 8.6 + 14.4) ppm, assigned to H2 + H1. Assignments of the ^{1}H resonances are summarised in Table 6.3.

The ^{13}C CP MAS NMR spectrum of GaPO-34[miHF] was assigned using the 2D CP HETCOR spectrum shown in Figure 6.5(b). Correlations are observed between H6 and C6 (36.7 ppm), H4 and C4 (122.7 ppm), H5 and C5 (124.0 ppm) and H2 and C2 (134.1 ppm). While the analogous spectrum of GaPO-34[pyHF] allows the identification of C3 (128.6 ppm), the correlations between H2 and C2, and H4 and C4 have the same ^{1}H shift and cannot be distinguished by this approach. However, by correlating the ^{13}C resonances with the ^{1}H DQCs, using the ^{1}H(DQ)-^{13}C CP HETCOR pulse sequence shown in Figure 6.6(a) to give the spectrum shown in Figure 6.6(b), assignment is possible. The ^{1}H DQC at δ_{DQ} = 23.1 ppm can be

Table 6.3. Experimental isotropic chemical shifts and assignments of ^{1}H, ^{13}C and ^{19}F resonances for GaPO-34[miHF] and GaPO-34[pyHF], using the numbering scheme of Scheme 6.1.

species	δ_{iso} (ppm)	species	δ_{iso} (ppm)	species	δ_{iso} (ppm)
GaPO-34[miHF]					
H2	8.2(1)	C2	134.1(1)	F	–98.4 (5)
H3	12.3(1)	C4	122.7(1)		
H4	7.7(2)	C5	124.0(1)		
H5	7.4(2)	C6	36.7(1)		
H6	3.8(1)				
H_2O	3.4(2)				
GaPO-34[pyHF]					
H1	14.4(1)	C2	141.5(1)	F	–102.0(5)
H2	8.6(1)	C3	128.6(1)		
H3	8.1(1)	C4	147.8(1)		
H4	8.6(1)				
H_2O	3.3(2)				

assigned to H1 + H2, and only C2 would be expected to correlate with this DQC (with the short recoupling time of two rotor periods (40 μs) of BABA pulses used). The ^{13}C resonance at 141.5 ppm can, therefore, be assigned to C2, with the remaining resonance, at 147.8 ppm, assigned to C4. This assignment is in agreement with the integrated intensities of the resonances in the ^{13}C CP MAS NMR spectrum in Figure 6.4(b), which are 2.2 : 2.4 : 1.0 for C2 : C3 : C4 (expected intensity ratio of 2 : 2 : 1). However, CP MAS cannot be relied upon to be quantitative, whereas the assignment achieved using the ^{1}H(DQ)-^{13}C CP HETCOR experiment is unambiguous. The assignments of the ^{13}C resonances are summarised in Table 6.3.

The ^{19}F MAS NMR spectra of both materials contain a single resonance in the shift range corresponding to bridging F in GaPOs (Figure 1.5). This is to be expected from the crystal structure of GaPO-34[miHF], which contains one bridging

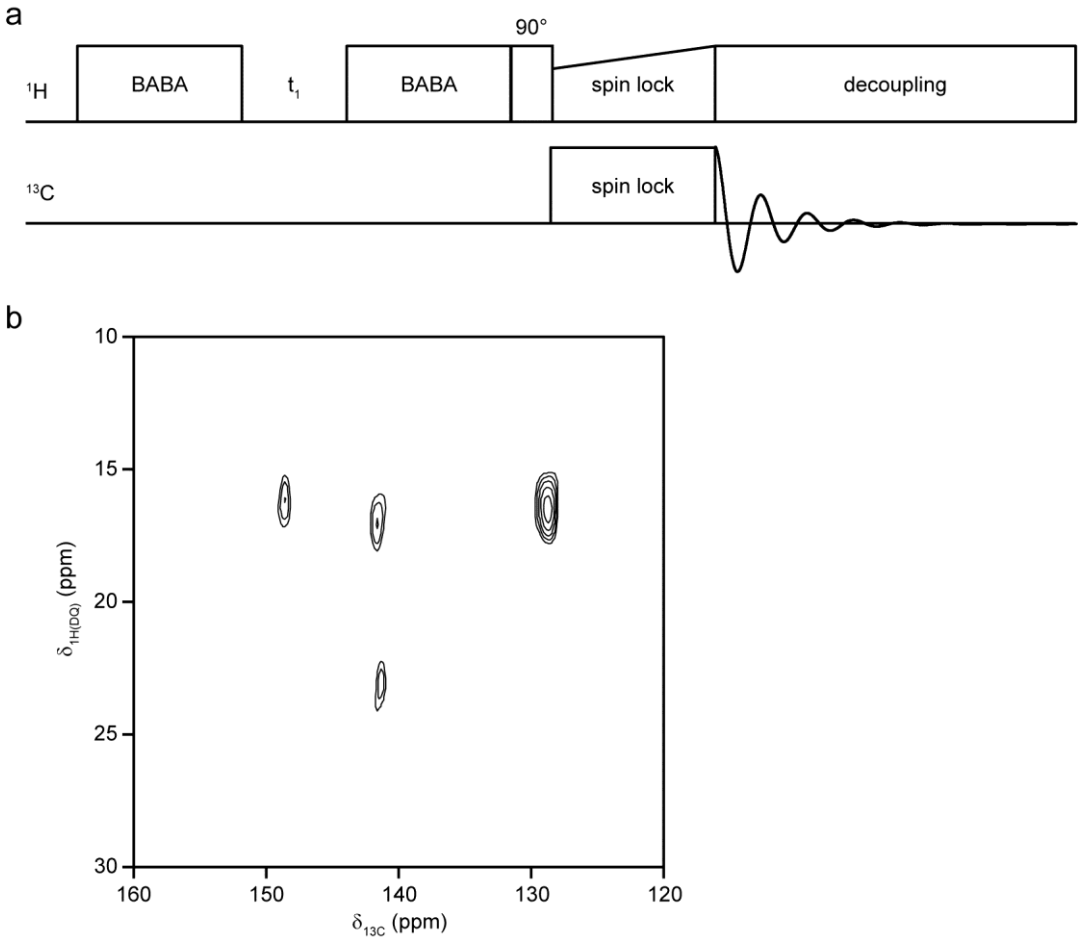

Figure 6.6 (a) The pulse sequence for the ^{1}H(DQ)-^{13}C CP HETCOR experiment. (b) ^{1}H(DQ)-^{13}C CP HETCOR NMR spectrum of GaPO-34[pyHF].

F species, and the similar result for GaPO-34[pyHF] confirms the similarity of their structures, although the chemical shift difference should be noted. The ^{19}F chemical shift is –98.4 ppm for GaPO-34[miHF] and –102.0 ppm for GaPO-34[pyHF]. It can be seen from Figure 1.5 that F contained within D4R units has a higher shift than that bridging between two Ga species, with F bound to a single Ga yielding the lowest chemical shifts. As the mean Ga-F bond length is typically longest in D4R units and shortest for terminal F, it has been proposed that the ^{19}F chemical shift increases with increasing Ga-F bond length,[9, 10] suggesting that the Ga-F bonds are shorter (and, hence, stronger) in GaPO-34[pyHF]. However, as discussed previously, chemical shifts in solids are rarely influenced by only one structural parameter, and further evidence would be required to evaluate this suggestion.

In conclusion, the ^{1}H, ^{13}C, ^{19}F, ^{31}P, ^{69}Ga and ^{71}Ga NMR spectra of GaPO-34[miHF] and GaPO-34[pyHF] have been recorded. The spectra have been assigned through a variety of two-dimensional NMR experiments and first-principles DFT calculations. It was demonstrated that NMR parameters calculated assuming that the water molecule present in GaPO-34[miHF] hops rapidly between the two positions located by Bragg diffraction show good agreement with the experimental data. However, further work would be required in order to confirm that disorder of the H_2O is dynamic rather than static. It would appear that there is greater disorder present in GaPO-34[pyHF], which may be responsible for the lack of published crystal structure, although $^{69/71}Ga$ NMR experiments indicate that this disorder gives rise to only a small distribution of NMR parameters. The nature of the disorder has not been explored in detail, but is likely to arise from static or dynamic disorder of the pyH^+ cations and H_2O molecules present within the pores of the material. Deuteration of both materials (*e.g.*, by synthesising the materials in a deuterated reaction medium or exchanging NH/H_2O protons for deuterons in a deuterated atmosphere) would allow for investigation of the motion of H_2O within the pores, using variable-temperature ^{2}H NMR experiments.

6.4.2 Phase Transformations Occurring on Heating

Thermogravimetric analysis (TGA) of GaPO-34[miHF] (Figure 6.7(a)) reveals three mass losses below 500 °C. Firstly, at 80-100 °C, ~1% mass is lost, corresponding to the loss of one molecule of H_2O per unit cell (where one unit cell has the formula $[Ga_3P_3O_{12}F{\cdot}C_4H_7N{\cdot}0.5(H_2O)]_2$). A second mass loss occurs between ~350 and 400 °C in the TGA trace, but the *in-situ* powder XRD patterns shown in Figure 6.7(b) indicate that the material undergoes a phase change at a slightly lower temperature, and the phase change is complete by 350 °C. The mass loss at this stage is ~4%, although the precise mass loss is hard to determine as, almost immediately following this mass loss, the third mass loss, of ~12% begins, and is complete by ~500 °C. The combined mass loss of ~16% is consistent with the loss of miHF (expected mass loss of 16.8%), yielding the calcined $GaPO_4$ framework, GaPO-34(calcined). The calcined material has been characterised in the literature, by solid-state NMR[2] and XRD.[1, 2, 11] The framework has the CHA topology and its rhombohedral symmetry

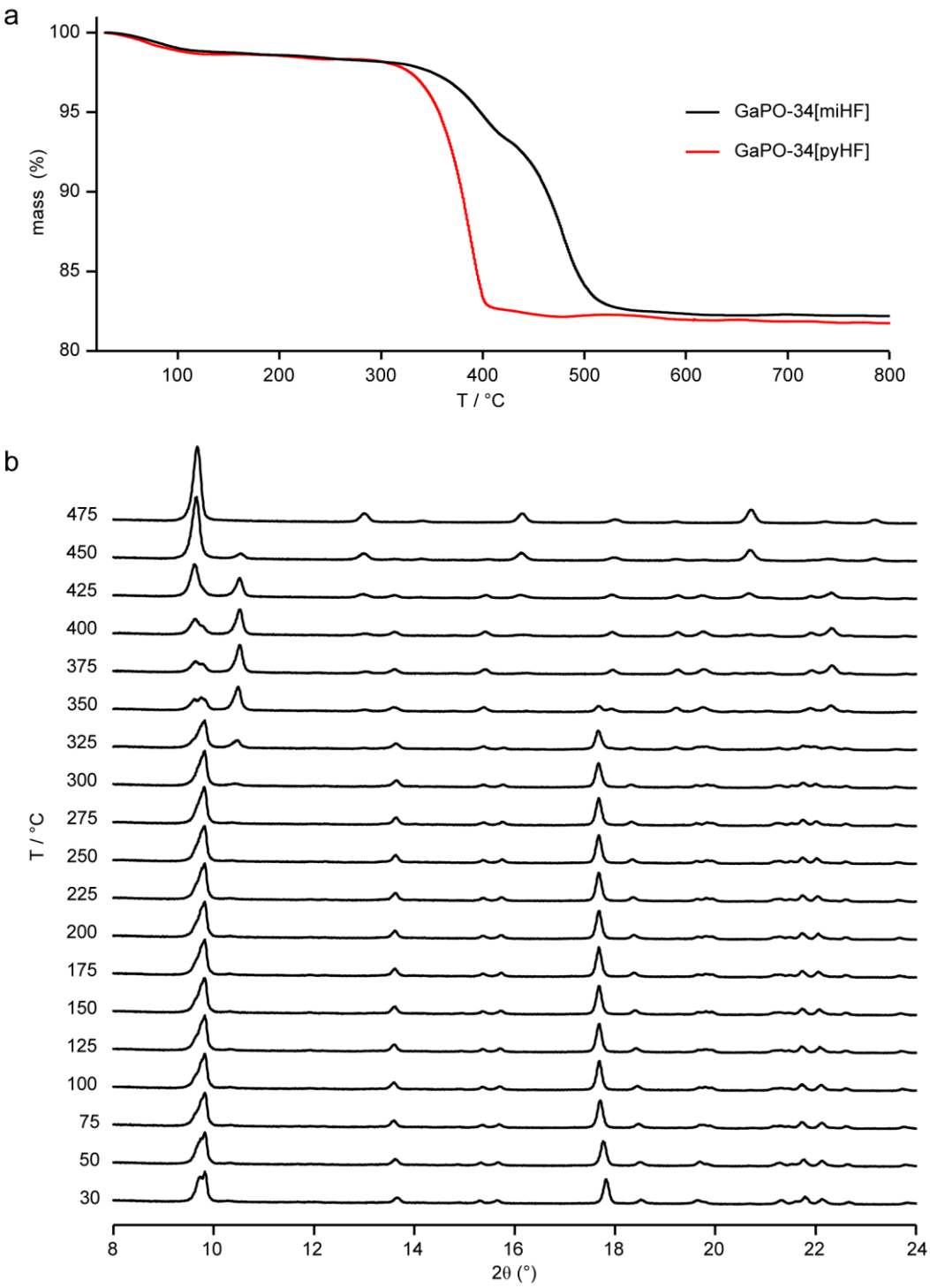

Figure 6.7. (a) TGA traces for GaPO-34[miHF] (black) and GaPO-34[pyHF] (red). (b) *In-situ* powder XRD patterns of GaPO-34[miHF] heated to the indicated temperature.

(space group $R\bar{3}$) gives rise to one crystallographically-distinct Ga(IV) species and one distinct P species. The ^{31}P and ^{71}Ga MAS NMR spectra of GaPO-34(calcined) are shown in Figure 6.8, and the NMR parameters calculated by CASTEP 5.5.2[2] are in good agreement with the experimental values, as summarised in Table 6.4. However, it is clear from Figure 6.7 that the calcination of GaPO-34[miHF] occurs in two stages, with a crystalline intermediate phase formed at ~350 °C. Schott-Darie *et al*. also observed a two-stage mass loss process and obtained a powder XRD pattern for the high-temperature intermediate, which was reported to form at 315 °C in that work.[1] However, no structural determination for this high-temperature intermediate phase was carried out, and there was no discussion of possible chemical and physical transformations that may have occurred to give rise to this material. The present study, therefore, sought to identify the high-temperature intermediate using a combination of solid-state NMR and DFT calculations.

In an attempt to prepare and characterise this intermediate phase, a sample of GaPO-34[miHF] was heated to 330 °C under air for 2 hours, and then packed into a vial while hot (~300 °C). No special precautions were taken to exclude air from the vial, but the lid was sealed with film until the sample was characterised by solid-state NMR. The ^{31}P MAS NMR spectrum of this sample (Figure 6.9) contained four sharp resonances at –12.2, –16.2, –19.3 and –22.9 ppm, with an integrated intensity ratio of 1 : 1 : 1 : 1. While this could be seen as evidence for a change in the symmetry of the material, it would also be reasonable to suggest that the resonance at –19.3 ppm corresponds to some GaPO-34(calcined) within the sample. This is to be expected, given that no accurate calibration of the furnace was carried out prior to preparation of this sample, and it is possible that the temperature was higher than assumed. There is no evidence in the spectrum of any remaining GaPO-34[miHF] (*i.e.*, resonances at –0.8, –12.0 and –20.0 ppm). The assignment of the resonance at –19.3 ppm to GaPO-34(calcined) is supported by the fact that this resonance disappears upon exposure of the sample to air during packing and unpacking of the rotor, as shown in Figure 6.9(b). This is consistent with the formation of GaPO-34(calcined, hydrated), which will be discussed in the following section. The other three resonances, however, remain sharp and have an approximately 1 : 1 : 1 integrated intensity ratio (although accurate integration is complicated by the overlap of resonances from this phase and

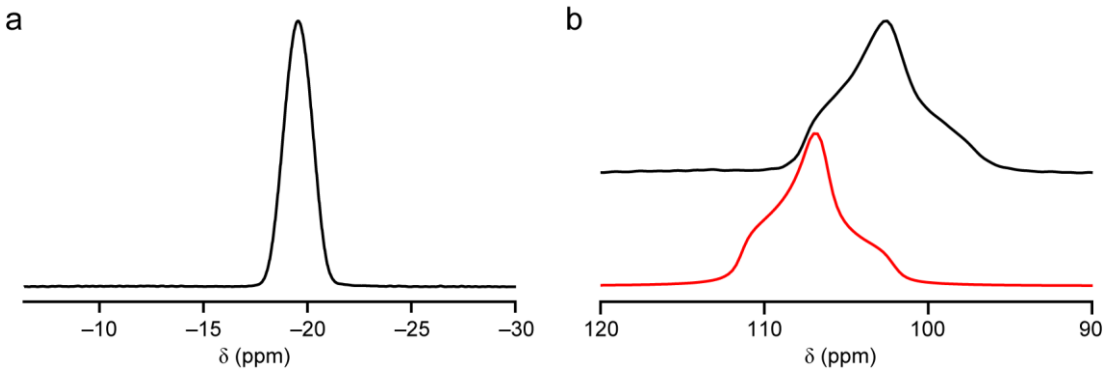

Figure 6.8. (a) ^{31}P (14.1 T, 25 kHz MAS) and (b) ^{71}Ga (20.0 T, 30 kHz MAS) NMR spectra of GaPO-34(calcined). In part (b) a spectrum simulated using the calculated parameters given in Table 6.4 is shown in red.

the calcined, hydrated material). This suggests a relatively small structural modification of the GaPO-34[miHF] to obtain the observed intermediate phase.

The high-field ^{71}Ga MAS NMR spectrum (Figure 6.10) of the sample (after exposure to ambient moisture) reveals a sharp resonance corresponding to Ga(IV) and a broad, lower-intensity resonance between 45 and –75 ppm. While some of the low-intensity resonance can be attributed to Ga(V) and Ga(VI) in GaPO-34(calcined, hydrated) (see Section 6.4.3), it appears that there is also some Ga(V/VI) in the intermediate phase. The resonance corresponding to Ga(IV) cannot be described well with a single resonance broadened by the second-order quadrupolar interaction, but this is unsurprising as there are three distinct P species observed by ^{31}P NMR, so one would also expect three distinct Ga species. It is also clear from the asymmetric

Table 6.4. Experimental (exp.) and calculated (calc.) NMR parameters for GaPO-34(calcined). Calculations were carried out using CASTEP 5.5.2.[2]

Species	δ_{iso} (ppm)		C_Q / MHz		η_Q	
	exp.	calc.	exp.	calc.	exp.	calc.
P	–19.5(2)	–20.3				
Ga	107.5(5)	114.3	3.20(5)	3.01	0.80(5)	0.89

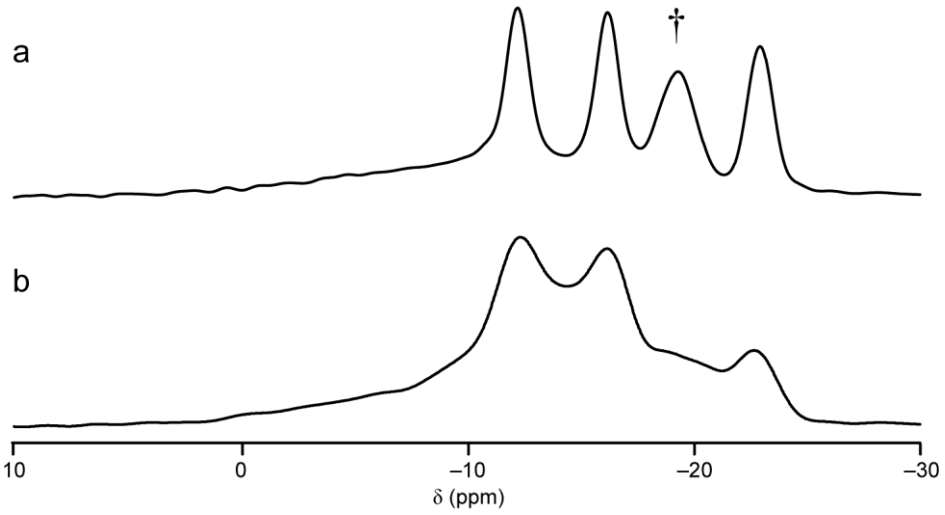

Figure 6.9. ^{31}P NMR spectra of (a) GaPO-34[miHF] after heating to 330 °C (14.1 T, 25 kHz MAS) and (b) the same sample after exposure to ambient moisture (9.4 T, 10 kHz MAS). In (a), the resonance assigned to GaPO-34(calcined) is marked †.

broadening of the lineshape that there is some disorder present, which will further complicate spectral analysis. The integrated intensity ratio of the Ga(IV) : Ga(V/VI) is approximately 2 : 1, the same as for the as-prepared GaPO, further supporting a relatively small structural modification of GaPO-34[miHF] to give this intermediate. The position of the Ga(V/VI) resonance suggests that the species present is five-coordinate, as the isotropic chemical shift range for such species is approximately 10 to 55 ppm.[12, 13] Attempts to obtain the NMR parameters for this resonance and to separate the two expected Ga(IV) species in order to obtain NMR parameters for

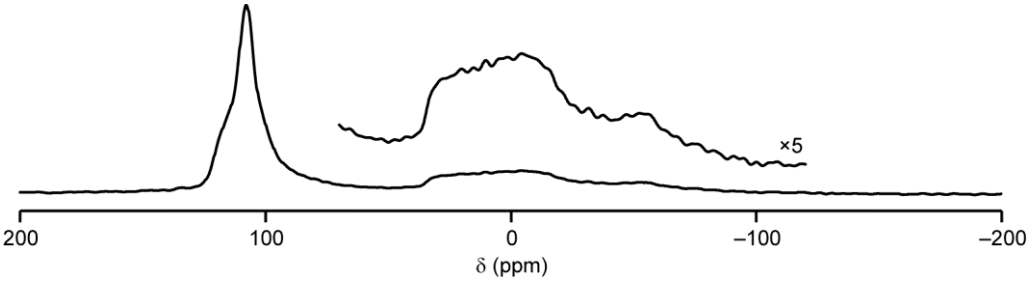

Figure 6.10. ^{71}Ga (20.0 T, 60 kHz MAS) NMR spectrum of GaPO-34[miHF] after heating to 330 °C, followed by exposure of the sample to ambient moisture. The inset shows vertical expansion of the Ga(V/VI) region (from 70 to –120 ppm).

them using a 3QMAS NMR experiment at 20.0 T were unsuccessful. It is believed that, owing to the combination of relatively rapid MAS and the correspondingly small sample volume, the experiment was simply too insensitive to allow observation of resonances for this sample in the limited time available at the national high-field facility. However, the presence of Ga(V) rather than Ga(VI) indicates that the Ga-F bonds must have changed (rather than the Ga-O bonds, which are still present in the fully-calcined material). Further evidence that the Ga-F bonds have been broken comes from the ^{19}F NMR spectrum of the material, shown in Figure 6.11. The spectrum was recorded with signal averaging for 128 transients (*cf.* 64 transients for Figure 6.4(c)) and contains only background signal and a low-intensity resonance at –122.7 ppm, corresponding to traces of the PTFE reference sample in the caps of the rotor. This suggests that the first step of the calcination is dehydrofluorination (calculated mass loss of 3.3%, *cf.* ~4% observed experimentally). This is surprising, as such a process has only been reported once before in the literature, by Oliver *et al.*, for AlPO-34[pyHF] (also known as UT6).[14] Some caution should be taken when interpreting the results of Oliver *et al.*, however, as there is a clear discrepancy between the published formula for the material, $Al_3P_3O_{12}$·pyHF·0.15H_2O (0.6 % by mass H_2O) and the 6% mass loss assigned to H_2O. This discrepancy in the water content of the material will clearly have a significant impact on the calculated and experimental mass losses (expressed in %), and drawing a reliable conclusion about the occurrence of a low-temperature dehydrofluorination in AlPO-34[pyHF] is not possible. In addition to the limited literature reports of dehydrofluorination of phosphate frameworks, "chemical intuition" suggests that the organic component of the material will be more susceptible to heat-induced degradation than the inorganic component. However, as shown by the ^{1}H MAS NMR spectrum of the sample (Figure 6.12(a)), the H3 resonance is absent, while the rest of the SDA appears intact (*cf.* Figure 6.4). An attempt to assign the remaining resonances by a ^{1}H DQMAS NMR experiment (Figure 6.12(b)), was unsuccessful, owing to the low resolution of the spectrum, indicative of disorder within the material. It should also be noted that two resonances may correspond to H_2O in the sample. One of these ($\delta_{SQ} \approx 6.1$ ppm) corresponds to H_2O in the calcined, hydrated phase (see Section 6.4.3), whereas the other ($\delta_{SQ} \approx 4.1$ ppm) might arise from hydration of the dehydrofluorinated phase.

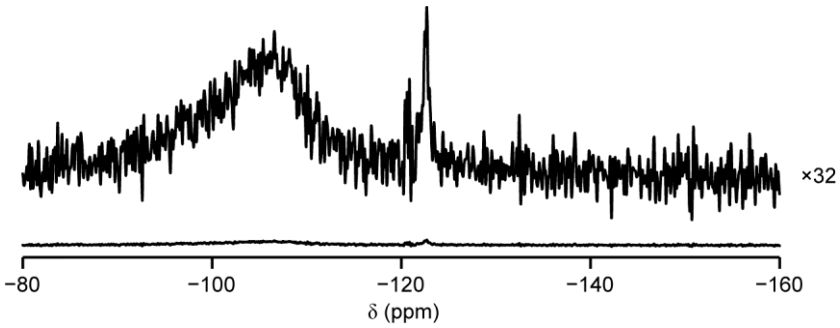

Figure 6.11. ^{19}F (14.1 T, 50 kHz MAS) NMR spectrum of GaPO-34[mi].

The presence of this H_2O would explain the observation of Ga(V), despite the absence of F^- within the material. The ^{13}C CP MAS NMR spectrum of the material, shown in Figure 6.12(c), confirms that 1-methylimidazole is intact but deprotonated, as four well-defined resonances are observed at 139.2, 128.8, 124.5 and 34.8 ppm – similar to the positions of the resonances observed for GaPO-34[miHF], with the differences (of 0.5 to 6.1 ppm) likely to arise predominantly from deprotonation of the SDA. DFT calculations carried out at the B3LYP/6-311+G(d,p) theory level for a single mi or miH^+ species in the gas phase (using GAUSSIAN09) yield approximate ^{13}C δ_{iso} (neglecting any effects of the surrounding framework in the real materials). These shifts (referenced using the four ^{13}C chemical shifts of GaPO-34[miHF]) are

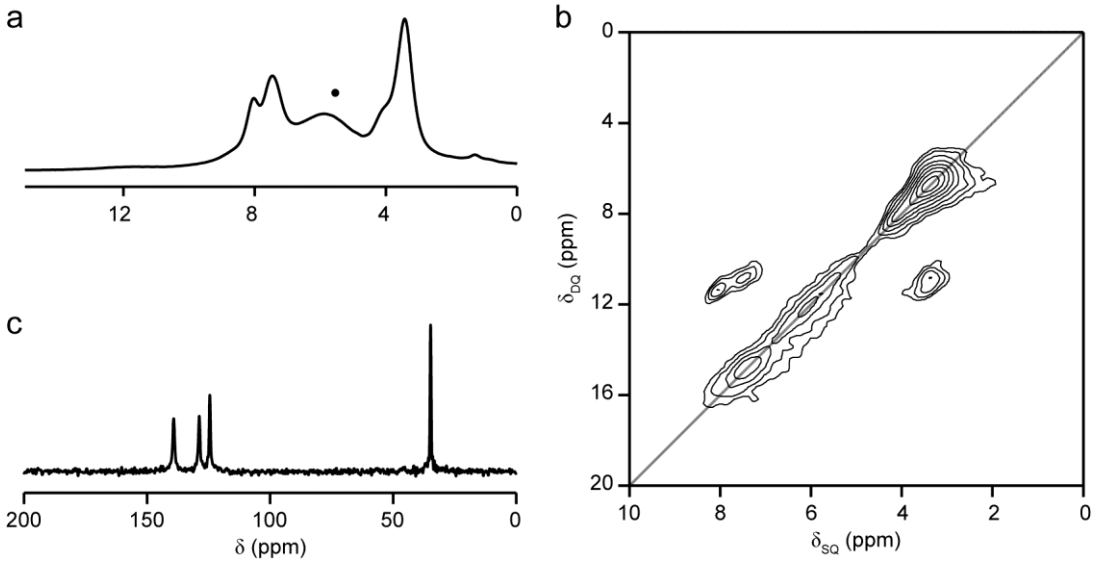

Figure 6.12. (a) ^{1}H (14.1 T, 60 kHz MAS), (b) ^{1}H (14.1 T, 60 kHz DQMAS) and (c) ^{13}C (14.1 T, 12.5 kHz CP MAS) NMR spectra of GaPO-34[mi]. In (b) the $\delta_{DQ} = 2\delta_{SQ}$ diagonal is indicated in grey.

summarised in Table 6.5 and, while the absolute values of the shifts are in relatively poor agreement with experiment, a tentative assignment can be made based on the relative ordering of the shifts.

Given that solid-state NMR and TGA indicate that the high-temperature intermediate is GaPO-34[mi] ($Ga_6P_6O_{24}$·2mi), it was possible to generate an initial structural model for this material simply by removing the H_2O and 2HF from the crystal structure of GaPO-34[miHF]. However, the coordination environment of Ga1 (formerly Ga(VI), with two Ga-F-Ga bridges) is highly distorted, as shown in Figure 6.13. Indeed, the structure was so distorted that attempts to calculate its electronic structure prior to structural optimisation using CASTEP were unsuccessful unless the material was treated as metallic, with the electronic structure including eight additional (unoccupied) bands.[15] After 200 iterations of optimisation using this approach, the structure looked "reasonable" on visual inspection and optimisation was carried out for a further 200 iterations with the material treated as an insulator (as for all other structural optimisations in this thesis). However, no significant structural changes were observed during these iterations, so the optimisation was not continued to completion. The largest atomic force in the final structure was 0.19 eV $Å^{-1}$ (for one of the P3 atoms), with average forces of 0.04 eV $Å^{-1}$ (H), 0.10 eV $Å^{-1}$ (C), 0.11 eV $Å^{-1}$ (N), 0.06 eV $Å^{-1}$ (O), 0.10 eV $Å^{-1}$ (P) and 0.04 eV $Å^{-1}$ (Ga), indicating that the structure was close to an energy minimum and only small changes would result upon full optimisation. The final structure is shown in Figure 6.14(a), and the cif files for the starting and two partially-optimised structures are provided in the electronic information accompanying this thesis. The simulated powder XRD pattern for this structure does not agree well with the experimental pattern obtained from *in-situ* diffraction experiments, as shown in Figure 6.14(b). This may arise from the fact that the very high atomic forces in the starting structure could have led CASTEP to locate merely a local minimum, rather than the global minimum. In addition, the NMR parameters calculated for this structure, summarised in Table 6.6, do not agree well with experiment, but this may be expected since, as evidenced by the ^{1}H DQMAS NMR spectrum (Figure 6.12), there is some H_2O present within the material at room temperature, which was not included in the structural model considered here.

Table 6.5. ^{13}C isotropic chemical shifts obtained from calculations carried out for gas-phase molecules of mi and miH^+ (calc), and from experimental ^{13}C CP MAS NMR spectra of GaPO-34[mi] and GaPO-34[miHF] (exp).

Species	δ_{iso}^{calc} (ppm)	δ_{iso}^{exp} (ppm)
miH^+		
C2	131.4	134.1
C4	121.9	122.7
C5	125.1	124.0
C6	34.2	36.7
mi		
C2	135.5	139.2
C4	131.6	128.8
C5	117.2	124.5
C6	28.5	34.8

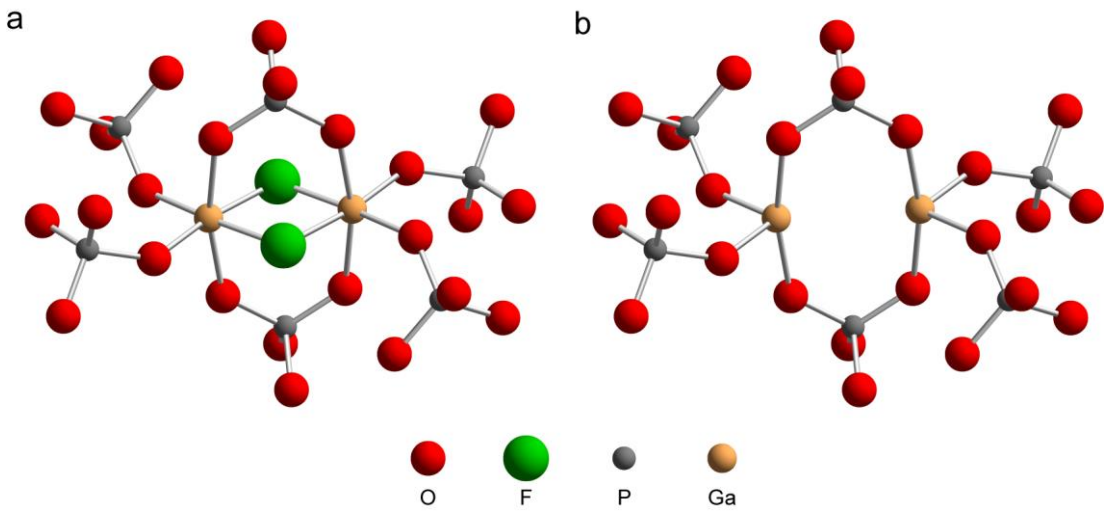

Figure 6.13. The local environment of Ga1 (a) before and (b) after removal of the fluoride. The structure is taken from the published structure of GaPO-34[miHF].

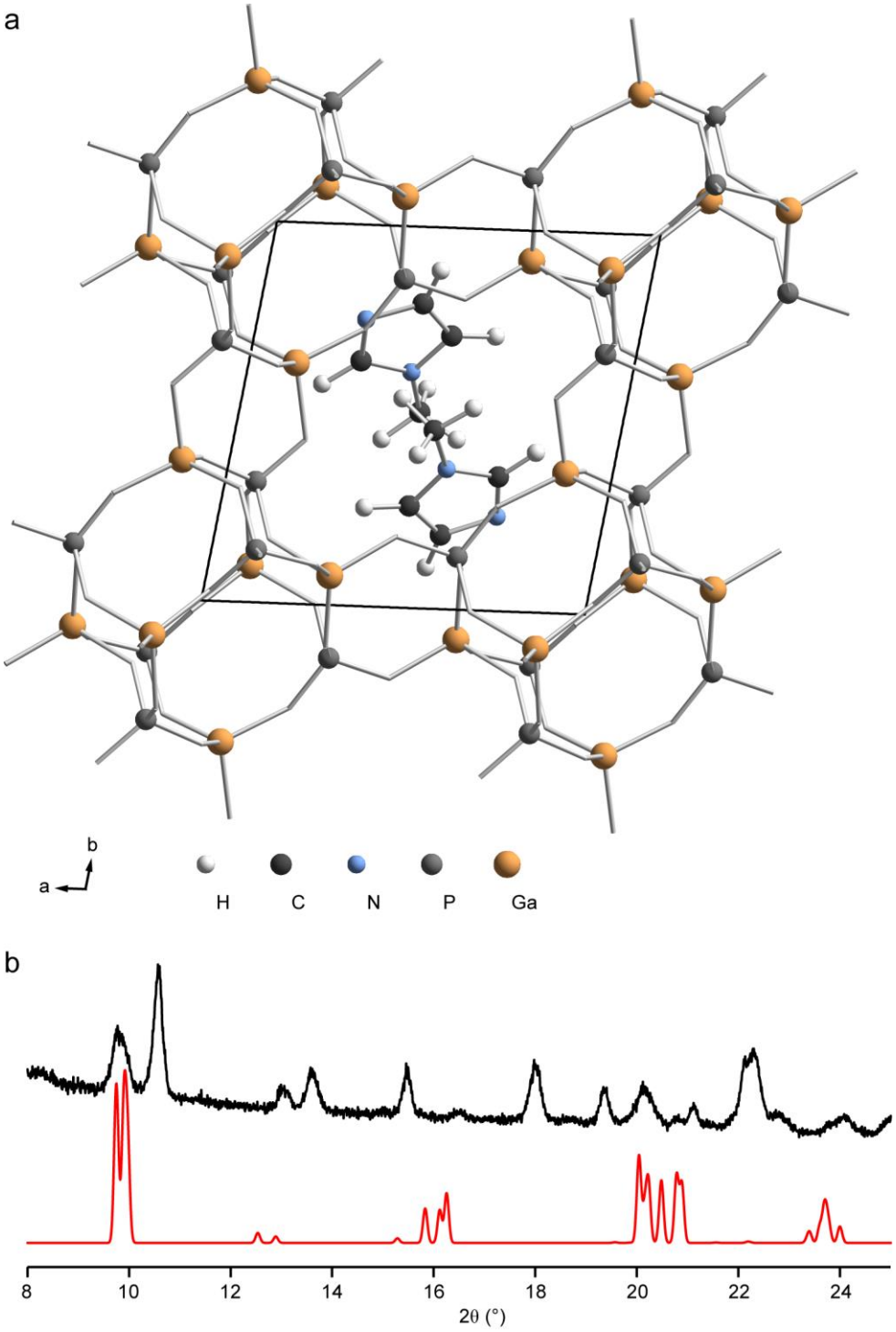

Figure 6.14. (a) The optimised structure of GaPO-34[mi], derived from the optimised structure of GaPO-34[miHF] as described in the text. (b) The simulated XRD pattern for the structure in part (a) (red) and the experimental *in-situ* XRD pattern of GaPO-34[mi] (black).

Table 6.6. Calculated (CASTEP 6) ^{31}P and ^{71}Ga NMR parameters for the partially-optimised (400 iterations, as described in the text) structural model of GaPO-34[mi].

Species	δ_{iso} (ppm)	C_Q / MHz	η_Q
P1	–3.7		
P2	–13.9		
P3	–21.0		
Ga1	73.4	7.0	0.97
Ga2	99.8	3.2	0.81
Ga3	106.0	13.4	0.88

The number of H_2O molecules per unit cell of GaPO-34[mi] has not yet been determined by, *e.g.*, TGA. However, integration of the ^{1}H MAS NMR spectrum (Figure 6.12) yields an approximate ratio of 1 : 3 for **H**$_2$O : C**H**$_3$, although the significant overlap of the resonances in this spectrum means that this ratio must be treated with caution. The integrated intensities of the ^{71}Ga resonances suggest that one in every three Ga is five-coordinate (*i.e.*, bound to H_2O). However, the intensity of the ^{71}Ga resonances will depend on the quadrupolar nutation rates, which are unlikely to be similar for Ga(IV) and Ga(V), possibly leading to a non-quantitative spectrum. Assuming a Ga(IV) : Ga(V) ratio of 2 : 1, this may be obtained by including a single bridging H_2O per unit cell (**H**$_2$O : C**H**$_3$ ratio of 1 : 3), or two "terminal" H_2O per unit cell (**H**$_2$O : C**H**$_3$ ratio of 2 : 3). Macfarlane investigated several structural models of GaPO-34[mi] containing different numbers and arrangements of H_2O molecules, but was unable to obtain good agreement with experimental NMR parameters for any of the models investigated.[15] As was discussed for AlPO-53(A) in Chapter 5, the AIRSS approach[16] may allow the automated searching of a much wider range of potential structures could be generated for GaPO-34[mi], without relying on "chemical intuition" to suggest locations for H_2O and mi. The use of AIRSS to investigate the structure of GaPO-34[mi] will, therefore, be carried out in the future.

Given the evidence of the solid-state NMR experiments, it seems clear that the high-temperature intermediate phase corresponds to the dehydrofluorinated

GaPO-34[mi], even if a detailed picture of the structure of the material remains elusive. It seems plausible that, having removed the HF, both the framework and guest species will be neutrally charged and, therefore, rather than heating the material further to achieve calcination, a low-temperature "solvent exchange" route, as shown schematically in Figure 6.15, could be a potential route to removing the mi from the pores of the GaPO. While this is not particularly useful for GaPO-34, which has a reasonable thermal stability, such a low-temperature SDA removal process may be of benefit in the preparation of active forms of less thermally-stable GaPO frameworks that could not be prepared by direct calcination. However, this scheme may not be particularly generally applicable, as the TGA trace for GaPO-34[pyHF], shown in Figure 6.7(a), indicates that a dehydrofluorinated intermediate does not exist over an appreciable temperature range and loss of pyHF occurs in a single step, yielding GaPO-34(calcined) (in contrast to the multi-step calcination process reported by Oliver *et al*. for the analogous AlPO-34[pyHF][14]). The reason for this difference may be explained by the different Ga-F bond strengths, observed by ^{19}F NMR spectroscopy, as discussed above. As GaPO-34[pyHF] has stronger Ga-F bonds then GaPO-34[miHF], release of HF will occur at higher temperature, which coincides with combustion of the pyridine SDA. Further investigation is, therefore, required in order to determine whether low-temperature dehydrofluorination is, indeed, a more general phenomenon that could be extended to other GaPO frameworks of potential interest by, *e.g.*, using an alternative SDA.

6.4.3 GaPO-34(calcined, hydrated) and GaPO-34(collapsed)

Water is rapidly adsorbed by GaPO-34(calcined) exposed to ambient conditions. The ^{31}P MAS NMR spectrum of the resulting GaPO-34(calcined, hydrated) is shown in Figure 6.16(a). The spectrum contains a broad resonance between 0 and –20 ppm, described by a single Gaussian-type lineshape centred at –10.7 ppm. In addition, seven sharper resonances are observed, at –10.8, –11.7, –12.8, –13.7, –16.8, –17.4 and –20.1 ppm. The widths of the sharp resonances (80 to 260 Hz, *cf*. 110 to 220 Hz in GaPO-34[miHF]) suggest an ordered material, whereas the broader resonance is indicative of a continuous distribution of chemical shifts, arising from a less ordered or amorphous phase. It is, therefore, possible that part of the material (~37% by ^{31}P integrated intensities) became amorphous upon calcination or hydration. However, as

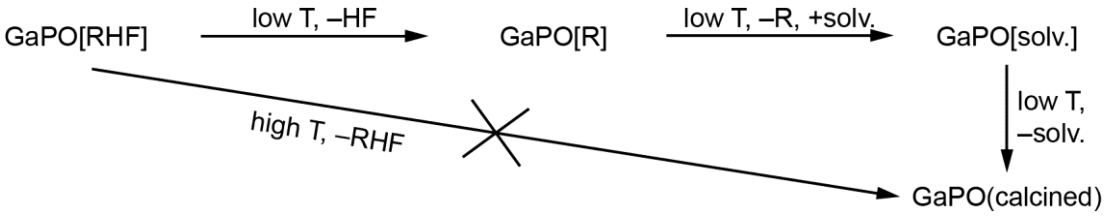

Figure 6.15. Scheme for a possible low-temperature calcination process, in which a GaPO containing F^- and the SDA, RH^+, is heated gently to remove HF, cooled to room temperature and stirred with a low-boiling-point solvent (solv.) to wash out R molecules, and then gently heated to remove solvent, yielding the calcined GaPO.

shown in Figure 6.16(b) both this broader resonance and the sharper resonances display similar ^{1}H-^{31}P CP build-up behaviour, indicating that all observed P species are similarly close to H_2O in GaPO-34(calcined, hydrated).

The ^{71}Ga MAS NMR spectrum of GaPO-34(calcined, hydrated) contains three resonances, assigned to Ga(IV), Ga(V) and Ga(VI) as indicated in Figure 6.17. However, the Gaussian/Lorentzian nature of the three resonances (as opposed to characteristic second-order quadrupolar broadening) is indicative of several distinct

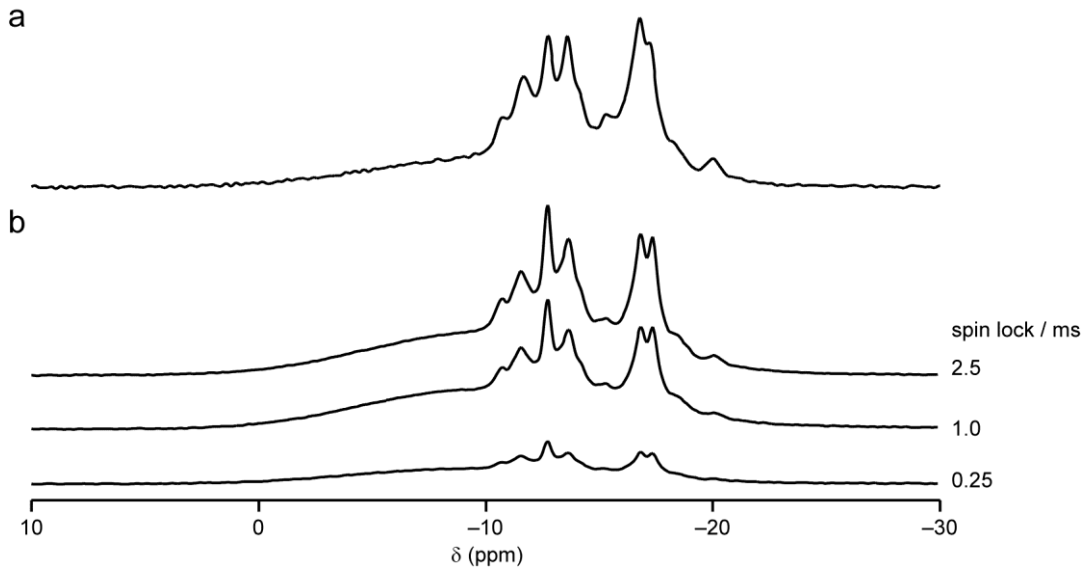

Figure 6.16. ^{31}P (a) 14.1 T, 25 kHz MAS and (b) 14.1 T, 12.5 kHz CP MAS NMR spectra of GaPO-34(calcined, hydrated). In part (b), the spin lock durations used were as indicated and the same vertical scale is used for all three spectra.

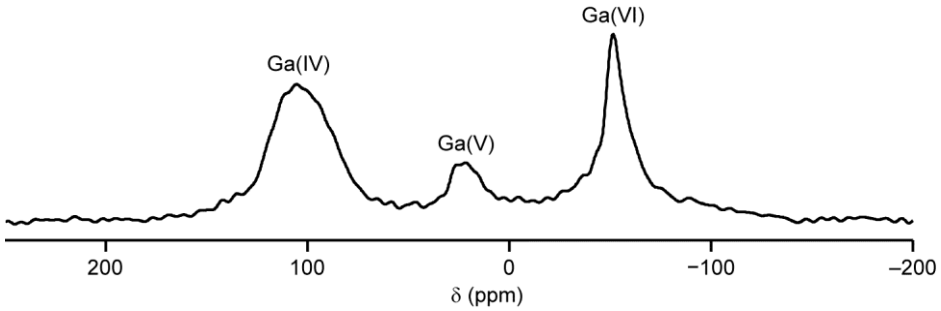

Figure 6.17. ^{71}Ga (20.1 T, 62.5 kHz MAS) NMR spectrum of GaPO-34(calcined, hydrated).

Ga species contributing to each resonance, and a small distribution of Ga NMR parameters for each species. Integration of the three resonances yields a ratio of approximately 2 : 1 : 2 for Ga(IV) : Ga(V) : Ga(VI). While high-field (20.0 T) high-resolution 3QMAS experiments were attempted in order to resolve distinct Ga species, the inherent inefficiency of the MQMAS experiment, particularly in the fast (60 kHz) MAS regime required in order to provide suitable separation of isotropic resonances and SSBs, meant that no useful data could be recorded in the limited experimental time available at the national facility.

The ^{1}H MAS NMR spectrum of GaPO-34(calcined, hydrated) is shown in Figure 6.18, and contains a single resonance at ~5.5 ppm. However the breadth of this resonances (FWHH = 1 kHz, 1.7 ppm) could be indicative of some disorder, or the presence of several distinct types of H_2O in the structure of GaPO-34(calcined, hydrated).

In order to learn more about the structure of GaPO-34(calcined, hydrated), it is informative to consider the case of the analogous AlPO, AlPO-34. A sample of calcined SIZ-4 (which has the same framework as AlPO-34, but is prepared ionothermally[17, 18]) was hydrated under ambient conditions, and ^{31}P and ^{27}Al NMR spectra were recorded every day for a week, and then at the end of the following week, as shown in Figure 6.19. Initially, the material exhibits a single ^{31}P resonance, at –30.1 ppm, and a single ^{27}Al resonance (δ_{iso} = 39.6 ppm, C_Q = 3.0 MHz, η_Q = 0.9), consistent with the single unique Al and P species present in the crystal structure. As with GaPO-34(calcined), the material rapidly hydrates and hydration is essentially

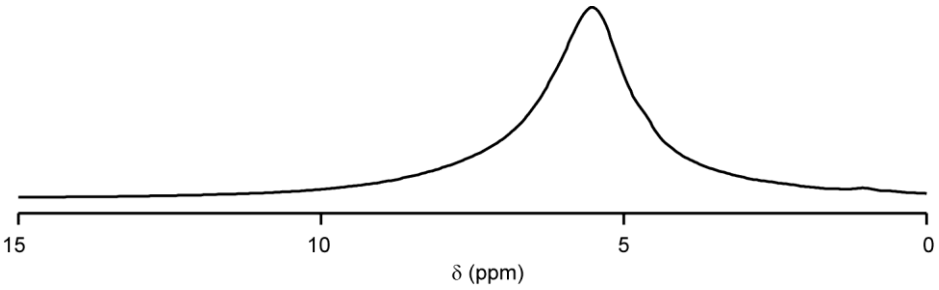

Figure 6.18. ^{1}H (14.1 T, 60 kHz MAS) NMR spectrum of GaPO-34(calcined, hydrated).

complete within one day. The ^{27}Al NMR spectrum exhibits resonances for Al(IV), Al(V) and Al(VI). This material has been characterised extensively by Tuel *et al.*,[19] Poulet *et al.*[20] and Seymour *et al.*,[21] and the ^{27}Al 3QMAS NMR spectrum[21] reveals three Al(IV) species, one Al(V) species, and two Al(VI) species in the fully-hydrated "phase B" of the material. (*i.e.*, giving rise to a 3 : 1 : 2 ratio of Al(IV) : Al(V) : Al(VI) in this phase). However, at temperatures just above room temperature, phase B, which contains 12 molecules of H_2O per unit cell, converts to phase A, with the loss of a single molecule of H_2O per unit cell.[19, 20] Phase A has not been well characterised, but it seems likely that the small variations between the ^{27}Al and ^{31}P NMR spectra from day to day can be explained by the presence of an equilibrium between the two low-temperature hydrated phases (the temperature of the room was maintained at 19.0(2) °C, but the humidity varied significantly as mentioned in Chapter 5). Indeed, closer inspection of the ^{31}P MAS NMR spectra of two different samples of GaPO-34(calcined, hydrated), shown in Figure 6.20, reveal small changes in the positions and intensities of resonances, possibly indicating the existence of either more than one hydrated phase of GaPO-34, or some variation in the degree of hydration of the material.

The powder XRD pattern of GaPO-34(calcined, hydrated) is shown in Figure 6.21, along with that simulated for the structure of phase B of hydrated AlPO-34.[20] It can be seen that the two patterns bear significant similarities, but the small amount of sample used for the XRD experiment meant that the quality of data is insufficient to attempt structural refinement. While the structure published by Poulet *et al.*[20] could be used as a starting point in determining the positions of H_2O molecules within

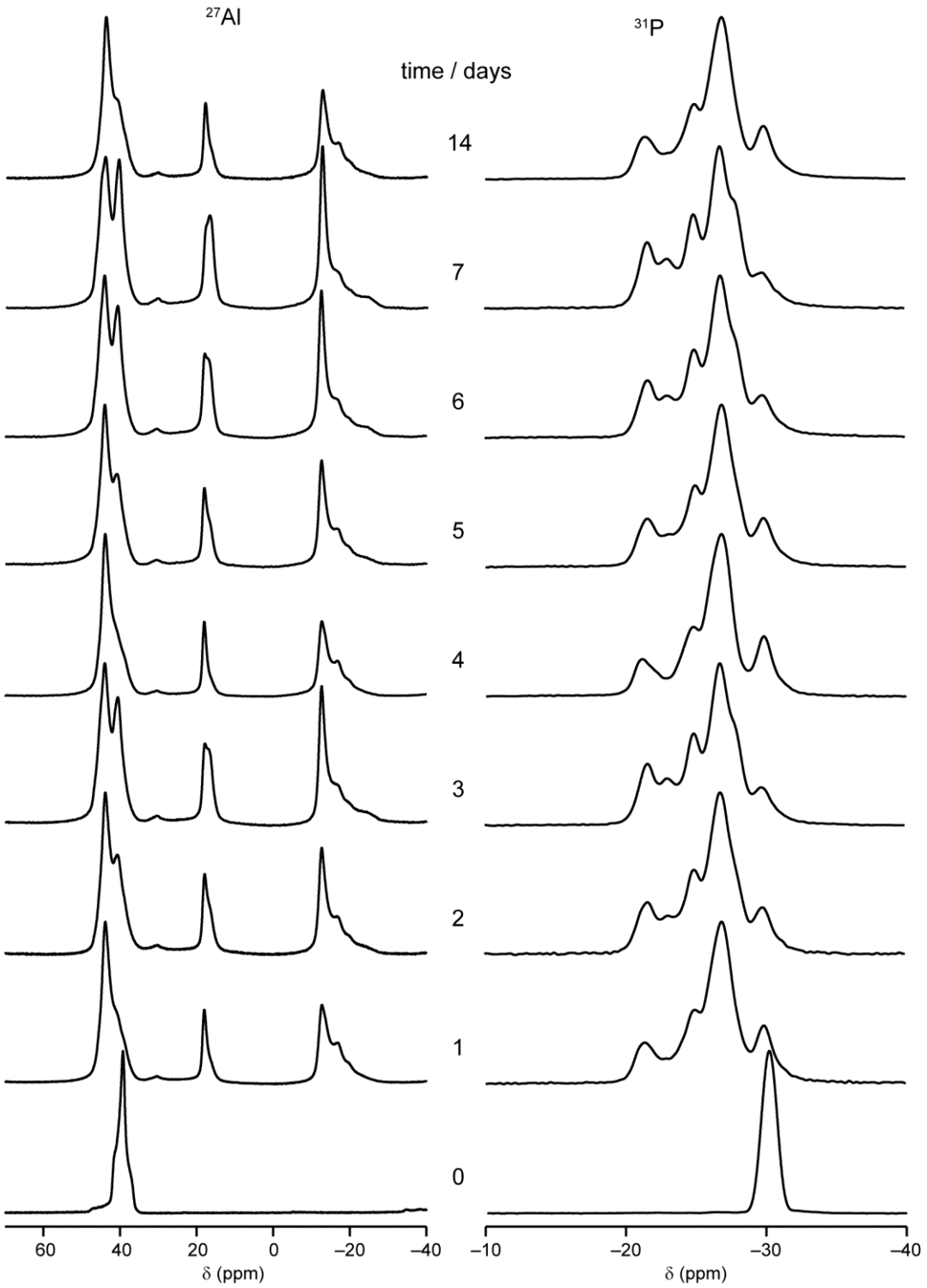

Figure 6.19. ^{31}P and ^{27}Al (14.1 T, 14 kHz MAS) NMR spectra of calcined AlPO-34 exposed to ambient conditions for the indicated time.

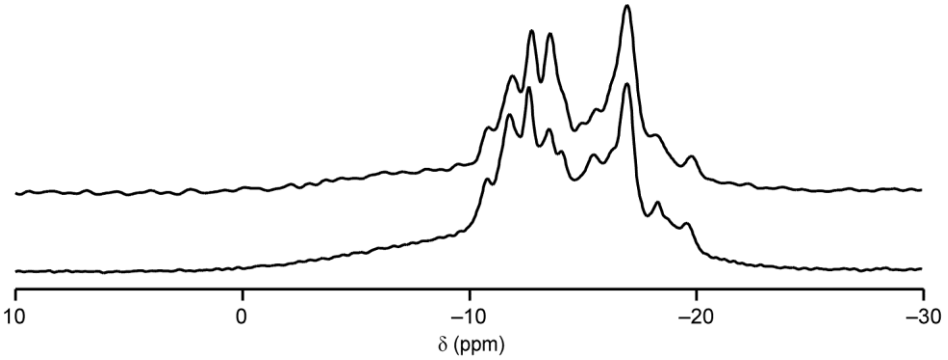

Figure 6.20. ^{31}P (20.0 T, 30 kHz MAS) NMR spectra of two different samples of GaPO-34(calcined, hydrated).

GaPO-34(calcined, hydrated), the above evidence suggests that there may actually be more than one form of hydrated GaPO-34 (similar to AlPO-34). Furthermore, the fact that the published unit cell for the AlPO contains only 6 P species means that it would be impossible, without using a supercell, to obtain the number of observed distinct ^{31}P chemical shifts (~12). Therefore, the possibility of investigating this material by DFT optimisation of a starting model based on the published structure of the AlPO will not be considered further here.

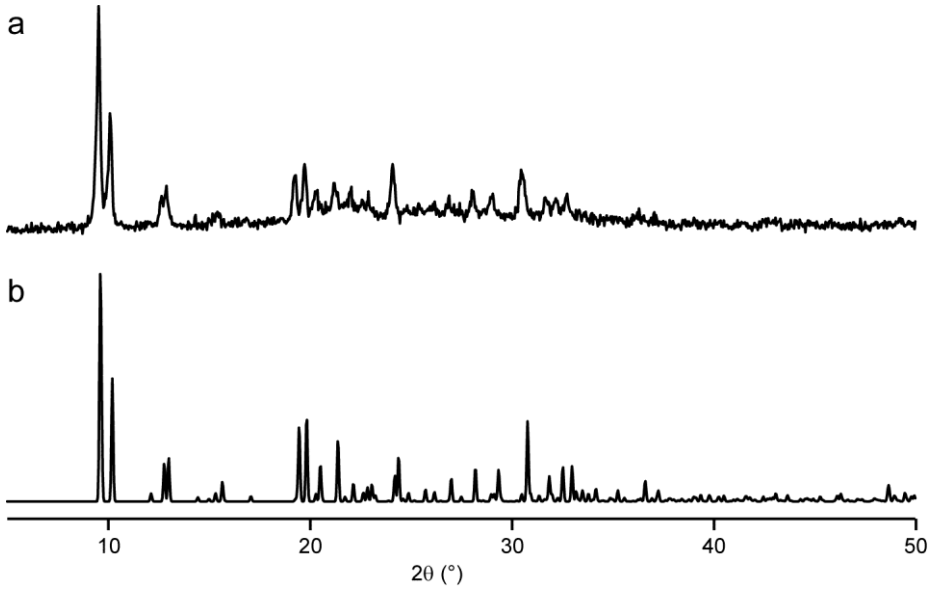

Figure 6.21. (a) Experimental powder XRD pattern for GaPO-34(calcined, hydrated) and (b) simulated powder XRD pattern for phase B of hydrated AlPO-34.

While GaPO-34(calcined, hydrated) is apparently stable indefinitely at room temperature, heating the material to 200 °C (*i.e.*, above the typical temperatures for H_2O loss from microporous materials, but below the temperature required for calcination of GaPO-34 to the (stable) $GaPO_4$ framework) does not yield GaPO-34(calcined), as one would expect (by comparison with AlPOs). Instead, the framework of the hydrated GaPO appears to "collapse" upon heating, with no peaks observed in the *in-situ* powder XRD pattern (Figure 6.22). The ^{31}P MAS NMR spectrum, shown in Figure 6.23(a), appears to confirm this, with a broad resonance observed between 0 and –25 ppm, which can be described by a single Gaussian lineshape, centred at –12.3 ppm. There is a small shoulder present at –19.0 ppm (*cf.* –19.5 ppm for GaPO-34(calcined)), contributing ~3.1% of the total spectral intensity, which may be indicative of a small amount of crystalline material remaining within the sample (such a small amount of crystalline material would not be observed by the *in-situ* XRD experiments, especially if the particle size were small). The ^{1}H MAS NMR spectrum (Figure 6.23(b)) contains a broad resonance, centred at 6.0 ppm, suggesting that there is still H_2O present within the material. The ^{71}Ga NMR spectrum, shown in Figure 6.23(c) indicates the presence of both Ga(IV) (50 to 130 ppm) and some higher-coordinate Ga (–90 to 50 ppm). The position of the Ga(V/VI) resonance indicates that this is most likely to arise from Ga(V), but the broadness of the resonances precludes further analysis. As for the GaPO-34(calcined, hydrated), high-field 3QMAS NMR experiments were unsuccessful, and further work is required to obtain a more detailed picture of the local structure in GaPO-34(collapsed).

In most applications, it is advantageous to be able to dry microporous materials after exposure to moisture, thereby reducing the need for strictly anhydrous operating conditions and allowing recovery of the material after exposure to water. Therefore, reversal of the hydration of GaPO-34(calcined) is a necessary step before GaPO-34 can be considered as potentially useful. In the original report of the collapse of GaPO-34, by Amri *et al.*,[2] GaPO(hydrated) was heated to 200 °C in the *in-situ* XRD apparatus, which may not have allowed for sufficiently rapid venting of H_2O vapour, leading essentially to a high-pressure steaming of the material, rather than dehydration. Therefore, the present work examined alternative approaches to

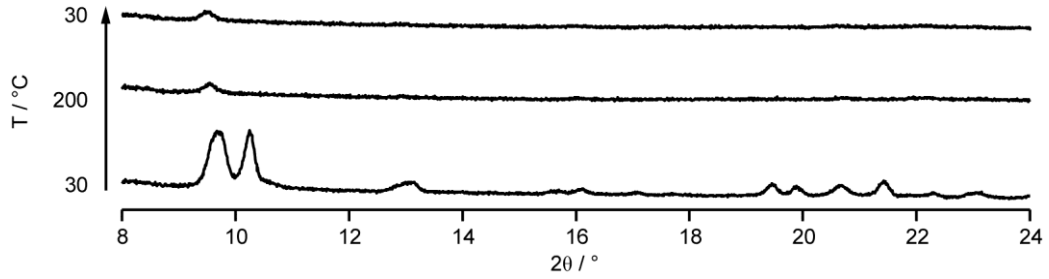

Figure 6.22. *In-situ* powder XRD patterns of GaPO-34(calcined, hydrated) heated to the indicated temperature.

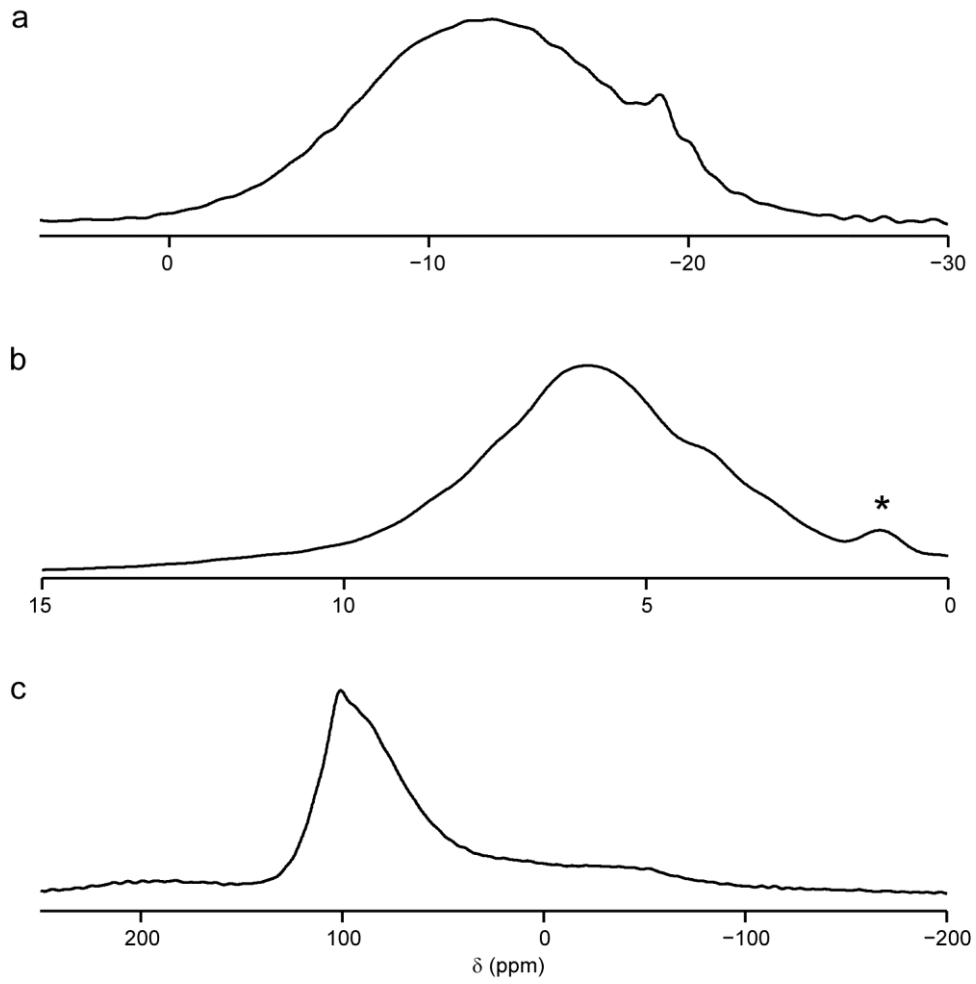

Figure 6.23. (a) ^{31}P (14.1 T, 20 kHz MAS), (b) ^{1}H (14.1 T, 60 kHz MAS), and (c) ^{71}Ga (20.0 T, 60 kHz MAS) NMR spectra of GaPO-34(collapsed). The asterisk in part (b) denotes a background resonance commonly observed in spectra recorded with the 1.3 mm probe used.

removing the water, without causing framework collapse.[15] A batch of GaPO-34(calcined, hydrated) was prepared and split into five portions. The first of these was heated at the low temperature of 45 °C for 2 days, and it can be seen from the ^{31}P NMR spectrum in Figure 6.24(a) that this treatment had little effect. The second portion was heated to 80 °C for 2 days and the ^{31}P NMR spectrum of the resulting material, shown in Figure 6.24(b), shows a significant change from the starting material. There is a broad resonance between –2 and –18 ppm, and a sharp resonance at –19.2 ppm, with a relative integrated intensity ratio of 2.8 : 1 (*cf.* 32 : 1 for GaPO-34(collapsed), above). Assuming that the sharp resonance corresponds to GaPO-34(calcined), this result suggests that the lower-temperature heating in a drying oven (more room for H_2O vapour to escape than in the *in-situ* XRD apparatus) may be a suitable route to the drying of GaPO-34(calcined, hydrated) without loss of the framework structure. Heating the third and fourth portions to 110 °C for 1 and 2 days, respectively, yielded materials with the ^{31}P NMR spectra shown in Figures 6.24(c and d), respectively. The integrated intensity ratio of the broad and sharp resonances decreases as the heating is continued (0.8 : 1 after 1 day and 0.6 : 1 after 2 days), although ~38% of the P remained in the phase giving rise to the broad resonance after heating for 2 days. Given that the proportion of this phase decreases with increased temperature and heating time, it is possible that it corresponds not to the true "collapsed" phase, but to some disordered, partially-hydrated phase, the chemical shift range for which merely coincides with that of GaPO-34(collapsed). The final portion of GaPO-34(calcined, hydrated) was placed under static vacuum in a vacuum desiccator for 5 days. The ^{31}P NMR spectrum of the resulting material is shown in Figure 6.24(e), and contains the sharp resonance at –19.5 ppm, as well as a series of resonances between –3.5 and –18.0 ppm. These resonances do not correspond to GaPO-34(calcined, hydrated) or GaPO-34(collapsed) or the broad resonance observed in the samples "dried" by heating. Therefore, it is assumed that they arise from a partially-hydrated (but still relatively ordered) phase of GaPO-34. The resonance arising from GaPO-34(calcined), at –19.5 ppm contributes ~33% of the total spectral intensity. Had more sample been available, the next logical step of this investigation would have been to subject GaPO-34(calcined, hydrated) to either dynamic vacuum or a combination of vacuum and heating, such that the H_2O would

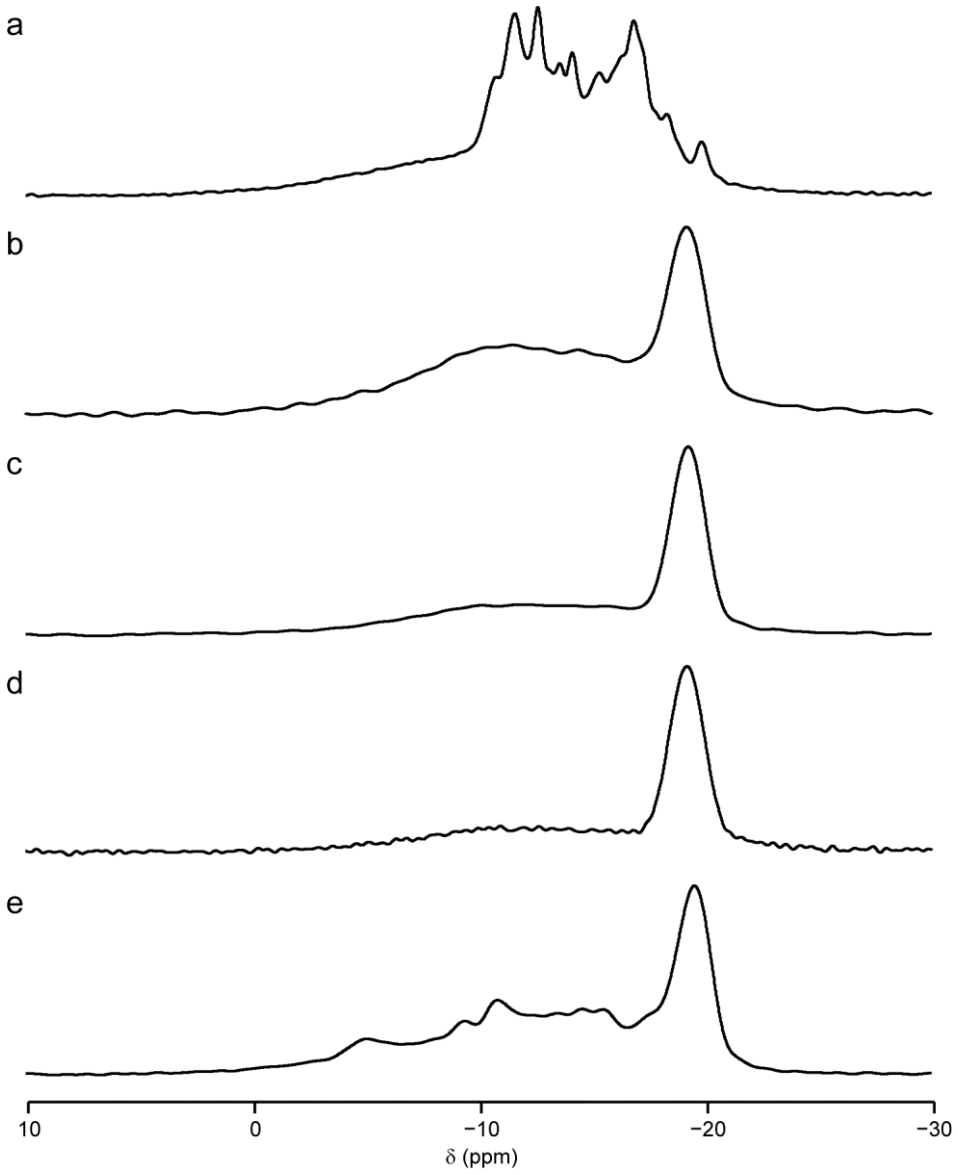

Figure 6.24. ^{31}P (14.1 T, 25 kHz MAS) NMR spectra of GaPO-34(calcined, hydrated) subjected to (a) heating to 45 °C for 2 days, (b) heating to 80 °C for 2 days, (c) heating to 110 °C for 1 day, (d) heating to 110 °C for 2 days and (e) static vacuum for 5 days.

rapidly be removed completely from the system, preventing any possible steaming of the sample. However, most further attempted syntheses of GaPO-34 yielded a mixture of GaPO-34 with impurity phases (discussed in greater detail below) and no further pure GaPO-34(calcined, hydrated) was prepared for this work. Future syntheses will be carried out in order to complete this investigation into dehydration of GaPO-34(calcined, hydrated).

6.4.4 Common Impurity Phases

As has been noted above, the synthesis of GaPO-34 often yields one or more additional phases, which may appear as impurities, or as the major phase present. One of these phases is the dense $GaPO_4$ phase, berlinite (the $GaPO_4$ analogue of quartz).[22] The structure of $GaPO_4$ berlinite is shown in Figure 6.25(a), and contains a single crystallographically-distinct Ga species, and one distinct P species. An unsuccessful attempt at the solvothermal synthesis of the AEN-type GaPO-M2[3] yielded a sample of pure $GaPO_4$ berlinite, and the ^{31}P and ^{71}Ga MAS NMR spectra of this sample are shown in Figures 6.25(b and c). A single ^{31}P resonance is observed at –10.4 ppm, and a single ^{71}Ga resonance is observed with δ_{iso} = 111.1 ppm, C_Q = 8.8 MHz and η_Q = 0.5. The ^{71}Ga NMR parameters agree well with those observed in the literature[13] but the ^{31}P δ_{iso} is different from that observed by Turner *et al.*,[23] (–9.6 ppm) owing to the different chemical shift references used. The δ_{iso} values were used to reference calculated ^{31}P and ^{71}Ga chemical shifts for the CASTEP 6 calculations reported in this chapter. The experimental and calculated C_Q and η_Q are in reasonable agreement, as summarised in Table 6.7.

The second impurity phase was observed by Schott-Darie *et al*. in the synthesis of GaPO-34[pyHF].[1] In this work, the impurity phase shall be known as GaPO-X[pyHF] (and GaPO-X[miHF] for the miHF-containing analogue) Although limited characterisation data were reported in the literature, two ^{19}F resonances were observed at –111.1 and –131.5 ppm, the ^{13}C signal was observed to be very weak, a total mass loss of ~12% was observed on calcination, and the powder XRD pattern was reported for the range 2.5 to 30° 2θ. The weak ^{13}C signal and the relatively small mass loss were attributed to the inclusion of relatively little pyHF (or py) within the framework, suggesting that it may be more dense than GaPO-34[pyHF]. However, it is also possible that the material is porous, but with small pore windows, slowing the release of products of the decomposition of the SDA. This would mean that the apparent mass loss upon heating rapidly in a TGA experiment is an inaccurate representation of the true mass lost achieved by maintaining a high calcination temperature for an extended period of time (as in actual calcination). The only interpretation of the ^{19}F NMR spectrum was that the material contained fluorine.

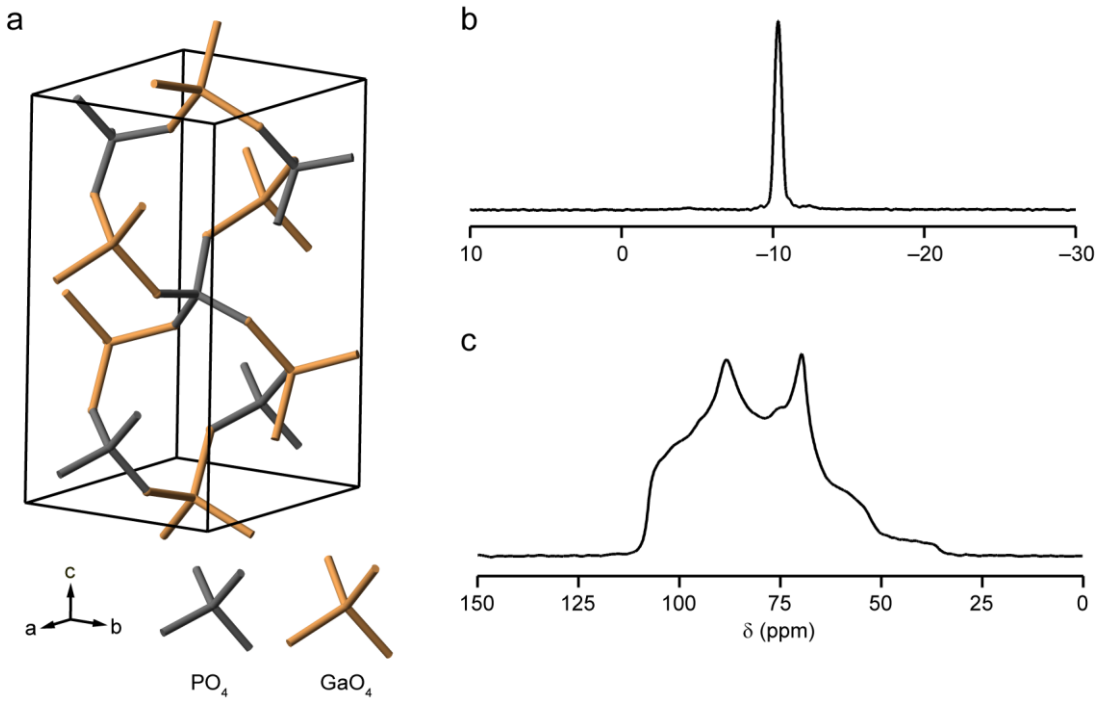

Figure 6.25. (a) The crystal structure of $GaPO_4$ berlinite.[22] (b) ^{31}P (14.1 T, 12.5 kHz MAS) and (c) ^{71}Ga (20.0 T, 60 kHz MAS) NMR spectra of $GaPO_4$ berlinite.

Reference to Figure 1.4 suggests that the resonances correspond to bridging fluoride, although the resonance at –131.5 is at the edge of the range of known ^{19}F chemical shifts for bridging fluoride, perhaps suggesting particularly short Ga-F bonds.

Two samples of GaPO-X were prepared for this work; a pure sample of GaPO-X[pyHF] and a relatively pure (containing a small amount of $GaPO_4$ berlinite) sample of GaPO-X[miHF], prepared by Professor Richard Walton. These samples were characterised in more detail for this work, with the aim of determining the

Table 6.7 The experimental and calculated (using CASTEP 6) ^{31}P and ^{71}Ga NMR parameters for $GaPO_4$ berlinite.

	δ_{iso} (ppm)		C_Q / MHz		η_Q	
Species	exp.	calc.	exp.	calc.	exp.	calc.
P	–10.4(1)	–10.4[a]				
Ga	111.1(10)	111.1[a]	8.8(2)	8.13	0.5(1)	0.77

a. $GaPO_4$ berlinite was used to reference the calculated (using CASTEP 6) ^{31}P and ^{71}Ga chemical shifts throughout this chapter.

structure of GaPO-X. The powder XRD pattern of GaPO-X[miHF] is shown in Figure 6.26, and is similar to the pattern for GaPO-X[pyHF], published by Schott-Darie *et al.*,[1] confirming the structural similarities between the two phases, even though they contain different SDAs.

The ^{1}H, ^{13}C, ^{19}F and ^{31}P MAS NMR spectra of GaPO-X[miHF] are shown in Figure 6.27 and, from the number of resonances present, it can be appreciated that GaPO-X has a considerably more complicated structure than GaPO-34. The ^{1}H NMR spectrum of GaPO-X[miHF] contains resonances assigned to H3 (12.5 ppm) and H6 (3.6 ppm). In order to assign the resonances between 4 and 10 ppm, a DQMAS NMR spectrum was recorded, with one block of BABA pulses used to excite and convert the DQCs. The spectrum, shown in Figure 6.28, indicates that the resonance centred on ~6.5 ppm corresponds to $\mathbf{H}_2$O (strong diagonal resonance with no off-diagonal DQCs), while resonances at ~7.0 and ~8.7 ppm correspond to H2 and H5 (in close proximity to H6). The resonance at ~8.7 ppm can be assigned to H2, (also in close proximity to H3). The resonance corresponding to H4 (close proximity to H3) can be identified at ~9.4 ppm. However, the width of the resonances means that a full assignment of all features in the ^{1}H MAS NMR spectrum is not possible. One point to note is that the resonance at 4.9 ppm in the MAS NMR spectrum does not appear in the DQMAS NMR spectrum, indicating that it may arise from HO^{-} species. The possibility of non-fluoride anions within the material cannot immediately be discounted when the ^{19}F NMR spectrum is considered. The ^{19}F NMR spectrum contains three resonances, with isotropic shifts of –112.9, –130.1 and –134.2 ppm, indicating the presence of three (rather than two, as observed by Schott-Darie *et al.*[1]) distinct types of bridging fluoride. The integrated intensity ratio of these resonances is 1.0 : 1.6 : 1.4, even when a very long repeat interval of 300 s (typical values for ^{19}F are 3-10 s) was used to ensure complete relaxation. While it could be argued that this ratio is close to 2 : 3 : 3, it is also possible that there exist both hydroxide and fluoride anions within GaPO-X, probably in some disordered (non-periodic) arrangement, as previously observed for the AlPOs, CJ2 and cloverite.[24, 25]

The ^{13}C CP MAS NMR spectrum of GaPO-X[miHF] contains three regions of intensity; broad resonances from 133 to 140 and 117 to 126 ppm, and a sharper

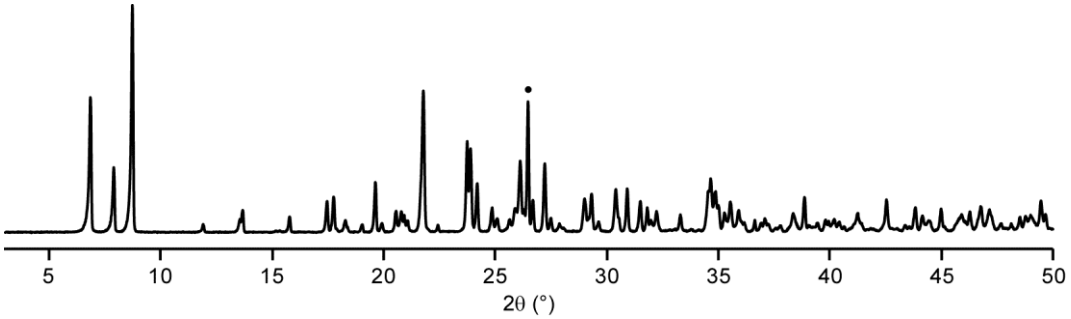

Figure 6.26. Powder XRD pattern of GaPO-X[miHF]. The 012 peaks of $GaPO_4$ berlinite is marked •.

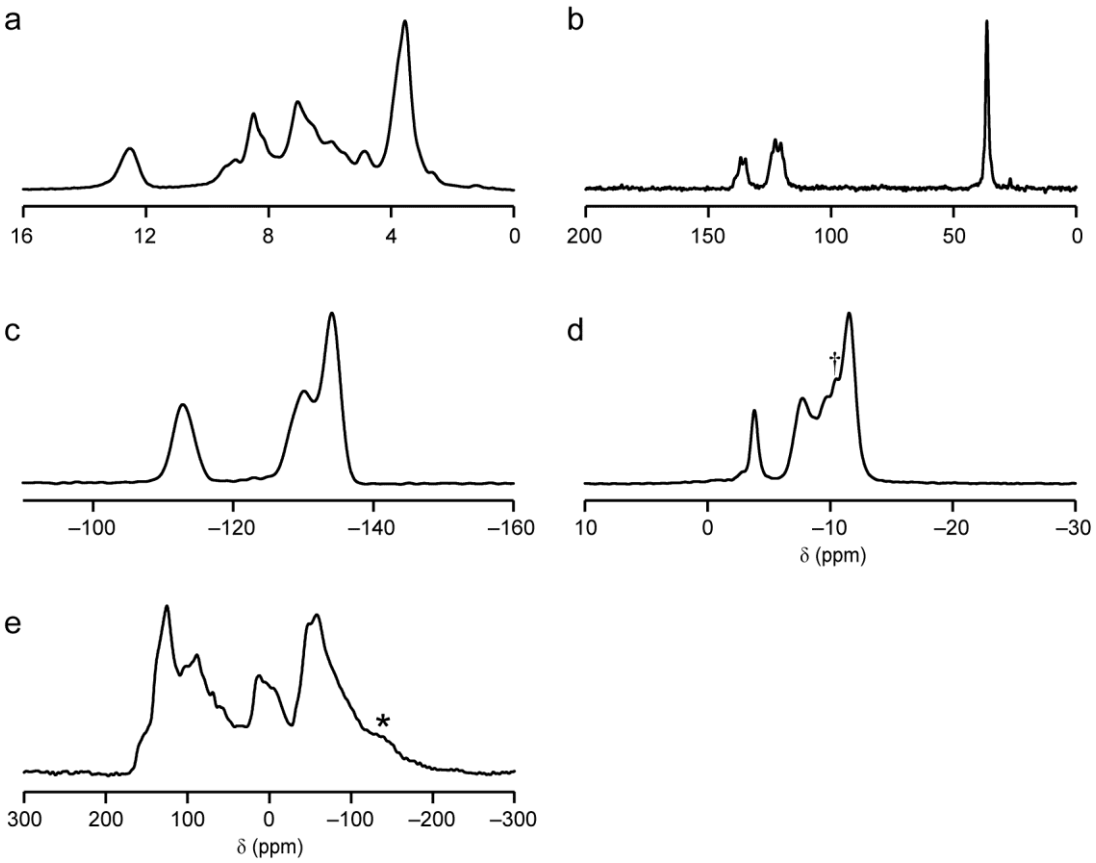

Figure 6.27. (a) ^{1}H (14.1 T, 60 kHz MAS), (b) ^{13}C (14.1 T, 12.5 kHz CPMAS), (c) ^{19}F (14.1 T, 55 kHz MAS), (d) ^{31}P (14.1 T, 14 kHz MAS) and (e) ^{71}Ga (20.0 T, 60 kHz MAS) NMR spectra of GaPO-X[miHF]. In part (d), the resonance arising from $GaPO_4$ berlinite is marked † and, in part (e), the asterisk denotes a SSB.

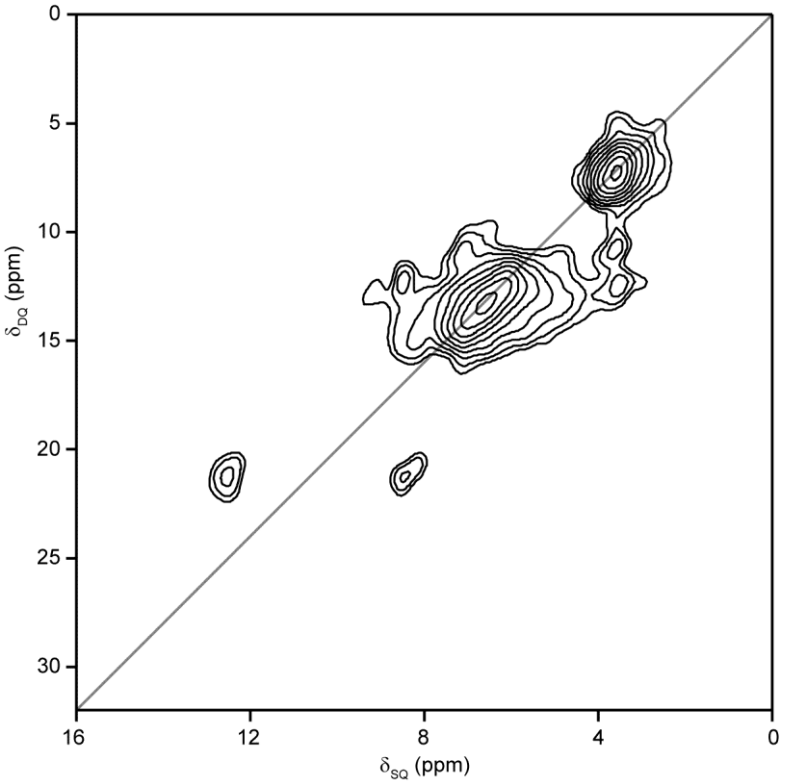

Figure 6.28. ^{1}H (14.1 T, 60 kHz DQMAS), NMR spectrum of GaPO-X[miHF]. The $\delta_{DQ} = 2\delta_{SQ}$ diagonal is indicated in grey.

one at ~36.5 ppm. These regions are close to the shifts of miH^{+} in GaPO-34[miHF], but also reasonably close to those of mi in GaPO-34[mi], with the exception of the resonance at 128.8 ppm in GaPO-34[mi], which is absent for GaPO-X[miHF]. Therefore, it is likely that the SDA is miH^{+} rather than mi in GaPO-X[miHF] (as also indicated by ^{1}H NMR), with the broadened resonances indicating some disorder.

The ^{31}P MAS NMR spectrum of GaPO-X[miHF] contains a resonance at –3.8 ppm and a series of overlapped resonances between –7 and –13 ppm. These shifts are all relatively high for ^{31}P in GaPOs, possibly owing to small average P-O-Ga bond angles, indicative of P-O-Ga(V/VI) linkages. In order to confirm that all ^{31}P resonances arise from the same phase (*i.e.*, are close in space), a ^{31}P DQMAS NMR spectrum was recorded using five rotor periods of POST-C7 recoupling to excite the DQCs. The spectrum, shown in Figure 6.29, confirms the presence of $GaPO_4$ berlinite, as the strong on-diagonal resonance at (–10.4, –20.8) ppm does not correlate to any of the other resonances. The increased intensity of this resonance in the DQMAS NMR spectrum relative to the MAS NMR spectrum arises from the fact

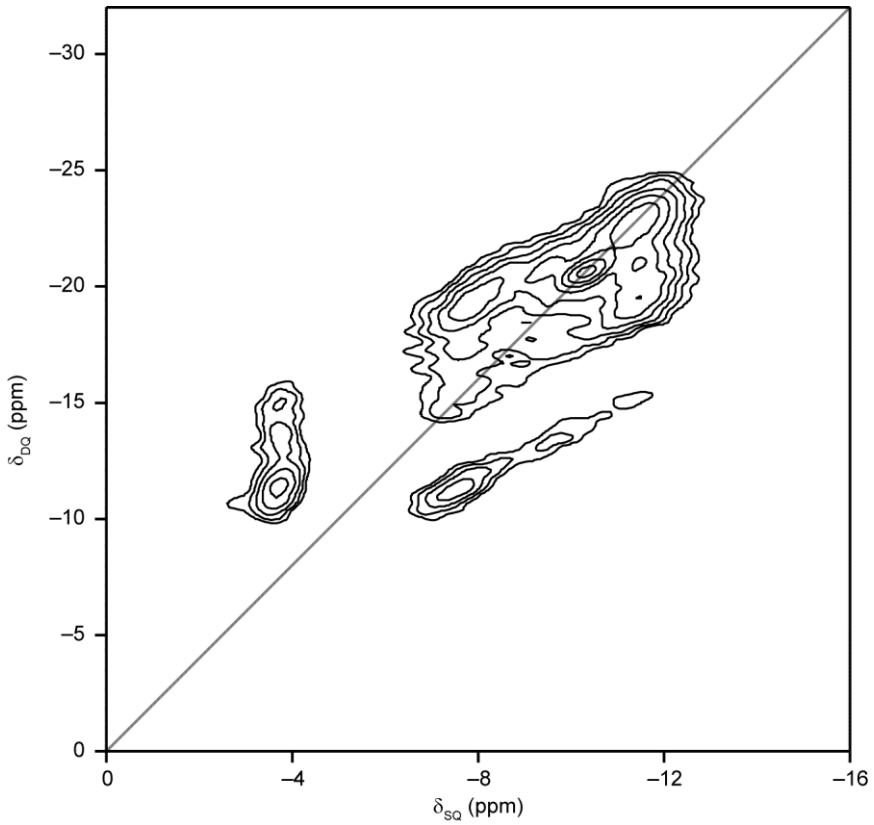

Figure 6.29. (a) ^{31}P (14.1 T, 10 kHz DQMAS) NMR spectrum of GaPO-X[miHF]. The $\delta_{DQ} = 2\delta_{SQ}$ diagonal is indicated in grey.

that a saturation train was used to record the DQMAS NMR spectrum, in order to allow a shorter repeat interval. It can be seen that the resonance at –3.8 ppm corresponds to a P species close in space to those with shifts between –7.4 and –11.6 ppm, indicating that GaPO-X[miHF] is a single phase. The ^{31}P DQMAS NMR spectrum also allows the identification of some distinct ^{31}P resonances within the –7 to –13 ppm region, with isotropic shifts of –7.7, –8.8, –9.6, –10.3 and –11.6 ppm, indicating the presence of at least six distinct P species in GaPO-X[miHF]. The ^{71}Ga NMR spectrum of GaPO-X[miHF], shown in Figure 6.27(e), contains multiple resonances with asymmetric broadening characteristic of a small distribution of NMR parameters, as would be expected from a disordered material. While no high-resolution ^{71}Ga NMR spectrum has yet been achieved for this sample, it is clear from the positions of the resonances that Ga(IV), Ga(V) and Ga(VI) are all present.

As noted above, a very long repeat interval was required in order to obtain a quantitative ^{19}F NMR spectrum. T_1 was measured for each F species using a

saturation recovery experiment, and was 6.2 and 6.3 s for the resonances at –130.1 and –134.2 ppm, respectively, but 59.6 s for the resonance at –112.9 ppm, indicating that this resonance arises from a F species in a very different environment from the other two F species. This difference may arise from the presence of two F-containing phases within the sample assumed to be a single phase, "GaPO-X[miHF]". The ^{19}F DQMAS NMR spectrum (recorded using three blocks of BABA pulses to excite and convert the DQCs), shown in Figure 6.30(a), shows no DQCs between the resonance at –112.9 ppm and the other two resonances, whereas the other two resonances can clearly be seen to result from F species that are close in space. This suggests that there may be two F-containing phases present within the sample. However, the ^{19}F-^{31}P CP HETCOR spectrum shown in Figure 6.30(b) clearly shows a correlation between the ^{31}P resonance at –11.7 ppm and all three F species, confirming that all observed P and F species occur within the same phase.

The ^{1}H, ^{13}C, ^{19}F and ^{31}P MAS NMR spectra of GaPO-X[pyHF] are shown in Figure 6.31. Comparison with Figure 6.27 shows many similarities, particularly for ^{19}F and ^{31}P, as would be expected from two such similar structures. The ^{1}H NMR spectrum of GaPO-X[pyHF] is somewhat easier to interpret than that of the miHF analogue – H1 can be identified at 13.4 ppm, confirming the SDA is protonated, H2-4 all contribute to the broad region of spectral intensity between 4.5 and 9.5 ppm, and **H**$_2$O can be clearly identified at 3.5 ppm in this spectrum, as there is no overlap with any of the resonances from the SDA. The identification of H_2O at 3.5 ppm is in contradiction to the shift of 6.5 ppm, suggested above for GaPO-X[miHF], although the 3.5 ppm is in much closer agreement with the shifts observed for GaPO-34[miHF] (3.4 ppm) and GaPO-34[pyHF] (3.3 ppm). Therefore, in order to confirm the assignment of **H**$_2$O, and in an attempt to obtain further information on the resonances between 4.5 and 9.5 ppm, a DQMAS NMR spectrum (Figure 6.32) was recorded, with two loops of BABA pulses used to excite and convert the DQCs. The intense on-diagonal DQC at (3.5, 7) ppm confirms the assignment of this resonance to **H**$_2$O. However, while some features can be resolved in the H2-H4 region, the extent of the overlap of the resonances is too great to allow detailed analysis, and it is not possible to determine whether any of the resonances correspond to O**H**, or whether they all arise from the pyH^+. Future attempts to assign this spectrum will

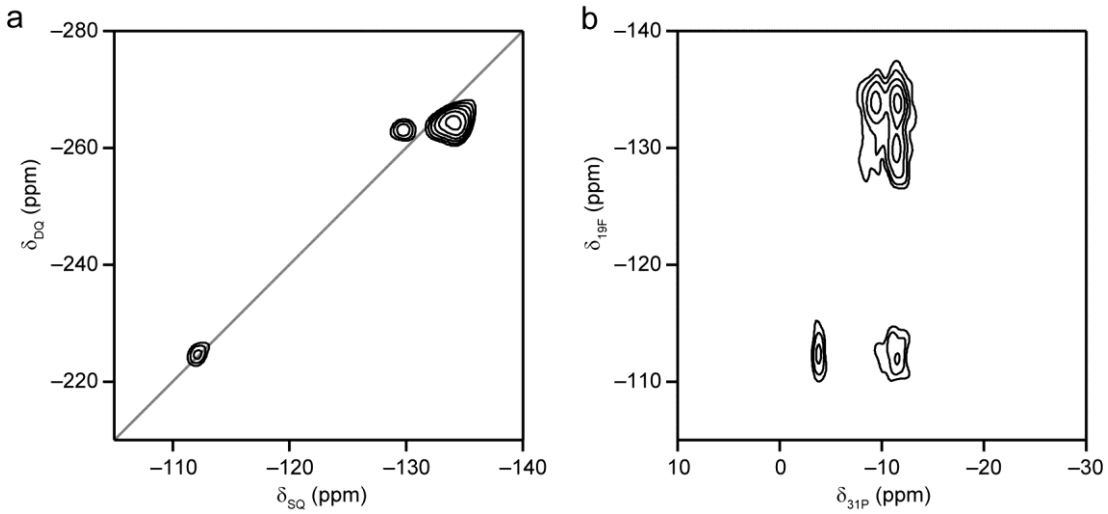

Figure 6.30. (a) ^{19}F (14.1 T, 55 kHz DQMAS) NMR spectrum of GaPO-X[miHF]. The $\delta_{DQ} = 2\delta_{SQ}$ diagonal is indicated in grey. (b) ^{19}F-^{31}P (14.1 T, 50 kHz MAS) CP HETCOR spectrum of GaPO-X[miHF].

involve recording ^{1}H-^{13}C correlation spectra, which may allow for the identification of any O**H** resonances present.

The ^{19}F NMR spectrum is similar to that of GaPO-X[miHF], containing three resonances, with isotropic shifts of –113.0, –128.9 and –132.8 ppm. Again, all three

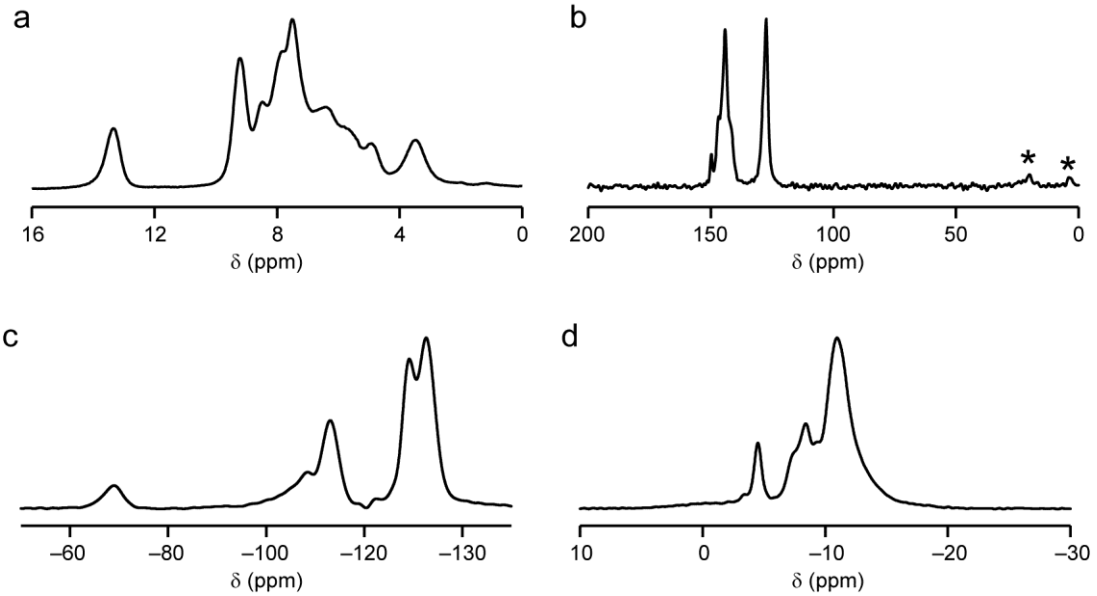

Figure 6.31. (a) ^{1}H (14.1 T, 60 kHz MAS), (b) ^{13}C (14.1 T, 12.5 kHz CPMAS), (c) ^{19}F (14.1 T, 60 kHz MAS) and (d) ^{31}P (14.1 T, 10 kHz MAS) NMR spectra of GaPO-X[pyHF]. Asterisks denote SSBs.

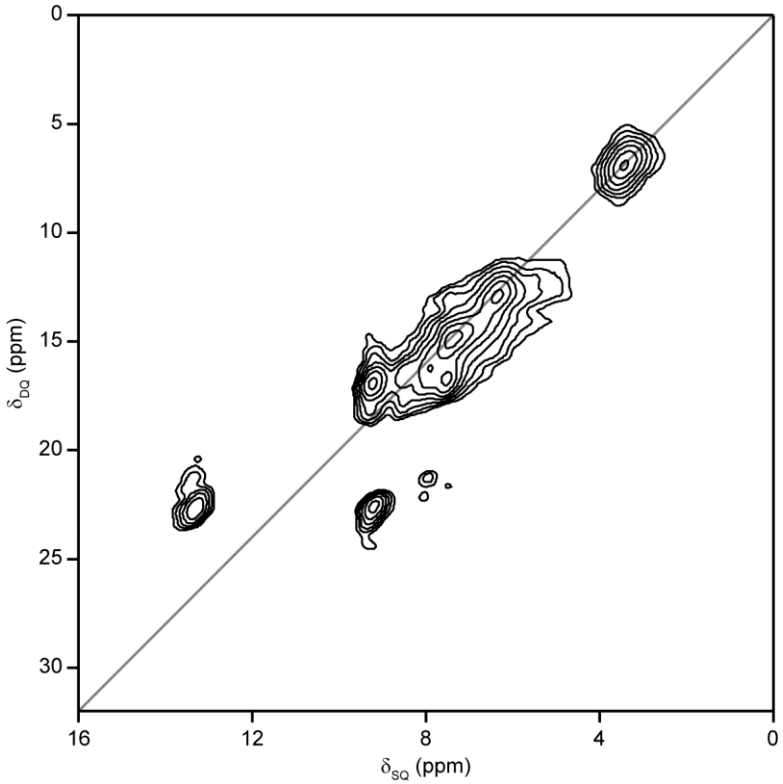

Figure 6.32. ^{1}H (14.1 T, 60 kHz DQMAS), NMR spectrum of GaPO-X[pyHF]. The $\delta_{DQ} = 2\delta_{SQ}$ diagonal is indicated in grey.

resonances are in the expected shift range for bridging fluoride. In addition, two lower-intensity resonances are observed at –69.0 and –108.2 ppm. These resonances are assumed to arise from an unidentified F-containing impurity, as no such resonances were observed for GaPO-X[miHF], and the resonance at –69 ppm is more characteristic of F^{-} in a D4R (*i.e.*, a structural feature that would require a different framework topology from that observed for GaPO-X[miHF], which is unlikely given the other similarities between the ^{19}F and ^{31}P NMR spectra, discussed below). The integrated intensity ratio of the three resonances from GaPO-X[pyHF] is 1.0 : 1.0 : 1.8, (300 s recycle interval). It is interesting that, while the isotropic shifts of the F species in GaPO-X[pyHF] and GaPO-X[miHF] are almost identical, their integrated intensity ratios are very different; an observation that may be explained if there is a random amount of substitution of HO^{-} for F^{-} in both samples. However, further investigation would be required to confirm this suggestion.

The ^{13}C CP MAS NMR spectrum of GaPO-X[pyHF] contains a resonance at 127.4 ppm and a region of spectral intensity between ~140 and 150 ppm, which

clearly contains numerous overlapping resonances. These regions match reasonably well with the shifts from pyH^+ in GaPO-34[pyHF], although, as was observed for GaPO-X[miHF], the broadened resonances likely indicate that the material is disordered. It should be noted that, in contrast to the claims of Schott-Darie *et al.*,[1] the amount of ^{13}C signal obtained from GaPO-X[pyHF] was not noticeably lower than would be typical for most microporous materials, perhaps indicating some error in experimental setup or an unreported impurity in the sample in the earlier work.

The ^{31}P MAS NMR spectrum of GaPO-X[miHF] contains a resonance at –4.5 ppm and a series of overlapped resonances between –6.5 and –14 ppm. While the overall lineshape is not identical to that of GaPO-X[miHF], this is to be expected as the different SDAs will most likely lead to slight differences in bond lengths and angles in the framework, as was observed for GaPO-34 with different SDAs. No evidence of $GaPO_4$ berlinite was observed for this sample, although it is possible that some of the spectral intensity arises from the F-containing impurity observed by ^{19}F NMR. Unlike the case of GaPO-X[miHF], the ^{31}P resonances in GaPO-X[pyHF] are too overlapped to allow reliable decomposition to determine the number of crystallographically distinct P species, even with a DQMAS experiment (not shown).

As discussed above, the original TGA experiment of Schott-Darie *et al.*[1] did not mimic the true calcination process, and may have led to a spuriously low total mass loss being observed. To investigate this possibility, samples of GaPO-X[miHF] and GaPO-X[pyHF] were subjected to TGA, with the heating continued up to 1000 °C, and maintained at that temperature for 2.75 h. The total mass loss observed was ~17-18% (*i.e.*, similar to GaPO-34[miHF] and GaPO-34[pyHF]), as shown in Figure 6.33, indicating that the material contains more SDA than initially assumed. However, the fact that prolonged heating is required to achieve complete calcination indicates that the pore windows may be much smaller in GaPO-X than GaPO-34. It is clear that calcination of either form of GaPO-X is a complicated multi-step process, which cannot currently be interpreted, as the exact stoichiometry of the material is not known. However, it is hoped that TGA combined with mass spectrometry (TGA-MS) experiments might be capable of providing further insight into the changes occurring during each mass loss.

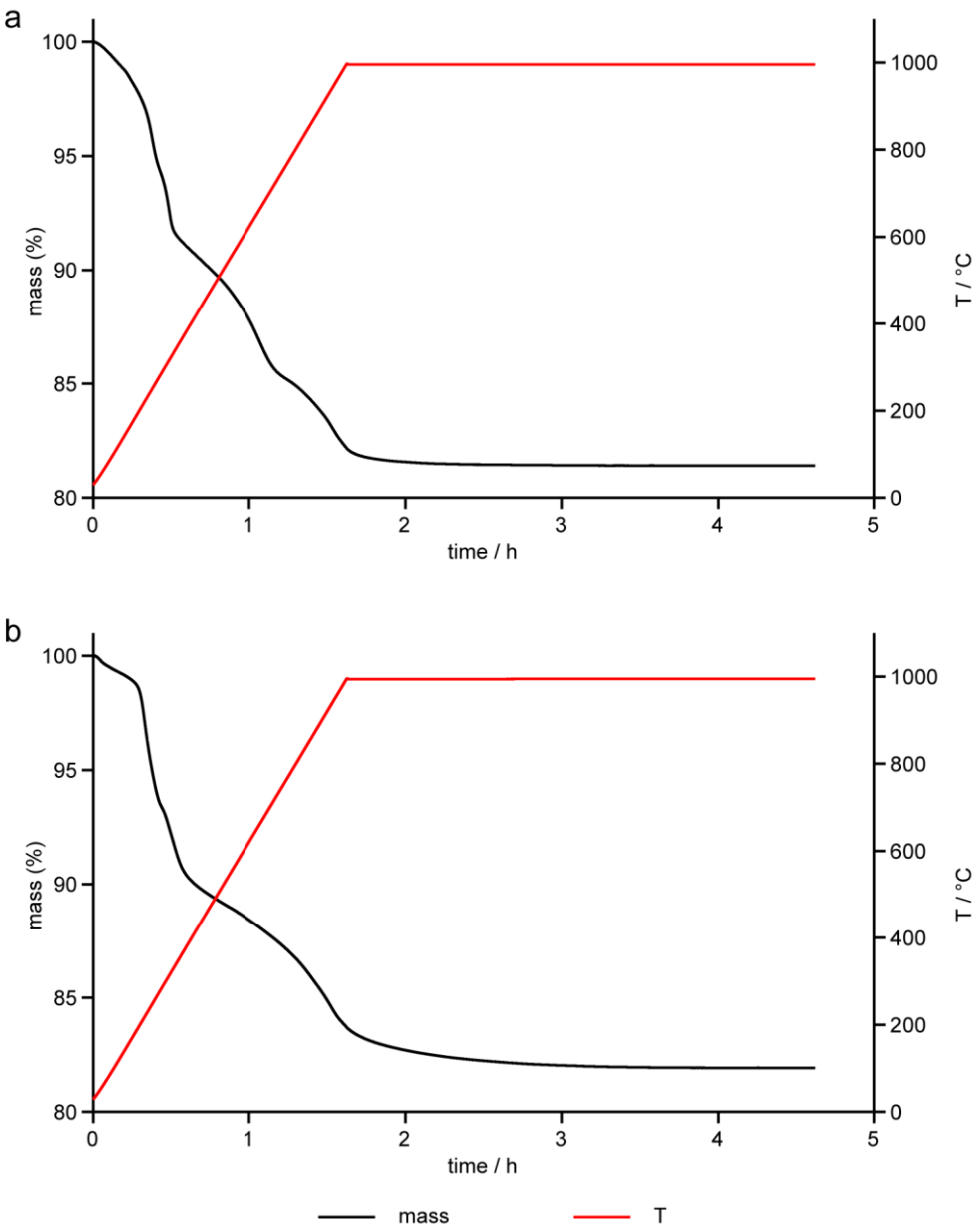

Figure 6.33. Plots of sample mass and temperature as a function of time during a TGA-DSC experiment for (a) GaPO-X[miHF] and (b) GaPO-X[pyHF].

While no in-depth investigation has yet been carried out into the impact of the Ga_2O_3 starting material on the outcome of the reaction, it is possible that this should form the focus of further investigation. The ^{31}P MAS NMR spectra of two samples of "GaPO-34[miHF]" prepared following the same procedure are shown in Figures 6.34(a and b). The first sample was prepared using Ga_2O_3 generated from old (very hydrated) $Ga(NO_3)_3$ that had a paste-like consistency before heating. The second sample was prepared using Ga_2O_3 generated from new (dry) $Ga(NO_3)_3$, that was

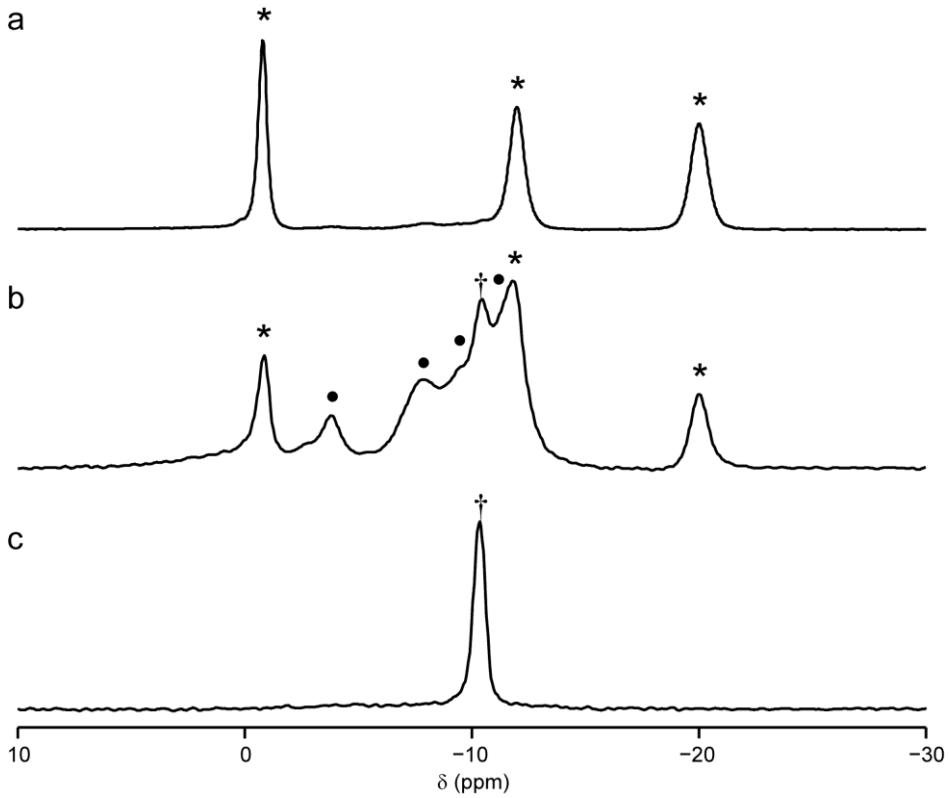

Figure 6.34. ^{31}P (14.1 T, 12.5-25 kHz MAS) NMR spectra of the solid product of attempted syntheses of GaPO-34[miHF], in which the Ga source was (a) Ga_2O_3 generated from old, hydrated $Ga(NO_3)_3$, (b) Ga_2O_3 generated from new, dry $Ga(NO_3)_3$ and (c) aqueous $Ga(NO_3)_3$ added directly to the reaction mix. Resonances from GaPO-34[miHF], GaPO-X[miHF] and $GaPO_4$ berlinite are marked *, • and †, respectively.

supplied as hard chunks. It can be seen that the degree of hydration of the initial gallium nitrate would appear to have a significant effect on the product, with the less hydrated starting material giving rise to a mixture of GaPO-34[miHF], GaPO-X[miHF] and $GaPO_4$ berlinite, whereas the more hydrated starting material yielded predominantly GaPO-34[miHF], with only traces of GaPO-X[miHF]. Schott-Darie *et al*. generated the Ga_2O_3 from an aqueous solution of $Ga(NO_3)_3$,[1] suggesting that the hydration state of the gallium nitrate has a significant effect on the nature of the Ga precursor formed. Playford *et al*. have recently shown that Ga_2O_3 has many phases,[26] and, while the reaction conditions employed here should yield only "δ-Ga_2O_3", this "phase" is actually a mixture of amorphous, β- and ε- phases of Ga_2O_3, and it is possible that the degree of hydration of the starting $Ga(NO_3)_3$ may influence the

proportions of the different phases present in the δ-Ga_2O_3 precursor to GaPO-34. In a separate synthesis, the decomposition of $Ga(NO_3)_3$ was omitted and the Ga source added to the autoclave was simply aqueous $Ga(NO_3)_3$. By ^{31}P MAS NMR spectroscopy, (Figure 6.34(c)) this reaction yielded almost entirely $GaPO_4$ berlinite. It would, therefore, appear that the outcome of the reaction is kinetically determined and, when the concentration of free Ga^{3+} is too high, the reaction will tend to form the dense phase (as this requires interaction only between Ga^{3+} and PO_4^-) whereas, when the concentration of free Ga^{3+} is reduced by using the less soluble Ga_2O_3 precursor, the reaction will tend to form GaPO-X and GaPO-34, both of which require interactions between Ga^{3+}, PO_4^-, HF and mi or py. While it seems likely that altering the proportions of the amorphous, β- and ε- Ga_2O_3 present in the δ-Ga_2O_3 precursor would alter its solubility, it is currently unclear whether a more soluble Ga^{3+} source will favour the formation of GaPO-34 or GaPO-X.

6.4.5 Conclusions

This chapter has reported the synthesis and characterisation of several phases of GaPO-34 that can be accessed starting from GaPO-34[RHF], where R = pyridine (py) or 1-methylimidazole (mi), as well as some commonly-formed impurities.

The as-prepared GaPO-34[pyHF] and GaPO-34[pyHF] were characterised by multinuclear solid-state NMR, including a combination of ^{69}Ga and ^{71}Ga NMR spectra recorded at high field (20.0 T). While only ^{71}Ga NMR spectra are normally recorded, owing to the lower gyromagnetic ratio and larger electric quadrupole moment of ^{69}Ga, work presented here showed that the combination of the two nuclei can be used to obtain more reliable Ga NMR parameters in the presence of disorder (particularly in GaPO-34[pyHF]).

It was shown that calcination of GaPO-34[pyHF] occurs in a single step, with loss of pyHF at ~375 °C resulting in the fully-calcined GaPO-34(calcined). However, calcination of GaPO-34[miHF] is a two-step process, with initial loss of HF at ~315 °C resulting in GaPO-34[mi], which contains neutral mi rather than miHF. The loss of HF was confirmed by ^{1}H and ^{19}F NMR and TGA, while the presence of mi was confirmed by ^{13}C NMR. While further work is required to determine the crystal

structure of GaPO-34[mi], the ^{31}P NMR spectrum indicates that the material contains three distinct P species – the same as GaPO-34[miHF], suggesting a relatively small structural change occurs on dehydrofluorination. The second step of calcination of GaPO-34[miHF] involves loss of mi at ~400 °C, yielding GaPO-34(calcined).

GaPO-34(calcined) can adsorb atmospheric moisture to give the hydrated GaPO-34(hydrated). GaPO-34(hydrated) appears to exhibit superficial similarities with the hydrated form of the analogous AlPO, AlPO-34, as observed by powder XRD. However, the ^{31}P NMR spectrum reveals that the GaPO contains many more distinct P species than the AlPO, indicating that the unit cell of the GaPO might be related to a supercell of the AlPO. In addition, it is possible that GaPO-34(hydrated) is actually a mixture of two hydrated phases, as is known for the AlPO, which exists in two forms with 11 or 12 H_2O molecules per unit cell. Further work is, therefore, required to obtain more detailed information on the structure of GaPO-34(hydrated).

The heating of GaPO-34(hydrated) does not yield GaPO-34(calcined), as would be expected (and as is observed for hydrated AlPO-34) and, instead, the apparently amorphous material, GaPO-34(collapsed) is obtained. This collapse is not desirable if GaPO-34 is to be considered for potential applications, as it would have to be handled in strictly anhydrous conditions and replaced rather than dried if it came into contact with moisture. This chapter presented preliminary investigations into alternative conditions for drying GaPO-34(hydrated), including heating at lower temperatures (40-110 °C) and evacuation at room temperature. It was shown that partial dehydration occurs under vacuum, and future work will investigate the possibility of combining gentle heating and dynamic vacuum to obtain fully dried GaPO-34(calcined) from GaPO-34(hydrated) without framework collapse.

The synthesis of GaPO-34 often yields samples containing the dense phase $GaPO_4$ berlinite and the unidentified phase, GaPO-X[RHF]. Relatively pure samples of $GaPO_4$ berlinite, GaPO-X[miHF] and GaPO-X[pyHF] were obtained and characterised by multinuclear solid-state NMR for this work. The NMR parameters for $GaPO_4$ berlinite agreed with those known in the literature, and were used to reference ^{31}P and ^{71}Ga chemical shifts calculated by DFT. TGA indicated that GaPO-X contains similar amounts of SDA (pyHF or miHF) to GaPO-34, although

prolonged heating at 1000 °C was required in order to achieve complete calcination, indicating that the pores of the framework are smaller (or have smaller windows). ^{1}H, ^{13}C and ^{71}Ga NMR indicated that the material is disordered, and its crystal structure has not yet been determined. However, the presence of at least six distinct P and three distinct bridging F species was revealed by ^{31}P and ^{19}F NMR, respectively, which will provide constraints to aid structural determination.

The influence of the Ga source on the phase formed in the attempted synthesis was investigated. It was shown that nominally "amorphous Ga_2O_3" prepared by thermal decomposition of hydrated (or aqueous) gallium nitrate was the most reliable Ga source for the preparation of GaPO-34. On the other hand, addition of aqueous $Ga(NO_3)_3$ directly to the reaction mixture led to $GaPO_4$ berlinite. Further investigation would be required in order to determine reaction conditions that would reliably yield GaPO-X.

6.5 REFERENCES

1. C. Schott-Darie, H. Kessler, M. Soulard, V. Gramlich and E. Benazzi, *Stud. Surf. Sci. Catal.*, **1994**, *84*, 101.

2. M. Amri, S. E. Ashbrook, D. M. Dawson, J. M. Griffin, R. I. Walton and S. Wimperis, *J. Phys. Chem. C*, **2012**, *116*, 15084.

3. Q. B. Kan, F. P. Glasser and R. R. Xu, *J. Mater. Chem.*, **1993**, *3*, 983.

4. E. McHale, *BSc Thesis*, University of St Andrews, 2011.

5. S. Grimme, *J. Comput. Chem.*, **2006**, *27*, 1787.

6. E. R. McNellis, J. Meyer and K. Reuter, *Phys. Rev. B*, **2009**, *80*, 205414.

7. GAUSSIAN09, revision A.01. M. J. Frisch *et al*., Gaussian, Inc., Wallingford, CT, **2009**.

8. P. Pyykko, *Mol. Phys.*, **2008**, *106*, 1965.

9. L. Lakiss, A. Simon-Masseron and J. Patarin, *Micropor. Mesopor. Mater.*, **2005**, *84*, 50.

10. A. Matijasic, B. Marler, J. C. M. Acevedo, L. Josien and J. Patarin, *Chem. Mater.*, **2003**, *15*, 2614.

11. M. Amri and R. I. Walton, *Chem. Mater.*, **2009**, *21*, 3380.

12. S. M. Bradley, R. F. Howe and R. A. Kydd, *Magn. Reson. Chem.*, **1993**, *31*, 883.

13. D. Massiot, T. Vosegaard, N. Magneron, D. Trumeau, V. Montouillout, P. Berthet, T. Loiseau and B. Bujoli, *Solid State Nucl. Magn. Reson.*, **1999**, *15*, 159.

14. S. Oliver, A. Kuperman, A. Lough and G. A. Ozin, *J. Mater. Chem.*, **1997**, *7*, 807.

15. L. E. Macfarlane, *BSc Thesis*, University of St Andrews, 2013.

16. C. J. Pickard and R. J. Needs, *J. Phys. Condens. Mat.*, **2011**, *23*, 053201.

17. E. R. Parnham and R. E. Morris, *Chem. Mater.*, **2006**, *18*, 4882.

18. E. R. Cooper, C. D. Andrews, P. S. Wheatley, P. B. Webb, P. Wormald and R. E. Morris, *Nature*, **2004**, *430*, 1021.

19. A. Tuel, S. Caldarelli, A. Meden, L. B. McCusker, C. Baerlocher, A. Ristic, N. Rajic, G. Mali and V. Kaucic, *J. Phys. Chem. B*, **2000**, *104*, 5697.

20. G. Poulet, P. Sautet and A. Tuel, *J. Phys. Chem. B*, **2002**, *106*, 8599.

21. V. R. Seymour, E. C. Pearson, R. E. Morris and S. E. Ashbrook, *8th Alpine Conference on Solid-State NMR*, Chamonix-Mont Blanc, France, **2013**.

22. O. Baumgartner, A. Preisinger, P. W. Krempl and H. Mang, *Z. Kristallogr.*, **1984**, *168*, 83.

23. G. L. Turner, K. A. Smith, R. J. Kirkpatrick and E. Oldfield, *J. Magn. Reson.*, **1986**, *70*, 408.

24. C. Martineau, B. Bouchevreau, Z. Tian, S.-J. Lohmeier, P. Behrens and F. Taulelle, *Chem. Mater.*, **2011**, *23*, 4799.

25. C. Martineau, C. Mellot-Draznieks and F. Taulelle, *Phys. Chem. Chem. Phys.*, **2011**, *13*, 18078.

26. H. Y. Playford, A. C. Hannon, E. R. Barney and R. I. Walton, *Chem. Eur. J.*, **2013**, *19*, 2803.

7 SUMMARY

This thesis has demonstrated the use of a combination of solid-state NMR spectroscopy, chemical synthesis (including isotopic enrichment), and first-principles DFT calculations to provide insight into the local structures of a number of microporous inorganic materials.

The first class of materials studied was MOFs, in which the presence of paramagnetic ions was found to have a range of effects on the ^{13}C NMR spectra, depending on the nature of the interactions between the nuclei and unpaired electrons. In the MOFs based on Cu^{2+} dimers, HKUST-1 and STAM-1, large isotropic shifts of up to ~850 ppm were observed for ^{13}C, as well as rapid T_1 and T_2 relaxation. In the CPO-27 series, which contains chains of metal ions, very large isotropic shifts were observed, as well as much larger paramagnetic shift anisotropies, owing to the interaction of each carbon nucleus with a large number of unpaired electrons. Again, T_1 and T_2 relaxation were very rapid. In the final series of MOF studied, the lanthanide-based Ln(btc)(dmu)$_2$, T_1 and T_2 relaxation were still rapid (for Ln = Nd), but only small isotropic and anisotropic effects were observed, owing to the limited through-bond interactions between lanthanide ions and their ligands and leaving only the through-space interactions.

The synthesis of H_3btc with selective ^{13}C labelling, and the corresponding ^{13}C-labelled MOFs, allowed the ^{13}C NMR spectra of HKUST-1 and STAM-1 to be assigned fully and unambiguously. Following the assignment of the spectra, it was shown that the isotropic shift of the resonance for the Cu-bound carboxylate groups appears to be a sensitive probe of the nature of the other Cu-bound guest species, potentially allowing natural-abundance ^{13}C NMR spectra to be used to probe the host-guest interactions within MOFs. The isotopic labelling schemes reported here could also be extended to Nd(btc)(dmu)$_2$, enabling a greater understanding of the ^{13}C NMR spectrum and, consequently, the structure of the MOF.

The second class of materials studied was AlPOs. It was shown that the (generally accurate) NMR parameters calculated by DFT could rapidly be predicted with experimentally-relevant accuracy using simple relationships with structural

parameters (*e.g.*, bond lengths and angles). While this work requires some extension to include as-prepared and guest-loaded systems, the principles demonstrated here indicate that an accuracy comparable to DFT-level calculations can be achieved for the NMR parameters of even very large systems on the timescale of seconds, offering the possibility to complement high-throughput structural calculations with high-throughput NMR calculations – an advance that would allow direct comparison of structural models with experiment in applications such as catalysis. A version of the DIStortion analysis COde (DISCO), capable of calculating the NMR parameters for calcined AlPOs is included in the supplementary material for this thesis.

The ambient hydration of JDF-2 to AlPO-53(A) – an unusual process, where guest species are adsorbed into the pores of an AlPO already containing the SDA – was investigated, and observed to occur slowly, with incomplete hydration after ~3 months. The resulting structure of AlPO-53(A) was observed to be disordered and a series of DFT calculations on possible models for the disorder revealed that it is likely that the published orientations of the methylammonium species are incorrect. However, a detailed description of the disorder was not obtained, owing to the significant computational cost of structural optimisation for each model. Further theoretical (*e.g.*, AIRSS or MD calculations) and experimental (including ^{27}Al-^{31}P and ^{13}C-^{15}N correlations, isotopic enrichment and variable-temperature NMR) work is planned in order to achieve an understanding of the disorder present in AlPO-53(A). These studies are likely to provide valuable insight into the behaviour of small molecules (here H_2O and methylammonium) within the pores of the material.

The third class of materials studied was GaPOs, particularly GaPO-34 and related materials. The two as-prepared forms of GaPO-34, GaPO-34[miHF] and GaPO-34[pyHF], were characterised by multinuclear solid-state NMR, and their calcination to GaPO-34(calcined) investigated by TGA and *in-situ* powder XRD. It was observed that the intermediate dehydrofluorinated phase, GaPO-34[mi] exists between ~325-400 °C when GaPO-34[miHF] is heated, while no such intermediate is observed for GaPO-34[pyHF]. The intermediate was characterised by multinuclear solid-state NMR and some structural models were discussed. However, its precise structure remains unclear. The calcined material was observed to be stable under

anhydrous conditions, but to hydrate rapidly to GaPO-34(calcined, hydrated) when exposed to air. The hydrated material was shown also to be stable under ambient conditions, but to collapse upon heating in an attempt to dry the material, yielding instead the amorphous GaPO-34(collapsed). Partial dehydration without collapse was achieved by both gentle heating of the material, and evacuation of the material at room temperature. This indicates that the calcined GaPO-34 framework is stable to both heating and moisture, when applied separately, but not simultaneously.

This work has provided valuable insight into the phase transitions present in GaPOs. In particular, the relatively low-temperature dehydrofluorination process is very rare in microporous materials, and has not yet been identified in the literature for GaPOs. It is also generally assumed that hydration alone is sufficient to cause collapse of calcined GaPOs, whereas it was demonstrated here that GaPO-34(calcined, hydrated) exhibits long-term stability, providing it is not heated. The development of procedures for drying calcined, hydrated GaPOs would open up this class of materials to many potential industrial applications.

The impurity phases, $GaPO_4$ berlinite and GaPO-X (containing miHF or pyHF) were synthesised and investigated by multinuclear solid-state NMR. While the structure of GaPO-X was not determined completely, much structural information has been determined from the solid-state NMR experiments, including the presence of three distinct types of bridging fluoride, the fact that the SDAs are protonated and disordered, and the fact that GaPO-X is a single phase (although both GaPO-X[miHF] and GaPO-X[pyHF] were observed to contain some impurities). Calcination of GaPO-X was studied by TGA, and it would appear that the process is more complicated than for GaPO-34, with heating to 1000 °C for ~3 h required to remove all of the SDA and HF, perhaps indicating multiple SDA environments or smaller pore windows. Structural characterisation of GaPO-X is an important step to understanding the roles of the SDAs in the synthesis of GaPO-34/GaPO-X, and whether the synthesis can be optimised to provide pure GaPO-34 and GaPO-X, or whether the two phases are too structurally similar to allow this.

APPENDIX A. EXTENDED FIGURE CAPTIONS

The following figure captions provide full NMR experimental details for the spectra shown in the relevant figures. Unless otherwise stated, all pulses were applied with $\nu_1 \approx 100$ kHz. The match condition for CP experiments and any pulses or delays involved in the decoupling sequences used were experimentally optimised prior to recording the reported spectra.

Figure 1.4. (b) ^{27}Al (14.1 T, 20 kHz MAS) NMR spectrum of AlPO-14 containing isopropylammonium hydroxide as the SDA/anion pair. The spectrum was recorded with signal averaging for 128 transients with a repeat interval of 10 s.

Figure 2.10. (d) ^{13}C (9.4 T) NMR spectrum of a static sample of 1[^{13}C]-glycine, recorded with signal averaging for 3424 transients with a repeat interval of 10 s.

Figure 2.13. (d) ^{13}C (14.1 T, 12.5 kHz CP MAS) NMR spectrum of solid H_3btc, recorded with signal averaging for 3072 transients with a repeat interval of 3 s. A spin-lock period of 1 ms was used, with a ramped pulse (90-100%) applied to ^{1}H. Decoupling of ^{1}H was achieved using the TPPM-15 decoupling sequence with $\nu_1 \approx$ 100 kHz in both cases.

Figure 2.18. (a) Experimental (14.1 T) and simulated ^{27}Al and ^{31}P NMR spectra for calcined AlPO-14. The ^{27}Al NMR spectrum was recorded with 10 kHz MAS. Signal averaging was carried out for 32 transients with a repeat interval of 1 s. The ^{31}P NMR spectrum was recorded with 14 kHz MAS. Signal averaging was carried out for 4 transients with a repeat interval of 30 s. Simulated spectra use NMR parameters calculated for the experimental and optimised structures, as indicated.

Figure 3.1. (b) The effects of MAS at the indicated rotation rate on the ^{119}Sn spectrum of SnO_2 (14.1 T). Spectra were recorded with signal averaging carried out for 32 transients with a repeat interval of 30 s.

Figure 3.2. The ^{13}C (9.4 T) NMR spectrum of 1[^{13}C]-glycine with (a) no resolution enhancement, (b) TPPM-15 decoupling ($\nu_1 \approx 50$ kHz), (c) 6 kHz MAS, (d) 6 kHz MAS and TPPM-15 decoupling ($\nu_1 \approx 50$ kHz). Insets in parts (c) and (d) show the isotropic resonance and asterisks are denoted by spinning sidebands. All spectra were recorded with signal averaging carried out for 3424 transients with a repeat interval of 10 s.

Figure 3.3. (a) ^{71}Ga NMR spectra of a static sample of $GaPO_4$ berlinite recorded at B_0 field strengths of 14.1 T and 20.0 T. Spectra were recorded using a spin-echo pulse sequence with τ delays of 18.6 μs (14.1 T) and 20 μs (20.0 T). Signal averaging was carried out for 7168 (14.1 T) and 1776 (20.0 T) transients with a repeat interval of 0.5 s (14.1 T) or 3 s (20.0 T).

Figure 3.4. (a) ^{27}Al (9.4 T, 12.5 kHz MAS) NMR spectrum of the AlPO, SIZ-4. The spectrum was recorded with signal averaging for 128 transients with a repeat interval of 5 s. The pulse length was experimentally optimised to provide maximum excitation of the resonances arising from the STs. (b) ^{71}Ga (20.0 T) NMR spectrum of $GaPO_4$ berlinite, acquired with and without MAS (60 kHz). Spectra were recorded using a spin-echo pulse sequence with τ delays of 20 μs (static) and 33.33 μs (MAS). Signal averaging was carried out for 1776 (static) and 3696 (MAS) transients with a repeat interval of 3 s (static) or 1 s (MAS).

Figure 3.5. (a) The pulse sequence and coherence transfer pathway for a z-filtered amplitude-modulated MQMAS experiment, shown here for 3QMAS. (b) The ^{87}Rb (14.1 T, 20 kHz 3QMAS) NMR spectrum of RbNO3, acquired using the experiment shown in part (a). The spectrum was recorded with signal averaging for 96 transients for each of 256 t_1 increments of 50 μs with a repeat interval of 250 ms. Excitation and conversion pulses were applied with $\nu_1 \approx 120$ kHz and the CT-selective pulse had $\nu_1 \approx 8$ kHz. (c) The spectrum shown in part (b) after a shearing transformation has been applied. In parts (b) and (c) the sum projections perpendicular to δ_1 and δ_2 are shown.

Figure 3.7. (a) The pulse sequence and coherence transfer pathway for a split-t_1 shifted-echo phase-modulated MQMAS experiment, shown here for 3QMAS for I = 3/2 (top) and I > 3/2 (below), where k and k' depend on I. (b) The ^{87}Rb (14.1 T, 20 kHz MAS) 3QMAS NMR spectrum of $RbNO_3$, acquired using the experiment shown in (a). The projections perpendicular to δ_1 and δ_2 are shown. The spectrum was recorded with signal averaging for 96 transients for each of 96 t_1 increments of 158.33 μs with a repeat interval of 250 ms. Excitation and conversion pulses were applied with $\nu_1 \approx 120$ kHz and the CT-selective pulse had $\nu_1 \approx 8$ kHz. (c) Cross-sections parallel to δ_2, extracted from the spectrum in (b) Fits to the cross-sections are shown in red, with $\delta_{iso} = -30.9$ ppm, $C_Q = 1.62$ MHz, $\eta_Q = 0.6$ for Rb1, $\delta_{iso} = -28.1$ ppm, $C_Q = 2.06$ MHz, $\eta_Q = 0.9$ for Rb2, and $\delta_{iso} = -26.6$ ppm, $C_Q = 1.63$ MHz, $\eta_Q = 0.3$ for Rb3.

Figure 3.8. (c) Experimental CP build-up curves for L-alanine (9.4 T, 10 kHz MAS). Spectra were recorded with signal averaging for 256 transients with a repeat interval of 3 s. A ramped pulse (90-100%) applied to ^{1}H during spin locking. Decoupling of ^{1}H was achieved using the TPPM-15 decoupling sequence with $\nu_1 \approx 80$ kHz.

Figure 3.10. ^{71}Ga (static, 14.1 T) NMR spectrum of $GaPO_4$ berlinite, acquired using (b) the spin echo pulse sequence and (c) the CPMG pulse sequence with $1/\tau = 3$ kHz (black line). The spectra in parts (b) and (c) were both recorded with signal averaging carried out for 7168 transients with a repeat interval of 0.5 s. In both experiments, $\nu_1 \approx 120$ kHz. 200 pulses were applied in the CPMG echo train.

Figure 4.5. ^{13}C (14.1 T, 12.5 kHz CP MAS) NMR spectra of (a) STAM-1 and (b) HKUST-1. Spectra were recorded with signal averaging for 6144 transients for STAM-1 and HKUST-1, respectively, with a repeat interval of 3 s (STAM-1) or 1 s (HKSUT-1). A spin-lock period of 1 ms was used, with a ramped pulse (90-100%) applied to ^{1}H. Decoupling of ^{1}H was achieved using SPINAL-32 and TPPM-15 decoupling sequences for STAM-1 and HKUST-1, respectively, with $\nu_1 \approx 100$ kHz in both cases.

Figure 4.6. ^{13}C (60 kHz MAS) spin-echo NMR spectra of as-made (a) HKUST-1 and (b) STAM-1. Spectra were recorded using a spin-echo pulse sequence with a rotor-synchronised delay of 16.67 μs. Signal averaging was carried out for 327,680 transients with a repeat interval of 20 ms.

Figure 4.7. (a) Expansion of the spectrum from Figure 4.6(a). (b) ^{13}C (14.1 T, 60 kHz MAS) NMR spectrum of HKUST-1 (c) ^{13}C (14.1 T, 60 kHz MAS) NMR spectrum of STAM-1. Spectra in (b) and (c) were recorded using a spin-echo pulse sequence with a rotor-synchronised delay of 16.67 μs. Signal averaging was carried out for 2,010,112 (HKUST-1) and 2,160,000 (STAM-1) transients with a repeat interval of 20 ms. In both cases, the transmitter frequency was at 850 ppm. Spectra were processed with 500 Hz Lorentzian broadening.

Figure 4.8. ^{13}C (14.1 T, 60 kHz MAS) NMR spectra of (a) HKUST-1 and (b) STAM-1, recorded using a spin-echo pulse sequence with a rotor-synchronised delay of 16.67 μs. For each sub-spectrum, signal averaging was carried out for 327,680 transients with a repeat interval of 20 ms. Sub-spectra were recorded with the transmitter offset at 100 and 850 ppm, and coadded after processing. In (a), the individual sub-spectra (grey) are shown the summed spectrum (black).

Figure 4.9. ^{13}C (14.1 T 12.5 kHz CP MAS) NMR spectra of (a) H_3btc and (b) tmbtc. Solution-phase (7.05 T, $(CD_3)_2SO$) ^{13}C NMR spectra of (c) H_3btc and (d) tmbtc. In (c) and (d), the multiplet at 39.52 ppm arises from the solvent and was used to reference the spectra. Spectra in (a) and (b) were recorded with signal averaging for 3072 (H_3btc) and 4096 (tmbtc) transients with a repeat interval of 3 s. A spin-lock period of 1 ms was used, with a ramped pulse (90-100%) applied to ^{1}H. Decoupling of ^{1}H was achieved using the TPPM-15 decoupling sequence with $\nu_1 \approx 100$ kHz in both cases. Spectra in (c) and (d) were recorded with signal averaging for 800 transients with a repeat interval of 1.5 s and an acquisition time of 1.8 s (total time between pulses of 3.3 s). Low-power WALTZ16 decoupling of ^{1}H was applied during acquisition.

Figure 4.10. ^{13}C (14.1 T, 11 kHz CP MAS) NMR spectrum of Zn-btc prepared in an attempt to synthesise Zn-HKUST-1. The spectrum was recorded with signal averaging for 1736 transients with a repeat interval of 3 s. A spin-lock period of 1.5 ms was used, with a ramped pulse (90-100%) applied to ^{1}H. Decoupling of ^{1}H was achieved using the TPPM-15 decoupling sequence with $\nu_1 \approx 100$ kHz.

Figure 4.11. Plots of the intensity of the ^{13}C resonances observed for HKUST-1 and STAM-1 in ^{13}C CP MAS NMR spectra with different spin-lock durations. Intensities are plotted relative to spin-echo experiments carried out under comparable conditions. 131072 Spectra were recorded with signal averaging for 131,072 transients with a repeat interval of 20 ms. A ramped spin-locking pulse (90-100%) was applied to ^{1}H. A ^{13}C spin echo with a rotor-synchronised delay of 16.67 μs was applied between polarisation transfer and acquisition to refocus broader resonances.

Figure 4.12. ^{13}C (14.1 T, 60 kHz MAS) NMR spectra of (a) $^{13}C(2)$-HKUST-1, (b) $^{13}C(2,6)$-STAM-1, (c) $^{13}C(1,3)$-HKUST-1 and (d) $^{13}C(1,3,4,5)$-STAM-1.In (b) and (d), the insets show the region between 190 and 160 ppm for the labelled (black) and natural-abundance (grey) MOFs. All spectra are the sum of two sub-spectra recorded with the transmitter offset at 100 and 850 ppm. Spectra were recorded using a spin-echo pulse sequence with a rotor-synchronised delay of 16.67 μs. For each sub-spectrum, signal averaging was carried out for (a and b) 32,768 and (c and d) 40,960 transients with a repeat interval of 100 ms. The insets in (b) and (d) are from the spectrum in Figure 4.8(b).

Figure 4.14. ^{1}H (14.1 T, 60 kHz MAS) NMR spectra of (a) HKUST-1 and (b) STAM-1. ^{1}H-^{13}C (14.1 T, 50 kHz MAS) CP-HETCOR spectra of (c) HKUST-1 and

(d) STAM-1. Spectra in (a) and (b) were recorded using a spin-echo pulse sequence with a rotor-synchronised delay of 16.67 μs. Signal averaging was carried out for 256 transients with a repeat interval of 20 ms. The spectrum in (c) was recorded with signal averaging for 45,056 transients with a repeat interval of 40 ms for each of 30 t_1 increments of 40 μs. The spectrum in (d) was recorded with signal averaging for 40,960 transients with a repeat interval of 40 ms for each of 40 t_1 increments of 40 μs. In (a), resonances marked † are commonly observed in spectra recorded for samples packed in 1.3 mm rotors, where small amounts of contaminants in the rotor end caps can lead to moderately intense resonances.

Figure 4.15. ^{13}C NMR spectra of (a) HKUST-1 and (b) STAM-1 recorded at B_0 field strengths of 14.1 T (60 KHz MAS, 327680 transients for each of 2 sub-spectra) and 20.0 T (58 kHz MAS, 65536 transients for each of 5 sub-spectra). Spectra were recorded using a spin-echo pulse sequence with a rotor-synchronised delay of 16.67 μs (60 kHz) or 17.24 μs (58 kHz) and a repeat interval of 100 ms.

Figure 4.16. Plots of the isotropic positions of the resonances observed for (a) C1, (b) C2 and (c) C3 in HKUST-1 against 1000/T. Data from the two different series of temperature measurements are shown as open (shim temperature controlled) and filled (no shim temperature control) points. Spectra were recorded with (a) signal averaging for 65536 (shim temperature controlled) or 131072 (no shim temperature control) transients with a repeat interval of 20 ms, and (b and c) signal averaging for 20480 transients with a repeat interval of 100 ms (shim temperature controlled) or 65536 transients with a repeat interval of 25 ms (no shim temperature control). All spectra were recorded at 60 kHz MAS using a spin-echo pulse sequence with a rotor-synchronised echo of 16.67 μs. Spectra were recorded with the transmitter offset to (a) 850 ppm and (b and c) 100 ppm.

Figure 4.19. Plots of the isotropic positions of the resonances observed for (a) C2, (b) C3, (c) C4, (d) C5, (e) C6 and (f) C7 in STAM-1 against 1000/T. Data from the two series of experiments are shown as open (shim temperature controlled) and filled (no shim temperature control) points. In parts (a and b), trend lines are plotted for the combined data set. The point shown in grey in part (b) was excluded from the calculation of the trend line. Spectra were recorded with signal averaging for 32768 transients with a repeat interval of 100 ms (shim temperature controlled) or 65536 transients with a repeat interval of 25 ms (no shim temperature control). All spectra were recorded at 60 kHz MAS using a spin-echo pulse sequence with a rotor-synchronised delay of 16.67 μs. The transmitter offset was 100 ppm for all spectra.

Figure 4.20. ^{1}H (20.0 T, 60 kHz MAS) NMR spectra of (a) HKUST-1 and (b) STAM-1 recorded at the indicated temperature. (c) Plot of the isotropic shifts of H3 in HKUST-1 against 1/T. All spectra were recorded with signal averaging for 128 transients with a repeat interval of 100 ms.

Figure 4.22. ^{13}C (14.1 T, 60 kHz MAS) NMR spectra of (a) deh-HKUST-1, (b) deh-STAM-1, (c) HKUST-1[H_2O] and (d) STAM-1[H_2O]. Spectra were recorded as two sub-spectra with signal averaging for (a and b) 51200 or (c and d) 102400 transients per sub-spectrum with repeat intervals of (a and c) 100, (b) 50, and (d) 20 ms. A spin-echo pulse sequence was used with a rotor-synchronised echo of 16.67 μs. The transmitter offsets for the two sub-spectra were 100 and 850 ppm.

Figure 4.23. ^{13}C (14.1 T, 60 kHz MAS) NMR spectra of (a) HKUST-1[H_2O], (b) HKUST-1[MeOH] and (c) HKUST-1[EtOH]. Spectra were recorded as two sub-spectra with signal averaging for (a) 102400 or (b and c) 51200 transients per sub-spectrum with a repeat interval of 100 ms. A spin-echo pulse sequence was used with a rotor-synchronised echo of 16.67 μs. The transmitter offsets for the two sub-spectra were 100 and 850 ppm.

Figure 4.24. (a) ^{13}C (14.1 T, 60 kHz MAS) NMR spectrum of HKUST-1[NO]. ^{13}C (14.1 T, 14 kHz MAS) NMR spectra of HKUST-1[NO] (d) before and (e) after exposure to moist air for a week. The spectra in (d and e) are plotted on the same vertical intensity scale. (f) ^{13}C (14.1 T, 60 kHz MAS) NMR spectrum of STAM-1[NO]. Spectra were recorded with signal averaging for (a, d and e) 102400 and (f) 65536 transients with a repeat interval of 100 ms. Spectra in (a and f) are the result of coadding two sub-spectra with the transmitter offset to 100 and 850 ppm, while spectra in (d and e) were recorded with the transmitter offset to 40 ppm. A spin-echo pulse sequence with a rotor-synchronised echo of (a and f) 16.67 or (d and e) 71.43 μs was used.

Figure 4.25. ^{13}C (14.1 T, 60 kHz MAS) NMR spectra of (a) HKUST-1[metro], (b) HKUST-1[metro+NO] and (c) HKUST-1[metro+H_2O]. (d) ^{13}C (14.1 T, 12.5 kHz CP MAS) NMR spectrum of solid metro. Spectra in were recorded with signal averaging for (a) 782336, (b) 364544, (c) 131072 and (d) 3072 transients with a repeat interval of (a) 0.05, (b) 0.2, (c) 0.1 and (d) 3 s. In (a-c) a spin-echo pulse sequence was used with a rotor-synchronised echo of 16.67 μs. In (d) cross polarisation from ^{1}H (5 ms spin lock) was employed, with a ramped spin-locking pulse (90-100%) applied to ^{1}H. TPPM-15 decoupling of ^{1}H was applied during acquisition (d only).

Figure 4.28. ^{2}H (14.1 T) NMR spectra of (a) ^{2}H(3)-HKUST-1 and (b) deh-^{2}H(3)-HKUST-1 recorded with (a) 10 or (b) 15 kHz MAS and static samples. The MAS NMR spectra were recorded with signal averaging for (a) 8192 and (b) 4096 transients with a repeat interval of (a) 0.25 and (b) 0.5 s. A spin-echo pulse sequence was used with a rotor-synchronised echo of (a) 100 and (b) 66.67 μs. Prior to acquisition of the spectra, the magic angle was set by minimising the linewidths of the ^{2}H SSBs of deuterated oxalic acid ($C_2O_4D_2.2D_2O$). Static spectra were recorded with signal averaging for (a) 33792 and (b) 58208 transients with a repeat interval of 0.25 s. A quadrupolar echo pulse sequence was used with an echo of 6 μs.

Figure 4.29. ^{2}H (14.1 T) NMR spectra of ^{2}H(7)-STAM-1, recorded with 5 kHz MAS (left) and a static sample (right). The spectra were recorded with signal averaging for 4096 (MAS) and 52352 (static) transients with a repeat interval of 0.5 (MAS) and 1 (static) s. The MAS spectrum as recorded using a spin-echo pulse sequence with a rotor-synchronised delay of 200 μs. The static spectrum was recorded using a quadrupolar echo pulse sequence with an delay of 5 μs. Prior to acquisition of the spectra, the magic angle was set by minimising the linewidths of the ^{2}H SSBs of $C_2O_4D_2.2D_2O$.

Figure 4.31. ^{13}C (14.1 T, 12.5 kHz CP MAS) NMR spectra of (a) CPO-27-Mg, (b) CPO-27-Zn and (c) CPO-27-Zn-[MeOH]. Spectra were recorded with signal averaging for (a) 3072, (b) 1704 and (c) 4096 transients with a repeat interval of (a and c) 3 and (b) 5 s. Cross polarisation from ^{1}H (1 ms spin lock) was employed, with a ramped spin-locking pulse (90-100%) applied to ^{1}H. TPPM-15 decoupling of ^{1}H (ν_1 ~72 kHz) was applied during acquisition.

Figure 4.32. CP build-up behaviour of the ^{13}C resonances observed for (a) CPO-27-Mg and CPO-27-Zn. Spectra were recorded at (a) 14.1 and (b) 9.4 T with signal averaging for 3072 transients with repeat intervals of (a) 3 and (b) 4 s. During cross polarisation a ramped spin-locking pulse (90-100%) was applied to ^{1}H. TPPM-15 decoupling of ^{1}H was applied during acquisition.

Figure 4.33. ^{1}H-^{13}C INEPT correlation spectrum of CPO-27-Mg (14.1 T, 12.5 kHz MAS), recorded with signal averaging for 80 transients with a repeat interval of 3 s for each of 140 t_1 increments of 161.41 μs. Homonuclear decoupling of ^{1}H during t_1 was achieved using the eDUMBO22$_1$ scheme, and heteronuclear decoupling of ^{1}H during acquisition was achieved using TPPM-15.

Figure 4.35. ^{1}H (14.1 T, 60 kHz MAS) NMR spectra of (a) CPO-27-Zn and (b) CPO-27-Zn[MeOH], recorded with signal averaging for 8 transients with a repeat interval of 3 s.

Figure 4.36. ^{1}H and ^{13}C (14.1 T, 60 kHz MAS) NMR spectra of (a) CPO-27-Ni, (b) CPO-27-Co and (c) CPO-27-Mn. ^{13}C NMR spectra were acquired with frequency stepping over 6 steps of 75 kHz (CPO-27-Ni) and with a single frequency step for CPO-27-Co and CPO-27-Mn. For ^{1}H, signal averaging was carried out for (a) 512 or (b and c) 1024 transients with a repeat interval of 100 ms. For ^{13}C, signal averaging was carried out for (a) 131072, (b) 200000 and (c) 94896 transients with a repeat interval of (a) 50, (b) 20 and (c) 250 ms (per sub-spectrum, in (a)). In all cases, a spin-echo pulse sequence was used with a rotor-synchronised delay of 16.67 μs.

Figure 4.37. ^{13}C (14.1 T) NMR spectra of CPO-27-Ni acquired with (a) 60 kHz and (b) 50 kHz MAS. Resonances believed to be the isotropic resonances are indicated with dots. Spectra were acquired as a series of sub-spectra, with signal averaging for 131072 transients with a repeat interval of 50 ms for each sub –spectrum. The transmitter offsets for the sub-spectra were –1400, –700, 0, 700, 1400 and 2100 ppm (steps of ~106 kHz) and ν_1 was 125 kHz. Sub-spectra were recorded using a spin-echo pulse sequence with rotor-synchronised delays of (a) 16.67 and (b) 20 μs.

Figure 4.39. (a) ^{13}C (14.1 T, 12.5 kHz CP MAS) NMR spectrum of La(btc)(dmu)$_2$, recorded with signal averaging for 6144 transients with a repeat interval of 5 s. Cross polarisation from ^{1}H (1 ms spin lock) was employed, with a ramped spin-locking pulse (90-100%) applied to ^{1}H. CW decoupling of ^{1}H was applied during acquisition.

Figure 4.40. ^{13}C NMR spectrum of Nd(btc)(dmu)$_2$, recorded at (a) 14.1 T with 60 kHz MAS and (b) 20.0 T with 62.5 kHz MAS. Spectra were recorded with signal averaging for (a) 467968 and (b) 262144 transients with a repeat interval of 100 ms. A spin-echo pulse sequence was used with a rotor-synchronised delay of (a) 16.67 and (b) 16 μs.

Figure 5.27. ^{31}P (14.1 T, 12.5 kHz MAS) NMR spectra of JDF-2 and AlPO-53(A), recorded with signal averaging for 2 transients with a repeat interval of 1200 s.

Figure 5.28. (a) The conversion of JDF-2 to AlPO-53(A), expressed as x_A, against time. (b) The ^{31}P (14.1 T, 12.5 kHz MAS) NMR spectra of the mixture of JDF-2 and AlPO-53(A) obtained after hydration of JDF-2 for the indicated time. Spectra were recorded with signal averaging for 2 transients with a repeat interval of 1200 s.

Figure 5.29. The ^{31}P (14.1 T, 12.5 kHz MAS) NMR spectra of (a) AlPO-53(A), (b) AlPO-53(A) prepared by submerging JDF-2 in water for 7 days. Spectra were recorded with signal averaging for (a) 32 and (b) 2 transients with repeat intervals of (a) 30 and (b) 1200 s.

Figure 5.30. ^{1}H (14.1 T, 60 kHz MAS), ^{13}C (14.1 T, 12.5 kHz CP MAS), ^{15}N (9.4 T, 5 kHz CP MAS) and ^{27}Al (14.1 T, 12.5 kHz MAS) NMR spectra of JDF-2. Spectra were recorded with signal averaging for 8 (^{1}H), 32 (^{27}Al), 512 (^{13}C) or 1600 (^{15}N) transients with repeat intervals of 3 (^{13}C), 5 (^{1}H and ^{27}Al) or 90 (^{15}N) s. Cross polarisation from ^{1}H was employed for the ^{13}C (1 ms spin lock) and ^{15}N (3 ms spin lock) spectra, with a ramped spin-locking pulse (90-100%) applied to ^{1}H. For both spectra, TPPM-15 decoupling of ^{1}H was applied during acquisition. The ^{15}N FID was truncated, even after 61 ms acquisition, and the spectrum shown was processed with 5 Hz Lorentzian broadening.

Figure 5.31. The ^{1}H (14.1 T, 60 kHz DQMAS) NMR spectrum of JDF-2. The spectrum was recorded with signal averaging for 16 transients for each of 300 t_1 increments of 16.67 μs with a repeat interval of 5 s. DQCs were created and reconverted using one block of BABA pulses.

Figure 5.32. (a) ^{27}Al (14.1 T, 14 kHz 3QMAS) NMR spectrum of JDF-2, recorded using a shifted-echo split-t_1 pulse sequence. Signal averaging was carried out for 288 transients with a 1 s repeat interval for each of 120 t_1 increments of 142.8 μs. The delay used to allow acquisition of a whole echo was 6.5 ms.

Figure 5.33. ^{1}H (14.1 T, 60 kHz MAS), ^{13}C (14.1 T, 12.5 kHz CP MAS), ^{15}N (9.4 T, 5 kHz CP MAS) and ^{27}Al (14.1 T, 14 kHz MAS) NMR spectra of AlPO-53(A). Spectra were recorded with signal averaging for 8 (^{1}H), 16 (^{27}Al), 512 (^{13}C) or 29696 (^{15}N) transients with repeat intervals of 2 (^{27}Al) or 3 (^{1}H, ^{13}C and ^{15}N) s. Cross polarisation from ^{1}H was employed for the ^{13}C (1 ms spin lock) and ^{15}N (3 ms spin lock) spectra, with a ramped spin-locking pulse (90-100%) applied to ^{1}H. For both spectra, TPPM-15 decoupling of ^{1}H was applied during acquisition. The ^{15}N FID was truncated, even after 61 ms acquisition, and the spectrum shown was processed with 2.5 Hz Lorentzian broadening.

Figure 5.34. ^{1}H (14.1 T, 60 kHz DQMAS) NMR spectrum of AlPO-53(A). The spectrum was recorded with signal averaging for 16 transients for each of 266 t_1 increments of 33.33 μs with a repeat interval of 3 s. DQCs were created and

reconverted using one block of BABA pulses.

Figure 5.35. ^{1}H-^{13}C (14.1 T, 12.5 kHz MAS) J-transferred INEPT spectrum of AlPO-53(A), recorded with signal averaging for 224 transients with a repeat interval of 3 s for each of 80 t_1 increments of 161.41 μs. Homonuclear decoupling of ^{1}H during t_1 was achieved using the eDUMBO22$_1$ scheme, and heteronuclear decoupling of ^{1}H during acquisition was achieved using TPPM-15.

Figure 5.36. The ^{27}Al (14.1 T, 14 kHz 3QMAS) NMR spectrum of AlPO-53(A), recorded using a z-filtered pulse sequence, and then sheared as described in Chapter 3. Signal averaging was carried out for 192 transients with a repeat interval of 1.5 s for each of 144 t_1 increments of 71.43 μs.

Figure 5.37. ^{31}P (14.1 T, 10 kHz DQMAS) NMR spectrum of AlPO-53(A), recorded with signal averaging for 32 transients with a repeat interval of 30 s for each of 84 t_1 increments of 100 μs. DQCs were excited and converted using 4 rotor periods (400 μs, 28 blocks) POST-C7 pulses with ν_1 = 70 kHz. Correlations between the four main resonances are indicated by solid red lines and between the main resonances and those at –15.0 and –18 to –20 ppm are indicated with broken lines. The $\delta_{DQ} = 2\delta_{SQ}$ diagonal is indicated in grey.

Figure 6.2. (a) ^{31}P (14.1 T, 25 kHz MAS), (b) ^{71}Ga (14.1 T, 28 kHz MAS), (c) ^{71}Ga (20.0 T, 30 kHz MAS) and (d), ^{71}Ga (20.0 T, 30 kHz MAS) sheared z-filtered 3QMAS NMR spectra of GaPO-34[miHF] and GapO-34[pyHF]. Spectra were recorded with signal averaging for (a) 8 (GaPO-34[miHF]) or 16 (GaPO-34[pyHF]) transients with a repeat interval of 60 s, (b and c) 1024 transients with a repeat interval of 0.5 s and (d) 480 (GaPO-34[miHF]) or 120 (GaPO-34[pyHF]) transients with a repeat interval of 0.5 s for each of 136 t_1 increments of 3.33 (GaPO-34[miHF]) or 5 (GaPO-34[pyHF]) μs. Spectra in (b and c) were recorded using a spin-echo pulse sequence with rotor synchronised delays of 35.71 and 33.33 μs, respectively.

Figure 6.3. ^{69}Ga (20.0 T, 62.5 kHz MAS) NMR spectra of (a) GaPO-34[miHF] and (b) GaPO-34[pyHF], recorded using a spin-echo pulse sequence with a rotor-synchronised delay of 16 μs. Signal averaging was carried out for 8192 transients with a repeat interval of 0.5 s.

Figure 6.4. (a) ^{1}H (14.1 T, 60 kHz MAS) (b) ^{13}C (14.1 T, 12.5 kHz CP MAS) and (c) ^{19}F (14.1 T, 55 kHz MAS) NMR spectra of GaPO-34[miHF] and GaPO-34[pyHF].

Spectra were recorded with signal averaging for (a) 32, (b) 576 (GaPO-34[miHF]) or 384 (GaPO-34[pyHF]) and (c) 64 transients with repeat intervals of (a) 3 and (b and c) 5 s. Cross polarisation from ^{1}H (1 ms spin lock) was employed for the ^{13}C NMR spectrum with a ramped spin-locking pulse (90-100%) applied to ^{1}H. TPPM-15 decoupling of ^{1}H (ν_1 ~110 kHz) was applied during acquisition.

Figure 6.5. (a) ^{1}H (14.1 T, 60 kHz DQMAS) NMR spectra of GaPO-34[miHF] and GaPO-34[pyHF], recorded with signal-averaging for 64 transients for each of 300 (GaPO-34[miHF]) or 96 (GaPO-34[pyHF]) t_1 increments of 16.67 (GaPO-34[miHF] or 33.33 μs (GaPO-34[pyHF]). DQCs were excited and converted using one block of BABA pulses. (b) ^{1}H-^{13}C (14.1 T, 50 kHz MAS) CP HETCOR NMR spectra of GaPO-34[miHF] and GaPO-34[pyHF], recorded with signal-averaging for 2048 transients for each of 26 (GaPO-34[miHF]) or 48 (GaPO-34[pyHF]) t_1 increments of 80 μs. Cross polarisation with a ramped spin-locking pulse (90-100%) applied to ^{1}H was used to transfer magnetisation to ^{13}C, with a spin-lock duration of 250 (GaPO-34[miHF]) or 200 (GaPO-34[pyHF] μs. CW decoupling of ^{1}H (ν_1 ~10 kHz) was applied during acquisition.

Figure 6.6. (b) the ^{1}H(DQ)-^{13}C (14.1 T, 50 kHz MAS) CP HETCOR NMR spectrum of GaPO-34[pyHF], recorded with signal averaging for 4096 transients with a repeat interval of 1.5 s for each of 24 t_1 increments of 40 μs. Cross polarisation with a ramped spin-locking pulse (90-100%) applied to ^{1}H was used to transfer magnetisation to ^{13}C, with a spin-lock duration of 250 μs. CW decoupling of ^{1}H (ν_1 ~10 kHz) was applied during acquisition.

Figure 6.8. (a) ^{31}P (14.1 T, 25 kHz MAS) NMR and (b) ^{71}Ga (20.0 T, 30 kHz MAS) NMR spectra of GaPO-34(calcined), recorded with signal averaging for (a) 8 and (b) 192 transients with a repeat interval of 3 s.

Figure 6.9. ^{31}P NMR spectra of (a) GaPO-34[miHF] after heating to 330 °C (14.1 T, 25 kHz MAS) and (b) the same sample after exposure to ambient moisture (9.4 T, 10 kHz MAS). Spectra were recorded with signal averaging for (a) 8 and (b) 16 transients with a repeat interval of (a) 300 and (b) 10 s. The spectrum in (b) was recorded using a spin-echo pulses sequence with a rotor-synchronised delay of 100 μs. In (a), the resonance assigned to GaPO-34(calcined) is marked †.

Figure 6.10. ^{71}Ga (20.0 T, 60 kHz MAS) NMR spectrum of GaPO-34[miHF] after heating to 330 °C, followed by exposure of the sample to ambient moisture. The

spectrum was recorded using a spin-echo pulse sequence with a rotor-synchronised delay of 16.67 μs. Signal averaging was carried out for 4096 transients with a repeat interval of 0.5 s.

Figure 6.11. ^{19}F (14.1 T, 50 kHz MAS) NMR spectrum of GaPO-34[mi], recorded using a spin-echo pulse sequence with a rotor-synchronised delay of 20 μs. Signal averaging was carried out for 128 transients with a repeat interval of 10 s.

Figure 6.12. (a) ^{1}H (14.1 T, 60 kHz MAS), (b) ^{1}H (14.1 T, 60 kHz DQMAS) and (c) ^{13}C (14.1 T, 12.5 kHz CP MAS) NMR spectra of GaPO-34[mi]. Spectra were recorded with signal averaging for (a) 256, (b) 32 and (c) 1024 transients with repeat intervals of (a and c) 3 and (b) 1 s. In (b), 300 t_1 increments of 16.67 μs were recorded, with DQCs excited and converted using one rotor period of BABA pulses. Cross polarisation from ^{1}H (1 ms spin lock) was employed for the ^{13}C NMR spectrum with a ramped spin-locking pulse (90-100%) applied to ^{1}H. TPPM-15 decoupling of ^{1}H (ν_1 ~72 kHz) was applied during acquisition.

Figure 6.16. (a) ^{31}P (14.1 T, 25 kHz MAS) NMR and (b) ^{31}P (14.1 T, 12.5 kHz CP MAS) NMR spectra of GaPO-34(calcined, hydrated). Spectra were recorded with signal averaging for (a) 8 and (b) 512 transients with repeat intervals of (a) 60 and (b) 3 s. In (a), a saturation train was used to reduce the repeat interval required. In (b), cross polarisation from ^{1}H (spin lock durations of 0.25, 1 and 2.5 ms) was employed, with a ramped spin-locking pulse (90-100%) applied to ^{1}H. CW decoupling of ^{1}H (ν_1 ~80 kHz) was applied during acquisition.

Figure 6.17. ^{71}Ga (20.0 T, 62.5 kHz MAS) NMR spectrum of GaPO-34(calcined, hydrated), recorded with signal averaging for 4096 transients with a repeat interval of 0.5 s. A spin-echo pulse sequence was used, with a rotor-synchronised delay of 16 μs.

Figure 6.18. ^{1}H (14.1 T, 60 kHz MAS) NMR spectrum of GaPO-34(calcined, hydrated), recorded with signal averaging for 16 transients with a repeat interval of 3 s. A spin-echo pulse sequence was used, with a rotor-synchronised delay of 16.67 μs.

Figure 6.19. ^{31}P and ^{27}Al (14.1 T, 14 kHz MAS) NMR spectra of calcined AlPO-34 exposed to ambient conditions for the indicated time. Spectra were recorded with signal averaging for 8 (^{31}P, ^{27}Al day 0) or 32 (^{27}Al, all other days) transients with a repeat interval of 30 (^{31}P) or 5 (^{27}Al) s.

Figure 6.20. ^{31}P (20.0 T, 30 kHz MAS) NMR spectra of the same sample of GaPO-34(calcined, hydrated), recorded on different days. Spectra were recorded with signal averaging for 64 (upper spectrum) or 32 (lower spectrum) transients with a repeat interval of 60 s.

Figure 6.23. (a) ^{1}H (14.1 T, 60 kHz MAS), (b) ^{31}P (14.1 T, 20 kHz MAS) and (c) ^{71}Ga (20.0 T, 60 kHz MAS) NMR spectra of GaPO-34(collapsed). Spectra were recorded with signal averaging for (a and b) 16 and (c) 4096 transients with a repeat interval of (a) 3, (b) 120 and (c) 0.5 s. The spectra in parts (a and c) were recorded using a spin-echo pulse sequence, with rotor-synchronised delays of 16.67 μs.

Figure 6.24. ^{31}P (14.1 T, 25 kHz MAS) NMR spectra of GaPO-34(calcined, hydrated) subjected to (a) heating to 45 °C for 2 days, (b) heating to 80 °C for 2 days, (c) heating to 110 °C for 1 day, (d) heating to 110 °C for 2 days and (e) static vacuum for 5 days. Spectra were recorded with signal averaging for (a, b and e) 16 or (c and d) 8 transients with repeat intervals of (a, b, d and e) 120 or (c) 5 s.

Figure 6.25. (b) ^{31}P (14.1 T, 12.5 kHz MAS) and (c) ^{71}Ga (20.0 T, 60 kHz MAS) NMR spectra of $GaPO_4$ berlinite. Spectra were recorded with signal averaging for (b) 8 and (c) 3696 transients with repeat intervals of (b) 30 and (c) 1 s. The ^{71}Ga spectrum as recorded using a spin-echo pulse sequence with a rotor-synchronised delay of 16.67 μs.

Figure 6.27. (a) ^{1}H (14.1 T, 60 kHz MAS), (b) ^{13}C (14.1 T, 12.5 kHz CPMAS), (c) ^{19}F (14.1 T, 55 kHz MAS), (d) ^{31}P (14.1 T, 14 kHz MAS) and (e) ^{71}Ga (20.0 T, 60 kHz MAS) NMR spectra of GaPO-X[miHF]. Spectra were recorded with signal averaging for (a and c) 16, (b) 5120, (d) 32 and (e) 8192 transients with repeat intervals of (a and b) 3, (c) 300, (d) 30 and (e) 0.5 s. The spectra in (a, c and e) were recorded using a spin-echo pulse sequence with rotor-synchronised delays of (a and e) 16.67 and (b) 18.18 μs. In (b), cross polarisation from ^{1}H (1 ms spin lock) was employed, with a ramped spin-locking pulse (90-100%) applied to ^{1}H. TPPM-15 decoupling of ^{1}H (ν_1 ~72 kHz) was applied during acquisition.

Figure 6.28. ^{1}H (14.1 T, 60 kHz DQMAS), NMR spectrum of GaPO-X[miHF], recorded with signal averaging for 16 transients with a repeat interval of 3 s for each of 148 t_1 increments of 16.67 μs. DQCs were excited and converted using one rotor period of BABA pulses.

Figure 6.29. (a) ^{31}P (14.1 T, 10 kHz DQMAS) NMR spectrum of GaPO-X[miHF],

recorded with signal averaging for 48 transients with a repeat interval of 10 s for each of 122 t_1 increments of 100 μs. DQCs were excited and converted using five rotor periods of POST-C7 pulses. A saturation train was employed to reduce the repeat interval.

Figure 6.30. (a) ^{19}F (14.1 T, 55 kHz DQMAS) NMR spectrum of GaPO-X[miHF], recorded with signal averaging for 64 transients with a repeat interval of 30 s for each of 28 t_1 increments of 18.18 μs. DQCs were excited and converted using three rotor periods of BABA pulses. (b) ^{19}F-^{31}P (14.1 T, 50 kHz MAS) CP HETCOR spectrum of GaPO-X[miHF], recorded with signal averaging for 48 transients with a repeat interval of 20 s for each of 82 t_1 increments of 20 μs. The spin lock duration was 2.5 ms.

Figure 6.31. (a) ^{1}H (14.1 T, 60 kHz MAS), (b) ^{13}C (14.1 T, 12.5 kHz CPMAS), (c) ^{19}F (14.1 T, 60 kHz MAS) and (d) ^{31}P (14.1 T, 10 kHz MAS) NMR spectra of GaPO-X[pyHF]. Spectra were recorded with signal averaging for (a, c and d) 16 and (b) 4096 transients with repeat intervals of (a and b) 3, (c) 300 and (d) 30 s. In (b), cross polarisation from ^{1}H (1 ms spin lock) was employed, with a ramped spin-locking pulse (90-100%) applied to ^{1}H. TPPM-15 decoupling of ^{1}H (ν_1 ~100 kHz) was applied during acquisition. In (c), the spectrum was recorded using a spin-echo pulse sequence with a rotor-synchronised delay of 16.67 μs.

Figure 6.32. ^{1}H (14.1 T, 60 kHz DQMAS), NMR spectrum of GaPO-X[pyHF], recorded with signal averaging for 32 transients with a repeat interval of 4 s for each of 128 t_1 increments of 33.33 μs. DQCs were excited and converted using one rotor period of BABA pulses.

Figure 6.34. ^{31}P (14.1 T) NMR spectra of the solid product of attempted syntheses of GaPO-34[miHF] in which the Ga source was (a) Ga_2O_3 generated from old, hydrated $Ga(NO_3)_3$, (b) Ga_2O_3 generated from new, dry $Ga(NO_3)_3$ and (c) aqueous $Ga(NO_3)_3$ added directly to the reaction mix. Spectra were recorded with MAS rates of (a) 25, (b) 12.5 and (c) 14 kHz with signal averaging for (a) 16, (b) 8 and (c) 4 transients with repeat intervals of (a) 300, (b) 5 and (c) 20 s.

APPENDIX B. COMMON LINKERS IN MOFS

Table B.1 shows some of the linkers commonly used in the synthesis of MOFs, and their common abbreviations. The abbreviation is often used as a chemical entity, so that, for example, the terephthalate (benzene-1,4-dicarboxylate) linker is abbreviated to bdc, and terephthalic acid can be written as H_2bdc. In the case of dhtp, the linker may exist as the fully deporotonated-dhtp^{4-}, or the doubly-deprotonated H_2dhtp^{2-}.[1]

Table B.1. Some common linkers used in the synthesis of MOFs.

Linker	Abbreviation(s)	MOF(s)[a]	References
benzene-1,4-dicarboxylic acid (terephthalic acid) 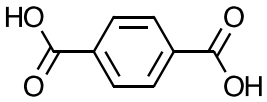	H_2bdc	MOF-5, MIL-53, MIL-101, Sc(bdc)	2-10
2-bromo terephthalic acid 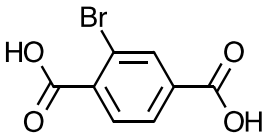	H_2Br-bdc	IRMOF-2, MIL-53(Fe)-Br	11, 12
2-amino terephthalic acid 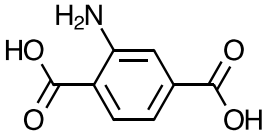	H_2NH_2-bdc, abdc	IRMOF-3, MIL-53(Fe)-NH_2, Sc(NH_2-bdc)	10-13
2-nitroterephthalic acid 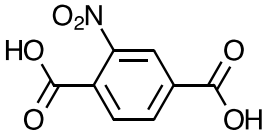	H_2NO_2-bdc	Sc(NO_2-bdc)	10
acetylene dicarboxylic acid 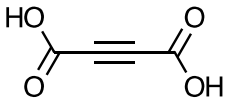	H_2adc	IRMOF-0	14

Linker	Abbreviation(s)	MOF(s)[a]	References
terphenyl dicarboxylic acid 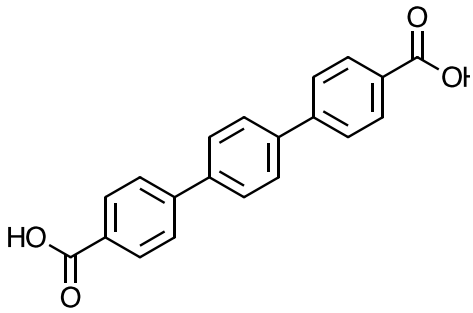	H_2tpdc	IRMOF-16	11
benzene-1,3,5-tricarboxylic acid (trimesic acid) 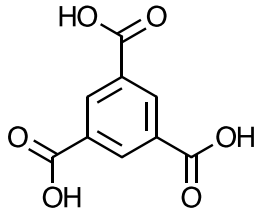	H_3btc	HKUST-1, MIL-100, Zn-btc	15-18
monomethyl trimesate 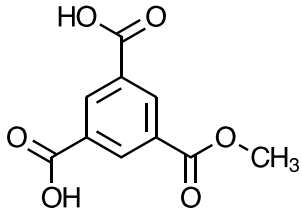	H_2mmbtc	STAM-1	19
dimethyl trimesate[b] 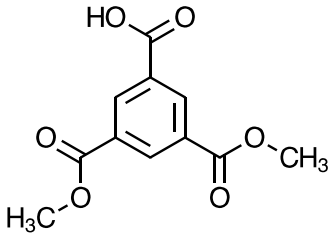	Hdmbtc	-	

Linker	Abbreviation(s)	MOF(s)[a]	References
trimethyl trimesate[b] 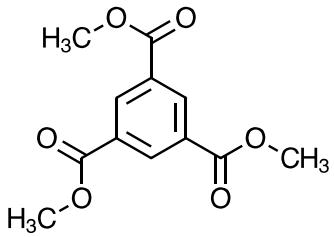	tmbtc	-	
2,5-dihydroxy terephthalic acid 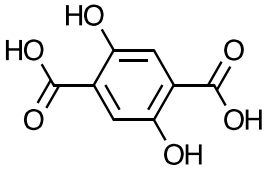	H_4dhtp	CPO-26, CPO-27, MIL-53(Fe)-$(OH)_2$	1, 12, 20
4-pyridin-4-ylbenzoic acid 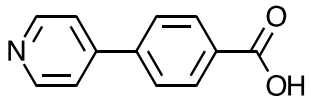	Hpba	$Ln_7(\mu_3$-$OH)_8(pba)_9(H_2O)_6\cdot 4ClO_4\cdot 3HL\cdot nH_2O$	21

a. MOFs given are examples, rather than an exhaustive list.

b. Hdmbtc and tmbtc cannot act as linkers in MOFs, but are included in this table for completeness.

REFERENCES

1. P. D. C. Dietzel, R. Blom and H. Fjellvåg, *Eur. J. Inorg. Chem.*, **2008**, 3624.

2. H. Li, M. Eddaoudi, T. L. Groy and O. M. Yaghi, *J. Am. Chem. Soc.*, **1998**, *120*, 8571.

3. Lebedev, O. I.; Millange, F.; Serre, C.; Van Tendeloo, G. and Férey, G. *Chem. Mater.*, **2005**, *17*, 6525.

4. C. Serre, F. Millange, C. Thouvenot, M. Nogues, G. Marsolier, D. Louer and G. Férey, *J. Am. Chem. Soc.*, **2002**, *124*, 13519.

5. G. Férey, M. Latroche, C. Serre, F. Millange, T. Loiseau and A. Percheron-Guegan, *Chem. Commun.*, **2003**, 2976.

6. S. R. Miller, P. A. Wright, C. Serre, T. Loiseau, J. Marrot and G. Férey, *Chem. Commun.*, **2005**, 3850.

7. F. Millange, G. Férey, M. Morcrette, C. Serre, M. L. Doublet, J. M. Greneche and J. M. Tarascon, *Proceedings of the 15th International Zeolite Conference*, **2007**, 170.

8. Anokhina, E. V.; Vougo-Zanda, M.; Wang, X. Q. and Jacobson, A. J. *J. Am.*

Chem. Soc., **2005**, *127*, 15000.
9. K. Barthelet, J. Marrot, D. Riou and G. Férey, *Angew. Chem. Int. Ed.*, **2001**, *41*, 281.
10. Mowat, J. P. S.; Miller, S. R.; Griffin, J. M.; Seymour, V. R.; Ashbrook, S. E.; Thompson, S. P.; Fairen-Jimenez, D.; Banu, A. M.; Düren, T and Wright, P. A. *Inorg. Chem.*, **2011**, *50*, 10844.
11. M. Eddaoudi, J. Kim, N. Rosi, D. Vodak, J. Wachter, M. O'Keeffe and O. M. Yaghi, *Science*, **2002**, *295*, 469.
12. T. Devic, P. Horcajada, C. Serre, F. Salles, G. Maurin, B. Moulin, D. Heurtaux, G. Clet, A. Vimont, J.-M. Greneche, B. Le Ouay, F. Moreau, E. Magnier, Y. Filinchuk, J. Marrot, J.-C. Lavalley, M. Daturi and G. Férey, *J. Am. Chem. Soc.*, 2010, **132**, 1127.
13. Couck, S.; Denayer, J. F.M.; Baron, G. V.; Remy, T.; Gascon, J. and Kapteijn, F. *J. Am. Chem. Soc.*, **2009**, *131*, 6326.
14. D. J. Tranchemontagne, J. R. Hunt and O. M. Yaghi, *Tetrahedron*, **2008**, *64*, 8553.
15. S. S. Y. Chui, S. M. F. Lo, J. P. H. Charmant, A. G. Orpen and I. D. Williams, *Science*, **1999**, *283*, 1148.
16. P. Horcajada, S. Surble, C. Serre, D.-Y. Hong, Y.-K. Seo, J.-S. Chang, J.-M. Greneche, I. Margiolaki and G. Férey, *Chem. Commun.*, **2007**, 2820.
17. Cendak, T.; Čelič, T. B.; Rangus, M.; Logar, N. Z.; Mali, G. and Kaučič, V. *7th Alpine Conference on Solid-State NMR*, Chamonix-Mont Blanc, France, **2011**.
18. Čelič, T. B.; Mazaj, M.; Guillou, N.; Kaučič, V. and Logar, N. Z. *3rd Croatian-Slovenan Symposium on Zeolites*, Zagreb, Croatia, **2010**.
19. M. I. H. Mohideen, B. Xiao, P. S. Wheatley, A. C. McKinlay, Y. Li, A. M. Z. Slawin, D. W. Aldous, N. F. Cessford, T. Dueren, X. Zhao, R. Gill, K. M. Thomas, J. M. Griffin, S. E. Ashbrook and R. E. Morris, *Nature Chem.*, **2011**, *3*, 304.
20. P. D. C. Dietzel, Y. Morita, R. Blom and H. Fjellvag, *Angew. Chem. Int. Ed.*, **2005**, *44*, 6354.
21. W.-H. Fang, L. Cheng, L. Huang and G.-Y. Yang, *Inorg. Chem.*, **2013**, *52*, 6.

APPENDIX C. MATRIX REPRESENTATIONS OF I_X, I_Y AND I_Z OPERATORS

Spin $I = 1/2$

$$I_x = \frac{1}{2}\begin{pmatrix} 0 & 1 \\ 1 & 0 \end{pmatrix} \qquad I_y = \frac{i}{2}\begin{pmatrix} 0 & -1 \\ 1 & 0 \end{pmatrix} \qquad I_z = \frac{1}{2}\begin{pmatrix} 1 & 0 \\ 0 & -1 \end{pmatrix}$$

Spin $I = 1$

$$I_x = \frac{1}{\sqrt{2}}\begin{pmatrix} 0 & 1 & 0 \\ 1 & 0 & 1 \\ 0 & 1 & 0 \end{pmatrix} \quad I_y = \frac{i}{\sqrt{2}}\begin{pmatrix} 0 & -1 & 0 \\ 1 & 0 & -1 \\ 0 & 1 & 0 \end{pmatrix} \quad I_z = \begin{pmatrix} 1 & 0 & 0 \\ 0 & 0 & 0 \\ 0 & 0 & -1 \end{pmatrix}$$

Spin $I = 3/2$

$$I_x = \frac{1}{2}\begin{pmatrix} 0 & \sqrt{3} & 0 & 0 \\ \sqrt{3} & 0 & 2 & 0 \\ 0 & 2 & 0 & \sqrt{3} \\ 0 & 0 & \sqrt{3} & 0 \end{pmatrix} \quad I_y = \frac{i}{2}\begin{pmatrix} 0 & -\sqrt{3} & 0 & 0 \\ \sqrt{3} & 0 & -2 & 0 \\ 0 & 2 & 0 & -\sqrt{3} \\ 0 & 0 & \sqrt{3} & 0 \end{pmatrix} \quad I_z = \frac{1}{2}\begin{pmatrix} 3 & 0 & 0 & 0 \\ 0 & 1 & 0 & 0 \\ 0 & 0 & 1 & 0 \\ 0 & 0 & 0 & 3 \end{pmatrix}$$

Spin $I = 5/2$

$$I_x = \frac{1}{2}\begin{pmatrix} 0 & \sqrt{5} & 0 & 0 & 0 & 0 \\ \sqrt{5} & 0 & \sqrt{8} & 0 & 0 & 0 \\ 0 & \sqrt{8} & 0 & 3 & 0 & 0 \\ 0 & 0 & 3 & 0 & \sqrt{8} & 0 \\ 0 & 0 & 0 & \sqrt{8} & 0 & \sqrt{5} \\ 0 & 0 & 0 & 0 & \sqrt{5} & 0 \end{pmatrix} \quad I_y = \frac{i}{2}\begin{pmatrix} 0 & -\sqrt{5} & 0 & 0 & 0 & 0 \\ \sqrt{5} & 0 & -\sqrt{8} & 0 & 0 & 0 \\ 0 & \sqrt{8} & 0 & -3 & 0 & 0 \\ 0 & 0 & 3 & 0 & -\sqrt{8} & 0 \\ 0 & 0 & 0 & \sqrt{8} & 0 & -\sqrt{5} \\ 0 & 0 & 0 & 0 & \sqrt{5} & 0 \end{pmatrix}$$

$$I_x = \frac{1}{2}\begin{pmatrix} 5 & 0 & 0 & 0 & 0 & 0 \\ 0 & 3 & 0 & 0 & 0 & 0 \\ 0 & 0 & 1 & 0 & 0 & 0 \\ 0 & 0 & 0 & -1 & 0 & 0 \\ 0 & 0 & 0 & 0 & -3 & 0 \\ 0 & 0 & 0 & 0 & 0 & -5 \end{pmatrix}$$

APPENDIX D. SELECTED PRIMARY AND SECONDARY CHEMICAL SHIFT REFERENCES

Table D.1. The chemical shifts (δ_{iso}) of the reference compounds used in this thesis.

Nucleus	Compound	δ_{iso} (ppm)
$^{1/2}$H	tetramethylsilane (TMS)	0.00
	L-alanine	8.5 (N**H**$_3$)
	$C_2O_4D_2.2D_2O$	16.5 ppm (CO_2**D**)
^{13}C	TMS	0.00
	L-alanine	20.5 (**C**H$_3$)
	β-glycine	175.3 (**C**O$_2$)
	$(CD_3)_2SO$	39.52
^{15}N	nitromethane	0.00[a]
	β-glycine	–347.4
^{19}F	$CFCl_3$	0.00
	poly(tetrafluoroethylene)	–122.7
^{23}Na	0.1 M $NaCl_{(aq)}$	0.00
	NaCl	7.8[b]
^{27}Al	1.1 M $Al(NO_3)_{3\ (aq)}$	0.00
	Aluminium tris(acetylacetonate)	0.00[c]
^{31}P	85 wt.% $H_3PO_{4\ (aq)}$	0.00
	BPO_4	–29.6[d]
$^{69/71}$Ga	1.1 M $Ga(NO_3)_{3\ (aq)}$	0.00
	$GaPO_4$ berlinite	111.2
^{87}Rb	0.01 M $RbCl_{\ (aq)}$	0.00
	$RbNO_3$	note e

a. Liquid NH_3 is also used as a common primary reference compound. To convert from the liquid NH_3 scale to the nitromethane scale, it is necessary to subtract 379.5 ppm.[2]

b. The negligible C_Q of ^{23}Na in NaCl allows for the approximation that the intensity maximum of the resonance occurs at the isotropic chemical shift.

c. Equivalent, but more practically relevant reference points are the left-hand horn (–1.1 ppm at 14.1 T) and the centre of gravity (–4.2 ppm at 9.4 T).

d. The shift for BPO_4 has also been reported as –31.2 ppm,[3] which can cause some confusion as the two reference scales are only separated by 1.6 ppm.

e. The isotropic shifts and quadrupolar coupling constants in $RbNO_3$ are temperature (*i.e.*, MAS-rate) dependent, as reported by Skibsted and Jakobsen.[3]

REFERENCES

1. S. P. Brown, M. Perez-Torralba, D. Sanz, R. M. Claramunt and L. Emsley, J. Am. Chem. Soc., **2002**, *124*, 1152.
2. K. J. D. MacKenzie and M. E. Smith, *Multinuclear Solid-State NMR of Inorganic Materials*, 1st edn., Elsevier Science Ltd, Oxford, UK, **2002**.
3. J. Skibsted and H. J. Jakobsen, *J. Phys. Chem. A*. **1999**, *103*, 7958.

APPENDIX E. COEFFICIENTS AND ROTATION MATRIX ELEMENTS FOR SECOND-ORDER QUADRUPOLAR PERTURBATION THEORY

The coefficients A^{l}_{I,m_I} are given in Table E.1.

Table E.1. The coefficients A^{l}_{I,m_I} for half-integer-spin nuclei.

I	m_I	A^{0}_{I,m_I}	A^{2}_{I,m_I}	A^{4}_{I,m_I}
3/2	$\pm$3/2	$\pm$6/5	0	$\mp$6/5
	$\pm$1/2	$\mp$2/5	$\mp$8/7	$\pm$54/35
5/2	$\pm$5/2	$\pm$20/3	$\pm$40/21	$\mp$60/7
	$\pm$3/2	$\mp$4/5	$\mp$40/7	$\pm$228/35
	$\pm$1/2	$\mp$16/15	$\mp$64/21	$\pm$144/35
7/2	$\pm$7/2	$\pm$98/5	$\pm$56/7	$\mp$996/35
	$\pm$5/2	$\pm$2	$\mp$80/7	$\pm$330/35
	$\pm$3/2	$\mp$54/15	$\mp$96/7	$\pm$606/35
	$\pm$1/2	$\mp$2	$\mp$40/7	$\pm$54/7
9/2	$\pm$9/2	$\pm$216/5	$\pm$144/7	$\mp$2332/35
	$\pm$7/2	$\pm$56/5	$\mp$16	$\pm$24/5
	$\pm$5/2	$\mp$4	$\mp$200/7	$\pm$228/7
	$\pm$3/2	$\mp$36/5	$\mp$24	$\pm$156/5
	$\pm$1/2	$\mp$16/5	$\mp$64/7	$\pm$432/35

The functions $B^0(\eta_Q)$, $B^2(\eta_Q, \alpha, \beta, \gamma)$ and $B^4(\eta_Q, \alpha, \beta, \gamma)$ are given by:

$$B^0(\eta_Q) = \left(1 + \frac{\eta_Q^2}{3}\right) , \tag{E.1}$$

$$B^2\left(\eta_Q, \alpha, \beta, \gamma\right) = \left(1 - \frac{\eta_Q^2}{3}\right) D^2_{0,0}(\alpha, \beta, \gamma)$$

$$- \frac{\sqrt{2}}{\sqrt{3}} \eta_Q \left(D^2_{0,2}(\alpha, \beta, \gamma) + D^2_{0,-2}(\alpha, \beta, \gamma)\right) , \tag{E.2}$$

$$B^4\left(\eta_Q, \alpha, \beta, \gamma\right) = \left(1 + \frac{\eta_Q^2}{18}\right) D^4_{0,0}(\alpha, \beta, \gamma)$$

$$+ \frac{\sqrt{10}}{6} \eta_Q \left(D^4_{0,2}(\alpha, \beta, \gamma) + D^4_{0,-2}(\alpha, \beta, \gamma)\right)$$

$$+ \frac{35}{18\sqrt{70}} \eta_Q^2 \left(D^4_{0,4}(\alpha, \beta, \gamma) + D^4_{0,-4}(\alpha, \beta, \gamma)\right) , \tag{E.3}$$

The Wigner rotation matrix elements, $D^l_{m,m'}(\alpha, \beta, \gamma)$, are defined as

$$D^l_{m,m'}(\alpha, \beta, \gamma) = d^l_{m,m'}(\beta) e^{-i\left(\alpha m' + \gamma m\right)} , \tag{E.4}$$

where the reduced Wigner rotation matrix elements, $d^l_{m,m'}(\beta)$, are given by

$$d^2_{0,0}(\beta) = \frac{1}{2}(3\cos^2\beta - 1) , \tag{E.5}$$

$$d^2_{0,2}(\beta) = \frac{\sqrt{3}}{\sqrt{8}} \sin^2\beta , \tag{E.6}$$

$$d^4_{0,0}(\beta) = \frac{1}{8}(35\cos^4\beta - 30\cos^2\beta + 3) , \tag{E.7}$$

$$d^4_{0,2}(\beta) = -\frac{\sqrt{10}}{128}(14\cos 4\beta - 8\cos 2\beta - 6) , \tag{E.8}$$

$$d^4_{0,4}(\beta) = \frac{\sqrt{70}}{128}(\cos 4\beta - 4\cos 2\beta + 3) . \tag{E.9}$$

The terms, $b^0(\eta_Q)$, $b^2(\eta_Q, \beta', \gamma')$ and $b^4(\eta_Q, \beta', \gamma')$, required to describe the second-order perturbation under magic angle spinning are

$$b^0(\eta_Q) = \left(1 + \frac{\eta_Q^2}{3}\right) , \tag{E.10}$$

$$b^2\left(\eta_Q, \beta', \gamma'\right) = \left(1 - \frac{\eta_Q^2}{3}\right) d^2_{0,0}(\beta', \gamma') - \frac{\sqrt{8}}{\sqrt{3}} \eta_Q d^2_{2,0}(\beta') \cos 2\gamma' , \tag{E.11}$$

$$b^4\left(\eta_Q, \beta', \gamma'\right) = \left(1 + \frac{\eta_Q^2}{18}\right) d^4_{0,0}(\beta') + \frac{\sqrt{10}}{3} \eta_Q d^4_{2,0}(\beta') \cos 2\gamma' + \frac{\sqrt{70}}{18} \eta_Q^2 d^4_{4,0}(\beta') \cos 4\gamma' . \tag{E.12}$$

APPENDIX F. IMPORTANT GRADIENTS FOR MQMAS EXPERIMENTS

Table F.1 lists the most relevant gradients in an unsheared MQMAS experiment. These are the direction of the fourth-rank second-order quadrupolar anisotropic broadening, R, (the isotropic dimension is perpendicular to this gradient), and gradients along which broadening arising from a distribution of chemical shifts or quadrupolar parameters appear ($dist_{CS}$ and $dist_Q$, respectively). Upon a shearing transformation, the sheared ω_1 position, ω_1', becomes

$$\omega_1' = \frac{1}{1+|R|}(\omega_1 - R\omega_2) \quad . \tag{F.1}$$

The gradients resulting from this transformation (or observed in a split-t_1 experiment[1]) are given in Table F.2.

Table F.1. Gradients for the isotropic dimension, R, distribution of chemical shift parameters ($dist_{CS}$), and distribution of quadrupolar parameters ($dist_Q$).

I	MQ transition	R	$dist_{CS}$	$dist_Q$
3/2	3Q	–7/9	3	–3
5/2	3Q	19/12	3	3/4
	5Q	–25/12	5	–25/4
7/2	3Q	101/45	3	9/5
	5Q	11/9	5	–1
	7Q	–161/45	7	–49/5
9/2	3Q	91/36	3	9/4
	5Q	95/36	5	5/4
	7Q	7/18	7	–7/2
	9Q	–31/6	9	–27/2

Table F.2. Gradients for the distribution of chemical shift parameters ($dist_{CS}$) and distribution of quadrupolar parameters ($dist_Q$) in a sheared z-filtered (or split-t_1) MQMAS spectrum.

I	MQ transition	$dist_{CS}$	$dist_Q$
3/2	3Q	17/8	–5/4
5/2	3Q	17/31	–10/31
	5Q	85/37	–50/37
7/2	3Q	17/73	–10/73
	5Q	17/10	–1
	7Q	238/103	140/103
9/2	3Q	17/127	–10/127
	5Q	85/131	–50/131
	7Q	119/25	–14/5
	9Q	85/37	–50/37

REFERENCES

1. S. P. Brown and S. Wimperis, *J. Magn. Reson.*, **1997**, *124*, 279.

APPENDIX G. POSITION OF THE CENTRE OF GRAVITY OF RESONANCES IN MQMAS SPECTRA

Table G.1 gives the δ_1 and δ_2 coordinates of the centre of gravity of the resonances in non-sheared or sheared MQMAS spectra, as a function of the isotropic chemical shift, δ_{iso} and the isotropic quadrupolar shift, δ_Q.

Table G.1. Coordinates for the position of the centre of gravity of a resonance in a MQMAS experiment as a function of isotropic chemical shift, δ_{iso}, and isotropic quadrupolar shift, δ_Q.

I	MQ transition		non-sheared z-filtered experiment	sheared z-filtered or split-t_1 experiment
3/2	3Q	δ_1	$3\delta_{iso} + (6/5)\delta_Q$	$(17/8)\delta_{iso} + (1/2)\delta_Q$
		δ_2	$\delta_{iso} - (2/5)\delta_Q$	$\delta_{iso} - (2/5)\delta_Q$
5/2	3Q	δ_1	$3\delta_{iso} - (4/5)\delta_Q$	$(17/31)\delta_{iso} + (32/93)\delta_Q$
		δ_2	$\delta_{iso} - (16/15)\delta_Q$	$\delta_{iso} - (16/15)\delta_Q$
	5Q	δ_1	$5\delta_{iso} + (20/3)\delta_Q$	$(85/37)\delta_{iso} + (160/111)\delta_Q$
		δ_2	$\delta_{iso} - (16/15)\delta_Q$	$\delta_{iso} - (16/15)\delta_Q$
7/2	3Q	δ_1	$3\delta_{iso} - (54/15)\delta_Q$	$(17/73)\delta_{iso} + (20/73)\delta_Q$
		δ_2	$\delta_{iso} - 2\delta_Q$	$\delta_{iso} - 2\delta_Q$
	5Q	δ_1	$5\delta_{iso} + 2\delta_Q$	$(17/10)\delta_{iso} + 2\delta_Q$
		δ_2	$3\delta_{iso} - 2\delta_Q$	$\delta_{iso} - 2\delta_Q$
	7Q	δ_1	$7\delta_{iso} - (98/5)\delta_Q$	$(238/103)\delta_{iso} + (280/103)\delta_Q$
		δ_2	$\delta_{iso} - 2\delta_Q$	$\delta_{iso} - 2\delta_Q$

APPENDIX H. POWDER XRD PATTERNS FOR CPO-27

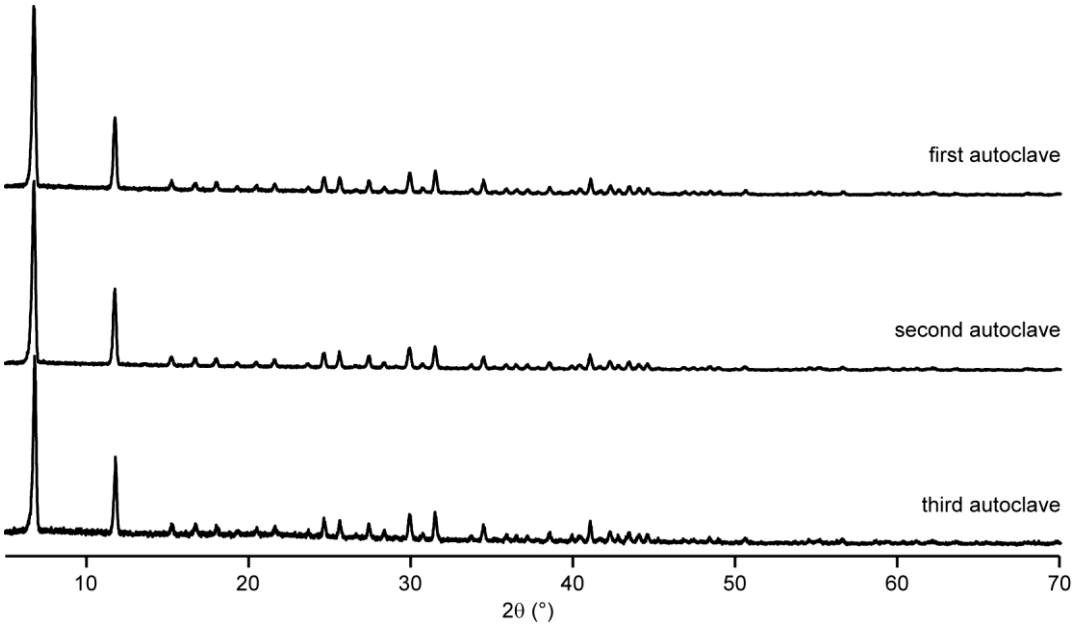

Figure H.1. Powder XRD patterns of the three samples of CPO-27-Mg prepared for this work.

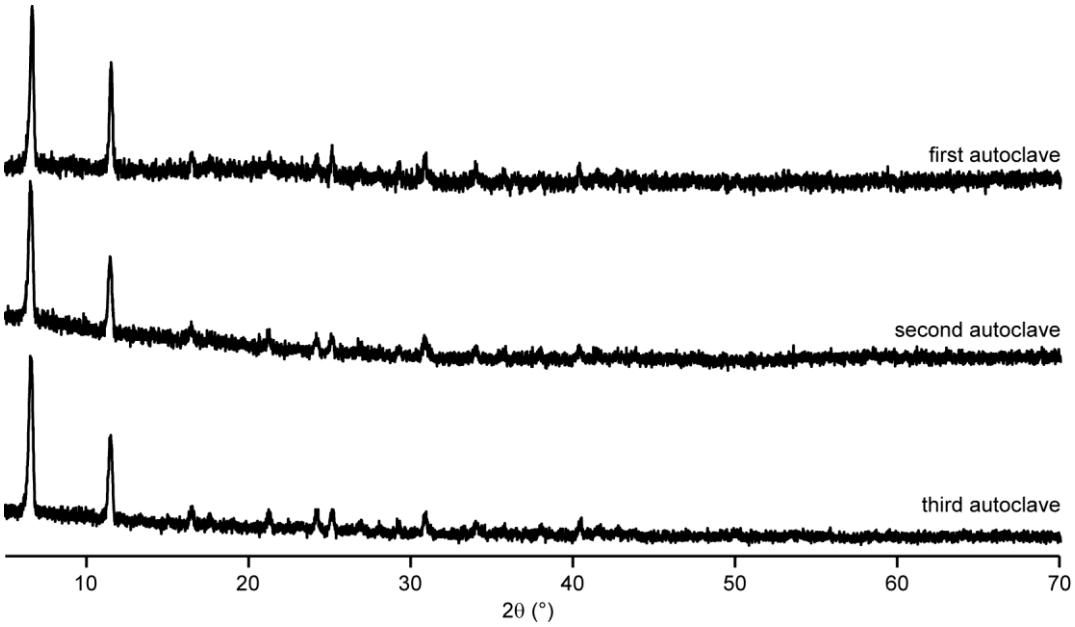

Figure H.2. Powder XRD patterns of the three samples of CPO-27-Mn prepared for this work.

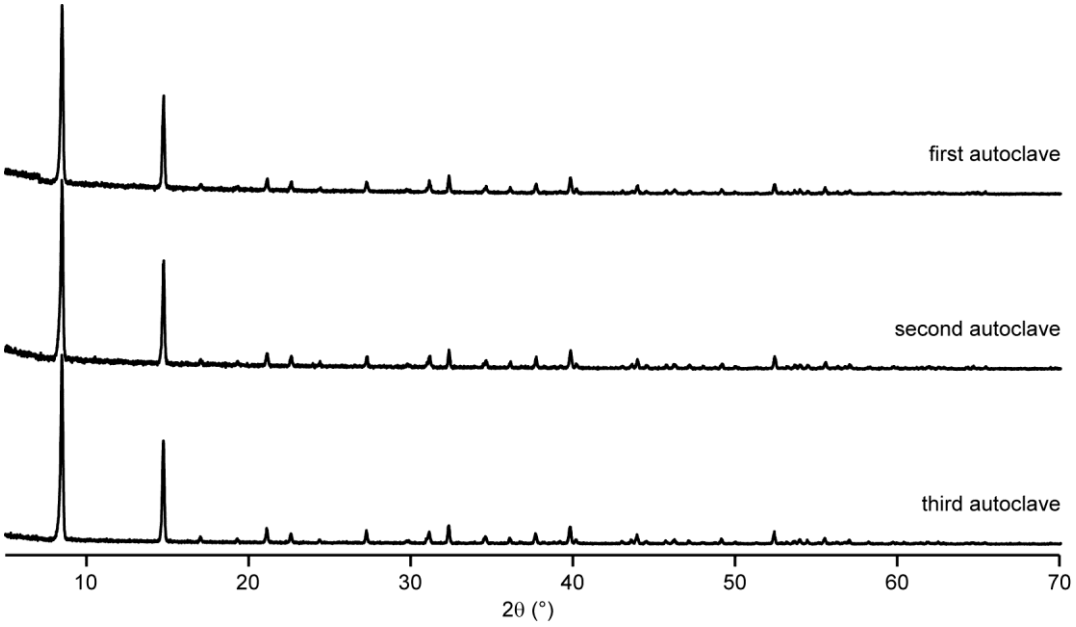

Figure H.3. Powder XRD patterns of the three samples of CPO-27-Co prepared for this work.

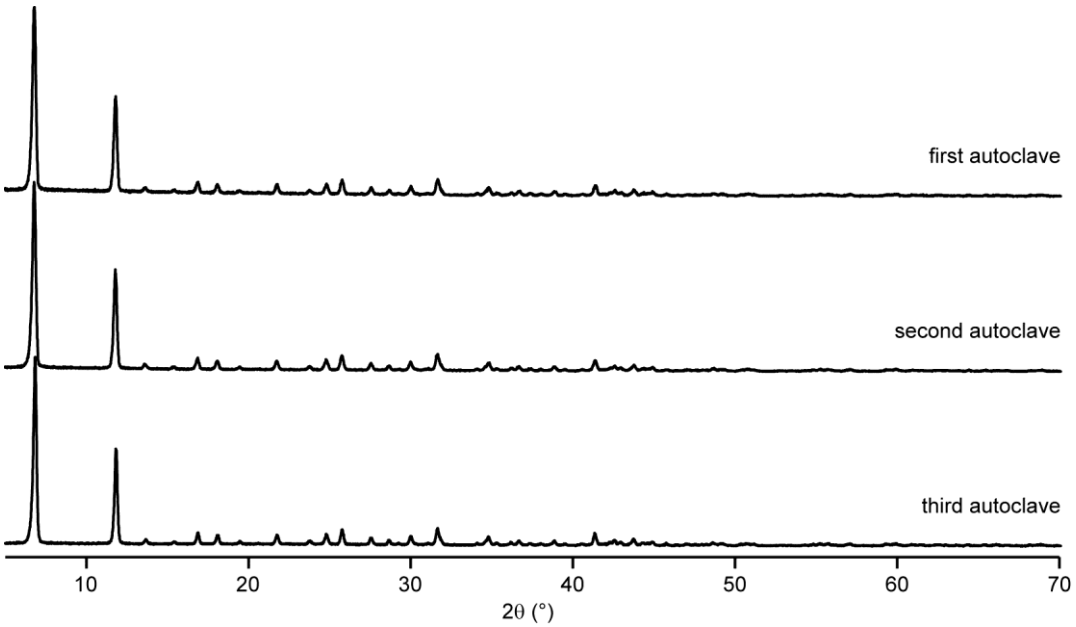

Figure H.4. Powder XRD patterns of the three samples of CPO-27-Ni prepared for this work.

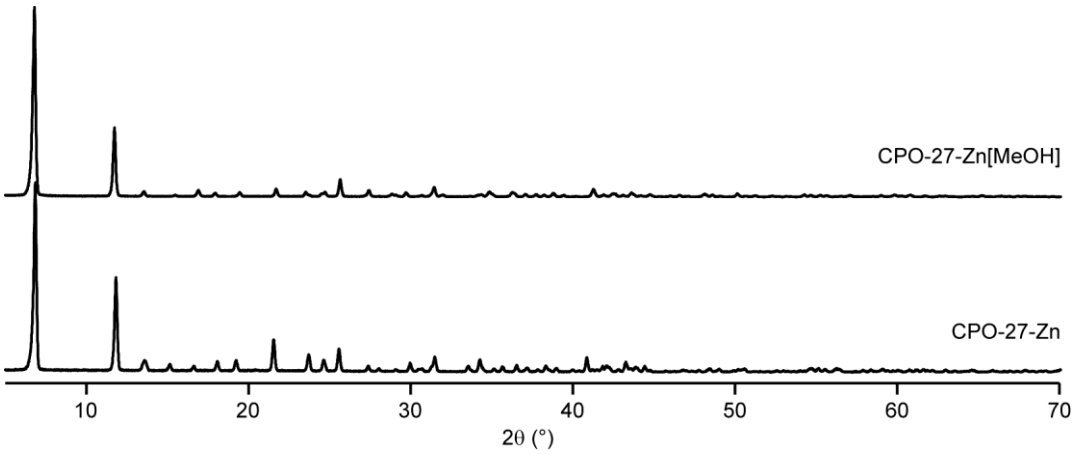

Figure H.5. Powder XRD patterns of the CPO-27-Zn and CPO-27-Zn[MeOH] prepared for this work.

APPENDIX I. FURTHER DETAIL OF SOLUTION-PHASE NMR SPECTRA

1[^{13}C],3,5-Trimethylbenzene ^{1}H NMR (7.05 T, $CDCl_3$) δ (ppm): 6.96 (m, 1H C**H**), 2.43 (t+dt (2H+1H), $^{4}J_{HH}$ = 0.4 Hz, $^{1}J_{HC}$ = 126.1 Hz, C**H**$_3$). ^{13}C NMR 138.2 (d+d $^{2}J_{CC}$ = 43.9 Hz, $^{4}J_{CC}$ = 4.0 Hz, quat. **C**), 127.5 (d+d, $^{3}J_{CC}$ = 3.2 Hz, $^{5}J_{CC}$ = 0.9 Hz, **C**H), 21.7 (s, **C**H_3).

Benzene-1[^{13}C],3,5-tricarboxylic acid ^{1}H NMR (7.05 T, $(CD_3)_2SO$) δ (ppm): 8.6 (s+d $^{3}J_{HC}$ = 2.9 Hz ($^{4}J_{HH}$,$^{5}J_{HC}$ < 1.0 Hz) C**H**). ^{13}C NMR: 168.4 (s, **C**O_2H), 134.4 (d+d, $^{1}J_{CC}$ = 70.0, $^{3}J_{CC}$ = 3.6 Hz quat. **C**), 134.7 (s ($^{2}J_{CC}$, $^{4}J_{CC}$<1 Hz), **C**H).

1,3,5-triethyl-[U ^{13}C]benzene ^{1}H NMR (7.05 T, $CDCl_3$) δ (ppm): 6.92 (m 1H C**H**). 2.66 (q $^{2}J_{HH}$ = 7.6 Hz 3H C**H**$_2$). 1.29 (q $^{2}J_{HH}$ = 7.6 Hz 4H C**H**$_3$). ^{13}C NMR: 144.6 (td, $^{1}J_{CC}$ = 57.2 Hz, $^{4}J_{CC}$ = 7.5 Hz) quat. **C**), 125.2 (td, $^{1}J_{CC}$ = 57.2, $^{3}J_{CC}$ = 7.5 Hz **C**H), 29.3 (s, **C**H_2), 16.1 (s, **C**H_3).

[U-^{13}C]benzene-1,3,5-tricarboxylic acid ^{1}H NMR (7.05 T, $(CD_3)_2SO$) δ (ppm): 8.64 (s C**H**). ^{13}C NMR: 165.8 (s **C**O_2H), 125-135 (m+m **C**H and quat. **C**).

Trimethyl benzene-1,3,5-tricarboxylate ^{13}C NMR (7.05 T, $(CD_3)_2SO$) δ (ppm): 164.5 (s, **C**O_2CH_3), 133.4 (s, **C**H), 130.9 (s, quat. **C**), 52.8 (s, **C**H_3).

Disodium methyl benzene-1,3,5-tricarboxylate ^{1}H NMR (7.05 T, $(CD_3)_2SO$) δ (ppm): 8.60 (t, 1H $^{4}J_{HH}$ = 1.6 Hz, **H3**), 8.41 (d, 2H, $^{4}J_{HH}$ = 1.6 Hz, **H4**), 3.85 (s, 3H **H7**).

Disodium 1′-methyl benzene-1[^{13}C],3,5-tricarboxylate and disodium 1′-methyl benzene-1,3[^{13}C],5-tricarboxylate ^{1}H NMR (7.05 T, D_2O) δ (ppm): 8.41 (d+dd, 2H, $^{4}J_{HH}$ = 1.6 Hz, $^{3}J_{HC}$ ≈ 3.4 Hz, **H4**). 8.36 (m, 1H, **H3**). 3.83 (s+d, 3H $^{3}J_{HC}$ ≈ 3.6 Hz **H7**).

Disodium 1′-methyl [U-^{13}C]benzene-1,3,5-tricarboxylate ^{1}H NMR (7.05 T, D_2O) δ (ppm): 8.42 (d, 2H, $^{4}J_{HH}$ = 1.7 Hz, **H4**). 8.36 (t, 1H, $^{4}J_{HH}$ = 1.7 Hz **H3**). 3.83 (s, 3H, **H7**).

APPENDIX J. RANDOMLY-GENERATED BOND LENGTHS AND ANGLES

All random numbers were generated using the RANDBETWEEN() function in Microsoft Excel, with the lower and upper limits (determined by studying the ranges of parameters in the literature) reported in Table J.1. Table J.2 shows the random $\theta_{POAl(i)}$ used in series 8 of the investigation into the effects of $\bar{\theta}_{POAl}$on the calculated ^{31}P σ_{iso}. Table J.3 shows the random $r_{PO(i)}$ used in series 13 of the investigation into the effects of $\bar{r}_{PO}$ on the calculated ^{31}P σ_{iso}. Table J.4 shows the random $\theta_{AlOP(i)}$ used in series 21 of the investigation into the effects of $\bar{\theta}_{AlOP}$ on the calculated ^{27}Al NMR parameters. Table J.5 shows the random r_{AlO} used in series 26 of the investigation into the effects of $\bar{r}_{AlOP}$ on the calculated ^{27}Al NMR parameters.

Table J.1. The upper and lower limits used in the random generation of the given structural parameters.

	θ_{POAl}	r_{PO}	θ_{AlOP}	r_{AlO}
upper limit	175°	1.58 Å	175°	1.82 Å
lower limit	115°	1.45 Å	115°	1.68 Å

Table J.2. The random $\theta_{POAl(i)}$ used in series 8 of the investigation into the effects of $\bar{\theta}_{POAl}$on the calculated ^{31}P σ_{iso}.

cluster	$\theta_{POAl(1)}$ (°)	$\theta_{POAl(2)}$ (°)	$\theta_{POAl(3)}$ (°)	$\theta_{POAl(4)}$ (°)
1[a]	131.52	136.68	137.15	158.65
2	128.19	137.04	135.31	163.96
3	136.01	116.83	127.20	138.75
4	127.16	133.98	164.98	164.48
5	155.43	150.19	163.96	133.23
6	130.13	163.28	119.68	137.44
7	130.50	162.64	132.08	163.46
8	153.35	126.86	163.97	137.84
9	122.87	148.97	167.41	151.90
10	128.17	129.46	119.85	140.48
11	154.50	157.42	130.28	121.45
12	147.54	136.77	132.28	162.12
13	124.46	121.48	159.87	140.74
14	115.62	156.96	160.63	120.29
15	134.11	119.70	117.33	116.59
16	146.11	127.33	148.03	115.58
17	127.70	145.55	132.42	123.83
18	164.08	127.73	132.13	134.30
19	159.18	139.99	129.75	157.02
20	129.96	144.71	117.13	125.17

a. The wavefunction for this cluster could not be minimised to a ground state and the results from this calculation are not included in the analysis.

Table J.3. The random $r_{PO(i)}$ used in series 13 of the investigation into the effects of $\bar{r}_{PO}$ on the calculated ^{31}P σ_{iso}.

cluster	$r_{PO(1)}$ / Å	$r_{PO(2)}$ / Å	$r_{PO(3)}$ / Å	$r_{PO(4)}$ / Å
1	1.54	1.51	1.55	1.56
2	1.51	1.55	1.50	1.49
3	1.57	1.45	1.49	1.56
4	1.57	1.52	1.48	1.53
5	1.46	1.52	1.50	1.52
6	1.52	153	1.55	1.49
7	1.56	1.55	1.52	1.48
8	1.52	1.55	1.51	1.47
9	1.54	1.51	1.52	1.54
10	1.47	1.45	1.49	1.50
11	1.45	1.50	1.47	1.53
12	1.51	1.46	1.46	1.50
13	1.52	1.46	1.52	1.51
14	1.49	1.55	1.46	1.48
15	1.54	1.45	1.49	1.55
16	1.49	1.51	1.50	1.49
17	1.52	1.56	1.49	1.50
18	1.55	1.46	1.56	1.50
19	1.47	1.45	146	1.48
20	1.49	154	1.48	1.50

Table J.4. The random $\theta_{AlOP(i)}$ used in series 21 of the investigation into the effects of $\bar{\theta}_{AlOP}$on the calculated ^{27}Al NMR parameters.

cluster	$\theta_{AlOP(1)}$ (°)	$\theta_{AlOP(2)}$ (°)	$\theta_{AlOP(3)}$ (°)	$\theta_{AlOP(4)}$ (°)
1	149.3	141.3	152.0	133.7
2	153.5	138.4	153.0	124.9
3	157.9	142.2	161.8	149.3
4	163.7	135.7	165.3	147.0
5	167.7	129.9	146.1	134.4
6	151.5	125.1	159.2	132.0
7	165.2	139.5	164.6	125.5
8	154.1	145.4	164.1	154.1
9	168.5	151.4	157.5	142.2
10	161.6	124.1	150.6	131.9
11	163.2	129.9	163.2	129.4
12	163.1	125.0	158.9	152.2
13	162.3	129.7	167.1	153.3
14	163.4	133.3	158.0	126.6
15	144.4	133.8	153.7	145.4
16	163.3	142.5	168.8	126.9
17	165.6	131.9	153.4	145.6
18	161.4	150.9	156.4	137.9
19	162.9	153.0	160.2	124.4
20	164.6	135.1	153.8	144.7

Table J.5. The random $r_{AlO(i)}$ used in series 26 of the investigation into the effects of $\bar{r}_{AlO}$ on the calculated ^{27}Al NMR parameters.

cluster	$r_{AlO(1)}$ / Å	$r_{AlO(2)}$ / Å	$r_{AlO(3)}$ / Å	$r_{AlO(4)}$ / Å
1	1.80	1.78	1.76	1.76
2	1.73	1.71	1.69	1.76
3	1.79	1.79	1.75	1.71
4	1.72	1.75	1.80	1.78
5	1.80	1.70	1.78	1.77
6	1.68	1.70	1.81	1.73
7	1.68	1.76	1.79	1.71
8	1.80	1.75	1.80	1.81
9	1.71	1.77	1.68	1.79
10	1.71	1.79	1.72	1.70
11	1.69	1.69	1.78	1.79
12	1.79	1.79	1.73	1.79
13	1.73	1.77	1.70	1.78
14	1.81	1.70	1.72	1.73
15	1.75	1.77	1.80	1.71
16	1.76	1.72	1.71	1.72
17	1.80	1.82	1.73	1.70
18	1.78	1.69	1.72	1.69
19	1.72	1.76	1.78	1.72
20	1.69	1.77	1.69	1.76

APPENDIX K. STRUCTURES OF CALCINED ALPOS USED IN CHAPTER 5

Table K.1. Structures of calcined AlPOs used in Chapter 5.

AlPO	structure type	database entry	reference
AlPO-5	published	ICSD 82863	1
AlPO-5	published and optimised	ICSD 88566	2
AlPO-5	published	ICSD 91671	3
AlPO-5	published	ICSD 91673	3
AlPO-8	published	ICSD 74462	4
AlPO-11	published	ICSD 63664	5
AlPO-14	published and optimised	ICSD 97901	6
AlPO-18	published	ICSD 71435	7
AlPO-31	published	ICSD 72374	8
AlPO-34 (110 K)	published		9
AlPO-34 (160 K)	published		9
AlPO-34 (210 K)	published		9
AlPO-34 (260 K)	published		9
AlPO-34 (310 K)	published		9
AlPO-34 (360 K)	published		9
AlPO-34 (410 K)	published		9
AlPO-34 (460 K)	published		9
AlPO-36	published and optimised	ICSD 67498	10
AlPO-41	published and optimised	ICSD 75906	11
AlPO-52	published	CrystMet 487056	12
AlPO-53(B)	published and optimised	ICSD 91679	13
AlPO-53(C)	published and optimised	ICSD 91681	13
AlPO-C	published	ICSD 69357	14
AlPO-D	published and optimised	ICSD 69358	14
AlPO-ZON	published	ICSD 98365	15
$AlPO_4$ berlinite	published and optimised	ICSD 9641	16
$AlPO_4$ crystobalite	published and optimised	ICSD 16651	17
STA-15	published	ICSD 166897	18
STA-2	optimised only[a]	CSD PAQJUM	19
$AlPO_4$ tridymite	optimised only[b]	ICSD 279582	20
UiO-12-500	published	ICSD 91682	21
VPI-5	published and optimised	ICSD 67593	22

a. The published structure of STA-2 is for the as-prepared materials. The SDA and HO^- anions were removed from the published structure prior to optimisation.

b. The published structure of tridymite contained unrealistic averaged Al-O-P bond angles of 180°, which made it impossible to calculate some of the distortion parameters investigated. Therefore, only the optimised structure was included in this study.

REFERENCES

1. A. J. Mora, A. N. Fitch, M. Cole, R. Goyal, R. H. Jones, H. Jobic and S. W. Carr, *J. Mater. Chem.*, **1996**, *6*, 1831.

2. T. Ikeda, K. Miyazawa, F. Izumi, Q. Huang and A. Santoro, *J. Phys. Chem. Solids*, **1999**, *60*, 1531.

3. G. J. Klap, H. van Koningsveld, H. Graafsma and A. M. M. Schreurs, *Micropor. Mesopor. Mater*., **2000**, *38*, 403.

4. D. M. Poojary and A. Clearfield, *Mater. Chem. Phys.*, **1993**, *35*, 301.

5. J. W. Richardson, J. J. Pluth and J. V. Smith, *Acta Crystallogr.*, **1988**, *B44*, 367.

6. R. W. Broach, S. T. Wilson and R. M. Kirchner, *Micropor. Mesopor. Mater.*, **2003**, *57*, 211.

7. A. Simmen, L. B. McKusker, C. Baerlocher and W. M. Meier, *Zeolites*, **1991**, *11*, 654.

8. J. M. Bennett and R. M. Kirchner, *Zeolites*, **1992**, *12*, 338.

9. M. Amri and R. I. Walton, *Chem. Mater*., **2009**, *21*, 3380.

10. P. A. Wright, S. Natarajan, J. M. Thomas, R. G. Bell, P. L. Gai-Boyes, R. H. Jones and J. Chen, *Angew. Chem. Int. Ed.* **1992**, *31*, 1472.

11. R. M. Kirchner and J. M. Bennett, *Zeolites*, **1994**, *14*, 523.

12. N. K. McGuire, C. A. Bateman, C. S. Blackwell, S. T. Wilson and R. M. Kirchner, *Zeolites*, **1995**, *15*, 460.

13. R. M. Kirchner, R. W. Grosse-Kunstleve, J. J. Pluth, S. T. Wilson, R. W. Broach and J. V. Smith, *Micropor. Mesopor. Mater.*, **2000**, *39*, 319.

14. E. B. Keller, W. M. Meier and R. M. Kirchner, *Solid State Ionics*, **1990**, *43*, 93.

15. M. Roux, C. Marichal, J. M. le Meins, C. Baerlocher and J. M. Chezeau, *Micropor. Mesopor. Mater.*, 2003, *63*, 163.

16. H. N. Ng and C. Calvo, *Can. J. Phys.*, **1976**, *54*, 638.

17. R. C. L. Mooney, *Acta Crystallogr.*, **1956**, *9*, 728.

18. Z. Han, A. L. Picone, A. M. Z. Slawin, V. R. Seymour, S. E. Ashbrook, W. Zhou, S. P. Thompson, J. E. Parker and P. A. Wright, *Chem. Mater.*, **2010**, *22*, 338.

19. G. W. Noble, P. A. Wright and A. Kvick, *Dalton Tansact.*, **1997**, *23*, 4485.

20. H. A. Graetsch, *Acta Crystallogr.*, **2001**, *C57*, 665.

21. K. O. Kongshaug, H. Fjellvåg, B. Klewe and K. P. Lillerud, *Micropor. Mesopor. Mater.*, **2000**, *39*, 333.

22. D. M. Poojary, J. O Perez and A. Clearfield, *J. Phys. Chem.*, **1992**, *96*, 7709

APPENDIX L. DESCRIPTION OF LINEAR REGRESSION PROCEDURES

The multivariate linear regression in Chapter 5 was carried out using the generalised linear model regression function of MATLAB. This function is called using the syntax "`model = glmfit(pred,resp)`" where `pred` is a (n × m) matrix of predictor variables (*i.e.*, the structural parameters, where each row represents a different site in the structure and each column represents a different structural parameter) and `resp` is the (n × 1) matrix of response variables (*i.e.*, the NMR parameter for the corresponding site). The result, `model`, is a (1 × m+1) matrix containing approximate coefficients for a linear regression of `resp` on `pred`. The `glmfit` function assumes that all parameters in `pred` are relevant to the values in `resp`, meaning that testing the relevance of a given structural parameter on `resp` is not possible without tedious manual alteration of the datasets to include or exclude the variable of interest, and comparison of the results. This process can be automated using the sequential feature selection function, `sequentialfs`, as in the MATLAB routine, dmd_sfs.m, included in the electronic information accompanying this thesis. The `sequentialfs` function, as used here, starts with an empty predictor matrix, and will add one column of `pred`, recalculate the linear regression coefficients (using `glmfit`) and determine whether the improvement in the model is statistically significant or not. If the improvement is significant, then the column is retained but, if not, the column is removed again and the routine proceeds to the next column. To allow easy determination of which columns from `pred` have been retained and ignored, `dmd_sfs` outputs both the model including only the retained columns, (termed `bft`) and a (1 × m+1) matrix, termed `BFT`, containing the coefficients from `bft` in the column corresponding to the correct variable in `pred`, and zero in all other columns. It is this routine that is described in the main text as linear regression with feature selection (LRFS).

APPENDIX M. FURTHER INFORMATION ON THE FORMAT OF DISCO INPUT AND OUTPUT

Table M.1. Keywords understood by DISCO.

Keyword	Description
`+`	denotes a comment line

`atoms_list_fract`	Starts a list of fractional coordinates, in the format
	`Al  0.4660  0.0000  0.3333`
	`Al  0.0000  0.4660  0.6667`
	where X is the atom type (Al, P and O are currently the only accepted atoms types). The list must be terminated with `end_atoms_list_fract`.

`batch_job_list`	Starts a list of jobs to run, in the format
	`job1`
	`job2`
	`...`
	where job1.in, job2.in, *etc.* are the input files for the jobs. The list must be terminated with `end_batch_job_list`.

`cell_abc`	Specifies the unit cell lengths in Å.
`cell_abg`	Specifies the unit cell angles in degrees.
`efg_cutoff_radius`	Specifies the maximum separation (in Å) between two atoms where the EFG contribution is assumed to be non-negligible. If not specified, the default value is 60 Å.
`efg_model`	Specifies the model to use for atomic charges in the point-charge model calculations of the EFG. Can be `default` (pure ionic charges) or `brownshannon` (uses the Brown-Shannon model, discussed in the main text).
`end_atoms_list_fract`	Terminates the list started with `atoms_list_fract`.
`end_batch_job_list`	Terminates the list started with `batch_job_list`.
`max_r_alo`	Defines the maximum Al-O bond length, in Å. The default value is 1.80 Å and, if the value must be increased to avoid error messages, the structure is probably unrealistic.
`max_r_alp`	Defines the maximum NNN Al-P separation length, in Å.
`max_r_op`	Defines the maximum O-P bond length, in Å. The default value is 1.60 Å and if the value must be increased to avoid error messages, the structure is probably unrealistic.

DISCO outputs three files for each job; *.log, *.struct and *.nmr. In batch job mode, disco_batch.log is generated. The .log file reports the progress of the job, and contains the unit cell parameters, fractional and Cartesian atomic coordinates, and the principal components of $\mathbf{V}^{PC}$. For example, the (abridged) .log file of berlinite is

```
Job start: 14.52:14.194
End of atoms list reached

Finished reading input file. Last line:

Unit cell parameters:
Lengths: a =   4.943003 b =   4.943007 c =  10.948000
Angles:  a =  90.000030 b =  90.000070 g = 120.000000

Fractional coordinates of atoms:
Al   1 abc 0.466000 0.000000 0.333330
...full list of fractional coordinates...
P    3 abc 0.532500 0.532500 0.499997

Cartesian coordinates of atoms:
Al   1 xyz   2.303435  -0.000004   3.649297
...full list of Cartesian coordinates...
P    3 xyz   1.316067   2.279503   5.473967
Starting calculation of local distortions.

Local distortions completed with no errors.

Starting calculation of EFG tensors.
EFG components (V_xx, V_yy, V_zz):
EFG tensors calculated using Brown-Shannon charges
Al   1 efg    0.001836    0.031034   -0.032870 q =  1.6806
... q is the atomic charge used for that atom...
P    3 efg   -0.021838   -0.068450    0.090288 q =  1.8580
Job end: 14.52:14.306
```

The *.struct file reports the structural distortion parameters for each atom in the unit cell and the *.nmr file reports the predicted values of σ_{iso}, σ_{ii} and, where appropriate, C_Q or $|C_Q|$.

APPENDIX N. CALCULATED NMR PARAMETERS FOR MODELS OF GAPO-34[MIHF] WITH DIFFERENT ORIENTATIONS OF H_2O

Calculations were carried out using CASTEP 6 with the G06 SEDC scheme applied. Table N.1 reports the NMR parameters calculated for the two optimised structures of GaPO-34[miHF]. The initial fractional coordinates of the O atoms of the H_2O molecules were (0.9356, 0.5203, 0.4772) for model 1 and (0.0644, 0.4797, 0.5228) for model 2.

Table N.1. The calculated (after structural optimisation) ^{31}P and ^{71}Ga NMR parameters for the two different models for H_2O in GaPO-34[miHF].

Species	δ_{iso} (ppm)		C_Q / MHz		η_Q	
	model 1	model 2	model 1	model 2	model 1	model 2
P1	–12.23	–13.80				
P1′	–13.45	–12.63				
P2	–11.23	–11.55				
P2′	–11.05	–11.29				
P3	–0.12	–1.33				
P3′	–1.32	–0.09				
Ga1	–56.03	–49.03	–5.22	–5.78	0.62	0.25
Ga1′	–48.84	–56.51	–5.84	–5.21	0.24	0.62
Ga2	–101.53	–99.41	–2.48	6.18	0.99	0.49
Ga2′	–99.24	–102.19	5.88	2.81	0.45	0.94
Ga3	–113.65	–112.85	10.34	10.92	0.93	0.80
Ga3′	–113.81	–114.02	10.87	10.21	0.78	0.94